



**UNIVERSITÄT PADERBORN**  
*Die Universität der Informationsgesellschaft*

---

**N-heterocyclic carbene based iron and ruthenium  
photosensitizer with amine donors –  
A systematic study on spectroscopic differences**

---

Dissertation

zur Erlangung des akademischen Grades eines  
Doktors der Naturwissenschaften

Dr. rer. nat.

Universität Paderborn  
Fakultät für Naturwissenschaften  
Department Chemie – Anorganische Chemie

von

Yannik Vukadinovic

Paderborn 2020



Datum der Einreichung: 12.10.2020

Datum der mündlichen Prüfung: 04.12.2020

Erster Gutachter: Prof. Dr. Matthias Bauer

Zweiter Gutachter: PD Dr. Hans Egold

Die experimentellen Untersuchungen wurden im Zeitraum Oktober 2016 bis September 2020 unter Anleitung von Prof. Dr. Matthias Bauer im Department Chemie der Universität Paderborn durchgeführt.



---

*„Wenn ich heute nicht erfolgreich bin, greife ich morgen wieder an.“*

*Mary Somerville*

## Abstract

A main aspect in the research field of photocatalytic water splitting is the investigation and development of new systems for a more efficient use of solar power. Until today, most light harvesting systems (photosensitizer) are based on noble metal compounds, which are advantageous due to their wide range of applications. Nevertheless, they do have some drawbacks which shall be considered, like high costs or a minor environmental sustainability. For this reason, a multitude of transition metal-based complexes were developed to act as an ecological friendly alternative, but these reveal a lack of efficiency due to their photophysical disadvantages.

Within this doctoral thesis, the influence of a methodical variation of new C<sup>N</sup>C-ligands was investigated in terms of the spectroscopic properties from according photosensitizer. Therefore, amine-functionalized bis-NHC-pyridine-ligands were synthesized as well as analyzed in terms of their spectroscopic properties and compared to their unfunctionalized analogues.

Subsequently these ligands were used to prepare a systematic series of new homoleptic iron-NHC complexes, to investigate how the varied ligand nature influences the properties of the respective complexes. The obtained complex series was analyzed in detail using different methods to examine its qualification regarding the use in photocatalytic applications. For this reason, the absorption properties and the redox behavior were made a major priority.

To further understand the ligand influence, a congruent series of homoleptic ruthenium-NHC complexes was synthesized and examined for similar properties. A direct comparison of iron- and ruthenium-NHC complexes allows statements regarding the ligand influence independent of the metal center.

The obtained results display a theoretical usability of the investigated complex series for photocatalytic applications. Additionally, the complex systems show a couple of exceptional features, which allow continuative operations to allow further steps towards sustainable catalysis using iron complexes.

## Kurzzusammenfassung

Ein Hauptaspekt im Forschungsgebiet der photokatalytischen Wasserspaltung ist die Entwicklung neuer Systeme zur effizienteren Nutzung von Sonnenenergie. Bisher vorhandene Photosensibilisatorsysteme basieren hierbei vorrangig auf edelmetallbasierten Komplexen, welche jedoch in ihren Kosten und ihrer Umweltverträglichkeit nachteilig sind. Aus diesem Grund ist bereits eine Vielzahl an Alternativen unter der Nutzung von unedlen Metallen entwickelt worden, welche jedoch aufgrund ihrer Effektivität eine industrielle Nutzung noch nicht realisierbar machen.

Im Rahmen dieser Dissertation wurde untersucht, welchen Einfluss die systematische Variation neuer C<sup>N</sup>C-Liganden auf die spektroskopischen Eigenschaften entsprechender Photosensibilisatoren hat. Hierzu gelang es zunächst Amin-funktionalisierte Bis-NHC-Pyridin-Liganden zu synthetisieren und ihre spektroskopischen Eigenschaften, mit denen der entsprechenden unfunktionalisierten Liganden zu vergleichen.

Anschließend wurde mithilfe dieser Liganden eine systematische Reihe bisher unbekannter homoleptischer Eisenkomplexe synthetisiert, um den Einfluss der veränderten Beschaffenheit der Liganden auf die Eigenschaften der jeweiligen Komplexe zu untersuchen. Die erhaltene Komplexreihe wurde mittels verschiedener Methoden detailliert charakterisiert und auf ihre Eignung im Hinblick auf die photokatalytische Wasserspaltung geprüft. Hierzu wurden vor allem die Absorptionseigenschaften und das Redox-Verhalten ausführlich analysiert.

Um den Einfluss der Liganden weitergehend zu untersuchen, diente eine übereinstimmende Komplexreihe homoleptischer Rutheniumkomplexe, welche hergestellt und ebenfalls auf ihre Eigenschaften hin untersucht wurde. Mithilfe von Kreuzvergleichen mit der zusammengehörigen Eisenverbindung konnte der Einfluss der Liganden unabhängig vom Metallzentrum untersucht werden.

Die erhaltenen Ergebnisse zeigen eine prinzipielle Nutzbarkeit der Systeme für photokatalytische Prozesse. Zusätzlich zeigen die Komplexsysteme eine Reihe außergewöhnlicher Eigenschaften, die durch weiterführende Arbeiten ein weiterer Schritt in Richtung nachhaltiger Katalyse sein können.

## **Eidesstaatliche Erklärung**

Hiermit versichere ich, die vorliegende Arbeit selbständig angefertigt und keine anderen als die von mir angegebenen Hilfsmittel verwendet zu haben. Wörtliche und sinngemäße Zitate wurden als solche gekennzeichnet und die Genehmigungen zur Veröffentlichung der urheberrechtlich geschützten Publikationen wurden eingeholt.

Paderborn, 12.10.2020

---

Yannik Vukadinovic

## Danksagung

An dieser Stelle möchte ich allen Menschen danken, die mich bei der Durchführung der praktischen Arbeiten und der Anfertigung dieser Arbeit in irgendeiner Form unterstützt haben.

Besonders Danken möchte ich Herrn Prof. Dr. Matthias Bauer für das interessante Thema und die Betreuung während der Zeit. Außerdem möchte ich ihm für die fachlichen Diskussionen danken, bei denen er mir stets mit Vor- und Ratschlägen zur Seite stand.

Herrn PD Dr. Hans Egold danke ich für die Übernahme des Zweitgutachtens, sowie seiner durchgehenden Hilfsbereitschaft und Unterstützung bei der NMR-Analytik.

Des Weiteren möchte ich mich bei allen anderen bedanken, die an der Erstellung dieser Arbeit behilflich waren: Für die Einkristallstrukturanalyse - Dr. Ulrich Flörke sowie Dr. Roland Schoch. Für die Massenspektrometrischen Analysen - Dr. Heinz Weber und Rodica Knaup sowie Dr. Adam Neuba und Christiane Gloger, denen ebenfalls für die elektrochemischen Analysen beziehungsweise den Elementaranalysen zu danken ist. Für die Messungen der zahlreichen NMR-Untersuchungen gilt mein Dank Frau Karin Stolte.

Ayla Pöpcke aus dem Arbeitskreis von Prof. Dr. Lochbrunner der Universität Rostock, möchte ich an dieser Stelle für die Aufnahme und Durchführung der transienten Absorptionsmessungen danken.

Dr. Lukas Burkhardt und Dr. Patrick Müller möchte ich für die Durchführung der zahlreichen theoretischen Rechnungen danken.

Den Studenten die im Rahmen von Bachelor-, Masterarbeiten, Vertiefungspraktika, Projektstudien und SHK-Stellen experimentell an dieser Arbeit mitgearbeitet haben, namentlich: Rene Rodriguez, Garrit Wicker und Lorena Fritsch danke ich für die Unterstützung. Besonders möchte ich Frau Anabel Miletic danken die über mehrere Jahre im Rahmen von Vertiefungspraktikum, Bachelorarbeit, Projektstudium und mehreren SHK-Stellen an der Erstellung dieser Arbeit mitgearbeitet hat.

Meinen Arbeitskollegen\innen möchte ich für die Arbeitsatmosphäre während der Zeit danken. Ein besonderer Dank gilt: Steffen Schlicher, Dr. Patrick Müller, Pia Rehsies, Tanja Hirschhausen, Dr. Regina Meinhardt, Dr. Maike Tünnermann und Dr. Hatice Soyler. Die für einige interessante und amüsante Kaffeepausen sowie Dienstreisen gesorgt haben.

## Danksagung

---

Dr. Jochen Ortmeyer danke ich für die humorvolle aber auch äußerst lehrreiche Zeit als SHK, Abschlussarbeiter oder Praktikant, die ich im Labor mitarbeiten durfte.

Meinen Freunden, Dr. Patrik Berg, Marie-Theres Berg und Carsten Schmiegel danke ich für die Hilfe während der Erstellung dieser Arbeit, sei es durch fachliche Diskussionen oder auch fachfremden Unterhaltungen die als Ablenkung auch mal ganze Abende füllen konnten.

Zum Abschluss möchte ich mich bei meinen Eltern, meinem Bruder Cedric und meiner Freundin Verena bedanken, die mir während des gesamten Studiums und der Zeit der Promotion immer Geduld, Verständnis und Zuversicht entgegenbrachten.

---

## Table of Contents

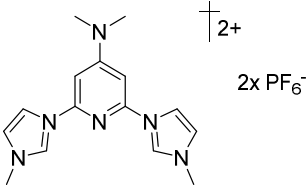
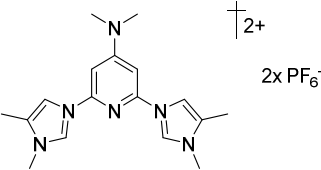
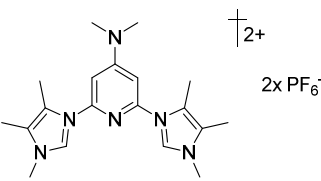
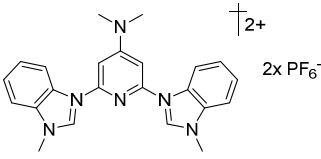
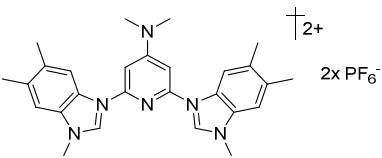
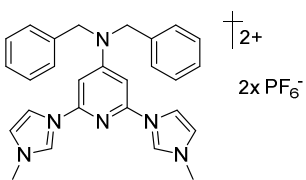
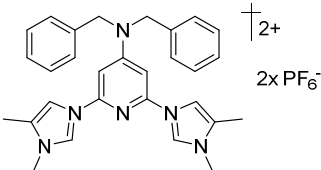
<b>1</b>	<b>Introduction</b> .....	<b>- 1 -</b>
1.1	Energy crisis .....	- 1 -
1.2	Renewable Hydrogen production .....	- 2 -
1.3	Photocatalytic water splitting .....	- 3 -
1.4	Photosensitizer .....	- 6 -
<b>2</b>	<b>Aim of work</b> .....	<b>- 20 -</b>
<b>3</b>	<b>New NHC-ligand systems</b> .....	<b>- 22 -</b>
3.1	Introduction and synthetic planning .....	- 22 -
3.2	Synthesis .....	- 23 -
3.3	Crystal structures .....	- 25 -
3.4	NMR-Spectroscopy .....	- 27 -
3.5	Spectroscopic properties.....	- 30 -
3.6	Redox properties.....	- 34 -
3.7	Chapter summary .....	- 35 -
<b>4</b>	<b>Homoleptic Fe(II) complexes</b> .....	<b>- 36 -</b>
4.1	Synthesis .....	- 36 -
4.2	Crystal structures .....	- 37 -
4.3	Spectroscopic properties.....	- 41 -
4.4	Cyclic voltammetry .....	- 51 -
4.5	Fe(III) complexes .....	- 57 -
4.6	pH dependency.....	- 59 -
4.7	X-Ray emission spectroscopy .....	- 63 -
4.8	Chapter summary .....	- 66 -

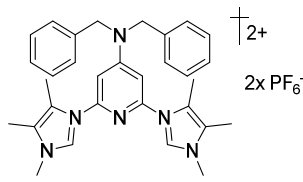
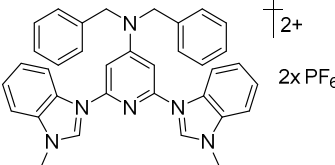
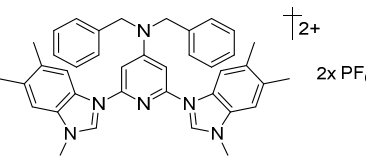
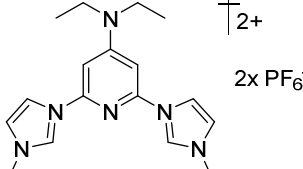
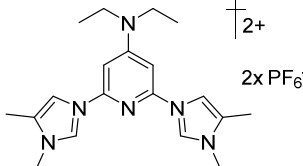
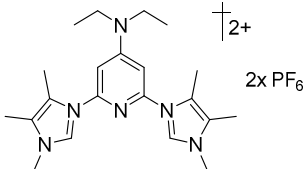
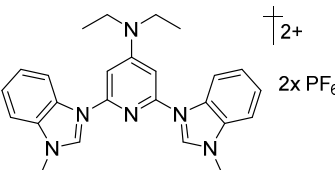
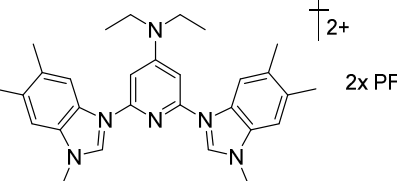
<b>5 Homoleptic Ru(II) Complexes</b> .....	<b>- 67 -</b>
5.1 Synthesis .....	- 67 -
5.2 Crystal structures .....	- 68 -
5.3 Spectroscopic properties .....	- 71 -
5.4 Cyclic voltammetry .....	- 80 -
5.5 Chapter summary.....	- 84 -
<b>6 Summary and Conclusion</b> .....	<b>- 86 -</b>
<b>7 Experimental Part</b> .....	<b>- 91 -</b>
7.1 General Information on equipment and chemicals.....	- 91 -
7.2 Annotations on the used analytical and spectroscopic methods .....	- 91 -
7.3 Precursor and Ligand synthesis .....	- 94 -
7.4 Synthesis of the tridentate C <sup>N</sup> C ligands.....	- 110 -
7.5 Synthesis of mononuclear iron(II) complexes .....	- 125 -
7.6 Synthesis of homoleptic mononuclear Ru(II) complexes .....	- 140 -
<b>References</b> .....	<b>- 155 -</b>
<b>List of figures</b> .....	<b>- 169 -</b>
<b>List of tables</b> .....	<b>- 172 -</b>
<b>Publications and Beamtimes</b> .....	<b>- 173 -</b>
<b>Publication permission</b> .....	<b>- 174 -</b>
<b>Appendix</b> .....	<b>- 175 -</b>

## List of abbreviations

arom.	Aromatic (NMR)
aliph.	Aliphatic (NMR)
av	Average
br	Broad (NMR, IR)
C <sub>carb</sub>	Carbene C-atom (NMR)
CV	Cyclic voltammetry
ddd, dd, d	(Double)-(double)-doublet (NMR)
DMF	N,N'-Dimethylformamide
DMSO	Dimethyl sulfoxide
ESI-MS	Electrospray-ionization mass spectrometry
EXAFS	Extended X-Ray absorption fine structure
HERFD	High energy resolution fluorescence detected
HOMO	Highest occupied molecular orbital
LMCT	Ligand to metal charge transfer
LUMO	Lowest unoccupied molecular orbital
m	Multiplet (NMR), middle (IR)
MeCN	Acetonitrile
MLCT	Metal to ligand charge transfer
NHE	normal hydrogen electrode
NHC	N-Heterocyclic carbene
NMR	Nuclear magnetic resonance
q	Quartet (NMR)
quint	Quintet (NMR)
s	Singulet (NMR), strong (IR)
sh	shoulder (UV/Vis)
dt, t	(Double)-Triplet (NMR)
w	weak (IR)
XANES	X-Ray absorption near edge structure

## Table of ligands

Denomination	Structure	Name (Abbreviation)
L1		N,N-Dimethyl-2,6-Bis(1-methylimidazole-3-yl)Pyridine-4-Amine  (BIP <sup>NMe2</sup> )
L2		N,N-Dimethyl-2,6-Bis(1,5-dimethylimidazole-3-yl)Pyridine-4-Amine  (BmiP <sup>NMe2</sup> )
L3		N,N-Dimethyl-2,6-Bis(1,4,5-Trimethylimidazole-3-yl)Pyridine-4-Amine  (BdmiP <sup>NMe2</sup> )
L4		N,N-Dimethyl-2,6-Bis(1-methylbenzimidazole-3-yl)Pyridine-4-Amine  (BbP <sup>NMe2</sup> )
L5		N,N-Dimethyl-2,6-Bis(1,5,6-trimethylbenzimidazole-3-yl)Pyridine-4-Amine  (BmbP <sup>NMe2</sup> )
L6		N,N-Dibenzyl-2,6-Bis(1-methylimidazole-3-yl)Pyridine-4-Amine  (BIP <sup>Benzyl</sup> )
L7		N,N-Dibenzyl-2,6-Bis(1,5-dimethylimidazole-3-yl)Pyridine-4-Amine  (BmiP <sup>Benzyl</sup> )

<b>L8</b>		<p>N,N-Dibenzyl-2,6-Bis(1,4,5-trimethylimidazole-3-yl)Pyridine-4-Amine</p> <p><b>(BdmiP<sup>BenzyI</sup>)</b></p>
<b>L9</b>		<p>N,N-Dibenzyl-2,6-Bis(1-methylbenzimidazole-3-yl)Pyridine-4-Amine</p> <p><b>(BbP<sup>BenzyI</sup>)</b></p>
<b>L10</b>		<p>N,N-Dibenzyl-2,6-Bis(1,5,6-trimethylbenzimidazole-3-yl)Pyridine-4-Amine</p> <p><b>(BmbP<sup>BenzyI</sup>)</b></p>
<b>L11</b>		<p>N,N-Diethyl-2,6-Bis(1-methylimidazole-3-yl)Pyridine-4-Amine</p> <p><b>(BIP<sup>NEt2</sup>)</b></p>
<b>L12</b>		<p>N,N-Diethyl-2,6-Bis(1,5-dimethylimidazole-3-yl)Pyridine-4-Amine</p> <p><b>(BmiP<sup>NEt2</sup>)</b></p>
<b>L13</b>		<p>N,N-Diethyl-2,6-Bis(1,4,5-trimethylimidazole-3-yl)Pyridine-4-Amine</p> <p><b>(BdmiP<sup>NEt2</sup>)</b></p>
<b>L14</b>		<p>N,N-Diethyl-2,6-Bis(1-methylbenzimidazole-3-yl)Pyridine-4-Amine</p> <p><b>(BbP<sup>NEt2</sup>)</b></p>
<b>L15</b>		<p>N,N-Diethyl-2,6-Bis(1,5,6-trimethylbenzimidazole-3-yl)Pyridine-4-Amine</p> <p><b>(BmbP<sup>NEt2</sup>)</b></p>

**List of complexes**

<b>C1</b>	$[\text{Fe}(\text{BIP}^{\text{NMe}_2})_2]^{2+} (2x \text{PF}_6^-)$	<b>C16</b>	$[\text{Ru}(\text{BIP}^{\text{NMe}_2})_2]^{2+} (2x \text{PF}_6^-)$
<b>C2</b>	$[\text{Fe}(\text{BmIP}^{\text{NMe}_2})_2]^{2+} (2x \text{PF}_6^-)$	<b>C17</b>	$[\text{Ru}(\text{BmIP}^{\text{NMe}_2})_2]^{2+} (2x \text{PF}_6^-)$
<b>C3</b>	$[\text{Fe}(\text{BdmIP}^{\text{NMe}_2})_2]^{2+} (2x \text{PF}_6^-)$	<b>C18</b>	$[\text{Ru}(\text{BdmIP}^{\text{NMe}_2})_2]^{2+} (2x \text{PF}_6^-)$
<b>C4</b>	$[\text{Fe}(\text{BbP}^{\text{NMe}_2})_2]^{2+} (2x \text{PF}_6^-)$	<b>C19</b>	$[\text{Ru}(\text{BbP}^{\text{NMe}_2})_2]^{2+} (2x \text{PF}_6^-)$
<b>C5</b>	$[\text{Fe}(\text{BmbP}^{\text{NMe}_2})_2]^{2+} (2x \text{PF}_6^-)$	<b>C20</b>	$[\text{Ru}(\text{BmbP}^{\text{NMe}_2})_2]^{2+} (2x \text{PF}_6^-)$
<b>C6</b>	$[\text{Fe}(\text{BIP}^{\text{NBn}_2})_2]^{2+} (2x \text{PF}_6^-)$	<b>C21</b>	$[\text{Ru}(\text{BIP}^{\text{NBn}_2})_2]^{2+} (2x \text{PF}_6^-)$
<b>C7</b>	$[\text{Fe}(\text{BmIP}^{\text{NBn}_2})_2]^{2+} (2x \text{PF}_6^-)$	<b>C22</b>	$[\text{Ru}(\text{BmIP}^{\text{NBn}_2})_2]^{2+} (2x \text{PF}_6^-)$
<b>C8</b>	$[\text{Fe}(\text{BdmIP}^{\text{NBn}_2})_2]^{2+} (2x \text{PF}_6^-)$	<b>C23</b>	$[\text{Ru}(\text{BdmIP}^{\text{NBn}_2})_2]^{2+} (2x \text{PF}_6^-)$
<b>C9</b>	$[\text{Fe}(\text{BbP}^{\text{NBn}_2})_2]^{2+} (2x \text{PF}_6^-)$	<b>C24</b>	$[\text{Ru}(\text{BbP}^{\text{NBn}_2})_2]^{2+} (2x \text{PF}_6^-)$
<b>C10</b>	$[\text{Fe}(\text{BmbP}^{\text{NBn}_2})_2]^{2+} (2x \text{PF}_6^-)$	<b>C25</b>	$[\text{Ru}(\text{BmbP}^{\text{NBn}_2})_2]^{2+} (2x \text{PF}_6^-)$
<b>C11</b>	$[\text{Fe}(\text{BIP}^{\text{NEt}_2})_2]^{2+} (2x \text{PF}_6^-)$	<b>C26</b>	$[\text{Ru}(\text{BIP}^{\text{NEt}_2})_2]^{2+} (2x \text{PF}_6^-)$
<b>C12</b>	$[\text{Fe}(\text{BmIP}^{\text{NEt}_2})_2]^{2+} (2x \text{PF}_6^-)$	<b>C27</b>	$[\text{Ru}(\text{BmIP}^{\text{NEt}_2})_2]^{2+} (2x \text{PF}_6^-)$
<b>C13</b>	$[\text{Fe}(\text{BdmIP}^{\text{NEt}_2})_2]^{2+} (2x \text{PF}_6^-)$	<b>C28</b>	$[\text{Ru}(\text{BdmIP}^{\text{NEt}_2})_2]^{2+} (2x \text{PF}_6^-)$
<b>C14</b>	$[\text{Fe}(\text{BbP}^{\text{NEt}_2})_2]^{2+} (2x \text{PF}_6^-)$	<b>C29</b>	$[\text{Ru}(\text{BbP}^{\text{NEt}_2})_2]^{2+} (2x \text{PF}_6^-)$
<b>C15</b>	$[\text{Fe}(\text{BmbP}^{\text{NEt}_2})_2]^{2+} (2x \text{PF}_6^-)$	<b>C30</b>	$[\text{Ru}(\text{BmbP}^{\text{NEt}_2})_2]^{2+} (2x \text{PF}_6^-)$

# 1 Introduction

## 1.1 Energy crisis

To enable secure energy supply for mankind is one of the most challenging topics of research so far. Since fossil fuels have been the primary energy source for decades, the exploitation of resources like coal, mineral oil, or natural gas, will end someday due to their limited availability. Even if their use is unlimited, the production and combustion of those energy sources has led to immense problems for climate and humanity.<sup>1-3</sup> For instance, the worldwide amount of greenhouse gases emitted by fuel combustion in the period from 1970 up to 2015 has doubled, as illustrated in **figure 1-1**.

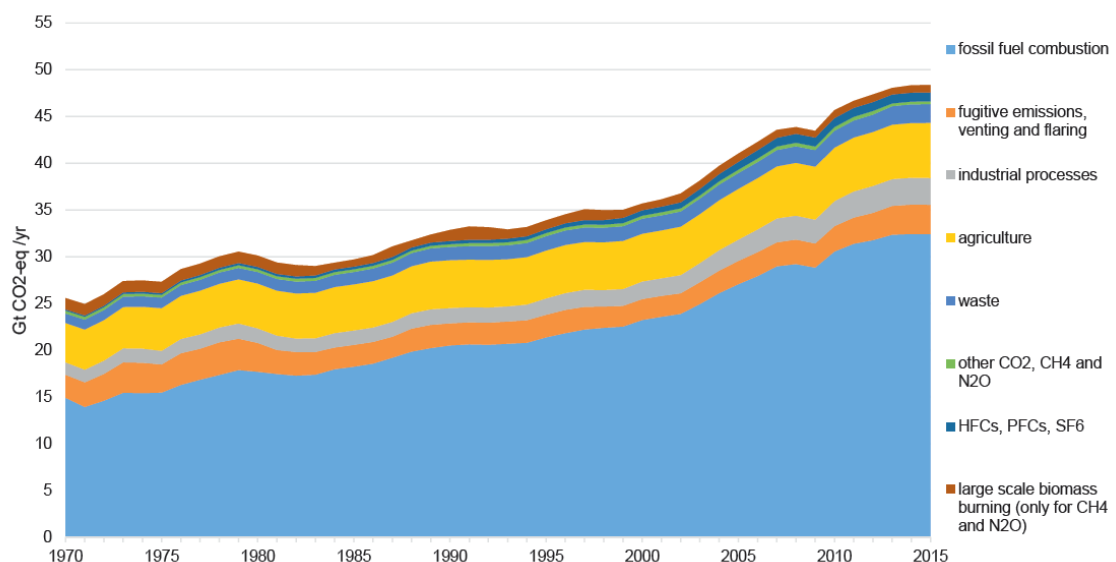


**Figure 1-1:** Global greenhouse gas emissions 1970-2015.<sup>4</sup>

This alarming development eventuates in an intensified greenhouse effect and thereby an accelerating climate change.<sup>5</sup> To counteract the climate change, the interest in reducing the dependence on fossil fuels and replacing them by more climate-friendly alternatives has been increasing over the years. Therefore, plants for energy sources like wind power, hydro power or solar energy are built extensively. This leads to an increased amount of energy production covered by sustainable sources, as shown in **figure 1-2**. In Germany, the quantity of energy produced by renewable sources nearly increased tenfold within the time span from 1990 to 2015. Meaning a quarter of the overall energy production is attributable to such sources. To entirely switch to a power supply by renewable sources, other ways must be found for using combustibles in large scale applications. One upcoming alternative is hydrogen due to its high specific energy of approximately

33.3 kWh/kg which is roughly three times higher than diesel (12.6 kWh/kg) or petrol (12.8 kWh/kg).<sup>6</sup>

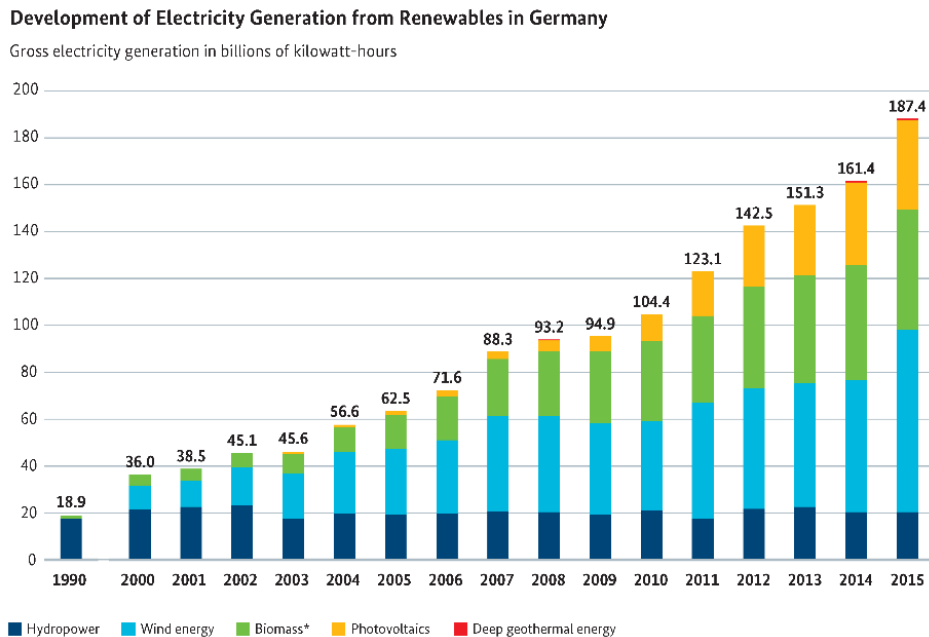


*Figure 1-2: Development of Electricity Generation from Renewables in Germany.*<sup>7</sup>

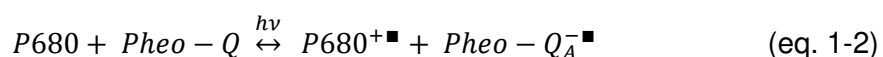
## 1.2 Renewable Hydrogen production

Considering hydrogen as a high potential future energy source, a major task is the generation and storage of it. Since hydrogen has been used as chemical reactant for decades, essential ways of production are mostly energy and emission intensive processes like steam reforming of methane, the partial oxidation of hydrocarbons or coal gasification. With the limited resources available for those processes and the aim of a sustainable energy production, water splitting becomes a highly attractive alternative to generate hydrogen. The longest-known method for water splitting is electrolysis. With 237 kJ/mol required for the splitting of hydrogen and oxygen, performance of this process requires a lot of energy due to efficiency rates up to 80 %.<sup>8-11</sup> Since this process can be improved by means of sustainability with use of energy generated from sustainable sources. A desirable approach to enhance its overall energy balance is to replace the initial energy needed. For this reason, the photocatalytic water splitting is an increasing field of research. This method combines the advantages of electrolysis in terms of sustainability and being emission free, with the use of an unlimited and free accessible energy source like sunlight. The central aspect of the development of water splitting

systems is the simultaneous generation of hydrogen and oxygen by using the provided photon energy of sunlight. The resulting overall redox reaction is shown in **equation 1-1**.



This general idea is based on photosynthesis, where the oxidation of water with the use of sunlight to generate oxygen is naturally happening inside plants in the photosystem II.<sup>12-14</sup> This bioprotein acts as a water-plastoquinone-oxido-reductase and cycles through a three step reaction cascade. In the first step, a light-induced charge separation is caused, leading to the formation of a radical pair consisting of a chlorophyll  $\alpha$  complex (P680), and pheopytin  $\alpha$  (pheo) in combination with a special plastoquinone-9 molecule ( $Q_A$ ) (**equation 1-2**).



Following this initial step, a reduction of plastoquinone to plastoquinol takes place, with  $Q_A^{-\bullet}$  as reducing agent. Finally, the oxidative water splitting into  $O_2$  and four protons at a manganese based catalytic site via a four-step sequence driven by  $P680^{+\bullet}$  proceeds.<sup>15-17</sup> Due to the complexity of this process, the structure activity correlation is not enlightened totally to this point.<sup>18,19</sup> This leads to the simplification of the overall reaction by division into an oxidative part (**equation 1-3**) leading to the formation of molecular oxygen and a reductive part (**equation 1-4**) leading to the formation of molecular hydrogen.



Usually in research both sub-processes are investigated separately from each other due to the complexity of electron transfer mechanisms. In case of oxygen four electrons are transferred in the oxidation process to generate one oxygen molecule, whereas the proton reduction requires two electrons for the generation of a hydrogen molecule. Even though hydrogen is a potential future energy source, the creation of a reasonable system for fuel production must incorporate both mechanisms in one process. This thesis focuses on the sub-process of reductive photocatalytic water splitting.

### 1.3 Photocatalytic water splitting

Since HONDA and FUJISHIMA reported the first light driven water splitting on a  $TiO_2$  single-crystal electrode by band-gap excitation in 1972, the research field of semiconductor based water splitting is studied extensively.<sup>20</sup> Since then, a variety of efficient systems

have been developed, with a multitude of metals. The overall concept involves metal oxides in their highest oxidation state with an electron configuration of  $d^0$  or  $d^{10}$ .<sup>21,22</sup> The operating principle of those materials is the excitation of electrons from the valence band (VB) into the conduction band (CB) by irradiation of visible light, which is shown in **figure 1-3**. The excited electrons leave a hole in the valence band which creates charge separation between VB and CB.

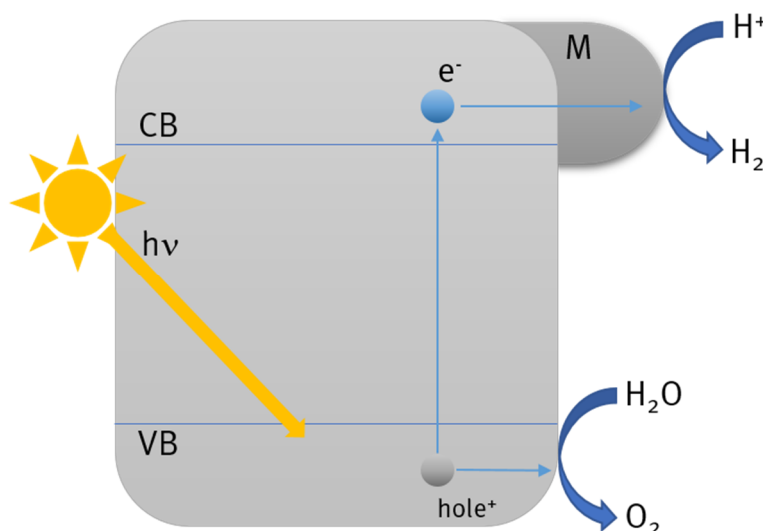


**Figure 1-3:** Schematic procedure of water splitting by a semiconductor.

Important for an effective catalysis is a suitable width of the band gap between valence and conduction band. Also, the bottom level of the conduction band has to be more negative than the redox potential of the  $H^+/H_2$  reduction (0 V vs. NHE), whereas the top level of the valence band has to be more positive than the redox potential of the  $O_2/H_2O$  oxidation (1.23 eV).<sup>23</sup> The holes respective electrons than migrate to the surface to accomplish a hydrogen (HER) or oxygen evolving reaction (OER).<sup>23–25</sup> Because pure oxides are hardly active for such catalytic reactions, semiconductor materials are doped with co-catalyst materials which consist of platinum-group elements<sup>26–28</sup> or earth-abundant elements.<sup>29,30</sup>

As a result, from the given band structure of the semiconductor the mode of action is already given for heterogeneous water splitting systems. Thereby, construction of a homogeneous system is attached to a multitude of potentials for change. Generally, homogeneous water reduction systems consist of these three components: A photosensitizer (PS), a water reduction catalyst (WRC) and a sacrificial agent as electron donor (ED) for recovering the photosensitizer after excitation. The connection between those compounds determines the differentiation between multi-component system and single-component system. In both cases, irradiation of the photosensitizer leads to excitation of an electron into an excited state. This electron is then further transported to

the water-reduction catalyst to conduct a hydrogen evolving reaction. The formally oxidized photosensitizer (PS<sup>+</sup>) is reduced by the sacrificial agent to return into the initial state, from where it can start another reaction cascade for proton reduction. This reaction cascade mechanism is comparable for both cases, the multi-component and single-component system, with varieties resulting from the different structure (**figure 1-4**).

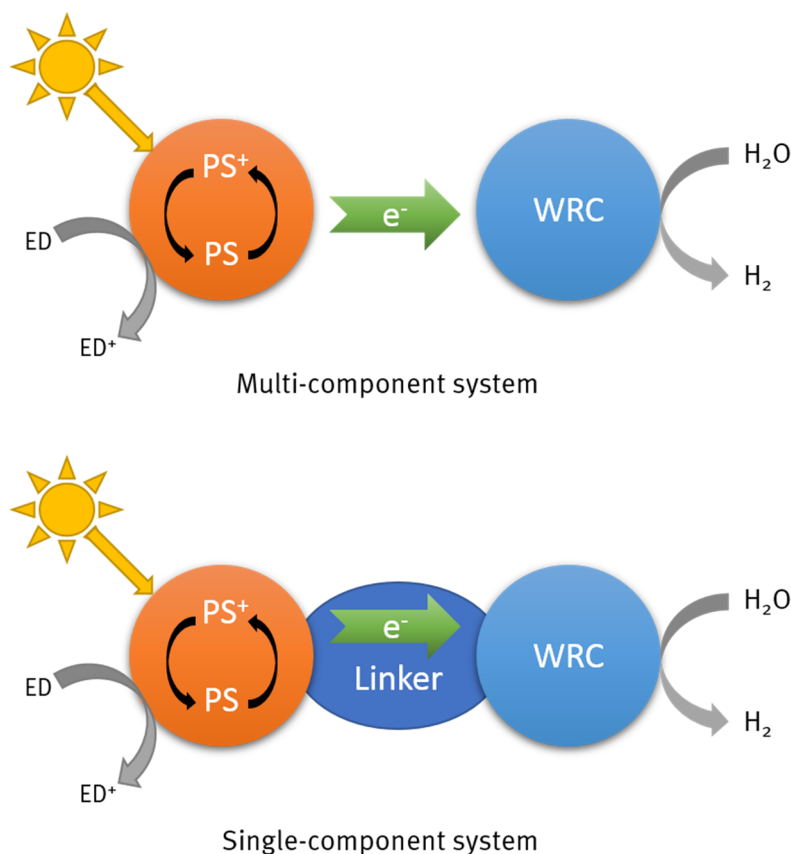


**Figure 1-4:** Schematic structure of a multi-component system (top) and a single-component system (bottom).

In multi-component systems the photosensitizer and the water-reduction catalyst are spatially separated from each other. Consequently, the electron transfer from the PS to the WRC is an intermolecular process, which either is depending on diffusion processes or is realized by transfer agents. These reagents need a high reversible reduction potential, thus viologens have established for this purpose.<sup>31–34</sup> Path-independent multi-component systems suffer from efficiency losses due to diffusion limited transfer rates and uncontrolled recombination reactions with the electron donating agent.<sup>35–37</sup>

A synthetically more sophisticated approach is the design of a single-component system (**figure 1-4**). These possess a molecular connection between the PS and the WRC via an organic linker molecule, which allows a targeted electron transfer alongside the redox potentials. The chance of higher chemical stability as well as a more efficient electron transfer caused high interest in such systems, despite the enhanced synthetical demand.

By variation of the organic linker molecule the chemical and optical properties of the system can be influenced.<sup>38-41</sup> Since the hydrogen evolving reaction requires two electrons for generation of a hydrogen molecule, even the PS to WRC ratio can be adjusted by modification of the organic linker pattern. In a dyad system the PS must run through two excitation circles to supply the electrons needed. Selection of suitable linker molecules can lead to an arrangement of two PS with one WRC, resulting in provision of two electrons by one excitation circle each.<sup>42</sup> To this point a definite statement whether a 2:1 ratio improves the catalytic performance is unresolved, due to the multitude of different factors which have to be considered. Despite the fact that the amount of systems known in the literature is increasing rapidly over the past years, only a few efficient dyad systems are known.<sup>42,43</sup> The demands for efficient catalysis involve a high catalytic rate of the WRC, a fast and purposeful electron-transfer alongside the linker and a high excitation rate at the photosensitizer, which will be elucidated meticulously in the following chapter.

## 1.4 Photosensitizer

### 1.4.1 General requirements

As the first and potentially prime component in the photocatalytic hydrogen evolving cascade, photosensitizers must fulfill different requirements. Since the general idea of photoinduced hydrogen production by using sunlight, the main requirement of a PS is the excitability by visible light. Within the excitation process an electron is elevated from the initial state into an energetically higher excited state, as shown in **figure 1-5**. Typically for  $d^6$ -low spin complexes, ground state (GS) excitation ( $d \rightarrow \pi^*$ ) leads to occupation of a metal-to-ligand charge transfer (MLCT) state while maintaining the spin. A very fast intersystem crossing (ISC) within femtoseconds (fs) causes allocation of a triplet MLCT ( $^3\text{MLCT}$ ). With this state enabling the electron transfer and further catalysis, stabilization and continuously elongation of the MLCT lifetime is intended. At this point several deactivation processes are possible. Direct deactivation from the  $^3\text{MLCT}$  into the GS could lead to luminescence, in this case phosphorescence caused by the triplet-singlet transition or determined by the energetic gap between  $^3\text{MLCT}$  and GS a radiation free relaxation.

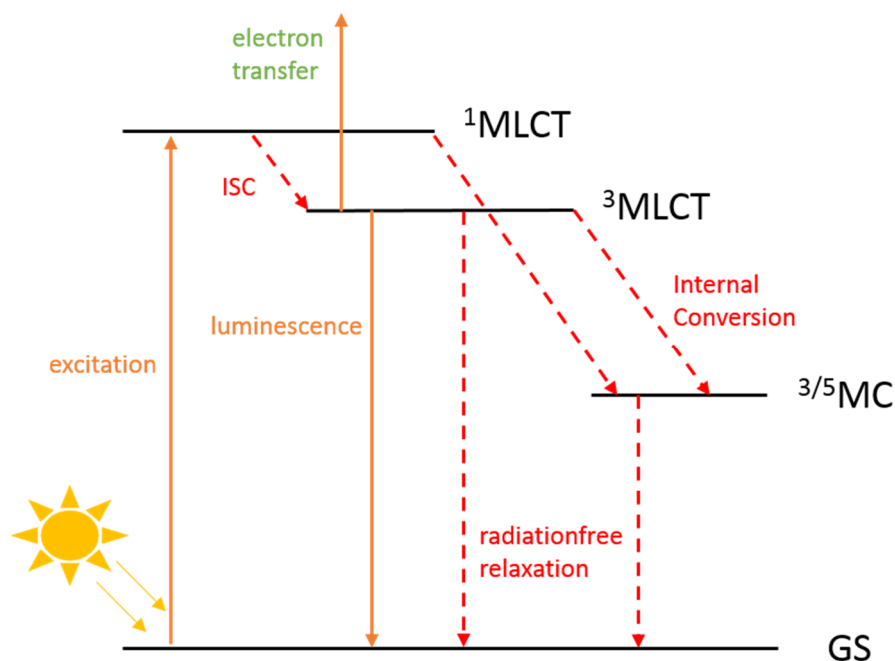


**Figure 1-5:** Simplified excitation scheme for a  $d^6$ -metal-complex with weak ligand field splitting.

For metal complexes with weak ligand field splitting, metal-centered states ( $3/5$ MC) are energetical close to the  $3$ MLCT states and could act as spin-trap, since they lead to a fast deactivation, causing a diminution of the catalytic active  $3$ MLCT state. Hence, a population of the MC states results in deactivation into the GS. Optimization of the photosensitizer can be achieved by destabilizing the MC states and thereby elongate the  $3$ MLCT lifetime. Since the energetic position of the MLCT and the MC states is depending on the metal center and the coordinating ligands, a certain degree of influence can be exerted.<sup>44–48</sup> Once the electron is elevated to the  $3$ MLCT and transferred to the WRC, it is crucial for an effective subsequent photocatalysis to ensure a total reversible recovery of the photosensitizer. Therefore, two quenching mechanisms are postulated, whereby both affect the regeneration pathway of the photosensitizer<sup>49</sup> (**figure 1-6**). On the one hand, the oxidative quenching denotes the MLCT process and further electron transfer as a formal oxidation of the metal center followed by reduction of the sacrificial agent. In sum, the metal-electron donor interaction happens after the electron transfer (left pathway **figure 1-6**).

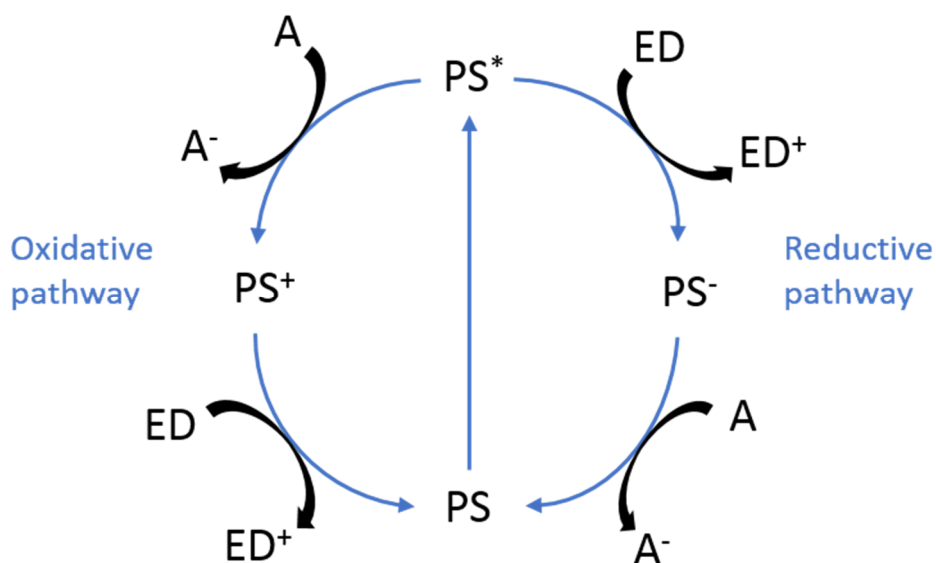


**Figure 1-6:** Schematic mechanism of oxidative and reductive quenching.

On the other hand, in the reductive quenching mechanism describes the interaction of the metal center with the sacrificial agent before an electron transfer implying a preceding reduction of the metal center (right pathway **figure 1-6**).

### 1.3.2 Ruthenium

Based on the afore mentioned aspects, noble metals played a major role in photocatalysis for decades due to their intrinsic properties.<sup>50–52</sup> Since the first photocatalytic application for  $[\text{Ru}(\text{bpy})_3]^{2+}$  was reported by HEDSTRAND *et al.*<sup>53</sup> in 1978 (**figure 1-7**), the use of noble metals as photocatalysts was established in organic synthesis. The large number of examples in which Ru(II) or Ir(III) photocatalysts have been used, bears from a multitude of organic conversions<sup>54–57</sup> to a variety of inorganic applications.<sup>58–61</sup>

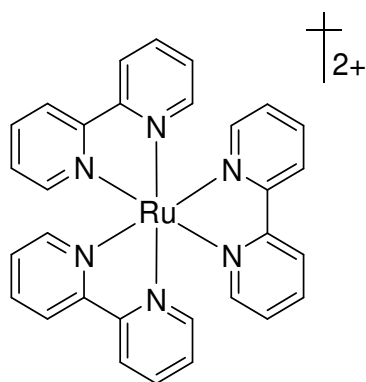


**Figure 1-7:**  $[\text{Ru}(\text{bpy})_3]$  first reported example of a ruthenium photocatalyst.

Therefore, it was perceived that the position of the MC and MLCT excited states, can be affected due to the selection of the ligand type. The ligand species determines the resulting ligand field splitting and the redox properties of the catalyst.<sup>62–65</sup> A schematic representation for a weak and strong ligand field is shown in **figure 1-8**. In a strong ligand field (**figure 1-8 (a)**) the  $^3\text{MC}$  typically is more destabilized than the  $^3\text{MLCT}$ , resulting in slow deactivation via luminescence from the  $^3\text{MLCT}$  into the GS, which can be found in case of  $[\text{Ru}(\text{bpy})_3]$ . A weak ligand field (**figure 1-8 (b)**) leads to more stabilized MC states, and thereby a fast radiation free deactivation cascade from the MLCT via the MC into the GS. The occupation of the anti-bonding MC states also entails the possibility of ligand dissociation resulting in decomposition of the initial ligand field.<sup>61</sup> To elongate the MLCT lifetime and improve the catalytic activity of the  $[\text{Ru}(\text{bpy})_3]$  core structure, functionalization of the bpy-ligand with electronic withdrawing substituents leads to an increased oxidation potential, whereas electron-donating substituents lead to an decreased oxidation potential for the  $\text{Ru}^{\text{II}}/\text{Ru}^{\text{III}}$  pair.<sup>66,67</sup>

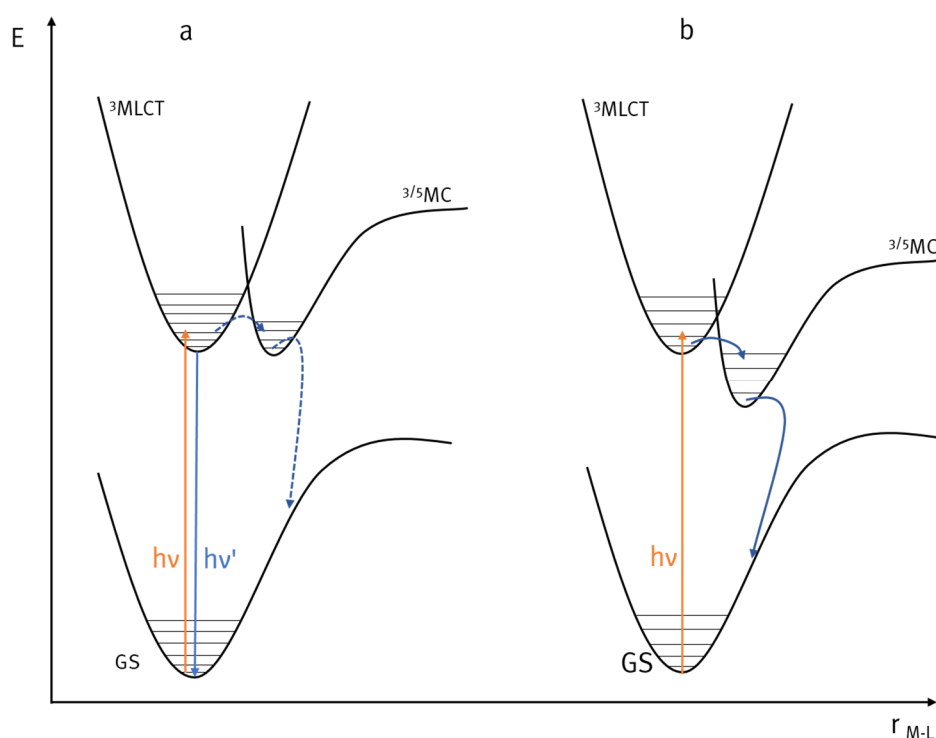


**Figure 1-8:** Schematic representation for  $^3\text{MLCT}$  and  $^3\text{MC}$  location in a strong(a) and weak (b) ligand field in case of  $[\text{Ru}(\text{bpy})_3]$ .

Problematic with the use of bidentate ligands in heteroleptic complexes is the formation of enantiomeric complex material. To solve this problem chemical equivalent ligands like terpyridine were used to build enantiopure complex material of  $[\text{Ru}(\text{tpy})_2]$ . Since then, a lot of different substitutions were made at the terpyridine ligand, to modify the electronic structure.<sup>68</sup> The use of those ligands allows the enantiopure synthesis of heteroleptic complexes, albeit they decrease the octahedral coordination geometry due to the larger

bite angles caused by the structure of the ligand. As a result, the ligand-metal orbital overlap reduces, which causes a decrease of the ligand field splitting. For this reason, several strategies were developed to restore the octahedral geometry, while maintaining tridentate ligand coordination.<sup>69–73</sup>

The use of polypyridine ligands engenders a whole series of efficient photocatalysts for hydrogen production. In 2006 the group of SAKAI *et al.* reported a  $[\text{Ru}(\text{bpy})_3]$  type photosensitizer, but they replaced a bipyridine ligand by a phenanthroline moiety enabling direct connection to the platinum catalyst center<sup>74</sup> (**figure 1-9**). Similar approaches followed by the groups of RAU *et al.*<sup>41</sup>, NA *et al.*<sup>75</sup> or ELVINGTON *et al.*<sup>76</sup>.

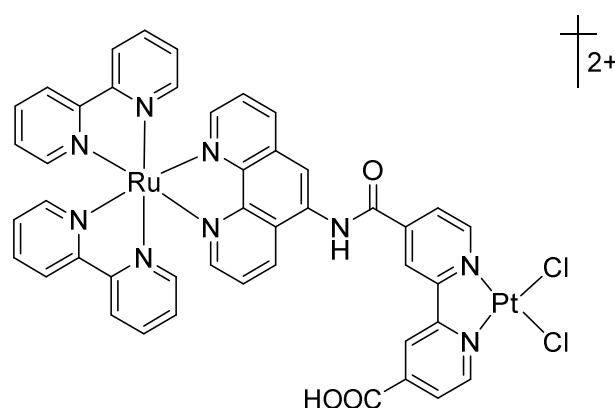


**Figure 1-9:**  $[\text{Ru}(\text{bpy})_2(5\text{-amino-phen})]^{2+}$  based catalytic system for hydrogen production by SAKAI *et al.*<sup>74</sup>

In 2008 FIHRI *et al.* reported a similar structured photocatalytic system, the ruthenium photosensitizer was coordinated like it was reported by SAKAI *et al.* before, but instead of a peptide bond connection the linker was modified by another heterocycle attached to a pyridine ring as shown in **figure 1-10**.<sup>77,78</sup> The usage of a cobalt catalytic center was the first step towards a sustainable system design.

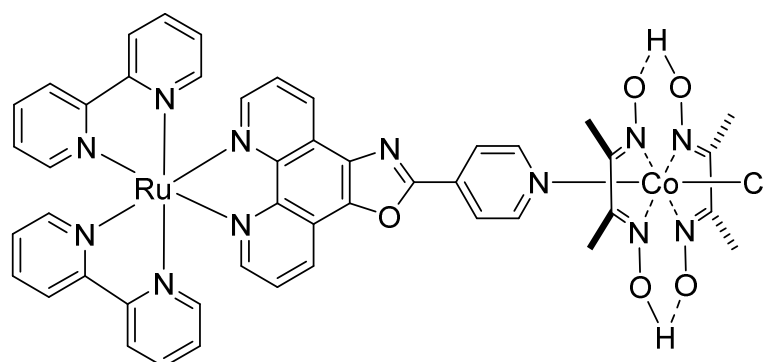


**Figure 1-10:** Single-component system with cobalt catalyst by FIHRI *et al.*<sup>77</sup>

Remarkably, they were able to increase the turnover number (TON) using cobalt as catalyst compared to the previously known systems by SAKAI *et al.*<sup>74</sup>, RAU *et al.*<sup>41</sup> or BREWER *et al.*<sup>76</sup> who rely on noble metal catalysts like platinum chloride, palladium

chloride or rhenium chloride. The high efficiency and its comparatively low costs led to use of cobalt catalysts as a standard motif in hydrogen evolving systems.<sup>79–81</sup> To increase the overall efficiency of those systems the quantum yield of the photosensitizer motif was further optimized. Therefore, different strategies were applied, ranging from replacing ruthenium by iridium as center metal,<sup>82</sup> enhancing the octahedral coordination<sup>69,73</sup> or increasing the ligand field splitting by use of strong sigma donor ligands.<sup>83</sup> For this purpose either the use of cyclometalating ligands, which were published in the early 90's by SAUVAGE et al.<sup>84,85</sup> or CONSTABLE et al.<sup>86</sup> were introduced and led to promising photosensitizers for dye-sensitized solar cells<sup>87</sup>. Or the use of carbene ligands, leading to an increase of the ligand field splitting, which were originally reported by SON et al.<sup>88</sup> In their first report in 2004, they describe the synthesis of bidentate pyridine-carbene and tridentate pyridine-bis-carbene-ligands and their respective Ru(II) complexes which are shown in **figure 1-11**. In this study they investigated the influence of substitution of a pyridine functionality by a carbene within the  $\text{Ru}(\text{bpy})_3^{2+}$  and  $\text{Ru}(\text{tpy})_2^{2+}$  analogues.

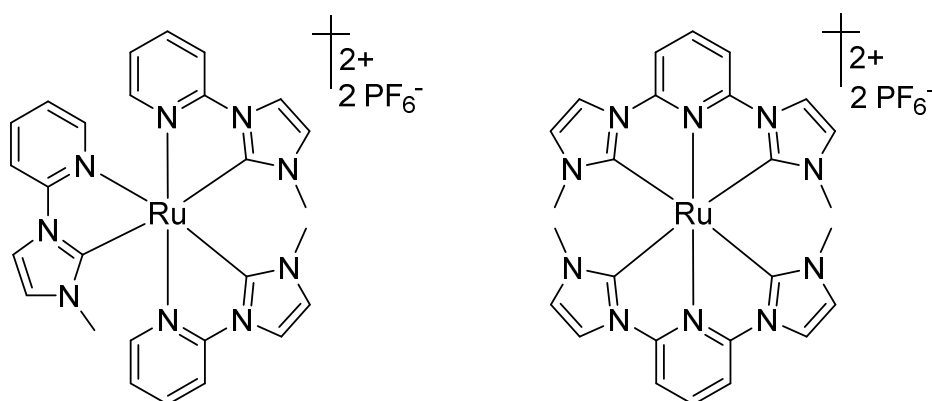


**Figure 1-11:** Carbene including Ru-PS analogues of  $\text{Ru}(\text{bpy})_3$  (left) and  $\text{Ru}(\text{tpy})_2$  (right) by SON et al.<sup>88</sup>

The tridentate complex (**figure 1-11 (right)**) showed very encouraging optical properties with an <sup>3</sup>MLCT lifetime of 3.1  $\mu\text{s}$  in water. In the endeavor of sustainable material use this ligand strategy was adapted for earth abundant metals like iron as explained in **chapter 1.3.3**.

### 1.3.3 Iron

As explained, iridium and ruthenium based photocatalysts have been widely used in the past due to their intrinsic properties.<sup>56</sup> Despite their wide range of applications, they do have some drawbacks which shall be considered. Primary, both elements are very rare, wherefore their mining is costly and the application on large scales might be questionable. Furthermore, these noble metals inhibit a toxicity even in small traces, which could be

prevented with replacement by less toxic materials. One possibility is to replace Ir(III) and Ru(II) by their lighter homologues Co(III) and Fe(II). Despite both transition metals are available in large amounts, their use as photocatalysts is associated with different challenges. Since this thesis deals with the synthesis of iron complexes exclusively, following the challenges handling the switch from ruthenium to iron are explained in detail.

Iron as a smaller atom, compared to its bigger homologue ruthenium, possesses a smaller d-orbital overlap with the surrounding ligands, resulting in a weaker interaction between the metal center and the ligands. This leads to a smaller ligand field splitting in iron complexes compared to the ruthenium analogue, as schematically shown in **figure 1-12**. For a long lifetime of the MLCT states the relative energetic position of the  $^3/5\text{MC}$  states is important, since a population of the MC states leads to a deactivation and consequently no catalytic activity. For ruthenium complexes, the energetic position of those MC states is close to the  $^3\text{MLCT}$  states, as explained in detail in **chapter 1.3.2**, leading to slow deactivation processes and long MLCT lifetimes. In case of iron complexes, the MC states are considerably more stabilized leading to an ultrafast deactivation cascade back to the ground state. Additionally, iron is characterized by a weaker bonding affinity which results in easier structural changes of the metal-ligand geometry or bond length. Unfortunately those deactivation processes are occurring more likely and on a faster timescale and thus the changes induced by population of the MC states can appear more easily.

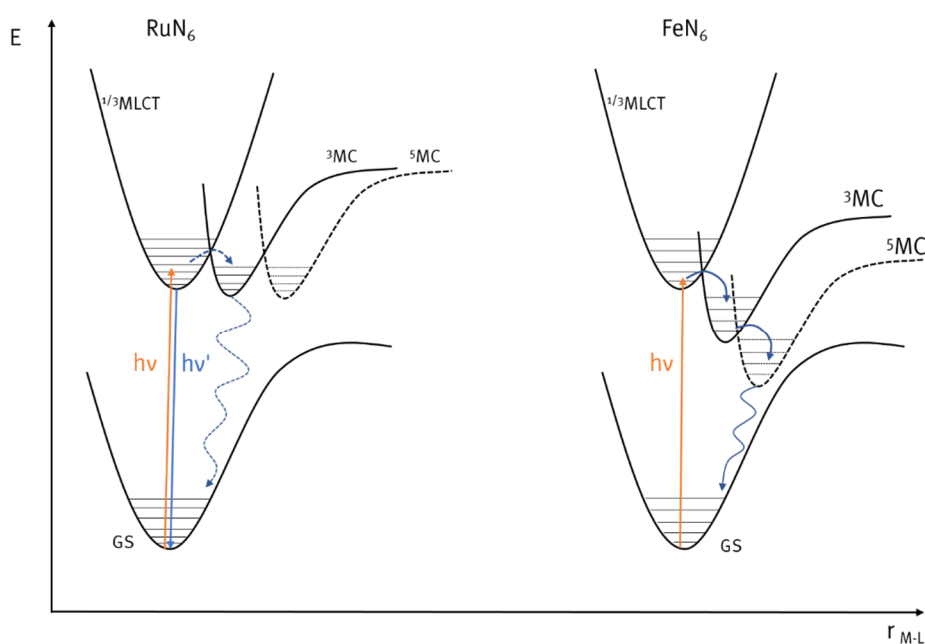


**Figure 1-12:** Schematic representation of MLCT and MC state energies for polypyridine Ru(II) and Fe(II) complexes

This can be imagined as the horizontal rate in the reaction cascade pictured in **figure 1-12**. The ruthenium deactivation cascade involves a lot of movement along the r-axis, whereas the iron deactivation proceeds a lot faster along the energy axis into the GS. This behavior also affects the luminescence properties of iron-polypyridine complexes. With the deactivation happening within the femtosecond time scale.<sup>89</sup> No luminescence could be observed for different iron complexes, whose ruthenium analogues are prominent for the long lasting luminescence.<sup>90</sup> The MLCT states in case of Fe(bpy)<sub>3</sub>, Fe(phen)<sub>3</sub> or Fe(tpy)<sub>2</sub> are depopulated faster into the MC states, than luminescence processes into the GS can occur.

Since the location of the energetic states are relative, the design of efficient iron-based photosensitizer needs to fulfill several preconditions. The intended conditions involve adjustment of the energetic states, meaning destabilization of the MC states more than the MLCT states to converge to a ruthenium like scenario. To accomplish this, strong donating ligands should be used to elevate the  $e_g^*$  orbitals, resulting in destabilization of the MC states. Simultaneously to stabilize the MLCT states, the  $\pi^*$  orbitals of the ligands must be reduced in energy. This can be achieved by an enlargement of the ligand  $\pi$  system, resulting in a decreased  $\pi - \pi^*$  gap of the ligand orbitals, or introduction of functional groups with high acceptor ability, to lower the LUMO orbitals synonymous with the MLCT states. This strategy was followed with the use of tridentate bis-pyridine carbene ligands, whose development is further elucidated in the following.

#### 1.3.4 Iron-C<sup>N</sup>C photosensitizer

Since pyridine-bis-carbene ligands were reported by SON et al.<sup>88</sup> and showed interesting properties for Ru(II) complexes, (see **chapter 1.3.2**), the use of this ligand type was adapted by WÄRNMARK et al.<sup>91</sup> in 2013 synthesizing a homoleptic tridentate pyridine-bis-carbene iron(II) complex (**figure 1-13**). Within their study they investigated the influence of the attached alkyl groups at the imidazolydene by using methyl or *tert*butyl groups. As it was reported for ruthenium, the introduction of NHC moieties increased the ligand field splitting significantly. Hence they were able to detect a <sup>3</sup>MLCT lifetime for the methylene alkylated complex of 9 ps, which is 62 times longer than the respective Fe(terpy)<sub>2</sub> complex with a MLCT lifetime of 145 fs.<sup>92</sup> Investigation of the *tert*butyl alkylated complex showed comparatively short lifetimes (300 fs), due to the steric shielding of the bulky substituents.

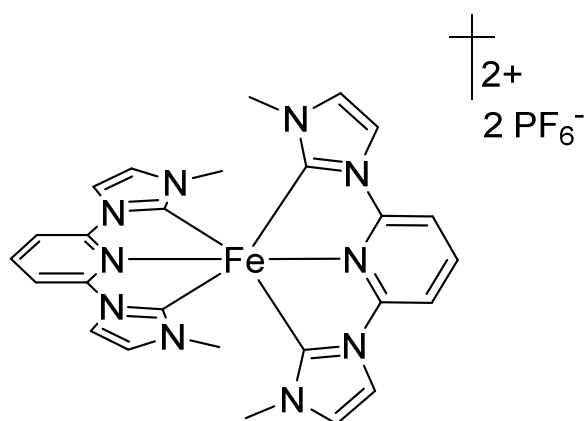


**Figure 1-13:** First homoleptic FeNHC complex reported by WÄRNMARK *et al.*<sup>91</sup>

The promoting donating character of the carbene moieties, which is visible by short Fe-carbene bond length, is hindered resulting in a decreased metal-ligand interaction and therefore explaining the different MLCT lifetime timescale.<sup>91–93</sup> The alkylation was further investigated by GROS *et al.*, revealing affirmation regarding their first assumption of direct correlation between lifetime and steric demand of the alkyl substituent.<sup>94</sup> Whereas, further elongation of the MLCT lifetime was targeted, a different approach was used increasing the  $\pi$  system of the ligand, and variation of the NHC ligand count by ZIMMER *et al.*<sup>95</sup> Their study showed that the more Fe-carbene bonds are introduced to the system, the higher the HOMO energy level rises. However, they reported the same trend for the LUMO energy due to the reduced amount of pyridine functionalities remaining in the system.<sup>95</sup> Nonetheless, their study revealed approval using  $\pi$ -system elongation because of an improved optical absorption. A combination of an increased  $\pi$ -system, while maintaining the NHC count was presented by LIU *et al.* in 2016 using benzimidazolylene instead of imidazolylene (**figure 1-14**).<sup>96</sup>

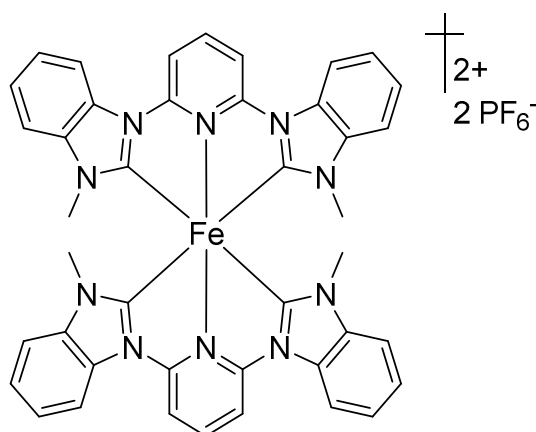


**Figure 1-14:** Homoleptic Fe-NHC complex with increased  $\pi$ -system by LIU *et al.*<sup>96</sup>

Combination of both strategies showed success, hence a  $^3\text{MLCT}$  lifetime of 16 ps was detected, accepting a small blueshift of the MLCT absorption spectra. Detailed investigation yielded a reduction of the ligand-based LUMO levels due to the extended ligand  $\pi$ -system. Simultaneously a significant stabilization of the  $t_{2g}$  orbitals (HOMO levels) is observed due to the improved  $\pi$ -accepting character of the benzimidazolydene. Hence the HOMO levels are effected more than the LUMO levels, this results in a larger HOMO-LUMO gap which explains the observed hypsochromic shift in the MLCT absorption (**figure 1-15**).<sup>92</sup> Another reported strategy was the replacement of the central ring of the tridentate ligand by pyrazine or pyrimidine moieties, to modify the  $\pi$ -accepting properties.<sup>97</sup> Introduction of another heteroatom in the central ring leads to a diminished acceptor character of the pyrazine moiety, eventuate in a decreased HOMO-LUMO gap (**figure 1-15**).

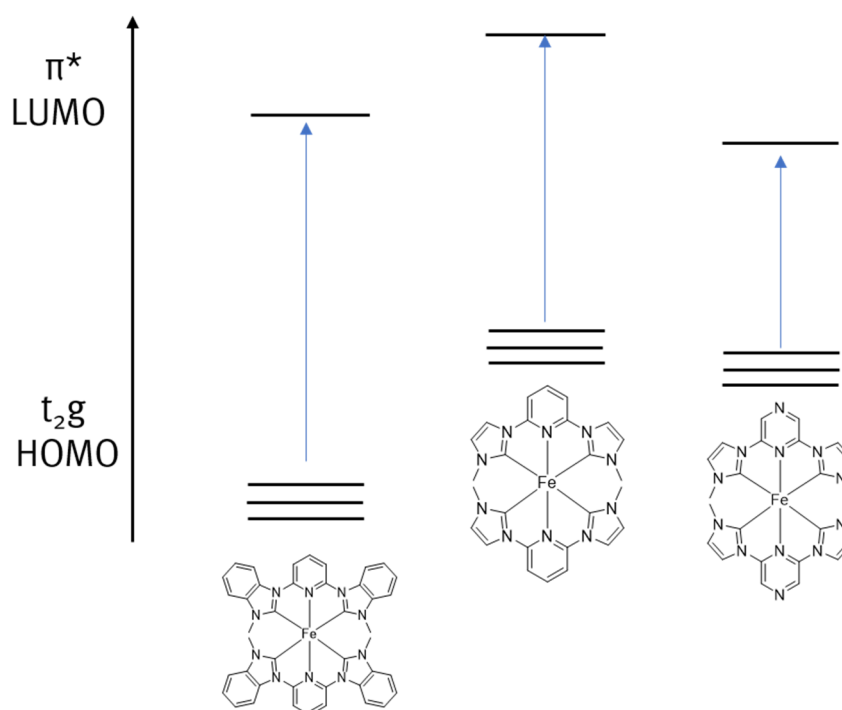


**Figure 1-15:** Change of the HOMO-LUMO gap by modification of the ligand system.

The observed MLCT lifetimes were detected to be 23 ps for the pyrazine-imidazolydene complex and 33 ps for the analogue pyrazine-benzimidazolydene complex. Because increasing the ligand  $\pi$ -system seems to be convenient, additional functionalization of the pyridine backbone showed to be beneficial. In 2015, the two independent working groups of GROS and SUNDSTRÖM reported the addition of a carboxylic group in the ligand backbone to be favorable for elongation of the MLCT lifetime as well as enabling immobilization on a semiconductor surface.<sup>98,99</sup> They reported a modification of the known imidazolydene complex (**figure 1-16 (left)**), and showed significant bathochromic shifts in the optical absorption spectrum caused by the carboxylic group. The measured MLCT

lifetime was found to be 16.5 ps, caused by the carboxylic acid function. The same effect was reported for the benzimidazolylene complex (**figure 1-16 (right)**), increasing its MLCT lifetime up to 26 ps.<sup>96</sup>

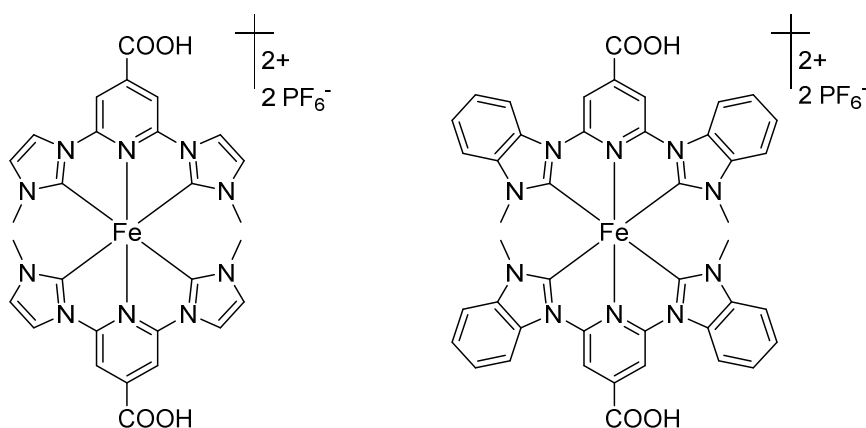


**Figure 1-16:** Immobilizable homoleptic Fe-NHC complexes by working groups of GROS<sup>98</sup> and WÄRNMARK<sup>99</sup>

The beneficial effect of the electron withdrawing carboxylic group was further used for attachment of the iron compound onto a TiO<sub>2</sub> semiconductor surface, making them the first assembled dye-sensitized solar cells (DSSC) with iron-carbene complexes. Although their solar-to-current efficiency was rather poor, they revealed high potential by high efficient electron injection into TiO<sub>2</sub> nanoparticles.<sup>99,100</sup> Taking up this idea, a theoretical study was published showing the high potential of using chromophores like anthracene as functional group in the ligand backbone. The anthracene triplet state was found to act as a possible energy reservoir, which could lead to an extended excited state decay by targeted electron transfer.<sup>101</sup>

Analogical to this approach, ZIMMER *et al.* reported a single-component system including two transition metals using a heteroleptic iron PS consisting of a tridentate bis-imidazolylene pyridine ligand, and a functionalized terpyridine based ligand, which is elongated by a pyridine moiety in the backbone (**figure 1-17**).<sup>102,103</sup> The use of the 2,6-diisopropylphenyl (DIPP) alkyl fragment, was necessary to enable the preparation of the heteroleptic complex, despite the known side effects of bulky alkyl substituents.

Aware of the unfavorable use of terpyridine instead of bis-carbene ligands, they were able to detect lifetimes in the picosecond timescale. Interestingly the MLCT lifetime of the pure photosensitizer, appears to be shorter than, in the single-component system.<sup>102</sup> Consequently they concluded a high impact of the pulling effect of the cobalt fragment, which would further elongate the MLCT lifetime, if strengthened by ligand design for example by increasing the amount of NHC moieties.

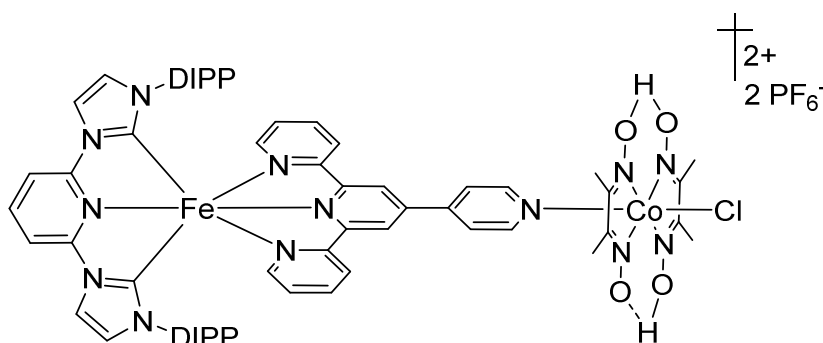


**Figure 1-17:** One-component system by ZIMMER *et al.*

Considering strong ligand design by carbene moieties, WÄRNMARK *et al.* used bidentate ligands to synthesize an octahedral iron complex saturated by coordination of six mesoionic carbene functions.<sup>104,105</sup> Mesoionic carbenes show increased  $\sigma$ -donor strength compared to classic NHC-ligands supplemental to their modest  $\pi$ -acceptor properties.<sup>106–109</sup> By using bidentate 4,4'-bis(1,2,3-triazol-5-ylidene) (btz) ligands, the octahedral coordination geometry was improved due to an increasing metal-ligand overlap resulting in a better ligand field splitting (**figure 1-18**). Saturation of the iron center with mesoionic NHC donor ligands results in a shift of the Fe(II/III) redox couple to significantly lower values compared to the known tridentate ligands bearing four NHC functions. As a result, this complex was found to be oxidized into the Fe(III) state under ambient conditions and is characterized in its Fe(II) state under anaerobic conditions. Electronic configuration investigation revealed five electrons in the  $t_{2g}$  ligand orbital, the lowest energy transitions observed in electron absorption spectroscopy are excitations from ligand  $\pi$  orbitals to metal centered orbitals (LMCT). This complex was the first reported iron complex to show photoluminescence in solution, resulting from spin allowed transitions from the  $^2\text{LMCT}$  state into the doublet ground state ( $^2\text{GS}$ ). This is different to the beforehand discussed, classic tridentate Fe(II)-NHC  $d^6$  complexes, where the charge transfer occurs via the  $^3\text{MLCT}$  state.

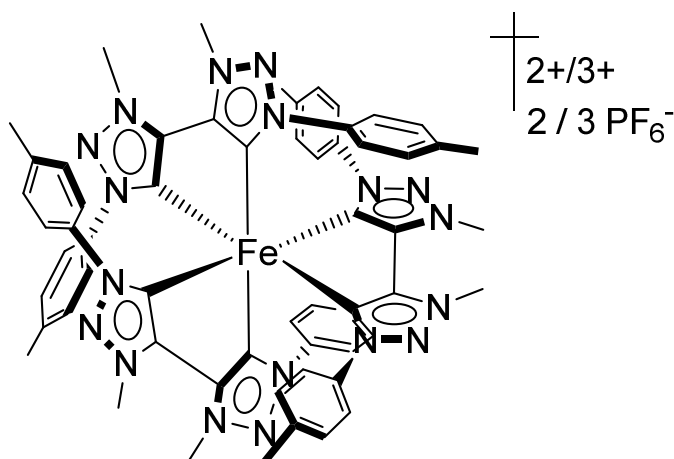


**Figure 1-18:** Homoleptic bidentate Fe(btz)<sub>3</sub>-complex by WÄRNMARK *et al.*<sup>104</sup>

In the Fe(III) state, the complex showed an  $^2\text{LMCT}$  lifetime of 100 ps, which was surpassed by the reduced Fe(II) form with a  $^3\text{MLCT}$  lifetime of 528 ps. Explanation for this immense increased lifetime compared to the Fe(III) state is given by the spin-forbidden transition from the  $^3\text{MLCT}$  to the  $^1\text{GS}$ .

### 1.3.5 Influence of N-Donors

As showed in the introduction before, several strategies were followed to elongate the  $^3\text{MLCT}$  lifetime and therefore to minimize the HOMO-LUMO gap. To this point in this comparatively young research field, several iron photosensitizers with either non functionalization or an electron-withdrawing group (EWG) were presented.

In a study by MAESTRI *et al.* a series of 14 different  $[\text{Ru}(\text{II})(\text{terpy-x})(\text{terpy-y})]$  was investigated with regard to their photophysical and electrochemical properties, whereby -X and -Y abbreviate functionalization of different acceptor and donor moieties.<sup>110</sup> As a main part of this study they investigated the properties of  $[\text{Ru}(\text{II})(\text{terpy-NMe}_2)_2]$  as pure donor complex and  $[\text{Ru}(\text{II})(\text{terpy-SO}_2\text{Me}_2)_2]$  as pure acceptor complex. Surprisingly, they observed a decrease of the MLCT energy in both cases when compared to the non-functionalized complex (**figure 1-19**). Simultaneously the ligand-centered bands are shifted bathochromic in case of the  $[\text{Ru}(\text{II})(\text{terpy-SO}_2\text{Me}_2)_2]$  complex and hypsochromic in case of  $[\text{Ru}(\text{II})(\text{terpy-NMe}_2)_2]$ .

After further investigation, incorporating heteroleptic complexes into the study, they observed a more pronounced stabilizing effect of the accepting groups to the  $\pi^*$ - ligand centered orbitals as they observed for the HOMO  $\pi(t_{2g})$  metal centered-orbitals (**figure 1-19** [(A-tpy)Ru(tpy-A)]). Additionally, no charge compensation in the formal oxidizing event of a MLCT transfer was observed, attributable to the accepting property of the functional group causing an increased oxidation potential of the  $\text{Ru}^{\text{II/III}}$  redox pair. Vice versa, the donor-functionalized complexes showed a decrease of the MLCT energy due to a more destabilizing effect to the HOMO  $\pi(t_{2g})$  metal centered orbitals than the LUMO  $\pi^*(e_g)$  ligand orbitals (**figure 1-19** [(D-tpy)Ru(tpy-D)]). This results in a lower  $\text{Ru}^{\text{II/III}}$  redox potential because of the ability of charge stabilization by the electron-donating groups.

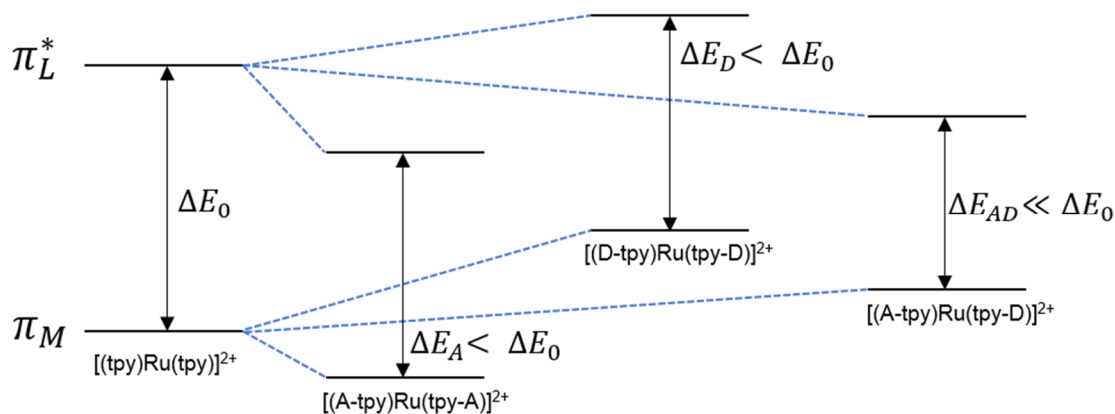


**Figure 1-19:** Schematic effect of ligand functionalization on the HOMO-LUMO gap for different  $\text{Ru}(\text{terpy})_2$  complexes

For a series of heteroleptic complexes they observed an even more pronounced shift of the MLCT energy to lower values, which is explained by the concurring effect of donor and acceptor group to the complex orbitals. As a result, a stabilizing effect to the  $\pi_L^*$  is observed resulting from the acceptor moiety, whereby the  $\pi_M$  ( $t_{2g}$ ) orbitals are destabilized by the donor moiety, leading to the smallest HOMO-LUMO gap ( $\Delta E_{AD} \ll \Delta E_0$ ) (**figure 1-19**  $[(\text{A-tpy})\text{Ru}(\text{tpy-D})]$ ).<sup>110</sup>

Although the effect of electron accepting functional groups has been adapted to iron-NHC photosensitizers and investigated with the same outcome of a decreased HOMO-LUMO gap (**chapter 1.3.4**) the influence of electron donating groups has not been investigated for iron NHC-compounds to this point.

## 2 Aim of work

In respect of sustainability the main goal of this work is the synthesis of new iron-based photosensitizer compounds using different N-heterocyclic carbene ligands. To this point literature known iron-NHC complexes are solely build by ligands functionalized with electron withdrawing groups. To bridge the gap between complexes with electron withdrawing groups and various other functionalization's a series of new C<sup>N</sup>C ligands with different amine functionalities and carbene moieties is synthesized and characterized (**figure 2-1**). Since ruthenium complexes of amine functionalized terpyridine ligands show encouraging absorption properties too, the difficult separation of properties between NHC vs pyridine is investigated via an systematic approach.<sup>92,110,111</sup>

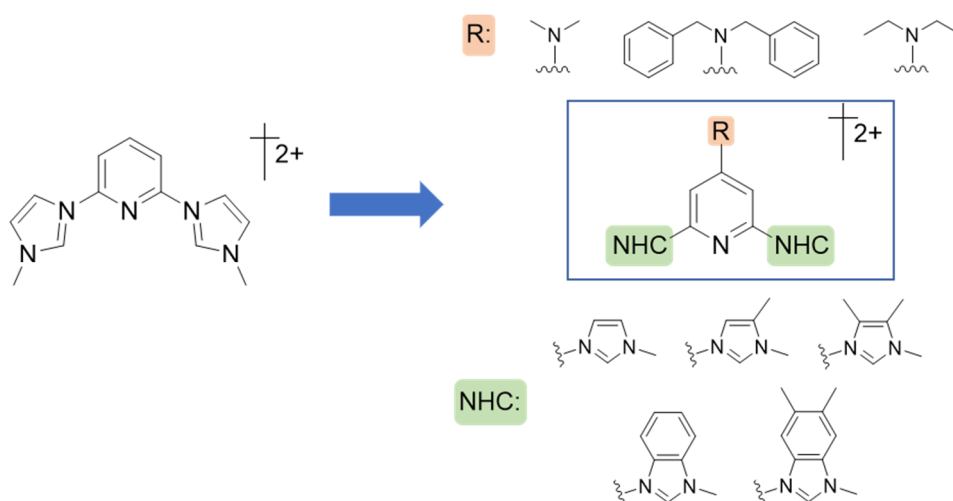


**Figure 2-1:** Structure of the ligand set used for the systematic study.

To increase the sustainability of this process, the use of precious metals is to be replaced by transition metals such as iron. Because iron complexes suffer from a small ligand field splitting, the destabilizing effect caused by donating amine groups onto the ligands  $\pi^*$  orbital and the resulting influence on the complex properties, is of special interest. Therefore, the obtained ligands are used to form a series of homoleptic Fe(II) complexes. The systematic ligand variation allows to draw conclusions about influence of the donor functionalization, which is investigated by detailed analysis of the photophysical and electrochemical properties.

To validate the results a corresponding series of Ru(II) complexes is synthesized, since ruthenium shows different preconditions by means of an intrinsic larger ligand field splitting. The influence of the novel amine functionalized carbene ligands can be directly compared to analogues functionalized [Ru(tpy)<sub>2</sub>] complexes and represents a new

contribution to future photocatalytic systems. A detailed analysis of the ruthenium complex series allows further information on the variability of the HOMO-LUMO gap.

Therefore, a direct cross comparison between the corresponding iron and ruthenium complexes can then show the influence of the ligands on the respective metal center. This will show whether the use of amine functionalized ligands can be a possible step towards increasing the efficiency of photocatalytic systems.

### 3 New NHC-ligand systems

#### 3.1 Introduction and synthetic planning

For an effective development of catalyst systems, which can be used on an industrial scale to produce hydrogen, a detailed understanding of every subcomponent is inevitable. Especially photosensitizers as a sub-component in catalytic systems must meet requirements since their excitation into the catalytic active state shall happen with high efficiency in the optical spectra of light. In addition, the lifetime of those excited states ought to be as large as possible, because of the following process of electron transfer. Moreover, they are expected to be resilient to the redox process for a large durability of the process.

Based on these demands, a systematic variation of the ligand system is one possibility to have bearing on the electronic structure of the respective photosensitizer. The so obtained structure – activity relationship allows to draw conclusions about the directive of catalyst design in the future.

For this reason, new N-heterocyclic carbene-ligands (**figure 3-1**) are developed, which are systematically varied in the backbone of the central pyridine ring as well as on their carbene functionality.

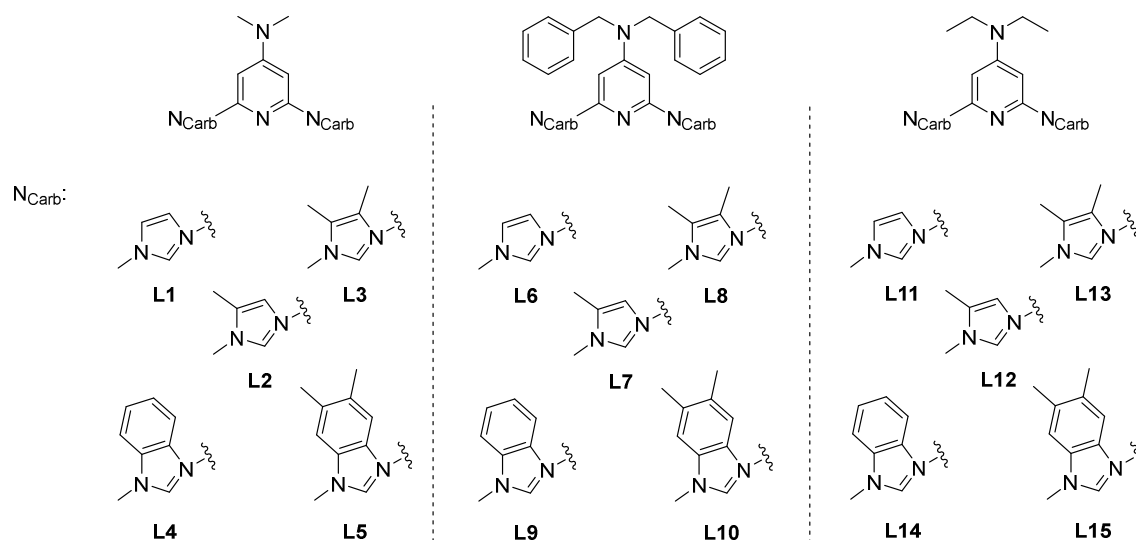


**Figure 3-1:** Overview over the synthesized NHC-ligand systems.

The variation of the ligand system can be divided into three classes, which is defined by the functionalization of the pyridine backbone in each case. The first class is characterized by a dimethylamine group (**L1-L5**), similarly to the known organic catalyst DMAP. The second class is specified by a dibenzylamine group in the backbone (**L6-L10**) increasing

the steric volume of the ligand system. The last category is determined by a diethyl group (**L11-L15**) which is in between the steric influence of the second group and the first one, as well as not having an aromatic system. All classes are subdivided into the consisting five different imidazolylene functionalizations.

### 3.2 Synthesis

The synthetic strategy starts with the synthesis of the collective precursor stage 2,6-dichloropyridine-4-amine (**4**). Therefore, the well-established procedures of HAY *et al.*<sup>112</sup> and BREIVOGEL *et al.*<sup>113</sup> are adopted onto the dichloro-derivative (**figure 3-2**).

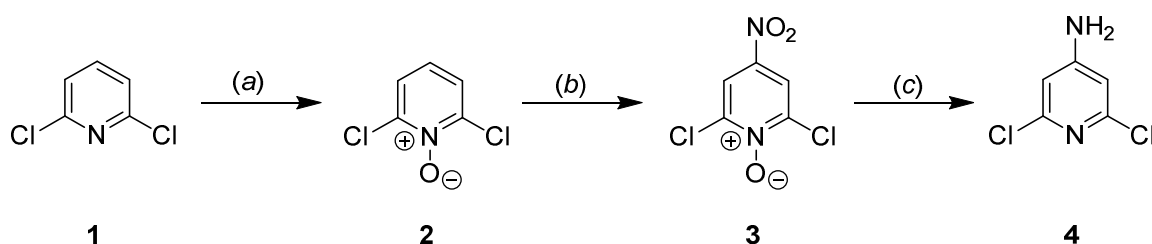


**Figure 3-2:** Synthesis of precursor 2,6-dichloropyridine-4-amine **4**.

(a) Trifluoroacetic acid, H<sub>2</sub>O<sub>2</sub> (35 %);<sup>112</sup> (b) H<sub>2</sub>SO<sub>4</sub> (96 %), HNO<sub>3</sub> (65 %);<sup>112</sup>  
 (c) AcOH (100 %), Fe-Powder.<sup>113</sup>

Synthesis of precursor **4**, 2,6-dichloropyridine-4-amine, is carried out over a three-stage synthesis starting with 2,6-dichloropyridine. In the first step **1** is oxidized in trifluoroacetic acid by treatment with a 35 % hydrogen peroxide solution to the respective N-oxide (**2**).<sup>112</sup> The oxidation of the nitrogen atom allows a selective nitration in 4-position by reaction with nitro sulfuric acid (**3**).<sup>112</sup> In the last step the N-oxide as well as the nitro-functionality are reduced to the final product (**4**) using glacial acetic acid and iron-powder.<sup>113</sup> The amine **4** can be obtained with an overall yield of 40 %. Based on the amine, several different transformations can be made, which lead to the respective ligand classes (**figure 3-3**). In the first case the amine **4** is deprotonated in a dehydrated mixture of DMF and THF 50:50 using sodium hydride. Following, an addition of methyl iodide to the deprotonated species. This leads to the dimethylamine derivate **5** which is then brought to reaction with the different imidazole derivatives. For the synthesis of **6** the amine **4** likewise is deprotonated using sodium hydride in dehydrated acetonitrile as solvent. Afterwards, the reaction mixture is treated with benzyl bromide leading to the precursor **6**. The third class of ligand systems can be achieved by using the same reaction pathway as used in the first case, replacing the methyl iodide by ethyl iodide. This reaction then results in product **7**.

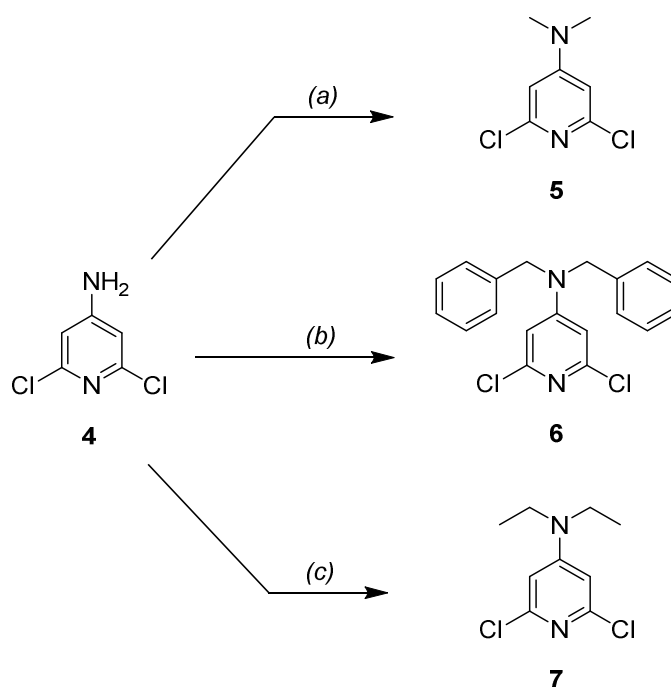


**Figure 3-3:** Synthesis of the different precursor **5-7**

(a) DMF/THF, NaH, MeI; (b) MeCN, NaH, BnBr; (c) DMF/THF, NaH, EtI.

For attachment of the imidazole derivatives different synthetic strategies are tested. The literature known protocol for a neat coupling between the pyridine core and a N-methylated imidazole structure is tested under several conditions but remain unsuccessful due to the reduced reactivity caused by N-donor addition.<sup>94,98,114–116</sup> Another two-step approach is based on a copper catalyzed Ullmann reaction.<sup>117–119</sup> Therefore, the pyridine precursors **5-7** as well as their brominated derivatives are brought to reaction with the imidazole derivative and sodium carbonate as base, catalyzed by copper(II)oxide. The successful synthesis of precursor molecules **8-22** is achieved for the chlorinated and the brominated version of **5-7** with better yields in case of the brominated species. Due to the elaborately work up process of the Ullmann reaction, the established working procedure is based on a nucleophilic substitution of the chloride by an *in-situ* generated deprotonated secondary amine of the imidazole.<sup>120–124</sup> The imidazole derivative is added to a solution of NaH resulting in deprotonation of the secondary amine. The resulting sodium-diazole salt is then brought to reaction with the dihalogenated pyridine resulting in a nucleophilic substitution of the chloride by the deprotonated amine. This procedure is preferred on grounds of high yields and a fast and easy work up procedure since the cooled reaction mixture is poured into ice cold water resulting in precipitation of the raw product. The intermediates **8-22** are further methylated using iodomethane to obtain the ligands **L1-L15**. The obtained iodine salts received through reaction with methyl iodide are purified in an initial step by a salt metathesis reaction.

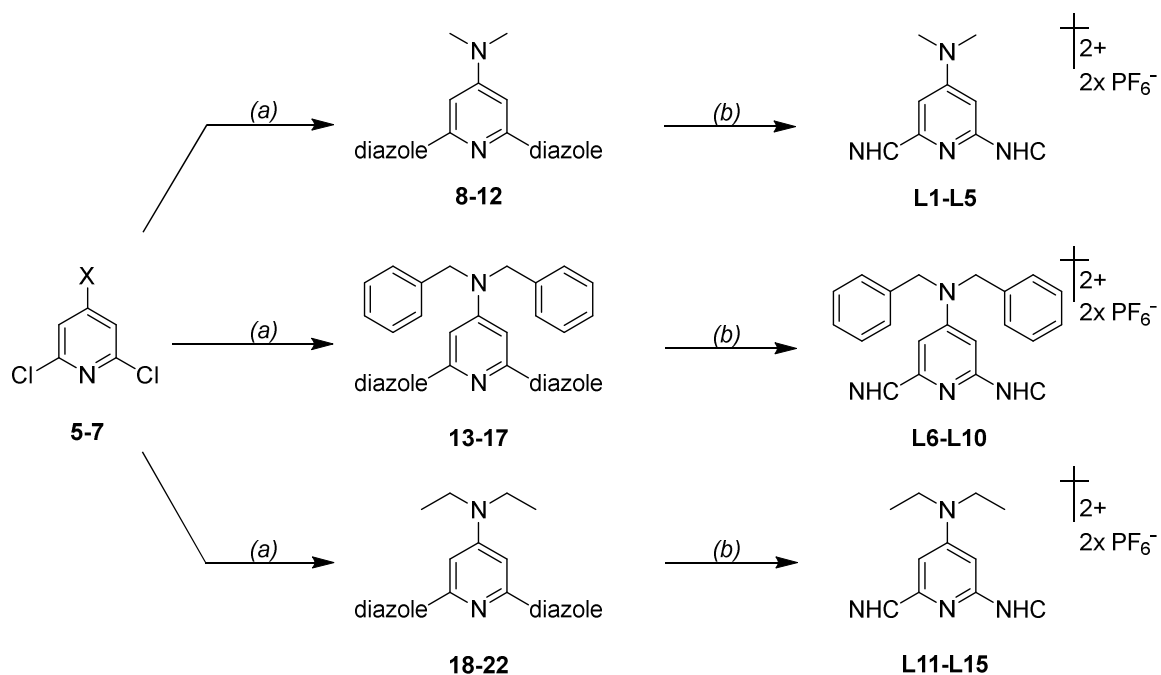


**Figure 3-4:** Two-step synthetic protocol for synthesis of ligand **L1-L15**

(a) NaH, diazole, DMF; (b) MeI, MeCN, KPF<sub>6</sub>.

For this purpose, the obtained crude product is suspended in water and filtered into a saturated aqueous solution of potassium hexafluorophosphate. The resulting precipitate is filtered and washed with diethyl ether to receive the pure ligand material. The two-step procedure is shown in **figure 3-4**. The overall synthetic route incorporates 6 steps with an overall yield of 12-15 % of the ligand material. Based on their spectroscopic behavior the ligands **L1-L3**, **L6-L8** and **L11-L13** are simplified termed as monocyclic carbenes, whereas the ligands **L4-L5**, **L9-L10** and **L14-L15** are labeled as bicyclic carbenes due to the elongated  $\pi$ -system through addition of a phenyl ring.

### 3.3 Crystal structures

Suitable single crystals for X-ray diffraction measurements can be obtained by slow gas phase diffusion of diethyl ether into an acetonitrile solution of the ligands **L1**, **L4** and **L6**. The results of the X-ray diffraction measurements for the ligands are shown in **figure 3-5**. A comparison of selected bond length and angles are summarized in **table 3-1**. Ligand [**BIP**<sup>NMe<sub>2</sub></sup>][PF<sub>6</sub>]<sub>2</sub> (**L1**) crystallizes in the space group C2/c (**figure 3-5** (top)). The ligand [**BbP**<sup>NMe<sub>2</sub></sup>][PF<sub>6</sub>]<sub>2</sub> (**L4**) with the extended  $\pi$ -system crystallizes in the C2/c space group as well (**figure 3-5** (bottom left)), whereas [**BIP**<sup>NBn<sub>2</sub></sup>][PF<sub>6</sub>]<sub>2</sub> (**L6**), crystallizes in the space group P 21/n and show a nearly perfectly planar arrangement of the three-ring system with 6 molecules in an asymmetric unit cell (**figure 3-5** (bottom right)). In general, the three-ring arrangement show similar arrays with a nearly planar alignment of the central pyridine

ring with the carbene moiety. In case of the larger benzimidazole carbene moiety the carbene atoms are rotated towards the pyridine plane in a 34.5°-degree angle due to the steric requirement, minimizing the repulsion between pyridine and benzimidazole. The dimethylamine group in case of ligand **L1** and **L4** is directed in accordance with the pyridine plane, due to the  $sp^2$  hybridization at the nitrogen atom. The steric requirement of the benzyl groups leads to a torsion of the amine substituents in **L6**, with an approximative orthogonal orientation of benzyl functionalization's (83.4° and 79.6° degree) to the pyridine plane.

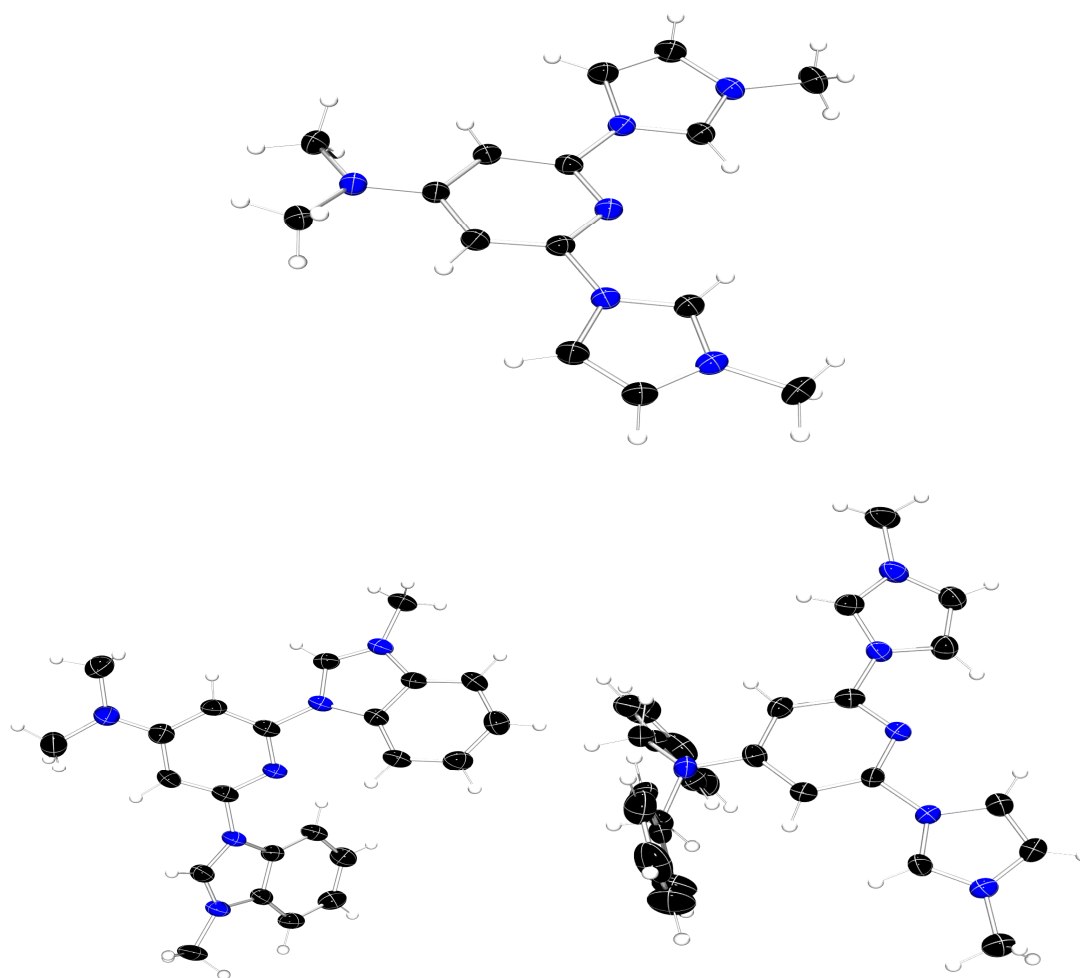


**Figure 3-5:** Single crystal structure of  $[BIP^{NMe_2}][PF_6]_2$  (**L1**) (top),  $[BbP^{NMe_2}][PF_6]_2$  (**L4**) (bottom left) and  $[BIP^{NBn_2}][PF_6]_2$  (**L6**) (bottom right)(ellipsoids with 50 % probability level).

The  $C_{pyr}-N_{azole}$ -bond lengths are similarly independent of size or orientation of the diazole connected to the pyridine ring. Inside the carbene moiety the two different  $N_{azole}-C_{carbene}$  bond lengths slightly differ, showing shorter bond lengths to the outer methylene group due to saturation of the ringside nitrogen atom by higher electron density inside the pyridine ring. The  $N_{aliph.}-C_{pyridine}$  bond length reveals to be independent from amine functionalization.

Despite the different bond lengths between C<sub>Carbene</sub> and both N<sub>azole</sub> the binding angle N<sub>azole</sub>-C<sub>carbene</sub>-N<sub>azole</sub> does not change independent of monocyclic or bicyclic carbene moiety.

Likewise, the N<sub>pyr</sub>-C<sub>pyr</sub>-N<sub>azole</sub> binding angle is comparable for all three ligands. Through rotation of the benzimidazole moieties contrary to the pyridine plane and the minimized steric repulsion, the mentioned binding angle is not affected throughout the series.

**Table 3-1:** Selected bond length and binding angles for the obtained ligand crystal structures

	L1	L4	L6
<b>Bond length [Å]</b>			
N <sub>azole</sub> -C <sub>pyridine</sub>	1.437(2)	1.431(3)	1.434(6)
N <sub>azole</sub> -N <sub>ring</sub> -C <sub>carb</sub>	1.342(2)	1.341(3)	1.330(6)
C <sub>carbene</sub> -N <sub>methyl</sub> -C <sub>carb</sub>	1.326(2)	1.314(4)	1.311(6)
N <sub>aliph</sub> -C <sub>pyridine</sub>	1.344(3)	1.346(5)	1.349(6)
<b>Binding angles [°]</b>			
N <sub>azole</sub> -C <sub>carbene</sub> -N <sub>azole</sub>	108.35(16)	110.5(3)	109.1(5)
N <sub>pyridine</sub> -C <sub>pyridine</sub> -N <sub>azole</sub>	112.65(15)	113.2(3)	112.4(5)

### 3.4 NMR-Spectroscopy

All C<sup>N</sup>C ligand systems are thoroughly characterized by NMR-spectroscopy. For this purpose, <sup>1</sup>H, <sup>13</sup>C and <sup>15</sup>N values are compared in **table 3-2**, with all ligands characterized in deuterated DMSO as solvent. A comparison of the different δ-values of the according signals show interesting insights into the electronic properties of the ligands. Especially the chemical shift of the carbene signal, which is well known to directly correlate with the acidity of the carbene proton, is of special interest. All values are obtained for the twofold cationic hexafluorophosphate salts, although actual coordination takes place by the deprotonated uncharged species. This procedure is applied since the obtained values are compared with each other, enabling a general assessment of functionalization influence.

The carbene signal of all synthesized monocyclic carbene ligands reveal to be situated at lower δ-values, when compared to the unfunctionalized reference of 2,6-bisimidazolylidene-pyridine (**BIP**), showing its <sup>1</sup>H-NMR carbene signal at 10.24 ppm. As a

general trend methylation of the monocyclic NHC backbone results in a lower acidity of the carbene proton. This trend is carried forwards by second methylation of the imidazole backbone which causes a comparatively large shift towards lower frequencies. Revealing the lowest acidity of the carbene proton in case of the dimethylimidazole ligands (**L3**, **L8**, **L13**). Despite comparison with the reference is only directly possible in the **BIP**-ligand series, due to the observed direct influence of the backbone methylation, functionalization of the central pyridine ring has direct influence on the carbene acidity, too. The pure amine effect is visible at the  $C_{\text{pyridine-H}}$  signal with varying values from 7.50 - 6.85 ppm, which is a significant decrease compared to the reference **BIP** with its according signal at 8.01 ppm.

**Table 3-2:** Chemical shifts in  $\delta$  of selected NMR signals for NHC-ligands containing monocyclic carbenes at 303 K in DMSO in ppm.

	<b>L1</b>	<b>L2</b>	<b>L3</b>	<b>L6</b>	<b>L7</b>	<b>L8</b>	<b>L11</b>	<b>L12</b>	<b>L13</b>
<b><math>^1\text{H-NMR}</math></b>									
$C_{\text{carbene-H}}$	10.15	10.02	9.60	10.12	10.01	9.46	10.17	10.02	9.48
$C_{\text{pyridine-H}}$	7.25	7.16	7.20	7.50	7.39	6.85	7.18	7.12	7.11
<b><math>^{13}\text{C-NMR}</math></b>									
$C_{\text{carbene}}$	135.9	135.1	136.1	136.6	136.1	135.4	135.8	135.7	135.6
$C_{\text{pyridine-H}}$	95.9	95.0	103.1	96.4	95.5	104.3	94.9	95.3	102.1
<b><math>^{15}\text{N-NMR}</math></b>									
$N_{\text{pyridine}}$	218.0	217.0	219.4	222.0	212.1	236.3	218.3	217.8	242.5

In the  $^{13}\text{C-NMR}$  the observed trend for the carbene signal is not visible, showing nearly identical values around 135 ppm throughout the series. Remarkably the  $C_{\text{pyridine-H}}$  signal is shifted to higher  $\delta$ -values of about 10 ppm for all three dimethylimidazole ligands (**L3**, **L8**, **L13**). A similar phenomenon is observed in the  $^{15}\text{N-NMR}$ , with the dimethylimidazole ligands showing significant shifts for the  $N_{\text{pyridine}}$ .

Alike the observations made for the monocyclic carbene ligands, the enhanced derivatives reveal lower  $\delta$ -values for the carbene signal, compared to the unfunctionalized reference of 2,6-bisbenzimidazolylene-pyridine (**BbP**) with a  $^1\text{H-NMR}$  carbene signal at 10.66 ppm.

**Table 3-3:** Chemical shifts in  $\delta$  of selected NMR signals for NHC-ligands containing bicyclic carbenes at 303 K in DMSO in ppm.

	L4	L5	L9	L10	L14	L15
<b><math>^1\text{H-NMR}</math></b>						
<b>C<sub>carbene-H</sub></b>	10.49	10.36	10.41	10.28	10.45	10.38
<b>C<sub>pyridine-H</sub></b>	7.36	7.32	7.65	7.37	7.32	7.29
<b><math>^{13}\text{C-NMR}</math></b>						
<b>C<sub>carbene</sub></b>	143.4	136.6	136.2	140.9	143.6	141.8
<b>C<sub>pyridine-H</sub></b>	100.2	98.9	100.5	100.2	100.1	98.8
<b><math>^{15}\text{N-NMR}</math></b>						
<b>N<sub>pyridine</sub></b>	233.0	217.5	236.1	-	-	232.6

Albeit the carbene signal is shifted to lower values compared to the reference, enlargement still results in larger  $\delta$ -values than observed in the monocyclic analogues. The influence on  $\text{C-H}_{\text{carbene}}$  acidity by backbone methylation is visible, although less pronounced compared to the monocyclic series. This is reasonable, since a small change of the electronic structure caused by a nonpolar methyl group is further negligible with an increasing size of the overall system. The shift of the  $\text{C}_{\text{carbene}}$  signal compared to the reference is also visible in the  $^{13}\text{C-NMR}$  spectra, where the **BbP**-reference ligand resides at 147.1 ppm.

Unfortunately, the  $\text{N}_{\text{pyridine}}$  signal for all bicyclic carbene ligands showed very low intensity, which is shown for ligand **L5** in **figure 3-6** with the associated small peak marked with the red square. As a result of the low intensity, the corresponding signal cannot be detected for the ligands **L10** and **L14**. The remaining four ligands show significantly alternating values, so it is not possible to draw conclusions from this series.

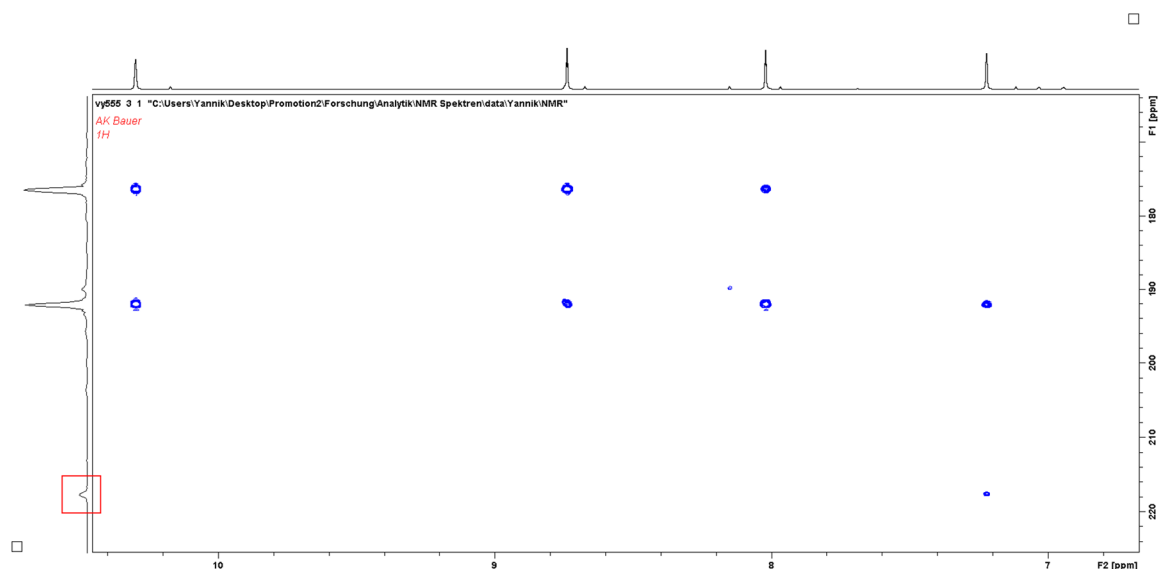


**Figure 3-6:**  $^{15}\text{N}$ -NMR spectra of ligand **L5** showing the small intensity of the  $N_{\text{pyridine}}$  signal.

### 3.5 Spectroscopic properties

UV/Vis spectra of the ligand systems are recorded at room temperature in acetonitrile solutions with an approximate concentration of  $1 \cdot 10^{-5}$  M. All ligands show a similar behavior independent of carbene moiety or pyridine functionalization. Two separate absorption maxima are observed around 280 nm and 235 nm which can be assigned to intraligand  $\pi \rightarrow \pi^*$  or  $n \rightarrow \pi^*$  transitions. In **figure 3-7**, the ligands containing monocyclic NHC-moieties are grouped along with same NHC functions. The bicyclic NHC-compounds are shown in **figure 3-8**. The investigated ligands are analyzed using the protonated  $\text{PF}_6$  salts, which is somewhat different to the chemical properties of the deprotonated free carbenes used in the complexation reaction. Since comparison among each other is possible due to the equal conditions, the effect of deprotonation is neglected in this observation. Within the ligand series only differences can be observed caused by the NHC moiety. While functionalization in the pyridine backbone has no big influence on the energetic location of the characteristic transition, methylation of the NHC moiety from imidazole (**L1**, **L6**, **L11**) to the dimethylimidazole (**L3**, **L8**, **L13**) causes a small hypsochromic shift. The situation is different in case of the bicyclic carbenes, where methylation of the backbone from benzimidazole (**L4**, **L9**, **L14**) to dimethylbenzimidazole (**L5**, **L10**, **L15**) leads to a small bathochromic shift.

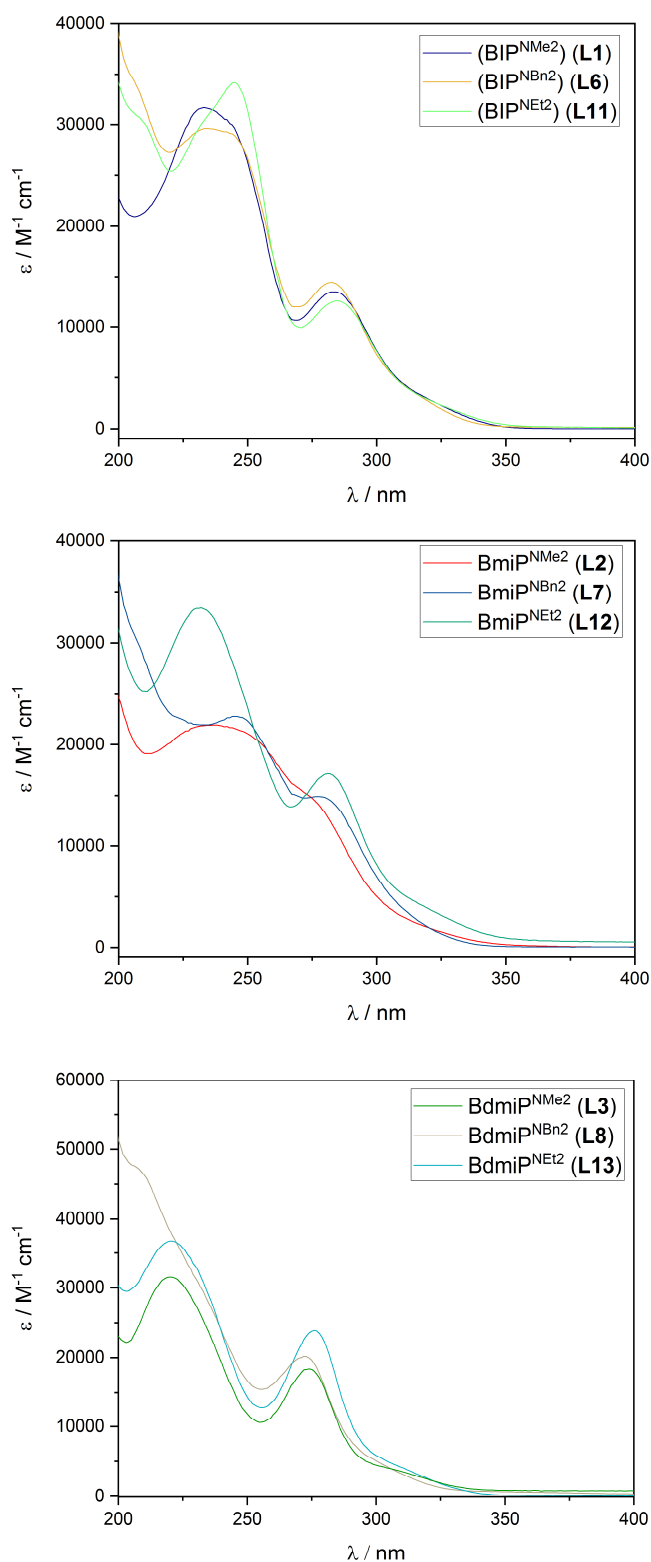


**Figure 3-7:** Compared UV/Vis spectra of monocyclic NHC containing ligands. Imidazole **BIP** (top), Methylimidazolylene **BmiP** (middle) and Dimethylimidazole **BdmIP** (bottom).

Comparison amongst the same carbene moiety displays no distinct trend regarding the extinction coefficient. By enlargement of the amine substituent from methylene to ethylene usually an increase of the extinction coefficient is observed, without diminution of the feature splitting.

The differentiability between both transition bands, diminishes with augmentation of the amine substituent when changing to larger moieties like **-NBn<sub>2</sub>**. Within the **-NBn<sub>2</sub>** ligand series a reduced splitting between both transitions is observed leading to an intense extinction coefficient below 225 nm but likewise no distinguishable second transition by further methylation of the carbene backbone.

Comparison with the used reference ligand **BIP** for the monocyclic carbene series shows a similar behavior, with two distinct transitions. The lowest energy transition is at 280 nm and is identical to the investigated ligand series. The higher energetic transition (**BIP**: 216 nm) is shifted to smaller wavelength of about 20 nm compared with the imidazole containing ligand in this series.

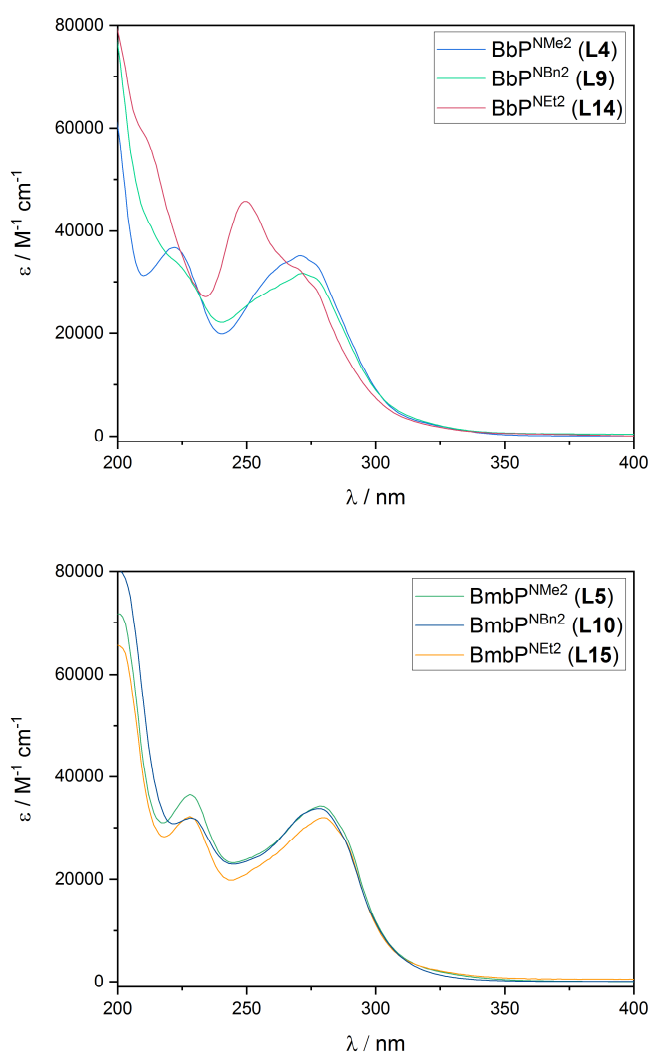


**Figure 3-8:** Compared UV/Vis spectra of bicyclic NHC containing ligands. Benzimidazole **BbP** (top) and dimethylbenzimidazole **BmbP** (bottom).

The ligands with elongated  $\pi$ -system (**BbP** and **BmbP**) show significant higher extinction coefficients as their associated smaller relatives. In the **BbP** series (figure 3-8 top) the vanishing of the higher energetic transition band can be observed for the dibenzylamine

(**L9**) and diethylamine ligand (**L14**) and results in small shoulders in the expected transition area around 225 nm. All absorption maxima and respective extinction coefficients are summarized in **table 3-4**.

Just as the monocyclic ligand series the benzimidazole containing ligands show a similar transition around 280 nm when compared to the respective reference ligand **BbP**. In contrast to the smaller ligand the second observed transition band is shifted to higher energies in case of **L4** by a value of 26 nm but remains identical to the reference in ligand **L14** (248 nm).

*Table 3-4: UV/Vis-data of ligands L1-L15 in DMSO at r.t..*

	Ligand	$\lambda$ [nm]	$\epsilon$ [ $M^{-1} cm^{-1}$ ]
<b>L1</b>	BIP <sup>NMe<sub>2</sub></sup>	282, 233	13493, 31689
<b>L2</b>	BmiP <sup>NMe<sub>2</sub></sup>	235	21902
<b>L3</b>	BdmiP <sup>NMe<sub>2</sub></sup>	273, 219	18368, 31538
<b>L4</b>	BbP <sup>NMe<sub>2</sub></sup>	271, 222	35179, 36825
<b>L5</b>	BmbP <sup>NMe<sub>2</sub></sup>	278, 227	34232, 36529
<b>L6</b>	BIP <sup>NBn<sub>2</sub></sup>	281, 233	14444, 29629
<b>L7</b>	BmiP <sup>NBn<sub>2</sub></sup>	279, 244	14857, 22798
<b>L8</b>	BdmiP <sup>NBn<sub>2</sub></sup>	273, 209	20146, 46322
<b>L9</b>	BbP <sup>NBn<sub>2</sub></sup>	271	31690
<b>L10</b>	BmbP <sup>NBn<sub>2</sub></sup>	277, 228	33754, 31929
<b>L11</b>	BIP <sup>NEt<sub>2</sub></sup>	284, 245	12574, 34164
<b>L12</b>	BmiP <sup>NEt<sub>2</sub></sup>	281, 231	17162, 33414
<b>L13</b>	BdmiP <sup>NEt<sub>2</sub></sup>	276, 219	23873, 36742
<b>L14</b>	BbP <sup>NEt<sub>2</sub></sup>	269, 248	32781, 45728
<b>L15</b>	BmbP <sup>NEt<sub>2</sub></sup>	280, 227	31988, 32182

For further information on the electronic properties of the ligand series, investigation of the emission properties for the tridentate C<sup>N</sup>C ligand systems are conducted using

freeze pumped acetonitrile solutions with an approximate concentration of  $1 \cdot 10^{-5} \text{ mol L}^{-1}$  equally to the absorption studies. As a result, no fluorescence is observed for any ligand system, despite high energy excitation wavelength of 260 nm and 220 nm

### 3.6 Redox properties

All ligand systems are investigated with respect to their redox properties using cyclic voltammetry. Therefore, the respective ligand sample ( $c = 1 \text{ mmol}$ ) and  $\text{NBu}_4\text{PF}_6$  ( $c = 100 \text{ mmol}$ ) as supporting electrolyte, are dissolved in dried and degassed acetonitrile. As a result of the ligand study no redox event is observed within the whole ligand series independent of increased  $\pi$ -system size or pyridine functionality. As an example, the scanned cyclic voltammogram of ligand **L1** is presented in **figure 3-9** in comparison with the unfunctionalized reference ligand. As seen, a ligand reduction is observed for the reference ligand at -1.92 V. Because of the higher electron density caused by the amine donor functionality the ligand reduction potential is further shifted to negative potentials, leading to no visible ligand reduction within the usable potential range for the acetonitrile solvent.

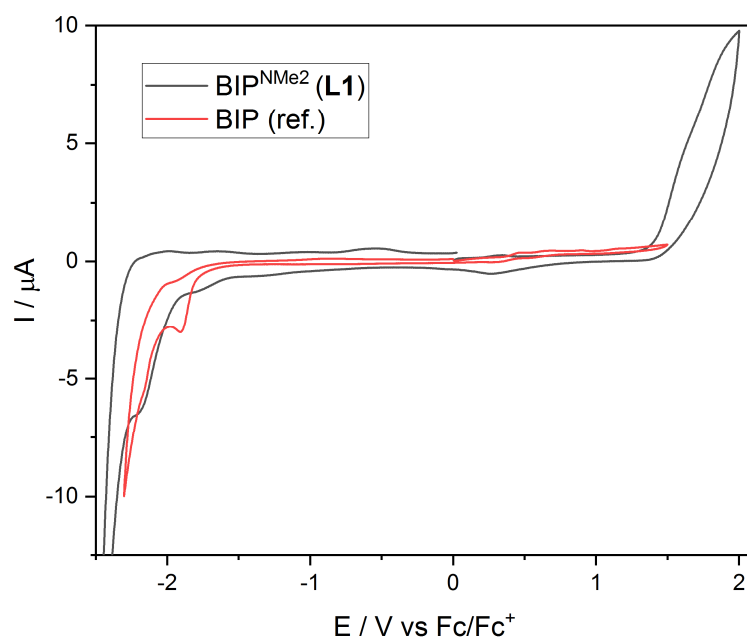


**Figure 3-9:** Total cyclic voltammogram of **L1** the unfunctionalized reference ligand (**BIP**) in acetonitrile at  $25^\circ \text{C}$  ( $v_s = 100 \text{ mV s}^{-1}$ ).

This characteristic is unfavorable for the intended application, especially because a MLCT transition and directed electron transfer includes ligand reduction along the catalytic cascade.

### 3.7 Chapter summary

The successful synthesis of 15 different amine functionalized ligands was described, of which nine were formed by monocyclic carbenes and six by bicyclic carbenes. Of these, three measurable single crystals could be obtained whose analysis showed similar properties in terms of bond length and angle. The  $^1\text{H-NMR}$  analysis showed that amine-functionalization of the pyridine ring lead to a slight influence on the acidity of the carbene proton, since the corresponding chemical shift of the proton signal is consistently lower than that of the non-functionalized reference ligand. Additionally, a correlating decrease in the acidity of the carbene proton with increasing alkylation of the carbene backbone was found. This effect was pronounced in the monocyclic series and was less pronounced in the bicyclic series, which generally showed higher carbene proton acidity than the monocyclic analogues. No significant differences between the ligand classes were found during the investigation of the absorption behavior. All ligands show two intense intraligand ( $\pi \rightarrow \pi^*$  or  $n \rightarrow \pi^*$ ) transitions in the wavelength range below 350 nm. The donating influence of the amine group could also be observed in the redox potential of the ligands, since here the potential is shifted to significantly more negative values than in the non-functionalized reference. Unfortunately, this led to the fact that a ligand reduction could not be detected because the expected potential is outside the usable measurement window of the used solvent.



## 4.2 Crystal structures

The octahedral geometry of the complex material allows growth of suitable single crystals for X-ray diffraction spectroscopy by gas phase diffusion of diethyl ether into a solution of the respective complex in acetonitrile. Suitable crystals are typically obtained within a few days. On a macroscopic scale crystal color and shape varies within the complex series as shown in **figure 4-2**.

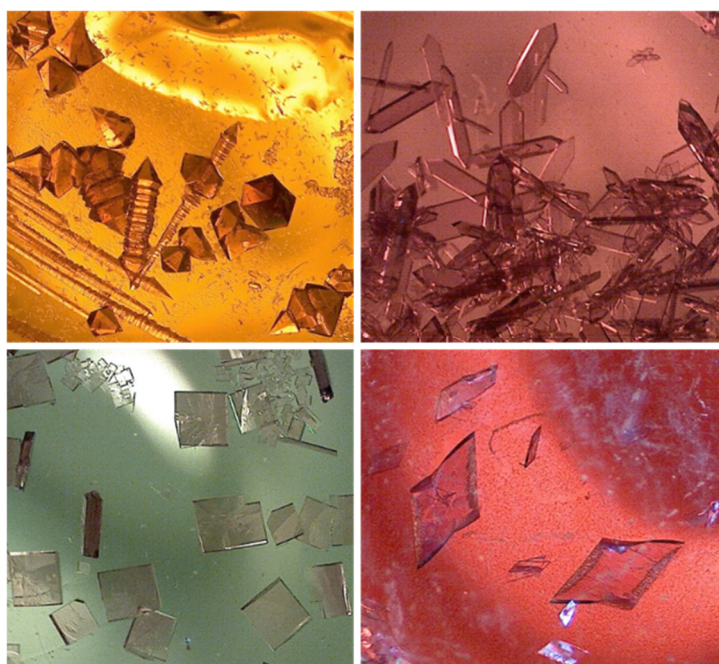


**Figure 4-2:** Crystal pictures of complexes  $[\text{Fe}(\text{BmIP}^{\text{NMe}_2})_2][\text{PF}_6]_2$  (top left);  $[\text{Fe}(\text{BdmIP}^{\text{NMe}_2})_2][\text{PF}_6]_2$  (top right);  $[\text{Fe}(\text{BmIP}^{\text{NBn}_2})_2][\text{PF}_6]_2$  (bottom left) and  $[\text{Fe}(\text{BbP}^{\text{NEt}_2})_2][\text{PF}_6]_2$  (bottom right) and their different shapes.

While complex  $[\text{Fe}(\text{BmIP}^{\text{NMe}_2})_2][\text{PF}_6]_2$  (**C2**) tends to form diamond-shaped crystals (**figure 4-2**; top left), the structural similar complex  $[\text{Fe}(\text{BdmIP}^{\text{NMe}_2})_2][\text{PF}_6]_2$  (**C3**) (**figure 4-2**; top right) builds up rectangular shaped plates with pointed peaks. The preference to build up plate shaped crystals is coherent with  $[\text{Fe}(\text{BmIP}^{\text{NBn}_2})_2][\text{PF}_6]_2$  (**C7**) (**figure 4-2**; bottom left), which incorporates a dimethylimidazolydene moiety, too. In contradistinction to  $[\text{Fe}(\text{BdmIP}^{\text{NMe}_2})_2][\text{PF}_6]_2$  (**C3**) the plates are square formed. The benzimidazolydene complex  $[\text{Fe}(\text{BbP}^{\text{NEt}_2})_2][\text{PF}_6]_2$  (**C14**) (**figure 4-2**, bottom right) tends to form octahedral appearing crystals.

Suitable single crystals can be obtained for complexes **C1-C4**, **C6-C7**, **C9** and **C11-C15**. A majority of the complexes crystallize triclinic in the P-1 space group (**C3**, **C7**, **C9**, **C13**), or monoclinic in either the C2/c space group (**C1**, **C2**) or others (**C14** in P21/n and **C15** in CC). In **table 4-1** the coordinating bond length of all analyzed complexes are summarized.

**Table 4-1:** Coordinating bond length and average in Å for all analyzed iron complexes.

	Bond length			
	Fe-N <sub>pyridine</sub>	average	Fe-C <sub>carbene</sub>	average
<b>C1</b>	1.920(1) 1.920(1)	1.920(1)	1.942(2) 1.944(2) 1.936(2) 1.940(2)	1.941(2)
<b>C2</b>	1.924(4) 1.924(4)	1.924(4)	1.951(5) 1.951(5) 1.956(5) 1.956(5)	1.953(5)
<b>C3</b>	1.915(1) 1.915(1)	1.915(1)	1.930(1) 1.932(1) 1.938(1) 1.947(1)	1.937(1)
<b>C4</b>	1.896(6) 1.919(6)	1.907(6)	1.901(7) 1.908(7) 1.927(8) 1.933(8)	1.917(6)
<b>C6</b>	1.891(8) 1.891(8)	1.891(8)	1.940(8) 1.940(8) 1.940(8) 1.940(8)	1.940(8)
<b>C7</b>	1.904(2) 1.905(2)	1.905(2)	1.939(3) 1.944(3) 1.944(3) 1.949(3)	1.944(3)
<b>C9</b>	1.904(5) 1.918(5)	1.911(5)	1.924(5) 1.928(6) 1.934(6) 1.948(6)	1.934(6)
<b>C12</b>	1.935(5) 1.935(5)	1.935(5)	1.964(8) 1.964(8) 1.979(8) 1.979(8)	1.971(8)
<b>C13</b>	1.909(1) 1.917(1)	1.913(1)	1.928(1) 1.928(1) 1.931(1) 1.936(1)	1.931(1)
<b>C14</b>	1.918(3) 1.921(3)	1.919(3)	1.932(3) 1.935(4) 1.935(3) 1.940(3)	1.935(3)
<b>C15</b>	1.896(4) 1.902(5)	1.899(5)	1.931(5) 1.932(5) 1.932(5) 1.936(5)	1.932(5)

Detailed analysis of those crystals shows similar coordination geometry for all complexes. Within the series of ligands, a slightly distorted octahedral geometry is found, showing slight differences in bond length caused by electronic influences of the ligands. The Fe-C<sub>carbene</sub> bond length is expected to shorten with increasing  $\sigma$ -donor strength of the carbene, considering the measurement errors, methylation of the imidazole ligand in 4-position have minor influences on the donor strength. Second methylation as well as enhancement of the  $\pi$ -system is leading to significant shorter bond length, based on the increased donor strength. Despite the differences in coordinating bond length the octahedral coordination geometry endures.

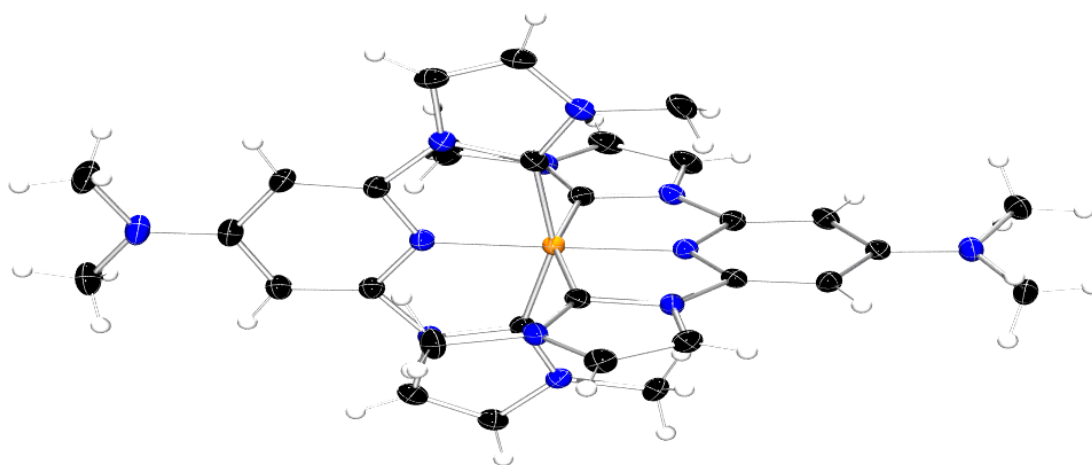


**Figure 4-3:** Single crystal structure of  $[\text{Fe}(\text{BIP}^{\text{NMe}_2})_2][\text{PF}_6]_2$  (C1) (ellipsoids with 50 % probability level)(counter ion omitted for clarity).

The crystal structure of  $[\text{Fe}(\text{BIP}^{\text{NMe}_2})_2][\text{PF}_6]_2$  (C1) is shown in **figure 4-3** and the distorted octahedral coordination is shown in magnified scale in **figure 4-4**, with simplification of

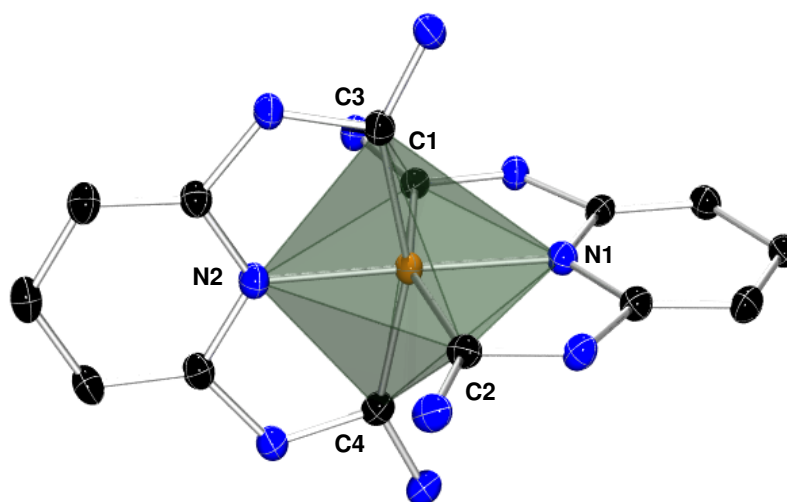


**Figure 4-4:** Enlarged coordination sphere of the iron center for  $[\text{Fe}(\text{BIP}^{\text{NMe}_2})_2][\text{PF}_6]_2$  (C1).

the ligand structure and a selection of the respective binding angles is summarized in **table 4-2**.

The observed distortion is caused by shorter Fe-C<sub>carbene</sub> bond lengths between the iron center and one ligand, while maintaining the same Fe-N<sub>pyridine</sub> distance. As listed in **table 4-2** the binding angles only slightly differ within the complex series regardless of the electronic differences of the ligands. As noted, the opposing nitrogen atoms are in line with a nearly perfect 180°-degree angle. Considering the maximum bond length and the consistent sp<sup>2</sup>-hybridized atoms laying in between the coordinating atoms a discrepancy of 22°-degree to the perfect octahedral geometry can be found inside the bite-angle between the two carbenes (C1-Fe-C2 or C3-Fe-C4). This variance to the perfect octahedral geometry can be reduced by extension of the ligand system. By insertion of additional atoms into the pyridine-imidazolylene bond the octahedral geometry can be improved with a transition from a 5- to 6-member chelate coordination. This has a large influence onto the photophysical properties of the complex.

**Table 4-2:** Selected coordinating binding angles for all analyzed iron complexes.

	<b>N1-Fe-N2</b>	<b>C1-Fe-C2</b>	<b>C3-Fe-C4</b>	<b>N2-Fe-C2</b>	<b>N1-Fe-C4</b>
<b>C1</b>	179.07(7)	157.68(8)	157.65(8)	101.18(8)	101.35(8)
<b>C2</b>	175.0(3)	156.81(19)	156.81(19)	97.79(1)	105.30(1)
<b>C3</b>	179.58(7)	158.17(7)	158.25(7)	100.74(7)	101.14(7)
<b>C4</b>	179.23(14)	157.74(15)	158.11(15)	100.62(14)	100.40(14)
<b>C6</b>	180.0(5)	158.7(4)	158.7(4)	100.7(2)	100.7(2)
<b>C7</b>	178.26(10)	158.72(13)	158.01(13)	102.54(11)	100.91(12)
<b>C9</b>	179.25(19)	158.4(2)	158.3(3)	101.9(2)	101.1(2)
<b>C12</b>	179.8(4)	156.4(3)	156.4(3)	101.6(3)	101.6(3)
<b>C13</b>	177.49(6)	158.47(7)	157.84(7)	99.03(7)	102.96(7)
<b>C14</b>	179.23(12)	157.43(14)	157.67(14)	101.33(13)	100.29(13)
<b>C15</b>	179.25(18)	158.26(19)	158.56(19)	100.13(19)	99.89(18)

The according strategy is applied by the groups of HEINZE and MCCUSKER using a methylamine or ethaneimine bridge in between the coordinating pyridines of polypyridine ligands. These extended ligands are used for the synthesis of chromium(II), ruthenium(II) and iron(II) complexes leading to an optimization of the octahedral geometry.<sup>113,125–127</sup>

The steric repulsion, causing rotation of the benzimidazole moiety in the pure ligand crystal structure, does not affect the binding properties of this enlarged ligand series of bicyclic carbenes. In **figure 4-5** the crystal structure of complex **C9** is shown since it differs the most from ligand **C1** in terms of the carbene moiety and the amine functionalization.

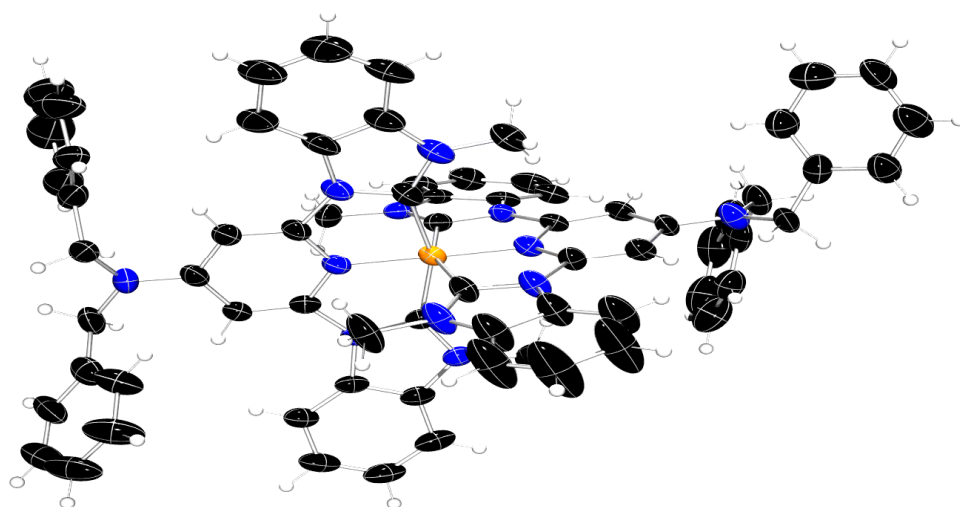


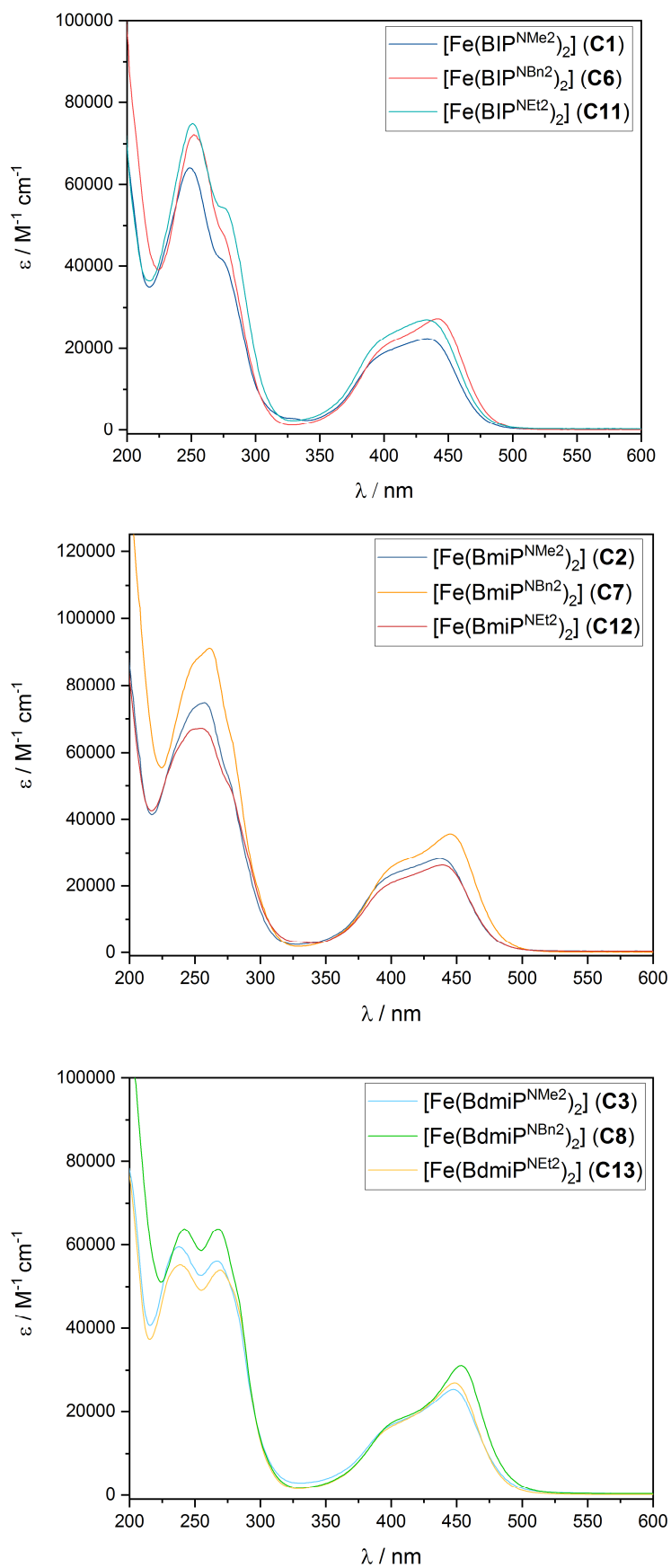
**Figure 4-5:** Single crystal structure of  $[\text{Fe}(\text{BbP}^{\text{NBn}2})_2][\text{PF}_6]_2$  (**C9**)(ellipsoids with 50 % probability level)(counter ion omitted for clarity).

The rotation of the benzyl ring system remains in a nearly orthogonal direction ( $88.17^\circ$  and  $85.85^\circ$ ) to the pyridine plane, with both ring systems inclined towards one another in a  $38^\circ$  angle. As observed, the iron center atom is bound closer to one of the ligands with  $\text{Fe}-\text{C}_{\text{carbene}}$  bond distances of  $1.924(5)$  and  $1.928(6)$  Å. The further bound ligand shows distances for the  $\text{Fe}-\text{C}_{\text{carbene}}$  bond of  $1.934(6)$  and  $1.948(6)$ , whereas the  $\text{Fe}-\text{N}_{\text{pyridine}}$  differs for both ligands in this complex, too. Throughout the whole complex series, the averaged  $\text{Fe}-\text{N}_{\text{pyridine}}$  distance varies from  $1.891(8)$  in complex **C6** to  $1.935(5)$  in complex **C12**, leading to differences in the averaged  $\text{Fe}-\text{C}_{\text{carbene}}$  bond length from  $1.917(6)$  in **C4** to  $1.971(8)$  in **C12** representing a deviation of  $0.06(2)$  Å.

### 4.3 Spectroscopic properties

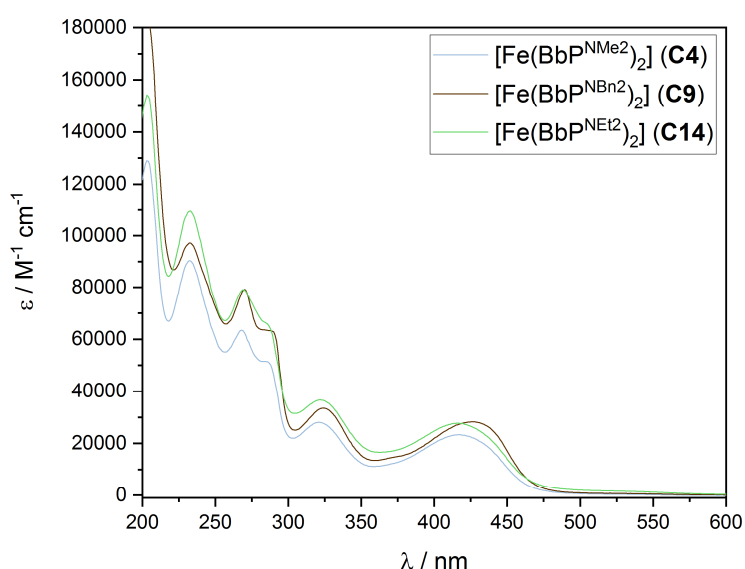
Because investigation of the photophysical properties by tuning the ligand system is a major goal of this thesis, all complexes are thoroughly investigated by UV/Vis-spectroscopy. The UV/Vis spectra are recorded at room temperature in acetonitrile

solutions with a concentration of  $1 \cdot 10^{-5}$  M. The complexes can be arranged in two groups according to their properties. Meaning a distribution of complexes containing monocyclic NHCs (**C1-C3**; **C6-C8**; **C11-C13**) or an extended  $\pi$ -system (**C4-C5**; **C9-C10**; **C14-C15**). A similar division based on different properties is not found in the pure ligand series. The optical different appearance is conspicuous due to the different colors of the complexes. In **figure 4-6** the UV/Vis spectra of the monocyclic NHC complexes are shown, whereby the complexes are plotted along with same NHC moieties. For all complexes the absorption spectra are composed of three main regions which is in line with similar complexes reported in the literature before (**table 4-3**).<sup>91,94,111</sup> The lowest energy feature, above 350 nm, is assigned to MLCT processes which consist of two independent transitions. For complexes with unfunctionalized ligands these transitions are usually asymmetric, with two to three separated maxima.<sup>95,98</sup> The lowest energy transition from 420-450 nm can be assigned to the Fe-pyridine charge transfer. Features at higher energies are allocated to the Fe-NHC charge transfer, usually around 380-420 nm. Due to the amine functionalization a decrease of the MLCT maxima splitting can be observed, leading to an indefinite differentiation between both transitions compared to unfunctionalized literature complexes.<sup>91</sup>



**Figure 4-6:** UV/Vis spectra of iron NHC-complexes containing monocyclic carbenes in acetonitrile at r.t.. Imidazole containing complexes (top); methylimidazole complexes (middle); dimethylimidazole complexes (bottom).

Since addition of an amine donor group onto the pyridine backbone leads to destabilization of the ligand  $\pi^*$ -energy level, a blueshift of the Fe-pyridine MLCT transition can be observed caused by the enlarged energy gap. As opposed to this, the carbenes are not affected by the increased electron density at the pyridine, leading to a similar energy position of the Fe-NHC MLCT transition as observed in unfunctionalized ligand complexes.<sup>91,99</sup> As a result band separation is decreased because the Fe-pyridine MLCT band shifts towards the Fe-NHC band. In general, an increased extinction coefficient can be observed for all dibenzyl amine functionalized complexes due to the increased  $\pi$ -system by the benzyl groups. Through methylation of the carbene backbone a change in the MLCT transition ratio between Fe-NHC and Fe-pyridine transition can be observed. For all imidazolydene complexes **[Fe(BIP<sup>NMe2</sup>)<sub>2</sub>] (C1)**, **[Fe(BIP<sup>NBn2</sup>)<sub>2</sub>] (C6)** and **[Fe(BIP<sup>NEt2</sup>)<sub>2</sub>] (C11)** the intensity ratio between both MLCT transitions is about 1:1, whereas the dimethylimidazole complexes **[Fe(BdmiP<sup>NMe2</sup>)<sub>2</sub>] (C3)**, **[Fe(BdmiP<sup>NBn2</sup>)<sub>2</sub>] (C8)** and **[Fe(BdmiP<sup>NEt2</sup>)<sub>2</sub>] (C13)** show an intensity ratio for both transitions of approximately 1:1.5. This means a significant change of the dipole moment within those transitions due to ligand methylation. Below 300 nm, intraligand transitions ( $\pi \rightarrow \pi^*$  and  $n \rightarrow \pi^*$ ) can be seen, whose intensity ratio is likewise affected by ligand methylation as well as the MLCT transitions. In the imidazole ligand series (**C1**, **C6**, **C11**) a second transition is visible as a shoulder at 275 nm. By first methylation of the ligand series (**C2**, **C7**, **C12**) the feature broadens, due to the increased intensity of the second feature. Second methylation is leading to two distinct features in the dimethylimidazole series (**C3**, **C8**, **C13**) with the same intensity. In the plain ligand series, the feature at approximately 275 nm is visible for all ligands, indicating the different influence on the iron center.



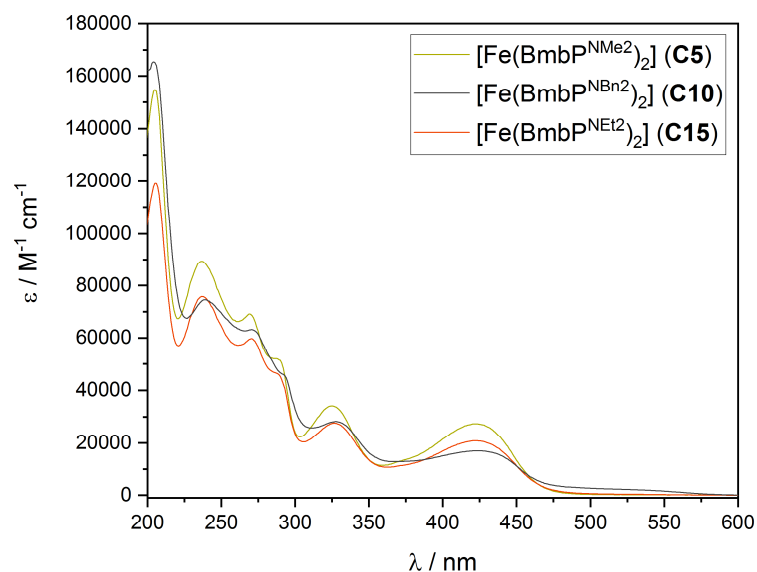


**Figure 4-7:** UV/Vis spectra of iron NHC-complexes containing carbenes with extended  $\pi$ -system in acetonitrile at r.t.. Benzimidazole containing complexes (top); dimethylbenzimidazole complexes (bottom).

The benzimidazole-2-ylidene and 5,6-dimethylbenzimidazole-2-ylidene complexes exhibit a distinct fine structure within their intra-ligand transitions ( $\pi \rightarrow \pi^*$  and  $n \rightarrow \pi^*$ ), with five pronounced features around 240 nm, 270 nm, 290 nm and 320 nm, which are assigned to the enlarged ligand  $\pi$ -system (**figure 4-7**). The MLCT energy feature is highly affected by the change from imidazolylidene to benzimidazolylidene showing no further splitting between the Fe-NHC and the Fe-pyridine transitions bands, resulting in one broad feature without fine structure. The MLCT maxima for both complex series are hypsochromic shifted by around 20 nm compared to the imidazole analogues, which is in line with literature known values and results from the electron accepting character of the benzimidazole-2-ylidenes.<sup>96</sup> Similar to the monocyclic carbene complexes, functionalization of the pyridine backbone leads to a shift of the Fe-pyridine band, explaining the appearance of the brought feature.

Due to all ligand variations, molar extinction coefficient values for the MLCT transitions differ in the 22000  $\text{M}^{-1} \text{cm}^{-1}$  to 35000  $\text{M}^{-1} \text{cm}^{-1}$  range. Comparison of the benzimidazolylidene complexes  $[\text{Fe}(\text{BbP}^{\text{NMe}_2})_2]$  (C4),  $[\text{Fe}(\text{BbP}^{\text{NBn}_2})_2]$  (C9) and  $[\text{Fe}(\text{BbP}^{\text{NEt}_2})_2]$  (C14) with their dimethylated analogues  $[\text{Fe}(\text{BmbP}^{\text{NMe}_2})_2]$  (C5),  $[\text{Fe}(\text{BmbP}^{\text{NBn}_2})_2]$  (C10) and  $[\text{Fe}(\text{BmbP}^{\text{NEt}_2})_2]$  (C15) show the same band structure, meaning a decreased influence of methylation to the ligand electronic structure as it is observed for the monocyclic carbenes.

**Table 4-3:** UV/Vis-data of homoleptic iron(II) complexes **C1-C15** in acetonitrile at r.t..

Complex	$\lambda$ [nm]	$\epsilon$ [ $M^{-1} \text{ cm}^{-1}$ ]
<b>C1</b> [Fe(BIP <sup>NMe2</sup> ) <sub>2</sub> ]	434, 249	22442, 64253
<b>C2</b> [Fe(BmiP <sup>NMe2</sup> ) <sub>2</sub> ]	436, 257	28163, 74668
<b>C3</b> [Fe(BdmiP <sup>NMe2</sup> ) <sub>2</sub> ]	447, 267, 238	25404, 56083, 59530
<b>C4</b> [Fe(BbP <sup>NMe2</sup> ) <sub>2</sub> ]	418, 321, 285, 268, 231, 202	23276, 28047, 51402, 63441, 90311, 128973
<b>C5</b> [Fe(BmbP <sup>NMe2</sup> ) <sub>2</sub> ]	422, 323, 289, 268, 236, 204	27311, 34094, 51625, 69145, 89349, 154815
<b>C6</b> [Fe(BIP <sup>NBn2</sup> ) <sub>2</sub> ]	442, 251	27264, 72235
<b>C7</b> [Fe(BmiP <sup>NBn2</sup> ) <sub>2</sub> ]	444, 260	35607, 91129
<b>C8</b> [Fe(BdmiP <sup>NBn2</sup> ) <sub>2</sub> ]	453, 268, 241	31077, 63784, 63877
<b>C9</b> [Fe(BbP <sup>NBn2</sup> ) <sub>2</sub> ]	426, 323, 287, 270, 233, 201	28224, 33524, 63290, 79267, 97203, 185406
<b>C10</b> [Fe(BmbP <sup>NBn2</sup> ) <sub>2</sub> ]	421, 326, 291, 270, 237, 203	16935, 28176, 45992, 63109, 74482, 165528
<b>C11</b> [Fe(BIP <sup>NEt2</sup> ) <sub>2</sub> ]	434, 251	26960, 74925
<b>C12</b> [Fe(BmiP <sup>NEt2</sup> ) <sub>2</sub> ]	438, 254	26203, 67119
<b>C13</b> [Fe(BdmiP <sup>NEt2</sup> ) <sub>2</sub> ]	449, 268, 238	26963, 53965, 55234
<b>C14</b> [Fe(BbP <sup>NEt2</sup> ) <sub>2</sub> ]	417, 322, 284, 270, 233, 203	27664, 36673, 66126, 78936, 109500, 154326
<b>C15</b> [Fe(BmbP <sup>NEt2</sup> ) <sub>2</sub> ]	423, 327, 289, 271, 236, 206	20838, 27554, 45903, 59615, 75871, 119040

In order to gain deeper insights into the electronic structure of the complexes, simulation of the lowest energy feature are carried out by DR. LUKAS BURKHARDT for a representative number of complexes (**figure 4-8**).<sup>128</sup> An overall good agreement between experimental and theoretical shift is observed for a majority of complexes except both benzimidazolydene compounds. Those compounds show a significant redshift in the computation when compared to the experimental spectra. An explanation for the systematic error regarding the benzimidazolydene complexes might be an increased static electron correlation, which is not adequately described by DFT.

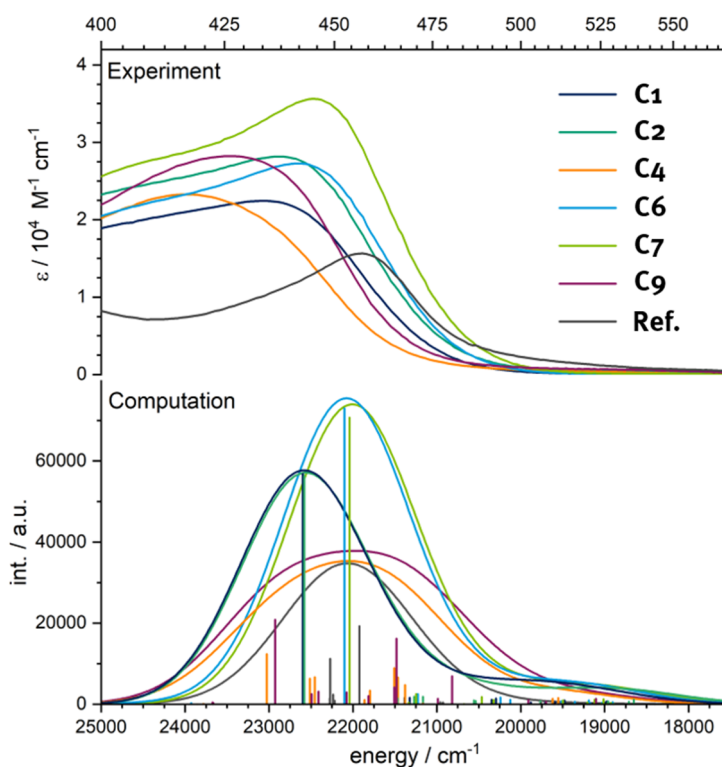


**Figure 4-8:** Experimental Vis spectra (top) in comparison with theoretical Vis spectra (bottom); TPSSh, D3BJ, def2-TZVPP, SMD (acetonitrile).<sup>128</sup>

For further detailed insights into the  $\pi$ -accepting character of the ligand series average Fe-3d populations of the bonding  $d\pi$  orbitals are analyzed. Because dimethylamine and dibenzylamine are representative for the maximal variability of the amine functionalization, the diethylamine complexes are excluded from this study. Like the approach for comparison of the optical absorption spectra, complexes with the same NHC moiety are compared to the respective unfunctionalized reference complex. The imidazolydene complexes  $[\text{Fe}(\text{BIP}^{\text{NMe}_2})_2]$  (C1) and  $[\text{Fe}(\text{BIP}^{\text{NBn}_2})_2]$  (C6) show a significant destabilization of all molecular levels when compared to the reference complex  $[\text{Fe}(\text{BIP})_2]$ . The electrostatic effect of the amine is mostly pronounced in a significant destabilization of the  $d\pi$  orbitals with z-character (figure 4-9) leading to a much smaller splitting within the  $d\pi$  orbitals.

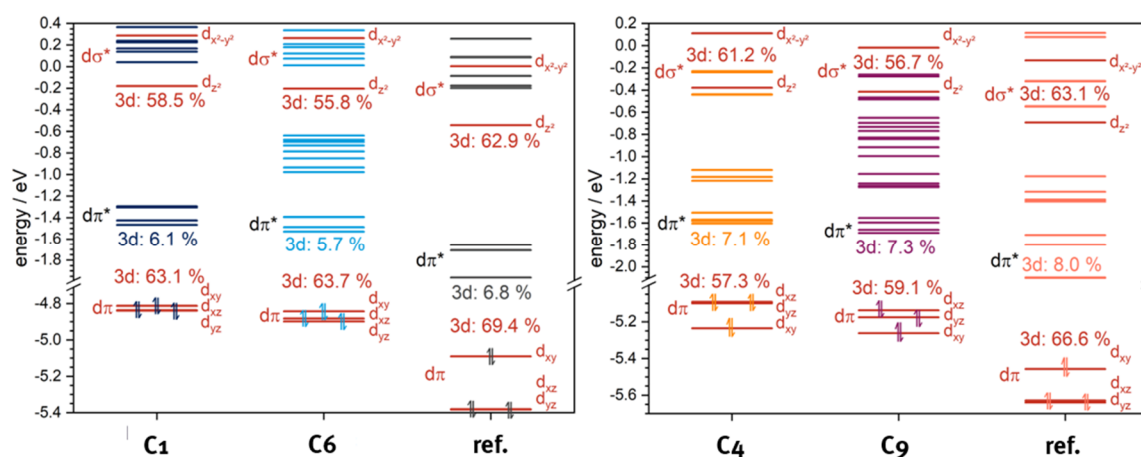


**Figure 4-9:** Molecular levels of imidazolydene and benzimidazolydene complexes compared to the respective unfunctionalized reference. TPSSH-D3; def2-TZVPP; SMD (acetonitrile).<sup>128</sup>

The opposite effect is observed for the antibonding  $d\pi^*$  orbitals, destabilizing the  $d_{z^2}$  less than the  $d_{xy}$  and  $d_{x^2-y^2}$ . This effect is even larger in the benzimidazolydene complex series resulting in an inverted order of the  $d\pi$  orbitals. The donating effect of the amine is further visible in the contribution of the 3d orbitals to the  $d\pi$  molecular orbitals, decreasing the Fe amount by circa 6 % from 69 % to 63 % in the imidazolydene case, and even stronger in the benzimidazolydene case from 66 % to roughly 59 %.

Since no luminescence can be observed for the complex series, transient absorption measurements are carried out to obtain information about the excited state dynamics. Therefore, in cooperation with the LOCHBRUNNER group, selected samples are measured in an acetonitrile solution to maintain the absorption conditions.

The time resolution of the ultrafast pump-probe spectroscopy is about 100 fs using excitation pulses centered at 450 nm and 400 nm. The transient spectra for the investigated complex series exhibit a very similar behavior. After optical excitation, intense negative signals are detected in the 380-480 nm area for all complexes, due to ground state bleaching (GSB). As it is seen in all spectra, the GSB echoes the MLCT absorption spectra and changes into positive signals above 480 nm corresponding to an excited state absorption (ESA). Similar to the UV/Vis spectra, comparison of the complexes is carried out for the same NHC moiety, therefore **figure 4-10** depicts the imidazolydene complexes **[Fe(BIP<sup>NMe2</sup>)<sub>2</sub>] (C1)** and **[Fe(BIP<sup>NBn2</sup>)<sub>2</sub>] (C6)**, complexes **[Fe(BmiP<sup>NMe2</sup>)<sub>2</sub>] (C2)** and **[Fe(BmiP<sup>NBn2</sup>)<sub>2</sub>] (C7)** are illustrated in **figure 4-11** and the benzimidazolydene complexes **[Fe(BbP<sup>NMe2</sup>)<sub>2</sub>] (C4)** and **[Fe(BbP<sup>NBn2</sup>)<sub>2</sub>] (C9)** are shown in **figure 4-12**. As a similarity, they are all showing two distinct time constants within the picosecond timescale.

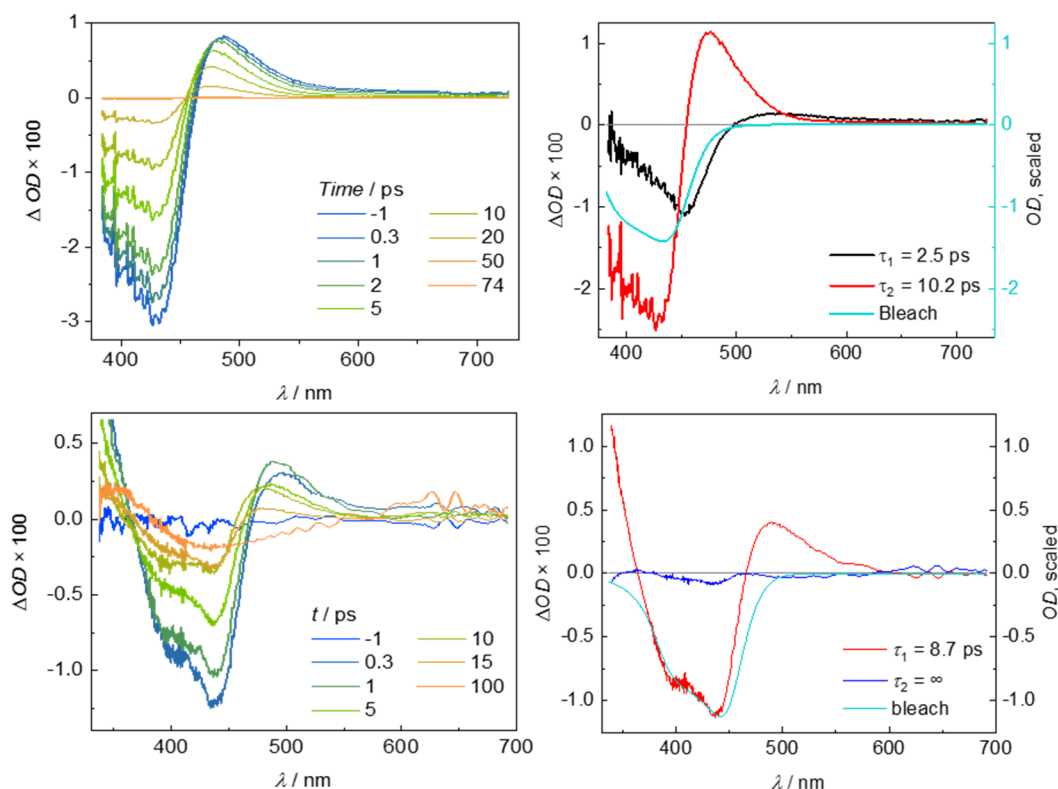


**Figure 4-10:** Transient absorption spectra (left) and decay associated amplitude spectra (right) with respective lifetimes of  $[\text{Fe}(\text{BIP}^{\text{NMe}_2})_2]$  (**C1**) (top) and  $[\text{Fe}(\text{BIP}^{\text{NBn}_2})_2]$  (**C6**) (bottom) with parallel polarization of excitation and retrieval pulse.<sup>128</sup>

By literature reports of GROS and HAACKE *et al.* a similar behavior is observed for imidazolydene and benzimidazolydene Fe(II) complexes.<sup>96,98</sup> In their case, two distinct time constants are detected, the first one is within a 100 fs scale which is assigned to an intersystem crossing from a direct populated hot <sup>3</sup>MLCT into a <sup>1</sup>MLCT. The second one is varying depending on the ligand framework from 10 to 26 ps, which is associated with the <sup>3</sup>MLCT lifetime, as it is described in **chapter 1.3.4**. These observations are confirmed by SUNDSTRÖM and WÄRNMARK *et al.* making the same interpretation for the unfunctionalized tridentate imidazolydene complex.<sup>91</sup> In our case the magnitude of the first time constant varies from 0.6 ps to 2.5 ps, which is too long for an ultrafast intersystem crossing. As an explanation this might be due to vibrational redistribution, which proceeds on such timescales and fits to the occurring shape of the decay associated spectra.<sup>129</sup> The first time-component for complex **C6** cannot be determined, because fitting with the amplitude spectra failed despite many attempts. The second and durable time constant, delineates the recovery of the GSB and contains the decay of the ESA. For all complexes investigated in this series the second time constant is around 10 ps fluctuating within 3 ps, the exact values for all complexes are summarized in **table 4-4**. This decay component is correlated to the <sup>3</sup>MLCT lifetime and appears to be less affected by ligand variation than it is reported before.<sup>91,95,98</sup>

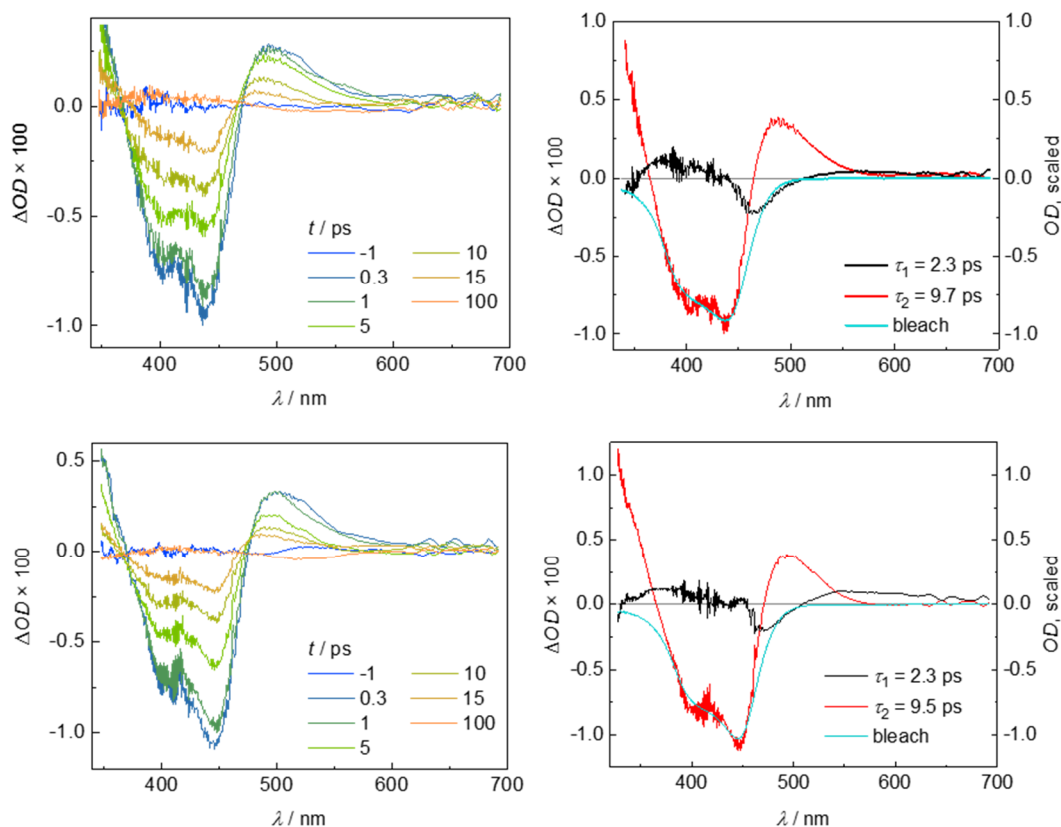


**Figure 4-11:** Transient absorption spectra (left) and decay associated amplitude spectra (right) with respective lifetimes of  $[\text{Fe}(\text{BmiP}^{\text{NMe}_2})_2]$  (C2) (top) and  $[\text{Fe}(\text{BmiP}^{\text{NBn}_2})_2]$  (C7) with parallel polarization of excitation and retrieval pulse.<sup>128</sup>

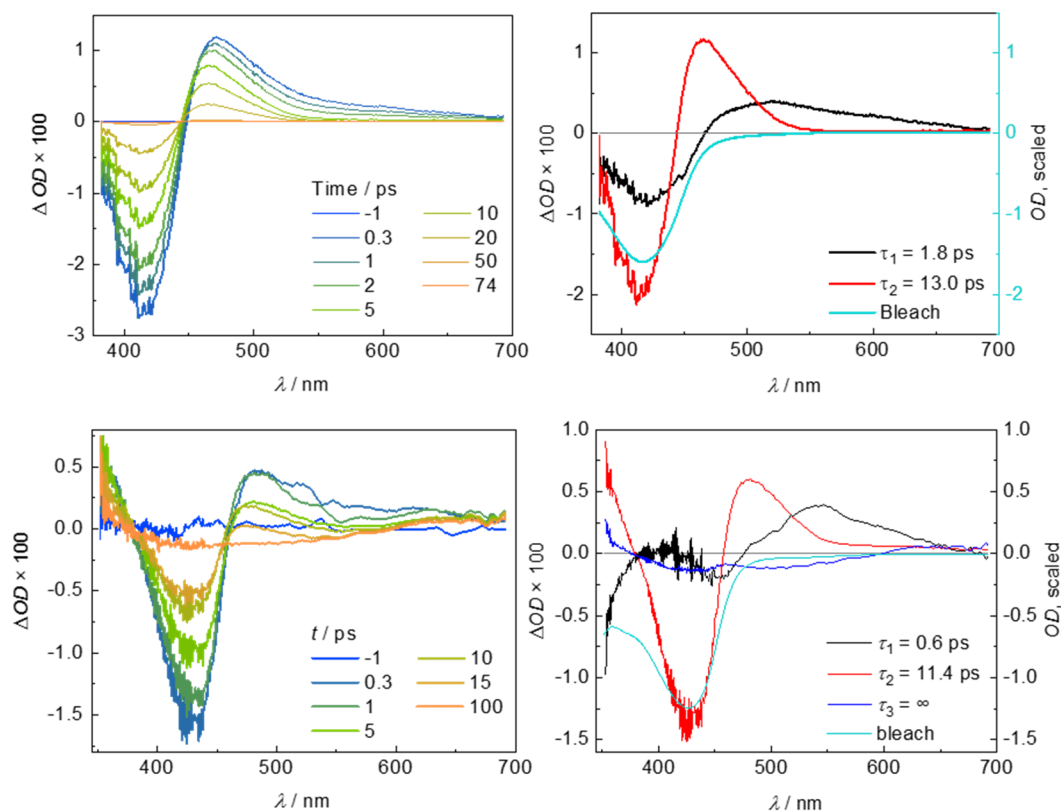


**Figure 4-12:** Transient absorption spectra (left) and decay associated amplitude spectra (right) with respective lifetimes of  $[\text{Fe}(\text{BbP}^{\text{NMe}_2})_2]$  (C4) (top) and  $[\text{Fe}(\text{BbP}^{\text{NBn}_2})_2]$  (C9) with parallel polarization of excitation and retrieval pulse.<sup>128</sup>

The effect of amine addition in the ligand backbone shows most influence on the  $^3\text{MLCT}$  lifetime of the benzimidazolylene complexes, (**figure 4-12**) which are determined by a fitting procedure with an uncertainty of  $\pm 0.5$  ps, decreasing them from 26 ps into almost half. For smaller ligand systems (**figure 4-10** and **4-11**) the influence of the amine can be neglected, revealing similar  $^3\text{MLCT}$  lifetimes as unfunctionalized complexes. Consequently, this indicates a dominating influence by the NHC moiety maintaining a catalytic active timeframe of 10 ps. Complex **C9** additionally shows a very long time-component which is attributed to fluctuation of the white light within this wavelength range. For an unequivocal assignment of the time constants, investigation of the redox properties is implemented, which is further elucidated in the following chapter.

**Table 4-4:** Obtained time constants from transient absorption spectroscopy for the iron complex series.

Complex	$\tau_1$ [ps]	$\tau_2$ [ps]
<b>C1</b> [Fe(BIP <sup>NMe2</sup> ) <sub>2</sub> ]	2.5 ( $\pm 0.5$ )	10.2 ( $\pm 0.5$ )
<b>C2</b> [Fe(BmiP <sup>NMe2</sup> ) <sub>2</sub> ]	2.3 ( $\pm 0.5$ )	9.7 ( $\pm 0.5$ )
<b>C4</b> [Fe(BbP <sup>NMe2</sup> ) <sub>2</sub> ]	1.8 ( $\pm 0.5$ )	13.0 ( $\pm 0.5$ )
<b>C6</b> [Fe(BIP <sup>NBn2</sup> ) <sub>2</sub> ]	-	8.7 ( $\pm 0.5$ )
<b>C7</b> [Fe(BmiP <sup>NBn2</sup> ) <sub>2</sub> ]	2.3 ( $\pm 0.5$ )	9.5 ( $\pm 0.5$ )
<b>C9</b> [Fe(BbP <sup>NBn2</sup> ) <sub>2</sub> ]	0.6 ( $\pm 0.5$ )	11.4 ( $\pm 0.5$ )

#### 4.4 Cyclic voltammetry

For all complexes electrochemical investigations are conducted in an acetonitrile solution using a concentration of 0.001 M. Tetrabutylammonium hexafluorophosphate ( $\text{Bu}_4\text{NPF}_6$ ) is used as supporting electrolyte with a concentration of 0.1 M. All redox potentials are referenced to the ferrocene/ferrocenium<sup>+</sup> ( $\text{Fc}/\text{Fc}^+$ ) redox couple as internal standard.

In general, the complex series reveals a similar electrochemical behavior, confirming the information obtained by UV/Vis spectroscopy. Almost all complexes are showing a reversible oxidation with  $E_{1/2}$  around 0 V and a second pseudo-reversible oxidation with an  $E_{1/2}$  around 1.3-1.6 V (**figure 4-13**). Within the complex series the first redox potential is considerably shifted towards lower potentials, compared to the unfunctionalized reference complex<sup>91,99</sup>, based on a reduced acceptor ability of the pyridine ring. As

explained in **chapter 3.6** no ligand reduction can be seen, which is also attributable to the amine donor. In a rough approximation, the electrochemical band gap ( $\Delta E_{gap} = E_{1/2ox} - E_{1/2red}$ ) of the reference complex is consulted, which has a value of 2.75 V.<sup>96</sup> Ignoring the influence of the amine donors on the band gap size and applying the known value of the reference to this system, the calculated reduction potential is about -2.77 V.

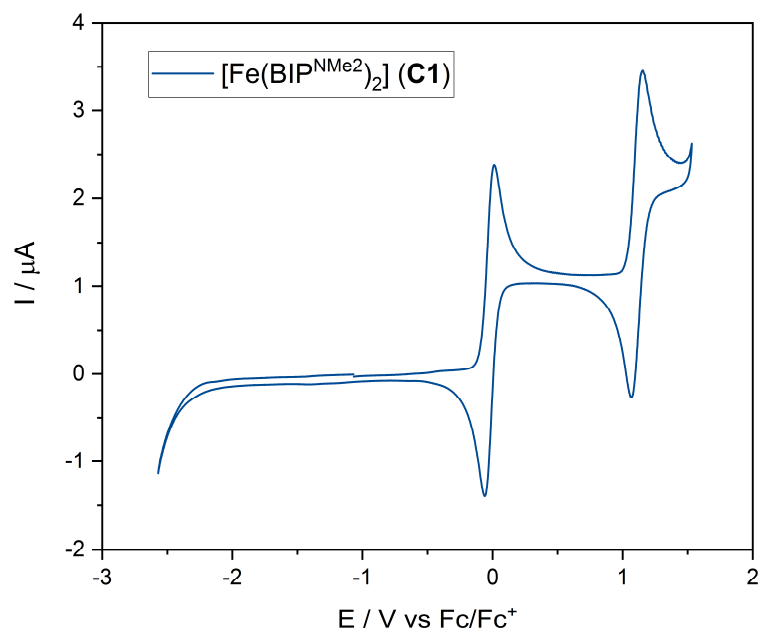


**Figure 4-13:** Total cyclic voltammogram of complex **C1** in acetonitrile at 25 °C ( $v = 100 \text{ mV s}^{-1}$ ).

Since amine functionalization leads to a decreased acceptor ability of the pyridine ring, and therefore an increased electron density at the iron center the shift of the redox potential within one functionalization class is directly attributable to the donor strength of the carbene moiety, like it is shown in **figure 4-14** for complexes **C1-C5**. With complex **C1** showing its first reversible oxidation at  $E_{1/2} = -0.02 \text{ V}$  and a peak separation between oxidation- and reduction potential of 69 mV, corresponding to the  $\text{Fe}^{\text{II}}/\text{Fe}^{\text{III}}$  crossover, methylation of the carbene backbone leads to an increased donor strength, shifting the first redox event to further negative values for complex **C2** ( $E_{1/2} = -0.06 \text{ V}$ ) and even further for complex **C3** ( $E_{1/2} = -0.13 \text{ V}$ ). Analysis of the redox event via the RANDLES-SEVCIK equation<sup>130,131</sup> by plotting the linear dependence of the forward current peak  $I_{pa}$  versus the square root of  $v$  reveal perfect reversibility for the whole complex series (**figure 4-15**). Complexes **C4** and **C5** with an enlarged  $\pi$ - system reveal more positive redox potentials, due to the known acceptor ability of the carbene moiety.<sup>132-136</sup> Similar to the monocyclic carbenes a slight shift to further negative potentials is observed from benzimidazole to dimethylbenzimidazole. Alike the observation made for the NMR signals, the shift is less pronounced as seen for the smaller ligands, due to the overall smaller effect of the methylene groups to the larger system.

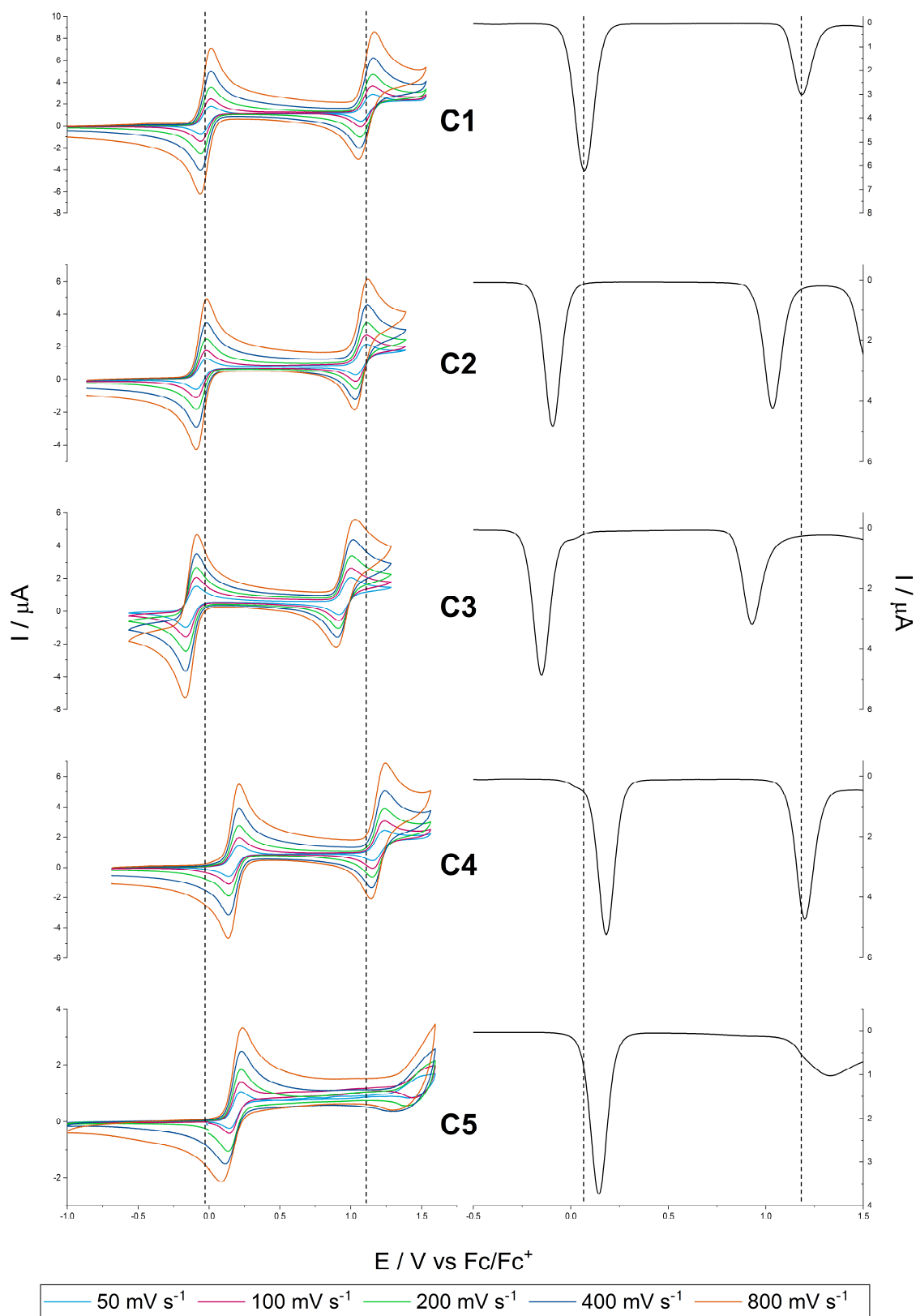


**Figure 4-14:** Cyclic voltammograms at different scan rates (left) and square-wave voltammograms (right) of complexes **C1 - C5** in acetonitrile at 25 °C.

The overall decreased redox potential of the Fe<sup>II/III</sup> couple allows a fast oxidation into the Fe<sup>III</sup> state, which likewise enables an efficient electron transfer as it is desired for photocatalytic applications. Unfortunately, the ligand class is less suitable for reception of an electron, limiting the use of amine functionalized complexes to multi-component-systems. Alternatively, amine functionalized ligands could act as donating part in a heteroleptic push-pull complex, which would benefit from the donating effect of the amine by predetermining the direction of the electron transfer alongside the pull-component. As a result of the diminished reduction potential, analysis of the transient absorption signal via differential spectra obtained by spectro-electrochemistry is impossible. Since the analyzed MLCT transition, denotes a formal oxidation of the metal center and a formal reduction of the ligand, comparison of the transient signal with the generated differential spectra can be clear proof for the proceeding event to its respective time constant. In case of the amine complexes, process - time constant assignment is realized based on empirical knowledge due to several measurements on similar complexes.

The second irreversible oxidation event for complex **C1** is observed at  $E_{1/2} = 1.11$  V with a peak separation of 85 mV and is presumably assigned with the Fe<sup>III</sup>/Fe<sup>IV</sup> oxidation couple. This oxidation event features the same trend as observed for the Fe<sup>II/III</sup> couple for the monocyclic carbene series but shows an exception in the bicyclic series with **C4** being the only complex showing this behavior and complex **C5**, whose second oxidation event is rather inconclusive.

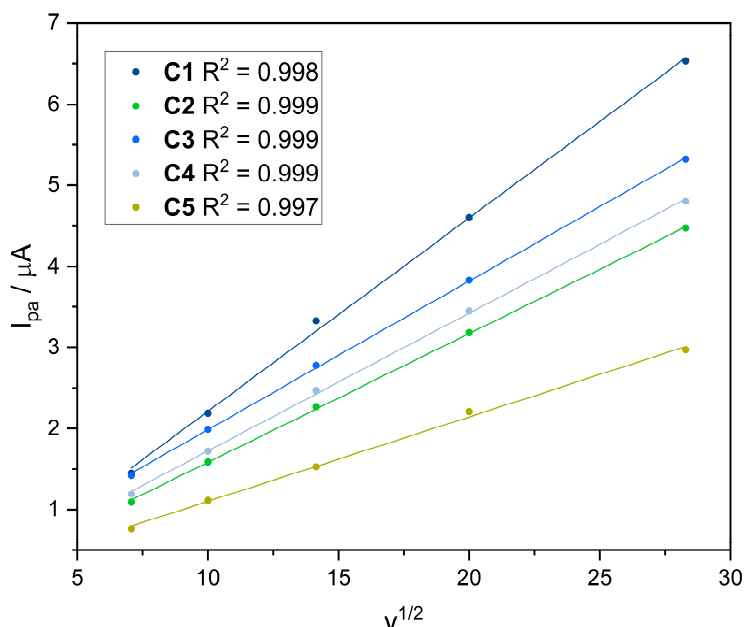


**Figure 4-15:** Randles-Sevcik plot for the first redox event of complexes **C1-C5**.

The half step potentials for all complexes are summarized in **table 4-5** and **4-6** showing slight influence of the amine functionalization. Within all ligand series, the observed trend

which is explained for the dimethylamine group in **figure 4-13** endures. Among the three kinds of different amines, the diethylamine reveals to inhabit the highest donor potential presumably due to the increased positive inductive effect of the ethyl group compared to the methylene group, leads to the most negative redox potentials. In turn, the dibenzylamine series shows the most positive redox potentials for the Fe<sup>II/III</sup> event, supposedly caused by a negative inductive effect and the resulting increased acceptor ability of the pyridine ring.

**Table 4-5:** Electrochemical data for iron NHC-complexes containing monocyclic carbenes in acetonitrile at r.t.. ( $\nu = 100 \text{ mV s}^{-1}$ ).

Complex	$E_{1/2} (\text{Fe}^{\text{II}}/\text{Fe}^{\text{III}})$ [V]	$\Delta E$ [mV]	$E_{1/2} \text{Ox}_{\text{II}}$ [V]	$\Delta E$ [mV]
<b>C1</b>	-0.02	69	1.11	85
<b>C2</b>	-0.06	68	1.05	166
<b>C3</b>	-0.12	68	0.95	87
<b>C6</b>	0.03	68	1.19	104
<b>C7</b>	-0.03	68	1.12	91
<b>C8</b>	-0.08	71	1.10	186
<b>C11</b>	-0.04	75	1.12	218
<b>C12</b>	-0.09	70		
<b>C13</b>	-0.13	73	0.97	168

**Table 4-6:** Electrochemical data for iron NHC-complexes containing bicyclic carbenes in acetonitrile at r.t. ( $\nu = 100 \text{ mV s}^{-1}$ ).

Complex	$E_{1/2} (\text{Fe}^{\text{II}}/\text{Fe}^{\text{III}})$ [V]	$\Delta E$ [mV]	$E_{1/2} \text{Ox}_{\text{II}}$ [V]	$\Delta E$ [mV]
<b>C4</b>	0.18	70	1.19	82
<b>C5</b>	0.12	60	-	-
<b>C9</b>	0.26	65	-	-
<b>C10</b>	0.22	77	-	-
<b>C14</b>	0.17	86	-	-
<b>C15</b>	0.11	78		

Change of the optical absorption related to the different oxidation states are revealed by spectro-electrochemical investigations of  $[\text{Fe}(\text{BIP}^{\text{NMe}_2})_2]$  (**C1**). For this purpose, an adequate voltage is applied to the complex solution, while UV/Vis spectra are detected simultaneously. For  $[\text{Fe}(\text{BIP}^{\text{NMe}_2})_2]$  (**C1**) the first oxidation event is investigated, using a voltage of 0.25 V (**fig. 4-14 (top)**) and -0.25 V for the respective reduction. As a result of electrolysis, the initial absorption spectra (**fig. 4-16 (red line)**) alters, shifting the intraligand transitions to higher energies in the  $\text{Fe}^{\text{III}}$  state. Additionally, a ligand to metal charge transfer (LMCT) band occurs in the 600 to 800 nm range. During the oxidation process, the analyte solution consistently becomes darker, because of the emerging LMCT transition, turning the solution color deep blue in the pure  $\text{Fe}^{\text{III}}$  state. Verification as well as a further characterization of the  $\text{Fe}^{\text{III}}$  species is described in **chapter 4.5**. Electrolysis using a voltage of 1.8 V generates an instable species, whose origin is expected to be the  $\text{Fe}^{\text{IV}}$  state. The intraligand transitions of the former  $\text{Fe}^{\text{III}}$  absorption spectra (**fig. 4-16 (bottom (blue line))**) are further redshifted, whereas the LMCT transition shifts into the near IR area.

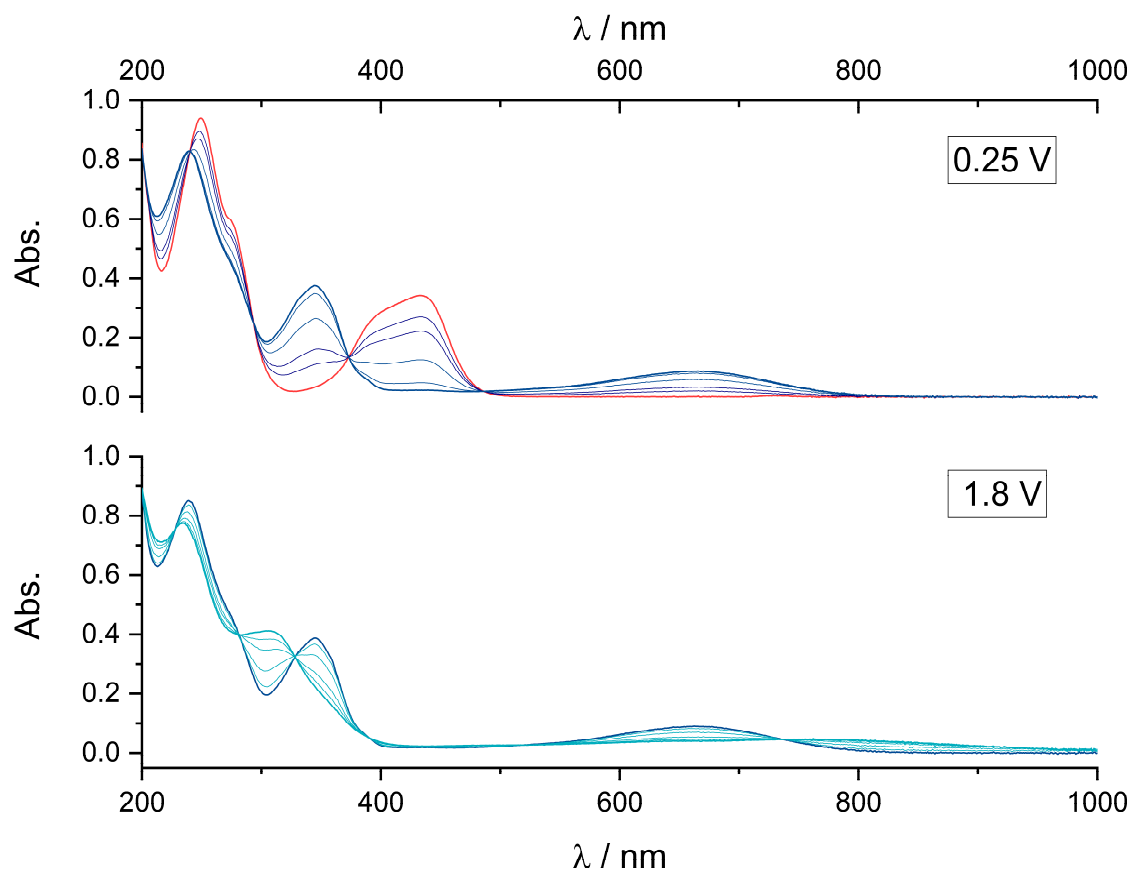


**Figure 4-16:** Change of the UV/Vis spectra during electrolysis of **C1** with an applied potential of 0.25 V (top) and 1.8 V (bottom).

This indicates the existence of an Fe<sup>IV</sup> species rather than oxidation of the ligand since no redox event is observed for pure ligand compounds. To clarify this issue, experiments are planned using X-ray emission spectroscopy while simultaneously applying a voltage to investigate the effect to the iron species. After complete electrolysis into this state, no reversible reduction can be realized which indicates a decomposition of the complex.

#### 4.5 Fe(III) complexes

In order to gain further information about the iron(III) species, isolation of the oxidized complexes is necessary. However, synthesis of the complex by using a Fe(III) precursor like FeCl<sub>3</sub> under the same reaction conditions leads to the respective Fe(II)-NHC complex due to the reductive effect of the free carbenes during complexation. Therefore chemical oxidation of the Fe(II) complex is conducted using three equivalents of NOPF<sub>6</sub> in an acetonitrile solution under inert conditions. The excess of NOPF<sub>6</sub> is necessary since stoichiometric use of the oxidizing agent only lead to partially oxidized reaction product. After addition of the NOPF<sub>6</sub> a spontaneous color change indicates the successful reaction. For purification of the obtained complex the solvent is removed, and the raw complex material is washed with dichloromethane. The higher charge of the Fe<sup>3+</sup> complex engenders a non-solubility in dichloromethane whereby the side products are sluiced out. Since the Fe(III) species is paramagnetic, conventional NMR spectroscopy is no longer suitable. But use of the EVANS method<sup>137–139</sup> allows determination of the effective magnetic moment  $\mu_{eff}$  and the quantity of unpaired electrons  $n$ .

**Table 4-7:**  $\mu_{eff}$  and  $n$  values for the investigated Fe(III) complexes.

	<b>Complex</b>	$\mu_{eff}$	$n$
<b>C1</b>	[Fe(III)(BIP <sup>NMe2</sup> ) <sub>2</sub> ]	2.24 ± 0.03	1.45 ± 0.04
<b>C2</b>	[Fe(III)(BmIP <sup>NMe2</sup> ) <sub>2</sub> ]	2.48 ± 0.06	1.68 ± 0.05
<b>C5</b>	[Fe(III)(BmbP <sup>NMe2</sup> ) <sub>2</sub> ]	2.27 ± 0.12	1.48 ± 0.09
<b>C6</b>	[Fe(III)(BIP <sup>NBn2</sup> ) <sub>2</sub> ]	2.36 ± 0.08	1.56 ± 0.06
<b>C8</b>	[Fe(III)(BdmiP <sup>NBn2</sup> ) <sub>2</sub> ]	1.81 ± 0.14	1.07 ± 0.12
<b>C12</b>	[Fe(III)(BmiP <sup>NEt2</sup> ) <sub>2</sub> ]	1.80 ± 0.08	1.08 ± 0.06
<b>C14</b>	[Fe(III)(BbP <sup>NEt2</sup> ) <sub>2</sub> ]	2.10 ± 0.10	1.32 ± 0.7

Under the assumption of maintained coordination geometry either a high-spin complex with five unpaired electrons or a low-spin complex with one unpaired electron exists, which is more likely due to the unchanged ligand field and the former existent Fe(II) ( $d^6$ ) low-spin complex. This assumption is verified by the obtained values for  $\mu_{eff}$  and  $n$  through the whole investigated series (**table 4-7**), although the obtained values are consistently larger than the theoretically expected value ( $\mu_{eff} = 1.73$ )<sup>140,141</sup> this behavior is explained by the distortion of the coordination geometry, which is observed and discussed in **chapter 4-2**. By investigation of the Fe(II) species using spectro-electrochemical monitoring, an impression of the absorption properties of the Fe(III) species can be obtained. For a deeper analysis and comparison of both species, UV/Vis spectra are recorded using the isolated Fe(III) compounds obtained by chemical oxidation. As an example the acquired spectra for **[Fe(III)(BIP<sup>NMe2</sup>)<sub>2</sub>][PF<sub>6</sub>]<sub>3</sub> (C1)** and **[Fe(III)(BbP<sup>NMe2</sup>)<sub>2</sub>][PF<sub>6</sub>]<sub>3</sub> (C4)** are shown in **figure 4-17**.

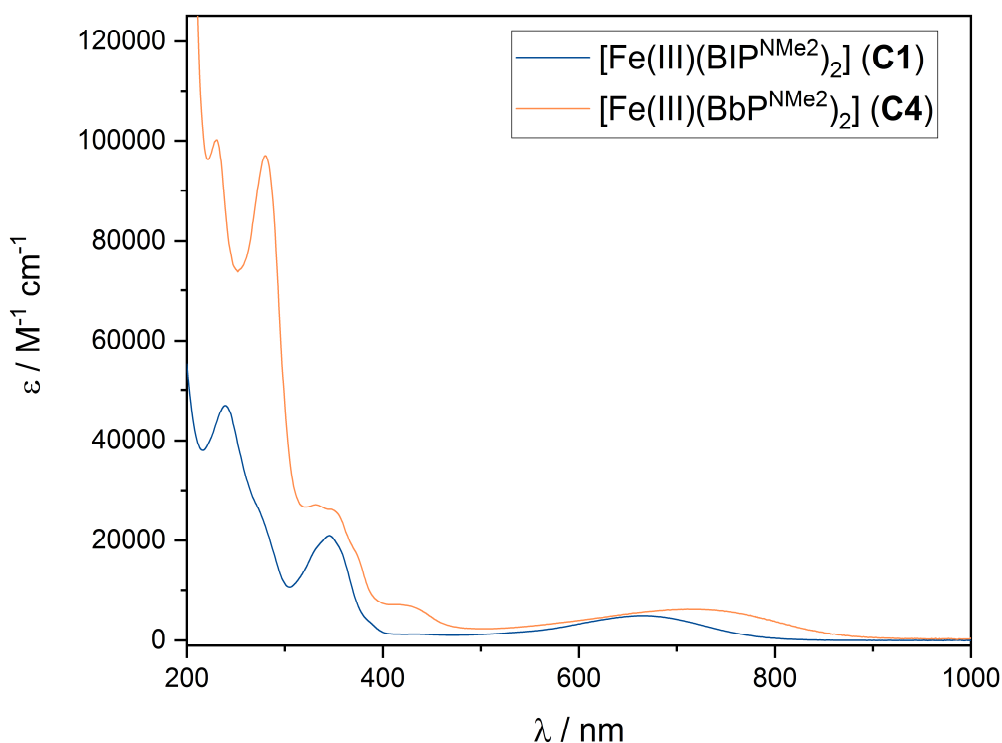


**Figure 4-17:** UV/Vis spectra of **[Fe(III)(BIP<sup>NMe2</sup>)<sub>2</sub>][PF<sub>6</sub>]<sub>3</sub> (C1)** and **[Fe(III)(BbP<sup>NMe2</sup>)<sub>2</sub>][PF<sub>6</sub>]<sub>3</sub> (C4)** in acetonitrile at r.t..

As a result, the UV/Vis spectra of the isolated Fe(III) species show a similar behavior as observed in spectro-electrochemistry experiments starting from Fe(II). The lowest energy transition is observed around 650 nm for monocyclic carbenes and around 710 nm for the investigated enlarged carbene complex. The former hypsochromic shift, which is observed in the Fe(II) species when changing the ligand from imidazole to benzimidazole, is reversed into a bathochromic shift of around 50 nm. The generated LMCT transition

( $\pi \rightarrow t_{2g}$ ), which is enabled due to the partial occupied  $t_{2g}$ -orbital of the  $d^5$  complex, shows a broad absorption range of 500-800 nm for **C1** with an absorption maximum at 665 nm and an even further range from 500-900 nm for **C4** with its maximum at 715 nm. Below 500 nm the observed changes match the known shifts by spectro-electrochemical investigation, shifting the intraligand transitions ( $\pi \rightarrow \pi^*$  and  $n \rightarrow \pi^*$ ) to lower wavelengths.

The extinction coefficient of the LMCT transition shows values around  $5000 \text{ M}^{-1} \text{ cm}^{-1}$ , which represents an expectable decrease compared to the MLCT transitions. The observed UV/Vis data for the investigated iron(III) complexes are shown in **table 4-8**.

**Table 4-8:** UV/Vis-data of selected homoleptic iron(III) complexes in acetonitrile at r.t.

	Complex	$\lambda$ [nm]	$\epsilon$ [ $\text{M}^{-1} \text{cm}^{-1}$ ]
<b>C1</b>	[Fe(III)(BIP <sup>NMe2</sup> ) <sub>2</sub> ][PF <sub>6</sub> ] <sub>3</sub>	665, 345, 237	4828, 20954, 46862
<b>C2</b>	[Fe(III)(BmiP <sup>NMe2</sup> ) <sub>2</sub> ][PF <sub>6</sub> ] <sub>3</sub>	652, 345, 258(sh), 234	6307, 30599, 53498, 65152
<b>C4</b>	[Fe(III)(BbP <sup>NMe2</sup> ) <sub>2</sub> ][PF <sub>6</sub> ] <sub>3</sub>	712, 420, 335, 279, 231, 202	6111, 6979, 26956, 97123, 100154, 180349
<b>C5</b>	[Fe(III)(BmbP <sup>NMe2</sup> ) <sub>2</sub> ][PF <sub>6</sub> ] <sub>3</sub>	701, 283, 204	4087, 85700, 160306
<b>C6</b>	[Fe(III)(BIP <sup>NBn2</sup> ) <sub>2</sub> ][PF <sub>6</sub> ] <sub>3</sub>	649, 345, 242	7136, 32833, 66820
<b>C8</b>	[Fe(III)(BdmIP <sup>NBn2</sup> ) <sub>2</sub> ][PF <sub>6</sub> ] <sub>3</sub>	629, 346, 270	5162, 22163, 73745
<b>C12</b>	[Fe(III)(BmIP <sup>NEt2</sup> ) <sub>2</sub> ][PF <sub>6</sub> ] <sub>3</sub>	655, 356, 252	4076, 15966, 56936
<b>C14</b>	[Fe(III)(BbP <sup>NEt2</sup> ) <sub>2</sub> ][PF <sub>6</sub> ] <sub>3</sub>	720, 272, 201	3675, 90380, 169116

## 4.6 pH dependency

In course of the conducted experiments, the iron complex series show a noticeable demeanor versus pH changes. Addition of acid lead to the formation of a sensitive red species, which slowly turns blue within hours. Since a blue color is assigned to the oxidized Fe(III) species, UV/Vis spectra are recorded comparing the final state of the acid induced transformation with the validated Fe(III) compounds by chemical oxidation and

spectro-electrochemical measurements (**figure 4-18**). As a result the induced transformation lead to the formation of the known Fe(III) species. To further understand the process of pH induced oxidation and foregone induced red species UV/Vis spectroscopic analysis is executed under inert conditions. Therefore, the analyzed stock solution as well as a diluted solution of trifluoromethane sulfuric acid is prepared using a glove box.

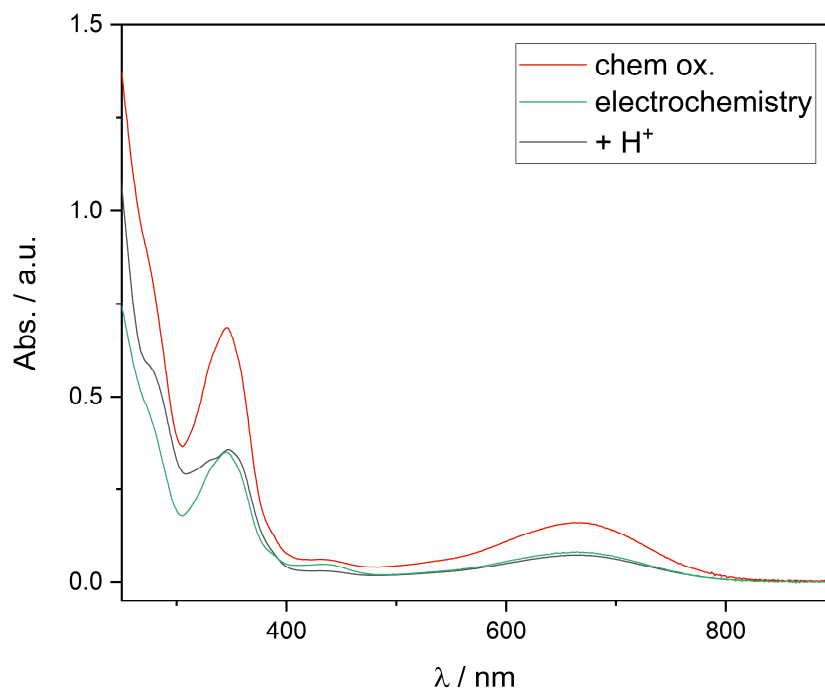


**Figure 4-18:** Obtained Fe(III) UV/Vis spectra by different oxidation methods in MeCN at r.t..

To exclude the possibility of time-resolved changes in the spectra, a plethora is measured for each equivalent of acid namely, right after addition, 2 minutes after addition and 10 minutes after addition. Since this acid-base reaction is expected to happen very fast, to that point the system shall be in an equilibrium. The resulting UV/Vis spectra are shown in **figure 4-19**, revealing a direct correlation with the added amount of acid. As it can be seen, a constant decrease of the former MLCT band intensity occurs, leading to a segregation into transitions with different maxima. With increasing amount of acid protonation of the amine function is becoming more likely, leading to an additional splitting of the MLCT transition band, revealing three distinct MLCT features. A bathochromic shift of the most intensive MLCT transition shifting the maximum from 433 nm to 481 nm is observed and is an explanation for the red color of the sample solution. Additionally, a decrease of the original MLCT transition is observed showing one maximum at 416 nm and a further transition at 350 nm. As known from the literature electron withdrawing groups like a carboxylic acids induce a significant bathochromic shift of the MLCT transition band, which is observed here to a smaller lesser extent.<sup>96,98,99,111</sup> Because the appearance of three MLCT transitions is unusual and unexpected in case of a twofold

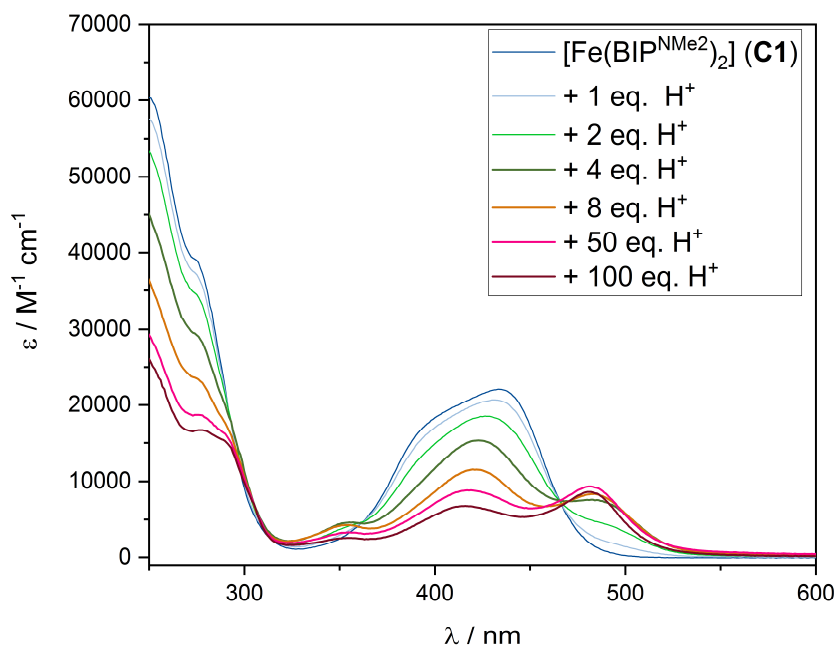


**Figure 4-19:** Alteration of the UV/Vis absorption of **C1<sup>+</sup>** after addition of various equivalents of acid.

protonation, UV/Vis spectra are simulated by DFT methods from DR. P. MÜLLER, for the simple and twofold protonation scenario (**figure 4-20**). As a result of the calculation, a high agreement of the experimental UV/Vis spectra is found with the calculated spectra for the simple protonated species. Both UV/Vis spectra are shown in **figure 4-20**, whereby the energy scale of the calculated spectra is shifted by 30 nm to match the experimental energy scale.

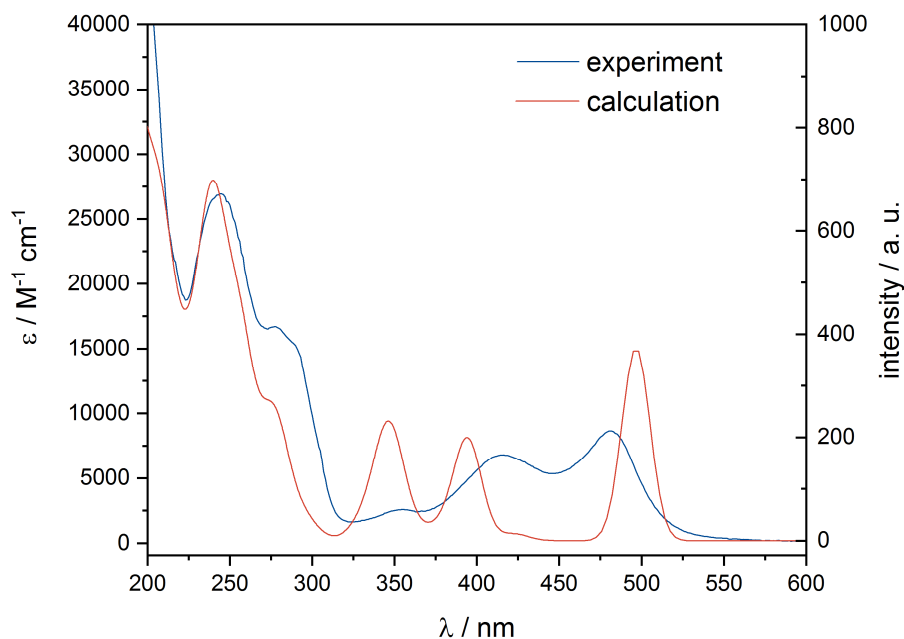


**Figure 4-20:** Experimental UV/Vis spectra and calculation for singular protonated species of **C1<sup>+</sup>** (theoretical scale is adjusted by -30 nm for a better agreement).

The UV/Vis of the terminal state reveals impressive similarities with the former mentioned complex with EWG-functionalized ligands, presumably due to the formation of a  $-NMe_2^+$  moiety.<sup>96,98,99</sup> The shift of the lowest energy MLCT transition induced by protonation overcompensates the initial hypsochromic shift induced by the amine functionality, leading to a bathochromic shift of 20 nm when compared to the complex with unfunctionalized ligands. It shall not go unmentioned, that functionalization by a pure EWG like the carboxylic group still exceeds this shift, showing its MLCT maxima at 520 nm.<sup>96</sup> But the diversity initiated by the amine group, allowing both donation and acceptance of electron density is a new feature in this complex class.

Albeit the sample solutions are prepared in a glove box, the oxidation process still occurs within a couple of hours. Presumably, this is due to a slow oxidation by molecular oxygen which is reported before for iron(II) complexes.<sup>142</sup> This hypothesis is supported by monitoring of the oxidation with simultaneous head space analysis of the gas-phase. As an observation, the oxidation happens faster, the more oxygen can be monitored in the gas phase. The heightened oxidation sensitivity in the protonated state, is somewhat surprising, as the induced acceptor feature shall lead to an increased oxidation potential, as it is shown for carboxylic acid functionalized complexes.<sup>98,111</sup> To understand the mechanism and the influence of the protonation onto the ligand and the respective shift of the oxidation potential, experiments are planned monitoring the redox potential during protonation via cyclic voltammetry. As a major disadvantage of this ligand class, the ligand reduction potential is shifted outside the visible potential range, which prevents monitoring of both redox events during protonation. Therefore, the ligand class shall be modified by less donating substituents, shifting the ligand reduction potential back into the visible range and enabling an *in-situ* monitoring of the potential shifts.

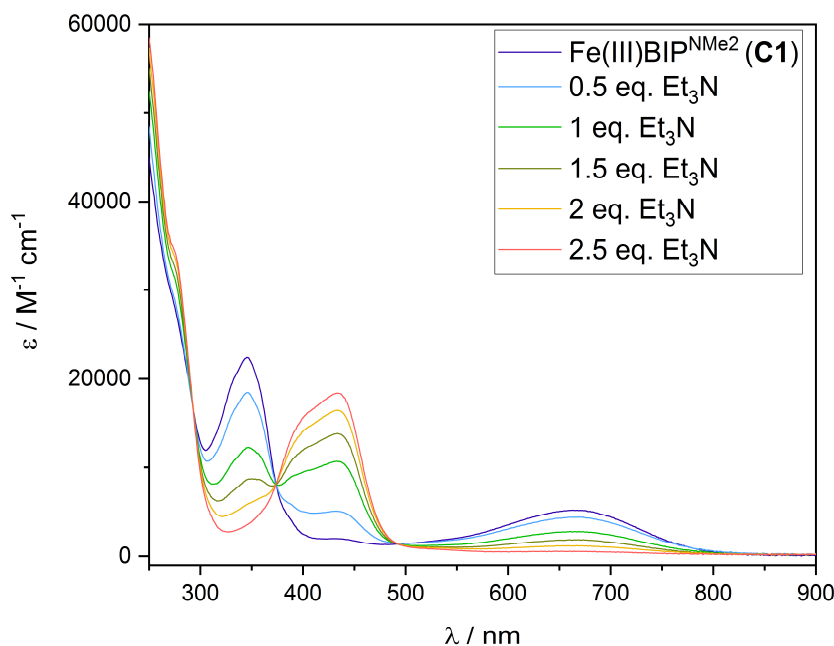


**Figure 4-21:** Alteration of the UV/vis spectra of **Fe(III)BIP<sup>NMe2</sup>** after addition of TEA in MeCN at r.t..

The severe protonation of the amine function becomes explicit, as the chemical oxidized Fe(III) species is investigated concerning the reduction ability. The implemented experiment for protonation is repeated under reversed conditions, using **[Fe(III)(BIP<sup>NMe2</sup>)<sub>2</sub>]** (**C1**) as starting material and adding specified amounts of a Et<sub>3</sub>N stock-solution (**figure 4-21**). As a result, complex reduction can be observed starting from addition of 0.5 eq Et<sub>3</sub>N. The reduction occurs to happen significantly faster, with total conversion in the Fe(II) state after adding a slight excess of base. The observed change in the UV/Vis spectra exactly match the results of chronoamperometric reduction.

## 4.7 X-Ray emission spectroscopy

To gain further insides, the complex series is investigated using X-ray emission spectroscopy. This technique is based on the excitation of an electron from a core state by a X-ray photon beam. As a result, the vacancy can be filled by an electron from different higher level. The radiative decay leads to emission of photons, which comprise information on the electronic structure depending on their origin. Classification of those emissions is implemented regarding the energy of the relaxation.

The lowest energy emission originates from the  $2p \rightarrow 1s$  and is called  $K\alpha$ . As a result of the low energy gap between excited and emissive states, the transition dipole moment is large and this emission reveals the highest intensity. Due to practical reasons, the used transition is the so called  $K\beta$  emission which is generated by the  $3p \rightarrow 1s$  transition. The

$K\beta$  exhibits two prominent spectral features. The intense higher energy feature is called  $K\beta_{1,3}$  and a weaker  $K\beta'$  signal, which is induced through 3p-3d exchange interaction. This exchange interaction increases by increasing number of unpaired electrons, resulting in a pronounced splitting of both features in a  $d^5$  high-spin complex. Nonetheless, the  $K\beta_{1,3}$  feature reveals information about the complexes itself, like oxidation state via the energy shift or covalency. While before mentioned transitions describe Core-to-Core (CtC) processes, the third occurring energy transition involves the valence orbitals, in example a Valence-to-Core (VtC) relaxation. This spectral feature describes the  $HOMO \rightarrow 1s$  transition and gives structural information due to direct ligand involvement. As mentioned before, the use of  $K\beta$  emission is preferred compared  $K\alpha$  emission, despite the lower intensity for practical reasons. Since the energy gap between the  $K\alpha$  and VtC is larger than between  $K\beta$  and the VtC, the latter ones are measurable within one experimental setup.

As an experimental approach the measurements are conducted in acetonitrile solutions with an approximate concentration of  $5 \cdot 10^{-3}$  mol/L. The spectra are recorded either at beamline P64 at the *Deutsche Elektronen Synchrotron* (DESY) in Hamburg or at beamline ID26 at the *European Synchrotron Radiation Facility* (ESRF) in Grenoble, France.

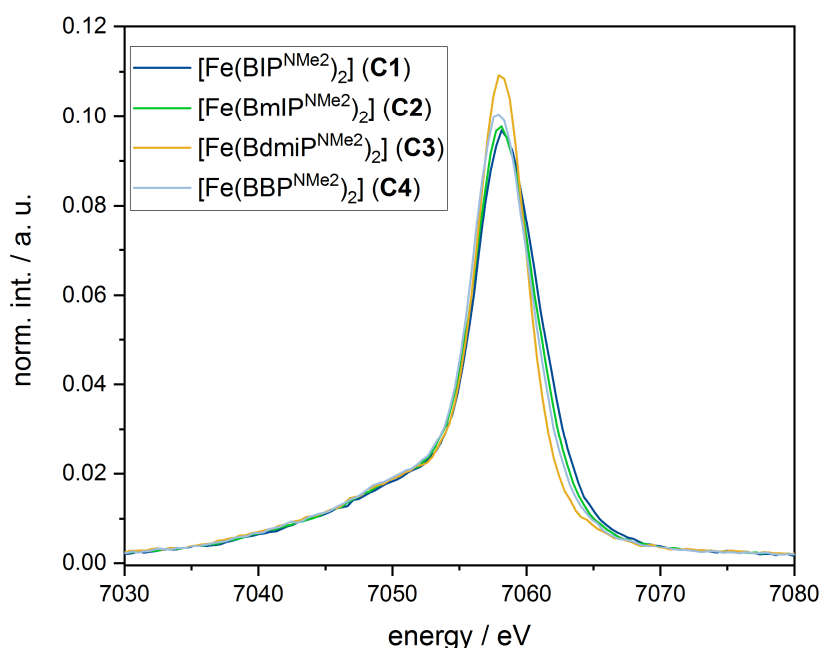


**Figure 4-22:**  $K\beta^{1,3}$  spectra of complexes **C1-C4** in acetonitrile at *r.t.*

The obtained  $K\beta_{1,3}$  spectra of complexes **C1-C4** are representatively shown in **figure 4-22**, revealing no visible feature for the  $K\beta'$  signal. This underlines the  $d^6$  low-spin Fe(II) character, with no unpaired electrons and an entirely occupied  $t_{2g}$ -orbital. Although all complexes remain in their Fe(II) state, slight shifts are visible within the spectrum due to small differences in the iron-ligand covalency. As described before, the difference in ligand

donor strength is leading to slight differences of electron density at the iron center which caused slight shifts within the complex series. For an exhaustive analysis the corresponding Fe(III) complexes are analyzed by X-ray emission spectroscopy, too. In **figure 4-23** the  $K\beta_{1,3}$  spectra of complex **C1** with its Fe(III) analogue are shown.

Alike the Fe(II) complex, no  $K\beta'$  signal can be observed at r.t., confirming the results of the EVANS-NMR method of low-spin Fe(III) complexes, with only one unpaired electron in the system. The observed energy shift between the Fe(II) and Fe(III) complex species is around 1 eV and varies in its magnitude. Because of the high complexity of the signal generating process, this shift depends on several influencing variables, which allow no reliable correlation with the oxidation state at this point. Nonetheless, it can be observed that the spectra are shifted towards higher energy values which imply an enlarged energy gap for the  $3p \rightarrow 1s$  transition.

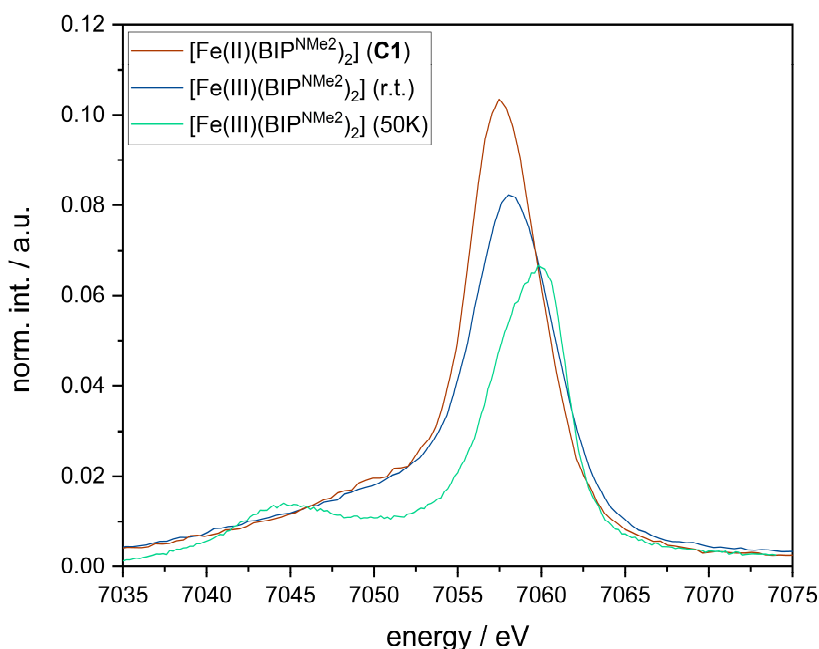


**Figure 4-23:**  $K\beta_{1,3}$  spectra of complex **C1** in its iron(II) and iron(III) state. Measured in acetonitrile at r.t. and 50 K.

Unexpectedly the Fe(III) analogue of complex **C1** reveal a distinct  $K\beta'$  signal equivalent to high-spin behavior when measured at low temperatures in this case 50 K (**figure 4-22**, green line) in a cryostat. The temperature decrease enables a spin-crossover into the  $d^5$ -high-spin state since this forms the thermodynamic stable product. This phenomenon is not enlightened totally to this point but will be further investigated in the future. Therefore, detailed experiments are planned to execute a stepwise cooling of the analyte solution with subsequent re-warming to obtain information about the transition temperature and the reversibility of the process.

## 4.8 Chapter summary

The new ligands were used to synthesize 15 new homoleptic Fe(II) complexes. These already showed optical differences as the complexes with monocyclic carbenes were obtained as yellow powder and the complexes of bicyclic carbenes as red powder. From eleven of these fifteen complexes measurable single crystals could be obtained. All of them showed a similar distorted octahedral coordination geometry independent of the size of the ligand system. When analyzing the absorption properties, all complexes show intense intraligand and MLCT transitions bands. The influence of the introduced amines can be seen when comparing the MLCT bands with the references used, which were formed from non-functionalized ligands. The separated asymmetric transitions between Fe-carbene and Fe-pyridine, which are known by the reference complex, are shifted towards each other due to the modification of the pyridine backbone and the associated lower accepting property. As none of the complexes showed fluorescence emission, transient absorption spectroscopy was performed to determine the lifetime of the  $^3\text{MLCT}$  states. As a result, the lifetime was found to be in the ten-picosecond region for all complexes, which for the monocyclic carbenes is only a small, but for the bicyclic carbenes is a significant lifetime reduction of this state. The negative shift of the redox potential, which has already been observed with the pure ligands, can also be observed in the complex series. Besides a significant shift of the  $\text{Fe}^{\text{III/II}}$  oxidation potential to values of -0.12 – 0 V for monocyclic carbene complexes and 0.1 - 0.25 V for bicyclic carbene complexes versus  $\text{Fc}/\text{Fc}^+$ , a second oxidation event can be observed in the area of 1 - 1.2 V vs.  $\text{Fc}/\text{Fc}^+$ , which is assigned to the  $\text{Fe}^{\text{III/IV}}$  oxidation couple. Due to the reduced oxidation potential it was possible to isolate and analyze material of the respective Fe(III) complexes. Corresponding analysis has shown that these are present in a  $d^5$  low spin configuration, whereby low temperature X-ray emission experiments have shown interesting spin crossover properties that need further investigation. In addition, the complexes showed a noticeable demeanor to different pH values due to amine functionalization. This enables the formation of a sensitive protonated species which leads to the conversion of the donating amine function into a positively charged ammonium function. This results in a bathochromic shift of the MLCT transition band, which exceeds the original MLCT transition of the unfunctionalized complex.

## 5 Homoleptic Ru(II) Complexes

### 5.1 Synthesis

For synthesis of the homoleptic ruthenium(II)-NHC complexes the literature protocol by PARK *et al.*<sup>88</sup> is used and slightly modified. Under an argon atmosphere  $\text{RuCl}_3 \cdot \text{H}_2\text{O}$  and the respective carbene ligand are dissolved in a small amount of ethylene glycol. The resulting black reaction mixture is stirred at  $180^\circ \text{C}$  for 4 hours, meanwhile the reaction mixture become brighter indicating the consumption of the starting material. The reaction mixture is brought to r.t. and the raw complex material is precipitated by addition of a saturated aqueous  $\text{KPF}_6$  solution (**figure 5-1**).

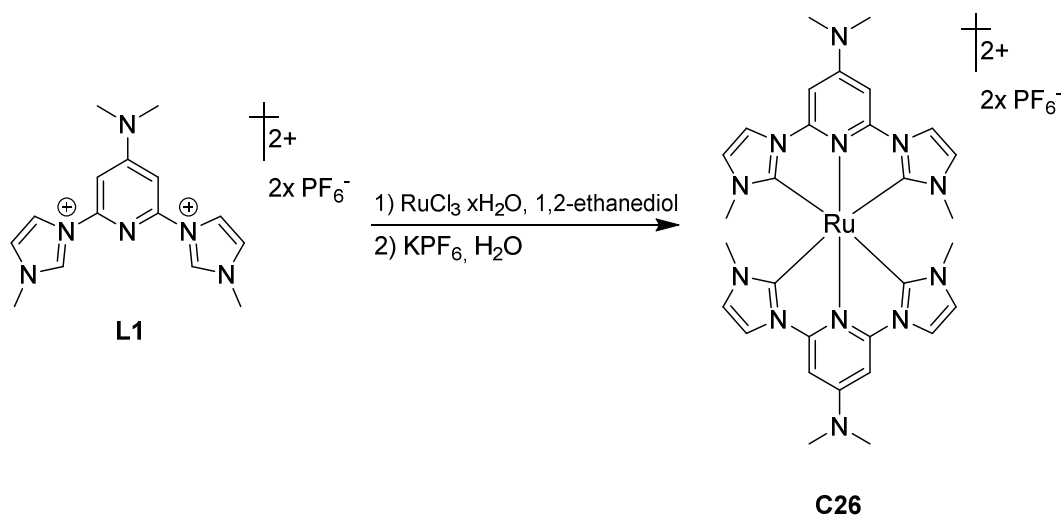


**Figure: 5-1:** Representative synthesis for ruthenium(II) complexes by example of complex  $[\text{Ru}(\text{BIP}^{\text{NMe}_2})_2][\text{PF}_6]_2$ .

Further purification is achieved by column chromatography using aluminum oxide and acetonitrile as eluent. All complexes are obtained as air stable bright yellow powder. Storage of the complex material is possible under aerobic conditions.

## 5.2 Crystal structures

Similar to the iron analogues suitable single crystals of the ruthenium(II) complexes **C16**, **C18-C20**, **C22**, **C25**, **C26** and **C28-C30** are obtained by gas phase diffusion of diethyl ether into an acetonitrile solution of the respective complex. The Ru-N<sub>pyridine</sub> and the Ru-C<sub>carbene</sub> bond length is summarized in **table 5-1**. The crystal structure of **[Ru(BIP<sup>NMe2</sup>)<sub>2</sub>][PF<sub>6</sub>]<sub>2</sub>** is shown exemplarily in **figure 5-1**.

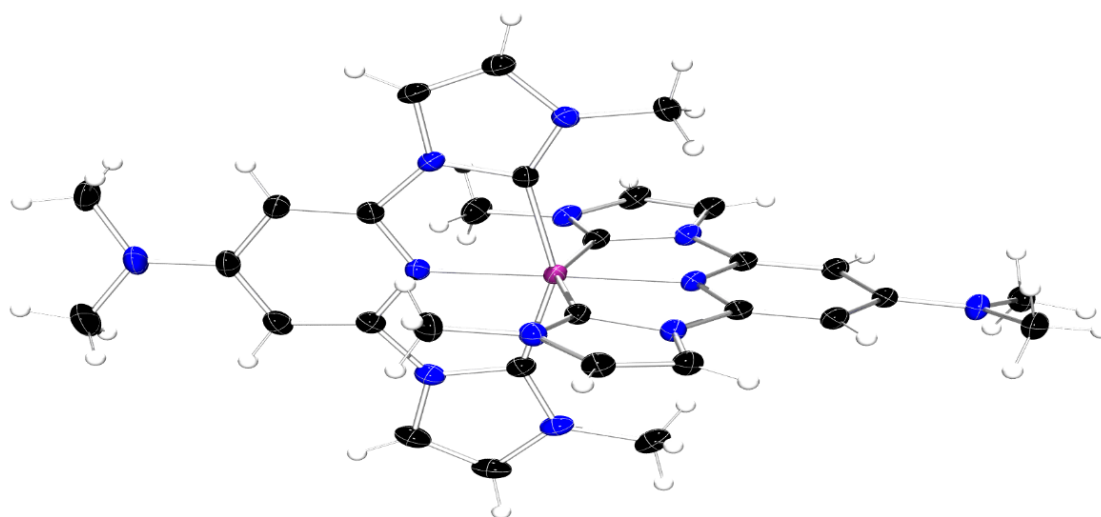


**Figure 5-1:** Single crystal structure of **[Ru(BIP<sup>NMe2</sup>)<sub>2</sub>][PF<sub>6</sub>]<sub>2</sub>** (**C16**) (ellipsoids with 50 % probability level)(counter ion omitted for clarity).

An attenuated effect of shorter bond length due to increasing  $\sigma$ -donor strength is expected compared to the iron analogues. Within the ruthenium series no obvious trend is noticed, probably caused by the much larger ruthenium ions, that lead to an increased coordination sphere. Nevertheless, the octahedral coordination geometry is present. Detailed data sets for all crystal structures are tabulated in the appendix. Identical to the iron complexes, distortion of the octahedral coordination is pronounced differently within the series of ruthenium complexes. A distorted coordination is shown in magnified scale in **figure 5-2**, for clarification of the tabulated coordination angles summarized in **table 5-2**. As visualized by the red box, a distorted octahedral ruthenium site is obvious, due to the limited bite angle of the ligands carbene moieties.

**Table 5-1:** Coordinating bond length and average in Å for all analyzed ruthenium complexes.

	Bond length			
	Ru-N <sub>pyridine</sub>	average	Ru-C <sub>carbene</sub>	average
<b>C16</b>	2.019 (1) 2.020 (1)	2.019 (1)	2.036 (2) 2.043 (2) 2.044 (2) 2.051 (2)	2.043 (2)
<b>C18</b>	2.014 (1) 2.020 (1)	2.017 (1)	2.037 (1) 2.039 (1) 2.041 (1) 2.048 (1)	2.041 (1)
<b>C19</b>	2.030 (1) 2.032 (1)	2.031 (1)	2.037 (3) 2.043 (3) 2.046 (2) 2.052 (2)	2.044 (3)
<b>C20</b>	2.018 (1) 2.018 (1)	2.018 (1)	2.032 (1) 2.034 (1) 2.036 (1) 2.037 (1)	2.035 (1)
<b>C22</b>	2.016 (3) 2.016 (3)	2.016 (3)	2.064 (3) 2.064 (3) 2.064 (3) 2.064 (3)	2.064 (3)
<b>C25</b>	2.018 (3) 2.019 (3)	2.019 (3)	2.038 (4) 2.038 (4) 2.048 (4) 2.048 (4)	2.043 (4)
<b>C26</b>	2.021 (3) 2.021 (3)	2.021 (3)	2.029 (4) 2.030 (4) 2.042 (4) 2.042 (4)	2.035 (4)
<b>C28</b>	2.020 (3) 2.023 (3)	2.021 (3)	2.041 (4) 2.044 (4) 2.051 (4) 2.060 (4)	2.049 (4)
<b>C29</b>	2.017 (3) 2.022 (3)	2.019 (3)	2.029 (3) 2.030 (3) 2.036 (3) 2.038 (3)	2.033 (3)
<b>C30</b>	2.015 (4) 2.020 (4)	2.017 (4)	2.029 (4) 2.036 (4) 2.040 (4) 2.042 (4)	2.036 (4)

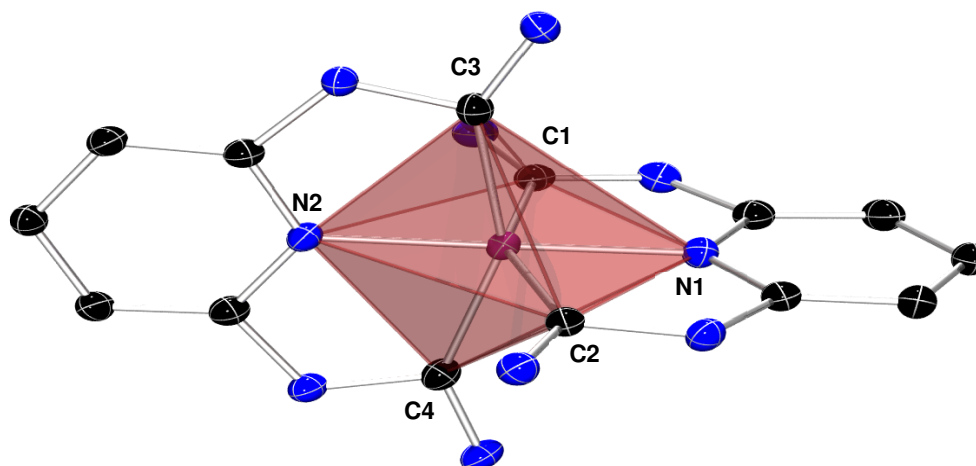


**Figure 5-2:** Magnified coordination sphere of the ruthenium center of  $[\text{Ru}(\text{BIP}^{\text{NMe}_2})_2][\text{PF}_6]_2$  (**C16**).

When comparing the different coordination angles, all complexes are oriented so the N1-Ru-N2 axis is horizontal, with the horizontal carbene pincer complex on the right to the ruthenium center. Since the orientation is not important inside an ideal octahedral coordination, its different in this case.

**Table 5-2:** Selected coordinating binding angles for all analyzed ruthenium complexes.

	<b>N1-Ru-N2</b>	<b>C1-Ru-C2</b>	<b>C3-Ru-C4</b>	<b>N2-Ru-C2</b>	<b>N1-Ru-C4</b>
<b>C16</b>	178.70 (7)	153.41 (9)	153.60 (9)	104.67 (8)	103.29 (8)
<b>C18</b>	178.85 (6)	153.01 (8)	153.39 (8)	102.66 (7)	104.38 (7)
<b>C19</b>	179.58 (8)	153.59 (8)	154.09 (6)	103.36 (9)	103.46 (9)
<b>C20</b>	178.17 (6)	154.22 (7)	154.07 (7)	103.06 (6)	101.29 (6)
<b>C22</b>	180.0 (1)	152.19 (18)	152.19 (18)	103.91 (9)	103.91 (9)
<b>C25</b>	177.53 (12)	155.06 (15)	154.43 (15)	104.12 (14)	105.18 (14)
<b>C26</b>	177.1 (2)	153.41 (17)	153.41 (17)	105.99 (15)	105.99 (15)
<b>C28</b>	177.11 (14)	153.45 (17)	153.33 (17)	103.37 (15)	106.04 (15)
<b>C29</b>	179.16 (11)	153.78 (13)	153.35 (12)	103.80 (12)	102.80 (12)
<b>C30</b>	178.70 (16)	154.01 (15)	154.03 (15)	103.75 (16)	104.24 (14)

By summary in **table 5-2** it is obvious that the binding angles only slightly differ within the complex series regardless of the electronic or steric differences of the ligands. Moreover, there is no big difference in binding angles compared to the iron analogues despite the larger size of the ruthenium central atom. Identical to the iron analogue, the size of the ligand framework does not affect the overall coordination geometry, as shown in **figure 5-3** for complex  $[\text{Ru}(\text{BmbP}^{\text{NBn2}})_2][\text{PF}_6]_2$  (**C25**).

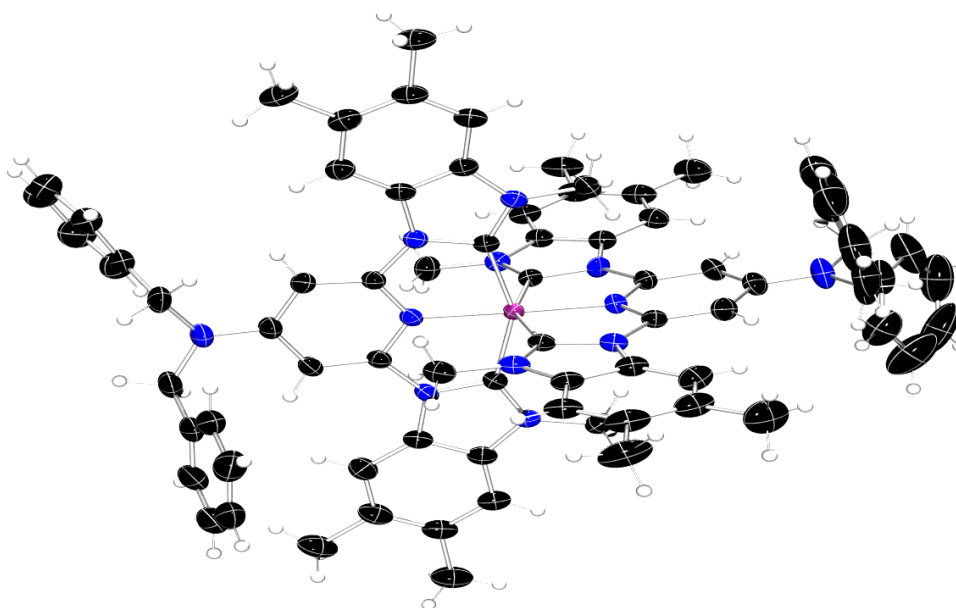


**Figure 5-3:** Single crystal structure of  $[\text{Ru}(\text{BmbP}^{\text{NBn2}})_2][\text{PF}_6]_2$  (**C25**) (ellipsoids with 50 % probability level)(counter ion omitted for clarity).

### 5.3 Spectroscopic properties

Since investigation of the photophysical properties influenced by amine donor functionalization is a main principle of this thesis, all ruthenium complexes are thoroughly investigated by UV/Vis-spectroscopy and compared with their iron analogues. The UV/Vis spectra are recorded at room temperature in acetonitrile solutions with a concentration of approximately  $1 \cdot 10^{-5} \text{ mol L}^{-1}$ . For reasons of clarity and comprehensibility the complexes are distributed similar to the iron analogues in terms of complexes with monocyclic NHCs (**C16-C18**; **C21-C23**; **C26-C28**) and complexes involving NHCs with extended  $\pi$ -system (**C19-C20**; **C24-C25**; **C29-C30**). In contrast to their iron equivalent no significant optical differences are observable, since all complexes appear as bright yellow solid. In general, a similar demeanor is observed in the UV/Vis spectra as for the amine functionalized iron complexes. In **figure 5-4** the UV/Vis spectra of complex **C1** and **C16** are shown to illustrate the high similarity between the iron and ruthenium species. The largest difference

between both complexes is observable by a shift of the MLCT energy of 55 nm towards higher energies, when changing the central atom from iron to ruthenium. This shift is reasoned by the intrinsic larger ligand field splitting of ruthenium, and as a result a larger  $t_{2g} \rightarrow \pi^*$  energy gap.<sup>143</sup> Since this difference depends on the metal ion, the similarity between both UV/Vis spectra increase in the region of ligand centered  $\pi \rightarrow \pi^*$  transitions.

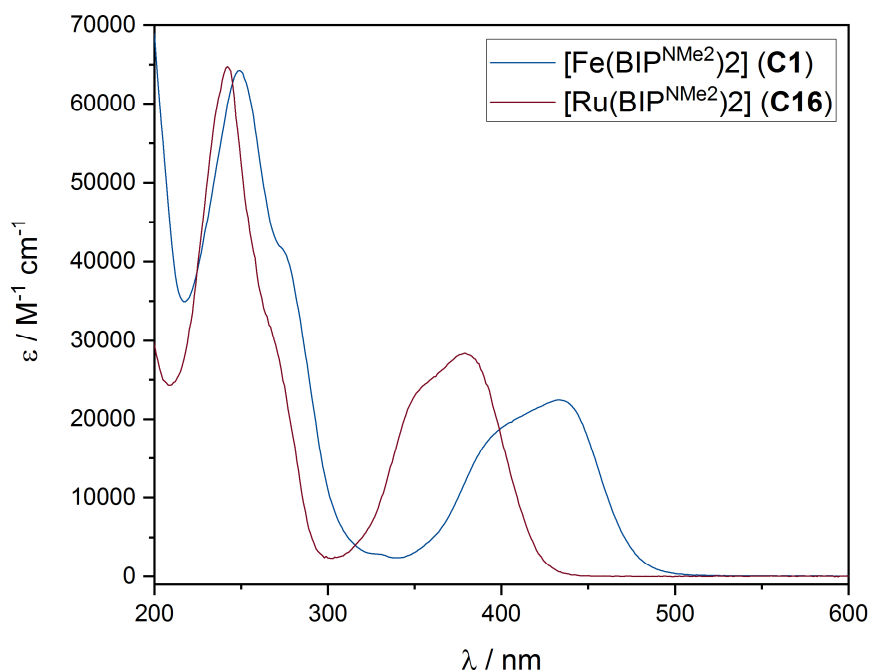


**Figure 5-4:** UV/Vis spectra of iron complex  $[\text{Fe}(\text{BIP}^{\text{NMe}_2})_2][\text{PF}_6]_2$  (C1) and ruthenium complex  $[\text{Ru}(\text{BIP}^{\text{NMe}_2})_2][\text{PF}_6]_2$  (C16).

In **figure 5-5** the UV/Vis spectra of the monocyclic NHC complexes are shown, whereby the complexes are plotted along with same NHC moieties. For all complexes, the absorption spectra are composed of two main absorption bands, which is comparable to similar complexes reported in the literature before.<sup>88,114,144</sup> Below 300 nm different  $\pi \rightarrow \pi^*$  and  $n \rightarrow \pi^*$  intra-ligand transitions are observed, which imply the existence of a shoulder in the range between 260-290 nm. Above 300 nm the lowest energy feature, is related to the MLCT processes, whose splitting is decreased for reasons explained for the iron analogues.<sup>88,144</sup> Caused by the amine functionalization the ligand  $\pi^*$ -energy level is destabilized leading to a blueshift of the Ru-pyridine MLCT transition. Because the carbenes are not affected of the functionalization the energy of the Ru-NHC transition remains the same as seen in complexes of unfunctionalized ligands. As a result, the Ru-pyridine transition is shifted into the Ru-NHC transition leading to an indefinite differentiation between both compared to unfunctionalized literature complexes.

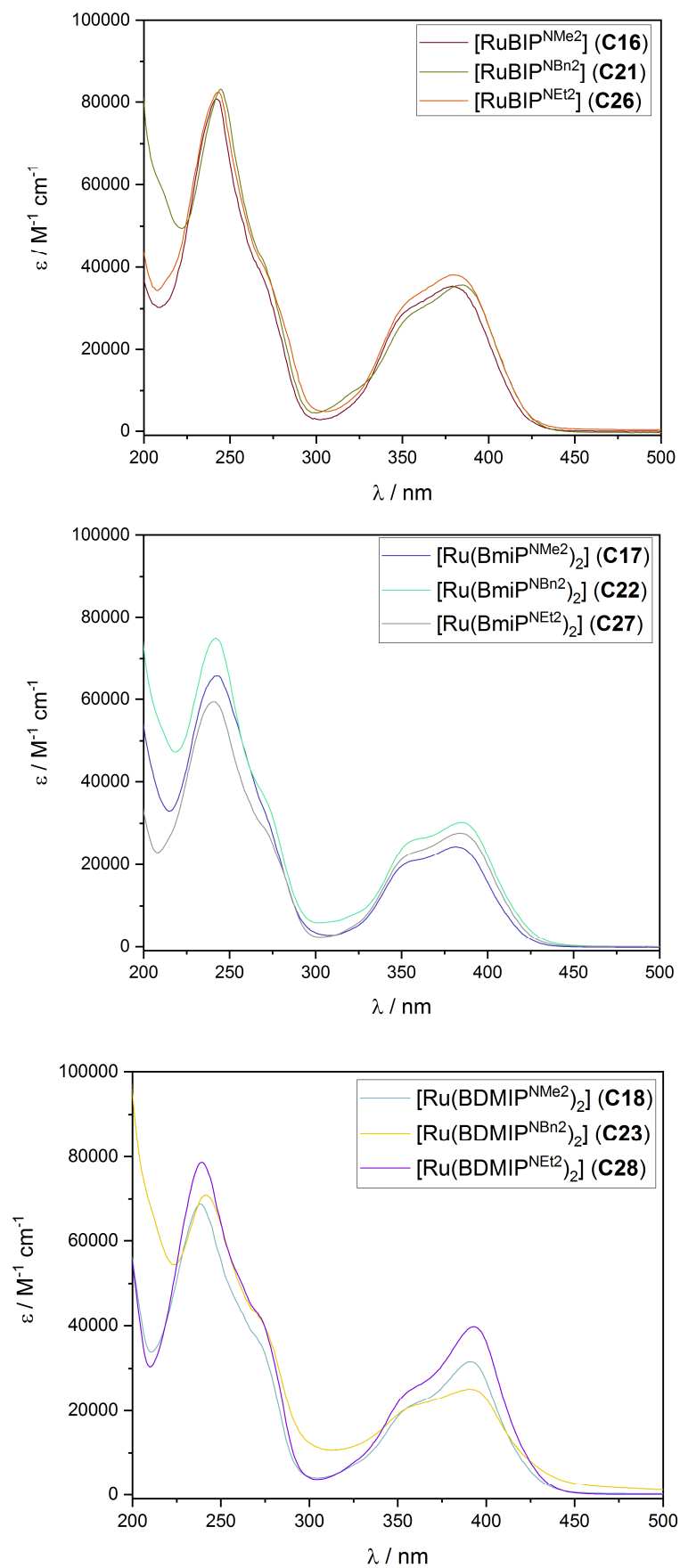


**Figure 5-5:** UV/Vis spectra of ruthenium NHC-complexes containing monocyclic carbenes in acetonitrile at r.t.. Imidazole containing complexes (top); methylimidazole complexes (middle); dimethylimidazole complexes (bottom).

Due to the use of different N-heterocyclic compounds, a varying degree of maxima splitting is observed. For the whole series of monocyclic NHC compounds the lowest energy transition emerges from 375-410 nm and can be assigned to the Ru-pyridine charge transfer. At higher energies, the feature assigned to the Ru-NHC charge transfer is often visible as a shoulder within the brought MLCT transition band, approximately around 330-375 nm. Identical to the iron complex series, a more distinct splitting of transition bands can be observed for the extended ligand systems (**figure 5-6**). For both series of NHC compounds, the lowest energy transition emerges at similar energy values from 350-385 nm and can be assigned to the Ru-pyridine charge transfer.

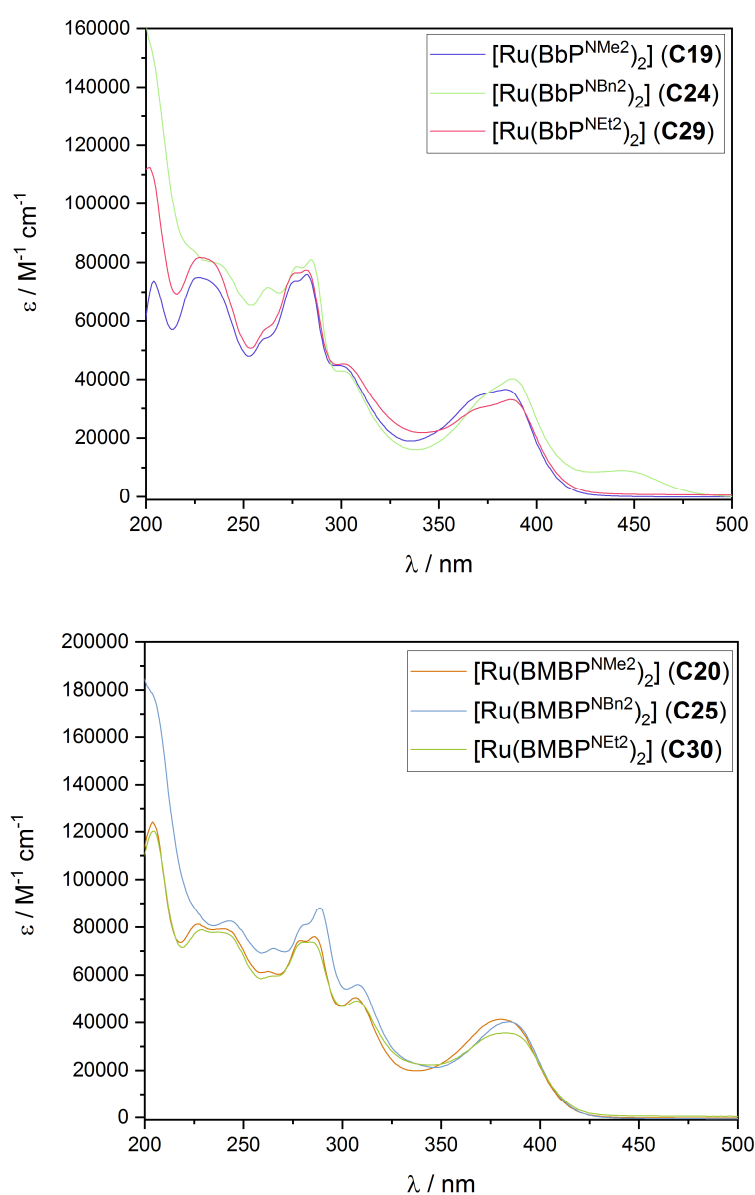


**Figure 5-6:** UV/Vis spectra of ruthenium NHC-complexes containing bicyclic carbenes in acetonitrile at r.t.. Benzimidazole containing complexes (top); Dimethylbenzimidazole complexes (bottom).

**Table 5-3:** UV/Vis-data of homoleptic ruthenium(II) complexes **C16-C30** in acetonitrile at r.t..

Complex		$\lambda$ [nm]	$\epsilon$ [ $M^{-1} cm^{-1}$ ]
<b>C16</b>	[Ru(BIP <sup>NMe2</sup> ) <sub>2</sub> ]	379, 241	28390, 64744
<b>C17</b>	[Ru(BmiP <sup>NMe2</sup> ) <sub>2</sub> ]	380, 353, 241	24317, 20541, 65847
<b>C18</b>	[Ru(BdmiP <sup>NMe2</sup> ) <sub>2</sub> ]	391, 354, 238	31615, 20505, 69440
<b>C19</b>	[Ru(BbP <sup>NMe2</sup> ) <sub>2</sub> ]	383, 282, 225, 203	36516, 75972, 74936, 73823
<b>C20</b>	[Ru(BmbP <sup>NMe2</sup> ) <sub>2</sub> ]	380, 307, 284, 278, 227, 204	41238, 50505, 75767, 74217, 81290, 123990
<b>C21</b>	[Ru(BIP <sup>NBn2</sup> ) <sub>2</sub> ]	384, 243	35606, 82991
<b>C22</b>	[Ru(BmiP <sup>NBn2</sup> ) <sub>2</sub> ]	384, 355, 242	30235, 25846, 74952
<b>C23</b>	[Ru(BdmiP <sup>NBn2</sup> ) <sub>2</sub> ]	391, 241	25104, 70994
<b>C24</b>	[Ru(BbP <sup>NBn2</sup> ) <sub>2</sub> ]	447, 387, 284, 276, 262, 235	8919, 40278, 80847, 78172, 71517, 80048
<b>C25</b>	[Ru(BmbP <sup>NBn2</sup> ) <sub>2</sub> ]	384, 307, 289, 278, 264, 242	40155, 56003, 88219, 79966, 71106, 82598
<b>C26</b>	[Ru(BIP <sup>NEt2</sup> ) <sub>2</sub> ]	380, 241	39980, 86307
<b>C27</b>	[Ru(BmiP <sup>NEt2</sup> ) <sub>2</sub> ]	383, 353, 240	35526, 22419, 76411
<b>C28</b>	[Ru(BdmiP <sup>NEt2</sup> ) <sub>2</sub> ]	393, 355, 270, 238	39778, 24656, 43428, 78631
<b>C29</b>	[Ru(BbP <sup>NEt2</sup> ) <sub>2</sub> ]	386, 301, 281, 275, 227, 202	33022, 45382, 77504, 76460, 81646, 112444
<b>C30</b>	[Ru(BmbP <sup>NEt2</sup> ) <sub>2</sub> ]	382, 307, 283, 280, 238, 227, 203	35551, 49106, 73684, 73599, 77787, 78808, 120195

The feature assigned to the Ru-NHC charge transfer is only visible in the benzimidazolydene series (**C19**; **C24**; **C29**), but likewise slightly distinct as a shoulder around 360 nm. For the dimethylbenzimidazolydene series (**C20**; **C25**; **C30**), both features are shifted towards each other, so no discriminability is possible anymore. In contrast to the monocyclic carbenes, a fine distinction of the  $\pi \rightarrow \pi^*$  and  $n \rightarrow \pi^*$  intra-ligand transitions is observed. Those significantly differ from their iron analogues showing two to three distinct peaks around 230 nm, 280 nm and 310 nm, whereas the latter one is only visible as a shoulder in the benzimidazolydene series.

The highlighted intra ligand transition bands show an even more detailed fine structure themselves. The summarized spectroscopic data are shown in **table 5-3**. Within the whole complex series, the extinction coefficient for the MLCT transition varies from 25000-40000  $\text{M}^{-1}\cdot\text{cm}^{-1}$  independent of the ligand size.

Since no fluorescence is observed for the iron complexes, the ruthenium complex series shows a similar behavior. Within the ruthenium complex series hardly any fluorescence signal is detected. This behavior is expectable for the iron series since no fluorescence emission is observed in the unfunctionalized iron complex either. However, nearly total fluorescence quenching is rather astounding for the ruthenium series, due to the intense fluorescence signal observed for the reference complex. The immense effect of the amine group is shown in **figure 5-7**, comparing the fluorescence signal of the unfunctionalized **[Ru(BIP)<sub>2</sub>]** with the weak fluorescence signal of complex **C17**, which is the only monocyclic complex revealing any detectable fluorescence signal at all.

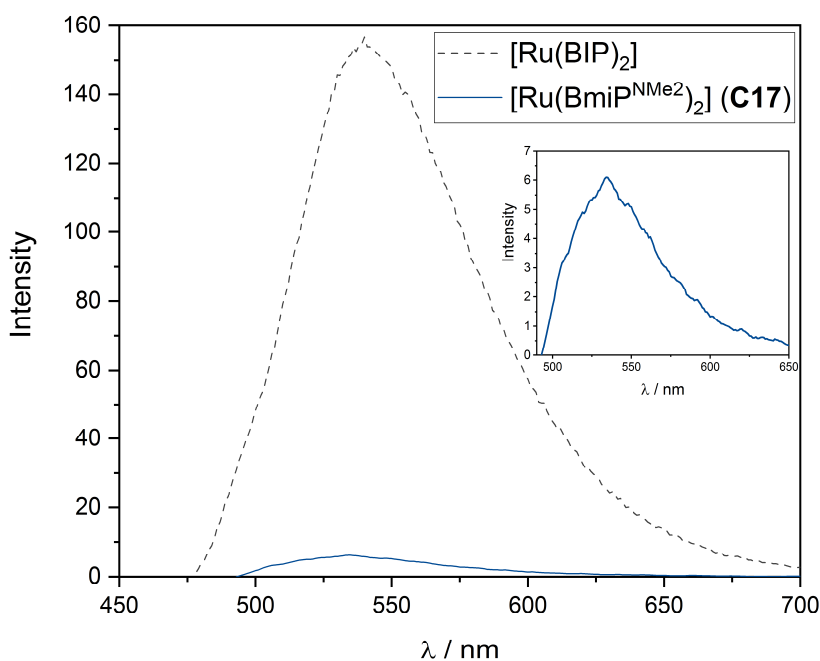


**Figure 5-7:** Compared fluorescence spectra of **C17** and reference complex **[Ru(BIP)<sub>2</sub>]** in acetonitrile at r.t.. Excitation wavelength 354 nm.

To further understand the reason for fluorescence quenching, subsequent experiments are realized to classify if there is no fluorescence occurring in **C16** and **C19** or if the fluorescence is quenched intermolecularly by the amine group of another complex molecule since amines are known to be active as fluorescence quenching agents. Therefore, quenching experiments are performed using the significant fluorescence signal of pure anthracene, since it is known to be quenched by tertiary amines like Et<sub>3</sub>N.<sup>145,146</sup> By time correlated single photon counting (TCSPC) the time constant for the singlet emission is determined, which benefits from independence of optical density. Following, defined equivalents of **C16** are added, remeasuring the time constant for the singlet emission. As a result, no quenching induced by **C16** can be observed. To countercheck the validity of the experimental approach, the experiment is repeated using Et<sub>3</sub>N as quenching agent. Hereby, affirmation of the experimental approach is achieved since a decrease of the fluorescence lifetime is observed. This elucidates the fact, that fluorescence of the complex is quenched intramolecularly, for example by vibrational relaxation of the amine group, and not intermolecularly by another molecule.

For this reason, transient absorption spectroscopy is measured for complexes **C16** and **C19** in acetonitrile by the LOCHBRUNNER group as representatives for the imidazole and benzimidazole ligand motif, to obtain information about the excited state dynamics. The time resolution of the ultrafast pump-probe spectroscopy is about 100 fs using frequency doubling of a Ti:sapphire laser system which generates excitation pulses centered at 400 nm. The transient spectra for both complexes exhibit a different behavior. In case of **C16** two distinct time components within the picosecond timescale are fitted with values of approximate 570 ps and 80 ps (**figure 5-8**). After optical excitation, a positive signal is detected above 420 nm for both time components with its maximum at around 605 nm. The negative signal below 420 nm is correlated to the ground state bleaching (GSB) merging into the positive signal of the excited state absorption (ESA). Both time components reveal a similar behavior, whereby the shorter one is mirrored along the x-axis into the negative area in case of a perpendicular polarization, which is attributable to rotational relaxation. The long living time component of approximately 560 ps is assigned to the <sup>3</sup>MLCT lifetime. The benzimidazolydene complex **C19** shows two distinct time constants as well, whereby the rotational relaxation happens on the same timescale than in the previous complex (**figure 5-9**). The positive signal shows a local maximum around 500 nm and a global maximum above 700 nm in both cases. The negative signal attributable to the GSB can be found below 410 nm. As distinct from **C16** and the observations made for the iron complex series the <sup>3</sup>MLCT lifetime shortens when changing to the enlarged benzimidazolydene system about 40 ps to values of approximate 500 ps.

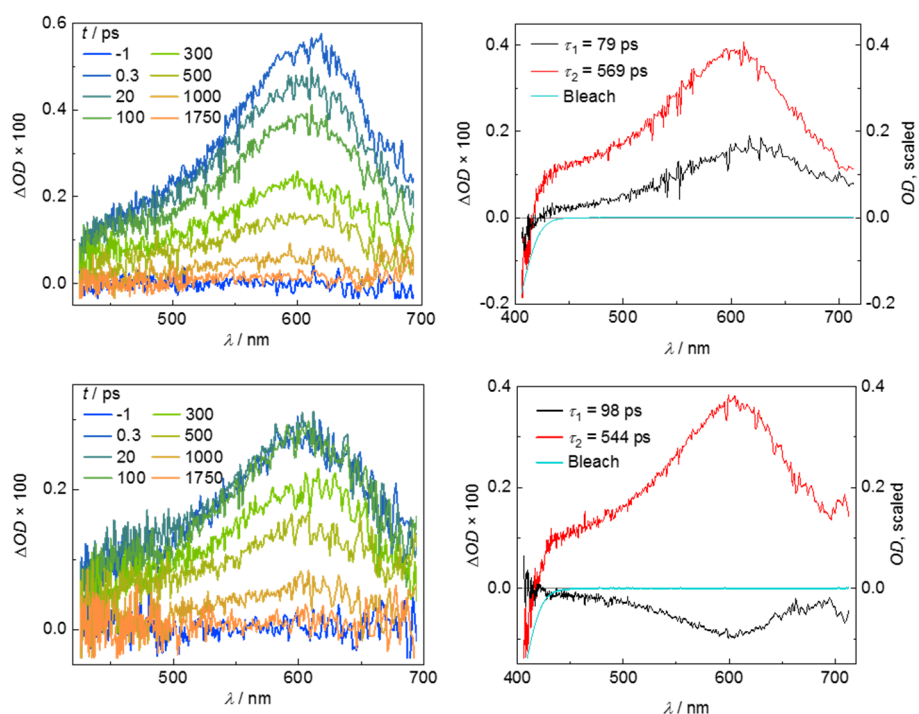


**Figure 5-8:** Transient absorption spectra (left) and decay associated amplitude spectra (right) with the respective lifetimes of  $[\text{Ru}(\text{BIP}^{\text{NMe}_2})_2]$  (**C16**) with parallel (top) and perpendicular (bottom) polarization of excitation and retrieval pulse.

In general, both complexes show a distinct increase of the  $^3\text{MLCT}$  lifetime when compared to the iron analogues due to the enlarged ligand field splitting. In case of the imidazolydene complexes **C1** and **C16** a 50-fold, and in case of the benzimidazolydene complexes **C4** and **C19** a 38-fold increase is observed.

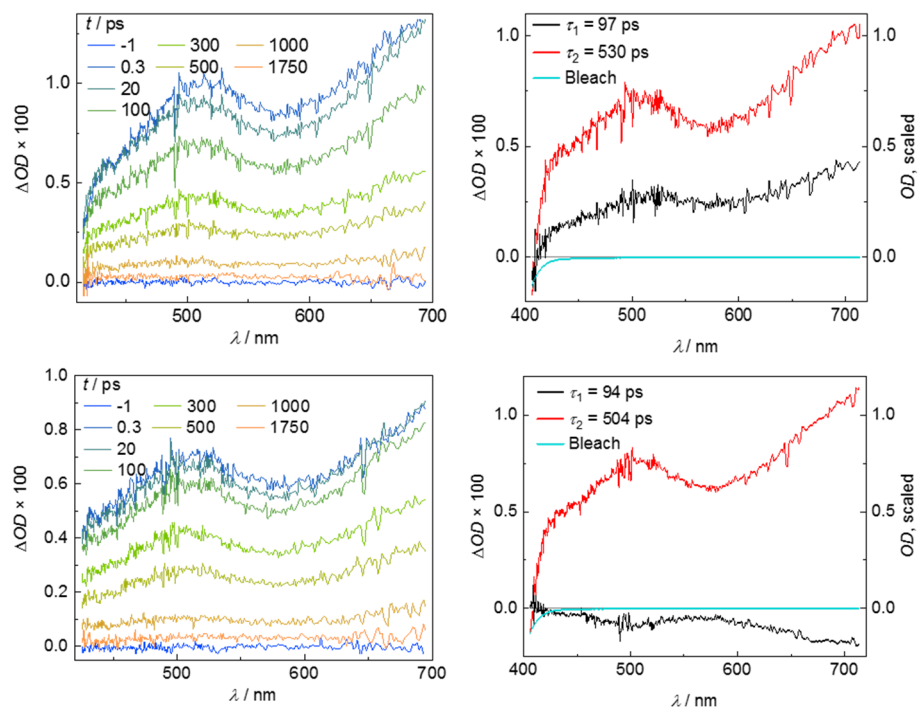


**Figure 5-9:** Transient absorption spectra (left) and decay associated amplitude spectra (right) with the respective lifetimes of  $[\text{Ru}(\text{BbP}^{\text{NMe}_2})_2]$  (**C19**) with parallel (top) and perpendicular (bottom) polarization of excitation and retrieval pulse.

To classify the magnitude of the amine influence, TCSPC is recorded for both reference complexes  $[\text{Ru}(\text{BIP})_2]$  and  $[\text{Ru}(\text{BbP})_2]$  to obtain information about their  $^3\text{MLCT}$  time constant. Therefore, decay curves of both complexes are recorded in a degassed acetonitrile solution. Following, data analysis is realized by fitting a second order polynomial function to the decay curve. In **figure 5-10** the decay curves are depicted as scatter diagram, with the respective fit shown as a line. The  $[\text{Ru}(\text{BIP})_2]$  and  $[\text{Ru}(\text{BbP})_2]$  reveal two separate time constants similar to the amine functionalized complexes **C16** and **C19**. Hereby the first decay constant is determined by values of 1.47 ns for  $[\text{Ru}(\text{BIP})_2]$  and 1.38 ns for  $[\text{Ru}(\text{BbP})_2]$ . As seen in the magnification of **figure 5-10** the first decay is not reproduced well by the fit, leading to an increased inaccuracy of the first time constant. Ongoing the fit shows improved reproduction of the decay curve leading to more reliable values for the second time constant in both cases.

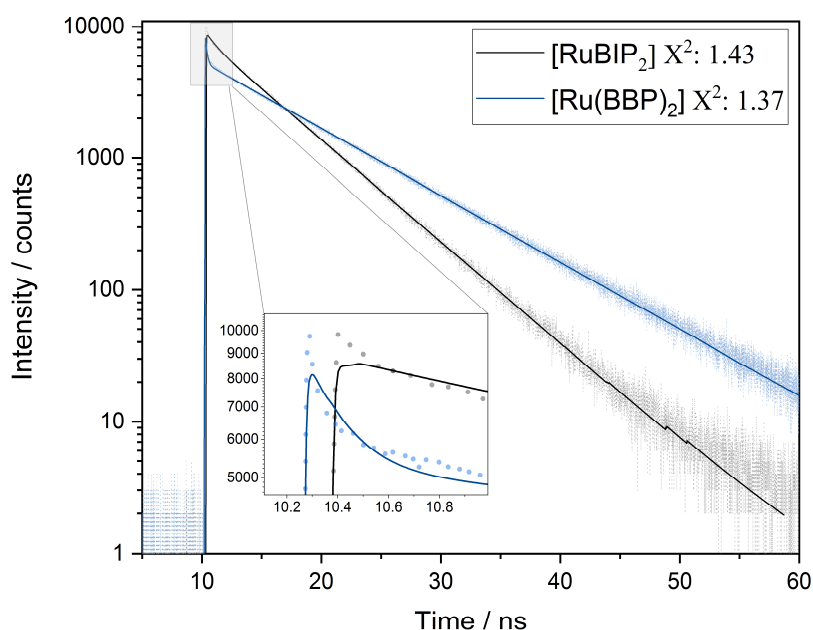


**Figure 5-10:** TCSPC decay and fit spectra for the  $[\text{Ru}(\text{BIP})_2]$  and  $[\text{Ru}(\text{BbP})_2]$  reference complex.

The second time constant shows values of 55.8 ns for the imidazole and 85.3 ns for the benzimidazole complex and differs from the values for **C16** and **C19** concerning magnitude and ratio. The strong decrease of the  $^3\text{MLCT}$  lifetime for the amine complexes is attributable to the destabilizing effect of the donating amine group onto the ligand  $\pi^*$ -orbital, leading to a fast deactivation due to convergence to the metal centered  $e_g$ -orbital. Nevertheless, this effect is much more pronounced than in the comparable iron complex series, with a 100-fold decrease of the  $^3\text{MLCT}$  lifetime. All observed time constants for the ruthenium complexes are summarized in **table 5-4**.

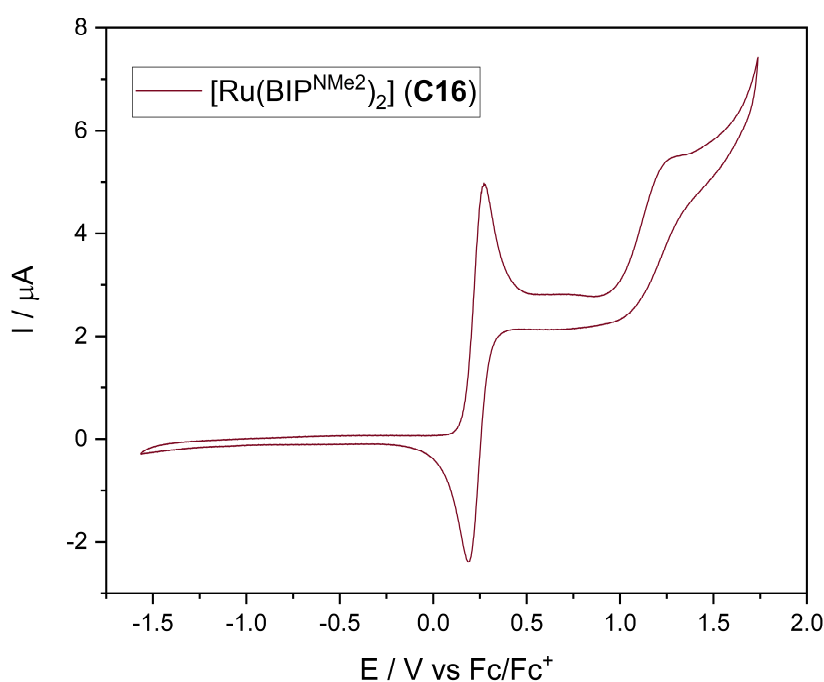
**Table 5-4:** Time constants obtained from transient absorption spectroscopy and TCSPC for the Ru-complexes.

Complex		$\tau_1$ [ps]	$\tau_2$ [ps]
<b>C16</b>	[Ru(BIP <sup>NMe2</sup> ) <sub>2</sub> ]	80	570
<b>C19</b>	[Ru(BbP <sup>NMe2</sup> ) <sub>2</sub> ]	95	500
-	[Ru(BIP) <sub>2</sub> ]	1470	55800
-	[Ru(BbP) <sub>2</sub> ]	1380	85300

## 5.4 Cyclic voltammetry

Exactly like executed for the iron series, all ruthenium complexes are investigated concerning their electrochemical properties, which are conducted in acetonitrile solutions using a concentration of 0.001 M. Tetrabutylammonium hexafluorophosphate (Bu<sub>4</sub>NPF<sub>6</sub>) is used as supporting electrolyte with a concentration of 0.1 M. All redox potentials are referenced to the ferrocene/ferrocenium<sup>+</sup> (Fc/Fc<sup>+</sup>) redox couple as internal standard.

In general, the complex series reveals a similar electrochemical behavior, confirming the information obtained by UV/Vis spectroscopy. All complexes are showing a reversible oxidation with E<sub>1/2</sub> corresponding to the Ru<sup>II</sup>/Ru<sup>III</sup> redox event around 0.25 V for monocyclic carbenes and around 0.35 V for the bicyclic carbene ligand series. The total cyclic voltammogram of complex **C16** is shown representatively in **figure 5-11**.

**Figure 5-11:** Total cyclic voltammogram of complex **C16** in acetonitrile at 25 °C ( $v = 400 \text{ mV s}^{-1}$ ).

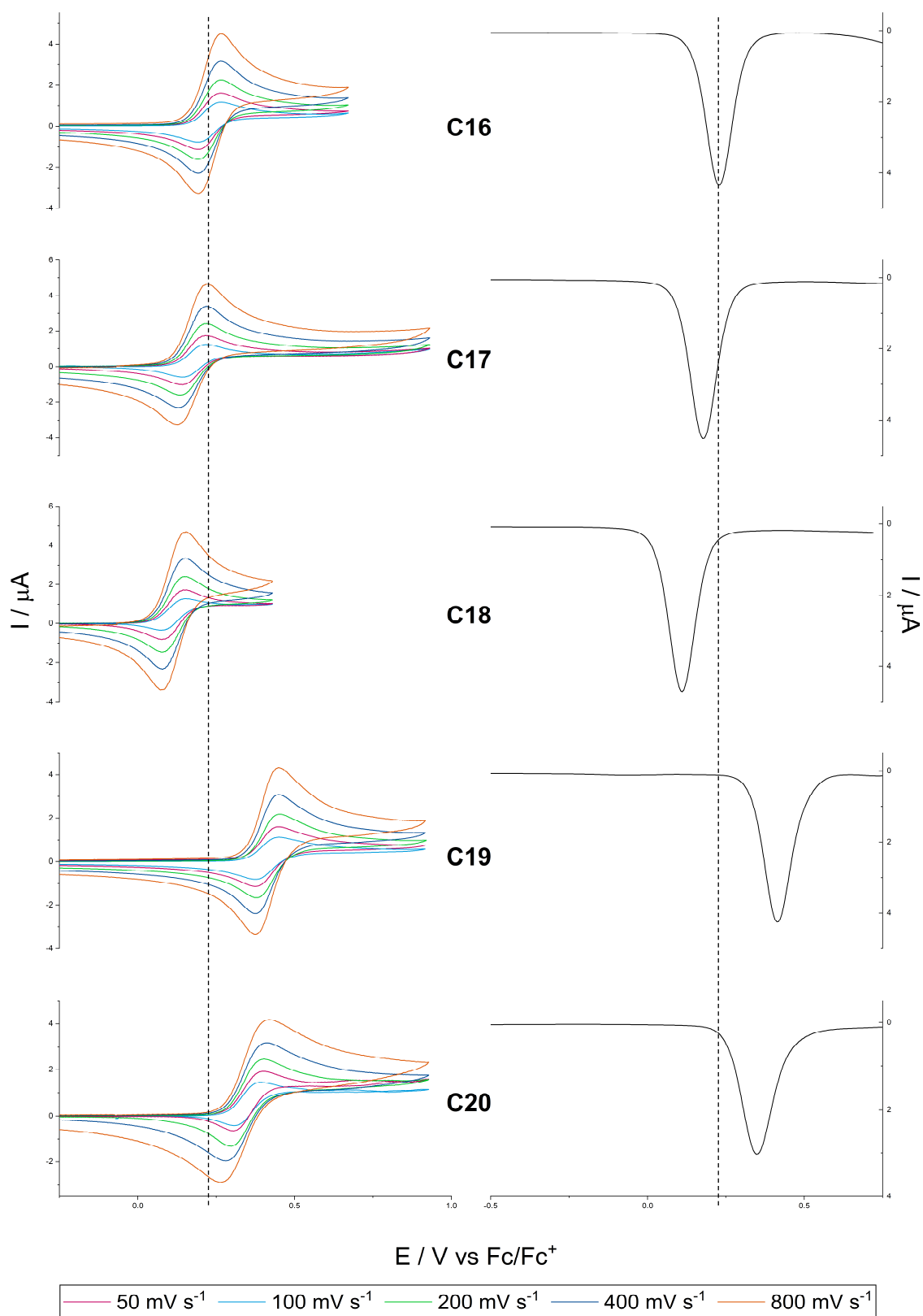


**Figure 5-12:** Cyclic voltammograms at different scan rates (left) and square-wave voltammograms (right) of complexes **C16- C20** in acetonitrile at 25° C.

Within the complex series, the first redox potential is considerably shifted towards lower potentials, compared to the unfunctionalized reference complex, attributable to the amine moiety.

Inside the same amine class (**C16-C20**) the ligands exert the same influence as observed for the iron complex series. The resulting cyclic voltammograms are shown in **figure 5-12** together with the respective square-wave voltammogram. Complex **C16** displays the reversible Ru<sup>II</sup>/Ru<sup>III</sup> redox event at 0.22 V vs Fc/Fc<sup>+</sup>, conterminously with a potential shift of +0.24 V compared to the Fe<sup>II</sup>/Fe<sup>III</sup> analogue. The potential of the Ru<sup>II/III</sup> redox couple is further shifted to lower values for complex **C17** (0.17 V) and **C18** (0.11 V). The previously mentioned accepting character of the enlarged benzimidazolylene systems, leads to a positive potential shift for complex **C19** (0.41 V) which is diminished by the methylene groups in **C20** (0.35 V). Reversibility of the redox event is illustrated by the Randles-Sevcik plot for **C16-C20** in **figure 5-13**.

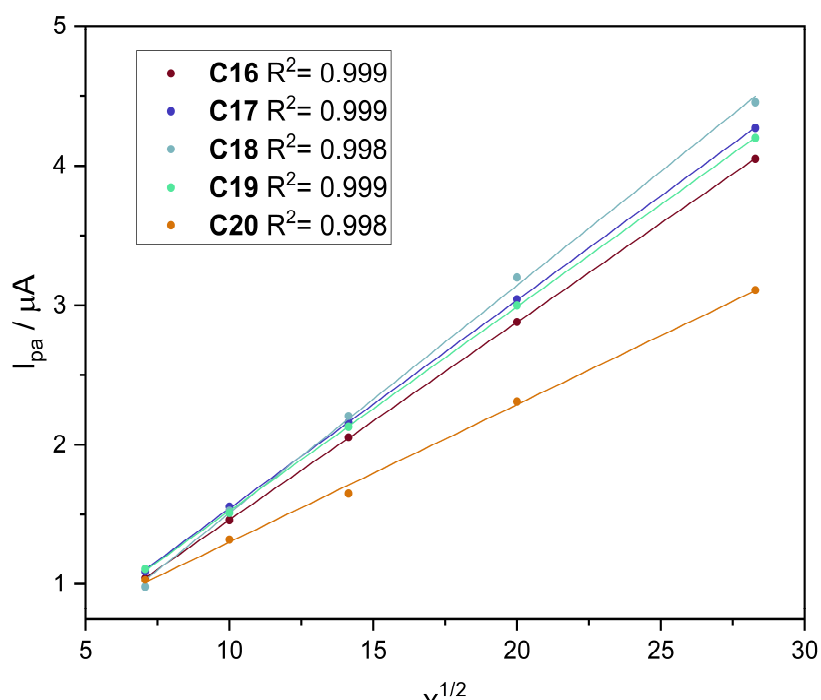


**Figure 5-13:** Randles-Sevcik plot for the redox event of **C16-C20**.

The shift of the redox potentials between the Ru<sup>II</sup>/Ru<sup>III</sup> couple and the respective Fe<sup>II</sup>/Fe<sup>III</sup> analogue shows constant values of around +0.23 V independent of the ligand. Within the complex series, slight shifts of the oxidation potential are noticeable, equal to the iron series. Albeit the potential of the oxidation event for the ruthenium center (Ru<sup>II/III</sup>) is shifted to significantly higher values, the ligand reduction remains in preferential. The

electrochemical data is summarized for the monocyclic carbene series in **table 5-5** and in **table 5-6** for the bicyclic counterpart.

**Table 5-5:** Electrochemical data for ruthenium NHC-complexes containing monocyclic carbenes in acetonitrile at r.t.. ( $\nu = 100 \text{ mV s}^{-1}$ ).

Complex	$E_{1/2} (\text{Ru}^{\text{II}}/\text{Ru}^{\text{III}})$ [V]	$\Delta E$ [mV]	E to $\text{Fe}^{\text{II/III}}$ [V]
<b>C16</b>	0.22	68	+0.24
<b>C17</b>	0.17	66	+0.23
<b>C18</b>	0.11	61	+0.23
<b>C21</b>	0.29	68	+0.26
<b>C22</b>	0.23	60	+0.26
<b>C23</b>	0.16	73	+0.24
<b>C26</b>	0.20	66	+0.24
<b>C27</b>	0.18	68	+0.27
<b>C28</b>	0.09	63	+0.22

**Table 5-6:** Electrochemical data for ruthenium NHC-complexes containing bicyclic carbenes in acetonitrile at r.t.. ( $\nu = 100 \text{ mV s}^{-1}$ ).

Complex	$E_{1/2} (\text{Ru}^{\text{II}}/\text{Ru}^{\text{III}})$ [V]	$\Delta E$ [mV]	E to $\text{Fe}^{\text{II/III}}$ [V]
<b>C19</b>	0.41	68	+0.23
<b>C20</b>	0.35	60	+0.23
<b>C24</b>	0.49	82	+0.23
<b>C25</b>	0.44	82	+0.22
<b>C29</b>	0.39	69	+0.22
<b>C30</b>	0.33	70	+0.22

Chronoamperometric investigations of complex **C16** and **C19** reveal an intense emerge of an LMCT band from 600 nm up to around 900 nm for both complexes during electrolysis using a voltage of 0.47 V (**C16**) or 0.66 V (**C19**) (**Figure 5-14**). The emerging LMCT transition spans from approximately 550-900 nm for complex **C16** and even further from 550-950 nm for complex **C19**. This behavior is observed for the iron analogues, too. Indicating a direct coherence between the energy of the MLCT in the Ru(II) state and the lowest energy feature of the emerging Ru(III) LMCT. The intraligand  $\pi \rightarrow \pi^*$  and  $n \rightarrow \pi^*$

transitions are exceptionless shifted to higher energies, whereas those transitions are shifted to higher energies in complex **C16** compared to **C19**.

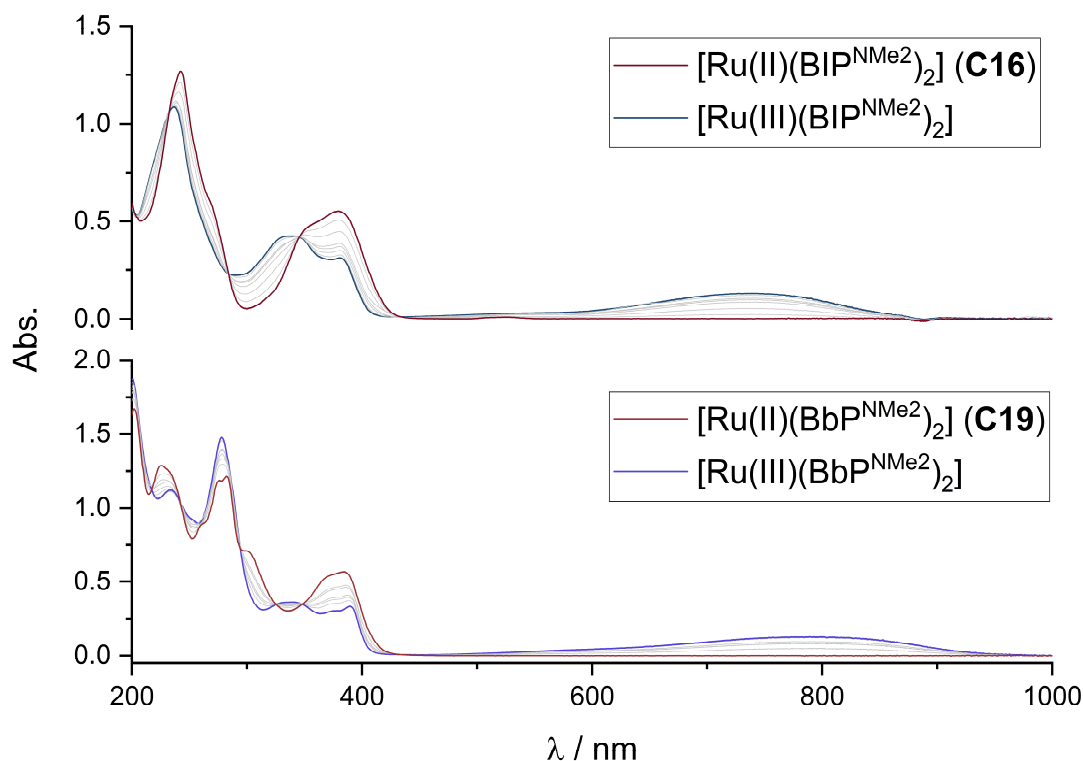


**Figure 5-14:** Change of the UV/Vis spectra during electrolysis of **C16** and **C19** with an applied potential of 0.47 V (top) and 0.66 V (bottom).

The brought emerging LMCT feature of the oxidized species, lead to a color change of the analyzed solution from yellow to blue. Indicating the same feature as observed for the iron analogues. Since the oxidation potential of the Ru<sup>II/III</sup> redox couple will enable a oxidation using NOPF<sub>6</sub> ( $E^{\circ}_{\text{ox}}$ : 0.87 V in MeCN<sup>147</sup>) synthetic isolation of the Ru<sup>III</sup> species is not accomplished to this point. In contrast to the iron analogue, the ruthenium complexes tend to decompose using an excess of oxidation agent.

## 5.5 Chapter summary

Analogous to the iron complex series, the new ligands were used to produce a corresponding ruthenium complex series. For ten of these complexes, measurable single crystals were obtained, which show a distorted octahedral coordination geometry similar to the iron derivatives. The larger ligand field splitting of the ruthenium center ion, which is manifested in the yellow color of the complex material, is also confirmed by UV/Vis investigations. These showed a shift of the MLCT band to higher energies, which confirm the larger gap between  $t_{2g} \rightarrow \pi^*$ . Compared to corresponding non-functionalized

ruthenium references, the same effect of the amine group on the splitting of the MLCT transitions could be detected as observed in the iron cases. Investigations of the emission properties showed a significantly reduced fluorescence compared to the reference. This property is probably due to the destabilizing effect of the amine on the ligands  $\pi^*$ -orbital, since destabilization reduces the energy gap to the metal-centered  $e_g$ -orbital, thus enabling a radiation-free deactivation. Due to the rapid radiationless deactivation, the  $^3\text{MLCT}$  lifetimes were also determined by transient absorption and showed an immense reduction of this state by a factor of 100 into the picosecond range compared to the corresponding unfunctionalized references. The negative shift in the oxidation potential observed in the iron series was also transferred to the ruthenium complexes shifting the oxidation potentials for the  $\text{Ru}^{\text{II/III}}$  couple to values of 0.1-0.3 V for monocyclic and 0.3-0.5 V for bicyclic carbene complexes.

## 6 Summary and Conclusion

Improving the efficiency of iron photosensitizers for photocatalytic applications is a fundamental step on the way to sustainable photocatalysis. In order to improve the efficiency, it is essential to understand the magnitude of influence by ligand variation applicable to the system. To gain further information about the amine influence onto NHC-ligands, a systematic series of new ligands was developed (**figure 6-1**). The ligand series was built from a central pyridine ring, which is functionalized in 2,4 and 6-position. In 4-position different amines were attached varying in size from dimethylamine (-NMe<sub>2</sub>) via diethylamine (-NEt<sub>2</sub>) to dibenzylamine (-NBn<sub>2</sub>). In 2,6-position the carbene ligand was attached, differing in size of the diazole ring size. The monocyclic series was based on imidazolylidene (**L1**, **L6**, **L11**), which is further varied by methylation in 3-position (**L2**, **L7**, **L12**) and even further by total methylation in 3,4-position (**L3**, **L8**, **L13**).

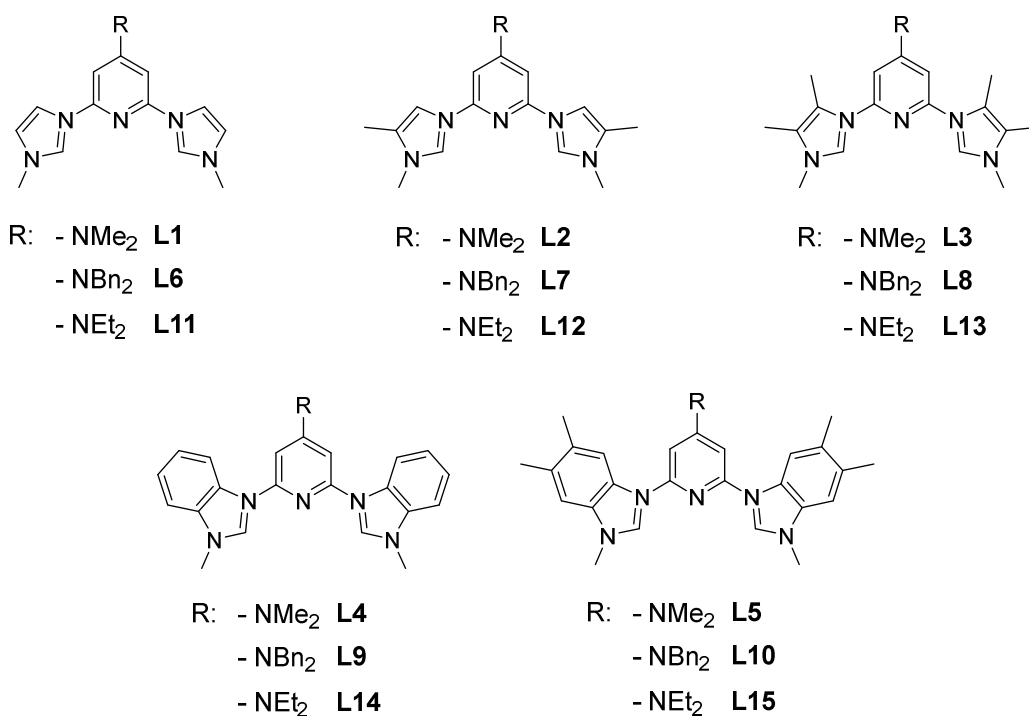


**Figure 6-1:** Summary of synthesized ligand systems.

Extension of the  $\pi$ -system was achieved by using benzimidazolylidene (**L4**, **L9**, **L14**) whose properties were compared to the dialkylated analogue 5,6-dimethylbenzimidazolylidene (**L5**, **L10**, **L15**). All ligand systems were characterized thoroughly, by means of NMR-spectroscopy and UV/Vis spectroscopy, whereby the influence of amine addition became obvious in cyclic voltammetry as well. The effect of amine addition was compared with the unfunctionalized analogue 2,6-bisimidazolylidene-pyridine (**BIP**) and it turned out that significant shifts were observable in terms of less

carbene-proton acidity or shifts of the ligand reduction potential which is unfavorable considering the envisaged application.

The obtained ligands were further used for complexation reactions resulting in the homoleptic Fe(II)-NHC compounds **C1-C15** (figure 6-2).

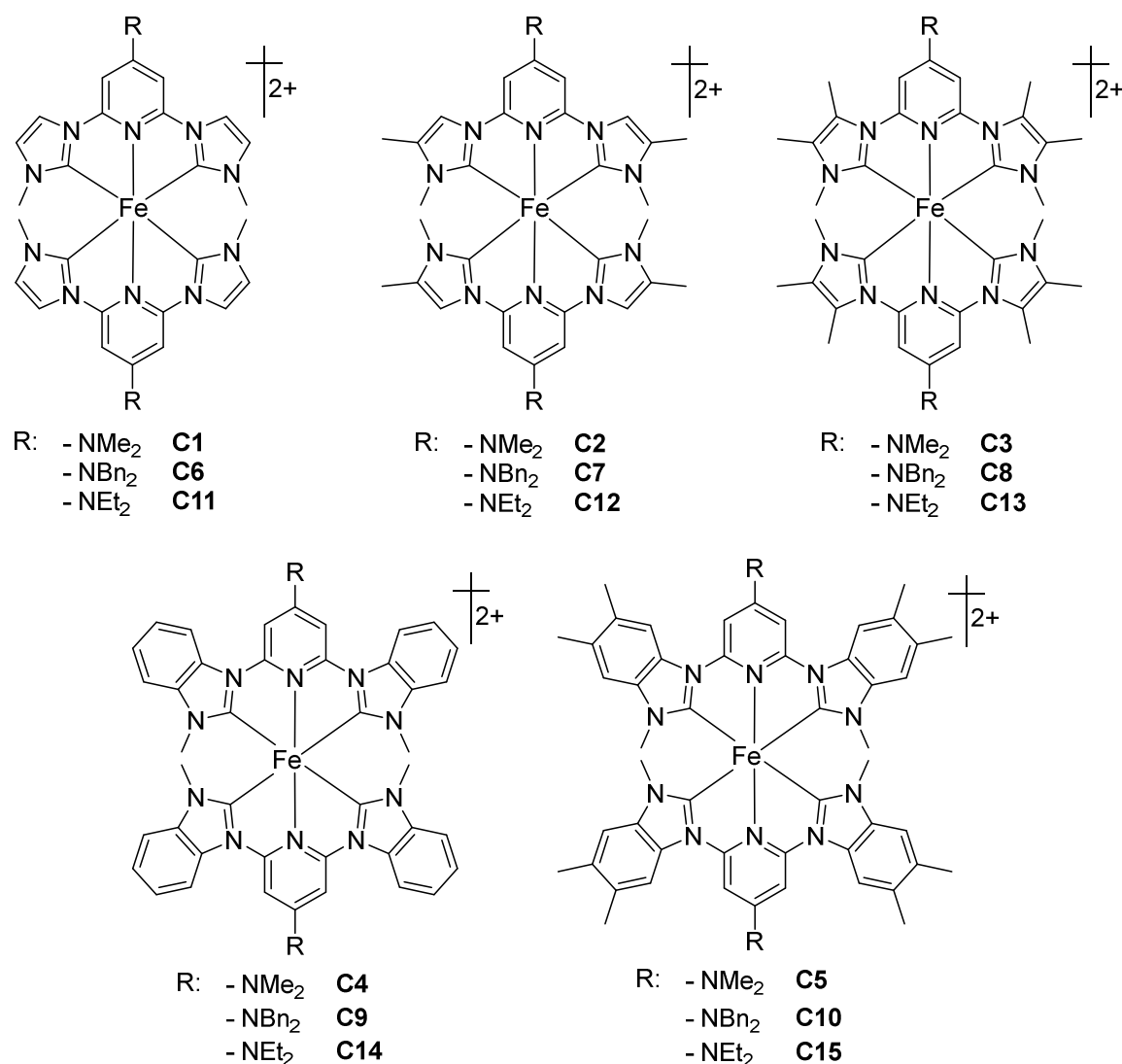


**Figure 6-2:** Summary of synthesized homoleptic Fe(II)-NHC compounds.

For most of the complex series, suitable single crystals could be obtained enabling a detailed analysis of the actual coordination geometry by X-ray diffractometry. As a result, all analyzed complexes showed a distorted octahedral coordination, limited by the bite angle between both carbene moieties. The variation of the imidazolidene backbone resulted in different Fe-NHC bond lengths, corresponding to the according  $\sigma$ -donor strength. Started with the aim of investigating the amine influence on the absorption properties, the series showed a MLCT transition band within the visible area. The maximum absorption was shifted towards higher energies equivalent to an increased HOMO-LUMO gap compared to the reference complex. This behavior distinguished the

NHC-containing complex series, from polypyridines and could be looked upon as a disadvantage concerning the envisaged application. Since no fluorescence could be detected for the complex series, the excited state lifetime of selected samples was determined using transient absorption spectroscopy. Despite the less favorable absorption properties, the MLCT lifetime only was found to be slightly shorter within the monocyclic carbene series compared to the reference complex. The influence of the amine functionalization showed greater impact onto the lifetime of the bicyclic series. All investigated complexes showed MLCT lifetimes in the 10 ps region. Further investigation of the redox properties showed significantly decreased redox potentials for the reversible Fe<sup>II/III</sup> redox couple. The observed decrease of the redox potential in the pure ligand compound resumes onto the complex series, shifting a second irreversible oxidation into an applicable potential range, which was attributable to the Fe<sup>III/IV</sup> redox couple. The first redox event for the monocyclic series showed a potential from -0.02 – - 0.13 V, whereas the potential drops by further methylation of the imidazolydene backbone. The bicyclic series showed much higher redox potentials attributable to the accepting character of the benzimidazolydene at about 0.2 V for the Fe<sup>II/III</sup> redox couple. The observed second redox event showed an approximate potential of 1.1 V in the monocyclic series and was observed only for complex **C4** in the bicyclic series at 1.19 V. A number of compounds could be isolated in the Fe(III) state, which were characterized in a low-spin state using the EVANS-method and X-ray emission spectroscopy.<sup>137–140</sup> Furthermore, the complex series showed a pH-dependency, starting with protonation of the amine function in an acidic environment and a simplified oxidation, likely triggered by molecular oxygen. A de novo readjustment of the pH to basic conditions showed reversibility of the process and lead to the former Fe(II) complex. Especially the ligands with extended  $\pi$ -system show promising absorption properties and allow easy access to the corresponding Fe(III) analogues due to the amine functionalization. A further extension of the system together with the possibility of protonation of the amine group can lead to an efficient absorption of the visible range.

To obtain further information about this new ligand class, a similar complex series is synthesized using Ru(II) as a center atom (**figure 6-3**). Like for the iron series, suitable single crystals are obtained for a majority of the Ru(II)-NHC compounds. The coordination geometry remains distorted octahedral, irrespective of the larger Ru-center atom, whereas the effect of bond length contraction due to increased  $\sigma$ -donation is not observed in the ruthenium series. Investigation of the absorption properties show high similarity between the iron and ruthenium complex series, albeit the ruthenium MLCT transition is shifted to smaller wavelengths by about 55 nm. The effect of carbene variation is decisive for the transition band structure, whereas amine functionalization shows minor influences on the

extinction coefficient. Interestingly the amine functionalization lead to an almost total fluorescence quenching for the complex series, which is contrary to the unfunctionalized reference complex. This property is probably due to the destabilizing effect of the amine on the ligands  $\pi^*$ -orbital, since destabilization leads to a convergence to the metal-centered  $e_g$ -orbital, meaning an alignment to the iron field splitting. In an experiment using time correlated single photon counting it is proven that the fluorescence is quenched intramolecularly for instance by vibrational relaxation of the amine group and not intermolecularly, like quenching by  $\text{Et}_3\text{N}$ , of another complex molecule. Electrochemical investigations show one reversible redox event for the whole ruthenium series, which exhibits the same trend of diminished potential by backbone methylation of the diazoles. The shift between the  $\text{Fe}^{\text{II/III}}$  and the  $\text{Ru}^{\text{II/III}}$  redox event is found to be about +0.23 V throughout the whole complex series, which shows that the influence of the ligands has the same effect on both metal centers.

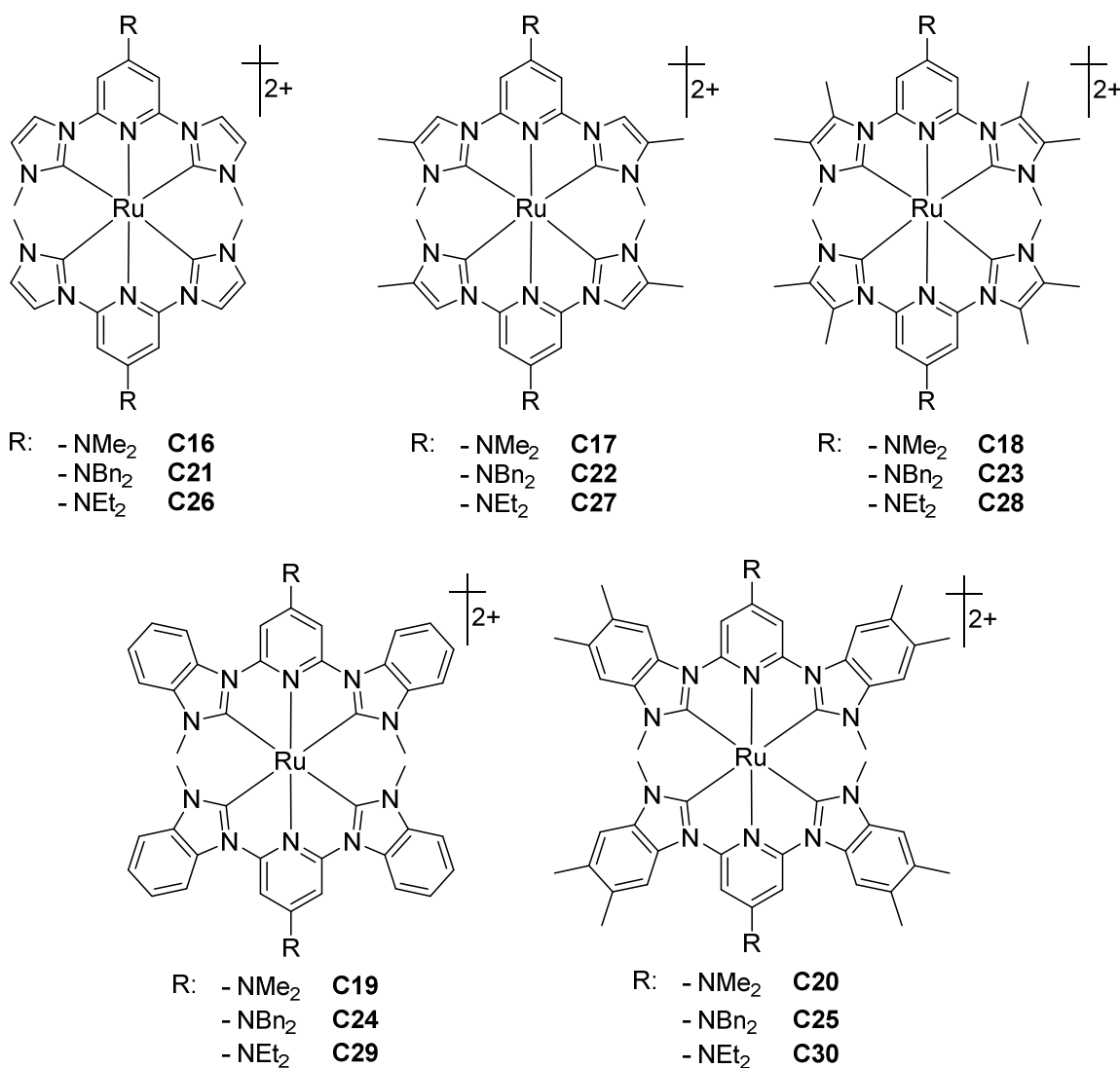


**Figure 6-3:** Summary of the synthesized homoleptic Ru(II)-NHC compounds.

As a result, the redox potential for the monocyclic series is found to be around 0.2 V and shifts to higher values of 0.4 V in the bicyclic series, due to the former mentioned accepting character of the benzimidazoles.

Summarizing, a series of 15 new amine functionalized tridentate NHC-ligands was synthesized, characterized, and used for the preparation of 15 iron and ruthenium complexes each. With the aim of studying the influence of amines onto the absorption- and electrochemical properties of the corresponding Fe(II)- and Ru(II)-NHC complexes, the results obtained have shown that the addition of amines to the ligand framework leads to an increased HOMO-LUMO gap, in contrast to polypyridine complexes. Made observations for ruthenium polypyridine complexes are not transferable to the respective Ru-NHC or Fe-NHC complexes, resulting in no enhanced efficiency for those photosensitizers. Anyway the iron complexes reveal other promising features, like a spin-crossover in the Fe(III) state or pH sensitivity. To further understand and confirm the spin-crossover and to determine the transition temperature, additional investigations using X-ray emission, or a superconducting quantum interference device (SQUID) are necessary. To understand the observed pH sensitivity more in-depth and to make use of the induced protonation, several comparable systems have to be synthesized varying in the amount of amine functions and combining them with an EWG group to build a push-pull system.

## 7 Experimental Part

### 7.1 General Information on equipment and chemicals

The synthesis of all compounds happens due to sensitivity against air or humidity of chemicals used under inert and anhydrous conditions. Therefore, standard Schlenk conditions are applied, and the used glass equipment is baked out at least three times and filled with pre-dried argon. All synthesis under inert conditions were carried out using water free solvents, which either were dried by literature references or picked from the solvent-drying plant by the firm *MBraun* model *MB SPS 800*.

The used chemicals were commercially purchased by following providers: *Sigma-Aldrich*, *abcr*, *TCI* and *Fisher Scientific*. All Chemicals were used for synthesis without further purification.

### 7.2 Annotations on the used analytical and spectroscopic methods

*NMR-Spectroscopy:*

$^1\text{H}$ -,  $^{13}\text{C}$  and  $^{15}\text{N}$ -Spectra of the different substances were recorded. These spectra are recorded by an NMR-spectrometer type *Avance 500* or a spectrometer type *Ascent 700* of company *Bruker* at the University of Paderborn. In case of the 500 MHz device the  $^1\text{H}$ -NMR-spectra are measured at a frequency of 500 MHz and the  $^{13}\text{C}$ -measurements are recorded at a frequency of 125 MHz. In case of the 700 MHz device the  $^1\text{H}$ -NMR-spectra are measured at a frequency of 700 MHz, the  $^{13}\text{C}$ -measurements are recorded at a frequency of 176 MHz and  $^{15}\text{N}$ -Spectra are recorded at 70.6 MHz. For measurement of the spectra the relevant substance is dissolved in an appropriate deuterated solvent which is specifically listed for each compound. The chemical shifts used indicated in ppm are related to the  $\delta$ -scale. For analysis of the spectra the software *Topspin* (version 4.0.6) by the firm *Bruker* is used. For correlation of the different signals to the belonging molecular parts two-dimensional NMR-spectra (COSY, HMBC, HMQC) are used.

*Mass spectrometry:*

The ESI-mass spectra were recorded using a quadrupole-time of flight-mass spectrometer (QTOF) type *Synapt 2G* by the firm *Waters*. The solvents used in each case are listed at each compound.

*X-ray diffraction analysis:*

Intensities for the X-ray diffraction analysis were recorded using the diffractometers type *AXS SMART APEX* or *D8 Venture* by the firm *Bruker* at 130 K. In case of the *AXS SMART APEX* MoK $\alpha$ -radiation ( $\varphi = 0.71073 \text{ \AA}$ ) is used in combination with a graphite monochromator.

*IR-Spectroscopy:*

The infrared spectra were measured with an IR-spectrometer *Vertex 70* by *Bruker*. Therefore, solid compounds were measured pure as powders using the ATR-technique.

*UV/Vis-Spectroscopy:*

For measurement of the UV/Vis-spectra a spectrometer *Cary 50* of firm *Varian* were used. The measurements were done at room temperature, whereas the used solvents were specified for every compound.

*Elemental analysis:*

The measurements of elemental analysis were realized with a device of type vario MICRO Cube of the company *Elementar*

*Electro chemistry:*

The cyclic- and square-wave-voltammograms were recorded at room temperature using the *Metrohm-Autolab Potentiostat PGSTAT 101* with a three-electrode arrangement. Therefore, a platinum-working electrode ( $d = 1 \text{ mm}$ ), an Ag/0.01 M AgNO<sub>3</sub>/MeCN-reference electrode and a platinum counter electrode were used. Recordings were executed using an inert argon atmosphere and water-free, degassed solvents. The complex concentration is 0.001 M using NBu<sub>4</sub>PF<sub>6</sub> (0.1 M) as supporting electrolyte. Ferrocene is used as internal standard and is added to the investigated solution after the

measurement. All potentials are referenced versus the ferrocene/ferrocenium (Fc/Fc<sup>+</sup>) redox couple.

*Magnetochemically investigation using the EVANS-Method:*

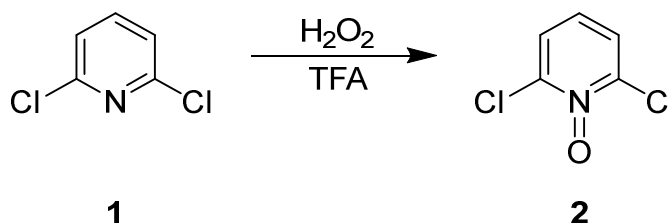
NMR-investigation of the paramagnetic complexes were conducted using the EVANS-Method to determine the effective magnetic moment  $\mu_{eff}$ .<sup>137-139,148</sup> For analysis the signal shift of a inert reference substance compared to the signal of the analyzed substance with paramagnetic influence are used. As reference the peak of the deuterated solvent itself is used. Suitable solvents shall show a solubility of the paramagnetic substance of at least 2.5 mg mL<sup>-1</sup> per unpaired electron to avoid overlap of reference- and sample-signals. For simultaneous measurement of reference and sample, a special NMR-tube is used which consists of an outer tube for the sample and an inner coaxial tube for the reference.

*Time-Correlated Single Photon Counting (TCSPC):*

The excited state lifetimes were measured using a *Horiba Ultima-01-DD*. The samples were prepared using freeze-pumped solvents with a concentration of approximate  $5 \cdot 10^{-5}$  M. The measurements were conducted with a 374 nm Laser diode and 10000 counts for each sample. The data analysis is realised with the software DAS6 provided by *Horiba*.

## 7.3 Precursor and Ligand synthesis

### 7.3.1 Synthesis of 2,6-dichloropyridine-N-oxide.



2,6-dichloropyridine (1 eq., 101 mmol) is dissolved in ice cold trifluoro acetic acid (120 mL). Following a dropwise addition of H<sub>2</sub>O<sub>2</sub> (30 ml) over 10 minutes. After complete addition the reaction mixture is stirred at 100° C for 4 hours and cooled to r.t.. Then 500 mL of cold distilled water are added, and the mixture is stirred for additional 10 minutes. The resulting precipitate is filtered, and the solution is extracted with dichloromethane (3 x 200 mL). The combined organic phases are washed with a saturated solution of K<sub>2</sub>CO<sub>3</sub> in water until the organic phase turned colorless. After drying of the organic phase over NaSO<sub>4</sub> the solvent is evaporated, and the raw product is recrystallized using acetone. The pure product is obtained as colorless crystalline needles.

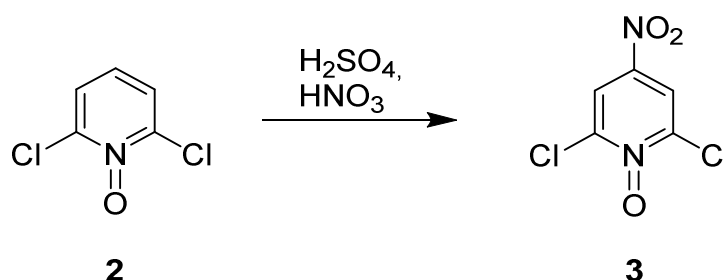
Yield: 73 %, (74.7 mmol).

**<sup>1</sup>H-NMR** (500 MHz, 30° C, CDCl<sub>3</sub>, δ [ppm]): 7.46 (d, <sup>3</sup>J<sub>HH</sub>: 7.83 Hz, 2H; CH<sub>arom.</sub>); 7.13 (t, <sup>3</sup>J<sub>HH</sub>: 7.78 Hz, 1H, CH<sub>arom.</sub>).

**<sup>13</sup>C-NMR** (125 MHz, 30° C, CDCl<sub>3</sub>, δ [ppm]): 143.5 (Cq); 125.2 (CH<sub>arom.</sub>); 124.6 (CH<sub>arom.</sub>).

**ESI-MS** (m/z (%)) (MeCN): 163.97 (100) [M+H<sup>+</sup>].

### 7.3.2 Synthesis of 2,6-dichloropyridine-4-nitro-N-oxide



2,6-dichloropyridine-N-oxide (1 eq; 48 mmol) is added to an ice cold mixture of  $\text{H}_2\text{SO}_4$  (0.85 mL  $\text{mmol}^{-1}$ ) and  $\text{HNO}_3$  (0.4 mL  $\text{mmol}^{-1}$ ). The reaction mixture is then heated to  $90^\circ\text{C}$  and stirred at this temperature for 18 h. After cooling to r.t. the reaction mixture is poured into a mixture of ice/water (500 mL) and the pH is adjusted to 14 using a 20 %-NaOH-solution, maintaining the temperature below  $10^\circ\text{C}$ . The resulting yellow precipitate is filtered and washed with cold water several times. The received raw product is recrystallized using chloroform resulting in the pure product as yellow needles.

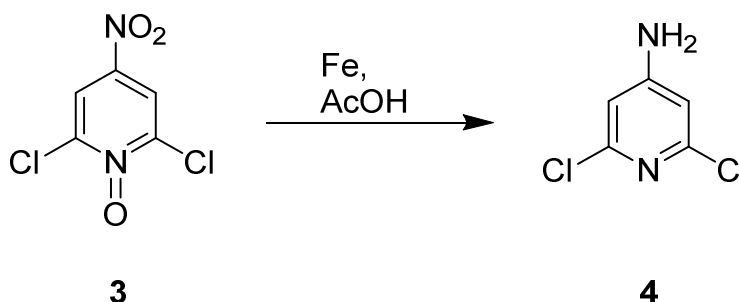
Yield: 60 %, (29.3 mmol).

$^1\text{H-NMR}$  (500 MHz,  $30^\circ\text{C}$ , DMSO,  $\delta$  [ppm]): 8.73 (s, 2H,  $\text{CH}_{\text{arom.}}$ ).

$^{13}\text{C-NMR}$  (125 MHz,  $30^\circ\text{C}$ , DMSO,  $\delta$  [ppm]): 151.5 (Cq); 143.6 (Cq); 120.7 ( $\text{CH}_{\text{arom.}}$ ).

**ESI-MS** (m/z (%))(MeOH+ $\text{H}^+$ ): 298.95 (100) [ $\text{M}+\text{H}^+$ ].

### 7.3.3 Synthesis of 2,6-dichloropyridine-4-amine



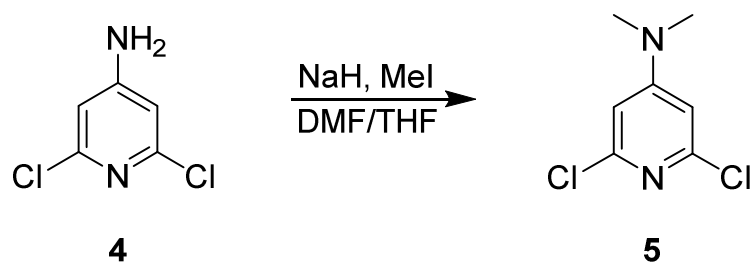
2,6-dichloropyridine-4-nitro-N-oxide (1 eq.; 62 mmol) is dissolved in glacial acetic acid (350 ml) and stirred at r.t.. Subsequently iron powder (5 eq.; 314 mmol) is added to the solution and the obtained suspension is stirred at  $100^\circ\text{C}$  for 1 h resulting in a color change of the mixture from bright grey to dark brown. After cooling to r.t. the suspension is cooled with an ice bath and the pH was adjusted to 14 using 20 % NaOH. The aqueous suspension is extracted with diethyl ether (3-5x 200 ml) and the combined organic phases are dried over  $\text{Na}_2\text{SO}_4$ . After removal of the solvent the raw product is obtained as a white powder. Purification of the product can be achieved using column chromatography (silica; DCM).

Yield: 88 %, (55 mmol).

$^1\text{H-NMR}$  (700 MHz,  $30^\circ\text{C}$ , DMSO,  $\delta$  [ppm]): 6.75 (br, 2H,  $\text{NH}_2$ ); 6.49 (s, 2H;  $\text{CH}_{\text{arom.}}$ ).

$^{13}\text{C-NMR}$  (176 MHz,  $30^\circ\text{C}$ , DMSO,  $\delta$  [ppm]): 158.2 (Cq); 149.2 (Cq); 106.5 ( $\text{CH}_{\text{arom.}}$ ).

**EI-MS** (m/z (%)): 161.97 (100) [ $\text{M}^+$ ].

7.3.4 Synthesis of 2,6-dichloro- *N,N'*-dimethylpyridine-4-amine

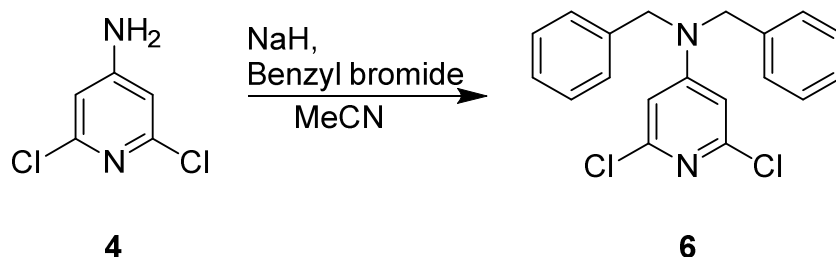
2,6-dichloropyridine-4-amine (1 eq.; 12 mmol) is added to an ice-cold solution of NaH (3 eq.; 36 mmol) in a mixture of DMF/THF (1:1; 30:30 ml) under argon atmosphere. The mixture is allowed to stir at 0° C for 30 minutes then iodomethane (3 eq., 36 mmol) is added and the reaction solution is stirred at 80 C for 5 h. After cooling to r.t. the reaction is quenched by a saturated solution of K<sub>2</sub>CO<sub>3</sub> in water. The obtained biphasic mixture is extracted with hexane (3 x 100 ml), and the combined hexane phases are dried over Na<sub>2</sub>SO<sub>4</sub>. After evaporation, the product is purified by column chromatography (silica; DCM: hexane 2:1) resulting in a white powder.

Yield: 90 %, (11 mmol).

<sup>1</sup>H-NMR (500 MHz, 30° C, CDCl<sub>3</sub>, δ [ppm]): 6.39 (s, 2H, CH<sub>arom.</sub>); 2.99 (s, 6H; CH<sub>3</sub>).

<sup>13</sup>C-NMR (500 MHz, 30° C, CDCl<sub>3</sub>, δ [ppm]): 157.6 (Cq); 151.0 (Cq); 108.0 (CH); 39.8 (CH<sub>3</sub>).

ESI-MS (m/z (%)) (MeOH): 191.0 (100) [M+H<sup>+</sup>]; 212.9 (28) [M+Na<sup>+</sup>].

7.3.5 Synthesis of *N,N'*-dibenzyl-2,6-dichloropyridine-4-amine

Under an argon atmosphere NaH (2.5 eq, 10 mmol) is dissolved in ice-cold acetonitrile. To the solution slowly 2,6-dichloropyridine-4-amine (1eq.; 4 mmol) is added and the mixture is stirred for additional 15 minutes. To the yellow solution benzyl bromide (8 eq.; 32 mmol) is added dropwise. The reaction mixture is stirred at reflux for 24 hours and after cooling to r.t. the solvent is removed under vacuum. The resulting yellow-white solid is purified using column chromatography (silica; DCM/hexane 3:1). The pure product is obtained as a white solid.

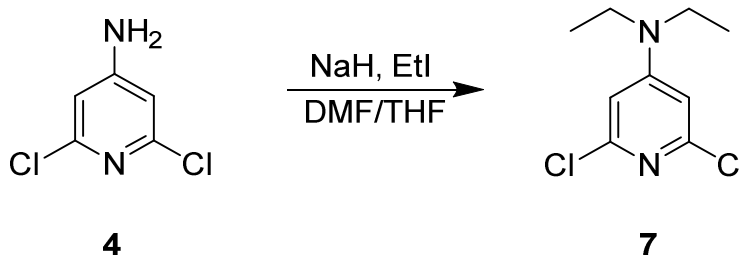
Yield: 68 %, (2.7 mmol).

**<sup>1</sup>H-NMR** (500 MHz, 30° C, DMSO,  $\delta$  [ppm]): 7.37 (d, 4H, CH<sub>arom.</sub>); 7.29 (t, 2H, CH<sub>arom.</sub>); 7.24 (d, 4H, CH<sub>arom.</sub>); 6.86 (s, 2H, CH<sub>arom.</sub>), 4.79 (s; 4H, CH<sub>2</sub>).

**<sup>13</sup>C-NMR** (125 MHz, 30° C, DMSO,  $\delta$  [ppm]): 156.4 (Cq); 140.2 (Cq); 136.6 (Cq); 128.8 (CH<sub>arom.</sub>); 127.3 (CH<sub>arom.</sub>); 126.6 (CH<sub>arom.</sub>); 109.7 (CH<sub>arom.</sub>); 53.5 (CH<sub>2</sub>).

**ESI-MS** (m/z (%)) (MeCN): 343.07 (100) [M+H<sup>+</sup>].

### 7.3.6 Synthesis of 2,6-dichloro- *N,N'*-diethylpyridine-4- amine



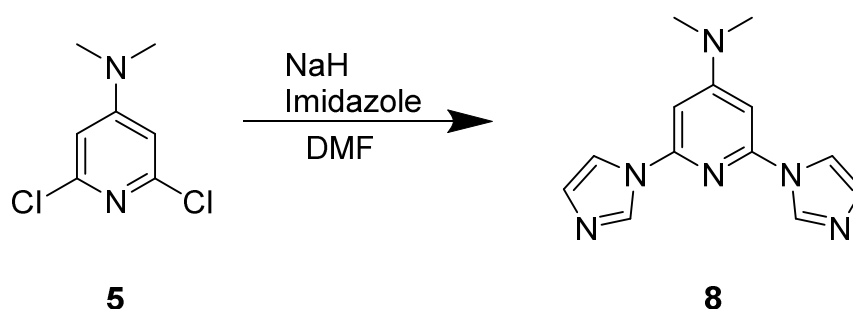
2,6-dichloropyridine-4-amine (1 eq.; 10 mmol) is added to an ice-cold solution of NaH (3 eq.; 30 mmol) in a mixture of DMF/THF (1:1; 30:30 ml) under argon atmosphere. The mixture is allowed to stir at 0 C for 30 minutes then iodoethane (3 eq.; 30 mmol) is added and the reaction solution is stirred at 80 C for 5 h. After cooling to r.t. the reaction is quenched by a saturated solution of K<sub>2</sub>CO<sub>3</sub> in water. The obtained biphasic mixture is extracted with ethyl acetate (3x 100 ml), and the combined organic ethyl acetate phases are dried over Na<sub>2</sub>SO<sub>4</sub>. After evaporation, the product is purified by column chromatography (silica; DCM: hexane 2:1) resulting in a white powder.

Yield: 95 %, (9.5 mmol).

**<sup>1</sup>H-NMR** (500 MHz, 30° C, DMSO,  $\delta$  [ppm]): 6.61 (s, 2H, CH<sub>arom.</sub>); 3.37 (q, 4H; <sup>3</sup>J<sub>HH</sub>: 7.12 Hz, CH<sub>2</sub>); 1.06 (t, 6H, <sup>3</sup>J<sub>HH</sub>: 7.04 Hz, CH<sub>3</sub>).

**<sup>13</sup>C-NMR** (500 MHz, 30° C, DMSO,  $\delta$  [ppm]): 155.3 (Cq); 149.8 (Cq); 104.3 (CH<sub>arom.</sub>); 43.7 (CH<sub>2</sub>); 11.8 (CH<sub>3</sub>).

**ESI-MS** (m/z (%)) (MeCN): 219.04 (100) [M+H<sup>+</sup>]; 241.0 (18) [M+Na<sup>+</sup>].

7.3.7 Synthesis of 2,6-bisimidazole-*N,N'*-dimethylpyridine-4-amine

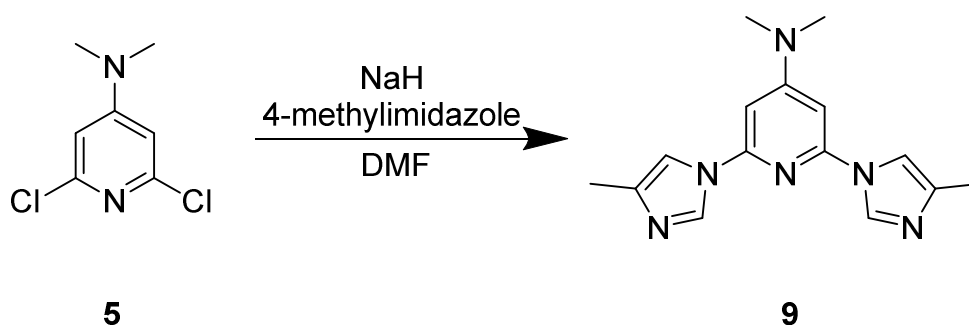
Under an argon atmosphere NaH (3.4 eq., 17 mmol) is dissolved in dry DMF (50 mL) and cooled with an ice-bath to 0 C. Then imidazole (3.3 eq., 16 mmol) is added portion wise. After complete addition the reaction mixture is stirred 1 h at 0 C and then allowed to warm to r.t.. At r.t. 2,6-dichloro-*N,N'*-dimethylpyridine-4-amine (1 eq., 5 mmol) is added and the mixture stirred at 130 C for 3 days. After cooling to r.t. the solution is poured into a mixture of ice/water (300 mL) and stirred for additional 10 minutes. The occurring white solid is filtered, washed with diethyl ether and dried under vacuum.

Yield: 74 %, (3.7 mmol).

**<sup>1</sup>H-NMR** (500 MHz, 30° C, DMSO,  $\delta$  [ppm]): 8.65 (t, 2H, CH<sub>arom.</sub>); 8.06 (t, 2H, CH<sub>arom.</sub>); 7.09 (s, 2H, CH<sub>arom.</sub>); 6.84 (s, 2H, CH<sub>arom.</sub>); 3.13 (s, 6H, CH<sub>3</sub>).

**<sup>13</sup>C-NMR** (500 MHz, 30° C, DMSO,  $\delta$  [ppm]): 158.6 (Cq); 148.6 (Cq); 135.6 (CH<sub>arom.</sub>); 129.8 (CH<sub>arom.</sub>); 117.0 (CH<sub>arom.</sub>); 92.5 (CH<sub>arom.</sub>); 39.6 (CH<sub>3</sub>).

**ESI-MS** (m/z (%))(MeCN): 255.13 (100) [M+H<sup>+</sup>]

7.3.8 Synthesis of 2,6-bis(4-methylimidazole)-*N,N'*-dimethylpyridine-4-amine

Under an argon atmosphere NaH (3.4 eq.; 24 mmol) is dissolved in dry DMF (50 mL) and cooled with an ice-bath to 0° C. Then 4-methylimidazole (3.3 eq.; 23 mmol) is added portion wise. After complete addition the reaction mixture is stirred 1 h at 0° C and then allowed to warm to r.t.. At r.t. 2,6-dichloro-*N,N'*-dimethylpyridine-4-amine (1 eq.; 7 mmol) is added and the mixture stirred at 130° C for 3 days. After cooling to r.t. the solution is

poured into a mixture of ice/water (300 mL) and stirred for additional 10 minutes. The aqueous phase is extracted with dichloromethane (3x 200 mL) and the organic phase is dried over Na<sub>2</sub>SO<sub>4</sub>. After evaporation of the solvents the product is obtained as white powder.

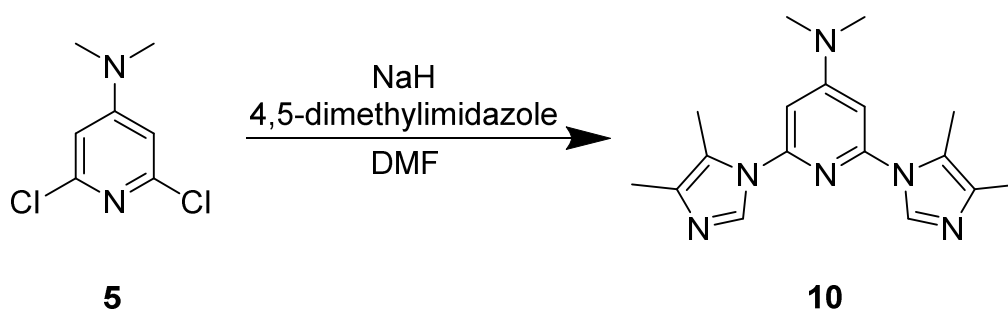
Yield: 76 %, (5.3 mmol).

**<sup>1</sup>H-NMR** (500 MHz, 30° C, CDCl<sub>3</sub>, δ [ppm]): 8.19 (s, 2H, CH<sub>arom.</sub>); 7.28 (s, 2H, CH<sub>arom.</sub>); 6.28 (s, 2H, CH<sub>arom.</sub>); 3.10 (s; 6H; CH<sub>3</sub>); 2.28 (s, 6H, CH<sub>3</sub>).

**<sup>13</sup>C-NMR** (125 MHz, 30° C, CDCl<sub>3</sub>, δ [ppm]): 158.2 (Cq); 149.3 (Cq); 139.7 (Cq), 134.5 (CH<sub>arom.</sub>), 112.8 (CH<sub>arom.</sub>), 92.01 (CH<sub>arom.</sub>), 39.9 (CH<sub>3</sub>); 13.9 (CH<sub>3</sub>).

**ESI-MS** (m/z (%)) (MeCN): 283.16 (100) [M+H<sup>+</sup>].

### 7.3.9 Synthesis of 2,6-bis(4,5-dimethylimidazole)-*N,N'*-dimethylpyridine-4-amine



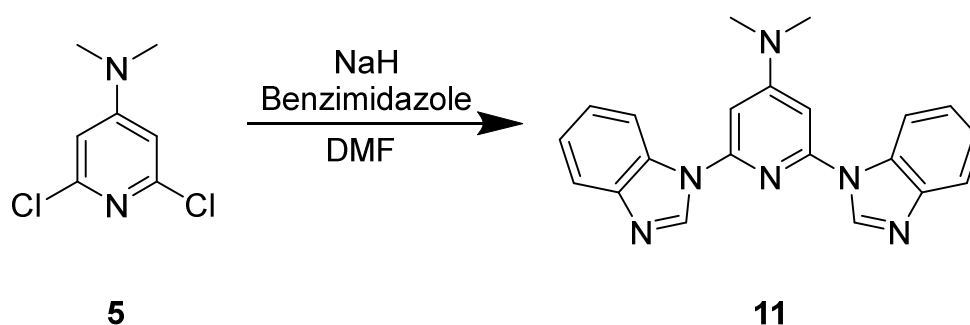
Under an argon atmosphere NaH (3.4 eq., 24 mmol) is dissolved in dry DMF (50 mL) and cooled with an ice-bath to 0° C. Then 4,5-dimethylimidazole (3.3 eq.; 23 mmol) is added portion wise. After complete addition the reaction mixture is stirred 1 h at 0° C and then allowed to warm to r.t.. At r.t. 2,6-dichloro- *N,N'*-dimethylpyridine-4-amine (1 eq.; 7 mmol) is added and the mixture stirred at 130° C for 3 days. After cooling to r.t. the solution is poured into a mixture of ice/water (300 mL) and stirred for additional 10 minutes. The resulting white precipitate is filtered, washed with diethyl ether and dried under vacuum.

Yield: 73 %, (5.1 mmol)

**<sup>1</sup>H-NMR** (500 MHz, 30° C, CDCl<sub>3</sub>, δ [ppm]): 7.75 (s, 2H, CH<sub>arom.</sub>); 6.38 (s, 2H, CH<sub>arom.</sub>); 3.08 (s, 6H, CH<sub>3</sub>); 2.28 (s; 6H; CH<sub>3</sub>); 2.18 (s, 6H, CH<sub>3</sub>).

**<sup>13</sup>C-NMR** (125 MHz, 30° C, CDCl<sub>3</sub>, δ [ppm]): 157.9 (Cq); 150.4 (Cq); 135.5 (Cq), 134.9 (CH<sub>arom.</sub>), 122.5 (Cq), 98.1 (CH<sub>arom.</sub>), 39.9 (CH<sub>3</sub>); 12.8 (CH<sub>3</sub>); 10.49 (CH<sub>3</sub>).

**ESI-MS** (m/z (%)) (MeCN): 311.19 (100) [M+H<sup>+</sup>].

7.3.10 Synthesis of 2,6-bis(benzimidazole)-*N,N'*-dimethylpyridine-4-amine

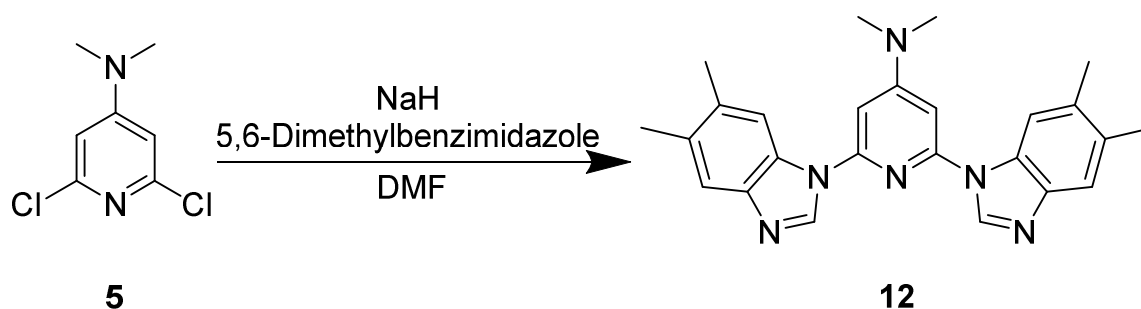
Under an argon atmosphere NaH (3.4 eq., 17 mmol) is dissolved in dry DMF (50 mL) and cooled with an ice-bath to 0° C. Then benzimidazole (3.3 eq.; 16.5 mmol) is added portion wise. After complete addition the reaction mixture is stirred 1 h at 0° C and then allowed to warm to r.t.. At r.t. 2,6-dichloro- *N,N'*-dimethylpyridine-4-amine (1 eq.; 5 mmol) is added and the mixture stirred at 130° C for 3 days. After cooling to r.t. the solution is poured into a mixture of ice/water (300 mL) and stirred for additional 10 minutes. The resulting white precipitate is filtered, washed with diethyl ether and dried under vacuum.

Yield: 75 %, (3.75 mmol).

**<sup>1</sup>H-NMR** (500 MHz, 30° C, DMSO,  $\delta$  [ppm]): 9.03 (s, 2H, CH<sub>arom.</sub>); 8.20 (dd, <sup>3</sup>J<sub>HH</sub>: 6.45 Hz, 2H, CH<sub>arom.</sub>); 7.79 (dd, <sup>3</sup>J<sub>HH</sub>: 6.33 Hz, 2H, CH<sub>arom.</sub>); 7.34 (m; 4H; CH<sub>arom.</sub>); 7.03 (s, 2H, CH<sub>arom.</sub>); 3.21 (s, 6H, CH<sub>3</sub>).

**<sup>13</sup>C-NMR** (125 MHz, 30° C, DMSO,  $\delta$  [ppm]): 158.6 (Cq); 149.9 (Cq); 144.7 (Cq), 143.1 (Cq), 132.6 (CH<sub>arom.</sub>), 124.3 (CH<sub>arom.</sub>), 123.4 (CH<sub>arom.</sub>), 120.4 (CH<sub>arom.</sub>), 114.2 (CH<sub>arom.</sub>), 95.6 (CH<sub>arom.</sub>), 39.8 (CH<sub>3</sub>).

**ESI-MS** (m/z (%)) (MeCN): 355.1 (100) [M+H<sup>+</sup>].

7.3.11 Synthesis of 2,6-bis(5,6-dimethylbenzimidazole)-*N,N'*-dimethylpyridine-4-amine

Under an argon atmosphere NaH (3.4 eq.; 20.5 mmol) is dissolved in dry DMF (50 mL) and cooled with an ice-bath to 0° C. Then 5,6-dimethylbenzimidazole (3.3 eq.; 20 mmol)

was added portion wise. After complete addition the reaction mixture is stirred 1 h at 0° C and then allowed to warm to r.t.. At r.t. 2,6-dichloro- *N,N'*-dimethylpyridine-4-amine (1 eq.; 6 mmol) is added and the mixture stirred at 130° C for 3 days. After cooling to r.t. the solution is poured into a mixture of ice/water (300 mL) and stirred for additional 10 minutes. The resulting white precipitate is filtered, washed with diethyl ether and dried under vacuum.

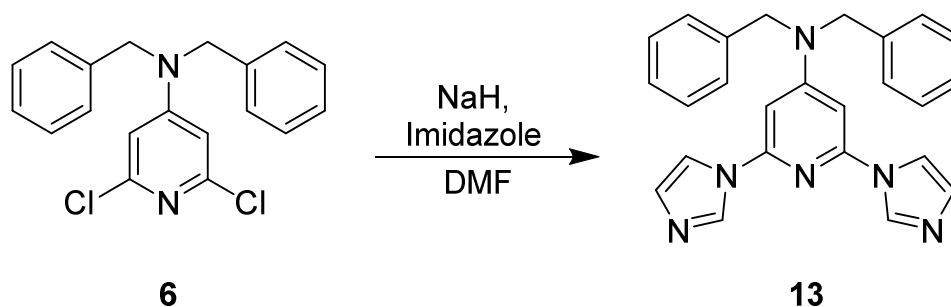
Yield: 77 %, (4.6 mmol)

**<sup>1</sup>H-NMR** (500 MHz, 30° C, DMSO,  $\delta$  [ppm]): 8.89 (s, 2H, CH<sub>arom.</sub>); 8.09 (s, 2H, CH<sub>arom.</sub>); 7.53 (s, 2H, CH<sub>arom.</sub>); 6.96 (s, 2H, CH<sub>arom.</sub>); 3.17 (s; 6H; CH<sub>3</sub>); 2.33 (s, 6H, CH<sub>3</sub>); 2.27 (s, 6H, CH<sub>3</sub>).

**<sup>13</sup>C-NMR** (125 MHz, 30° C, CDCl<sub>3</sub>,  $\delta$  [ppm]): 158.1 (Cq); 150.3 (Cq); 143.5 (Cq), 140.8 (CH<sub>arom.</sub>); 133.4 (Cq); 132.2 (Cq); 130.7 (Cq); 120.7 (CH<sub>arom.</sub>); 113.4 (CH<sub>arom.</sub>); 94.2 (CH<sub>arom.</sub>); 39.9 (CH<sub>3</sub>); 20.9 (CH<sub>3</sub>); 20.4 (CH<sub>3</sub>).

**ESI-MS** (m/z (%)) (MeCN): 411.23 (100) [M+H<sup>+</sup>], 821.456 (73) [2xM+H<sup>+</sup>].

### 7.3.12 Synthesis of *N,N'*-dibenzyl-2,6-bisimidazolpyridine-4-amine



Under an argon atmosphere NaH (3.4 eq., 29 mmol) is dissolved in dry DMF (50 mL) and cooled with an ice-bath to 0° C. Then imidazole (3.3 eq., 28 mmol) is added portion wise. After complete addition the reaction mixture is stirred 1 h at 0° C and then allowed to warm to r.t.. At r.t. *N,N'*-dibenzyl-2,6-dichloropyridine-4-amine (1 eq., 8.5 mmol) is added and the mixture stirred at 130° C for 3 days. After cooling to r.t. the solution is poured into a mixture of ice/water (300 mL) and stirred for additional 10 minutes. The occurring white solid is filtered, washed with diethyl ether and dried under vacuum.

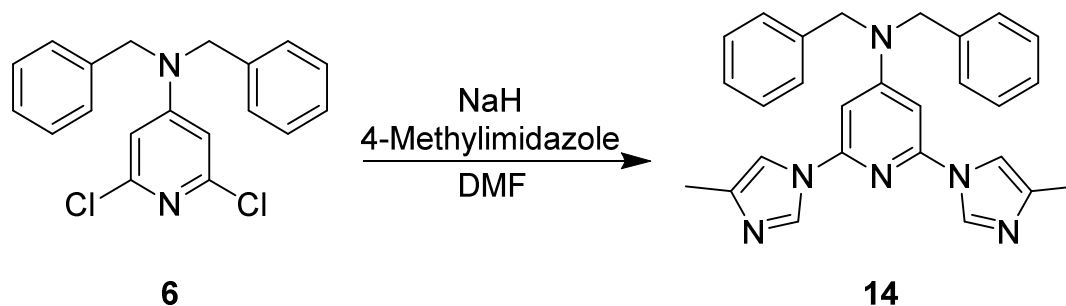
Yield: 81 %, (6.9 mmol).

**<sup>1</sup>H-NMR** (500 MHz, 30° C, DMSO,  $\delta$  [ppm]): 8.57 (s, 2H, CH<sub>arom.</sub>); 7.96 (s, 2H, CH<sub>arom.</sub>); 7.34 (m, 8H, CH<sub>arom.</sub>); 7.27 (t, <sup>3</sup>J<sub>HH</sub>: 7.07 Hz, 2H, CH<sub>arom.</sub>); 7.08 (s, 2H, CH<sub>arom.</sub>); 6.99 (s, 2H, CH<sub>arom.</sub>); 4.92 (s, 4H, CH<sub>2</sub>).

**$^{13}\text{C-NMR}$**  (125 MHz, 30° C, DMSO,  $\delta$  [ppm]): 158.0 (Cq); 148.8 (Cq); 137.4 (Cq); 135.5 (CH<sub>arom.</sub>); 129.8 (CH<sub>arom.</sub>); 128.7 (CH<sub>arom.</sub>); 127.3 (CH<sub>arom.</sub>); 127.1 (CH<sub>arom.</sub>); 116.9 (CH<sub>arom.</sub>); 93.2 (CH<sub>arom.</sub>); 53.0 (CH<sub>2</sub>).

**ESI-MS** (m/z (%)) (MeOH): 407.19 (100) [M+H<sup>+</sup>]; 204.10 (11) [M-Benzyl+H<sup>+</sup>].

### 7.3.13 Synthesis of *N,N'*-dibenzyl-2,6-bis(4-methyl)-imidazolpyridine-4-amine



Under an argon atmosphere NaH (3.5 eq.; 32 mmol) is dissolved in dry DMF (75 mL) and cooled with an ice-bath to 0° C. Then 4-methylimidazole (3.4 eq.; 31 mmol) is added portion wise. After complete addition, the reaction mixture is stirred 1 h at 0° C and then allowed to warm to room temperature. At r.t. *N,N'*-dibenzyl-2,6-dichloropyridine-4-amine (1 eq.; 9 mmol) is added and the mixture stirred at 130° C for 3 days. After cooling to r.t. the solution is poured into a mixture of ice/water (300 mL) and stirred for additional 10 minutes. The occurring yellow solid is filtered, washed with diethyl ether and dried under vacuum. The raw product is purified by column chromatography (silica/ hexane: EtOAc 100:0 → 0:100) and is obtained as a yellow crystalline solid after evaporation of the solvent.

Yield: 40 %, (3.6 mmol).

**$^1\text{H-NMR}$**  (500 MHz, 30° C, DMSO,  $\delta$  [ppm]): 8.49 (s, 2H, CH<sub>arom.</sub>); 7.67 (s, 2H, CH<sub>arom.</sub>); 7.35 (m, 8H, CH<sub>arom.</sub>); 7.26 (t,  $^3J_{\text{HH}}$ : 7.02 Hz, 2H, CH<sub>arom.</sub>); 6.92 (s, 2H, CH<sub>arom.</sub>); 4.90 (s, 4H, CH<sub>2</sub>); 2.16 (s, 6H, CH<sub>3</sub>).

**$^{13}\text{C-NMR}$**  (125 MHz, 30° C, DMSO,  $\delta$  [ppm]): 157.9 (Cq); 148.7 (Cq); 138.4 (Cq); 137.3 (CH<sub>arom.</sub>); 134.6 (Cq); 128.6 (CH<sub>arom.</sub>); 127.2 (CH<sub>arom.</sub>); 126.9 (CH<sub>arom.</sub>); 112.9 (CH<sub>arom.</sub>); 92.3 (CH<sub>arom.</sub>); 52.8 (CH<sub>2</sub>); 13.6 (CH<sub>3</sub>).

**ESI-MS** (m/z (%)) (MeCN): 435.23 (100) [M+H<sup>+</sup>].



portion wise. After complete addition the reaction mixture is stirred 1 h at 0° C and then allowed to warm to r.t.. At r.t. *N,N'*-dibenzyl-2,6-dichloropyridine-4-amine (1 eq.; 6 mmol) is added and the mixture stirred at 130° C for 3 days. After cooling to r.t. the solution is poured into a mixture of ice/water (300 mL) and stirred for additional 10 minutes. The occurring yellowish solid is filtered, washed with diethyl ether and dried under vacuum.

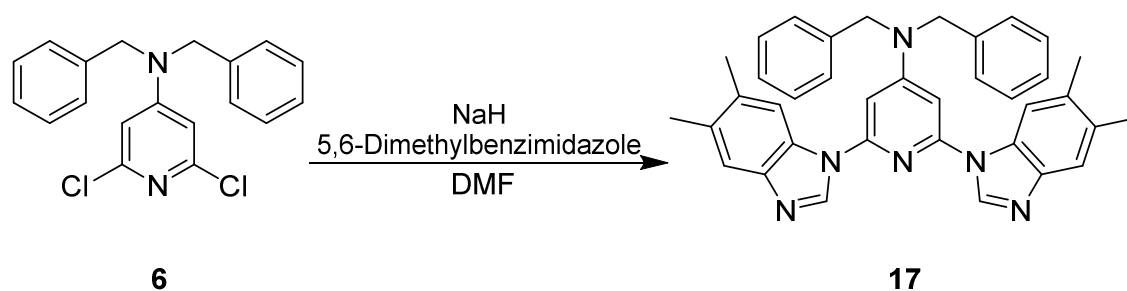
Yield: 97 % (5.8 mmol)

**<sup>1</sup>H-NMR** (500 MHz, 30° C, DMSO, δ [ppm]): 8.94 (s, 2H, CH<sub>arom.</sub>); 7.76 (d, <sup>3</sup>J<sub>HH</sub>: 8.01 Hz 2H, CH<sub>arom.</sub>); 7.75 (d, <sup>3</sup>J<sub>HH</sub>: 8.1 Hz; 2H, CH<sub>arom.</sub>); 7.43 (m, 8H, CH<sub>arom.</sub>); 7.36 (t, <sup>3</sup>J<sub>HH</sub>: 7.24 Hz; 2H, CH<sub>arom.</sub>); 7.30 (t, <sup>3</sup>J<sub>HH</sub>: 7.30 Hz, 2H, CH<sub>arom.</sub>); 7.20 (t, <sup>3</sup>J<sub>HH</sub>: 8.15 Hz, 2H, CH<sub>arom.</sub>), 7.01 (s, 2H, CH<sub>arom.</sub>); 5.07 (s, 4H, CH<sub>2</sub>).

**<sup>13</sup>C-NMR** (125 MHz, 30° C, DMSO, δ [ppm]): 157.3 (Cq); 149.3 (Cq); 144.3 (Cq); 142.6 (Cq); 137.4 (Cq); 131.9 (CH<sub>arom.</sub>); 128.9 (CH<sub>arom.</sub>); 127.4 (CH<sub>arom.</sub>); 127.3 (CH<sub>arom.</sub>); 126.9 (CH<sub>arom.</sub>); 123.9 (CH<sub>arom.</sub>); 122.9 (CH<sub>arom.</sub>); 120.1 (CH<sub>arom.</sub>); 112.8 (CH<sub>arom.</sub>); 96.6 (CH<sub>arom.</sub>); 54.4 (CH<sub>2</sub>).

**ESI-MS** (m/z (%)) (MeOH): 507.22 (100) [M+H<sup>+</sup>]; 1013.45 (18) [2xM+H<sup>+</sup>]; 529.21 (8) [M+Na<sup>+</sup>].

### 7.3.16 Synthesis of *N,N'*-dibenzyl-2,6-bis-benzimidazolpyridine-4-amine



Under an argon atmosphere NaH (3.4 eq.; 24.5 mmol) is dissolved in dry DMF (50 mL) and cooled with an ice-bath to 0° C. Then 5,6-dimethylbenzimidazole (3.3 eq.; 23.8 mmol) is added portion wise. After complete addition the reaction mixture is stirred 1 h at 0° C and then allowed to warm to r.t.. At r.t. *N,N'*-dibenzyl-2,6-dichloropyridine-4-amine (1 eq.; 7 mmol) is added and the mixture stirred at 130° C for 3 days. After cooling to r.t. the solution is poured into a mixture of ice/water (300 mL) and stirred for additional 10 minutes. The pile precipitate is filtered, washed with diethyl ether and dried under vacuum.

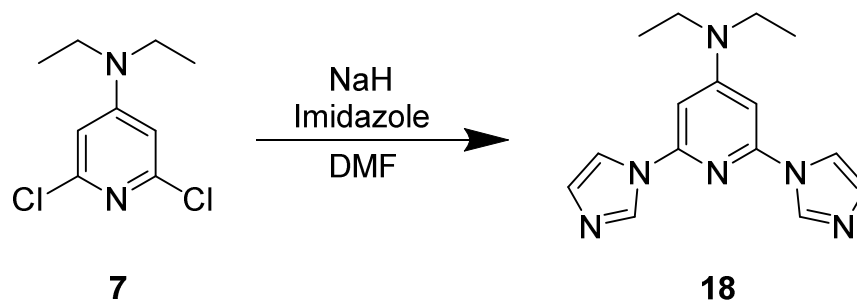
Yield: 73%, (5.1 mmol).

**<sup>1</sup>H-NMR** (500 MHz, 30° C, CDCl<sub>3</sub>, δ [ppm]): 8.40 (s, 2H, CH<sub>arom.</sub>); 7.58 (s, 2H, CH<sub>arom.</sub>); 7.45 (s, 4H, CH<sub>arom.</sub>); 7.38 (m, 8H, CH<sub>arom.</sub>); 6.73 (s, 2H, CH<sub>arom.</sub>); 4.89 (s, 4H, CH<sub>2</sub>), .2.36 (s, 6H, CH<sub>3</sub>); 2.22 (s, 6H, CH<sub>3</sub>).

**<sup>13</sup>C-NMR** (125 MHz, 30° C, CDCl<sub>3</sub>, δ [ppm]): 157.8 (Cq); 150.3 (Cq); 144.3 (Cq); 140.9 (Cq); 135.8 (Cq); 133.2 (Cq); 132.1 (CH<sub>arom.</sub>); 130.5 (Cq); 129.4 (CH<sub>arom.</sub>); 128.1 (CH<sub>arom.</sub>); 126.1 (CH<sub>arom.</sub>); 120.7 (CH<sub>arom.</sub>); 112.5 (CH<sub>arom.</sub>); 95.3 (CH<sub>arom.</sub>); 55.13 (CH<sub>2</sub>); 20.6 (CH<sub>3</sub>); 20.2 (CH<sub>3</sub>).

**ESI-MS** (m/z (%)) (MeCN): 563.29 (100) [M+H<sup>+</sup>]; 1125.57 (18) [2xM+H<sup>+</sup>]; 282.15 (25) [M<sup>2+</sup>].

### 7.3.17 Synthesis of 2,6-bisimidazole-*N,N'*-diethylpyridine-4-amine



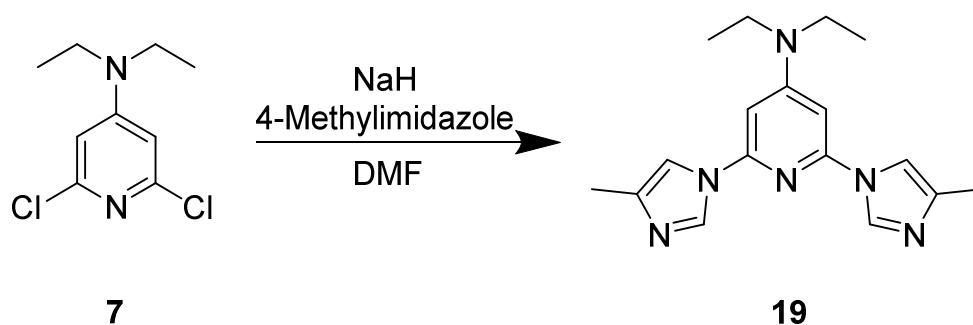
Under an argon atmosphere NaH (3.4 eq.; 14 mmol) is dissolved in dry DMF (50 mL) and cooled with an ice-bath to 0° C. Then imidazole (3.3 eq.; 13 mmol) is added portion wise. After complete addition the reaction mixture is stirred 1 h at 0° C and then allowed to warm to r.t.. At r.t. 2,6-dichloro- *N,N'*-diethylpyridine-4-amine (1 eq.; 4 mmol) is added and the mixture stirred at 130° C for 3 days. After cooling to r.t. the solution is poured into a mixture of ice/water (300 mL) and stirred for additional 10 minutes. The aqueous phase is extracted with dichloromethane (3x 200 mL) and the combined organic layers are dried over Na<sub>2</sub>SO<sub>4</sub>. After evaporation of the solvents the product is obtained as a white powder.

Yield: 81 %, (3.8 mmol).

**<sup>1</sup>H-NMR** (500 MHz, 30° C, CDCl<sub>3</sub>, δ [ppm]): 8.29 (s, 2H, CH<sub>arom.</sub>); 7.59 (s, 2H, CH<sub>arom.</sub>); 7.18 (s, 2H, CH<sub>arom.</sub>); 6.38 (s; 2H; CH<sub>arom.</sub>); 3.48 (q, <sup>3</sup>J<sub>HH</sub>: 7.12 Hz, 4H, CH<sub>2</sub>); 1.28 (t, <sup>3</sup>J<sub>HH</sub>: 7.26 Hz, 6H, CH<sub>3</sub>).

**<sup>13</sup>C-NMR** (125 MHz, 30° C, CDCl<sub>3</sub>, δ [ppm]): 156.4 (Cq); 149.8 (Cq); 135.3 (CH<sub>arom.</sub>), 130.6 (CH<sub>arom.</sub>), 116.5 (CH<sub>arom.</sub>), 92.6 (CH<sub>arom.</sub>), 44.8 (CH<sub>2</sub>), 12.5 (CH<sub>3</sub>).

**ESI-MS** (m/z (%)) (MeCN): 283.16 (100) [M+H<sup>+</sup>].

**7.3.18 Synthesis of 2,6-bis(4-methylimidazole)- *N,N'*-diethylpyridine-4-amine**

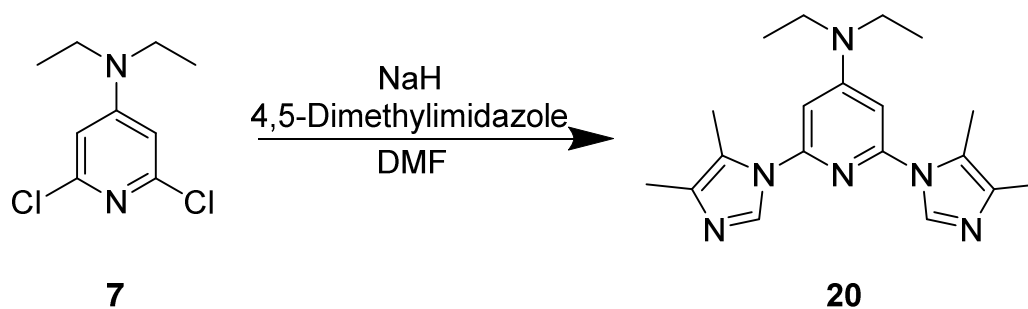
Under an argon atmosphere NaH (3.5 eq.; 24 mmol) is dissolved in dry DMF (50 mL) and cooled with an ice-bath to 0° C. Then 4-methylimidazole (3.3 eq.; 23 mmol) is added portion wise. After complete addition the reaction mixture is stirred 1 h at 0° C and then allowed to warm to r.t.. At r.t. 2,6-dichloro- *N,N'*-diethylpyridine-4-amine (1 eq.; 6.75 mmol) is added and the mixture stirred at 130° C for 3 days. After cooling to r.t. the solution is poured into a mixture of ice/water (300 mL) and stirred for additional 10 minutes. The aqueous phase is extracted with dichloromethane (3x 200 mL) and the combined organic layers are dried over Na<sub>2</sub>SO<sub>4</sub>. After evaporation of the solvents the product is obtained as a white powder.

Yield: 52 %, (3.5 mmol)

**<sup>1</sup>H-NMR** (500 MHz, 30° C, DMSO, δ [ppm]): 8.50 (d, <sup>4</sup>J<sub>HH</sub>: 1.28 Hz, 2H, CH<sub>arom.</sub>); 7.73 (s, 2H, CH<sub>arom.</sub>); 6.67 (s, 2H, CH<sub>arom.</sub>); 3.50 (q; <sup>3</sup>J<sub>HH</sub>: 7.07 Hz, 4H; CH<sub>2</sub>); 2.17 (s, 6H, CH<sub>3</sub>); 1.14 (d, <sup>3</sup>J<sub>HH</sub>: 7.12 Hz, 6H, CH<sub>3</sub>).

**<sup>13</sup>C-NMR** (125 MHz, 30° C, CDCl<sub>3</sub>, δ [ppm]): 156.4 (C<sub>q</sub>); 149.8 (C<sub>q</sub>); 138.6 (C<sub>q</sub>), 135.2 (CH<sub>arom.</sub>); 113.5 (CH<sub>arom.</sub>), 91.6 (CH<sub>arom.</sub>), 44.0 (CH<sub>2</sub>), 14.09 (CH<sub>3</sub>); 12.8 (CH<sub>3</sub>).

**ESI-MS** (m/z (%)) (MeCN): 311.19 (100) [M+H<sup>+</sup>].

7.3.19 Synthesis of 2,6-bis(4,5-dimethylimidazole)- *N,N'*-diethylpyridine-4-amine

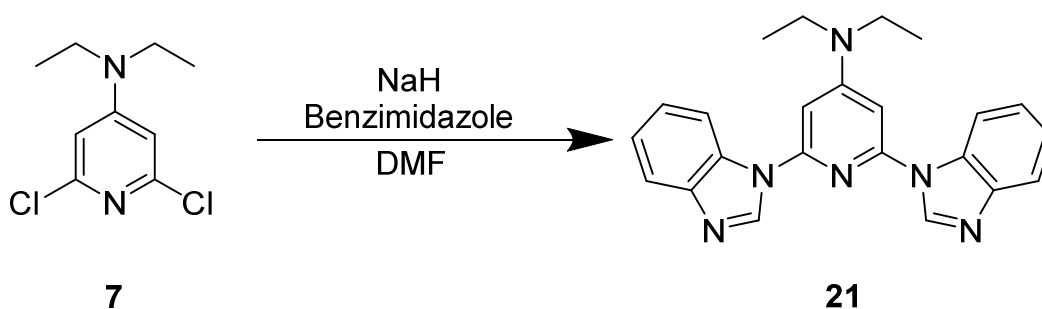
Under an argon atmosphere NaH (3.5 eq.; 24 mmol) is dissolved in dry DMF (75 mL) and cooled with an ice-bath to 0° C. Then 4,5-dimethylimidazole (3.3 eq.; 23 mmol) is added portion wise. After complete addition the reaction mixture is stirred 1 h at 0° C and then allowed to warm to r.t.. At r.t. 2,6-dichloro- *N,N'*-diethylpyridine-4-amine (1 eq.; 7 mmol) is added and the mixture stirred at 130° C for 3 days. After cooling to r.t. the solution is poured into a mixture of ice/water (300 mL) and stirred for additional 10 minutes. The obtained precipitate is filtered and washed with diethyl ether. After drying under vacuum, the product is obtained as a white solid.

Yield: 70 %, (4.9 mmol).

**<sup>1</sup>H-NMR** (500 MHz, 30° C, DMSO,  $\delta$  [ppm]): .7.90 (s, 2H, CH<sub>arom.</sub>); 6.62 (s, 2H, CH<sub>arom.</sub>); 3.48 (q; <sup>3</sup>J<sub>HH</sub>: 7.36 Hz, 4H; CH<sub>2</sub>); 2.26 (s, 6H, CH<sub>3</sub>); 2.09 (s, 6H, CH<sub>3</sub>); 1.14 (t, <sup>3</sup>J<sub>HH</sub>: 7.25 Hz, 6H, CH<sub>3</sub>).

**<sup>13</sup>C-NMR** (125 MHz, 30° C, DMSO,  $\delta$  [ppm]): 155.6 (Cq); 149.8 (Cq); 135.2 (CH<sub>arom.</sub>), 134.2 (Cq), 121.8 (Cq), 97.6 (CH<sub>arom.</sub>), 43.8 (CH<sub>2</sub>), 12.5 (CH<sub>3</sub>); 12.2 (CH<sub>3</sub>); 9.9 (CH<sub>3</sub>).

**ESI-MS** (m/z (%)) (MeCN): 339.22 (100) [M+H<sup>+</sup>].

7.3.20 Synthesis of 2,6-bis(benzimidazole)- *N,N'*-diethylpyridine-4-amine

Under an argon atmosphere NaH (3 eq.; 18 mmol) is dissolved in dry DMF (75 mL) and cooled with an ice-bath to 0° C. Then benzimidazole (2.8 eq.; 16 mmol) is added portionwise. After complete addition the reaction mixture is stirred 1 h at 0° C and then

allowed to warm to r.t.. At r.t. 2,6-dichloro-*N,N'*-diethylpyridine-4-amine (1 eq.; 6 mmol) is added and the mixture stirred at 130° C for 3 days. After cooling to r.t. the solution is poured into a mixture of ice/water (300 mL) and stirred for additional 10 minutes. The obtained precipitate is filtered and washed with diethyl ether. After drying under vacuum, the product is obtained as a white solid.

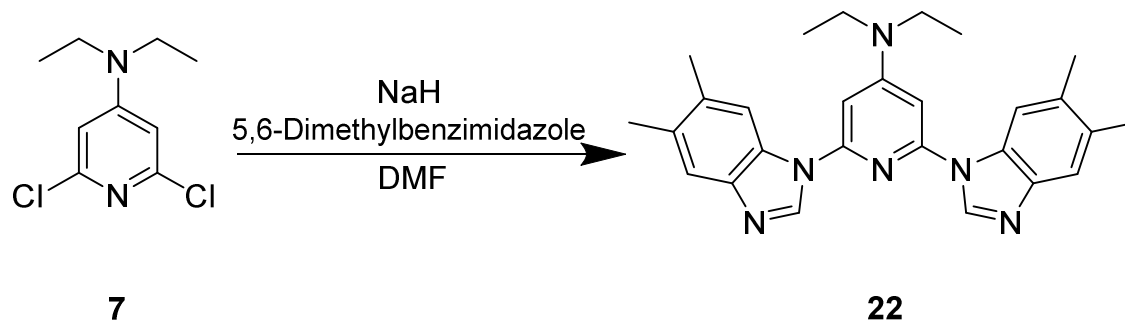
Yield: 62 %, (3.7 mmol).

**<sup>1</sup>H-NMR** (700 MHz, 30° C, DMSO,  $\delta$  [ppm]): .9.00 (s, 2H, CH<sub>arom.</sub>); 8.15 (m, 2H, CH<sub>arom.</sub>); 7.78 (m; 2H; CH<sub>arom.</sub>); 7.33 (m, 4H, CH<sub>arom.</sub>), 6.98 (s, 2H, CH<sub>arom.</sub>); 3.61 (q, <sup>3</sup>J<sub>HH</sub>: 7.20 Hz; 4H, CH<sub>2</sub>); 1.22 (t, <sup>3</sup>J<sub>HH</sub>: 6.48 Hz, 6H, CH<sub>3</sub>).

**<sup>13</sup>C-NMR** (176 MHz, 30° C, DMSO,  $\delta$  [ppm]): 155.9 (Cq); 149.8 (Cq); 144.2 (Cq); 142.7 (CH<sub>arom.</sub>); 132.2 (Cq); 123.7 (CH<sub>arom.</sub>); 122.8 (CH<sub>arom.</sub>); 119.8 (CH<sub>arom.</sub>); 113.6 (CH<sub>arom.</sub>); 94.7 (CH<sub>arom.</sub>); 43.8 (CH<sub>2</sub>); 12.3 (CH<sub>3</sub>).

**ESI-MS** (m/z (%)) (MeCN): 383.19 (100) [M+H<sup>+</sup>].

### 7.3.21 Synthesis of 2,6-bis(benzimidazole)- *N,N'*-diethylpyridine-4-amine



Under an argon atmosphere NaH (3.5 eq.; 10.5 mmol) is dissolved in dry DMF (75 mL) and cooled with an ice-bath to 0° C. Then 4,5-dimethylimidazole (3.3 eq.; 10.2 mmol) is added portion wise. After complete addition the reaction mixture is stirred 1 h at 0° C and then allowed to warm to r.t.. At r.t. 2,6-dichloro- *N,N'*-diethylpyridine-4-amine (1 eq.; 3 mmol) is added and the mixture stirred at 130° C for 3 days. After cooling to r.t. the solution is poured into a mixture of ice/water (300 mL) and stirred for additional 10 minutes. The obtained precipitate is filtered and washed with diethyl ether. After drying under vacuum, the product is obtained as a white solid.

Yield: 60 %, (1.81 mmol).

**<sup>1</sup>H-NMR** (500 MHz, 30° C, CD<sub>3</sub>Cl, δ [ppm]): 8.47 (s, 2H, CH<sub>arom.</sub>); 7.82 (s, 2H, CH<sub>arom.</sub>); 7.63 (s, 2H, CH<sub>arom.</sub>); 6.63 (s, 2H, CH<sub>arom.</sub>); 3.53 (s; 4H; CH<sub>2</sub>); 2.40 (s, 6H, CH<sub>3</sub>); 1.33 (s, 6H, CH<sub>3</sub>).

**<sup>13</sup>C-NMR** (125 MHz, 30° C, CDCl<sub>3</sub>, δ [ppm]): 155.9 (Cq); 150.5 (Cq); 143.3 (Cq); 140.7 (CH<sub>arom.</sub>), 133.1 (Cq), 132.0 (Cq); 130.7 (Cq); 120.6 (CH<sub>arom.</sub>); 112.9 (CH<sub>arom.</sub>), 94.1 (CH<sub>arom.</sub>); 44.8 (CH<sub>2</sub>), 20.7 (CH<sub>3</sub>), 20.2 (CH<sub>3</sub>), 12.4 (CH<sub>3</sub>).

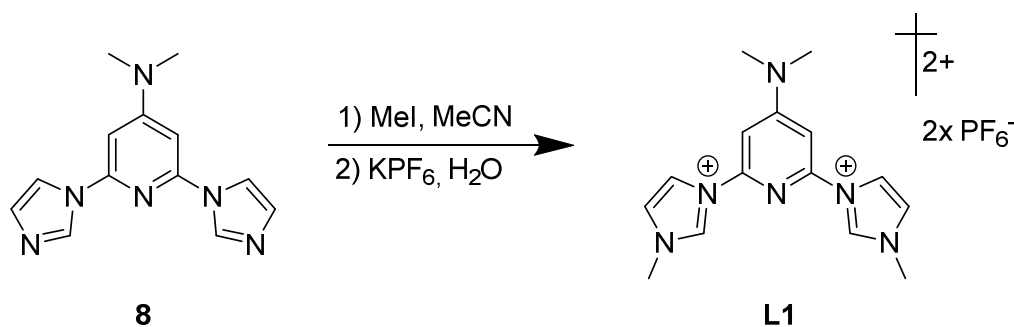
**ESI-MS** (m/z (%)) (MeCN): 439.25 (100) [M+H<sup>+</sup>].

## 7.4 Synthesis of the tridentate C<sup>N</sup>C ligands

### 7.4.1 General method for ligand synthesis

The respective ligand precursor (**8-22**) (1 eq., 5 mmol) is added to dry acetonitrile at r.t. under an argon atmosphere. Then iodomethane (3.5 eq., 17.5 mmol) is added slowly and the resulting reaction mixture is stirred at 85° C for 24 hours. After cooling to r.t. the solvent is evaporated and the resulting brownish solid is suspended in water. The suspension is filtered and directly dripped into a saturated solution of KPF<sub>6</sub> in water. When the counter ion metathesis is successful the resulting PF<sub>6</sub><sup>-</sup> salt is obtained precipitating from the aqueous solution. After filtration and washing with diethyl ether the respective ligands (**L1-L15**) are obtained as white to yellow powders.

### 7.4.2 Synthesis of 3,3'-(4-(dimethylamino)pyridine-2,6-diyl)bis(1-methylimidazole-3-ium) [BIP<sup>NMe2</sup>] (**L1**)



The product is obtained as a white solid. Suitable single crystals for X-ray diffraction measurements can be obtained by slow gas phase diffusion of diethyl ether into an acetonitrile solution of **L1**.

Yield: 79 %, (3.9 mmol).

**<sup>1</sup>H-NMR** (700 MHz, 30° C, DMSO, δ [ppm]): 10.15 (s, 2H, CH<sub>carb.</sub>); 8.70 (s, 2H, CH<sub>arom.</sub>); 8.00 (s, 2H, CH<sub>arom.</sub>); 7.25 (s, 2H, CH<sub>arom.</sub>); 4.00 (s, 6H, CH<sub>3</sub>); 3.22 (s, 6H, CH<sub>3</sub>).

**<sup>13</sup>C-NMR** (176 MHz, 30° C, DMSO, δ [ppm]): 158.8 (Cq); 146.1 (Cq); 135.9 (CH<sub>carb.</sub>); 124.7 (CH<sub>arom.</sub>); 119.2 (CH<sub>arom.</sub>); 95.1 (CH<sub>arom.</sub>); 39.9 (CH<sub>3</sub>); 36.5 (CH<sub>3</sub>).

**<sup>15</sup>N-NMR** (50.7 MHz, 30° C DMSO, δ [ppm]): 218.0 (N<sub>arom.</sub>); 192.2 (N<sub>arom.</sub>); 176.3 (N<sub>arom.</sub>); 76.1 (N<sub>aliph.</sub>).

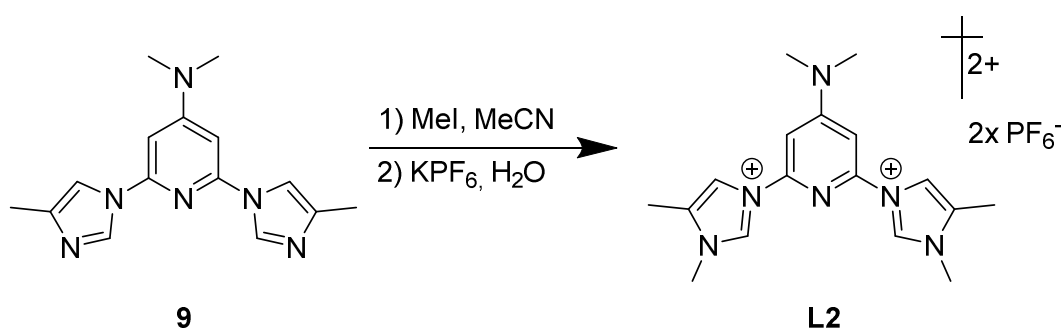
**ESI-MS** (m/z (%))(MeCN): 142.08 (100) [M<sup>2+</sup>].

**IR** (ATR,  $\tilde{\nu}$  [ $\text{cm}^{-1}$ ]): 3168w, 1629m, 1585w, 1540w, 1479w, 1450w, 1425w, 1361w, 1334w, 1234w, 1216w, 1176w, 1137w, 1093w, 1024w, 981w, 946w, 825s, 761m, 655w, 621w, 555s, 474w.

**UV/Vis** (MeCN,  $\lambda_{\text{max}}$  [nm] ( $\epsilon$  [ $\text{M}^{-1} \text{cm}^{-1}$ ])): 282 (13493); 233 (31689).

**Elemental analysis:** calculated for  $\text{C}_{15}\text{H}_{20}\text{F}_{12}\text{N}_6\text{P}_2$ : C: 31.37; H: 3.51; N: 14.63; found: C: 30.98; H: 3.67; N: 14.32.

### 7.4.3 Synthesis of 3,3'-(4-(dimethylamino)pyridine-2,6-diyl)bis(1,4-methylimidazole-3-ium) [BmiP<sup>NMe2</sup>] (L2)



The product is obtained as a white solid.

Yield: 62 %, (3.1 mmol).

**<sup>1</sup>H-NMR** (700 MHz, 30° C, DMSO,  $\delta$  [ppm]): 10.02 (s, 2H, CH<sub>carb.</sub>); 8.44 (s, 2H, CH<sub>arom.</sub>); 7.16 (s, 2H, CH<sub>arom.</sub>); 3.88 (s, 6H, CH<sub>3</sub>); 3.20 (s, 6H, CH<sub>3</sub>); 2.39 (s, 6H, CH<sub>3</sub>).

**<sup>13</sup>C-NMR** (176 MHz, 30° C, DMSO,  $\delta$  [ppm]): 158.6 (Cq); 145.9 (Cq); 135.1 (CH<sub>carb.</sub>); 132.6 (Cq); 115.7 (CH<sub>arom.</sub>); 95.0 (CH<sub>arom.</sub>); 39.7 (CH<sub>3</sub>); 33.9 (CH<sub>3</sub>); 8.7 (CH<sub>3</sub>)

**<sup>15</sup>N-NMR** (50.7 MHz, 30° C DMSO,  $\delta$  [ppm]): 217.0 (N<sub>arom.</sub>); 189.4 (N<sub>arom.</sub>); 178.4 (N<sub>arom.</sub>); 75.9 (N<sub>aliph.</sub>).

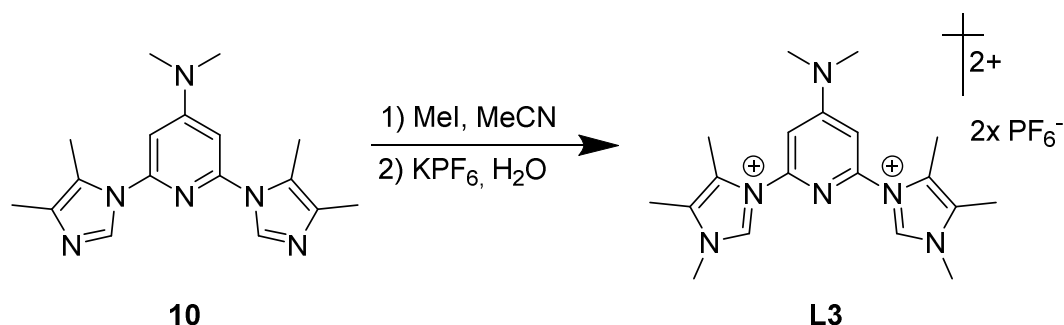
**ESI-MS** (m/z (%))(MeCN): 156.10 (100) [ $\text{M}^{2+}$ ], 457.16 (8) [ $\text{M}^{2+} + \text{PF}_6^-$ ].

**IR** (ATR,  $\tilde{\nu}$  [ $\text{cm}^{-1}$ ]): 3166w, 1635w, 1614w, 1537m, 1492w, 1448w, 1240w, 1218w, 1172w, 1124w, 1087w, 1031w, 981w, 945w, 831s, 81s, 738w, 655w, 626w, 555s, 509w, 335w.

**UV/Vis** (MeCN,  $\lambda_{\text{max}}$  [nm] ( $\epsilon$  [ $\text{M}^{-1} \text{cm}^{-1}$ ])): 235 (21902).

**Elemental analysis:** calculated for  $\text{C}_{17}\text{H}_{24}\text{F}_{12}\text{N}_6\text{P}_2$ : C: 33.90; H: 4.02; N: 13.95; found: C: 33.46; H: 4.19; N: 14.01.

#### 7.4.4 Synthesis of 3,3'-(4-(dimethylamino)pyridine-2,6-diyl)bis(1,4,5-methylimidazole-3-ium) [BdmiP<sup>NMe2</sup>] (L3)



The product is obtained as a white powder.

Yield: 83 %, (4.15 mmol)

**<sup>1</sup>H-NMR** (700 MHz, 30° C, DMSO,  $\delta$  [ppm]): 9.60 (s, 2H, CH<sub>carb.</sub>); 7.20 (s, 2H, CH<sub>arom.</sub>); 3.87 (s, 6H, CH<sub>3</sub>); 3.18 (s, 2H, CH<sub>3</sub>); 2.36 (s, 6H, CH<sub>3</sub>); 2.34 (s, 6H, CH<sub>3</sub>).

**<sup>13</sup>C-NMR** (176 MHz, 30° C, DMSO,  $\delta$  [ppm]): 158.5 (Cq); 147.2 (Cq); 136.1 (CH<sub>carb.</sub>); 128.4 (Cq); 126.4 (Cq); 103.1 (CH<sub>arom.</sub>); 40.2 (CH<sub>3</sub>); 34.4 (CH<sub>3</sub>); 9.9 (CH<sub>3</sub>); 8.3 (CH<sub>3</sub>).

**<sup>15</sup>N-NMR** (50.7 MHz, 30° C DMSO,  $\delta$  [ppm]): 219.4 (N<sub>arom.</sub>); 190.7 (N<sub>arom.</sub>); 175.0 (N<sub>arom.</sub>); 75.5 (N<sub>aliph.</sub>).

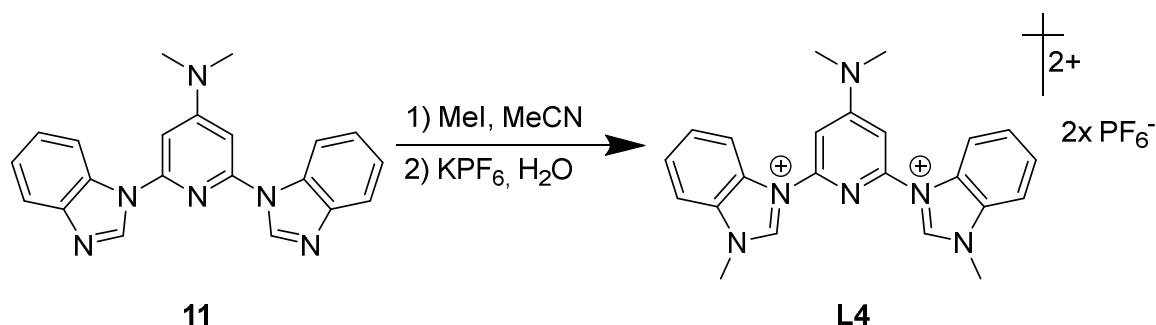
**ESI-MS** (m/z (%))(MeCN): 170.11 (100) [M<sup>2+</sup>], 467.14 (8) [M<sup>2+</sup>+I].

**IR** (ATR,  $\tilde{\nu}$  [cm<sup>-1</sup>]): 2360w, 2341w, 1645w, 1620w, 1542w, 1473w, 1456w, 1434w, 1334w, 1249w, 1230w, 1186w, 1137w, 991w, 840s, 819s, 740w, 667w, 642w, 557s, 420w, 354w, 291w, 248w, 225w.

**UV/Vis** (MeCN,  $\lambda_{\text{max}}$  [nm] ( $\epsilon$  [M<sup>-1</sup> cm<sup>-1</sup>])): 273 (18368); 219 (31538).

**Elemental analysis:** calculated for für C<sub>19</sub>H<sub>28</sub>F<sub>12</sub>N<sub>6</sub>P<sub>2</sub>: C: 36.20; H: 4.48; N: 13.33; found: C: 35.41; H: 4.10; N: 12.85.

### 7.4.5 Synthesis of 3,3'-(4-(dimethylamino)pyridine-2,6-diyl)bis(1-methylbenzimidazole-3-ium) [BbP<sup>NMe2</sup>] (L4)



The product is obtained as a voluminous white powder. Suitable single crystals for X-ray diffraction spectroscopy can be achieved by slow gas phase diffusion of diethyl ether into a solution of **L4** in acetonitrile.

Yield: 60 %, (3 mmol)

**<sup>1</sup>H-NMR** (700 MHz, 30° C DMSO,  $\delta$  [ppm]): 10.49 (s, 2H, CH<sub>carb.</sub>); 8.39 (d, <sup>3</sup>J<sub>HH</sub>: 8.27 Hz, 2H, CH<sub>arom.</sub>); 8.17 (d, <sup>3</sup>J<sub>HH</sub>: 8.27 Hz, 2H, CH<sub>arom.</sub>); 7.81 (t, <sup>3</sup>J<sub>HH</sub>: 7.81 Hz, 2H, CH<sub>arom.</sub>); 7.73 (t, <sup>3</sup>J<sub>HH</sub>: 8.06 Hz, 2H, CH<sub>arom.</sub>); 7.36 (s, 2H, CH<sub>arom.</sub>); 4.25 (s, 6H, CH<sub>3</sub>); 3.28 (s, 6H, CH<sub>3</sub>).

**<sup>13</sup>C-NMR** (176 MHz, 30° C DMSO,  $\delta$  [ppm]): 158.8 (Cq); 147.6 (Cq); 143.4 (CH<sub>carb.</sub>); 132.6 (Cq); 130.0 (Cq); 128.1 (CH<sub>arom.</sub>); 127.6 (CH<sub>arom.</sub>); 116.1 (CH<sub>arom.</sub>); 114.4 (CH<sub>arom.</sub>); 100.2 (CH<sub>arom.</sub>); 39.99 (CH<sub>3</sub>); 34.2 (CH<sub>3</sub>).

**<sup>15</sup>N-NMR** (50.7 MHz, 30° C DMSO,  $\delta$  [ppm]): 233.0 (N<sub>arom.</sub>); 173.2 (N<sub>arom.</sub>); 159.5 (N<sub>arom.</sub>); 74.8 (N<sub>aliph.</sub>).

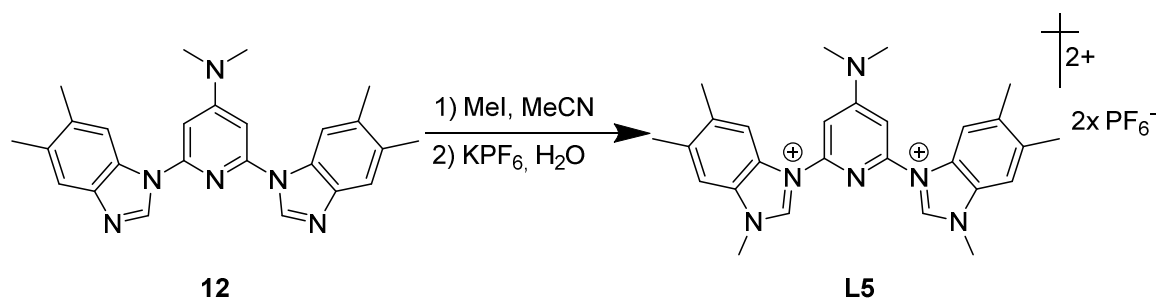
**ESI-MS** (m/z (%))(MeCN): 192.1 [M<sup>2+</sup>] (100); 401.2 [M<sup>+</sup>+OH] (22); 383.2 [M<sup>+</sup>] (4).

**IR** (ATR,  $\tilde{\nu}$  [cm<sup>-1</sup>]): 3165w, 3127w, 1621m, 1608m, 1576w, 1539w, 1490w, 1466w, 1430w, 1343w, 1237w, 1190w, 1162w, 1139w, 1129w, 1031w, 1015w, 983w, 936w, 826s, 781m, 763s, 644w, 556s, 424w, 258w.

**UV/Vis** (MeCN,  $\lambda_{\text{max}}$  [nm] ( $\epsilon$  [M<sup>-1</sup> cm<sup>-1</sup>])): 271 (35179); 222 (36802).

**Elemental analysis:** calculated for C<sub>23</sub>H<sub>24</sub>F<sub>12</sub>N<sub>6</sub>P<sub>2</sub>: C: 40.96; H: 3.59; N: 12.46; found: C: 41.11; H: 3.87; N: 12.65.

### 7.4.6 Synthesis of 3,3'-(4-(dimethylamino)pyridine-2,6-diyl)bis(1,5,6-trimethylbenzimidazole-3-ium) [BmbP<sup>NMe2</sup>] (L5)



The product is obtained as a voluminous white powder.

Yield: 52 %, (2.6 mmol)

**<sup>1</sup>H-NMR** (700 MHz, 30° C, DMSO,  $\delta$  [ppm]): 10.36 (s, 2H, CH<sub>carb.</sub>); 8.22 (s, 2H, CH<sub>arom.</sub>); 7.94 (s, 2H, CH<sub>arom.</sub>); 7.32 (s, 2H, CH<sub>arom.</sub>); 4.17 (s, 6H, CH<sub>3</sub>); 3.27 (s, 6H, CH<sub>3</sub>); 2.48 (s, 6H, CH<sub>3</sub>); 2.36 (s, 6H, CH<sub>3</sub>).

**<sup>13</sup>C-NMR** (176 MHz, 30° C, DMSO,  $\delta$  [ppm]): 158.2 (Cq); 147.4 (Cq); 141.7 (CH<sub>carb.</sub>); 137.3 (CH<sub>arom.</sub>); 136.9 (CH<sub>arom.</sub>); 130.7 (CH<sub>arom.</sub>); 127.9 (CH<sub>arom.</sub>); 115.4 (CH<sub>arom.</sub>); 113.5 (CH<sub>arom.</sub>); 98.9 (CH<sub>arom.</sub>); 40.0 (CH<sub>3</sub>); 33.6 (CH<sub>3</sub>); 20.1 (CH<sub>3</sub>); 19.9 (CH<sub>3</sub>).

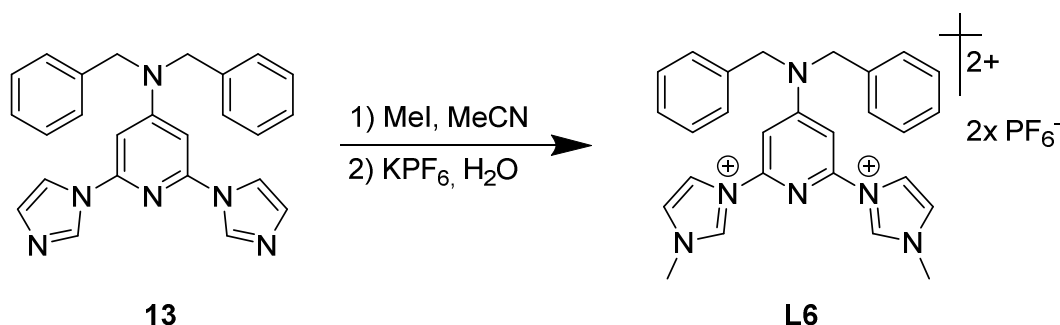
**<sup>15</sup>N-NMR** (50.7 MHz, 30° C DMSO,  $\delta$  [ppm]): 234.4 (N<sub>arom.</sub>); 172.2 (N<sub>arom.</sub>); 158.9 (N<sub>arom.</sub>); 74.2 (N<sub>aliph.</sub>).

**ESI-MS** (m/z (%))(MeCN): 220.14 (100) [M<sup>2+</sup>]; 585.24 (48) [M<sup>2+</sup>+PF<sub>6</sub><sup>-</sup>].

**IR** (ATR,  $\tilde{\nu}$  [cm<sup>-1</sup>]): 3170w, 3124w, 2956w, 1620m, 1573m, 1537m, 1492m, 1465w, 1432w, 1359w, 1292w, 1249w, 1215w, 1189w, 1141w, 1095w, 1004w, 879m, 821s, 740m, 651w, 626w, 592w, 555s, 432m, 387w, 264w, 223w.

**UV/Vis** (MeCN,  $\lambda_{\text{max}}$  [nm] ( $\epsilon$  [M<sup>-1</sup> cm<sup>-1</sup>])): 278 (34202); 227 (36529); 200 (71695).

### 7.4.7 Synthesis of *N,N'*-dibenzyl-2,6-bis(3-methylimidazole-3-ium)pyridine-4-amine [BIP<sup>NBn2</sup>] (**L6**)



The product is obtained as white solid. Suitable single crystals for X-ray diffraction spectroscopy can be achieved by slow gas phase diffusion of diethyl ether into a solution of **L6** in acetonitrile.

Yield: 87 %, (4.3 mmol).

**<sup>1</sup>H-NMR** (500 MHz, 30° C, DMSO,  $\delta$  [ppm]): 10.12 (s, 2H, CH<sub>carb.</sub>), 8.66 (d, <sup>4</sup>J<sub>HH</sub>: 1.99 Hz; 2H, CH<sub>arom.</sub>); 7.97 (d, <sup>4</sup>J<sub>HH</sub>: 1.98 Hz, 2H, CH<sub>arom.</sub>); 7.50 (s, 2H, CH<sub>arom.</sub>); 7.40 (m, 4H, CH<sub>arom.</sub>), 7.33 (m, 6H, CH<sub>arom.</sub>); 4.96 (s, 4H, CH<sub>2</sub>); 4.00 (s, 6H, CH<sub>3</sub>).

**<sup>13</sup>C-NMR** (125 MHz, 30° C, DMSO,  $\delta$  [ppm]): 159.4 (Cq); 147.1 (Cq); 136.6 (CH<sub>carb.</sub>); 129.3 (CH<sub>arom.</sub>); 128.0 (CH<sub>arom.</sub>); 127.5 (CH<sub>arom.</sub>); 125.2 (CH<sub>arom.</sub>); 119.6 (CH<sub>arom.</sub>); 96.4 (CH<sub>arom.</sub>); 52.5 (CH<sub>2</sub>); 36.6 (CH<sub>3</sub>).

**<sup>15</sup>N-NMR** (50.7 MHz, 30° C, DMSO,  $\delta$  [ppm]): 222.0 (N<sub>arom.</sub>); 192.4 (N<sub>arom.</sub>), 176.9 (N<sub>arom.</sub>); 97.2 (N<sub>aliph.</sub>).

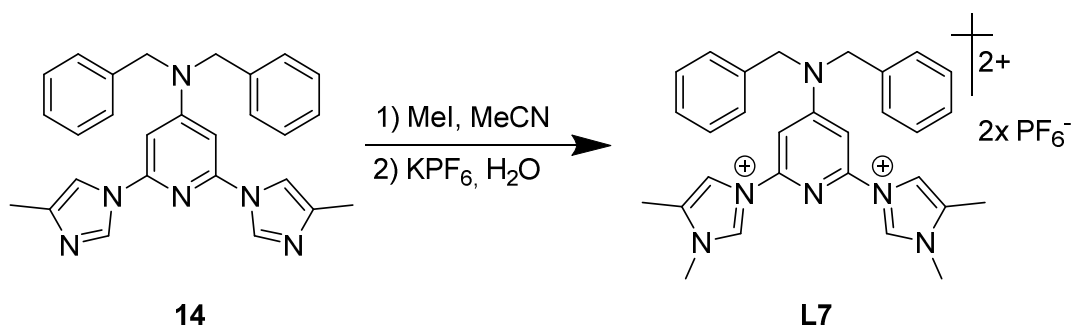
**ESI-MS** (m/z (%)) (MeCN): 218.11 (100) [M<sup>2+</sup>]; 421.21 (8) [M-CH<sub>3</sub><sup>+</sup>].

**IR** (ATR,  $\tilde{\nu}$  [cm<sup>-1</sup>]): 3169w, 1626m, 1583w, 1536sh, 1521w, 1496w, 1481w, 1454w, 1426w, 1357w, 1224w, 1202w, 1146w, 1088w, 1024w, 996w, 980w, 943w, 829s, 783w, 739m, 701w, 655w, 619w, 555s, 459w, 302w.

**UV/Vis** (MeCN,  $\lambda_{\text{max}}$  [nm] ( $\epsilon$  [M<sup>-1</sup> cm<sup>-1</sup>])): 281 (14444); 235 (29618).

**Elemental analysis:** calculated for C<sub>27</sub>H<sub>28</sub>F<sub>12</sub>N<sub>6</sub>P<sub>2</sub>: C: 44.64; H: 3.88; N: 11.57; found: C: 44.93; H: 4.01; N: 12.50.

### 7.4.8 Synthesis of *N,N'*-dibenzyl-2,6-bis(1-methylimidazole-3-ium)pyridine-4-amine [BmiP<sup>NBn2</sup>] (L7)



The product is obtained as a light-yellow powder.

Ausbeute: 87 %, (4.35 mmol)

**<sup>1</sup>H-NMR** (700 MHz, 30° C, DMSO,  $\delta$  [ppm]): 10.01 (s, 2H, CH<sub>carb.</sub>), 8.40 (s, 2H, CH<sub>arom.</sub>); 7.48 (s, 2H, CH<sub>arom.</sub>); 7.39 (s, 4H, CH<sub>arom.</sub>); 7.31 (s, 6H, CH<sub>arom.</sub>), 4.91 (s, 4H, CH<sub>2</sub>); 3.87 (s, 6H, CH<sub>3</sub>); 2.38 (s, 6H, CH<sub>3</sub>).

**<sup>13</sup>C-NMR** (176 MHz, 30° C, DMSO,  $\delta$  [ppm]): 158.9 (Cq); 146.7 6 (Cq); 136.1 (CH<sub>carb.</sub>); 135.2 (Cq) 132.6 (Cq); 128.8 (CH<sub>arom.</sub>); 127.5 (CH<sub>arom.</sub>); 127.0 (CH<sub>arom.</sub>); 115.7 (CH<sub>arom.</sub>); 95.5 (CH<sub>arom.</sub>); 52.3 (CH<sub>2</sub>); 33.8 (CH<sub>3</sub>); 8.6 (CH<sub>3</sub>).

**<sup>15</sup>N-NMR** (70.9 MHz, 30° C, DMSO,  $\delta$  [ppm]): 212.1 (N<sub>arom.</sub>); 189.5 (N<sub>arom.</sub>); 178.2 (N<sub>arom.</sub>); 97.5 (N<sub>aliph.</sub>).

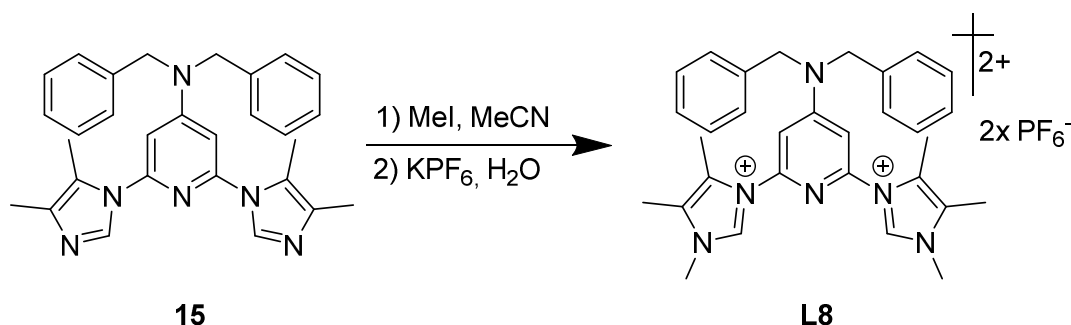
**ESI-MS** (m/z (%)) (MeCN): 232.13 (100) [M<sup>2+</sup>]; 609.235 (8) [M<sup>2+</sup> + PF<sub>6</sub><sup>-</sup>].

**IR** (ATR,  $\tilde{\nu}$  [cm<sup>-1</sup>]): 3162w, 1631m, 1610m, 1539w, 1523w, 1454w, 1357w, 1203w, 1184w, 1126w, 1091w, 1029w, 983w, 943w, 829s, 738m, 700w, 624w, 555s, 459w, 335w.

**UV/Vis** (MeCN,  $\lambda_{\text{max}}$  [nm] ( $\epsilon$  [M<sup>-1</sup> cm<sup>-1</sup>])): 279 (14797), 246 (22798).

**Elemental analysis:** calculated for C<sub>29</sub>H<sub>32</sub>F<sub>12</sub>N<sub>6</sub>P<sub>2</sub>: C: 46.14; H: 4.27; N: 11.24; found: C: 46.15; H: 4.52; N: 11.22.

### 7.4.9 Synthesis of *N,N'*-dibenzyl-2,6-bis(1,4,5-trimethylimidazole-3-ium)pyridine-4-amine [BdmiP<sup>NBn2</sup>] (L8)



The product is obtained as a light-yellow powder.

Yield: 37 %, (1.85 mmol)

**<sup>1</sup>H-NMR** (700 MHz, 30° C, MeCN,  $\delta$  [ppm]): 9.46 (s, 2H, CH<sub>carb.</sub>), 7.39 (t, <sup>3</sup>J<sub>HH</sub>: 7.41 Hz, 4H, CH<sub>arom.</sub>); 7.33 (d, <sup>3</sup>J<sub>HH</sub>: 7.22 Hz, 2H, CH<sub>arom.</sub>); 7.31 (d, <sup>3</sup>J<sub>HH</sub>: 7.40 Hz, 4H, CH<sub>arom.</sub>); 6.85 (s, 4H, CH<sub>arom.</sub>), 4.89 (s, 4H, CH<sub>2</sub>); 3.76 (s, 6H, CH<sub>3</sub>); 2.23 (s, 6H, CH<sub>3</sub>), 2.09 (s, 6H, CH<sub>3</sub>).

**<sup>13</sup>C-NMR** (125 MHz, 30° C, MeCN,  $\delta$  [ppm]): 159.3 (Cq); 148.1 (Cq); 136.7 (Cq); 135.4 (CH<sub>carb.</sub>); 130.1 (CH<sub>arom.</sub>); 129.8 (Cq); 128.8 (CH<sub>arom.</sub>); 127.8 (Cq); 127.7 (CH<sub>arom.</sub>); 104.3 (CH<sub>arom.</sub>); 55.5 (CH<sub>2</sub>); 34.8 (CH<sub>3</sub>); 9.8 (CH<sub>3</sub>); 8.4 (CH<sub>3</sub>).

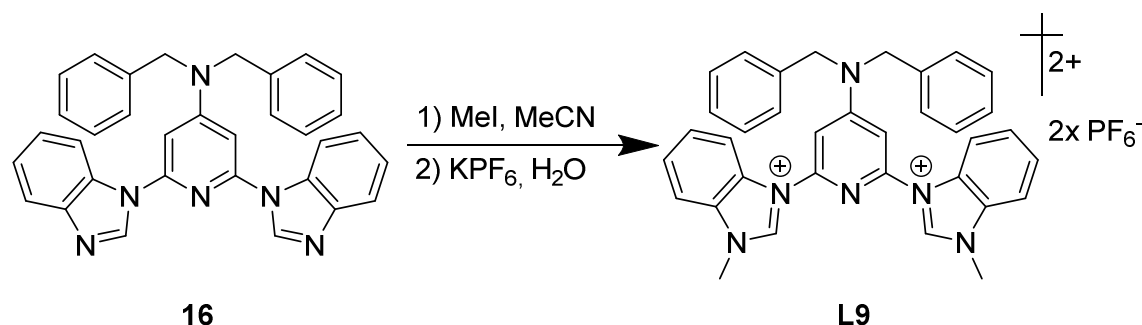
**<sup>15</sup>N-NMR** (90.7 MHz, 30° C, MeCN,  $\delta$  [ppm]): 236.3 (N<sub>arom.</sub>); 190.22 (N<sub>arom.</sub>); 173.8 (N<sub>arom.</sub>); 35.8 (N<sub>aliph.</sub>)

**ESI-MS** (m/z (%)) (MeCN): 246.16(100) [M<sup>2+</sup>]

**IR** (ATR,  $\tilde{\nu}$  [cm<sup>-1</sup>]): 3172w, 3120w, 1608m, 1573w, 1527m, 1486w, 1456w, 1361w, 1230w, 1215w, 1139w, 1076w, 897w, 831s, 738m, 729m, 698m, 630w, 557s, 453w, 291w, 279w.

**UV/Vis** (MeCN,  $\lambda_{\text{max}}$  [nm] ( $\epsilon$  [M<sup>-1</sup> cm<sup>-1</sup>])): 273 (20146), 209 (46322).

### 7.4.10 Synthesis of *N,N'*-dibenzyl-2,6-bis(1-methylbenzimidazole-3-ium)pyridine-4-amine [BbP<sup>NBn2</sup>] (L9)



The product is obtained as a light-yellow powder.

Yield: 56%, (2.8 mmol)

**<sup>1</sup>H-NMR** (500 MHz, 30° C, DMSO,  $\delta$  [ppm]): 10.41 (s, 2H, CH<sub>carb.</sub>), 8.16 (d, <sup>3</sup>J<sub>HH</sub>: 8.44 Hz, 2H, CH<sub>arom.</sub>); 7.96 (d, <sup>4</sup>J<sub>HH</sub>: 3.82 Hz 2H, CH<sub>arom.</sub>); 7.79 (t, <sup>3</sup>J<sub>HH</sub>: 7.63 Hz 2H, CH<sub>arom.</sub>); 7.65 (t, <sup>3</sup>J<sub>HH</sub>: 7.83 Hz 2H, CH<sub>arom.</sub>); 7.45 (m, 5H, CH<sub>arom.</sub>), 7.41 (m, 5H, CH<sub>arom.</sub>); 5.07 (s, 4H, CH<sub>2</sub>); 4.22 (s, 6H, CH<sub>3</sub>).

**<sup>13</sup>C-NMR** (125 MHz, 30° C, DMSO,  $\delta$  [ppm]): 158.2 (Cq); 147.4 (Cq); 143.0 (Cq); 136.2 (CH<sub>carb.</sub>); 132.4 (CH<sub>arom.</sub>); 129.5 (Cq) 129.1 (CH<sub>arom.</sub>); 127.8 (CH<sub>arom.</sub>); 127.7 (CH<sub>arom.</sub>); 127.2 (Cq); 126.9 (CH<sub>arom.</sub>); 115.2 (CH<sub>arom.</sub>); 114.2 (CH<sub>arom.</sub>); 100.5 (CH<sub>arom.</sub>); 53.6 (CH<sub>2</sub>); 33.9 (CH<sub>3</sub>).

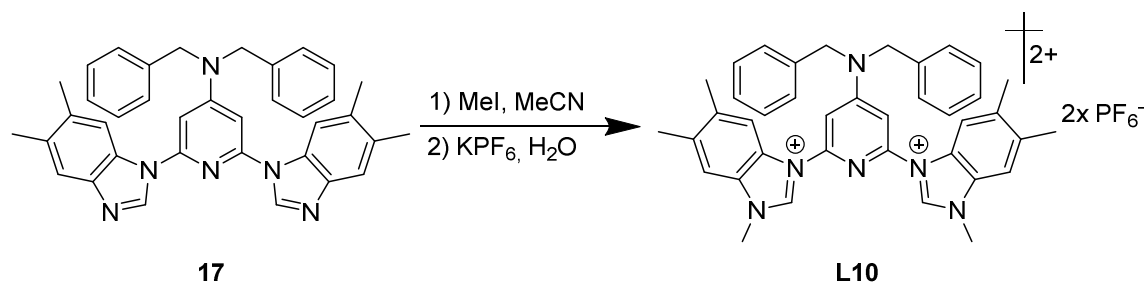
**<sup>15</sup>N-NMR** (90.7 MHz, 30° C, DMSO,  $\delta$  [ppm]): 236.1 (N<sub>arom.</sub>); 173.4 (N<sub>arom.</sub>); 160.2 (N<sub>arom.</sub>); 94.5 (N<sub>aliph.</sub>).

**ESI-MS** (m/z (%)) (MeCN): 268.1 (100) [M<sup>2+</sup>]; 681.2 (8) [M<sup>2+</sup>+PF<sub>6</sub><sup>-</sup>].

**IR** (ATR,  $\tilde{\nu}$  [cm<sup>-1</sup>]): 3161w, 3110w, 1624w, 1600m, 1574w, 1539w, 1524w, 1486w, 1453w, 1423w, 1351w, 1261w, 1229w, 1211w, 1140w, 1107w, 992w, 823s, 779m, 739m, 697m, 555s, 457w, 422w, 254w.

**UV/Vis** (MeCN,  $\lambda_{\text{max}}$  [nm] ( $\epsilon$  [M<sup>-1</sup> cm<sup>-1</sup>])): 271 (31690).

### 7.4.11 Synthesis of *N,N'*-dibenzyl-2,6-bis(1,6,7-trimethylbenzimidazole-3-ium)pyridine-4-amine [BmbP<sup>NBn2</sup>] (L10)



The product is obtained as a light-yellow powder.

Yield: 52 %, (2.6 mmol).

**<sup>1</sup>H-NMR** (700 MHz, 30° C, (CD<sub>3</sub>)<sub>2</sub>CO, δ [ppm]): 9.96 (s, 2H, CH<sub>carb-</sub>), 7.81 (s, 2H, CH<sub>arom.</sub>); 7.50 (s, 2H, CH<sub>arom.</sub>); 7.50 (s, 2H, CH<sub>arom.</sub>); 7.44 (m, 8H, CH<sub>arom.</sub>), 7.37 (s, 2H, CH<sub>arom.</sub>); 5.15 (s, 4H, CH<sub>2</sub>); 4.30 (s, 6H, CH<sub>3</sub>); 2.50 (s, 6H, CH<sub>3</sub>); 2.37 (s, 6H, CH<sub>3</sub>).

**<sup>13</sup>C-NMR** (176 MHz, 30° C, (CD<sub>3</sub>)<sub>2</sub>CO, δ [ppm]): 159.2 (Cq); 147.8 (Cq); 140.9 (CH<sub>carb.</sub>); 138.6 (Cq); 138.1 (Cq); 136.1 (Cq); 131.5 (Cq); 129.3 (CH<sub>arom.</sub>); 128.5 (Cq); 127.9 (CH<sub>arom.</sub>), 126.8 (CH<sub>arom.</sub>); 114.6 (CH<sub>arom.</sub>); 113.7 (CH<sub>arom.</sub>); 100.6 (CH<sub>arom.</sub>); 54.5 (CH<sub>2</sub>); 33.7 (CH<sub>3</sub>); 19.9 (CH<sub>3</sub>); 19.7 (CH<sub>3</sub>).

**<sup>15</sup>N-NMR** (90.7 MHz, 30° C, DMSO, δ [ppm]): 172.8 (N<sub>arom.</sub>); 159.1 (N<sub>arom.</sub>); 93.8 (N<sub>aliph.</sub>).

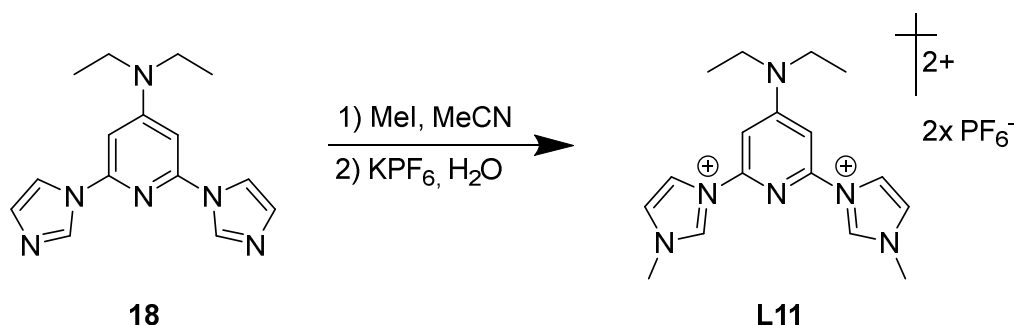
**ESI-MS** (m/z (%)) (MeCN): 296.16 (100) [M<sup>2+</sup>].

**IR** (ATR,  $\tilde{\nu}$  [cm<sup>-1</sup>]): 3166w, 1621m, 1600w, 1573w, 1542w, 1527w, 1486m, 1454m, 1355w, 1286w, 1207w, 1139w, 989w, 831s, 740m, 700m, 555s, 430m, 250m.

**UV/Vis** (MeCN,  $\lambda_{\text{max}}$  [nm] ( $\epsilon$  [M<sup>-1</sup> cm<sup>-1</sup>])): 277 (58156); 228 (54882).

**Elemental analysis:** calculated for C<sub>39</sub>H<sub>40</sub>F<sub>12</sub>N<sub>6</sub>P<sub>2</sub>: C: 53.07; H: 4.57; N: 9.52; found C: 52.78; H: 4.57; N: 9.89.

### 7.4.12 Synthesis of 3,3'-(4-(diethylamino)pyridine-2,6-diyl)bis(1-methyl-imidazole-3-ium) [BIP<sup>NEt2</sup>] (L11)



The product is obtained as a white powder. The Ligand is synthesized as part of the bachelor thesis by A. MILETIC where it is not characterized and discussed entirely.<sup>149</sup>

Yield: 69 %, (3.45 mmol)

**<sup>1</sup>H-NMR** (700 MHz, 30° C, DMSO,  $\delta$  [ppm]): 10.17 (s, 2H, CH<sub>carb.</sub>); 8.71 (t, <sup>4</sup>J<sub>HH</sub>:1.92 Hz, 2H, CH<sub>arom.</sub>); 7.99 (t, <sup>4</sup>J<sub>HH</sub>: 1.81 Hz, 2H, CH<sub>arom.</sub>); 7.18 (s, 2H, CH<sub>arom.</sub>); 3.99 (s, 6H, CH<sub>3</sub>); 3.61 (q, <sup>3</sup>J<sub>HH</sub>: 6.88 Hz, 4H, CH<sub>2</sub>); 1.19 (t, <sup>3</sup>J<sub>HH</sub>: 6.95 Hz, 6H, CH<sub>3</sub>).

**<sup>13</sup>C-NMR** (125 MHz, 30° C, DMSO,  $\delta$  [ppm]): 156.7 (Cq); 146.4 (Cq); 135.8 (CH<sub>carb.</sub>); 124.5 (CH<sub>arom.</sub>); 119.2 (CH<sub>arom.</sub>); 94.9 (CH<sub>arom.</sub>); 44.2 (CH<sub>2</sub>); 36.5 (CH<sub>3</sub>); 12.1 (CH<sub>3</sub>).

**<sup>15</sup>N-NMR** (50.7 MHz, 30° C CD<sub>3</sub>CN,  $\delta$  [ppm]): 218.3 (N<sub>arom.</sub>); 192.5 (N<sub>arom.</sub>); 176.1 (N<sub>arom.</sub>); 104.8 (N<sub>aliph.</sub>).

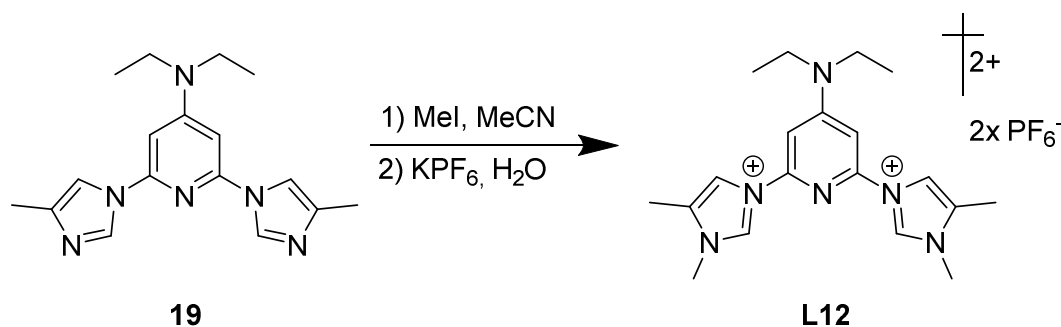
**ESI-MS** (m/z (%))(MeCN): 457.17 (100) [M<sup>2+</sup>+PF<sub>6</sub><sup>-</sup>]; 156.10 (60) [M<sup>2+</sup>]; 311.19 [M<sup>+</sup>].

**IR** (ATR,  $\tilde{\nu}$  [cm<sup>-1</sup>]): 3180w, 2970w, 1621m, 1537m, 1490w, 1355w, 1226m, 1188w, 1137w, 1097w, 979w, 815s, 655w, 621w, 555s, 470w, 304w.

**UV/Vis** (MeCN,  $\lambda_{\text{max}}$  [nm] ( $\epsilon$  [M<sup>-1</sup> cm<sup>-1</sup>])): 284 (12574), 243 (34119), 194 (41203).

**Elemental analysis:** calculated for C<sub>17</sub>H<sub>24</sub>F<sub>12</sub>N<sub>6</sub>P<sub>2</sub>: C: 33.90; H: 4.02; N: 13.95; found: C: 33.28; H: 3.96; N: 13.62.

### 7.4.13 Synthesis of 3,3'-[4-(diethylamino)pyridine-2,6-diyl]bis(1,4-methyl-imidazole-3-ium) [BmiP<sup>NEt2</sup>] (L12)



The product is obtained as a white powder.

Yield: 68 %, (3.42 mmol)

**<sup>1</sup>H-NMR** (700 MHz, 30° C, DMSO,  $\delta$  [ppm]): 10.02 (s, 2H, CH<sub>carb.</sub>); 8.45 (s, 2H, CH<sub>arom.</sub>); 7.12 (s, 2H, CH<sub>arom.</sub>); 3.90 (s, 6H, CH<sub>3</sub>); 3.60 (s, 4H, CH<sub>2</sub>); 3.35 (s, 6H, CH<sub>3</sub>); 2.40 (s, 6H, CH<sub>3</sub>); 1.21 (t, 6H, CH<sub>3</sub>).

**<sup>13</sup>C-NMR** (176 MHz, 30° C, DMSO,  $\delta$  [ppm]): 157.3 (C<sub>q</sub>); 147.0 (C<sub>q</sub>); 135.7 (CH<sub>carb.</sub>); 133.1 (C<sub>q</sub>); 116.5 (CH<sub>arom.</sub>); 95.3 (CH<sub>arom.</sub>); 44.8 (CH<sub>2</sub>); 34.5 (CH<sub>3</sub>); 12.7 (CH<sub>3</sub>); 9.3 (CH<sub>3</sub>).

**<sup>15</sup>N-NMR** (50.7 MHz, 30° C; DMSO,  $\delta$  [ppm]): 217.8 (N<sub>(arom.)</sub>); 189.8 (N<sub>(arom.)</sub>); 178.3 (N<sub>(arom.)</sub>); 104.2 (N<sub>(arom.)</sub>).

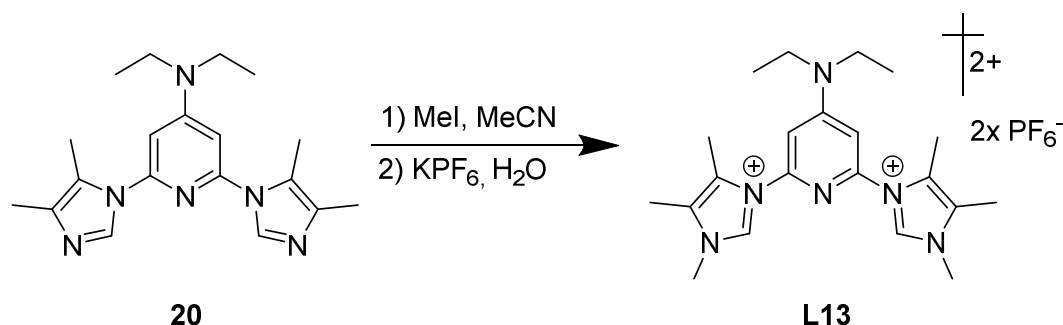
**ESI-MS** (m/z (%))(MeCN): 170.12 (100) [M<sup>2+</sup>].

**IR** (ATR,  $\tilde{\nu}$  [cm<sup>-1</sup>]): 3178w, 2366w, 1637w, 1616w, 1539w, 1494w, 1463w, 1429w, 1359w, 1222w, 1191w, 1161w, 1124w, 1087w, 979w, 835s, 740w, 657w, 605w, 555s, 513w, 335w.

**UV/Vis** (MeCN,  $\lambda_{\text{max}}$  [nm] ( $\epsilon$  [M<sup>-1</sup> cm<sup>-1</sup>])): 281 (17162), 231 (33414), 193 (37615).

**Elemental analysis:** calculated for C<sub>19</sub>H<sub>28</sub>F<sub>12</sub>N<sub>6</sub>P<sub>2</sub>: C: 36.20; H: 4.48; N: 13.33; found: C: 36.05; H: 4.76; N: 13.48.

### 7.4.14 Synthesis of 3,3'-(4-(diethylamino)pyridine-2,6-diyl)bis(1,4,5-methylimidazole-3-ium) [BdmiP<sup>NEt2</sup>] (L13)



The product is obtained as a white powder.

Yield: 78 %, (3.92 mmol)

**<sup>1</sup>H-NMR** (700 MHz, 30° C, DMSO, δ [ppm]): 9.48 (s, 2H, CH<sub>carb.</sub>); 7.11 (s, 2H, CH<sub>arom.</sub>); 3.85 (s, 6H, CH<sub>3</sub>); 3.55 (q, <sup>3</sup>J<sub>HH</sub>: 7.44 Hz, 4H, CH<sub>2</sub>); 2.34 (s, 6H, CH<sub>3</sub>); 2.32 (s, 6H, CH<sub>3</sub>); 1.18 (t, <sup>3</sup>J<sub>HH</sub>: 7.22 Hz, 6H, CH<sub>3</sub>).

**<sup>13</sup>C-NMR** (125 MHz, 30° C, DMSO, δ [ppm]): 156.1 (Cq); 147.1 (Cq); 135.6 (CH<sub>carb.</sub>); 127.8 (Cq); 126.0 (Cq); 102.1 (CH<sub>arom.</sub>); 44.2 (CH<sub>3</sub>); 33.7 (CH<sub>2</sub>); 11.9 (CH<sub>3</sub>); 9.3 (CH<sub>3</sub>); 7.6 (CH<sub>3</sub>).

**<sup>15</sup>N-NMR** (50.7 MHz, 30° C DMSO, δ [ppm]): 242.5 (N<sub>arom.</sub>); 190.3 (N<sub>arom.</sub>); 174.4 (N<sub>arom.</sub>); 103.7 (N<sub>aliph.</sub>).

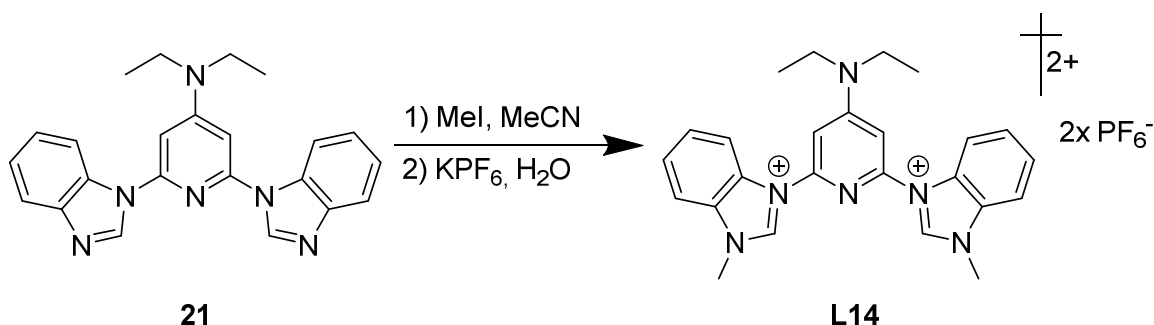
**ESI-MS** (m/z (%))(MeCN): 184.13 (100) [M<sup>2+</sup>]; 513.23 (95) [M<sup>2+</sup>+PF<sub>6</sub><sup>-</sup>].

**IR** (ATR,  $\tilde{\nu}$  [cm<sup>-1</sup>]): 3170w, 3120w, 2989w, 2368w, 1614m, 1573w, 1531m, 1488w, 1456w, 1355w, 1234m, 1199w, 1137w, 1083w, 985w, 833s, 738m, 700w, 671w, 638m, 622w, 555s, 430w, 293m, 223w.

**UV/Vis** (MeCN,  $\lambda_{\max}$  [nm] ( $\epsilon$  [M<sup>-1</sup> cm<sup>-1</sup>])): 276 (23873), 220 (36742).

**Elemental analysis:** calculated for C<sub>21</sub>H<sub>32</sub>F<sub>12</sub>N<sub>6</sub>P<sub>2</sub>: C: 38.31; H: 4.90; N: 12.76; found: C: 38.54; H: 4.96; N: 12.80.

### 7.4.15 Synthesis of 3,3'-(4-(diethylamino)pyridine-2,6-diyl)bis(1-methylbenzimidazole-3-ium) [BbP<sup>NEt2</sup>] (L14)



The product is obtained as a white powder. The Ligand is synthesized as part of the bachelor thesis by A. MILETIC where it is not characterized and discussed entirely.<sup>149</sup>

Yield: 66 %, (3.3 mmol)

**<sup>1</sup>H-NMR** (700 MHz, 30° C, DMSO,  $\delta$  [ppm]): 10.45 (s, 2H, CH<sub>carb.</sub>); 8.34 (s, 2H, CH<sub>arom.</sub>); 8.16 (s, 2H, CH<sub>arom.</sub>); 7.80 (s, 2H, CH<sub>arom.</sub>); 7.71 (s, 2H, CH<sub>arom.</sub>); 7.32 (s, 2H, CH<sub>arom.</sub>); 4.25 (s, 4H; CH<sub>2</sub>); 3.36 (s, 6H, CH<sub>3</sub>); 1.27 (s, 6H, CH<sub>3</sub>).

**<sup>13</sup>C-NMR** (125 MHz, 30° C, DMSO,  $\delta$  [ppm]): 157.0 (Cq); 148.3 (Cq); 143.6 (CH<sub>carb.</sub>); 132.8 (Cq); 130.3 (Cq) 128.3 (CH<sub>arom.</sub>); 127.8 (CH<sub>arom.</sub>); 116.3 (CH<sub>arom.</sub>); 114.6 (CH<sub>arom.</sub>); 100.1 (CH<sub>arom.</sub>); 44.9 (CH<sub>2</sub>); 34.43 (CH<sub>3</sub>); 12.7 (CH<sub>3</sub>).

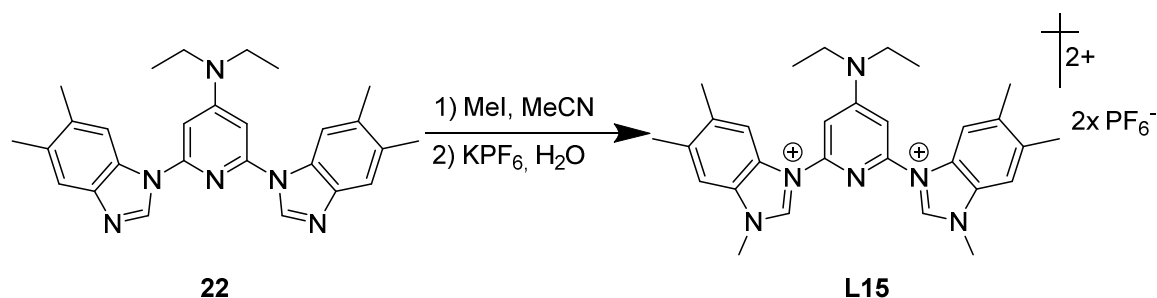
**<sup>15</sup>N-NMR** (50.7 MHz, 30° C DMSO,  $\delta$  [ppm]): 173.8 (N<sub>arom.</sub>); 159.5 (N<sub>arom.</sub>); 103.5 (N<sub>aliph.</sub>).

**ESI-MS** (m/z (%))(MeCN): 206.12 (100) [M<sup>2+</sup>]; 557.20 (75) [M<sup>2+</sup>+PF<sub>6</sub><sup>-</sup>].

**IR** (ATR,  $\tilde{\nu}$  [cm<sup>-1</sup>]): 3853w, 3749w, 3675w, 3648w, 3170w, 3118w, 2995w, 2366w, 2352w, 2161w, 2034w, 1972w, 1520m, 1575w, 1537w, 1492w, 1465w, 1359w, 1240w, 979w, 979s, 763m, 609s, 555s, 279w, 246m, 225m, 202m.

**UV/Vis** (MeCN,  $\lambda_{\text{max}}$  [nm] ( $\epsilon$  [M<sup>-1</sup> cm<sup>-1</sup>])): 268 (51704sh); 249 (72245).

### 7.4.16 Synthesis of 3,3'-(4-(diethylamino)pyridine-2,6-diyl)bis(1,5,6-trimethylbenzimidazole-3-ium) [BmbP<sup>NEt2</sup>] (L15)



The product is obtained as a light-yellow powder.

Yield: 63 %, (3.15 mmol)

**<sup>1</sup>H-NMR** (700 MHz, 30° C, DMSO,  $\delta$  [ppm]): 10.38 (s, 2H, CH<sub>carb.</sub>); 8.20 (s, 2H, CH<sub>arom.</sub>); 7.96 (s, 2H, CH<sub>arom.</sub>); 7.29 (s, 2H, CH<sub>arom.</sub>); 4.18 (s, 6H, CH<sub>3</sub>); 3.64 (s, 4H, CH<sub>2</sub>); 2.49 (s, 6H, CH<sub>3</sub>); 2.37 (s, 6H, CH<sub>3</sub>); 1.26 (s, 6H, CH<sub>3</sub>).

**<sup>13</sup>C-NMR** (125 MHz, 30° C, DMSO,  $\delta$  [ppm]): 156.3 (Cq); 147.7 (Cq); 141.8 (CH<sub>carb.</sub>); 137.2 (Cq); 136.8 (Cq); 130.6 (Cq); 128.1 (Cq); 115.4 (CH<sub>arom.</sub>); 113.5 (CH<sub>arom.</sub>); 98.8 (CH<sub>arom.</sub>); 44.3 (CH<sub>3</sub>); 33.6 (CH<sub>2</sub>); 20.1 (CH<sub>3</sub>); 19.9 (CH<sub>3</sub>); 12.1 (CH<sub>3</sub>).

**<sup>15</sup>N-NMR** (50.7 MHz, 30° C DMSO,  $\delta$  [ppm]): 232.6 (N<sub>arom.</sub>); 172.3 (N<sub>arom.</sub>); 158.3 (N<sub>arom.</sub>); 103.4 (N<sub>arom.</sub>).

**ESI-MS** (m/z (%))(MeCN): 234.14 (100) [M<sup>2+</sup>]

**IR** (ATR,  $\tilde{\nu}$  [cm<sup>-1</sup>]): 3170w, 3124w, 2989w, 2360w, 1618w, 1575w, 1531w, 1494w, 1465w, 1432w, 1386w, 1357w, 1309w, 1290w, 1247w, 1213w, 1182w, 1141w, 1097w, 1078w, 1026w, 989w, 968w, 877w, 817s, 748w, 655w, 626w, 590w, 555s, 472w, 430w.

**UV/Vis** (MeCN,  $\lambda_{\max}$  [nm] ( $\epsilon$  [M<sup>-1</sup> cm<sup>-1</sup>])): 287 (29724); 279 (31339); 251 (23335).

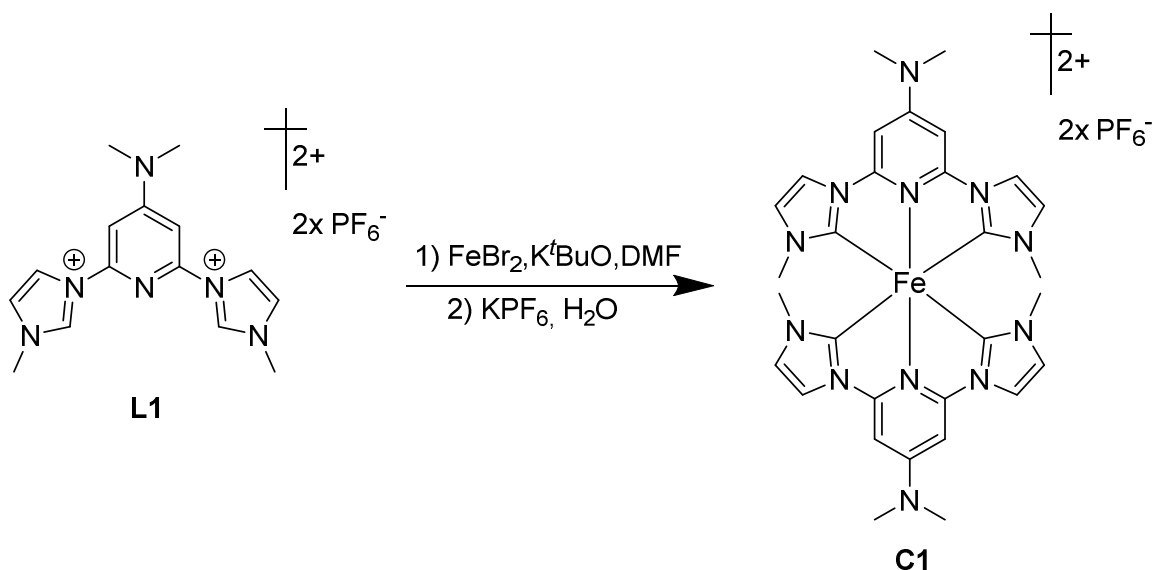
## 7.5 Synthesis of mononuclear iron(II) complexes

### 7.5.1 General method for iron complex synthesis

The complex synthesis varies within the time of the practical works. The first synthetic route used is well established in our group using LiHMDS as base to deprotonate the ligand in THF at  $-10^{\circ}\text{C}$ .<sup>95,97,150</sup> The complex synthesis is converted to a much simpler one described in the literature by the group of GROS.<sup>94,96</sup>

The respective ligand (**L1-L15**) (1 eq., 1 mmol) and  $\text{FeBr}_2$  (0.5 eq., 0.5 mmol) are added to dry DMF (15 mL) at r.t. under an argon atmosphere. Then  $\text{K}^t\text{BuO}$  (3.1 eq., 3.1 mmol) is added and the resulting reaction mixture is stirred at room temperature for 2 h. A saturated solution of  $\text{KPF}_6$  in water is added and the resulting suspension is stirred for another hour. The resulting precipitate is filtered and washed with diethyl ether. The obtained raw complex material is further purified using column chromatography (AluOx / MeCN).

### 7.5.2 Synthesis of $[\text{Fe}(\text{BIP}^{\text{NMe}_2})_2][\text{PF}_6]_2$ (**C1**)



Complex **C1** is obtained as bright-yellow powder. Suitable single crystals for X-ray diffraction spectroscopy can be obtained by slow diffusion of diethyl ether into an acetonitrile solution of **C1**.

Yield: 75 %, (0.37 mmol)

$^1\text{H-NMR}$  (500 MHz,  $(\text{CD}_3)_2\text{CO}$ ,  $30^{\circ}\text{C}$ ,  $\delta$  [ppm]): 8.29 (d,  $^3J_{\text{HH}} = 2.1$  Hz, 4H,  $\text{CH}_{\text{arom.}}$ ); 7.36 (s, 4H,  $\text{CH}_{\text{arom.}}$ ); 7.21 (d,  $^3J_{\text{HH}} = 2.1$  Hz, 4H,  $\text{CH}_{\text{arom.}}$ ); 3.31 (s, 12H,  $\text{CH}_3$ ); 2.81 (s, 12H,  $\text{CH}_3$ ).

$^{13}\text{C-NMR}$  (125 MHz,  $(\text{CD}_3)_2\text{CO}$ ,  $30^{\circ}\text{C}$ ,  $\delta$  [ppm]): 203.4 ( $\text{C}_{\text{qNHC}}$ ); 157.4 ( $\text{C}_{\text{q}}$ ); 153.6 ( $\text{C}_{\text{q}}$ ); 125.8 ( $\text{CH}_{\text{arom.}}$ ); 115.9 ( $\text{CH}_{\text{arom.}}$ ); 89.4 ( $\text{CH}_{\text{arom.}}$ ); 39.6 ( $\text{CH}_3$ ); 34.4 ( $\text{CH}_3$ ).

**$^{15}\text{N-NMR}$**  (50.7 MHz,  $(\text{CD}_3)_2\text{CO}$ , 30°C,  $\delta$  [ppm]): 203.7 ( $\text{N}_{\text{arom.}}$ ); 193.9 ( $\text{N}_{\text{arom.}}$ ); 179.5 ( $\text{N}_{\text{arom.}}$ ); 69.7 ( $\text{N}_{\text{aliph.}}$ ).

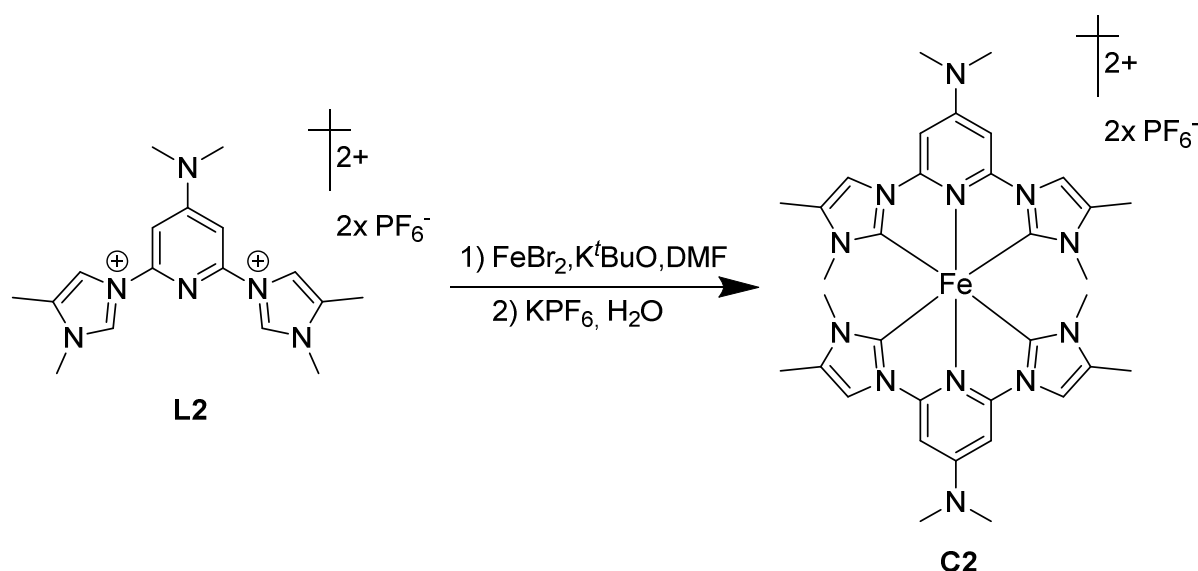
**ESI-MS** ( $m/z(\%)$ ) (MeCN): 310.12 (100) [ $\text{M}^{2+}$ ]; 303.119 (20) [ $\text{M-CH}_3^{2+}$ ].

**IR** (ATR,  $\tilde{\nu}$  [ $\text{cm}^{-1}$ ]): 3185w, 3148w, 2947w, 1634w, 1568w, 1531m, 1503w, 1482w, 1466m, 1435w, 1402m, 1341m, 1262m, 1235w, 1177m, 1125w, 1085w, 1067w, 1003w, 987w, 937w, 865sh, 827s, 801s, 748m, 695s, 684s, 636w, 582w, 553s, 490w, 417w, 378w, 323w, 272w, 239w.

**UV/Vis** (MeCN,  $\lambda_{\text{max}}$  [nm] ( $\epsilon$  [ $\text{M}^{-1} \text{cm}^{-1}$ ])): 432 (22425); 249 (64253).

**Elemental analysis:** calculated for  $\text{C}_{30}\text{H}_{36}\text{F}_{12}\text{FeN}_{12}\text{P}_2$ : C: 39.58; H: 3.99; N: 18.46; found: C: 39.68; H: 4.10; N: 18.43.

### 7.5.3 Synthesis of $[\text{Fe}(\text{BmIP}^{\text{NMe}_2})_2][\text{PF}_6]_2$ (**C2**)



Complex **C2** is obtained as bright-yellow powder. Suitable single crystals for X-ray diffraction spectroscopy can be obtained by slow diffusion of diethyl ether into an acetonitrile solution of **C2**.

Yield: 75 %, (0.37 mmol)

**$^1\text{H-NMR}$**  (500 MHz,  $\text{CD}_3\text{CN}$ , 30°C,  $\delta$  [ppm]): 7.66 (d,  $^4J_{\text{HH}} = 1.23$  Hz, 4H,  $\text{CH}_{\text{arom.}}$ ); 6.82 (s, 4H,  $\text{CH}_{\text{arom.}}$ ); 3.22 (s, 12H,  $\text{CH}_3$ ); 2.47 (s, 12H,  $\text{CH}_3$ ); 2.08 (s, 12H,  $\text{CH}_3$ ).

**$^{13}\text{C-NMR}$**  (125 MHz,  $\text{CD}_3\text{CN}$ , 30°C,  $\delta$  [ppm]): 204.4 ( $\text{C}_{\text{qNHC}}$ ); 158.0 ( $\text{C}_{\text{q}}$ ); 154.2 ( $\text{C}_{\text{q}}$ ); 134.4 ( $\text{CH}_{\text{arom.}}$ ); 113.3 ( $\text{CH}_{\text{arom.}}$ ); 89.5 ( $\text{CH}_{\text{arom.}}$ ); 40.7 ( $\text{CH}_3$ ); 32.1 ( $\text{CH}_3$ ); 9.9 ( $\text{CH}_3$ ).

**$^{15}\text{N-NMR}$**  (50.7 MHz,  $\text{CD}_3\text{CN}$ ,  $30^\circ\text{C}$ ,  $\delta$  [ppm]): 200.2 ( $\text{N}_{\text{arom.}}$ ); 194.3 ( $\text{N}_{\text{arom.}}$ ); 182.4 ( $\text{N}_{\text{arom.}}$ ); 69.4 ( $\text{N}_{\text{aliph.}}$ ).

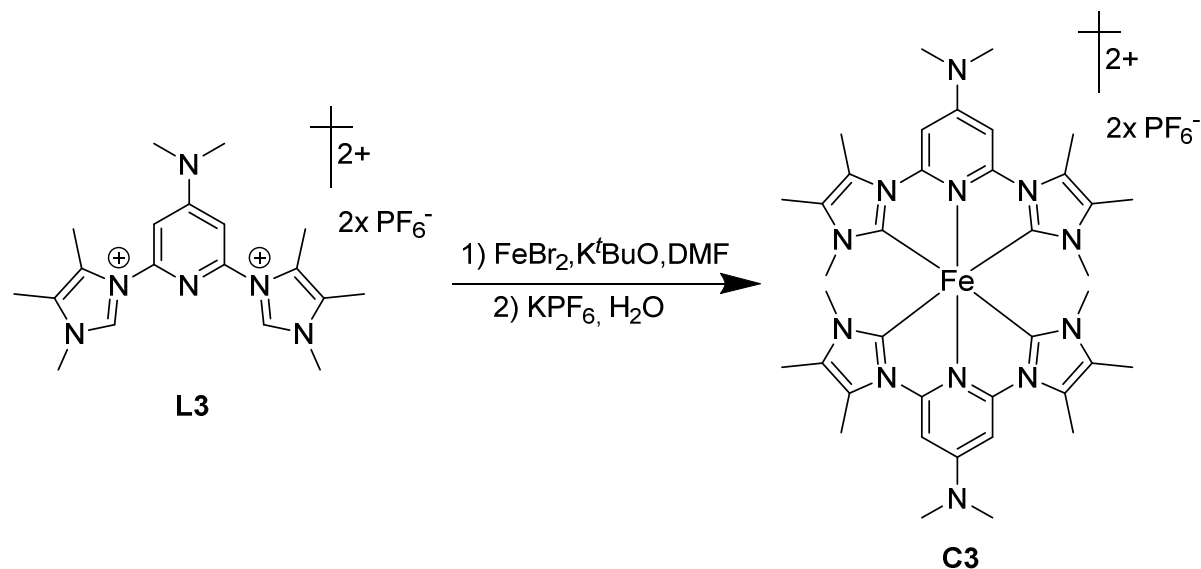
**ESI-MS** ( $m/z(\%)$ ) ( $\text{MeCN}$ ): 338.15 (100) [ $\text{M}^{2+}$ ]; 821.28 (8) [ $\text{M}^{2+} + \text{PF}_6^-$ ].

**IR** (ATR,  $\tilde{\nu}$  [ $\text{cm}^{-1}$ ]): 3648w, 3149w, 2931w, 2360w, 1645m, 1620m, 1539m, 1506w, 1436w, 1394m, 1336m, 1270m, 1240w, 1184w, 1166w, 1072w, 999w, 937w, 835s, 806sh, 752m, 698w, 607w, 555s, 501w, 410w, 378w, 349w.

**UV/Vis** ( $\text{MeCN}$ ,  $\lambda_{\text{max}}$  [nm] ( $\epsilon$  [ $\text{M}^{-1} \text{cm}^{-1}$ ])): 436 (28163); 257 (74668).

**Elemental analysis:** calculated for  $\text{C}_{34}\text{H}_{44}\text{F}_{12}\text{FeN}_{12}\text{P}_2$ : C: 42.25; H: 4.59; N: 17.39; found: C: 43.24; H: 4.97; N: 17.78.

### 7.5.4 Synthesis of $[\text{Fe}(\text{BdmIP}^{\text{NMe}_2})_2][\text{PF}_6]_2$ (**C3**)



Complex **C3** is obtained as bright-orange powder.

Yield: 67 %, (0.34 mmol)

**$^1\text{H-NMR}$**  (700 MHz,  $\text{CD}_3\text{CN}$ ,  $30^\circ\text{C}$ ,  $\delta$  [ppm]): 6.98 (s, 4H,  $\text{CH}_{\text{arom.}}$ ); 3.22 (s, 12H,  $\text{CH}_3$ ); 2.60 (s, 12H,  $\text{CH}_3$ ); 2.48 (s, 12H,  $\text{CH}_3$ ); 1.98 (s, 12H,  $\text{CH}_3$ ).

**$^{13}\text{C-NMR}$**  (176 MHz,  $\text{CD}_3\text{CN}$ ,  $30^\circ\text{C}$ ,  $\delta$  [ppm]): 203.0 ( $\text{C}_{\text{qNHC}}$ ); 156.3 ( $\text{C}_{\text{q}}$ ); 154.9 ( $\text{C}_{\text{q}}$ ); 129.1 ( $\text{C}_{\text{q}}$ ); 123.3 ( $\text{C}_{\text{q}}$ ); 90.6 ( $\text{CH}_{\text{arom.}}$ ); 39.8 ( $\text{CH}_3$ ); 31.6 ( $\text{CH}_3$ ); 10.8 ( $\text{CH}_3$ ); 8.2 ( $\text{CH}_3$ ).

**$^{15}\text{N-NMR}$**  (70.6 MHz,  $\text{CD}_3\text{CN}$ ,  $30^\circ\text{C}$ ,  $\delta$  [ppm]): 201.3 ( $\text{N}_{\text{arom.}}$ ); 199.7 ( $\text{N}_{\text{arom.}}$ ); 178.3 ( $\text{N}_{\text{arom.}}$ ); 67.6 ( $\text{N}_{\text{aliph.}}$ ).

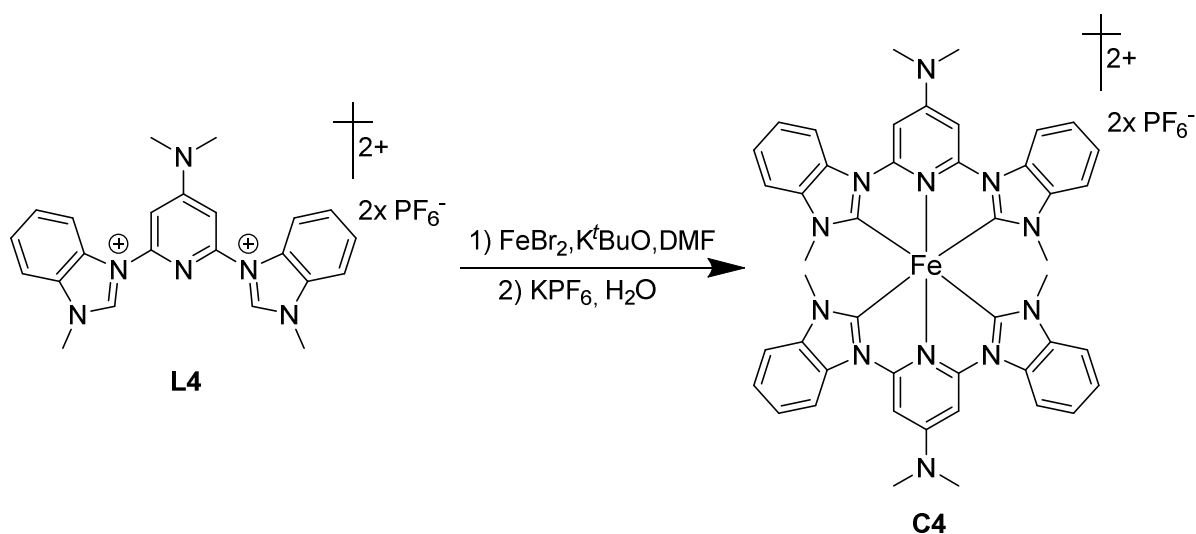
**ESI-MS** ( $m/z(\%)$ ) ( $\text{MeCN}$ ): 366.19 (100) [ $\text{M}^{2+}$ ]; 344.66 (25) [ $\text{M}^{2+} - \text{NMe}_2$ ].

**IR** (ATR,  $\tilde{\nu}$  [ $\text{cm}^{-1}$ ]): 1660w, 1625m, 1537w, 1494w, 1448w, 1388m, 1367w, 1334m, 1296w, 1211w, 1159w, 1097w, 1066w, 958w, 835s, 796m, 729w, 698w, 555s, 493w, 418w, 351w.

**UV/Vis** (MeCN,  $\lambda_{\text{max}}$  [nm] ( $\epsilon$  [ $\text{M}^{-1} \text{cm}^{-1}$ ])): 447 (25401); 397 (16474sh); 267 (56083); 238 (59530).

**Elemental analysis:** calculated for  $\text{C}_{38}\text{H}_{52}\text{F}_{12}\text{FeN}_{12}\text{P}_2$ : C: 44.63; H: 5.13; N: 16.44; found: C: 44.42; H: 5.06; N: 16.39.

### 7.5.5 Synthesis of $[\text{Fe}(\text{BbP}^{\text{NMe}_2})_2][\text{PF}_6]_2$ (**C4**)



Complex **C4** is obtained as red powder. Suitable single crystals for X-ray diffraction spectroscopy can be obtained by slow diffusion of diethyl ether into an acetonitrile solution of **C4**.

Yield: 62 %, (0.31 mmol).

**$^1\text{H-NMR}$**  (700 MHz,  $\text{CD}_3\text{CN}$ ,  $30^\circ\text{C}$ ,  $\delta$  [ppm]): 8.21 (d,  $^3J_{\text{HH}} = 8.4$  Hz, 4H,  $\text{CH}_{\text{arom.}}$ ); 7.45 (t,  $^3J_{\text{HH}} = 7.9$  Hz, 4H,  $\text{CH}_{\text{arom.}}$ ); 7.38 (t,  $^3J_{\text{HH}} = 7.7$  Hz, 4H,  $\text{CH}_{\text{arom.}}$ ); 7.36 (s, 4H,  $\text{CH}_{\text{arom.}}$ ); 7.31 (d,  $^3J_{\text{HH}} = 7.9$  Hz, 4H,  $\text{CH}_{\text{arom.}}$ ); 3.49 (s, 12H,  $\text{CH}_3$ ); 2.87 (s, 12H,  $\text{CH}_3$ ).

**$^{13}\text{C-NMR}$**  (125 MHz,  $\text{CD}_3\text{CN}$ ,  $30^\circ\text{C}$ ,  $\delta$  [ppm]): 214.9 ( $\text{C}_{\text{qNHC}}$ ); 158.6 ( $\text{C}_{\text{q}}$ ); 154.7 ( $\text{C}_{\text{q}}$ ); 139.3 ( $\text{C}_{\text{q}}$ ); 131.9 ( $\text{C}_{\text{q}}$ ); 125.3 ( $\text{CH}_{\text{arom.}}$ ); 124.5 ( $\text{CH}_{\text{arom.}}$ ); 112.5 ( $\text{CH}_{\text{arom.}}$ ); 111.0 ( $\text{CH}_{\text{arom.}}$ ); 91.6 ( $\text{CH}_{\text{arom.}}$ ); 41.2 ( $\text{CH}_3$ ); 32.4 ( $\text{CH}_3$ ).

**$^{15}\text{N-NMR}$**  (50.7 MHz,  $\text{CD}_3\text{CN}$ ,  $30^\circ\text{C}$ ,  $\delta$  [ppm]): 218.0 ( $\text{N}_{\text{arom.}}$ ); 187.9 ( $\text{N}_{\text{arom.}}$ ); 168.4 ( $\text{N}_{\text{arom.}}$ ); 72.9 ( $\text{N}_{\text{aliph.}}$ ).

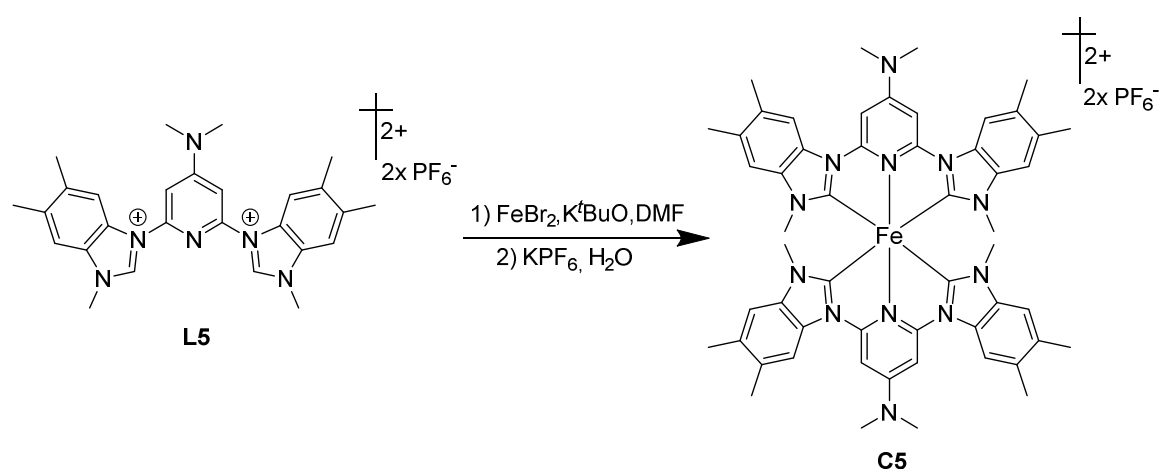
**ESI-MS** ( $m/z$ (%)) (MeCN): 410.15 (100) [ $\text{M}^{2+}$ ].

**IR** (ATR,  $\tilde{\nu}$  [ $\text{cm}^{-1}$ ]): 2930w, 2812w, 1673w, 1640m, 1601w, 1537w, 1499m, 1463w, 1438w, 1384m, 1334sh, 1305m, 1231s, 1189s, 1160s, 1124s, 1092s, 1022w, 981s, 939w, 875w, 829s, 789s, 734s, 690m, 671m, 636w, 587w, 555s, 456w, 431m, 393w, 349w, 281w.

**UV/Vis** (MeCN,  $\lambda_{\text{max}}$  [nm] ( $\epsilon$  [ $\text{M}^{-1} \text{cm}^{-1}$ ])): 416 (23271); 320 (28087); 268 (63441); 231 (90311); 202 (128973).

**Elemental analysis:** calculated for  $\text{C}_{46}\text{H}_{44}\text{F}_{12}\text{FeN}_{12}\text{P}_2$ : C: 49.74; H: 3.99; N: 15.13; found: C: 49.51; H: 4.50; N: 14.34.

### 7.5.6 Synthesis of $[\text{Fe}(\text{BmbP}^{\text{NMe}_2})_2][\text{PF}_6]_2$ (**C5**)



Complex **C5** is obtained as orange powder.

Yield: 55 %, (0.27 mmol)

**$^1\text{H-NMR}$**  (700 MHz,  $\text{CD}_3\text{CN}$ ,  $30^\circ\text{C}$ ,  $\delta$  [ppm]): 7.85 (s, 4H,  $\text{CH}_{\text{arom.}}$ ); 7.26 (s, 4H,  $\text{CH}_{\text{arom.}}$ ); 7.06 (s, 4H,  $\text{CH}_{\text{arom.}}$ ); 3.46 (s, 12H,  $\text{CH}_3$ ); 2.75 (s, 12H,  $\text{CH}_3$ ); 2.45 (s, 12H,  $\text{CH}_3$ ); 2.30 (s, 12H,  $\text{CH}_3$ ).

**$^{13}\text{C-NMR}$**  (125 MHz,  $\text{CD}_3\text{CN}$ ,  $30^\circ\text{C}$ ,  $\delta$  [ppm]): 212.9 ( $\text{C}_{\text{qNHC}}$ ); 157.43 ( $\text{C}_{\text{q}}$ ); 153.7 ( $\text{C}_{\text{q}}$ ); 136.6 ( $\text{C}_{\text{q}}$ ); 133.3 ( $\text{C}_{\text{q}}$ ); 132.4 ( $\text{C}_{\text{q}}$ ); 129.3 ( $\text{C}_{\text{q}}$ ); 111.6 ( $\text{CH}_{\text{arom.}}$ ); 110.4 ( $\text{CH}_{\text{arom.}}$ ); 90.0 ( $\text{CH}_{\text{arom.}}$ ); 40.1 ( $\text{CH}_3$ ); 31.1 ( $\text{CH}_3$ ); 19.2 ( $\text{CH}_3$ ).

**$^{15}\text{N-NMR}$**  (50.7 MHz,  $\text{CD}_3\text{CN}$ ,  $30^\circ\text{C}$ ,  $\delta$  [ppm]): 188.9 ( $\text{N}_{\text{arom.}}$ ); 186.4 ( $\text{N}_{\text{arom.}}$ ); 167.3 ( $\text{N}_{\text{arom.}}$ ); 72.5 ( $\text{N}_{\text{arom.}}$ ).

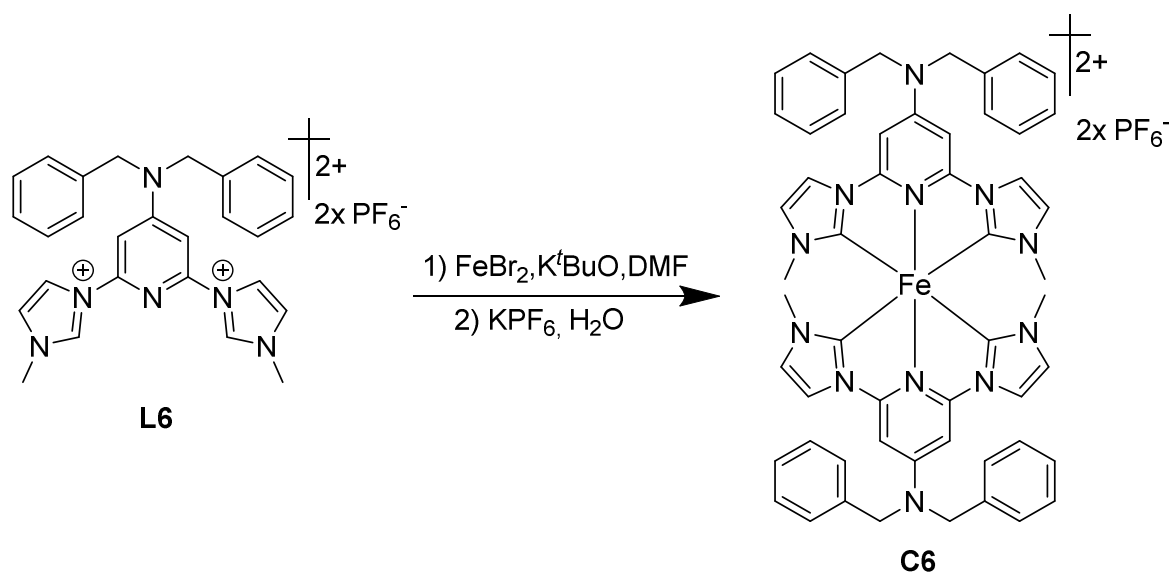
**ESI-MS** ( $m/z(\%)$ ) (MeCN): 466.220 (100) [ $\text{M}^{2+}$ ]; 310.814 (8) [ $\text{M}^{3+}$ ].

**IR** (ATR,  $\tilde{\nu}$  [ $\text{cm}^{-1}$ ]): 2921w, 2858sh, 1670w, 1639m, 1598w, 1535m, 1502m, 1446m, 1384m, 1330m, 1305m, 1238m, 1184m, 1159m, 1083m, 1002w, 875w, 827s, 788m, 756m, 736m, 686m, 657m, 617w, 576m, 555s, 522m, 449m, 416m, 352m, 293m.

**UV/Vis** (MeCN,  $\lambda_{\text{max}}$  [nm] ( $\epsilon$  [ $\text{M}^{-1} \text{cm}^{-1}$ ])): 422 (27311); 323 (34094); 287 (51991); 268 (69145); 236 (89349).

**Elemental analysis:** calculated for  $\text{C}_{54}\text{H}_{60}\text{F}_{12}\text{FeN}_{12}\text{P}_2$ : C: 53.04; H: 4.95; N: 13.74; found: C: 52.69; H: 5.05; N: 13.91.

### 7.5.7 Synthesis of $[\text{Fe}(\text{BIP}^{\text{NBn}2})_2][\text{PF}_6]_2$ (**C6**)



Complex **C6** is obtained as light-yellow powder. Suitable single crystals for X-ray diffraction spectroscopy can be obtained by slow diffusion of diethyl ether into an acetonitrile solution of **C6**.

Yield: 68 %, (0.34 mmol)

**$^1\text{H-NMR}$**  (700 MHz,  $\text{CD}_3\text{CN}$ ,  $30^\circ\text{C}$ ,  $\delta$  [ppm]): 7.78 (s, 4H,  $\text{CH}_{\text{arom.}}$ ); 7.39 (t,  $^3J_{\text{HH}} = 7.8$  Hz, 8H,  $\text{CH}_{\text{arom.}}$ ); 7.32 (m, 12H,  $\text{CH}_{\text{arom.}}$ ); 7.06 (s, 4H,  $\text{CH}_{\text{arom.}}$ ); 6.93 (d,  $^3J_{\text{HH}} = 2.1$  Hz, 4H,  $\text{CH}_{\text{arom.}}$ ); 4.92 (s, 8H,  $\text{CH}_2$ ); 2.61 (s, 12H,  $\text{CH}_3$ ).

**$^{13}\text{C-NMR}$**  (176 MHz,  $\text{CD}_3\text{CN}$ ,  $30^\circ\text{C}$ ,  $\delta$  [ppm]): 204.0 ( $\text{C}_{\text{qNHC}}$ ); 157.9 ( $\text{C}_{\text{q}}$ ); 154.6 ( $\text{C}_{\text{q}}$ ); 137.5 ( $\text{C}_{\text{q}}$ ); 129.7 ( $\text{CH}_{\text{arom.}}$ ); 128.4 ( $\text{CH}_{\text{arom.}}$ ); 127.9 ( $\text{CH}_{\text{arom.}}$ ); 126.7 ( $\text{CH}_{\text{arom.}}$ ); 116.5 ( $\text{CH}_{\text{arom.}}$ ); 91.1 ( $\text{CH}_{\text{arom.}}$ ); 54.6 ( $\text{CH}_2$ ); 35.4 ( $\text{CH}_3$ ).

**$^{15}\text{N-NMR}$**  (50.7 MHz,  $\text{CD}_3\text{CN}$ ,  $30^\circ\text{C}$ ,  $\delta$  [ppm]): 203.2 ( $\text{N}_{\text{arom.}}$ ); 197.9 ( $\text{N}_{\text{arom.}}$ ); 179.6 ( $\text{N}_{\text{arom.}}$ ), 90.1 ( $\text{N}_{\text{aliph.}}$ ).

**ESI-MS** ( $m/z(\%)$ ) ( $\text{MeCN}$ ): 462.19 (100) [ $\text{M}^{2+}$ ].

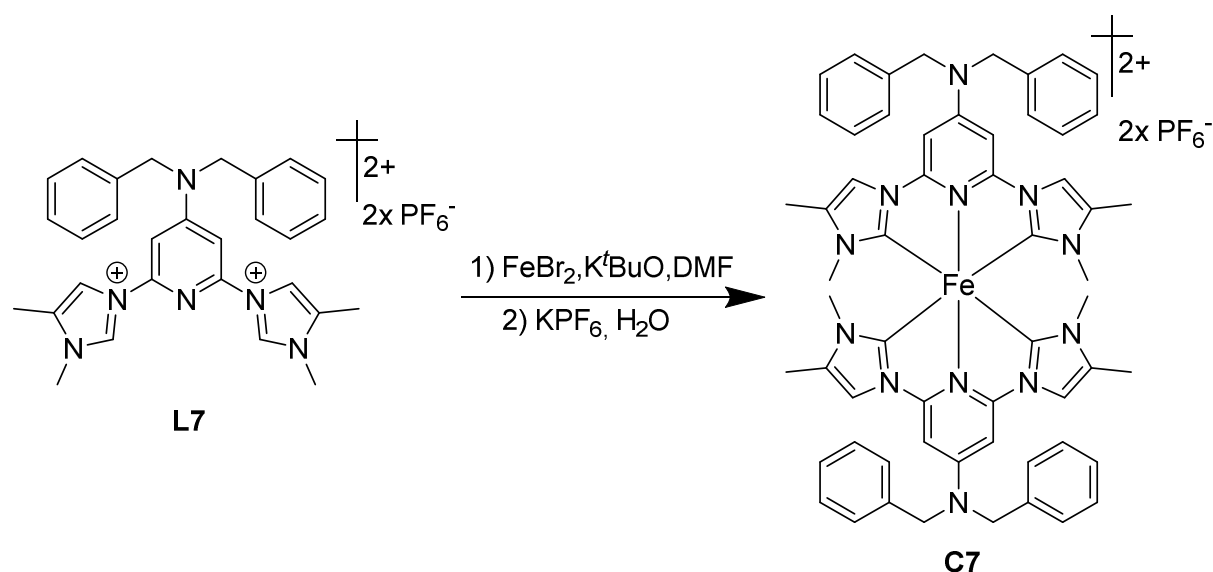
**IR** (ATR,  $\tilde{\nu}$  [ $\text{cm}^{-1}$ ]): 3168w, 3135w, 2916w, 2850w, 1729w, 1716w, 1640m, 1633m, 1603w, 1568w, 1539w, 1502m, 1480m, 1467w, 1450m, 1400m, 1343m, 1296w, 1270w, 1240m,

1255m, 1186w, 1155w, 1131m, 1085m, 1028w, 1000w, 981w, 945m, 899w, 837s, 808s, 728s, 694m, 616w, 555s, 485w, 454w, 408w, 375w, 349w, 317w, 265w, 226w.

**UV/Vis** (MeCN,  $\lambda_{\text{max}}$  [nm] ( $\epsilon$  [ $\text{M}^{-1} \text{cm}^{-1}$ ])): 442 (27264); 251 (72235).

**Elemental analysis:** calculated for  $\text{C}_{54}\text{H}_{52}\text{F}_{12}\text{FeN}_{12}\text{P}_2$ : C: 53.39; H: 4.31; N: 13.84; found: C: 52.74; H: 4.80; N: 13.03.

### 7.5.8 Synthesis of $[\text{Fe}(\text{BmlP}^{\text{NBn2}})_2][\text{PF}_6]_2$ (**C7**)



Complex **C7** is obtained as light-yellow powder. Suitable single crystals for X-ray diffraction spectroscopy can be obtained by slow diffusion of diethyl ether into an acetonitrile solution of **C7**.

Yield: 83 %, (0.41 mmol)

**$^1\text{H-NMR}$**  (500 MHz, 30°C,  $\text{CD}_3\text{CN}$ ,  $\delta$  [ppm]): 7.41 (d,  $^4J_{\text{HH}}$ : 1.28 Hz, 4H,  $\text{CH}_{\text{arom.}}$ ); 7.29 (t,  $^3J_{\text{HH}}$ : 7.2 Hz, 8H,  $\text{CH}_{\text{arom.}}$ ); 7.21 (d,  $^3J_{\text{HH}}$ : 7.1 Hz, 8H,  $\text{CH}_{\text{arom.}}$ ); 7.20 (t,  $^3J_{\text{HH}}$ : 7.3 Hz, 4H,  $\text{CH}_{\text{arom.}}$ ); 6.80 (s, 4H, CH); 4.82 (s, 8H,  $\text{CH}_2$ ); 2.34 (s, 12H,  $\text{CH}_3$ ); 1.93 (d,  $^4J_{\text{HH}}$ : 1.2 Hz, 12H,  $\text{CH}_3$ ).

**$^{13}\text{C-NMR}$**  (125 MHz, 30°C,  $\text{CD}_3\text{CN}$ ,  $\delta$  [ppm]): 204.3 ( $\text{C}_{\text{qNHC}}$ ); 157.77 (Cq); 154.6 (Cq); 137.7 (Cq); 134.8 (Cq); 129.8 ( $\text{CH}_{\text{arom.}}$ ); 128.5 ( $\text{CH}_{\text{arom.}}$ ); 127.9 ( $\text{CH}_{\text{arom.}}$ ); 113.3 ( $\text{CH}_{\text{arom.}}$ ); 90.5 ( $\text{CH}_{\text{arom.}}$ ); 55.2 ( $\text{CH}_2$ ); 31.0 ( $\text{CH}_3$ ); 9.9 ( $\text{CH}_3$ ).

**$^{15}\text{N-NMR}$**  (50.7 MHz,  $\text{CD}_3\text{CN}$ , 30°C,  $\delta$  [ppm]): 199.6 ( $\text{N}_{\text{arom.}}$ ); 197.6 ( $\text{N}_{\text{arom.}}$ ); 182.3 ( $\text{N}_{\text{arom.}}$ ); 88.8 ( $\text{N}_{\text{aliph.}}$ ).

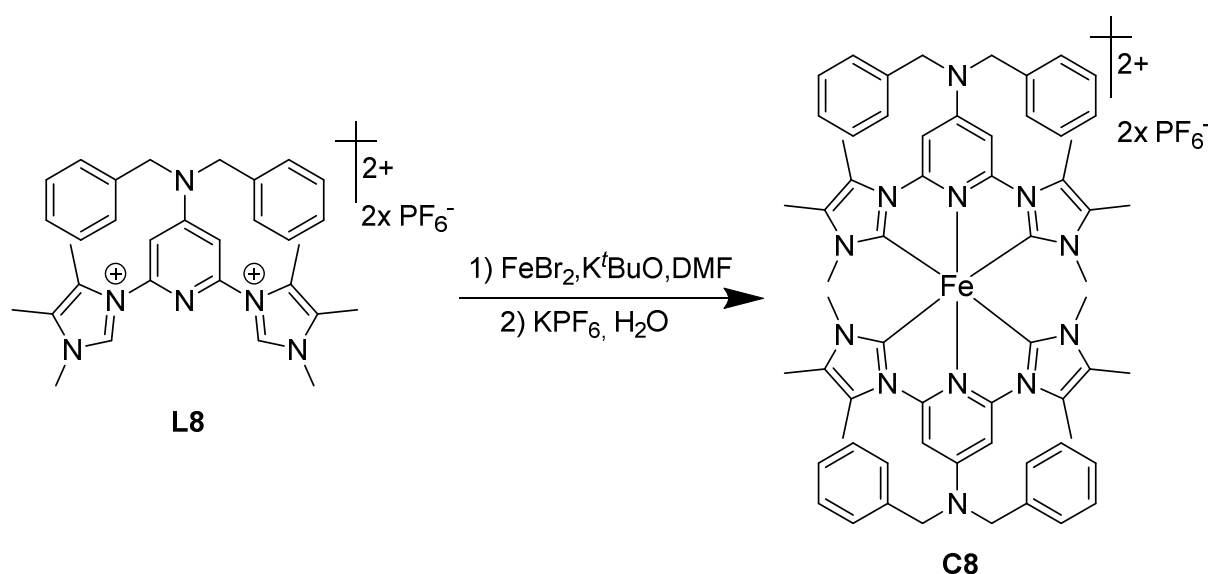
**ESI-MS** ( $m/z$ (%)) (MeCN): 490.21 (100) [ $\text{M}^{2+}$ ].

**IR** (ATR,  $\tilde{\nu}$  [ $\text{cm}^{-1}$ ]): 3141w, 3029w, 2929w, 2360w, 2323w, 1641m, 1620m, 1540w, 1506m, 1488m, 1454w, 1392m, 1348sh, 1332w, 1297w, 1272w, 1251w, 1209m, 1176w, 1155w, 1076w, 1027w, 1002w, 931w, 916w, 873w, 829s, 802s, 730m, 696m, 644m, 613w, 555s, 487w, 459w, 416w, 376w, 351w, 302w, 246w, 227w.

**UV/Vis** (MeCN,  $\lambda_{\text{max}}$  [nm] ( $\epsilon$  [ $\text{M}^{-1} \text{cm}^{-1}$ ])): 446 (35589); 262 (91039).

**Elemental analysis:** calculated for  $\text{C}_{58}\text{H}_{60}\text{F}_{12}\text{FeN}_{12}\text{P}_2$ : C: 54.81; H: 4.76; N: 13.22; found: C: 54.86; H: 4.86; N: 13.44.

### 7.5.9 Synthesis of $[\text{Fe}(\text{BdmIP}^{\text{NBn2}})_2][\text{PF}_6]_2$ (**C8**)



The complex **C8** is obtained as orange powder.

Yield: 37 %, (0.18 mmol)

**$^1\text{H-NMR}$**  (700 MHz,  $30^\circ\text{C}$ ,  $(\text{CD}_3)_2\text{CO}$ ,  $\delta$  [ppm]): 7.47 (d,  $^3J_{\text{HH}}$ : 7.4 Hz, 8H,  $\text{CH}_{\text{arom.}}$ ); 7.43 (t,  $^3J_{\text{HH}}$ : 7.4 Hz, 8H,  $\text{CH}_{\text{arom.}}$ ); 7.34 (t,  $^3J_{\text{HH}}$ : 7.2 Hz, 4H,  $\text{CH}_{\text{arom.}}$ ); 7.14 (s, 4H,  $\text{CH}_{\text{arom.}}$ ); 5.21 (s, 8H,  $\text{CH}_2$ ); 2.51 (s, 12H,  $\text{CH}_3$ ); 2.31 (s, 12H,  $\text{CH}_3$ ); 1.98 (s, 12H,  $\text{CH}_3$ ).

**$^{13}\text{C-NMR}$**  (176 MHz,  $30^\circ\text{C}$ ,  $(\text{CD}_3)_2\text{CO}$ ,  $\delta$  [ppm]): 202.3 ( $\text{C}_{\text{qNHC}}$ ); 154.9 ( $\text{C}_{\text{q}}$ ); 154.5 ( $\text{C}_{\text{q}}$ ); 137.1 ( $\text{C}_{\text{q}}$ ); 128.9 ( $\text{C}_{\text{q}}$ ); 129.9 ( $\text{CH}_{\text{arom.}}$ ); 127.5 ( $\text{C}_{\text{q}}$ ); 126.6 ( $\text{CH}_{\text{arom.}}$ ); 122.6 ( $\text{C}_{\text{q}}$ ); 92.2 ( $\text{CH}_{\text{arom.}}$ ); 56.3 ( $\text{CH}_2$ ); 31.0 ( $\text{CH}_3$ ); 10.2 ( $\text{CH}_3$ ); 7.6 ( $\text{CH}_3$ ).

**$^{15}\text{N-NMR}$**  (70.9 MHz,  $(\text{CD}_3)_2\text{CO}$ ,  $30^\circ\text{C}$ ,  $\delta$  [ppm]): 203.0 ( $\text{N}_{\text{arom.}}$ ); 201.2 ( $\text{N}_{\text{arom.}}$ ); 178.9 ( $\text{N}_{\text{arom.}}$ ); 86.4 ( $\text{N}_{\text{aliph.}}$ ).

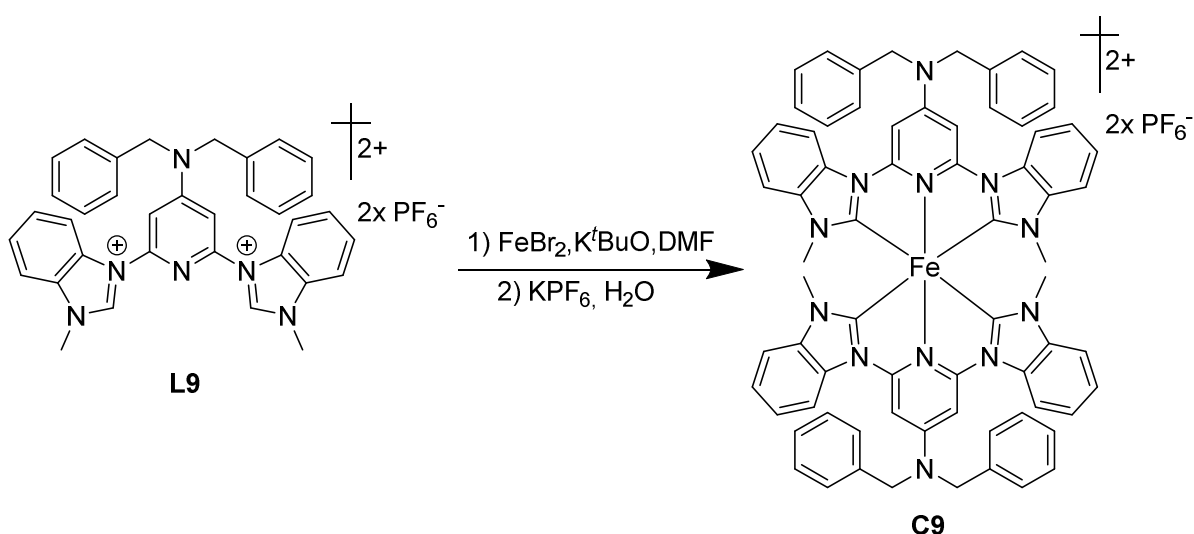
**ESI-MS** ( $m/z$ (%)) (MeCN): 518.25 (100) [ $\text{M}^{2+}$ ]; 345.50 (25) [ $\text{M}^{3+}$ ].

**IR** (ATR,  $\tilde{\nu}$  [ $\text{cm}^{-1}$ ]): 2927w, 1658w, 1631m, 1539w, 1513w, 1496w, 1450m, 1388m, 1350w, 1296w, 1240m, 1170w, 1139w, 1095w, 1066sh, 1027w, 954w, 833s, 796s, 736m, 698m, 555s, 493w, 460w, 420w, 387w, 351w, 248w, 212w.

**UV/Vis** (MeCN,  $\lambda_{\text{max}}$  [nm] ( $\epsilon$  [ $\text{M}^{-1} \text{cm}^{-1}$ ])): 453 (31077); 406 (18151); 266 (63838); 241 (63877).

**Elemental analysis:** calculated for  $\text{C}_{62}\text{H}_{68}\text{F}_{12}\text{FeN}_{12}\text{P}_2$ : C: 56.11; H: 5.17; N: 12.67; found: C: 55.95; H: 5.11; N: 12.80.

### 7.5.10 Synthesis of $[\text{Fe}(\text{BbP}^{\text{NBn}2})_2][\text{PF}_6]_2$ (**C9**)



Complex **C9** is obtained as dark red powder. Suitable single crystals for X-ray diffraction spectroscopy can be obtained by slow diffusion of diethyl ether into an acetonitrile solution of **C9**.

Yield: 60 %, (0.3 mmol)

**<sup>1</sup>H-NMR** (700 MHz, CD<sub>3</sub>CN, 30°C,  $\delta$  [ppm]): 7.62 (d,  $^3J_{\text{HH}} = 9.2$  Hz, 4H, CH<sub>arom.</sub>); 7.57 (d,  $^3J_{\text{HH}} = 7.6$  Hz, CH<sub>arom.</sub>); 7.49 (t,  $^3J_{\text{HH}} = 7.57$  Hz, 8H, CH<sub>arom.</sub>); 7.35 (m, 12H, CH<sub>arom.</sub>); 7.29 (s, 4H, CH<sub>arom.</sub>); 7.26 (m, 4H, CH<sub>arom.</sub>); 5.26 (s, 8H, CH<sub>2</sub>); 2.73 (s, 12H, CH<sub>3</sub>).

**<sup>13</sup>C-NMR** (125 MHz, CD<sub>3</sub>CN, 30°C,  $\delta$  [ppm]): 214.4 (Cq<sub>NHC</sub>); 157.6 (Cq); 154.5 (Cq); 139.2 (Cq); 137.9 (Cq); 131.6 (Cq); 130.2 (CH<sub>arom.</sub>); 128.8 (CH<sub>arom.</sub>); 127.9 (CH<sub>arom.</sub>); 125.3 (CH<sub>arom.</sub>); 124.3 (CH<sub>arom.</sub>); 111.7 (CH<sub>arom.</sub>); 111.2 (CH<sub>arom.</sub>); 93.3 (CH<sub>arom.</sub>); 57.2 (CH<sub>2</sub>); 32.2 (CH<sub>3</sub>).

**<sup>15</sup>N-NMR** (50.7 MHz, CD<sub>3</sub>CN, 30°C,  $\delta$  [ppm]): 191.9 (N<sub>arom.</sub>); 187.2 (N<sub>arom.</sub>); 168.6 (N<sub>arom.</sub>); 90.5 (N<sub>aliph.</sub>).

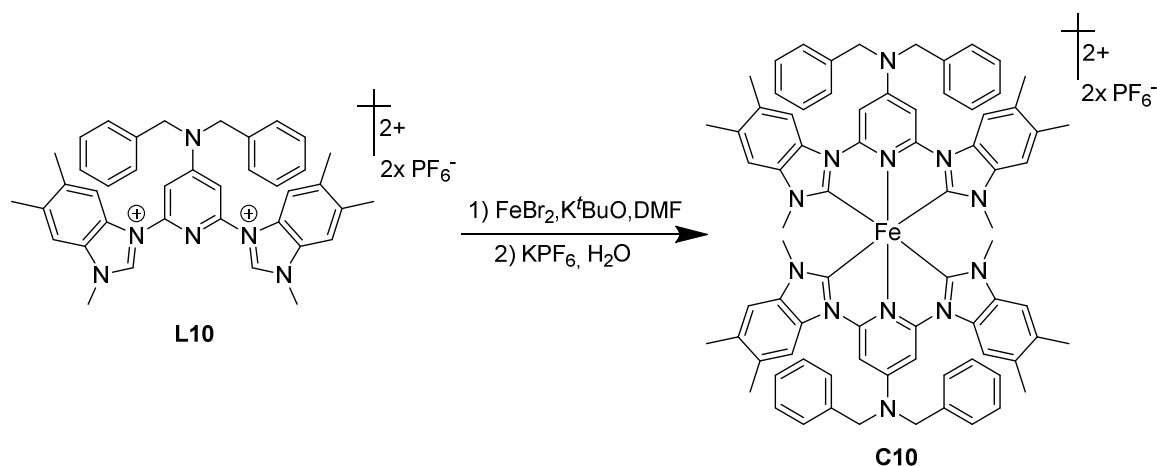
**ESI-MS** (m/z(%)) (MeCN): 562.22 (100) [M<sup>2+</sup>].

**IR** (ATR,  $\tilde{\nu}$  [cm<sup>-1</sup>]): 3060w, 3030w, 2360w, 2336w, 1640m, 1599m, 1540w, 1496m, 1452m, 1439m, 1385m, 1321m, 1293m, 1248w, 1231w, 1190m, 1138w, 1092m, 1022w, 939w, 828s, 791s, 731s, 696m, 635w, 585w, 555s, 546sh, 487w, 430m, 389w, 346w, 324w, 280w.

**UV/Vis** (MeCN,  $\lambda_{\text{max}}$  [nm] ( $\epsilon$  [M<sup>-1</sup> cm<sup>-1</sup>])): 426 (28209); 325 (33470); 289 (62795); 270 (79267); 232 (97195).

**Elemental analysis:** calculated for C<sub>70</sub>H<sub>60</sub>F<sub>12</sub>FeN<sub>12</sub>P<sub>2</sub>: C: 59.11; H: 4.27; N: 11.88; found: C: 59.21; H: 4.63; N: 11.69.

### 7.5.11 Synthesis of [Fe(BmbP<sup>NBn2</sup>)<sub>2</sub>][PF<sub>6</sub>]<sub>2</sub> (**C10**)



Complex **C10** is obtained as intense orange powder.

Yield: 43 %, (0.22 mmol)

**<sup>1</sup>H-NMR** (500 MHz, 30°C, CD<sub>3</sub>CN,  $\delta$  [ppm]): 7.55 (d, <sup>3</sup>J<sub>HH</sub>: 7.5 Hz, 8H, CH); 7.48 (t, <sup>3</sup>J<sub>HH</sub>: 7.7 Hz, 8H, C<sub>(17+19)</sub>H); 7.33 (t, <sup>3</sup>J<sub>HH</sub>: 7.6 Hz, 4H, C<sub>(18)</sub>H); 7.24 (s, 4H, C<sub>(9)</sub>H); 7.14 (s, 4H, C<sub>(12)</sub>H); 6.99 (s, 4H, C<sub>(4)</sub>H); 5.27 (s, 8H, C<sub>(14)</sub>H<sub>2</sub>); 2.59 (s, 12H, C<sub>(1)</sub>H<sub>3</sub>); 2.35 (s, 12H, C<sub>(8)</sub>H<sub>3</sub>); 2.26 (s, 12H, C<sub>(6)</sub>H<sub>3</sub>).

**<sup>13</sup>C-NMR** (125 MHz, 30°C, CD<sub>3</sub>CN,  $\delta$  [ppm]): 213.4 (C<sub>(2)</sub>q); 157.4 (C<sub>(13)</sub>q); 138.2 (C<sub>(15)</sub>q); 137.7 (C<sub>(3)</sub>q); 134.5 (C<sub>(5)</sub>q); 133.5 (C<sub>(7)</sub>q); 130.4 (C<sub>(17+19)</sub>H); 130.2 (C<sub>(10)</sub>q); 128.8 (C<sub>(18)</sub>H); 127.8 (C<sub>(16+20)</sub>H); 112.1 (C<sub>(9)</sub>H); 111.7 (C<sub>(4)</sub>H); 93.1 (C<sub>(12)</sub>H); 57.9 (C<sub>(14)</sub>H<sub>2</sub>); 32.1 (C<sub>(1)</sub>H<sub>3</sub>); 20.4 (C<sub>(8)</sub>H<sub>3</sub>); 20.3 (C<sub>(6)</sub>H<sub>3</sub>).

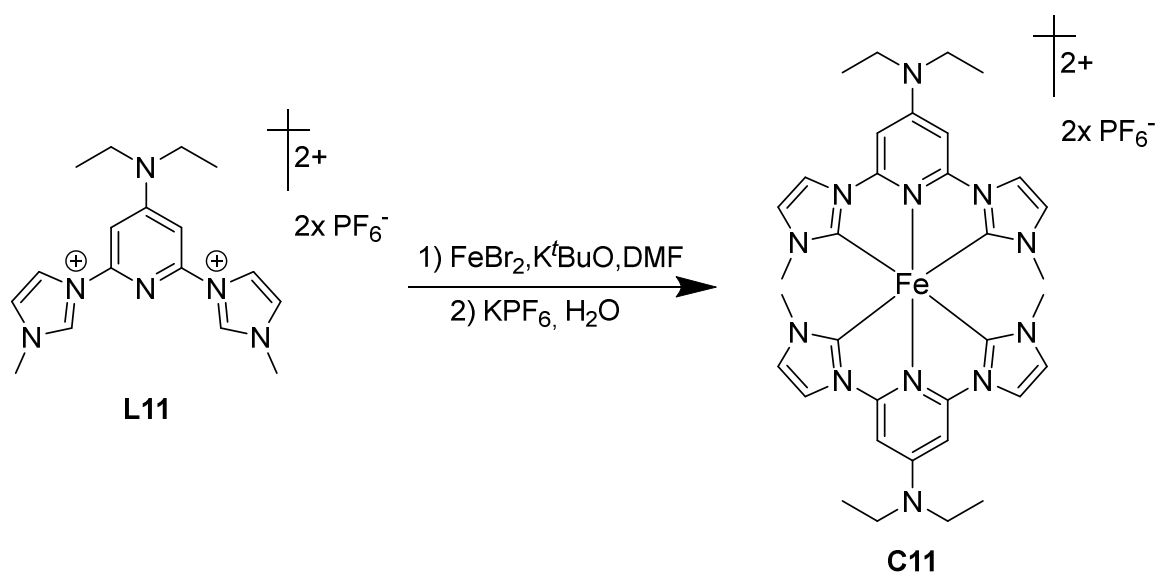
**<sup>15</sup>N-NMR** (50.7 MHz, CD<sub>3</sub>CN, 30°C,  $\delta$  [ppm]): 193.6 (N<sub>c</sub>); 186.9 (N<sub>b</sub>); 167.4 (N<sub>a</sub>); 89.5 (N<sub>d</sub>).

**ESI-MS** (m/z(%)) (MeCN): 618.28 (100) [M<sup>2+</sup>].

**IR** (ATR,  $\tilde{\nu}$  [ $\text{cm}^{-1}$ ]): 2360w, 1637w, 1600w, 1540w, 1498w, 1452w, 1386w, 1301w, 1220w, 1184w, 1078w, 1024w, 1000w, 966w, 914w, 835s, 794w, 736m, 696w, 613w, 555s, 486w, 455w, 426w, 352w, 291w, 254w.

**Elemental analysis:** calculated for  $\text{C}_{78}\text{H}_{76}\text{F}_{12}\text{FeN}_{12}\text{P}_2$ : C: 61.34; H: 5.02; N: 11.01; found: C: 10.91; H: 60.76; N: 5.02.

### 7.5.12 Synthesis of $[\text{Fe}(\text{BIP}^{\text{NEt}_2})_2][\text{PF}_6]_2$ (**C11**)



Complex **C11** is obtained as yellow powder. Complex **C11** is synthesized as part of the bachelor thesis by A. MILETIC but is not characterized entirely.<sup>149</sup>

Yield: 34 %, (0.17 mmol)

**$^1\text{H-NMR}$**  (700 MHz,  $\text{CD}_3\text{CN}$ ,  $30^\circ\text{C}$ ,  $\delta$  [ppm]): 7.93 (d,  $^3J_{\text{HH}}$ : 2.14 Hz; 4H, CH); 6.95 (d,  $^3J_{\text{HH}}$ : 2.14 Hz, 4H, CH); 6.90 (s, 4H, CH); 3.61 (q,  $^3J_{\text{HH}}$ : 7.64 Hz, 8H,  $\text{CH}_2$ ); 2.63 (s, 12H,  $\text{CH}_3$ ); 1.29 (t,  $^3J_{\text{HH}}$ : 7.11 Hz, 12H,  $\text{CH}_3$ ).

**$^{13}\text{C-NMR}$**  (176 MHz,  $\text{CD}_3\text{CN}$ ,  $30^\circ\text{C}$ ,  $\delta$  [ppm]): 203.7 (Cq); 155.4 (Cq); 153.9 (Cq); 125.7 (CH); 116.1 (CH); 89.4 (CH); 45.1 ( $\text{CH}_2$ ); 34.8 ( $\text{CH}_3$ ); 11.8 ( $\text{CH}_3$ ).

**$^{15}\text{N-NMR}$**  (50.7 MHz,  $\text{CD}_3\text{CN}$ ,  $30^\circ\text{C}$ ,  $\delta$  [ppm]): 203.6 ( $\text{N}_b$ ); 192.7 ( $\text{N}_c$ ); 178.9 ( $\text{N}_a$ ); 99.2 ( $\text{N}_d$ ).

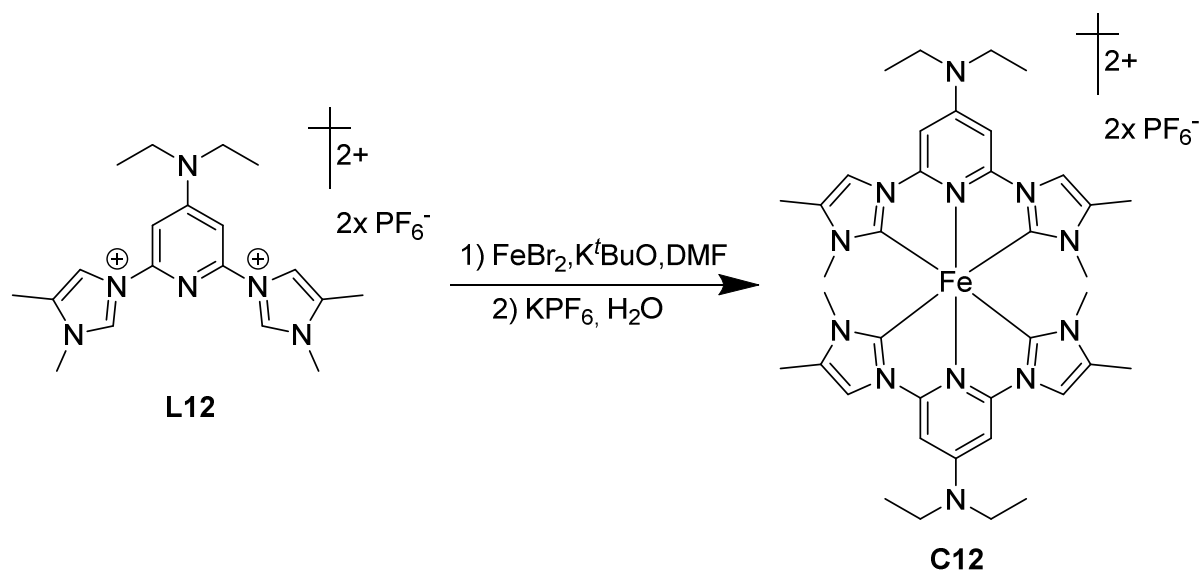
**ESI-MS** ( $m/z$ (%)) ( $\text{MeCN}$ ): 338.16 (100) [ $\text{M}^{2+}$ ], 225.44 (38) [ $\text{M}^{3+}$ ].

**IR** (ATR,  $\tilde{\nu}$  [ $\text{cm}^{-1}$ ]): 3145w, 2979w, 1635m, 1571w, 1529m, 1508w, 1488m, 1448w, 1404m, 1344m, 1166w, 1124w, 1080w, 1004w, 975w, 918w, 831s, 806s, 732m, 686m, 555s, 491w, 443w, 410w, 381w, 314w, 229w.

**UV/Vis** ( $\text{MeCN}$ ,  $\lambda_{\text{max}}$  [nm] ( $\epsilon$  [ $\text{M}^{-1}\text{cm}^{-1}$ ])): 430 (26981); 275 (54358); 251 (74925).

**Elemental analysis:** calculated for  $C_{34}H_{44}F_{12}FeN_{12}P_2$ : C: 42.25; H: 4.59; N: 17.39; found: C: 42.13; H: 4.66; N: 17.34.

### 7.5.13 Synthesis of $[Fe(BmIP^{NEt_2})_2][PF_6]_2$ (**C12**)



Complex **C12** is obtained as yellow powder.

Yield: 71 %, (0.35 mmol)

**<sup>1</sup>H-NMR** (700 MHz, acetone-d<sub>3</sub>, 30°C, δ [ppm]): 8.08 (d, <sup>4</sup>J<sub>HH</sub>:1.27 Hz, 4H, CH<sub>arom.</sub>); 7.25 (s, 4H, CH<sub>arom.</sub>); 3.71 (q, <sup>3</sup>J<sub>HH</sub>: 7.53 Hz, 8H, CH<sub>2</sub>); 2.69 (s, 12H, CH<sub>3</sub>); 2.15 (d, <sup>4</sup>J<sub>HH</sub>: 1.27 Hz, 12H, CH<sub>3</sub>); 1.30 (t, <sup>3</sup>J<sub>HH</sub>: 7.18 Hz, 12H, CH<sub>3</sub>).

**<sup>13</sup>C-NMR** (176 MHz, acetone-d<sub>3</sub>, 30°C, δ [ppm]): 203.8 (C<sub>qNHC</sub>); 155.4 (C<sub>q</sub>); 154.1 (C<sub>q</sub>); 133.5 (C<sub>q</sub>); 113.2 (CH<sub>arom.</sub>); 88.5 (CH<sub>arom.</sub>); 44.8 (CH<sub>2</sub>); 31.3 (CH<sub>3</sub>); 11.7 (CH<sub>3</sub>); 9.0 (CH<sub>3</sub>).

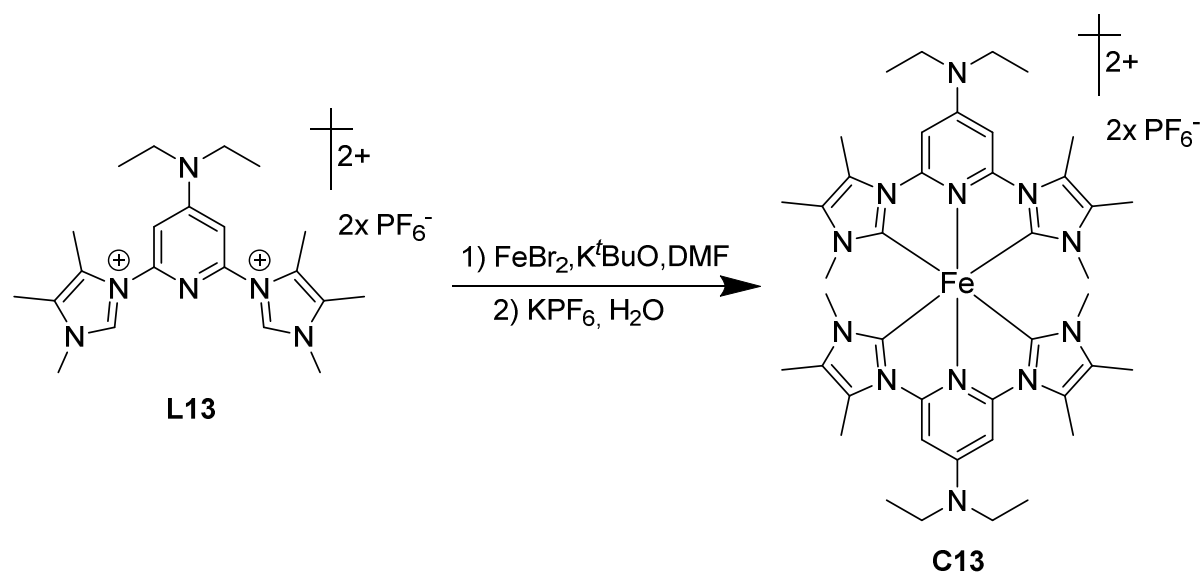
**<sup>15</sup>N-NMR** (50.7 MHz, acetone-d<sub>3</sub>, 30°C, δ [ppm]): 200.5 (N<sub>arom.</sub>); 192.6 (N<sub>arom.</sub>); 182.2 (N<sub>arom.</sub>); 98.9 (N<sub>aliph.</sub>).

**ESI-MS** (m/z(%)) (MeCN): 394.22 (100) [M<sup>2+</sup>].

**IR** (ATR,  $\tilde{\nu}$  [cm<sup>-1</sup>]): 3155w, 2921m, 2852w, 1922w, 1641m, 1620m, 1539m, 1508m, 1488m, 1452m, 1398m, 1353m, 1334m, 1278m, 1259m, 1232m, 1195m, 1153m, 1078m, 977m, 833s, 802s, 740m, 694m, 676m, 607m, 555s, 478m, 349m, 268m.

**UV/Vis** (MeCN,  $\lambda_{max}$  [nm] ( $\epsilon$  [M<sup>-1</sup> cm<sup>-1</sup>])): 438 (26193); 254 (67085).

**Elemental analysis:** calculated for  $C_{38}H_{52}F_{12}FeN_{12}P_2$ : C: 44.63; H: 5.13; N: 16.44; found: C: 45.21; H: 5.35; N: 15.84.

7.5.14 Synthesis of  $[\text{Fe}(\text{BdmIP}^{\text{NEt}_2})_2] [\text{PF}_6]_2$  (**C13**)

Complex **C13** is obtained as yellow powder. Suitable single crystals for X-ray diffraction spectroscopy can be obtained by slow diffusion of diethyl ether into an acetonitrile solution of **C13**.

Yield: 48 %, (0.24 mmol)

**$^1\text{H-NMR}$**  (700 MHz,  $\text{CD}_3\text{CN}$ ,  $30^\circ\text{C}$ ,  $\delta$  [ppm]): 7.00 (s, 4H,  $\text{CH}_{\text{arom.}}$ ); 3.64 (d,  $^3J_{\text{HH}}$ : 7.16 Hz, 8H,  $\text{CH}_2$ ); 2.63 (s, 12H,  $\text{CH}_3$ ); 2.55 (s, 12H,  $\text{CH}_3$ ); 2.03 (s, 12H,  $\text{CH}_3$ ); 1.33 (t,  $^3J_{\text{HH}}$ : 7.11 Hz, 12H,  $\text{CH}_3$ ).

**$^{13}\text{C-NMR}$**  (176 MHz,  $\text{CD}_3\text{CN}$ ,  $30^\circ\text{C}$ ,  $\delta$  [ppm]): 203.7 ( $\text{C}_{\text{qNHC}}$ ); 155.9 (Cq); 154.8 (Cq); 129.8 (Cq); 123.9 (Cq); 91.1 ( $\text{CH}_{\text{arom.}}$ ); 45.9 ( $\text{CH}_2$ ); 32.3 ( $\text{CH}_3$ ); 12.4 ( $\text{CH}_3$ ); 11.6 ( $\text{CH}_3$ ); 8.8 ( $\text{CH}_3$ ).

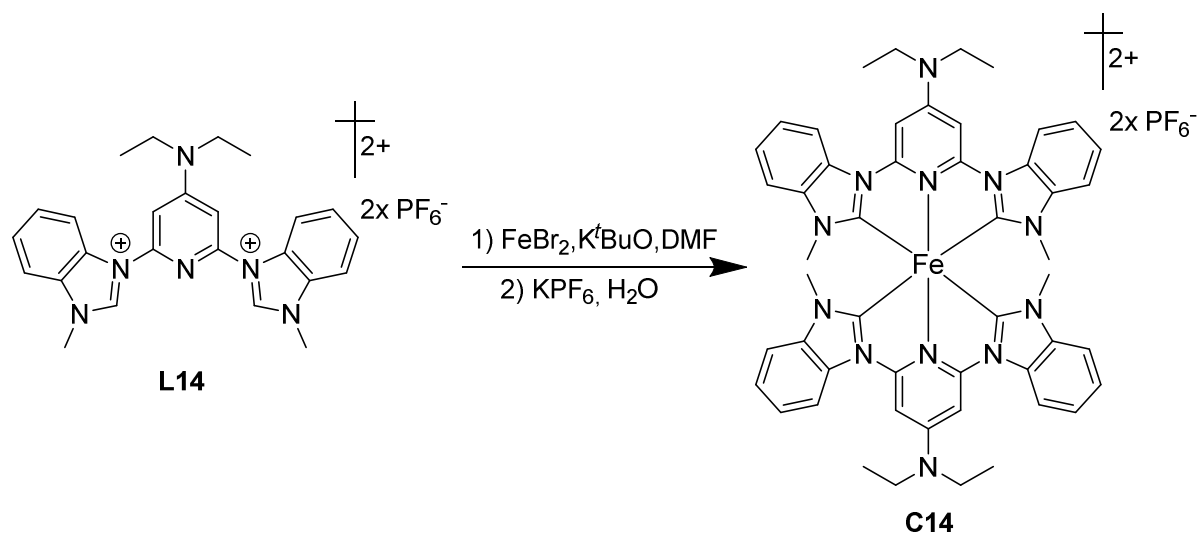
**$^{15}\text{N-NMR}$**  (50.7 MHz,  $\text{CD}_3\text{CN}$ ,  $30^\circ\text{C}$ ,  $\delta$  [ppm]): 201.5 ( $\text{N}_{\text{arom.}}$ ); 198.5 ( $\text{N}_{\text{arom.}}$ ); 178.9 ( $\text{N}_{\text{arom.}}$ ); 96.3 ( $\text{N}_{\text{aliph.}}$ ).

**ESI-MS** ( $m/z(\%)$ ) ( $\text{MeCN}$ ): 394.22 (100) [ $\text{M}^{2+}$ ].

**IR** (ATR,  $\tilde{\nu}$  [ $\text{cm}^{-1}$ ]): 2973w, 2933w, 1658w, 1623m, 1531m, 1485m, 1452m, 1386m, 1348m, 1299w, 1265m, 1203w, 1149w, 1093m, 1072m, 1008w, 962w, 833s, 796s, 736m, 698m, 555s, 493m, 414m, 351m, 214m.

**UV/Vis** ( $\text{MeCN}$ ,  $\lambda_{\text{max}}$  [nm] ( $\epsilon$  [ $\text{M}^{-1} \text{cm}^{-1}$ ])): 447 (26974); 400 (16556); 268 (53965); 238 (55234).

**Elemental analysis:** calculated for  $\text{C}_{42}\text{H}_{60}\text{F}_{12}\text{FeN}_{12}\text{P}_2$ : C: 46.76; H: 5.61; N: 15.58; found: C: 46.82; H: 5.60; N: 15.43.

7.5.15 Synthesis of  $[\text{Fe}(\text{BbP}^{\text{NEt}_2})_2][\text{PF}_6]_2$  (**C14**)

Complex **C14** is obtained as red powder. Suitable single crystals for X-ray diffraction spectroscopy can be obtained by slow diffusion of diethyl ether into an acetonitrile solution of **C14**.

Yield: 69 %, (0.34 mmol)

**$^1\text{H-NMR}$**  (700 MHz,  $\text{CD}_3\text{CN}$ ,  $30^\circ\text{C}$ ,  $\delta$  [ppm]): 8.16 (d,  $^3J_{\text{HH}}$ : 8.32 Hz; 4H,  $\text{CH}_{\text{arom.}}$ ); 7.48 (t,  $^3J_{\text{HH}}$ : 7.90 Hz, 4H,  $\text{CH}_{\text{arom.}}$ ); 7.41 (t,  $^3J_{\text{HH}}$ : 7.90 Hz 4H,  $\text{CH}_{\text{arom.}}$ ); 7.35 (s, 4H,  $\text{CH}_{\text{arom.}}$ ); 7.33 (d,  $^3J_{\text{HH}}$ : 7.90 Hz,  $\text{CH}_{\text{arom.}}$ ); 3.88 (q,  $^3J_{\text{HH}}$ : 7.20 Hz, 8H,  $\text{CH}_2$ ); 2.90 (s, 12H,  $\text{CH}_3$ ); 1.50 (t,  $^3J_{\text{HH}}$ : 7.22 Hz, 12H,  $\text{CH}_3$ ).

**$^{13}\text{C-NMR}$**  (125 MHz,  $\text{CD}_3\text{CN}$ ,  $30^\circ\text{C}$ ,  $\delta$  [ppm]): 214.3 ( $\text{C}_{\text{qNHC}}$ ); 155.7 (Cq); 154.3 (Cq); 138.5 (Cq); 131.2 (Cq); 124.5 ( $\text{CH}_{\text{arom.}}$ ); 123.8 ( $\text{CH}_{\text{arom.}}$ ); 111.6 ( $\text{CH}_{\text{arom.}}$ ); 110.3 ( $\text{CH}_{\text{arom.}}$ ); 90.6 ( $\text{CH}_{\text{arom.}}$ ); 45.5 ( $\text{CH}_2$ ); 31.7 ( $\text{CH}_3$ ); 11.8 ( $\text{CH}_3$ ).

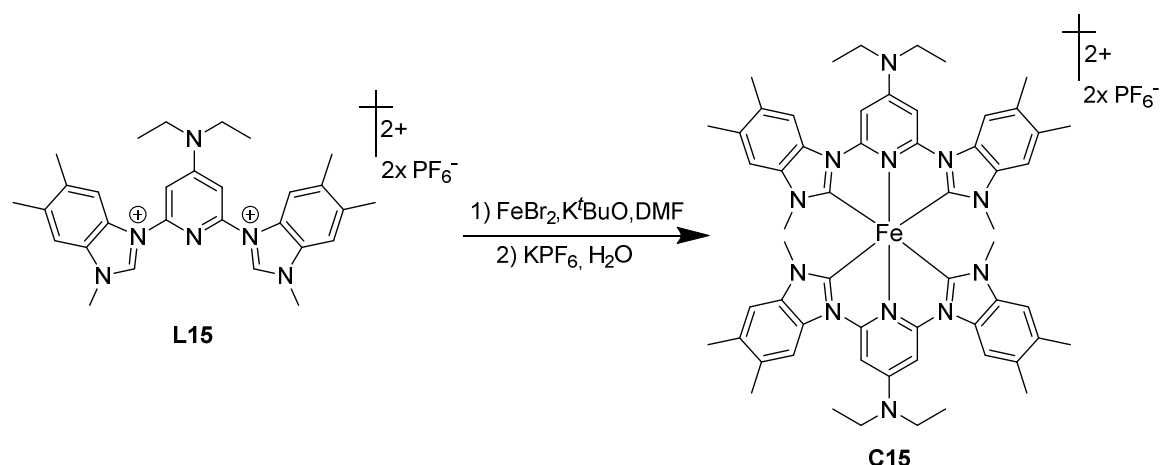
**$^{15}\text{N-NMR}$**  (70.9 MHz,  $\text{CD}_3\text{CN}$ ,  $30^\circ\text{C}$ ,  $\delta$  [ppm]): 198.2 ( $\text{N}_{\text{arom.}}$ ); 186.9 ( $\text{N}_{\text{arom.}}$ ); 168.5 ( $\text{N}_{\text{arom.}}$ ); 100.9 ( $\text{N}_{\text{aliph.}}$ ).

**ESI-MS** ( $m/z$ (%)) ( $\text{MeCN}$ ): 438.20 (100) [ $\text{M}^{2+}$ ], 446.18 (18) [ $\text{M}^{2+} + \text{O}_2$ ].

**IR** (ATR,  $\tilde{\nu}$  [ $\text{cm}^{-1}$ ]): 2977w, 2933w, 2362w, 1639m, 1600m, 1523m, 1500m, 1442m, 1390m, 1355m, 1323m, 1294w, 1270m, 1230w, 1207w, 1189m, 1157m, 1093m, 1024w, 979w, 833s, 790m, 732m, 690w, 671m, 634w, 588w, 555s, 493w, 432m, 387w, 347m, 281w.

**UV/Vis** ( $\text{MeCN}$ ,  $\lambda_{\text{max}}$  [nm] ( $\epsilon$  [ $\text{M}^{-1} \text{cm}^{-1}$ ])): 417 (27666), 322 (36673); 268 (879082); 231 (109359).

**Elemental analysis:** calculated for  $\text{C}_{50}\text{H}_{52}\text{F}_{12}\text{FeN}_{12}\text{P}_2$ : C: 51.47; H: 4.49; N: 14.41; found: C: 51.13; H: 4.66; N: 14.32.

7.5.16 Synthesis of  $[\text{Fe}(\text{BmbP}^{\text{NEt}_2})_2] [\text{PF}_6]_2$  (**C15**)

Complex **C15** is obtained as light red powder. Suitable single crystals for X-ray diffraction spectroscopy can be obtained by slow diffusion of diethyl ether into an acetonitrile solution of **C15**.

Yield: 32 %, (0.16 mmol)

**$^1\text{H-NMR}$**  (700 MHz,  $\text{CD}_3\text{CN}$ ,  $30^\circ\text{C}$ ,  $\delta$  [ppm]): 7.77 (s, 4H,  $\text{CH}_{\text{arom.}}$ ); 7.25 (s, 4H,  $\text{CH}_{\text{arom.}}$ ); 7.06 (s, 4H,  $\text{CH}_{\text{arom.}}$ ); 3.85 (q,  $^3J_{\text{HH}}$ : 7.12 Hz, 8H,  $\text{CH}_2$ ); 2.77 (s, 12H,  $\text{CH}_3$ ); 2.45 (s, 12H,  $\text{CH}_3$ ); 2.30 (s, 12H,  $\text{CH}_3$ ); 1.46 (t,  $^3J_{\text{HH}}$ : 7.26 Hz, 12H;  $\text{CH}_3$ ).

**$^{13}\text{C-NMR}$**  (176 MHz,  $\text{CD}_3\text{CN}$ ,  $30^\circ\text{C}$ ,  $\delta$  [ppm]): 214.0 (Cq); 156.4 (Cq); 155.1 (Cq); 137.7 (Cq); 134.4 (Cq); 133.4 (Cq); 130.4 (Cq); 112.5 ( $\text{CH}_{\text{arom.}}$ ); 111.51 ( $\text{CH}_{\text{arom.}}$ ); 90.9 ( $\text{CH}_{\text{arom.}}$ ); 46.2 ( $\text{CH}_2$ ); 32.2 ( $\text{CH}_3$ ); 20.3 ( $\text{CH}_3$ ); 20.2 ( $\text{CH}_3$ ); 12.4 ( $\text{CH}_3$ ).

**$^{15}\text{N-NMR}$**  (50.7 MHz,  $\text{CD}_3\text{CN}$ ,  $30^\circ\text{C}$ ,  $\delta$  [ppm]): 188.2 ( $\text{N}_{\text{arom.}}$ ); 167.9 ( $\text{N}_{\text{arom.}}$ ); 101.1 ( $\text{N}_{\text{aliph.}}$ ).

**ESI-MS** ( $m/z(\%)$ ) ( $\text{MeCN}$ ): 494.25 (100) [ $\text{M}^{2+}$ ].

**IR** (ATR,  $\tilde{\nu}$  [ $\text{cm}^{-1}$ ]): 2973w, 2927w, 1729w, 1639m, 1598w, 1535w, 1504m, 1444m, 1392m, 1351m, 1305w, 1269w, 1234w, 1186m, 1149w, 1070w, 1000w, 875w, 827s, 788m, 756w, 736w, 688m, 617w, 555s, 418w, 354w, 293w.

**UV/Vis** ( $\text{MeCN}$ ,  $\lambda_{\text{max}}$  [nm] ( $\epsilon$  [ $\text{M}^{-1} \text{cm}^{-1}$ ])): 421 (20860), 327 (27554), 287 (46352), 270 (59668); 236 (75871), 204 (119117).

**Elemental analysis:** calculated for  $\text{C}_{58}\text{H}_{68}\text{F}_{12}\text{FeN}_{12}\text{P}_2$ : C: 54.47; H: 5.36; N: 13.14; found: C: 54.19; H: 5.39; N: 13.02.

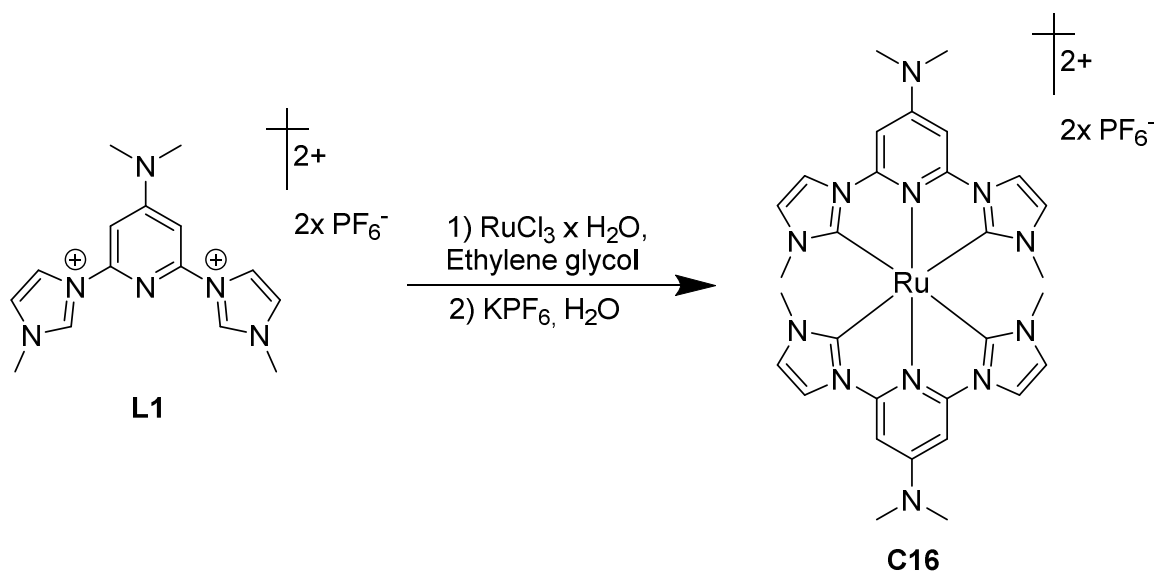
## 7.6 Synthesis of homoleptic mononuclear Ru(II) complexes

### 7.6.1 General synthetic procedure for Ru(II) complexes

For the synthesis of the homoleptic ruthenium complexes a modified procedure to the literature known protocol by PARK *et al.* is used.<sup>144</sup>

The respective ligand (**L1-L15**) (1 eq., 1 mmol) and RuCl<sub>3</sub>·xH<sub>2</sub>O (0.5 eq., 0.5 mmol) are added to ethylene glycol (15 mL) at r.t.. The resulting reaction mixture is heated to 180° C and stirred at that temperature for 5 hours. After cooling to r.t. a saturated solution of KPF<sub>6</sub> in water is added and the resulting suspension is stirred for another hour. The resulting precipitate is filtered and washed with diethyl ether. The obtained raw complex material is further purified using column chromatography (AluOx / MeCN).

### 7.6.2 Synthesis of [Ru(BIP<sup>NMe2</sup>)<sub>2</sub>] [PF<sub>6</sub>]<sub>2</sub> (**C16**)



The complex **C16** is obtained as bright yellow powder. Suitable single crystals for X-ray diffraction spectroscopy can be obtained by slow diffusion of diethyl ether into an acetonitrile solution of **C16**.

Yield: 44 %, (0.22 mmol)

<sup>1</sup>H-NMR (700 MHz, CD<sub>3</sub>CN, 30°C, δ [ppm]): 7.93 (d, <sup>3</sup>J<sub>HH</sub> = 1.7 Hz, 4H, CH<sub>arom.</sub>); 7.01 (s, 4H, CH<sub>arom.</sub>); 6.94 (d, <sup>3</sup>J<sub>HH</sub> = 1.73 Hz, 4H, CH<sub>arom.</sub>); 2.67 (s, 12H, CH<sub>3</sub>); 2.13 (s, 12H, CH<sub>3</sub>).

<sup>13</sup>C-NMR (176 MHz, CD<sub>3</sub>CN, 30°C, δ [ppm]): 192.6 (Cq); 156.4 (Cq); 151.4 (Cq); 123.4 (CH<sub>arom.</sub>); 115.9 (CH<sub>arom.</sub>); 89.4 (CH<sub>arom.</sub>); 39.8 (CH<sub>3</sub>); 35.1 (CH<sub>3</sub>).

**$^{15}\text{N-NMR}$**  (50.7 MHz,  $\text{CD}_3\text{CN}$ ,  $30^\circ\text{C}$ ,  $\delta$  [ppm]): 202.0 ( $\text{N}_{\text{arom.}}$ ); 189.9 ( $\text{N}_{\text{arom.}}$ ); 177.5 ( $\text{N}_{\text{arom.}}$ ); 68.7 ( $\text{N}_{\text{aliph.}}$ ).

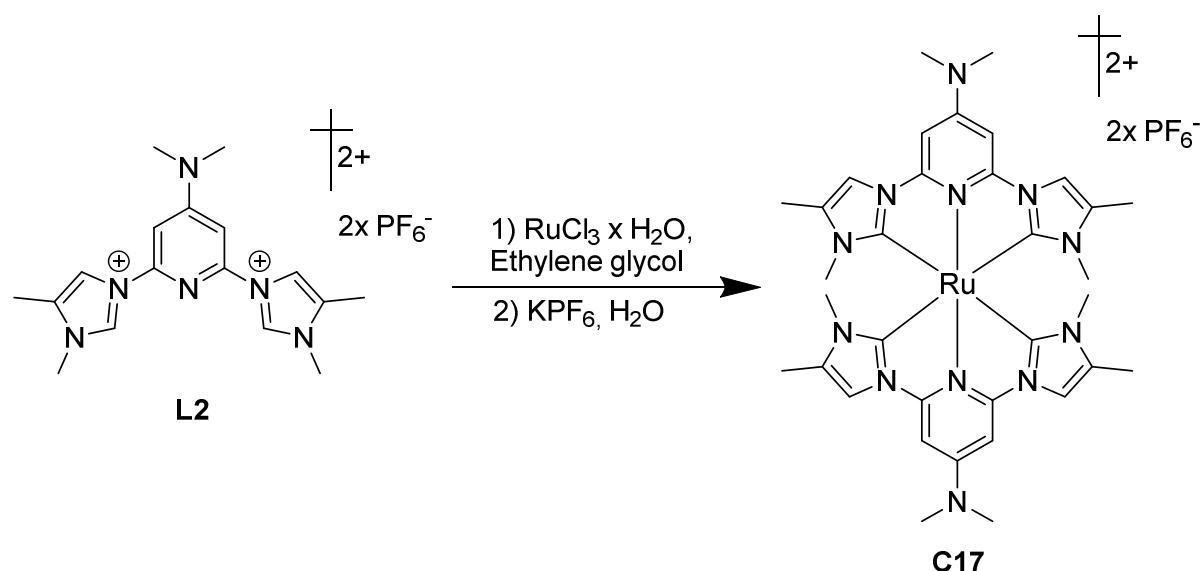
**ESI-MS** ( $m/z(\%)$ ) ( $\text{MeCN}$ ): 333.10 (100) [ $\text{M}^{2+}$ ]; 811.17 (4) [ $\text{M}^{2+} + \text{PF}_6^-$ ].

**IR** (ATR,  $\tilde{\nu}$  [ $\text{cm}^{-1}$ ]): 3182w, 3153w, 2945w, 2361w, 2336w, 1634m, 1574w, 1515m, 1505w, 1481w, 1447w, 1403m, 1344m, 1280w, 1267m, 1242w, 1178w, 1126w, 1088w, 1009w, 937m, 876w, 837s, 823s, 804s, 729m, 716m, 684s, 595w, 555s, 488w, 463w, 438w, 381w, 361w, 306w, 281w, 221w.

**UV/Vis** ( $\text{MeCN}$ ,  $\lambda_{\text{max}}$  [nm] ( $\epsilon$  [ $\text{M}^{-1} \text{cm}^{-1}$ ])): 379 (28390); 241 (64744).

**Elemental analysis:** calculated for  $\text{C}_{30}\text{H}_{36}\text{F}_{12}\text{RuN}_{12}\text{P}_2$ : C: 37.70; H: 3.80; N: 17.59; found: C: 37.78; H: 4.13; N: 17.65.

### 7.6.3 Synthesis of $[\text{Ru}(\text{BmIP}^{\text{NMe}_2})_2][\text{PF}_6]_2$ (**C17**)



The complex **C17** is obtained as bright yellow powder.

Yield: 54 %, (0.27 mmol)

**$^1\text{H-NMR}$**  (700 MHz,  $\text{CD}_3\text{CN}$ ,  $30^\circ\text{C}$ ,  $\delta$  [ppm]): 7.68 (d,  $^4J_{\text{HH}} = 1.3$  Hz, 4H,  $\text{CH}_{\text{arom.}}$ ); 6.90 (s, 4H,  $\text{CH}_{\text{arom.}}$ ); 3.26 (s, 12H,  $\text{CH}_3$ ); 2.54 (s, 12H,  $\text{CH}_3$ ); 2.08 (d,  $^4J_{\text{HH}} = 1.27$  Hz, 12H,  $\text{CH}_3$ ).

**$^{13}\text{C-NMR}$**  (176 MHz,  $\text{CD}_3\text{CN}$ ,  $30^\circ\text{C}$ ,  $\delta$  [ppm]): 193.7 (Cq); 157.2 (Cq); 152.2 (Cq); 132.5 (Cq); 113.4 ( $\text{CH}_{\text{arom.}}$ ); 89.5 ( $\text{CH}_{\text{arom.}}$ ); 40.7 ( $\text{CH}_3$ ); 33.2 ( $\text{CH}_3$ ); 9.9 ( $\text{CH}_3$ ).

**$^{15}\text{N-NMR}$**  (70.9 MHz,  $\text{CD}_3\text{CN}$ ,  $30^\circ\text{C}$ ,  $\delta$  [ppm]): 199.0 ( $\text{N}_{\text{arom.}}$ ); 190.5 ( $\text{N}_{\text{arom.}}$ ); 180.8 ( $\text{N}_{\text{arom.}}$ ); 68.2 ( $\text{N}_{\text{aliph.}}$ ).

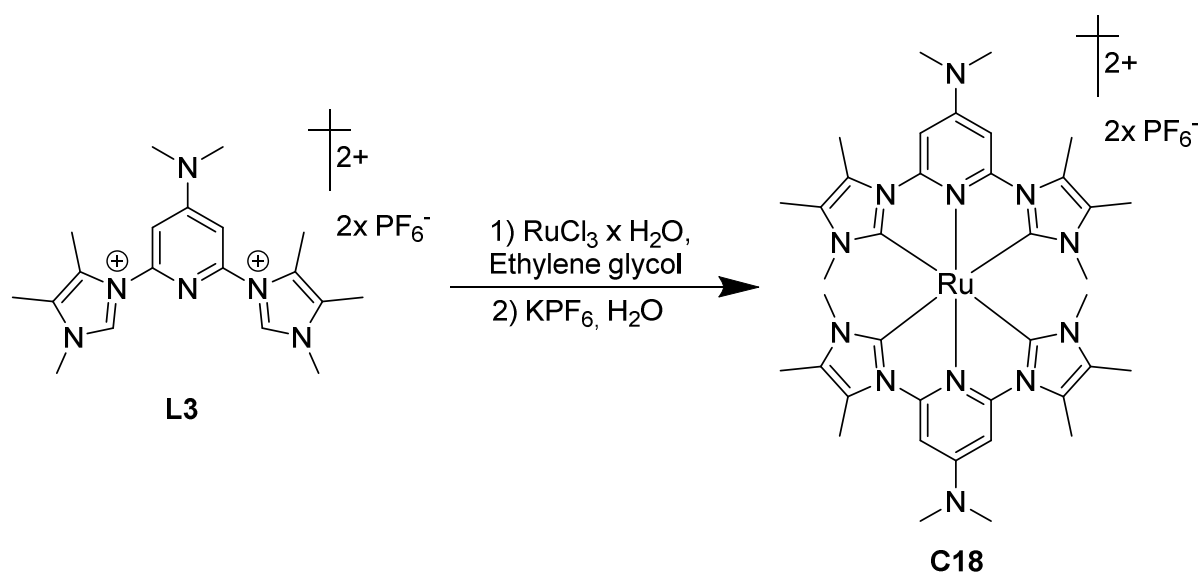
**ESI-MS** ( $m/z(\%)$ ) ( $\text{MeCN}$ ): 489.21 (100) [ $\text{M}^{2+}$ ]; 1123.37 (8) [ $\text{M}^{2+} + \text{PF}_6^-$ ].

**IR** (ATR,  $\tilde{\nu}$  [ $\text{cm}^{-1}$ ]): 3149w, 2933w, 1641m, 1620m, 1537m, 1504w, 1456w, 1434m, 1398m, 1336m, 1261w, 1240m, 1189w, 1166m, 1072w, 1000w, 937w, 835s, 804s, 752m, 694m, 678m, 555s, 501w, 474w, 349m, 279w.

**UV/Vis** (MeCN,  $\lambda_{\text{max}}$  [nm] ( $\epsilon$  [ $\text{M}^{-1} \text{cm}^{-1}$ ]): 380 (24317); 353 (20541), 241 (65847).

**Elemental analysis:** calculated for  $\text{C}_{34}\text{H}_{44}\text{F}_{12}\text{RuN}_{12}\text{P}_2$ : C: 40.36; H: 4.38; N: 16.61; found: C: 40.44; H: 4.70; N: 16.82.

#### 7.6.4 Synthesis of $[\text{Ru}(\text{BdmlP}^{\text{NMe}_2})_2] [\text{PF}_6]_2$ (**C18**)



The complex **C18** is obtained as yellow powder. Suitable single crystals for X-ray diffraction spectroscopy can be obtained by slow diffusion of diethyl ether into an acetonitrile solution of **C18**.

Yield: 32 % (0.16 mmol)

**$^1\text{H-NMR}$**  (700 MHz,  $\text{CD}_3\text{CN}$ ,  $30^\circ\text{C}$ ,  $\delta$  [ppm]): 7.07 (s, 4H,  $\text{CH}_{\text{arom.}}$ ); 3.20 (s, 12H,  $\text{CH}_3$ ); 2.59 (s, 12H,  $\text{CH}_3$ ); 2.49 (s, 12H,  $\text{CH}_3$ ); 1.93 (s, 12H,  $\text{CH}_3$ ).

**$^{13}\text{C-NMR}$**  (176 MHz,  $\text{CD}_3\text{CN}$ ,  $30^\circ\text{C}$ ,  $\delta$  [ppm]): 193.0 (Cq); 156.0 (Cq); 153.6 (Cq); 127.8 (Cq); 123.9 (Cq); 91.4 ( $\text{CH}_{\text{arom.}}$ ); 40.4 ( $\text{CH}_3$ ); 33.3 ( $\text{CH}_3$ ); 11.87 ( $\text{CH}_3$ ); 8.75 ( $\text{CH}_3$ ).

**$^{15}\text{N-NMR}$**  (50.7 MHz,  $\text{CD}_3\text{CN}$ ,  $30^\circ\text{C}$ ,  $\delta$  [ppm]): 200.4 ( $\text{N}_{\text{arom.}}$ ); 194.8 ( $\text{N}_{\text{arom.}}$ ); 177.4 ( $\text{N}_{\text{arom.}}$ ); 66.3 ( $\text{N}_{\text{aliph.}}$ ).

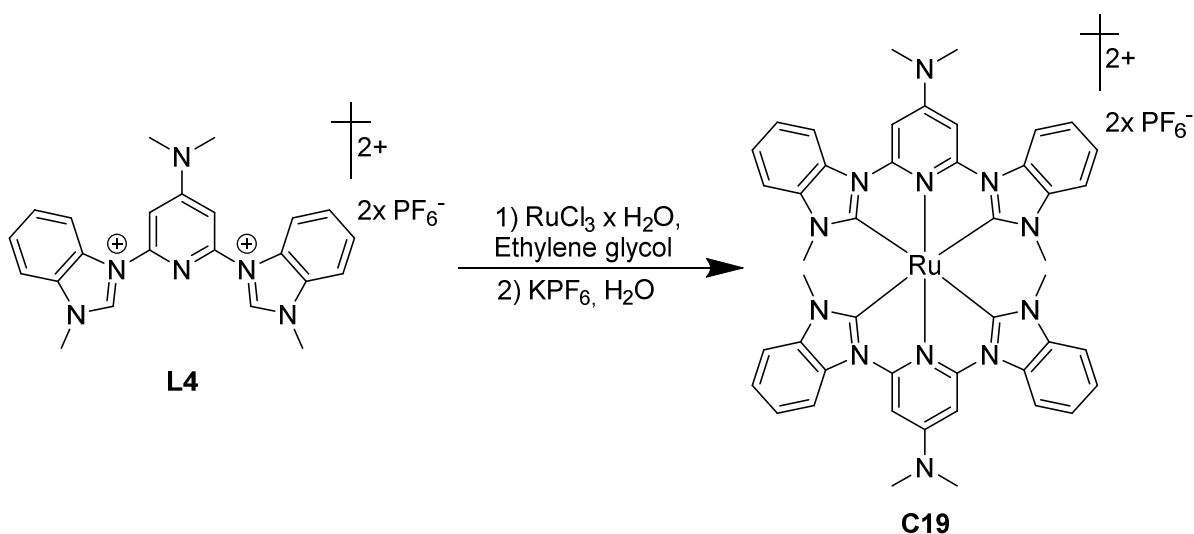
**ESI-MS** ( $m/z$ (%)) (MeCN): 389.17 (100) [ $\text{M}^{2+}$ ]; 923.31 (18) [ $\text{M}^{2+} + \text{PF}_6^-$ ].

**IR** (ATR,  $\tilde{\nu}$  [ $\text{cm}^{-1}$ ]): 3170w, 3116w, 2935w, 1616m, 1571w, 1537m, 1444w, 1394w, 1332w, 1226m, 1180w, 1139w, 1097w, 1068w, 989w, 825s, 740m, 676w, 638w, 555s, 281m, 225w.

**UV/Vis** (MeCN,  $\lambda_{\text{max}}$  [nm] ( $\epsilon$  [ $\text{M}^{-1} \text{cm}^{-1}$ ])): 391 (31615); 354 (20505); 238 (69440).

**Elemental analysis:** calculated for  $\text{C}_{38}\text{H}_{52}\text{F}_{12}\text{RuN}_{12}\text{P}_2$ : C: 42.74; H: 4.91; N: 15.74; found: C: 42.31; H: 5.19; N: 16.17.

### 7.6.5 Synthesis of $[\text{Ru}(\text{BbP}^{\text{NMe}_2})_2] [\text{PF}_6]_2$ (**C19**)



The complex **C19** is obtained as yellow powder. Suitable single crystals for X-ray diffraction spectroscopy can be obtained by slow diffusion of diethyl ether into an acetonitrile solution of **C19**.

Yield: 60 %, (0.3 mmol)

**$^1\text{H-NMR}$**  (700 MHz,  $\text{CD}_3\text{CN}$ ,  $30^\circ\text{C}$ ,  $\delta$  [ppm]): 8.25 (d,  $^3J_{\text{HH}} = 8.4$  Hz, 4H,  $\text{CH}_{\text{arom.}}$ ); 7.48 (t,  $^3J_{\text{HH}} = 9.0$  Hz 4H,  $\text{CH}_{\text{arom.}}$ ); 7.48 (s, 4H,  $\text{CH}_{\text{arom.}}$ ); 7.40 (t,  $^3J_{\text{HH}} = 9.0$  Hz, 4H,  $\text{CH}_{\text{arom.}}$ ); 7.30 (d,  $^3J_{\text{HH}} = 7.5$  Hz, 4H,  $\text{CH}_{\text{arom.}}$ ); 3.51 (s, 12H,  $\text{CH}_3$ ); 2.89 (s, 12H,  $\text{CH}_3$ ).

**$^{13}\text{C-NMR}$**  (176 MHz,  $\text{CD}_3\text{CN}$ ,  $30^\circ\text{C}$ ,  $\delta$  [ppm]): 202.4 (Cq); 156.6 (Cq); 151.9 (Cq); 136.5 (Cq); 131.1 (Cq); 124.4 ( $\text{CH}_{\text{arom.}}$ ); 123.7 ( $\text{CH}_{\text{arom.}}$ ); 111.9 ( $\text{CH}_{\text{arom.}}$ ); 110.5 ( $\text{CH}_{\text{arom.}}$ ); 90.7 ( $\text{CH}_{\text{arom.}}$ ); 40.1 ( $\text{CH}_3$ ); 32.3 ( $\text{CH}_3$ ).

**$^{15}\text{N-NMR}$**  (50.7 MHz,  $\text{CD}_3\text{CN}$ ,  $30^\circ\text{C}$ ,  $\delta$  [ppm]): 186.0 ( $\text{N}_{\text{arom.}}$ ); 167.4 ( $\text{N}_{\text{arom.}}$ ); 71.4 ( $\text{N}_{\text{aliph.}}$ ).

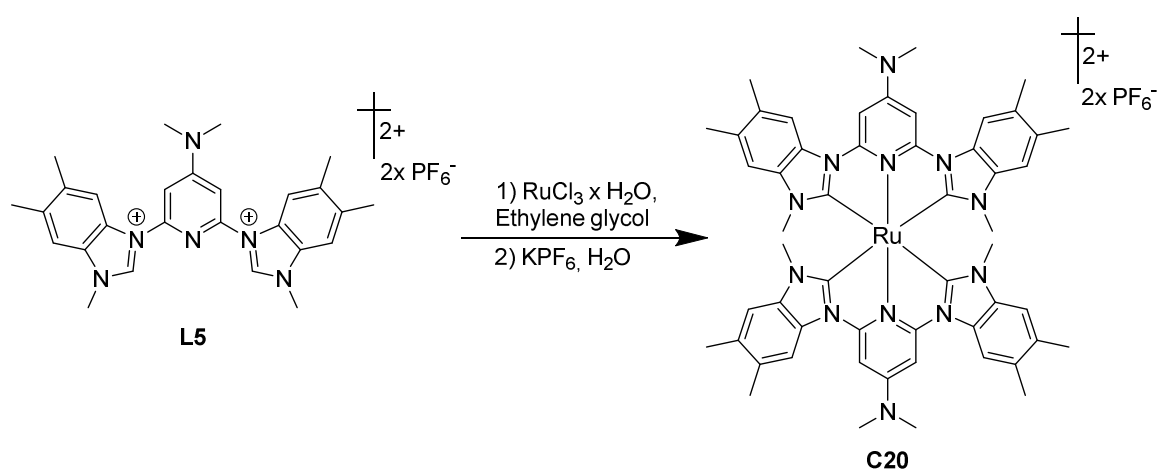
**ESI-MS** ( $m/z$ (%)) (MeCN): 433.14 (100) [ $\text{M}^{2+}$ ]; 426.13 (32) [ $\text{M}^{2+}-\text{CH}_3$ ]; 288.7 (7) [ $\text{M}^{3+}$ ].

**IR** (ATR,  $\tilde{\nu}$  [ $\text{cm}^{-1}$ ]): 3656w, 2941w, 2875w, 1639m, 1598w, 1531m, 1496m, 1461m, 1440m, 1390s, 1334m, 1317m, 1292m, 1232w, 1182w, 1161m, 1091m, 1022w, 937w, 827s, 784s, 732s, 669m, 630w, 586w, 555s, 428m, 347m, 256m.

**UV/Vis** (MeCN,  $\lambda_{\text{max}}$  [nm] ( $\epsilon$  [ $\text{M}^{-1} \text{cm}^{-1}$ ])): 383 (36516); 282 (75972); 225 (74936); 203 (73823).

**Elemental analysis:** calculated for  $\text{C}_{46}\text{H}_{44}\text{F}_{12}\text{RuN}_{12}\text{P}_2$ : C: 47.80; H: 3.84; N: 14.54; found: C: 47.17; H: 3.90; N: 14.65.

### 7.6.6 Synthesis of $[\text{Ru}(\text{BmbP}^{\text{NMe}_2})_2] [\text{PF}_6]_2$ (**C20**)



The complex **C20** is obtained as dark yellow powder. Suitable single crystals for X-ray diffraction spectroscopy can be obtained by slow diffusion of diethyl ether into an acetonitrile solution of **C20**.

Yield: 56 %, (0.28 mmol)

**$^1\text{H-NMR}$**  (700 MHz,  $\text{CD}_3\text{CN}$ ,  $30^\circ\text{C}$ ,  $\delta$  [ppm]): 7.92 (s, 4H,  $\text{CH}_{\text{arom.}}$ ); 7.41 (s, 4H,  $\text{CH}_{\text{arom.}}$ ); 7.07 (s, 4H,  $\text{CH}_{\text{arom.}}$ ); 3.51 (s, 12H,  $\text{CH}_3$ ); 2.80 (s, 12H,  $\text{CH}_3$ ); 2.48 (s, 12H,  $\text{CH}_3$ ); 2.31 (s, 12H,  $\text{CH}_3$ ).

**$^{13}\text{C-NMR}$**  (176 MHz,  $\text{CD}_3\text{CN}$ ,  $30^\circ\text{C}$ ,  $\delta$  [ppm]): 201.5 (Cq); 156.6 (Cq); 151.9 (Cq); 134.9 (Cq); 133.6 (Cq); 132.7 ( $\text{CH}_{\text{arom.}}$ ); 129.6 ( $\text{CH}_{\text{arom.}}$ ); 112.2 ( $\text{CH}_{\text{arom.}}$ ); 110.9 ( $\text{CH}_{\text{arom.}}$ ); 90.2 ( $\text{CH}_{\text{arom.}}$ ); 40.1 ( $\text{CH}_3$ ); 32.1 ( $\text{CH}_3$ ); 19.3 ( $\text{CH}_3$ ); 19.1 ( $\text{CH}_3$ ).

**$^{15}\text{N-NMR}$**  (50.7 MHz,  $\text{CD}_3\text{CN}$ ,  $30^\circ\text{C}$ ,  $\delta$  [ppm]): 186.7 ( $\text{N}_{\text{arom.}}$ ); 185.5 ( $\text{N}_{\text{arom.}}$ ); 167.4 ( $\text{N}_{\text{arom.}}$ ); 71.4 ( $\text{N}_{\text{aliph.}}$ ).

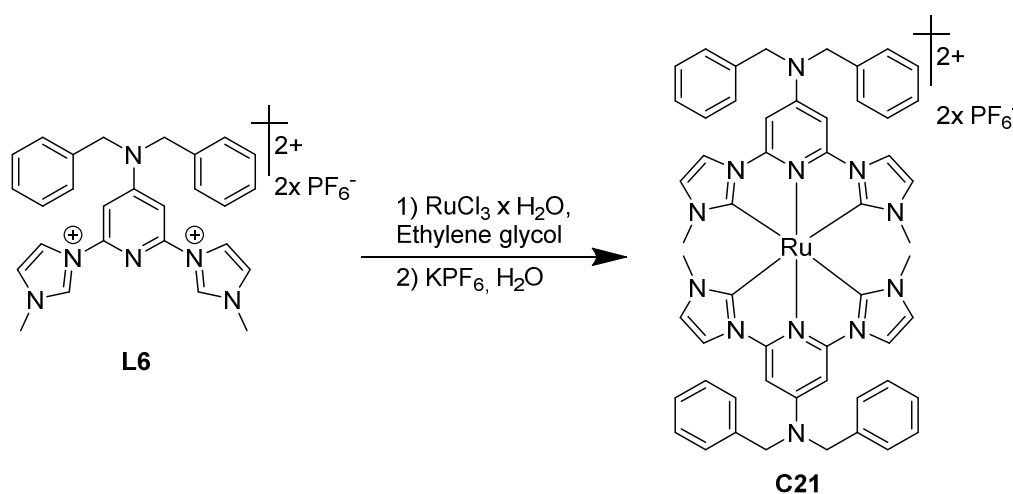
**ESI-MS** ( $m/z$ (%)) (MeCN): 433.14 (100) [ $\text{M}^{2+}$ ]; 426.13 (32) [ $\text{M}^{2+}-\text{CH}_3$ ]; 288.7 (7) [ $\text{M}^{3+}$ ].

**IR** (ATR,  $\tilde{\nu}$  [ $\text{cm}^{-1}$ ]): 2921w, 2360w, 2323w, 1969w, 1637m, 1598w, 1531m, 1494m, 1463m, 1444m, 1390m, 1328w, 1309m, 1161m, 1083w, 1068w, 1000w, 827s, 788m, 756w, 736w, 680m, 617w, 555s, 424w, 399w, 271m.

**UV/Vis** (MeCN,  $\lambda_{\text{max}}$  [nm] ( $\epsilon$  [ $\text{M}^{-1} \text{cm}^{-1}$ ])): 380 (41238); 307 (50505); 284 (75767); 278 (74217); 227 (81290); 204 (123990).

**Elemental analysis:** calculated for  $\text{C}_{54}\text{H}_{60}\text{F}_{12}\text{RuN}_{12}\text{P}_2$ : C: 51.14; H: 4.77; N: 13.25; found: C: 50.72; H: 5.15; N: 13.32.

### 7.6.7 Synthesis of $[\text{Ru}(\text{BIP}^{\text{NBn}2})_2][\text{PF}_6]_2$ (**C21**)



The complex **C21** is obtained as dark yellow powder.

Yield: 74 %, (0.37 mmol)

**$^1\text{H-NMR}$**  (700 MHz,  $\text{CD}_3\text{CN}$ ,  $30^\circ\text{C}$ ,  $\delta$  [ppm]): 7.78 (d,  $^3J_{\text{HH}} = 2.3$  Hz, 4H,  $\text{CH}_{\text{arom.}}$ ); 7.39-7.32 (m, 20H,  $\text{CH}_{\text{arom.}}$ ); 7.12 (s, 4H,  $\text{CH}_{\text{arom.}}$ ); 6.90 (d,  $^3J_{\text{HH}} = 2.4$  Hz,  $\text{CH}_{\text{arom.}}$ ); 4.96 (s, 8H,  $\text{CH}_2$ ); 2.66 (s, 12H,  $\text{CH}_3$ ).

**$^{13}\text{C-NMR}$**  (176 MHz,  $\text{CD}_3\text{CN}$ ,  $30^\circ\text{C}$ ,  $\delta$  [ppm]): 193.4 (Cq); 157.2 (Cq); 152.7 (Cq); 137.7 ( $\text{CH}_{\text{arom.}}$ ); 129.8 ( $\text{CH}_{\text{arom.}}$ ); 128.6 ( $\text{CH}_{\text{arom.}}$ ); 128.1 ( $\text{CH}_{\text{arom.}}$ ); 124.6 (Cq); 116.85 ( $\text{CH}_{\text{arom.}}$ ); 91.1 ( $\text{CH}_{\text{arom.}}$ ); 54.8 ( $\text{CH}_2$ ); 36.2 ( $\text{CH}_3$ )

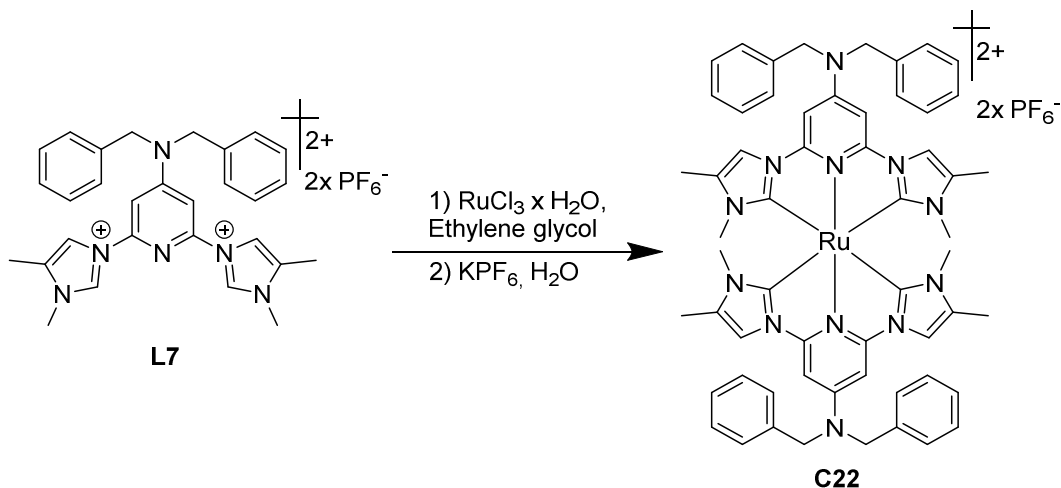
**$^{15}\text{N-NMR}$**  (50.7 MHz,  $\text{CD}_3\text{CN}$ ,  $30^\circ\text{C}$ ,  $\delta$  [ppm]): 201.9 ( $\text{N}_{\text{arom.}}$ ); 193.1 ( $\text{N}_{\text{arom.}}$ ); 177.9 ( $\text{N}_{\text{arom.}}$ ); 89.0 ( $\text{N}_{\text{aliph.}}$ ).

**ESI-MS** ( $m/z$ (%)) (MeCN): 513.20 (100) [ $\text{M}^{2+}$ ]; 468.17 (8) [ $\text{M}^{2+}$ -Benzyl].

**IR** (ATR,  $\tilde{\nu}$  [ $\text{cm}^{-1}$ ]): 3180w, 3133w, 2630w, 2327w, 2052w, 1992w, 1635m, 1571w, 1537w, 1494m, 1450m, 1402m, 1344m, 1269w, 1218m, 1132w, 1081w, 1027w, 1002w, 935w, 829s, 7129m, 682s, 615w, 555s, 457w, 378w, 304w.

**UV/Vis** (MeCN,  $\lambda_{\max}$  [nm] ( $\epsilon$  [ $M^{-1} \text{ cm}^{-1}$ ])): 384 (35606); 243 (82991).

### 7.6.8 Synthesis of $[\text{Ru}(\text{BmlP}^{\text{NBn}2})_2] [\text{PF}_6]_2$ (**C22**)



The complex **C22** is obtained as bright yellow powder. Suitable single crystals for X-ray diffraction spectroscopy can be obtained by slow diffusion of diethyl ether into an acetonitrile solution of **C22**.

Yield: 28 %, (0.14 mmol)

**$^1\text{H-NMR}$**  (700 MHz,  $\text{CD}_3\text{CN}$ ,  $30^\circ\text{C}$ ,  $\delta$  [ppm]): 7.53 (d,  $^4J_{\text{HH}} = 1.3$  Hz, 4H,  $\text{CH}_{\text{arom}}$ ); 7.43 (t;  $^3J_{\text{HH}} = 6.88$  Hz, 8H,  $\text{CH}_{\text{arom}}$ ); 7.40 (d,  $^3J_{\text{HH}} = 6.88$  Hz, 8H,  $\text{CH}_{\text{arom}}$ ); 7.35 (t,  $^3J_{\text{HH}} = 6.88$  Hz, 4H,  $\text{CH}_{\text{arom}}$ ); 7.00 (s, 4H,  $\text{CH}_{\text{arom}}$ ); 4.99 (s, 8H,  $\text{CH}_2$ ); 2.55 (s, 12H,  $\text{CH}_3$ ); 2.08 (d,  $^4J_{\text{HH}} = 1.2$  Hz, 12H,  $\text{CH}_3$ ).

**$^{13}\text{C-NMR}$**  (176 MHz,  $\text{CD}_3\text{CN}$ ,  $30^\circ\text{C}$ ,  $\delta$  [ppm]): 192.8 (Cq); 156.1 (Cq); 151.6 (Cq); 136.9 (Cq); 132.0 (Cq); 129.0 ( $\text{CH}_{\text{arom}}$ ); 127.7 ( $\text{CH}_{\text{arom}}$ ); 127.2 ( $\text{CH}_{\text{arom}}$ ); 112.4 ( $\text{CH}_{\text{arom}}$ ); 89.5 ( $\text{CH}_{\text{arom}}$ ); 54.2 ( $\text{CH}_2$ ); 32.4 ( $\text{CH}_3$ ); 9.1 ( $\text{CH}_3$ ).

**$^{15}\text{N-NMR}$**  (50.7 MHz,  $\text{CD}_3\text{CN}$ ,  $30^\circ\text{C}$ ,  $\delta$  [ppm]): 198.6 ( $\text{N}_{\text{arom}}$ ); 193.0 ( $\text{N}_{\text{arom}}$ ); 181.1 ( $\text{N}_{\text{arom}}$ ); 87.9 ( $\text{N}_{\text{aliph}}$ ).

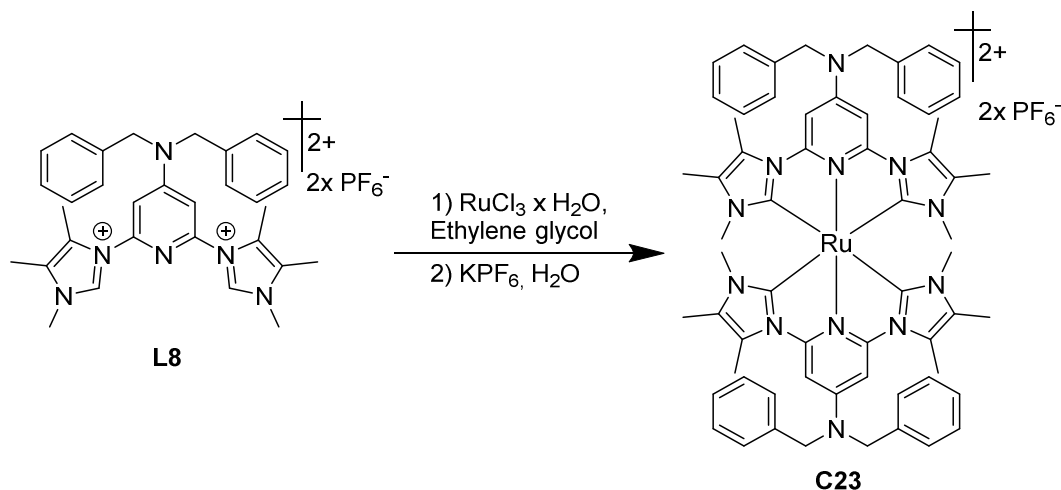
**ESI-MS** ( $m/z$ (%)) (MeCN): 485.17 (100) [ $M^{2+}$ ].

**IR** (ATR,  $\tilde{\nu}$  [ $\text{cm}^{-1}$ ]): 3149w, 3141w, 3033w, 2925w, 2364w, 2050w, 1953w, 1922w, 1772w, 1716w, 1639w, 1620m, 1539w, 1494m, 1452m, 1396m, 1336m, 1297w, 1265w, 1236w, 1209m, 1176w, 1155w, 1078w, 1027w, 1000w, 829s, 802s, 743m, 694m, 609w, 555s, 457w, 418w, 397w, 349w, 325w, 279w, 246w, 225w.

**UV/Vis** (MeCN,  $\lambda_{\max}$  [nm] ( $\epsilon$  [ $M^{-1} \text{ cm}^{-1}$ ])): 384 (30235), 355 (25846); 242 (74952).

**Elemental analysis:** calculated for  $C_{58}H_{60}F_{12}RuN_{12}P_2$ : C: 52.93; H: 4.60; N: 12.77; found: C: 52.84; H: 4.90; N: 13.05.

### 7.6.9 Synthesis of $[Ru(BdmIP^{NBn2})_2][PF_6]_2$ (**C23**)



The complex **C23** is obtained as bright yellow powder.

Yield: 23 %, (0.12 mmol)

**$^1H$ -NMR** (700 MHz,  $CD_3CN$ ,  $30^\circ C$ ,  $\delta$  [ppm]): 7.40 (m, 16H,  $C_{arom.}$ ); 7.32 (t,  $^3J_{HH}$ : 6.89 Hz, 4H,  $CH_{arom.}$ ); 7.02 (s, 4H,  $CH_{arom.}$ ); 5.06 (s, 8H,  $CH_2$ ); 2.42 (s, 12H,  $CH_3$ ); 2.19 (s, 12H,  $CH_3$ ); 1.90 (s, 12H,  $CH_3$ ).

**$^{13}C$ -NMR** (176 MHz,  $CD_3CN$ ,  $30^\circ C$ ,  $\delta$  [ppm]): 192.7 (Cq); 154.9 (Cq); 153.4 (Cq); 138.1 (Cq); 130.0 ( $CH_{arom.}$ ); 128.6 ( $CH_{arom.}$ ); 128.0 (Cq); 127.6 ( $CH_{arom.}$ ); 123.6 (Cq); 93.3 ( $CH_{arom.}$ ); 57.2 ( $CH_2$ ); 33.3 ( $CH_3$ ); 11.7 ( $CH_3$ ); 8.8 ( $CH_3$ ).

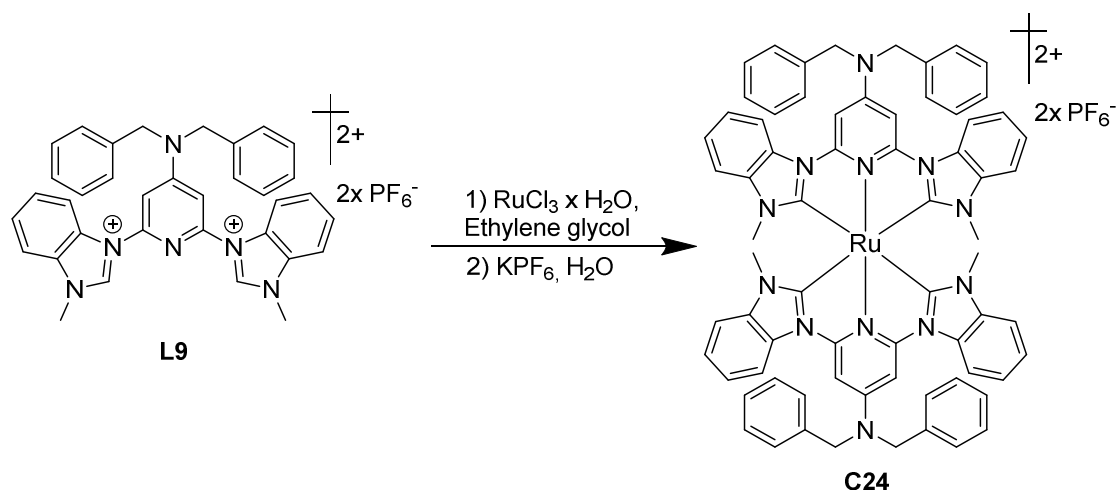
**$^{15}N$ -NMR** (50.7 MHz,  $CD_3CN$ ,  $30^\circ C$ ,  $\delta$  [ppm]): 199.9 ( $N_{arom.}$ ); 197.5 ( $N_{arom.}$ ); 177.6 ( $N_{arom.}$ ); 84.0 ( $N_{aliph.}$ ).

**ESI-MS** (m/z(%)) (MeCN): 541.23 (100) [ $M^{2+}$ ].

**IR** (ATR,  $\tilde{\nu}$  [ $cm^{-1}$ ]): 1953w, 1658w, 1627m, 1537w, 1513w, 1494w, 1450w, 1392w, 1351w, 1296w, 1234m, 1168w, 1139w, 1097w, 1027w, 954w, 833s, 798m, 738m, 694m, 628w, 555s, 457w, 372w, 347w, 331w, 293w, 248w.

**UV/Vis** (MeCN,  $\lambda_{max}$  [nm] ( $\epsilon$  [ $M^{-1} cm^{-1}$ ])): 391 (25104), 241 (70994).

**Elemental analysis:** calculated for  $C_{62}H_{68}F_{12}RuN_{12}P_2$ : C: 54.26; H: 4.99; N: 12.25; found: C: 52.93; H: 5.12; N: 12.26.

7.6.10 Synthesis of  $[\text{Ru}(\text{BbP}^{\text{NBn}2})_2][\text{PF}_6]_2$  (**C24**)

The complex **C24** is obtained as bright yellow powder. Suitable single crystals for X-ray diffraction spectroscopy can be obtained by slow diffusion of diethyl ether into an acetonitrile solution of **C24**.

Yield: 47 %, (0.23 mmol)

**$^1\text{H-NMR}$**  (700 MHz,  $\text{CD}_3\text{CN}$ ,  $30^\circ\text{C}$ ,  $\delta$  [ppm]): 7.40 (d,  $^4J_{\text{HH}}$ : 1.38 Hz; 4H,  $\text{CH}_{\text{arom.}}$ ); 7.28 (m, 14H,  $\text{CH}_{\text{arom.}}$ ); 7.22 (m, 18H,  $\text{CH}_{\text{arom.}}$ ); 6.80 (s, 4H,  $\text{CH}_{\text{arom.}}$ ); 4.82 (s, 8H;  $\text{CH}_{\text{arom.}}$ ); 2.34 (s, 12H,  $\text{CH}_3$ ).

**$^{13}\text{C-NMR}$**  (176 MHz,  $\text{CD}_3\text{CN}$ ,  $30^\circ\text{C}$ ,  $\delta$  [ppm]): 204.5 (Cq); 157.9 (Cq); 154.7 (Cq); 137.8 (Cq); 134.9 (Cq); 130.1 (Cq); 129.9 ( $\text{CH}_{\text{arom.}}$ ); 128.6 ( $\text{CH}_{\text{arom.}}$ ); 128.1 ( $\text{CH}_{\text{arom.}}$ ); 127.9 ( $\text{CH}_{\text{arom.}}$ ); 113.3 ( $\text{CH}_{\text{arom.}}$ ); 90.5 ( $\text{CH}_{\text{arom.}}$ ); 55.4 ( $\text{CH}_2$ ); 32.3 ( $\text{CH}_3$ ).

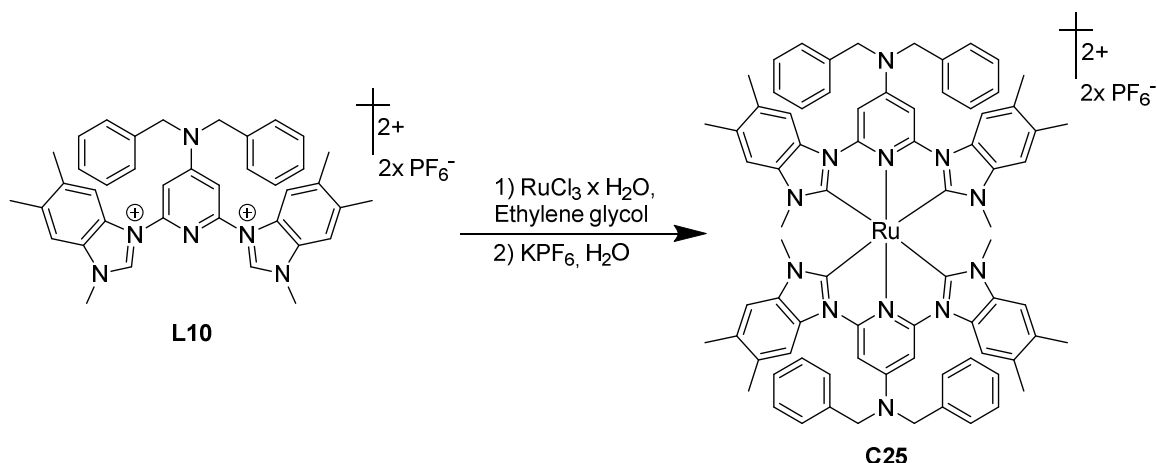
**$^{15}\text{N-NMR}$**  (50.7 MHz,  $\text{CD}_3\text{CN}$ ,  $30^\circ\text{C}$ ,  $\delta$  [ppm]): 199.7 ( $\text{N}_{\text{arom.}}$ ); 197.8 ( $\text{N}_{\text{arom.}}$ ); 182.5 ( $\text{N}_a$ ); 89.0 ( $\text{N}_{\text{aliph.}}$ ).

**ESI-MS** ( $m/z$ (%)) ( $\text{MeCN}$ ): 433.14 (100) [ $\text{M}^{2+}$ ]; 288.76 (8) [ $\text{M}^{3+}$ ]

**IR** (ATR,  $\tilde{\nu}$  [ $\text{cm}^{-1}$ ]): 2360w, 1637m, 1598w, 1539w, 1494w, 1452w, 1390m, 1323w, 1294w, 1245w, 1184w, 1139w, 1093w, 1022w, 939w, 835s, 792m, 732m, 696m, 607w, 555m, 466w, 426w, 345w, 331w, 262w, 237w.

**UV/Vis** ( $\text{MeCN}$ ,  $\lambda_{\text{max}}$  [nm] ( $\epsilon$  [ $\text{M}^{-1} \text{cm}^{-1}$ ])): 447 (8919); 387 (40278); 284 (80847), 276 (78172), 262 (71517), 235 (80048).

**Elemental analysis:** calculated for  $\text{C}_{70}\text{H}_{60}\text{F}_{12}\text{RuN}_{12}\text{P}_2$ : C: 57.57; H: 4.14; N: 11.51; found: C: 56.27; H: 4.61; N: 11.97.

7.6.11 Synthesis of  $[\text{Ru}(\text{BmbP}^{\text{NBn}2})_2] [\text{PF}_6]_2$  (**C25**)

The complex **C25** is obtained as bright yellow powder. Suitable single crystals for X-ray diffraction spectroscopy can be obtained by slow diffusion of diethyl ether into an acetonitrile solution of **C25**.

Yield: 56 %, (0.28 mmol)

**$^1\text{H-NMR}$**  (700 MHz,  $\text{CD}_3\text{CN}$ ,  $30^\circ\text{C}$ ,  $\delta$  [ppm]): 7.61 (d,  $^3J_{\text{HH}}$ : 7.82 Hz, 8H,  $\text{CH}_{\text{arom.}}$ ); 7.51 (t,  $^3J_{\text{HH}}$ : 8.04 Hz, 8H,  $\text{CH}_{\text{arom.}}$ ); 7.35 (t,  $^3J_{\text{HH}}$ : 7.42 Hz, 4H,  $\text{CH}_{\text{arom.}}$ ); 7.28 (d,  $^4J_{\text{HH}}$ : 3.99 Hz, 8H,  $\text{CH}_{\text{arom.}}$ ); 7.01 (s, 4H,  $\text{CH}_{\text{arom.}}$ ); 5.33 (s, 8H,  $\text{CH}_2$ ); 2.66 (s, 12H,  $\text{CH}_3$ ); 2.37 (s, 12H,  $\text{CH}_3$ ); 2.27 (s, 12H,  $\text{CH}_3$ ).

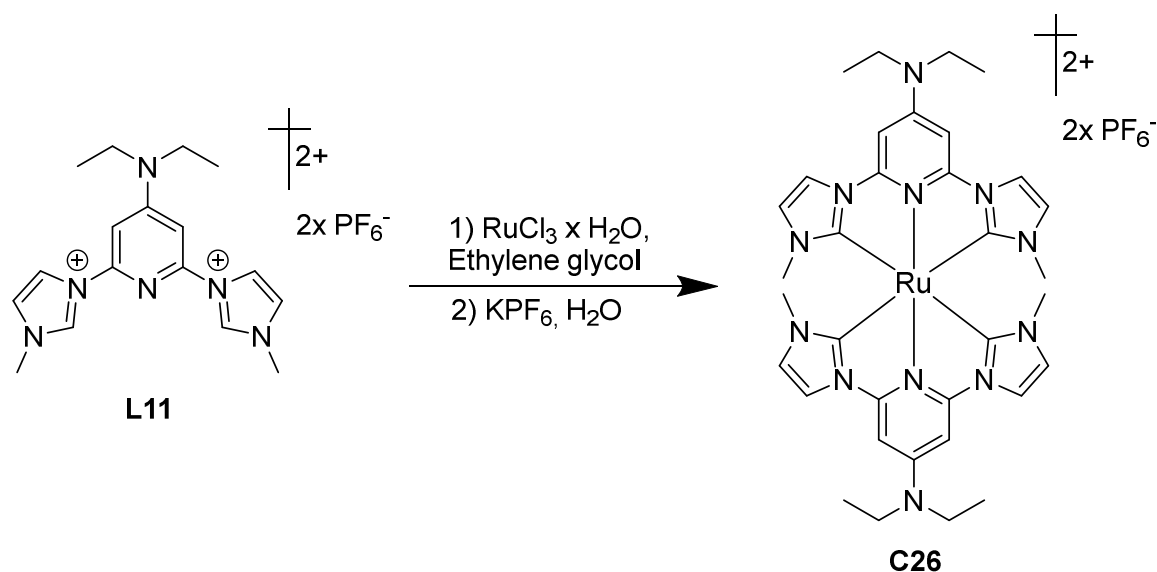
**$^{13}\text{C-NMR}$**  (176 MHz,  $\text{CD}_3\text{CN}$ ,  $30^\circ\text{C}$ ,  $\delta$  [ppm]): 202.0 (Cq); 156.4 (Cq); 152.6 (Cq); 138.1 (Cq); 135.9 (Cq); 134.7 (Cq); 133.7 (Cq); 130.4 (Cq); 130.3 ( $\text{CH}_{\text{arom.}}$ ); 128.7 ( $\text{CH}_{\text{arom.}}$ ); 127.5 ( $\text{CH}_{\text{arom.}}$ ); 112.5 ( $\text{CH}_{\text{arom.}}$ ); 112.1 ( $\text{CH}_{\text{arom.}}$ ); 93.1 ( $\text{CH}_{\text{arom.}}$ ); 57.8 ( $\text{CH}_2$ ); 33.0 ( $\text{CH}_3$ ); 20.3 ( $\text{CH}_3$ ); 20.1 ( $\text{CH}_3$ ).

**$^{15}\text{N-NMR}$**  (50.7 MHz,  $\text{CD}_3\text{CN}$ ,  $30^\circ\text{C}$ ,  $\delta$  [ppm]): 190.1 ( $\text{N}_{\text{arom.}}$ ); 185.1 ( $\text{N}_{\text{arom.}}$ ); 166.2 ( $\text{N}_{\text{arom.}}$ ); 86.8 ( $\text{N}_{\text{aliph.}}$ ).

**ESI-MS** ( $m/z(\%)$ ) ( $\text{MeCN}$ ): 641.26 (100) [ $\text{M}^{2+}$ ]; 634.26 (15) [ $\text{M}^{2+}-\text{CH}_3$ ].

**IR** (ATR,  $\tilde{\nu}$  [ $\text{cm}^{-1}$ ]): 2979w, 2360w, 2337w, 1731w, 1637w, 1600w, 1558w, 1539w, 1519w, 1496w, 1454w, 1392m, 1338w, 1307w, 1255w, 1218w, 1176w, 1135w, 1081w, 1026w, 1000w, 968w, 916w, 837s, 790w, 757w, 736m, 696w, 680w, 615w, 555m, 480w, 459w, 424w, 399w, 374w, 302w, 271w, 246w, 225w.

**UV/Vis** ( $\text{MeCN}$ ,  $\lambda_{\text{max}}$  [nm] ( $\epsilon$  [ $\text{M}^{-1} \text{cm}^{-1}$ ])): 384 (40155), 307 (56003), 289 (88219), 278 (79966), 264 (71106), 242 (82598).

7.6.12 Synthesis of  $[\text{Ru}(\text{BIP}^{\text{NEt}_2})_2][\text{PF}_6]_2$  (**C26**)

The complex **C26** is obtained as bright yellow powder. Suitable single crystals for X-ray diffraction spectroscopy can be obtained by slow diffusion of diethyl ether into an acetonitrile solution of **C26**. Complex **C26** is synthesized as part of the bachelor thesis by A. MILETIC<sup>149</sup> but is not characterized entirely.

Yield: 56 %, (0.28 mmol)

**<sup>1</sup>H-NMR** (500 MHz, CD<sub>3</sub>CN, 30°C, δ [ppm]): 7.96 (d, <sup>3</sup>J<sub>HH</sub> = 2.1 Hz, 4H, CH<sub>arom.</sub>); 6.97 (s, 4H, CH<sub>arom.</sub>); 6.93 (d, <sup>3</sup>J<sub>HH</sub> = 2.11 Hz, 4H, CH<sub>arom.</sub>); 3.65 (q, <sup>3</sup>J<sub>HH</sub> = 7.02 Hz, 8H, CH<sub>2</sub>); 2.69 (s, 12H, CH<sub>3</sub>); 1.31 (t, <sup>3</sup>J<sub>HH</sub> = 7.03 Hz, 12H, CH<sub>3</sub>).

**<sup>13</sup>C-NMR** (125 MHz, CD<sub>3</sub>CN, 30°C, δ [ppm]): 204.6 (Cq); 156.1 (Cq); 154.7 (Cq); 126.6 (CH<sub>arom.</sub>); 116.9 (CH<sub>arom.</sub>); 90.3 (CH<sub>arom.</sub>); 45.9 (CH<sub>2</sub>); 35.6 (CH<sub>3</sub>); 12.7 (CH<sub>3</sub>).

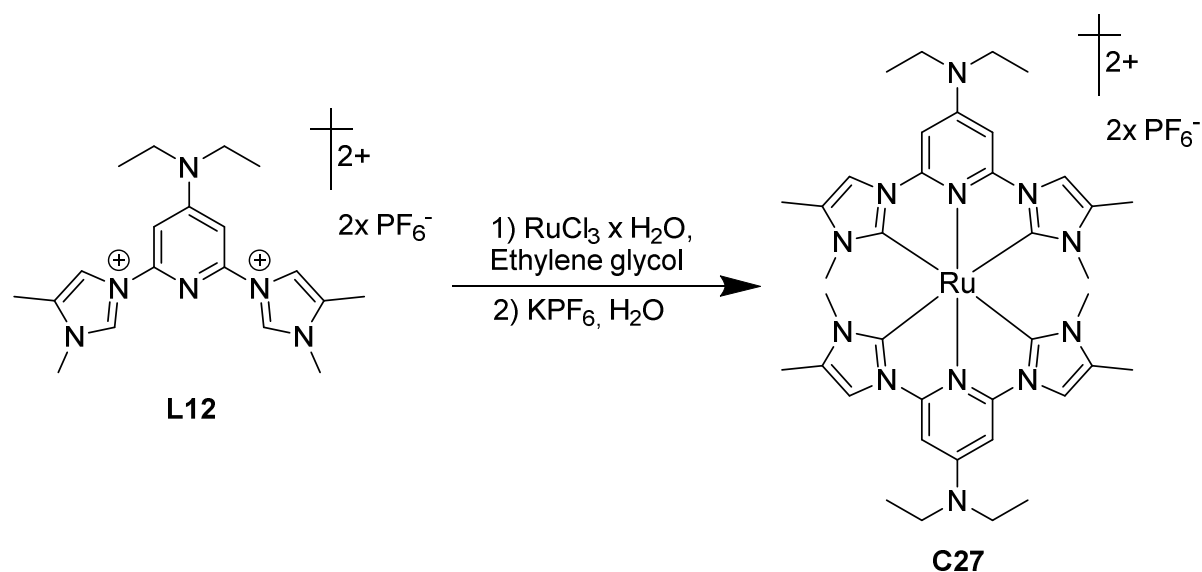
**<sup>15</sup>N-NMR** (50.7 MHz, CD<sub>3</sub>CN, 30°C, δ [ppm]): 202.2 (N<sub>arom.</sub>); 188.5 (N<sub>arom.</sub>); 177.3 (N<sub>arom.</sub>); 98.0 (N<sub>aliph.</sub>).

**ESI-MS** (m/z(%)) (MeCN): 361.14 (100) [M<sup>2+</sup>]; 867.25 (10) [M<sup>2+</sup>+PF<sub>6</sub>].

**IR** (ATR,  $\tilde{\nu}$  [cm<sup>-1</sup>]): 3182w, 3143w, 2971w, 2941w, 1635m, 1573w, 1525m, 1502w, 1486m, 1452w, 1402m, 1348m, 1249m, 1162w, 1126w, 1078w, 1002w, 979w, 838s, 817s, 725m, 680m, 555s, 462w, 379w, 306w, 221w.

**UV/Vis** (MeCN, λ<sub>max</sub> [nm] (ε [M<sup>-1</sup> cm<sup>-1</sup>])): 380 (39980), 241 (86307).

**Elemental analysis:** calculated for C<sub>34</sub>H<sub>44</sub>F<sub>12</sub>RuN<sub>12</sub>P<sub>2</sub>: C: 40.36; H: 4.38; N: 16.61; found: C: 40.33; H: 4.54; N: 16.59.

7.6.13 Synthesis of  $[\text{Ru}(\text{BmIP}^{\text{NEt}_2})_2] [\text{PF}_6]_2$  (**C27**)

The complex **C27** is obtained as yellow powder.

Yield: 54 %, (0.27 mmol)

**$^1\text{H-NMR}$**  (700 MHz,  $\text{CD}_3\text{CN}$ ,  $30^\circ\text{C}$ ,  $\delta$  [ppm]): 7.71 (d,  $^4J_{\text{HH}} = 1.6$  Hz, 4H,  $\text{CH}_{\text{arom.}}$ ); 6.87 (s, 4H,  $\text{CH}_{\text{arom.}}$ ); 3.64 (q,  $^3J_{\text{HH}} = 7.01$  Hz, 8H,  $\text{CH}_2$ ); 2.57 (s, 12H,  $\text{CH}_3$ ); 2.08 (d,  $^4J_{\text{HH}} = 1.3$  Hz, 12H,  $\text{CH}_3$ ); 1.31 (t,  $^3J_{\text{HH}} = 6.91$  Hz, 12H,  $\text{CH}_3$ ).

**$^{13}\text{C-NMR}$**  (176 MHz,  $\text{CD}_3\text{CN}$ ,  $30^\circ\text{C}$ ,  $\delta$  [ppm]): 193.9 (Cq); 155.2 (Cq); 152.6 (Cq); 132.5 (Cq); 113.6 ( $\text{CH}_{\text{arom.}}$ ); 89.2 ( $\text{CH}_{\text{arom.}}$ ); 45.7 ( $\text{CH}_2$ ); 33.1 ( $\text{CH}_3$ ); 12.6 ( $\text{CH}_3$ ); 9.9 ( $\text{CH}_3$ ).

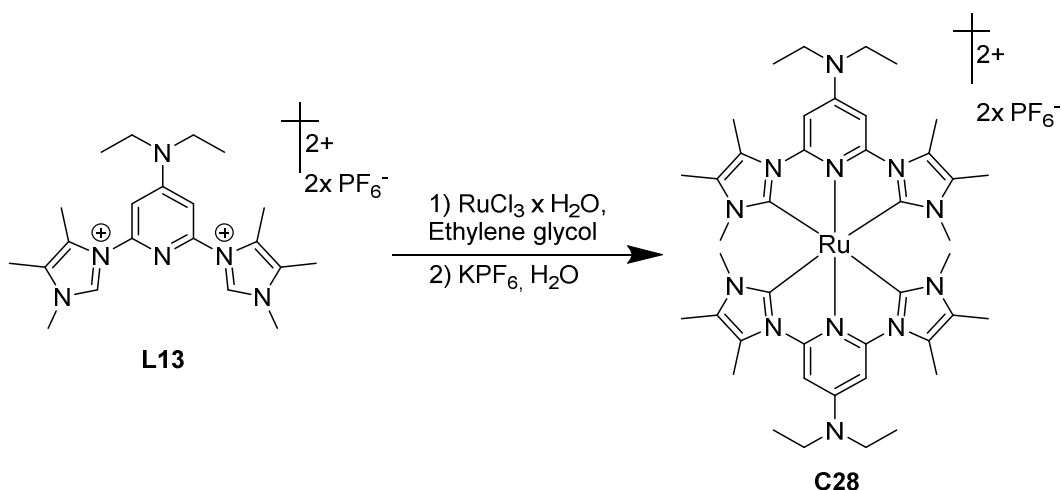
**$^{15}\text{N-NMR}$**  (50.7 MHz,  $\text{CD}_3\text{CN}$ ,  $30^\circ\text{C}$ ,  $\delta$  [ppm]): 198.9 ( $\text{N}_{\text{arom.}}$ ); 188.1 ( $\text{N}_{\text{arom.}}$ ); 180.5 ( $\text{N}_{\text{arom.}}$ ); 97.4 ( $\text{N}_{\text{aliph.}}$ ).

**ESI-MS** (m/z(%)) (MeCN): 389.18 (100) [ $\text{M}^{2+}$ ].

**IR** (ATR,  $\tilde{\nu}$  [ $\text{cm}^{-1}$ ]): 2975w, 2890w, 2360w, 1641m, 1620w, 1537w, 1525w, 1506w, 1488w, 1454w, 1396w, 1353w, 1334w, 12748w, 1259w, 1232w, 1193w, 1151w, 1078w, 977w, 837s, 802m, 740w, 694w, 676w, 603w, 555s, 478w, 351w.

**UV/Vis** (MeCN,  $\lambda_{\text{max}}$  [nm] ( $\epsilon$  [ $\text{M}^{-1} \text{cm}^{-1}$ ])): 383 (35526); 353 (22419); 240 (76411).

**Elemental analysis:** calculated for  $\text{C}_{38}\text{H}_{52}\text{F}_{12}\text{RuN}_{12}\text{P}_2$ : C: 42.47; H: 4.91; N: 15.74; found: C: 42.59; H: 5.04; N: 15.69.

7.6.14 Synthesis of  $[\text{Ru}(\text{BdmIP}^{\text{NEt}_2})_2] [\text{PF}_6]_2$  (**C28**)

The complex **C28** is obtained as bright yellow powder.

Yield: 61 % (0.30 mmol)

**$^1\text{H-NMR}$**  (700 MHz,  $\text{CD}_3\text{CN}$ ,  $30^\circ\text{C}$ ,  $\delta$  [ppm]): 7.11 (s, 4H,  $\text{CH}_{\text{arom.}}$ ); 3.63 (q,  $^3J_{\text{HH}}$ : 7.12 Hz, 8H,  $\text{CH}_2$ ); 2.63 (s, 12H,  $\text{CH}_3$ ); 2.57 (s, 12H,  $\text{CH}_3$ ); 1.99 (s, 12H,  $\text{CH}_3$ ) 1.33 (t,  $^3J_{\text{HH}}$ : 7.14 Hz, 12H,  $\text{CH}_3$ ).

**$^{13}\text{C-NMR}$**  (176 MHz,  $\text{CD}_3\text{CN}$ ,  $30^\circ\text{C}$ ,  $\delta$  [ppm]): 192.3 (Cq); 153.2 (Cq); 153.1 (Cq); 127.0 (Cq); 123.1 (Cq); 90.4 ( $\text{CH}_{\text{arom.}}$ ); 45.1 ( $\text{CH}_2$ ); 32.6 ( $\text{CH}_3$ ); 11.6 ( $\text{CH}_3$ ); 11.2 ( $\text{CH}_3$ ); 8.0 ( $\text{CH}_3$ ).

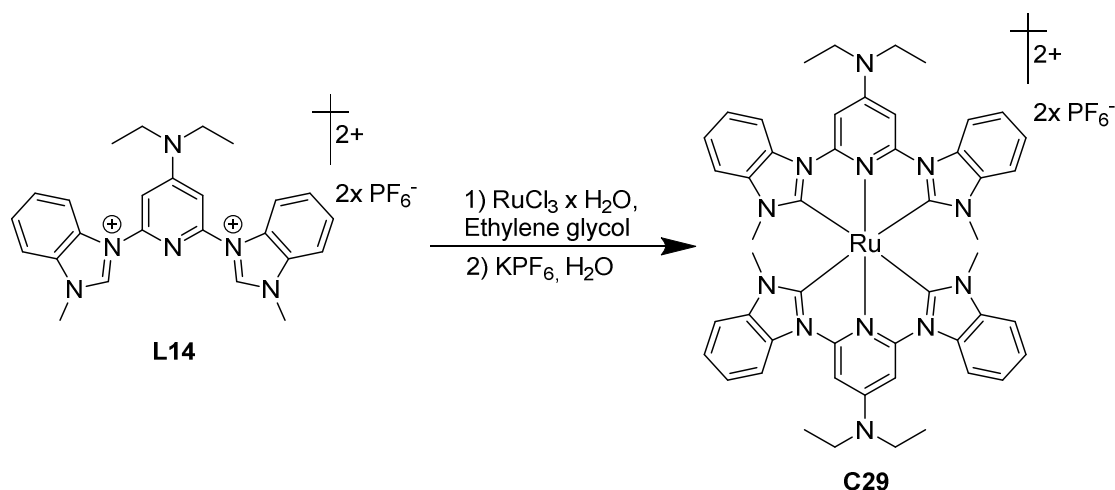
**$^{15}\text{N-NMR}$**  (50.7 MHz,  $\text{CD}_3\text{CN}$ ,  $30^\circ\text{C}$ ,  $\delta$  [ppm]): 200.6 ( $\text{N}_{\text{arom.}}$ ); 193.3 ( $\text{N}_{\text{arom.}}$ ); 177.4 ( $\text{N}_{\text{arom.}}$ ); 94.9 ( $\text{N}_{\text{aliph.}}$ ).

**ESI-MS** ( $m/z(\%)$ ) ( $\text{MeCN}$ ): 417.20 (100) [ $\text{M}^{2+}$ ].

**IR** (ATR,  $\tilde{\nu}$  [ $\text{cm}^{-1}$ ]): 2975w, 2053w, 1988w, 1656w, 1621m, 1525w, 1485w, 1450w, 1386w, 1351m, 1263m, 1193w, 1149w, 1093w, 1072w, 964w, 833s, 798m, 738w, 692w, 555s, 480w, 368w, 347w, 331w.

**UV/Vis** ( $\text{MeCN}$ ,  $\lambda_{\text{max}}$  [nm] ( $\epsilon$  [ $\text{M}^{-1} \text{cm}^{-1}$ ])): 393 (39778); 355 (24656); 270 (43428); 238 (78631).

**Elemental analysis:** calculated for  $\text{C}_{42}\text{H}_{60}\text{F}_{12}\text{RuN}_{12}\text{P}_2$ : C: 44.84; H: 5.38; N: 14.95; found: C: 44.21; H: 5.47; N: 14.69.

7.6.15 Synthesis of  $[\text{Ru}(\text{BbP}^{\text{NEt}_2})_2] [\text{PF}_6]_2$  (**C29**)

The complex **C29** is obtained as bright yellow powder. Suitable single crystals for X-ray diffraction spectroscopy can be obtained by slow diffusion of diethyl ether into an acetonitrile solution of **C29**.

Yield: 64 %, (0.32 mmol)

**$^1\text{H-NMR}$**  (700 MHz,  $\text{CD}_3\text{CN}$ ,  $30^\circ\text{C}$ ,  $\delta$  [ppm]): 8.21 (d,  $^3J_{\text{HH}} = 8.21$  Hz, 4H,  $\text{CH}_{\text{arom.}}$ ); 7.51 (t,  $^3J_{\text{HH}} = 7.89$  Hz, 4H,  $\text{CH}_{\text{arom.}}$ ); 7.49 (s, 4H,  $\text{CH}_{\text{arom.}}$ ); 7.43 (t,  $^3J_{\text{HH}} = 7.97$  Hz, 4H,  $\text{CH}_{\text{arom.}}$ ); 7.34 (d,  $^3J_{\text{HH}} = 7.93$  Hz, 4H,  $\text{CH}_{\text{arom.}}$ ); 3.91 (q,  $^3J_{\text{HH}} = 7.2$  Hz, 8H,  $\text{CH}_2$ ); 2.94 (s, 12H;  $\text{CH}_3$ ); 1.53 (t,  $^3J_{\text{HH}} = 7.2$  Hz, 12H,  $\text{CH}_3$ ).

**$^{13}\text{C-NMR}$**  (176 MHz,  $\text{CD}_3\text{CN}$ ,  $30^\circ\text{C}$ ,  $\delta$  [ppm]): 202.6 (Cq); 154.7 (Cq); 152.4 (Cq); 136.7 (Cq); 131.4 (Cq); 124.6 ( $\text{CH}_{\text{arom.}}$ ); 123.9 ( $\text{CH}_{\text{arom.}}$ ); 111.9 ( $\text{CH}_{\text{arom.}}$ ); 110.7 ( $\text{CH}_{\text{arom.}}$ ); 90.6 ( $\text{CH}_{\text{arom.}}$ ); 45.4 ( $\text{CH}_2$ ); 32.6 ( $\text{CH}_3$ ); 11.7 ( $\text{CH}_3$ ).

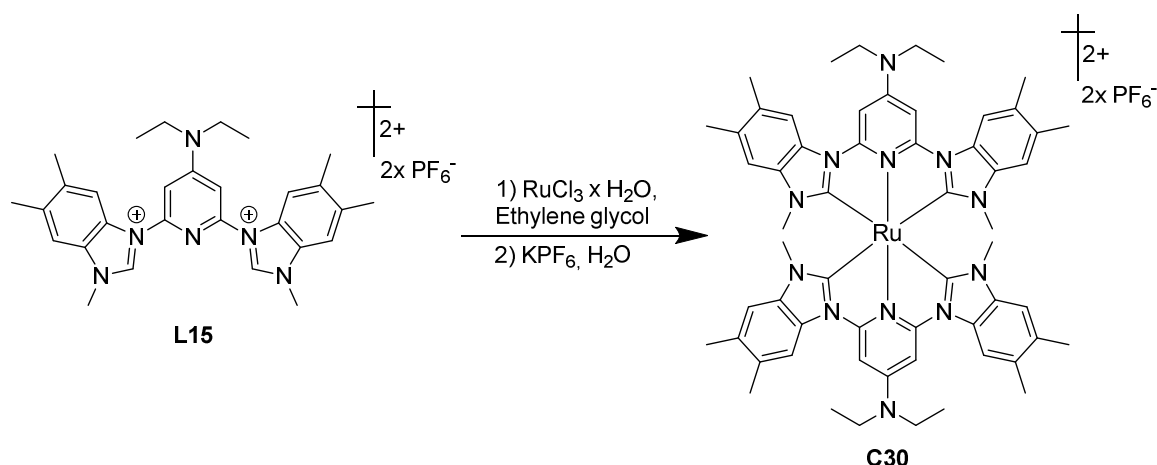
**$^{15}\text{N-NMR}$**  (50.7 MHz,  $\text{CD}_3\text{CN}$ ,  $30^\circ\text{C}$ ,  $\delta$  [ppm]): 185.3 ( $\text{N}_{\text{arom.}}$ ); 167.3 ( $\text{N}_{\text{arom.}}$ ); 100.3 ( $\text{N}_{\text{aliph.}}$ ).

**ESI-MS** ( $m/z(\%)$ ) ( $\text{MeCN}$ ): 461.17 (100) [ $\text{M}^{2+}$ ].

**IR** (ATR,  $\tilde{\nu}$  [ $\text{cm}^{-1}$ ]): 3116w, 2977w, 1618w, 1602w, 1575w, 1537w, 1488w, 1461w, 1429w, 1355w, 1344w, 1240w, 1182w, 1176w, 1137w, 1101w, 1076w, 1043w, 1014w, 979w, 829s, 779m, 763m, 651w, 578w, 555s, 426w, 347w, 260w, 219w.

**UV/Vis** ( $\text{MeCN}$ ,  $\lambda_{\text{max}}$  [nm] ( $\epsilon$  [ $\text{M}^{-1} \text{cm}^{-1}$ ])): 386 (33022); 301 (45382); 281 (77504); 275 (76460); 227 (81646); 202 (112444).

**Elemental analysis:** calculated for  $\text{C}_{50}\text{H}_{52}\text{F}_{12}\text{RuN}_{12}\text{P}_2$ : C: 49.55; H: 4.32; N: 13.87; found: C: 48.10; H: 4.30; N: 13.32.

7.6.16 Synthesis of  $[\text{Ru}(\text{BmbP}^{\text{NEt}_2})_2][\text{PF}_6]_2$  (**C30**)

The complex **C30** is obtained as bright yellow powder.

Yield: 42 % (0.21 mmol)

**$^1\text{H-NMR}$**  (700 MHz,  $\text{CD}_3\text{CN}$ ,  $30^\circ\text{C}$ ,  $\delta$  [ppm]): 7.87 (s, 4H,  $\text{CH}_{\text{arom.}}$ ); 7.43 (s, 4H,  $\text{CH}_{\text{arom.}}$ ); 7.12 (s, 4H,  $\text{CH}_{\text{arom.}}$ ); 3.92 (q,  $^3J_{\text{HH}}$ : 7.33 Hz, 8H,  $\text{CH}_2$ ); 2.86 (s, 12H,  $\text{CH}_3$ ); 2.51 (s, 12H,  $\text{CH}_3$ ); 2.35 (s, 12H,  $\text{CH}_3$ ); 1.56 (t,  $^3J_{\text{HH}}$ : 7.27 Hz, 12H,  $\text{CH}_3$ ).

**$^{13}\text{C-NMR}$**  (176 MHz,  $\text{CD}_3\text{CN}$ ,  $30^\circ\text{C}$ ,  $\delta$  [ppm]): 201.7 (Cq); 154.7 (Cq); 152.5 (Cq); 135.2 (Cq); 133.8 (Cq); 132.9 (Cq); 129.8 (Cq); 112.2 ( $\text{CH}_{\text{arom.}}$ ); 111.2 ( $\text{CH}_{\text{arom.}}$ ); 90.2 ( $\text{CH}_{\text{arom.}}$ ); 45.4 ( $\text{CH}_2$ ); 32.4 ( $\text{CH}_3$ ); 19.6 ( $\text{CH}_3$ ); 19.3 ( $\text{CH}_3$ ); 11.6 ( $\text{CH}_3$ ).

**$^{15}\text{N-NMR}$**  (50.7 MHz,  $\text{CD}_3\text{CN}$ ,  $30^\circ\text{C}$ ,  $\delta$  [ppm]): 202.6 ( $\text{N}_{\text{arom.}}$ ); 185.7 ( $\text{N}_{\text{arom.}}$ ); 165.9 ( $\text{N}_{\text{arom.}}$ ); 99.1 ( $\text{N}_{\text{aliph.}}$ ).

**ESI-MS** ( $m/z$ (%)) ( $\text{MeCN}$ ): 517.23 (100) [ $\text{M}^{2+}$ ]

**IR** (ATR,  $\tilde{\nu}$  [ $\text{cm}^{-1}$ ]): 2971w, 2052w, 1990w, 1729w, 1637w, 1621w, 1598w, 1529w, 1496w, 1465w, 1442w, 1392m, 1351w, 1311ww, 1265w, 1232w, 1176w, 1151w, 1070w, 1002w, 875w, 827s, 788m, 738w, 680m, 615w, 555s, 426w, 399w, 310w, 271w.

**UV/Vis** ( $\text{MeCN}$ ,  $\lambda_{\text{max}}$  [nm] ( $\epsilon$  [ $\text{M}^{-1} \text{cm}^{-1}$ ])): 382 (35551); 307 (49106); 283 (73684); 280 (73599); 238 (77787); 227 (78808); 203 (120195).

**Elemental analysis:** calculated for  $\text{C}_{58}\text{H}_{68}\text{F}_{12}\text{RuN}_{12}\text{P}_2$ : C: 52.61; H: 5.18; N: 12.69; found: C: 50.69; H: 5.17; N: 12.01.

---

## References

1. Peters, G. P. *et al.* Carbon dioxide emissions continue to grow amidst slowly emerging climate policies. *Nat. Clim. Chang.* **10**, 3–6; 10.1038/s41558-019-0659-6 (2020).
2. *Every breath we take. The lifelong impact of air pollution report of a working party* (Royal College of Physicians of London, London, 2016).
3. Stabile, L. *et al.* A novel approach to evaluate the lung cancer risk of airborne particles emitted in a city. *The Science of the total environment* **656**, 1032–1042; 10.1016/j.scitotenv.2018.11.432 (2019).
4. IEA - International Energy Agency (ed.). *CO2 emissions from fuel combustion* (2019).
5. Meinshausen, M. *et al.* Greenhouse-gas emission targets for limiting global warming to 2 degrees C. *Nature* **458**, 1158–1162; 10.1038/nature08017 (2009).
6. Edwards, P. P., Kuznetsov, V. L., David, W.I.F. & Brandon, N. P. Hydrogen and fuel cells: Towards a sustainable energy future. *Energy Policy* **36**, 4356–4362; 10.1016/j.enpol.2008.09.036 (2008).
7. Bundesministerium für Wirtschaft und Energie. Development of Electricity Generation from Renewables in Germany. Available at <https://www.bmwi.de/Redaktion/DE/Infografiken/Energie/entwicklung-stromerzeugung-erneuerbare-energien-deutschland.html>.
8. Shiva Kumar, S. & Himabindu, V. Hydrogen production by PEM water electrolysis – A review. *Materials Science for Energy Technologies* **2**, 442–454; 10.1016/j.mset.2019.03.002 (2019).
9. Carmo, M., Fritz, D. L., Mergel, J. & Stolten, D. A comprehensive review on PEM water electrolysis. *International Journal of Hydrogen Energy* **38**, 4901–4934; 10.1016/j.ijhydene.2013.01.151 (2013).
10. Buttler, A. & Spliethoff, H. Current status of water electrolysis for energy storage, grid balancing and sector coupling via power-to-gas and power-to-liquids: A review. *Renewable and Sustainable Energy Reviews* **82**, 2440–2454; 10.1016/j.rser.2017.09.003 (2018).
11. Millet, P. & Grigoriev, S. in *Renewable Hydrogen Technologies* (Elsevier2013), pp. 19–41.
12. Hoganson, C. W. & Babcock, G. T. A Metalloradical Mechanism for the Generation of Oxygen from Water in Photosynthesis. *Science (New York, N.Y.)* (1997).

13. Tommos, C. & Babcock, G. T. Oxygen Production in Nature: A light-driven Metalloradical Enzyme Process. *Accounts of chemical research*, 18–25 (1998).
14. Tommos, C. & Babcock, G. T. Proton and hydrogen currents in photosynthetic water oxidation. *Biochimica et Biophysica Acta*, 199–219 (2000).
15. Kern, J. & Renger, G. Photosystem II: structure and mechanism of the water:plastoquinone oxidoreductase. *Photosynthesis research* **94**, 183–202; 10.1007/s11120-007-9201-1 (2007).
16. Loll, B., Kern, J., Saenger, W., Zouni, A. & Biesiadka, J. Towards complete cofactor arrangement in the 3.0 Å resolution structure of photosystem II. *Nature* **438**, 1040–1044; 10.1038/nature04224 (2005).
17. Umena, Y., Kawakami, K., Shen, J.-R. & Kamiya, N. Crystal structure of oxygen-evolving photosystem II at a resolution of 1.9 Å. *Nature* **473**, 55–60; 10.1038/nature09913 (2011).
18. Suga, M. *et al.* Native structure of photosystem II at 1.95 Å resolution viewed by femtosecond X-ray pulses. *Nature* **517**, 99–103; 10.1038/nature13991 (2015).
19. Young, I. D. *et al.* Structure of photosystem II and substrate binding at room temperature. *Nature* **540**, 453–457; 10.1038/nature20161 (2016).
20. Fujishima, A. & Honda, K. Electrochemical Photolysis of Water at a Semiconductor Electrode. *Nature*, 37–38 (1972).
21. Li, X. *et al.* Engineering heterogeneous semiconductors for solar water splitting. *J. Mater. Chem. A* **3**, 2485–2534; 10.1039/C4TA04461D (2015).
22. Maeda, K. & Domen, K. New Non-Oxide Photocatalysts Designed for Overall Water Splitting under Visible Light. *J. Phys. Chem. C* **111**, 7851–7861; 10.1021/jp070911w (2007).
23. Kudo, A. & Miseki, Y. Heterogeneous photocatalyst materials for water splitting. *Chemical Society reviews* **38**, 253–278; 10.1039/b800489g (2009).
24. Chen, X., Shen, S., Guo, L. & Mao, S. S. Semiconductor-based photocatalytic hydrogen generation. *Chemical reviews* **110**, 6503–6570; 10.1021/cr1001645 (2010).
25. Hisatomi, T., Kubota, J. & Domen, K. Recent advances in semiconductors for photocatalytic and photoelectrochemical water splitting. *Chemical Society reviews* **43**, 7520–7535; 10.1039/c3cs60378d (2014).

- 
26. Linic, S., Christopher, P. & Ingram, D. B. Plasmonic-metal nanostructures for efficient conversion of solar to chemical energy. *Nature materials* **10**, 911–921; 10.1038/nmat3151 (2011).
27. Wang, C. & Astruc, D. Nanogold plasmonic photocatalysis for organic synthesis and clean energy conversion. *Chemical Society reviews* **43**, 7188–7216; 10.1039/c4cs00145a (2014).
28. Zhou, X., Liu, G., Yu, J. & Fan, W. Surface plasmon resonance-mediated photocatalysis by noble metal-based composites under visible light. *J. Mater. Chem.* **22**, 21337; 10.1039/c2jm31902k (2012).
29. Fukuzumi, S., Hong, D. & Yamada, Y. Bioinspired Photocatalytic Water Reduction and Oxidation with Earth-Abundant Metal Catalysts. *J. Phys. Chem. Lett.* **4**, 3458–3467; 10.1021/jz401560x (2013).
30. Du, P. & Eisenberg, R. Catalysts made of earth-abundant elements (Co, Ni, Fe) for water splitting: Recent progress and future challenges. *Energy Environ. Sci.* **5**, 6012; 10.1039/c2ee03250c (2012).
31. Graetzel, M. Artificial Photosynthesis: Water Cleavage into Hydrogen and Oxygen by Visible Light. *Accounts of chemical research*, 376–384 (1981).
32. Yonemoto, E. H. *et al.* Electron-Transfer Reactions of Ruthenium Trisbipyridyl-Viologen Donor-Acceptor Molecules: Comparison of the Distance Dependence of Electron-Transfer Rates in the Normal and Marcus Inverted Regions. *J. Am. Chem. Soc.*, 4786–4795 (1994).
33. Le, T. P., Rogers, J. E. & Kelly, L. A. Photoinduced Electron Transfer in Covalently Linked 1,8-Naphthalimide/Viologen Systems. *J. Phys. Chem. A* **104**, 6778–6785; 10.1021/jp000855y (2000).
34. Miller, D. & McLendon, G. Model Systems for Photocatalytic Water Reduction: Role of pH and Metal Colloid Catalysts. *Inorg. Chem.*, 950–953 (1981).
35. Fukuzumi, S., Ohkubo, K., Imahori, H. & Guldi, D. M. Driving Force Dependence of Intermolecular Electron-Transfer Reactions of Fullerenes. *Chem. Eur. J.*, 1585–1593 (2003).
36. Listorti, A., O'Regan, B. & Durrant, J. R. Electron Transfer Dynamics in Dye-Sensitized Solar Cells. *Chem. Mater.* **23**, 3381–3399; 10.1021/cm200651e (2011).
37. Durrant, J. R., Haque, S. A. & Palomares, E. Towards optimisation of electron transfer processes in dye sensitised solar cells. *Coordination Chemistry Reviews* **248**, 1247–1257; 10.1016/j.ccr.2004.03.014 (2004).
-

38. SAKAI, K. & OZAWA, H. Homogeneous catalysis of platinum(II) complexes in photochemical hydrogen production from water. *Coordination Chemistry Reviews* **251**, 2753–2766; 10.1016/j.ccr.2007.08.014 (2007).
39. Miyaji, M., Kitamoto, K., Ozawa, H. & Sakai, K. Synthesis and Characterization of a RuPt-Based Photo-Hydrogen-Evolving Molecular Device Tethered to a Single Viologen Acceptor. *Eur. J. Inorg. Chem.* **2017**, 1237–1244; 10.1002/ejic.201601346 (2017).
40. Tschierlei, S. *et al.* Photophysics of an intramolecular hydrogen-evolving Ru-Pd photocatalyst. *Chemistry (Weinheim an der Bergstrasse, Germany)* **15**, 7678–7688; 10.1002/chem.200900457 (2009).
41. Rau, S. *et al.* A supramolecular photocatalyst for the production of hydrogen and the selective hydrogenation of toluene. *Angewandte Chemie (International ed. in English)* **45**, 6215–6218; 10.1002/anie.200600543 (2006).
42. Ozawa, H. & Sakai, K. Photo-hydrogen-evolving molecular devices driving visible-light-induced water reduction into molecular hydrogen: structure-activity relationship and reaction mechanism. *Chemical communications (Cambridge, England)* **47**, 2227–2242; 10.1039/c0cc04708b (2011).
43. Lentz, C., Schott, O., Auvray, T., Hanan, G. S. & Elias, B. Design and photophysical studies of iridium(iii)-cobalt(iii) dyads and their application for dihydrogen photo-evolution. *Dalton transactions (Cambridge, England : 2003)* **48**, 15567–15576; 10.1039/c9dt01989h (2019).
44. Balzani, V., Juris, A. & Venturi, M. Luminescent and Redox-Active Polynuclear Transition Metal Complexes. *Chem. Rev.*, 759–833; 10.1021/cr941154y (1996).
45. Jakubikova, E. & Bowman, D. N. Fe(II)-Polypyridines as Chromophores in Dye-Sensitized Solar Cells: A Computational Perspective. *Accounts of chemical research* **48**, 1441–1449; 10.1021/ar500428t (2015).
46. Balzani, V., Credi, A. & Venturi, M. Photochemical conversion of solar energy. *ChemSusChem* **1**, 26–58; 10.1002/cssc.200700087 (2008).
47. Bignozzi, C. A. *et al.* The role of transition metal complexes in dye sensitized solar devices. *Coordination Chemistry Reviews* **257**, 1472–1492; 10.1016/j.ccr.2012.09.008 (2013).
48. Hennig, H. Homogeneous photo catalysis by transition metal complexes. *Coordination Chemistry Reviews*, 101–123 (1999).

- 
49. Amouyal, E. Photochemical production of hydrogen and oxygen from water: A review and state of the art. *Solar Energy Materials and Solar Cells* **38**, 249–276; 10.1016/0927-0248(95)00003-8 (1995).
50. Schultz, D. M. & Yoon, T. P. Solar synthesis: prospects in visible light photocatalysis. *Science (New York, N.Y.)* **343**, 1239176; 10.1126/science.1239176 (2014).
51. Ismail, A. A. & Bahnemann, D. W. Photochemical splitting of water for hydrogen production by photocatalysis: A review. *Solar Energy Materials and Solar Cells* **128**, 85–101; 10.1016/j.solmat.2014.04.037 (2014).
52. Bumajdad, A. & Madkour, M. Understanding the superior photocatalytic activity of noble metals modified titania under UV and visible light irradiation. *Physical chemistry chemical physics : PCCP* **16**, 7146–7158; 10.1039/c3cp54411g (2014).
53. Hedstrand, D. M., Kruizinga, W. H. & Kellogg, R. M. Light induced and dye accelerated reductions of phenacyl onium salts by 1,4-dihydropyridines. *Tetrahedron Letters*, 1255–1258 (1978).
54. Nicewicz, D. A. & MacMillan, D. W. C. Merging photoredox catalysis with organocatalysis: the direct asymmetric alkylation of aldehydes. *Science (New York, N.Y.)* **322**, 77–80; 10.1126/science.1161976 (2008).
55. Ischay, M. A., Anzovino, M. E., Du, J. & Yoon, T. P. Efficient visible light photocatalysis of 2+2 enone cycloadditions. *Journal of the American Chemical Society* **130**, 12886–12887; 10.1021/ja805387f (2008).
56. Prier, C. K., Rankic, D. A. & MacMillan, D. W. C. Visible light photoredox catalysis with transition metal complexes: applications in organic synthesis. *Chemical reviews* **113**, 5322–5363; 10.1021/cr300503r (2013).
57. Marzo, L., Pagire, S. K., Reiser, O. & König, B. Visible-Light Photocatalysis: Does It Make a Difference in Organic Synthesis? *Angewandte Chemie (International ed. in English)* **57**, 10034–10072; 10.1002/anie.201709766 (2018).
58. Mills, I. N., Porras, J. A. & Bernhard, S. Judicious Design of Cationic, Cyclometalated Ir(III) Complexes for Photochemical Energy Conversion and Optoelectronics. *Accounts of chemical research* **51**, 352–364; 10.1021/acs.accounts.7b00375 (2018).
59. Lowry, M. S. & Bernhard, S. Synthetically tailored excited states: phosphorescent, cyclometalated iridium(III) complexes and their applications. *Chemistry (Weinheim an der Bergstrasse, Germany)* **12**, 7970–7977; 10.1002/chem.200600618 (2006).

60. Shon, J.-H. & Teets, T. S. Molecular Photosensitizers in Energy Research and Catalysis: Design Principles and Recent Developments. *ACS Energy Lett.* **4**, 558–566; 10.1021/acsenergylett.8b02388 (2019).
61. Juris, A. & Balzani, V. Ru(II) polypyridine complexes: Photophysics, Photochemistry, Electrochemistry, and Chemiluminescence. *Coordination Chemistry Reviews*, 85–277 (1988).
62. Caspar, J. V. & Meyer, T. J. Photochemistry of MLCT excited states. Effect of nonchromophoric ligand variations on photophysical properties in the series cis-Ru(bpy)<sub>2</sub>L<sub>2</sub><sup>2+</sup>. *Inorg. Chem.*, 2444–2453 (1983).
63. Boyde, S., Strouse, G. F., Jones Jr., Wayne E. Jones Jr. & Meyer, T. J. The effect on MLCT excited states of electronic delocalization in the acceptor ligand. *J. Am. Chem. Soc.*, 7395–7396 (1990).
64. Indelli, M. T., Bignozzi, C. A., Scandola, F. & Collin, J.-P. Design of Long-Lived Ru(II) Terpyridine MLCT States. Tricyano Terpyridine Complexes. *Inorganic chemistry* **37**, 6084–6089; 10.1021/ic980060u (1998).
65. Bargawi, K. R., Llobet, A. & Meyer, T. J. Synthetic design of MLCT excited states. Ligand-substituted, mono-2,2'-bipyridine complexes of ruthenium(II). *J. Am. Chem. Soc.*, 7751–7759 (1988).
66. Lin, C. T., Böttcher, M. C., Creutz C. & Sutin N. Mechanism of the Quenching of the Emission of Substituted Polypyridineruthenium(II) Complexes by Iron(III). Chromium(III) and Europium(III) Ions. *J. Am. Chem. Soc.*, 6536–6544 (1976).
67. Balzani, V., Bolletta, F., Scandola, F. & Ballardini, R. Excited State Electron-Transfer Reactions of Transition Metal Complexes. *Pure & Appl. Chem.*, 299–311 (1979).
68. Goldsmith, J. I., Hudson, W. R., Lowry, M. S., Anderson, T. H. & Bernhard, S. Discovery and high-throughput screening of heteroleptic iridium complexes for photoinduced hydrogen production. *Journal of the American Chemical Society* **127**, 7502–7510; 10.1021/ja0427101 (2005).
69. Parada, G. A. *et al.* Tuning the electronics of bis(tridentate)ruthenium(II) complexes with long-lived excited states: modifications to the ligand skeleton beyond classical electron donor or electron withdrawing group decorations. *Inorganic chemistry* **52**, 5128–5137; 10.1021/ic400009m (2013).
70. Abrahamsson, M. *et al.* A new strategy for the improvement of photophysical properties in ruthenium(II) polypyridyl complexes. Synthesis and photophysical and

- electrochemical characterization of six mononuclear ruthenium(II) bisterpyridine-type complexes. *Inorganic chemistry* **44**, 3215–3225; 10.1021/ic048247a (2005).
71. Abrahamsson, M. *et al.* Six-membered ring chelate complexes of Ru(II): structural and photophysical effects. *Inorganic chemistry* **46**, 10354–10364; 10.1021/ic7011827 (2007).
72. Abrahamsson, M., Becker, H.-C. & Hammarström, L. Microsecond 3MLCT excited state lifetimes in bis-tridentate Ru(ii)-complexes: significant reductions of non-radiative rate constants. *Dalton transactions (Cambridge, England : 2003)* **46**, 13314–13321; 10.1039/c7dt02437a (2017).
73. Breivogel, A. *et al.* Push-Pull Design of Bis(tridentate) Ruthenium(II) Polypyridine Chromophores as Deep Red Light Emitters in Light-Emitting Electrochemical Cells. *Eur. J. Inorg. Chem.* **2014**, 288–295; 10.1002/ejic.201301226 (2014).
74. Ozawa, H., Haga, M.-a. & Sakai, K. A photo-hydrogen-evolving molecular device driving visible-light-induced EDTA-reduction of water into molecular hydrogen. *Journal of the American Chemical Society* **128**, 4926–4927; 10.1021/ja058087h (2006).
75. Na, Y. *et al.* Visible light-driven electron transfer and hydrogen generation catalyzed by bioinspired 2Fe<sub>2</sub>S complexes. *Inorganic chemistry* **47**, 2805–2810; 10.1021/ic702010w (2008).
76. Elvington, M., Brown, J., Arachchige, S. M. & Brewer, K. J. Photocatalytic hydrogen production from water employing a Ru, Rh, Ru molecular device for photoinitiated electron collection. *Journal of the American Chemical Society* **129**, 10644–10645; 10.1021/ja073123t (2007).
77. Fihri, A. *et al.* Cobaloxime-based photocatalytic devices for hydrogen production. *Angewandte Chemie (International ed. in English)* **47**, 564–567; 10.1002/anie.200702953 (2008).
78. Fihri, A., Artero, V., Pereira, A. & Fontecave, M. Efficient H<sub>2</sub>-producing photocatalytic systems based on cyclometalated iridium- and tricarbonylrhenium-diimine photosensitizers and cobaloxime catalysts. *Dalton transactions (Cambridge, England : 2003)*, 5567–5569; 10.1039/b812605b (2008).
79. Deponti, E. & Natali, M. Photocatalytic hydrogen evolution with ruthenium polypyridine sensitizers: unveiling the key factors to improve efficiencies. *Dalton transactions (Cambridge, England : 2003)* **45**, 9136–9147; 10.1039/c6dt01221c (2016).

80. Rupp, M. *et al.* Photocatalytic Hydrogen Evolution Driven by a Heteroleptic Ruthenium(II) Bis(terpyridine) Complex. *Inorganic chemistry* **58**, 9127–9134; 10.1021/acs.inorgchem.9b00698 (2019).
81. Losse, S., Vos, J. G. & Rau, S. Catalytic hydrogen production at cobalt centres. *Coordination Chemistry Reviews* **254**, 2492–2504; 10.1016/j.ccr.2010.06.004 (2010).
82. Jasimuddin, S., Yamada, T., Fukuju, K., Otsuki, J. & Sakai, K. Photocatalytic hydrogen production from water in self-assembled supramolecular iridium-cobalt systems. *Chemical communications (Cambridge, England)* **46**, 8466–8468; 10.1039/c0cc02486d (2010).
83. Hammarström, L. & Johansson, O. Expanded bite angles in tridentate ligands. Improving the photophysical properties in bistridentate RuII polypyridine complexes. *Coordination Chemistry Reviews* **254**, 2546–2559; 10.1016/j.ccr.2010.01.006 (2010).
84. Beley, M. *et al.* Luminescent Dinuclear Complexes Containing Ruthenium(II)- and Osmium(II)-Terpyridine-Type Chromophores Bridged by a Rigid Biscyclometalating Ligand. *Inorg. Chem.*, 2543–2547 (1994).
85. Collin, J.-P., Beley, M. & Sauvage, J.-P. A room temperature luminescent cyclometallated ruthenium(II) complex of 6-phenyl-2,2'-bipyridine. *Inorganica Chimica Acta*, 91–93 (1991).
86. Constable, E. C. & Cargill Thompson, Alexander M. W. Ligand Substitution Patterns Control Photophysical Properties of Ruthenium(II)-2,2':6',2''-Terpyridine Complexes—Room Temperature Emission from  $[\text{Ru}(\text{tpy})_2]^{2+}$  Analogues. *Polyhedron*, 2707–2709 (1992).
87. Wadman, S. H. *et al.* Cyclometalated ruthenium complexes for sensitizing nanocrystalline TiO<sub>2</sub> solar cells. *Chemical communications (Cambridge, England)*, 1907–1909; 10.1039/b703636a (2007).
88. Son, S. U. *et al.* Synthesis of Ru(II) complexes of N-heterocyclic carbenes and their promising photoluminescence properties in water. *Inorganic chemistry* **43**, 6896–6898; 10.1021/ic049514f (2004).
89. Zhang, W. *et al.* Tracking excited-state charge and spin dynamics in iron coordination complexes. *Nature* **509**, 345–348; 10.1038/nature13252 (2014).
90. Fink, D. W. & Ohnesorge, W. E. Temperature Effect on Charge-Transfer Luminescence Intensity of Some Transition Metal Ion Chelates. *J. Am. Chem. Soc.*, 4995–4998 (1969).

- 
91. Liu, Y. *et al.* Towards longer-lived metal-to-ligand charge transfer states of iron(II) complexes: an N-heterocyclic carbene approach. *Chemical communications (Cambridge, England)* **49**, 6412–6414; 10.1039/c3cc43833c (2013).
92. Kaufhold, S. & Wärnmark, K. Design and Synthesis of Photoactive Iron N-Heterocyclic Carbene Complexes. *Catalysts* **10**, 132; 10.3390/catal10010132 (2020).
93. Fredin, L. A. *et al.* Exceptional Excited-State Lifetime of an Iron(II)-N-Heterocyclic Carbene Complex Explained. *The journal of physical chemistry letters* **5**, 2066–2071; 10.1021/jz500829w (2014).
94. Duchanois, T. *et al.* Heteroleptic Pyridyl-Carbene Iron Complexes with Tuneable Electronic Properties. *Eur. J. Inorg. Chem.* **2014**, 3747–3753; 10.1002/ejic.201402356 (2014).
95. Zimmer, P. *et al.* The Connection between NHC Ligand Count and Photophysical Properties in Fe(II) Photosensitizers: An Experimental Study. *Inorganic chemistry* **57**, 360–373; 10.1021/acs.inorgchem.7b02624 (2018).
96. Liu, L. *et al.* A new record excited state (3)MLCT lifetime for metalorganic iron(ii) complexes. *Physical chemistry chemical physics : PCCP* **18**, 12550–12556; 10.1039/c6cp01418f (2016).
97. Darari, M. *et al.* Iron(ii) complexes with diaziny-NHC ligands: impact of  $\pi$ -deficiency of the azine core on photophysical properties. *Dalton transactions (Cambridge, England : 2003)*; 10.1039/c9dt01731c (2019).
98. Duchanois, T. *et al.* An Iron-Based Photosensitizer with Extended Excited-State Lifetime: Photophysical and Photovoltaic Properties. *Eur. J. Inorg. Chem.* **2015**, 2469–2477; 10.1002/ejic.201500142 (2015).
99. Harlang, T. C. B. *et al.* Iron sensitizer converts light to electrons with 92% yield. *Nature chemistry* **7**, 883–889; 10.1038/nchem.2365 (2015).
100. Fredin, L. A., Wärnmark, K., Sundström, V. & Persson, P. Molecular and Interfacial Calculations of Iron(II) Light Harvesters. *ChemSusChem* **9**, 667–675; 10.1002/cssc.201600062 (2016).
101. Francés-Monerris, A., Gros, P. C., Pastore, M., Assfeld, X. & Monari, A. Photophysical properties of bichromophoric Fe(II) complexes bearing an aromatic electron acceptor. *Theor Chem Acc* **138**, 13522; 10.1007/s00214-019-2471-9 (2019).
102. Zimmer, P. *et al.* Towards Noble-Metal-Free Dyads: Ground and Excited State Tuning by a Cobalt Dimethylglyoxime Motif Connected to an Iron N-Heterocyclic

- Carbene Photosensitizer. *Eur. J. Inorg. Chem.* **2018**, 5203–5214; 10.1002/ejic.201800946 (2018).
103. Zimmer, P. *et al.* N-Heterocyclic Carbene Complexes of Iron as Photosensitizers for Light-Induced Water Reduction. *Eur. J. Inorg. Chem.* **2017**, 1504–1509; 10.1002/ejic.201700064 (2017).
104. Chábera, P. *et al.* Fell Hexa N-Heterocyclic Carbene Complex with a 528 ps Metal-to-Ligand Charge-Transfer Excited-State Lifetime. *The journal of physical chemistry letters* **9**, 459–463; 10.1021/acs.jpcclett.7b02962 (2018).
105. Chábera, P. *et al.* A low-spin Fe(III) complex with 100-ps ligand-to-metal charge transfer photoluminescence. *Nature* **543**, 695–699; 10.1038/nature21430 (2017).
106. Guisado-Barrios, G., Bouffard, J., Donnadieu, B. & Bertrand, G. Crystalline 1H-1,2,3-triazol-5-ylidenes: new stable mesoionic carbenes (MICs). *Angewandte Chemie (International ed. in English)* **49**, 4759–4762; 10.1002/anie.201001864 (2010).
107. Schulze, B. *et al.* A heteroleptic bis(tridentate) ruthenium(II) complex of a click-derived abnormal carbene pincer ligand with potential for photosensitizer application. *Chemistry (Weinheim an der Bergstrasse, Germany)* **17**, 5494–5498; 10.1002/chem.201100045 (2011).
108. Liu, Y. *et al.* A heteroleptic ferrous complex with mesoionic bis(1,2,3-triazol-5-ylidene) ligands: taming the MLCT excited state of iron(II). *Chemistry (Weinheim an der Bergstrasse, Germany)* **21**, 3628–3639; 10.1002/chem.201405184 (2015).
109. Liu, Y., Persson, P., Sundström, V. & Wärnmark, K. Fe N-Heterocyclic Carbene Complexes as Promising Photosensitizers. *Accounts of chemical research* **49**, 1477–1485; 10.1021/acs.accounts.6b00186 (2016).
110. Maestri, M., Armaroli, N., Balzani, V., Constable, E. C. & Cargill Thompson, Alexander M. W. Complexes of the Ruthenium(II)-2,2':6',2"-terpyridine Family. Effect of Electron-Accepting and -Donating Substituents on the Photophysical and Electrochemical Properties. *Inorg. Chem.*, 2759–2767 (1995).
111. Duchanois, T. *et al.* NHC-Based Iron Sensitizers for DSSCs. *Inorganics* **6**, 63; 10.3390/inorganics6020063 (2018).
112. Hay, D. A. *et al.* A flexible synthesis of C-6 and N-1 analogues of a 4-amino-1,3-dihydroimidazo[4,5-c]pyridin-2-one core. *Tetrahedron Letters* **52**, 5728–5732; 10.1016/j.tetlet.2011.08.119 (2011).
113. Breivogel, A., Meister, M., Förster, C., Laquai, F. & Heinze, K. Excited state tuning of bis(tridentate) ruthenium(II) polypyridine chromophores by push-pull effects and bite

- angle optimization: a comprehensive experimental and theoretical study. *Chemistry (Weinheim an der Bergstrasse, Germany)* **19**, 13745–13760; 10.1002/chem.201302231 (2013).
114. Park, H.-J. & Chung, Y. K. Ru(II) complexes with N-heterocyclic carbene ligands or terpyridine analogues: synthesis, characterization, and electrochemical and proton-dependent spectrometric properties. *Dalton transactions (Cambridge, England : 2003)* **41**, 5678–5686; 10.1039/c2dt12283a (2012).
115. Churruca, F., SanMartin, R., Inés, B., Tellitu, I. & Domínguez, E. Hydrophilic CNC-Pincer Palladium Complexes: A Source for Highly Efficient, Recyclable Homogeneous Catalysts in Suzuki–Miyaura Cross-Coupling. *Adv. Synth. Catal.* **348**, 1836–1840; 10.1002/adsc.200606173 (2006).
116. Inés, B., SanMartin, R., Moure, M. J. & Domínguez, E. Insights into the Role of New Palladium Pincer Complexes as Robust and Recyclable Precatalysts for Suzuki–Miyaura Couplings in Neat Water. *Adv. Synth. Catal.* **351**, 2124–2132; 10.1002/adsc.200900345 (2009).
117. Tu, T., Feng, X., Wang, Z. & Liu, X. A robust hydrophilic pyridine-bridged bis-benzimidazolyliene palladium pincer complex: synthesis and its catalytic application towards Suzuki–Miyaura couplings in aqueous solvents. *Dalton transactions (Cambridge, England : 2003)* **39**, 10598–10600; 10.1039/c0dt01083a (2010).
118. Wang, L., Liu, N. & Dai, B. Metal-free site-selective C–N bond-forming reaction of polyhalogenated pyridines and pyrimidines. *RSC Adv.* **5**, 82097–82111; 10.1039/C5RA18653F (2015).
119. Lv, R., Wang, Y., Zhou, C., Li, L. & Wang, R. Efficient Copper-Catalyzed Ullmann Reaction of Aryl Bromides with Imidazoles in Water Promoted by a pH-Responsive Ligand. *ChemCatChem* **5**, 2978–2982; 10.1002/cctc.201300257 (2013).
120. MaGee, K. D. M. *et al.* Synthesis, Solid-state Structures, Solution Behaviour and Catalysis Studies of Nickel Complexes of Bis(benzimidazolin-2-ylidene)pyridine Pincer Ligands. *Aust. J. Chem.* **65**, 823; 10.1071/CH12044 (2012).
121. Kershaw Cook, L. J. *et al.* A Unified Treatment of the Relationship Between Ligand Substituents and Spin State in a Family of Iron(II) Complexes. *Angewandte Chemie (International ed. in English)* **55**, 4327–4331; 10.1002/anie.201600165 (2016).
122. Brown, D. H., Nealon, G. L., Simpson, P. V., Skelton, B. W. & Wang, Z. Silver and Palladium Complexes of a Bis(benzimidazolin-2-ylidene)pyridine Pincer Ligand. *Organometallics* **28**, 1965–1968; 10.1021/om801144m (2009).

123. McPhillie, M. J. *et al.* Structure-based ligand design of novel bacterial RNA polymerase inhibitors. *ACS medicinal chemistry letters* **2**, 729–734; 10.1021/ml200087m (2011).
124. Gunasekar, G. H. *et al.* A Covalent Triazine Framework, Functionalized with Ir/N-Heterocyclic Carbene Sites, for the Efficient Hydrogenation of CO<sub>2</sub> to Formate. *Chem. Mater.* **29**, 6740–6748; 10.1021/acs.chemmater.7b01539 (2017).
125. Moll, J. *et al.* Green Light Activation of Push-Pull Ruthenium(II) Complexes. *Chemistry (Weinheim an der Bergstrasse, Germany)*; 10.1002/chem.202000871 (2020).
126. Förster, C. & Heinze, K. Photophysics and photochemistry with Earth-abundant metals - fundamentals and concepts. *Chemical Society reviews* **49**, 1057–1070; 10.1039/c9cs00573k (2020).
127. Paulus, B. C., Adelman, S. L., Jamula, L. L. & McCusker, J. K. Leveraging excited-state coherence for synthetic control of ultrafast dynamics. *Nature* **582**, 214–218; 10.1038/s41586-020-2353-2 (2020).
128. Vukadinovic, Y. *et al.* When Donors Turn into Acceptors: Ground and Excited State Properties of FeII Complexes with Amine-Substituted Tridentate Bis-imidazole-2-ylidene Pyridine Ligands. *Inorganic chemistry* **59**, 8762–8774; 10.1021/acs.inorgchem.0c00393 (2020).
129. Cannizzo, A. *et al.* Light-induced spin crossover in Fe(II)-based complexes: The full photocycle unraveled by ultrafast optical and X-ray spectroscopies. *Coordination Chemistry Reviews* **254**, 2677–2686; 10.1016/j.ccr.2009.12.007 (2010).
130. Randles, J. E. B. A cathode Ray Polarograph. Part II - The Current-Voltage Curves. *Trans. Faraday Soc.*, 327–338 (1948).
131. Ševčík, A. Oscillographic Polarography with periodical triangular voltage. *Collect. Czech. Chem. Comm.*, 349–377 (1948).
132. Jacobsen, H., Correa, A., Poater, A., Costabile, C. & Cavallo, L. Understanding the M(NHC) (NHC=N-heterocyclic carbene) bond. *Coordination Chemistry Reviews* **253**, 687–703; 10.1016/j.ccr.2008.06.006 (2009).
133. Alcarazo, M., Stork, T., Anoop, A., Thiel, W. & Fürstner, A. Steering the surprisingly modular pi-acceptor properties of N-heterocyclic carbenes: implications for gold catalysis. *Angewandte Chemie (International ed. in English)* **49**, 2542–2546; 10.1002/anie.200907194 (2010).

134. Mercks, L., Labat, G., Neels, A., Ehlers, A. & Albrecht, M. Piano-Stool Iron(II) Complexes as Probes for the Bonding of N-Heterocyclic Carbenes: Indications for  $\pi$ -Acceptor Ability. *Organometallics* **25**, 5648–5656; 10.1021/om060637c (2006).
135. Fantasia, S., Petersen, J. L., Jacobsen, H., Cavallo, L. & Nolan, S. P. Electronic Properties of N-Heterocyclic Carbene (NHC) Ligands: Synthetic, Structural, and Spectroscopic Studies of (NHC)Platinum(II) Complexes. *Organometallics* **26**, 5880–5889; 10.1021/om700857j (2007).
136. Casson, L. A. *et al.* N-heterocyclic carbenes as  $\pi^*$ -acceptors in luminescent Re(I) tricarbonyl complexes. *Dalton transactions (Cambridge, England : 2003)* **40**, 11960–11967; 10.1039/c1dt11233c (2011).
137. Evans, D. F. 400. The determination of the paramagnetic susceptibility of substances in solution by nuclear magnetic resonance. *J. Chem. Soc.*, 2003; 10.1039/jr9590002003 (1959).
138. Evans, D. F. & James, T. A. Variable-temperature Magnetic-susceptibility Measurements of Spin Equilibria for Iron(III) Dithiocarbamates in Solution. *J. Chem. Soc., Dalton Trans.*, 723–726 (1979).
139. Evans, D. F., Fazakerley, G. V. & Phillips, R. F. Organometallic compounds of bivalent europium, ytterbium, and samarium. *J. Chem. Soc., A*, 1931; 10.1039/j19710001931 (1971).
140. Johnson Matthey, D. F. Evans. *Magnetic Susceptibility Balance Instruction Manual*. 3rd ed. (2004).
141. P.W. Selwood. *Magnetochemistry*. 2nd ed. (Interscience Publishers, New York, London, 1956).
142. Jones, A. M., Griffin, P. J. & Waite, T. D. Ferrous iron oxidation by molecular oxygen under acidic conditions: The effect of citrate, EDTA and fulvic acid. *Geochimica et Cosmochimica Acta* **160**, 117–131; 10.1016/j.gca.2015.03.026 (2015).
143. Albin, A. & Fasani, E. (eds.). *A Specialist Periodical Report - Photochemistry* (The Royal Society of Chemistry, Cambridge, 2017).
144. Park, H.-J., Yoo, S., Shin, I.-S., Chung, Y. K. & Kim, J. Color-Tunable Electrogenerated Chemiluminescence of Ruthenium N-Heterocyclic Carbene Complexes. *Electroanalysis* **25**, 1111–1115; 10.1002/elan.201200619 (2013).
145. Mac, M., Najbar, J. & Wirz, J. Fluorescence quenching of derivatives of anthracene by organic electron donors and acceptors in acetonitrile. Electron and proton transfer mechanism. *Chemical Physics Letters*, 187–194 (1995).

146. Lakowicz, J. R. *Principles of Fluorescence Spectroscopy* (Springer, 2010).
147. Connelly, N. G. & Geiger, W. E. Chemical Redox Agents for Organometallic Chemistry. *Chem. Rev.* **96**, 877–910; 10.1021/cr940053x (1996).
148. Baker, M. V., Field, L. D. & Hambley, T. W. Diamagnetic Paramagnetic Equilibria in Solutions of Bis(dialkylphosphino)ethane Complexes of Iron. *Inorg. Chem.*, 2872–2876 (1988).
149. Miletic, A. *Bachelorarbeit* (Universität Paderborn, 2018).
150. McGuinness, D. S., Gibson, V. C. & Steed, J. W. Bis(carbene)pyridine Complexes of the Early to Middle Transition Metals: Survey of Ethylene Oligomerization and Polymerization Capability. *Organometallics* **23**, 6288–6292; 10.1021/om049246t (2004).

## List of figures

<b>Figure 1-1:</b> Global greenhouse gas emissions 1970-2015.....	- 1 -
<b>Figure 1-2:</b> Development of Electricity Generation from Renewables in Germany.....	- 2 -
<b>Figure 1-3:</b> Schematic procedure of water splitting by a semiconductor. ....	- 4 -
<b>Figure 1-4:</b> Schematic structure of multi- and single-component system. ....	- 5 -
<b>Figure 1-5:</b> Simplified excitation scheme for a $d^6$ -metal-complex with weak ligand field splitting.....	- 7 -
<b>Figure 1-6:</b> Schematic mechanism of oxidative and reductive quenching. ....	- 8 -
<b>Figure 1-7:</b> $[\text{Ru}(\text{bpy})_3]$ first reported example of a ruthenium photocatalyst. ....	- 8 -
<b>Figure 1-8:</b> Schematic representation for $^3\text{MLCT}$ and $^3\text{MC}$ location in a strong and weak ligand field in case of $[\text{Ru}(\text{bpy})_3]$ . ....	- 9 -
<b>Figure 1-9:</b> $[\text{Ru}(\text{bpy})_2(5\text{-amino-phen})]^{2+}$ based catalytic system for hydrogen production by SAKAI et al. ....	- 10 -
<b>Figure 1-10:</b> Single-component system with cobalt catalyst by FIIHRI et al. ....	- 10 -
<b>Figure 1-11:</b> Carbene Ru-PS analogues of $\text{Ru}(\text{bpy})_3$ and $\text{Ru}(\text{tpy})_2$ by SON et al.....	- 11 -
<b>Figure 1-12:</b> Schematic representation of MLCT and MC state energies for polypyridine $\text{Ru}(\text{II})$ and $\text{Fe}(\text{II})$ complexes.....	- 12 -
<b>Figure 1-13:</b> First homoleptic FeNHC complex reported by WÄRNMARK et al.....	- 14 -
<b>Figure 1-14:</b> Homoleptic Fe-NHC complex with increased $\pi$ -system by LIU et al. ...	- 14 -
<b>Figure 1-15:</b> Change of the HOMO-LUMO gap by modification of the ligand.....	- 15 -
<b>Figure 1-16:</b> Immobilizable homoleptic Fe-NHC complexes by working groups of GROS and WÄRNMARK.....	- 16 -
<b>Figure 1-17:</b> One-component system by ZIMMER et al. ....	- 17 -
<b>Figure 1-18:</b> Homoleptic bidentate $\text{Fe}(\text{btz})_3$ -complex by WÄRNMARK et al.....	- 17 -
<b>Figure 1-19:</b> Schematic effect of ligand functionalization on the HOMO-LUMO gap for different $\text{Ru}(\text{terpy})_2$ complexes .....	- 19 -
<b>Figure 2-1:</b> Structure of the ligand set used for the systematic study. ....	- 20 -
<b>Figure 3-1:</b> Overview over the synthesized NHC-ligand systems. ....	- 22 -
<b>Figure 3-2:</b> Synthesis of precursor 2,6-dichloropyridine-4-amine <b>4</b> . ....	- 23 -
<b>Figure 3-3:</b> Synthesis of the different precursor <b>5-7</b> .....	- 24 -
<b>Figure 3-4:</b> Two-step synthetic protocol for synthesis of ligand <b>L1-L15</b> .....	- 25 -
<b>Figure 4-1:</b> Representative synthesis for iron(II) complexes by example of complex $[\text{Fe}(\text{BIP}^{\text{NMe}_2})_2][\text{PF}_6]_2$ . ....	- 36 -
<b>Figure 4-2:</b> Crystal pictures of complexes $[\text{Fe}(\text{BmIP}^{\text{NMe}_2})_2][\text{PF}_6]_2$ ; $[\text{Fe}(\text{BdmIP}^{\text{NMe}_2})_2][\text{PF}_6]_2$ ; $[\text{Fe}(\text{BmIP}^{\text{NBn}_2})_2][\text{PF}_6]_2$ and $[\text{Fe}(\text{BBP}^{\text{NEt}_2})_2][\text{PF}_6]_2$ and their different shapes.....	- 37 -
<b>Figure 4-3:</b> Single crystal structure of $[\text{Fe}(\text{BIP}^{\text{NMe}_2})_2][\text{PF}_6]_2$ ( <b>C1</b> ). ....	- 39 -

<b>Figure 4-4:</b> Enlarged coordination sphere of $[\text{Fe}(\text{BIP}^{\text{NMe}_2})_2][\text{PF}_6]_2$ ( <b>C1</b> ).....	- 39 -
<b>Figure 4-5:</b> Single crystal structure of $[\text{Fe}(\text{BBP}^{\text{NBn}_2})_2][\text{PF}_6]_2$ ( <b>C9</b> ).....	- 41 -
<b>Figure 4-6:</b> UV/Vis spectra of iron NHC-complexes containing monocyclic carbenes in acetonitrile at r.t.. Imidazole containing complexes; methylimidazole complexes; dimethylimidazole complexes.....	- 43 -
<b>Figure 4-7:</b> UV/Vis spectra of iron NHC-complexes containing carbenes with extended $\pi$ -system in acetonitrile at r.t.. Benzimidazole containing complexes; dimethylbenzimidazole complexes.....	- 45 -
<b>Figure 4-8:</b> Experimental Vis spectra in comparison with theoretical Vis spectra; TPSSh, D3BJ, def2-TZVPP, SMD.....	- 47 -
<b>Figure 4-9:</b> Molecular levels of imidazolydene and benzimidazolydene complexes compared to the respective unfunctionalized reference.....	- 48 -
<b>Figure 4-10:</b> Transient absorption spectra and decay associated amplitude spectra with respective lifetimes of $[\text{Fe}(\text{BIP}^{\text{NMe}_2})_2]$ ( <b>C1</b> ) and $[\text{Fe}(\text{BiP}^{\text{NBn}_2})_2]$ ( <b>C6</b> ) with parallel polarization of excitation and retrieval pulse.....	- 49 -
<b>Figure 4-11:</b> Transient absorption spectra and decay associated amplitude spectra with respective lifetimes of $[\text{Fe}(\text{BmiP}^{\text{NMe}_2})_2]$ ( <b>C2</b> ) and $[\text{Fe}(\text{BmiP}^{\text{NBn}_2})_2]$ ( <b>C7</b> ) with parallel polarisation of excitation and retrieval pulse.....	- 50 -
<b>Figure 4-12:</b> Transient absorption spectra (left) and decay associated amplitude spectra with respective lifetimes of $[\text{Fe}(\text{BbP}^{\text{NMe}_2})_2]$ ( <b>C4</b> ) and $[\text{Fe}(\text{BbP}^{\text{NBn}_2})_2]$ ( <b>C9</b> ) with parallel polarization of excitation and retrieval pulse.....	- 50 -
<b>Figure 4-13:</b> Total cyclic voltammogram of complex <b>C1</b> in acetonitrile at 25 °C.....	- 52 -
<b>Figure 4-14:</b> Cyclic voltammograms at different scan rates and square-wave voltammograms of complexes <b>C1 - C5</b> in acetonitrile at 25 °C.....	- 53 -
<b>Figure 4-15:</b> Randles-Sevcik plot for the first redox event of complexes <b>C1-C5</b> .....	- 54 -
<b>Figure 4-16:</b> Change of the UV/Vis spectra during electrolysis of <b>C1</b> with an applied potential of 0.25 V and 1.8 V.....	- 56 -
<b>Figure 4-17:</b> UV/Vis spectra of $[\text{Fe}(\text{III})(\text{BIP}^{\text{NMe}_2})_2][\text{PF}_6]_3$ ( <b>C1</b> ) and $[\text{Fe}(\text{III})(\text{BbP}^{\text{NMe}_2})_2][\text{PF}_6]_3$ ( <b>C4</b> ) in acetonitrile at r.t.....	- 58 -
<b>Figure 4-18:</b> Obtained Fe(III) UV/Vis spectra by different oxidation methods in MeCN at r.t.....	- 60 -
<b>Figure 5-1:</b> Single crystal structure of $[\text{Ru}(\text{BIP}^{\text{NMe}_2})_2][\text{PF}_6]_2$ ( <b>C16</b> ).....	- 68 -
<b>Figure 5-2:</b> Magnified coordination sphere of the ruthenium center of $[\text{Ru}(\text{BIP}^{\text{NMe}_2})_2][\text{PF}_6]_2$ ( <b>C16</b> ).....	- 70 -
<b>Figure 5-3:</b> Single crystal structure of $[\text{Ru}(\text{BmbP}^{\text{NBn}_2})_2][\text{PF}_6]_2$ ( <b>C25</b> ).....	- 71 -
<b>Figure 5-4:</b> UV/Vis spectra of iron complex $[\text{Fe}(\text{BIP}^{\text{NMe}_2})_2][\text{PF}_6]_2$ ( <b>C1</b> ) and ruthenium complex $[\text{Ru}(\text{BIP}^{\text{NMe}_2})_2][\text{PF}_6]_2$ ( <b>C16</b> ).....	- 72 -

---

<b>Figure 5-5:</b> UV/Vis spectra of ruthenium NHC-complexes containing monocyclic carbenes in acetonitrile at r.t.. Imidazole containing complexes; methylimidazole complexes; dimethylimidazole complexes.....	- 73 -
<b>Figure 5-6:</b> UV/Vis spectra of ruthenium NHC-complexes containing bicyclic carbenes in acetonitrile at r.t.. Benzimidazole containing complexes; Diemthylbenzimidazole complexes.....	- 74 -
<b>Figure 5-7:</b> Compared fluorescence spectra of <b>C17</b> and reference complex <b>[Ru(BIP)<sub>2</sub>]</b> in acetonitrile at r.t.. Excitation wavelength 354 nm.....	- 76 -
<b>Figure 5-8:</b> Transient absorption spectra and decay associated amplitude spectra with the respective lifetimes of <b>[Ru(BIP<sup>NMe<sub>2</sub>)<sub>2</sub>]</sup></b> ( <b>C16</b> ) with parallel and perpendicular polarisation of excitation and retrieval pulse.....	- 78 -
<b>Figure 5-9:</b> Transient absorption spectra (left) and decay associated amplitude spectra (right) with the respective lifetimes of <b>[Ru(BBP<sup>NMe<sub>2</sub>)<sub>2</sub>]</sup></b> ( <b>C19</b> ) with parallel and perpendicular polarisation of excitation and retrieval pulse.....	- 78 -
<b>Figure 5-10:</b> TCSPC decay and fit spectra for the <b>[Ru(BIP)<sub>2</sub>]</b> and <b>[Ru(BBP)<sub>2</sub>]</b> reference complex. ....	- 79 -
<b>Figure 5-11:</b> Total cyclic voltammogram of complex <b>C16</b> in acetonitrile at 25 °C.....	- 80 -
<b>Figure 5-12:</b> Cyclic voltammograms at different scan rates and square-wave voltammograms of complexes <b>C16- C20</b> in acetonitrile at 25° C. ....	- 81 -
<b>Figure 5-13:</b> Randles-Sevcik plot for the redox event of <b>C16-C20</b> . ....	- 82 -
<b>Figure 5-14:</b> Change of the UV/Vis spectra during electrolysis of <b>C16</b> and <b>C19</b> with an applied potential of 0.47 V and 0.66 V.....	- 84 -
<b>Figure 6-1:</b> Summary of synthesized ligand systems.....	- 86 -
<b>Figure 6-2:</b> Summary of synthesized homoleptic Fe(II)-NHC compounds. ....	- 87 -
<b>Figure 6-3:</b> Summary of the synthesized homoleptic Ru(II)-NHC compounds. ....	- 89 -

## List of tables

<b>Table 3-1:</b> Selected bond length and binding angles for the obtained ligand crystal structures .....	- 27 -
<b>Table 3-2:</b> Chemical shifts in $\delta$ of selected NMR signals for NHC-ligands containing monocyclic carbenes at 303 K in DMSO in ppm.....	- 28 -
<b>Table 3-3:</b> Chemical shifts in $\delta$ of selected NMR signals for NHC-ligands containing bicyclic carbenes at 303 K in DMSO in ppm.....	- 29 -
<b>Table 3-4:</b> UV/Vis-data of ligands <b>L1-L15</b> in DMSO at r.t.....	- 33 -
<b>Table 4-1:</b> Coordinating bond length for all analyzed iron complexes.....	- 38 -
<b>Table 4-2:</b> Selected coordinating binding angles for all analyzed iron complexes. ....	- 40 -
<b>Table 4-3:</b> UV/Vis-data of homoleptic iron(II) complexes <b>C1-C15</b> in acetonitrile .....	- 46 -
<b>Table 4-4:</b> Obtained time constants from transient absorption spectroscopy for the iron complex series. ....	- 51 -
<b>Table 4-5:</b> Electrochemical data for iron NHC-complexes containing monocyclic carbenes in acetonitrile at r.t.. ( $\nu = 100 \text{ mV s}^{-1}$ ).....	- 55 -
<b>Table 4-6:</b> Electrochemical data for iron NHC-complexes containing bicyclic carbenes in acetonitrile at r.t. ( $\nu = 100 \text{ mV s}^{-1}$ ).....	- 55 -
<b>Table 4-7:</b> $\mu_{eff}$ and $n$ values for the investigated Fe(III) complexes.....	- 57 -
<b>Table 4-8:</b> UV/Vis-data of selected homoleptic iron(III) complexes in acetonitrile.....	- 59 -
<b>Table 5-1:</b> Coordinating bond length and average in Å for all analyzed ruthenium complexes.....	- 69 -
<b>Table 5-2:</b> Selected coordinating binding angles for all ruthenium complexes.....	- 70 -
<b>Table 5-3:</b> UV/Vis-data of homoleptic ruthenium(II) complexes <b>C16-C30</b> in acetonitrile at r.t.....	- 75 -
<b>Table 5-4:</b> Obtained time constants from transient absorption spectroscopy and TCSPC for the Ru-complexes. ....	- 80 -
<b>Table 5-5:</b> Electrochemical data for ruthenium NHC-complexes containing monocyclic carbenes in acetonitrile at r.t.. ( $\nu = 100 \text{ mV s}^{-1}$ ).....	- 83 -
<b>Table 5-6:</b> Electrochemical data for ruthenium NHC-complexes containing bicyclic carbenes in acetonitrile at r.t.. ( $\nu = 100 \text{ mV s}^{-1}$ ).....	- 83 -

## Publications and Beamtimes

**Table 1:** List of Oral presentations

Place	Meeting	Date
Köln	Ligandendesign Workshop	30.8.2017

**Table 2:** List of Poster presentations

Place	Meeting	Date
Heidelberg	Koordinationschemie Tagung	11.03 - 13.03.2018
München	Koordinationschemie Tagung	03.03. - 05.03.2019

**Table 3:** List of Publications

1.	<u>Y. Vukadinovic</u> , L. Burkhardt, A. Pöpcke, A. Miletic, L. Fritsch, B. Altenburger, R. Schoch, A. Neuba, S. Lochbrunner, M. Bauer, „When Donors turn into Acceptors: Ground and excited state properties of Fe(II) complexes with amine-substituted tridentate bis-imidazole-2-ylidene pyridine ligands”, <i>Inorg. Chem.</i> , <b>2020</b> , <i>59</i> , 8762-8774.
2.	<u>Y. Vukadinovic</u> , P. Müller, A. Pöpcke, R. Schoch, A. Neuba, S. Lochbrunner, M. Bauer, „Homoleptic tridentate Ru(II)-NHC complexes with amine donors – Synthesis and Characterization”, <i>manuscript in preparation</i>
3.	L. Burkhardt, <u>Y. Vukadinovic</u> , M. Nowakowski, A. Kalinko, J. Rudolph, P.A. Carlsson, C.R. Jacob, M. Bauer, “Electronic Structure of the Hieber Anion [Fe(CO) <sub>3</sub> (NO)] <sup>-</sup> Revisited by X-ray Emission and Absorption Spectroscopy”, <i>Inorg. Chem.</i> , <b>2020</b> , <i>59</i> , 6 ,3551-3561

**Table 4:** List of Beamtimes

Institute	Beamline	Time frame
Hamburg/ DESY	P65	31.08. - 05.09.2017
Hamburg/ DESY	P64	26.10. - 01.11.2018
Hamburg/ DESY	P64	12.04. - 17.04.2019
Hamburg/ DESY	P64	07.11. – 13.11.2019
Hamburg/ DESY	P65	01.10. – 06.10.2020
Grenoble/ ESRF	ID26	21.02. - 27.02.2018
Grenoble/ ESRF	ID26	13.06. - 19.06.2018
Hyogo Japan/ Spring-8	SACLA	05.07. - 08.07.2019
Oxfordshire / Diamond	B18	24.07. - 29.07.2019

## Publication permission



RightsLink®



Home



Help



Email Support



Sign In



Create Account



### When Donors Turn into Acceptors: Ground and Excited State Properties of Fell Complexes with Amine-Substituted Tridentate Bis-imidazole-2-ylidene Pyridine Ligands

Author: Yannik Vukadinovic, Lukas Burkhardt, Ayla Pöpcke, et al

Publication: Inorganic Chemistry

Publisher: American Chemical Society

Date: Jul 1, 2020

Copyright © 2020, American Chemical Society

#### PERMISSION/LICENSE IS GRANTED FOR YOUR ORDER AT NO CHARGE

This type of permission/license, instead of the standard Terms & Conditions, is sent to you because no fee is being charged for your order. Please note the following:

- Permission is granted for your request in both print and electronic formats, and translations.
- If figures and/or tables were requested, they may be adapted or used in part.
- Please print this page for your records and send a copy of it to your publisher/graduate school.
- Appropriate credit for the requested material should be given as follows: "Reprinted (adapted) with permission from (COMPLETE REFERENCE CITATION). Copyright (YEAR) American Chemical Society." Insert appropriate information in place of the capitalized words.
- One-time permission is granted only for the use specified in your request. No additional uses are granted (such as derivative works or other editions). For any other uses, please submit a new request.

[BACK](#)

[CLOSE WINDOW](#)

## Appendix

### Crystal data for the ligand series

**Table A 1:** Crystal data and refinement method of **L1** and **L6**

	<b>L1</b>	<b>L4</b>
Identification code	yv_0012mm_a	v2932
Empirical formula	C <sub>15</sub> H <sub>20</sub> F <sub>12</sub> N <sub>6</sub> P <sub>2</sub>	C <sub>23</sub> H <sub>24</sub> F <sub>12</sub> N <sub>6</sub> P <sub>2</sub>
Formula weight [g mol <sup>-1</sup> ]	574.31	674.42
Temperature [K]	130(2)	130(2)
Wavelength [Å]	0.71073	0.71073
Crystal system	Monoclinic	Monoclinic
Space group	C2/c	C2/c
Unit cell dimensions [Å]; [°]	a = 14.652(2), $\alpha$ = 90 b = 11.531(2), $\beta$ = 102.590(4) c = 13.180(2), $\gamma$ = 90	a = 12.366(3), $\alpha$ = 90 b = 10.769(2), $\beta$ = 105.006(6) c = 21.267(4), $\gamma$ = 90
Volume [Å <sup>3</sup> ]	2173.2(7)	2735.4(10)
Z	4	4
Density (calculated) [Mg m <sup>-3</sup> ]	1.755	1.638
Absorption coefficient [mm <sup>-1</sup> ]	0.320	0.268
F(000)	1160	1368
Crystal size [mm <sup>3</sup> ]	? x ? x ?	0.490 x 0.220 x 0.210
$\theta$ range [°]	2.269 to 28.442	1.983 to 27.877
Index ranges	-19 ≤ h ≤ 19, -15 ≤ k ≤ 15, -17 ≤ l ≤ 17	-16 ≤ h ≤ 16, -14 ≤ k ≤ 14, -23 ≤ l ≤ 27
Reflections collected	14658	12655
Independent reflections	2738 [R(int) = 0.0211]	3264 [R(int) = 0.0573]
Completeness to $\theta$ [%]	99.9	100.0
Refinement method	Full-matrix least-squares on F <sup>2</sup>	Full-matrix least-squares on F <sup>2</sup>
Data / restraints/ parameters	2738 / 0 / 162	3264 / 0 / 235
Goodness of fit on F <sup>2</sup>	1.037	1.054
Final R indices	R1 = 0.0481, wR2 = 0.1253	R1 = 0.0621, wR2 = 0.1406
R indices (all data)	R1 = 0.0510, wR2 = 0.1279	R1 = 0.1029, wR2 = 0.1624
Extinction coefficient	n/a	n/a
Largest diff. peak and hole [e Å <sup>-3</sup> ]	0.828 and -0.612	0.543 and -0.386

---

<b>L6</b>	
Identification code	v2940
Empirical formula	C <sub>28</sub> H <sub>30</sub> F <sub>12</sub> N <sub>6</sub> P <sub>2</sub>
Formula weight [g mol <sup>-1</sup> ]	753.86
Temperature [K]	130(2)
Wavelength [Å]	0.71073
Crystal system	Monoclinic
Space group	P 21/n
Unit cell dimensions [Å]; [°]	a = 24.320(3), $\alpha$ = 90 b = 29.056(3), $\beta$ = 91.333(3) c = 27.468(3), $\gamma$ = 90
Volume [Å <sup>3</sup> ]	19404(4)
Z	24 (6 x 4)
Density (calculated) [Mg m <sup>-3</sup> ]	1.548
Absorption coefficient [mm <sup>-1</sup> ]	0.237
F(000)	9232
Crystal size [mm <sup>3</sup> ]	0.460 x 0.450 x 0.380
$\theta$ range [°]	1.092 to 27.878
Index ranges	-30 ≤ h ≤ 31, -38 ≤ k ≤ 36, -36 ≤ l ≤ 36
Reflections collected	184273
Independent reflections	46279 [R(int) = 0.2290]
Completeness to $\theta$ [%]	100.0
Refinement method	Full-matrix least-squares on F <sup>2</sup>
Data / restraints/ parameters	46279 / 0 / 2666
Goodness of fit on F <sup>2</sup>	0.885
Final R indices	R1 = 0.0797, wR2 = 0.1120
R indices (all data)	R1 = 0.2543, wR2 = 0.1619
Extinction coefficient	n/a
Largest diff. peak and hole [e Å <sup>-3</sup> ]	1.159 and -0.505

---

# $^1\text{H}$ - and $^{13}\text{C}$ -NMR-Spectra for the ligand series

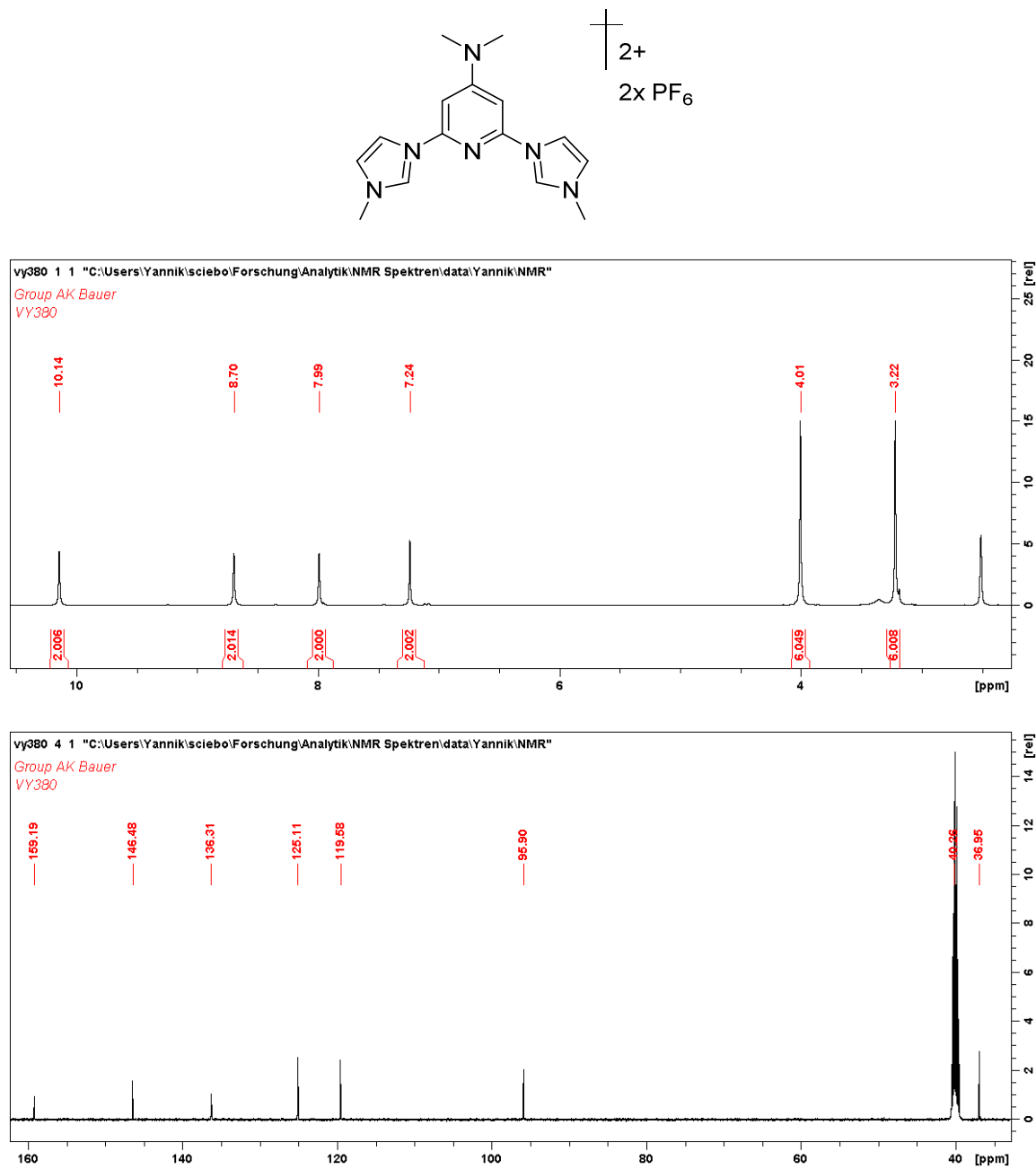


Figure A--0-1:  $^1\text{H}$ - (top) and  $^{13}\text{C}$ -NMR spectra (bottom) of  $\text{BIP}^{\text{NMe}_2}$  (L1) in DMSO at 303 K.

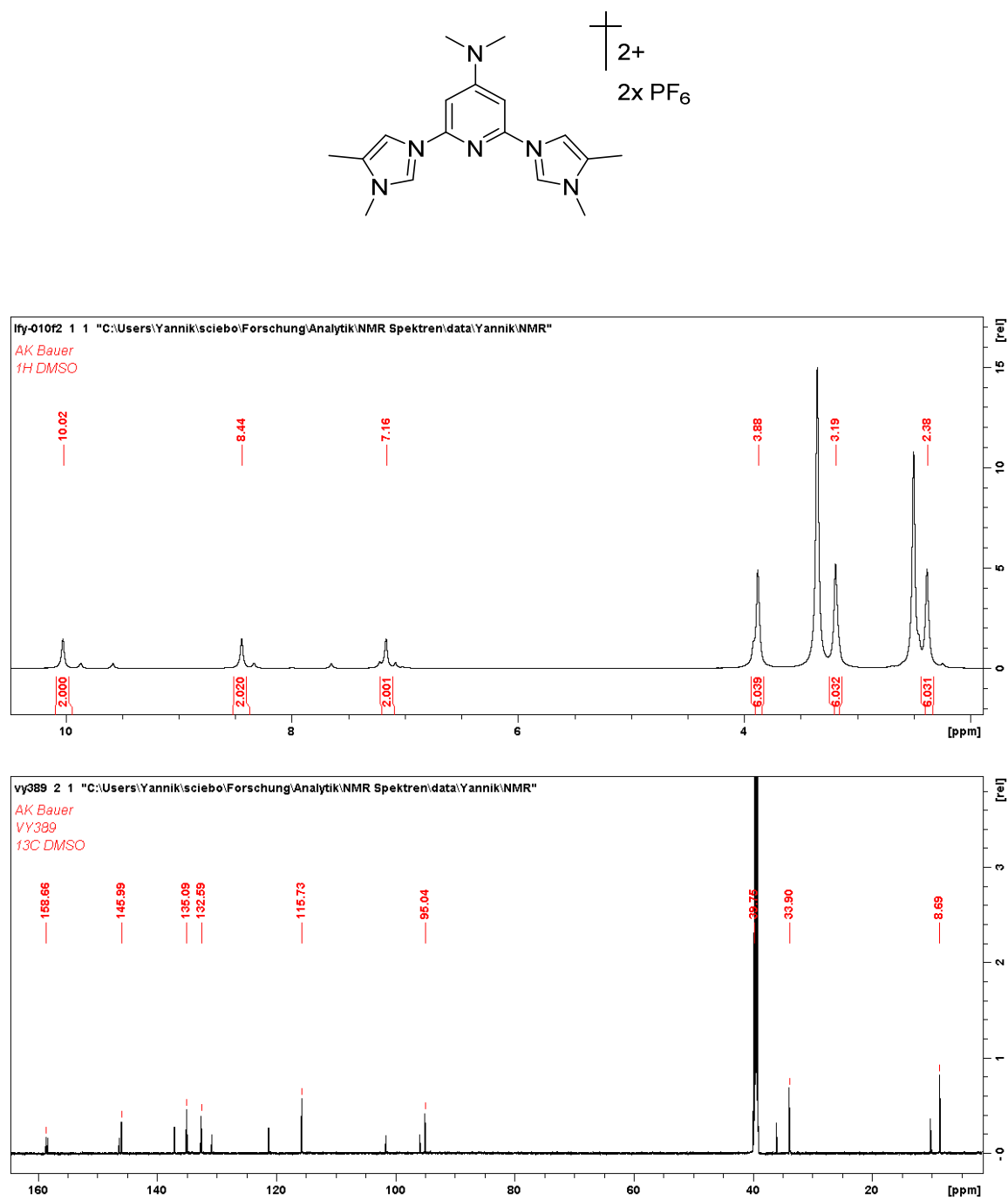


Figure A--0-2: <sup>1</sup>H- (top) and <sup>13</sup>C-NMR spectra (bottom) of BmiP<sup>NMe2</sup> (L2) in DMSO at 303 K.

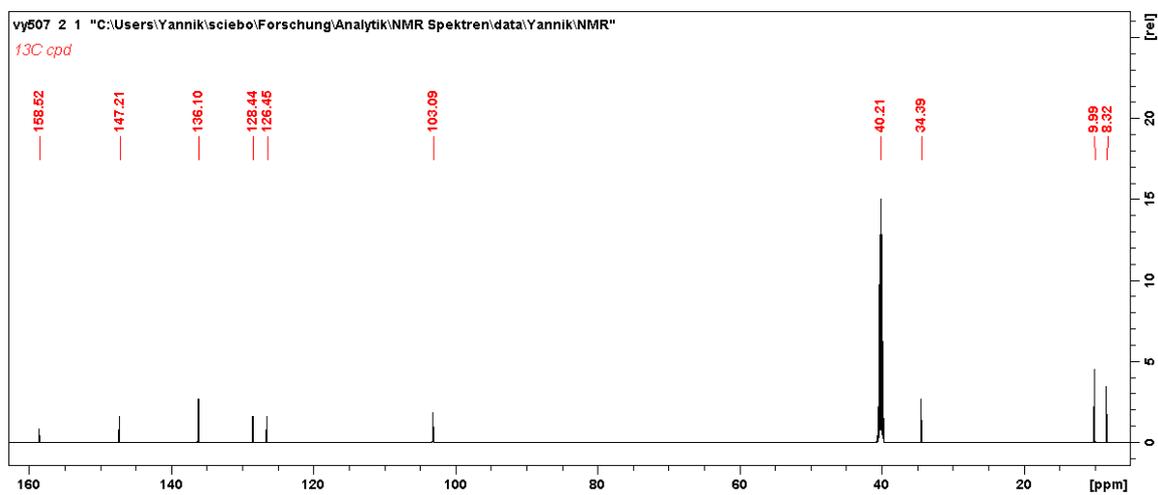
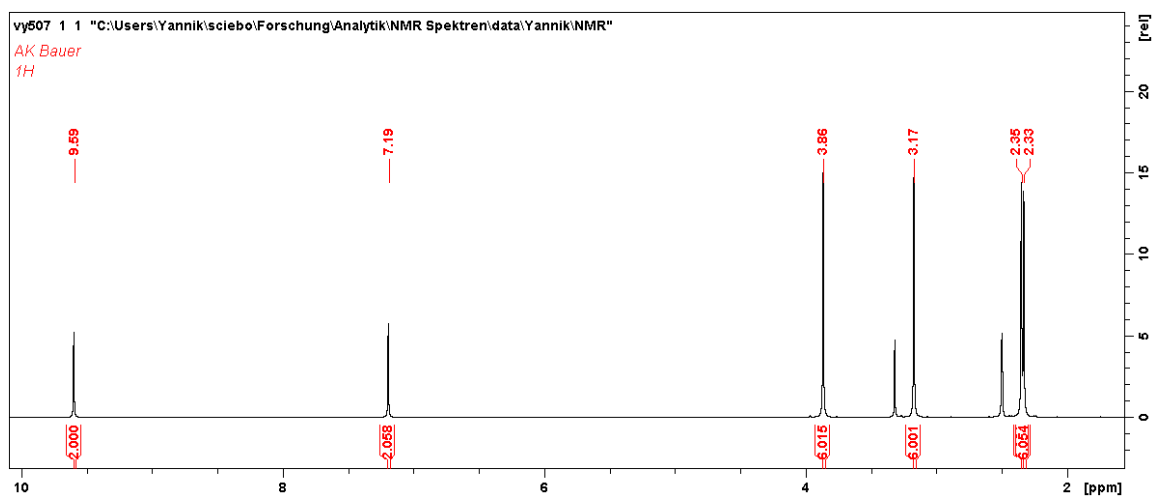
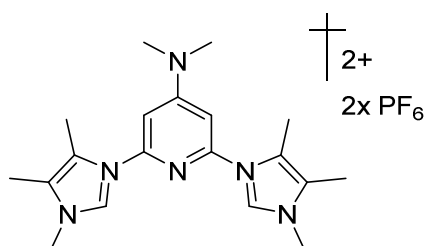


Figure A--0-3: <sup>1</sup>H- (top) and <sup>13</sup>C-NMR spectra (bottom) of **BdmipNMe<sub>2</sub> (L3)** in DMSO at 303 K.

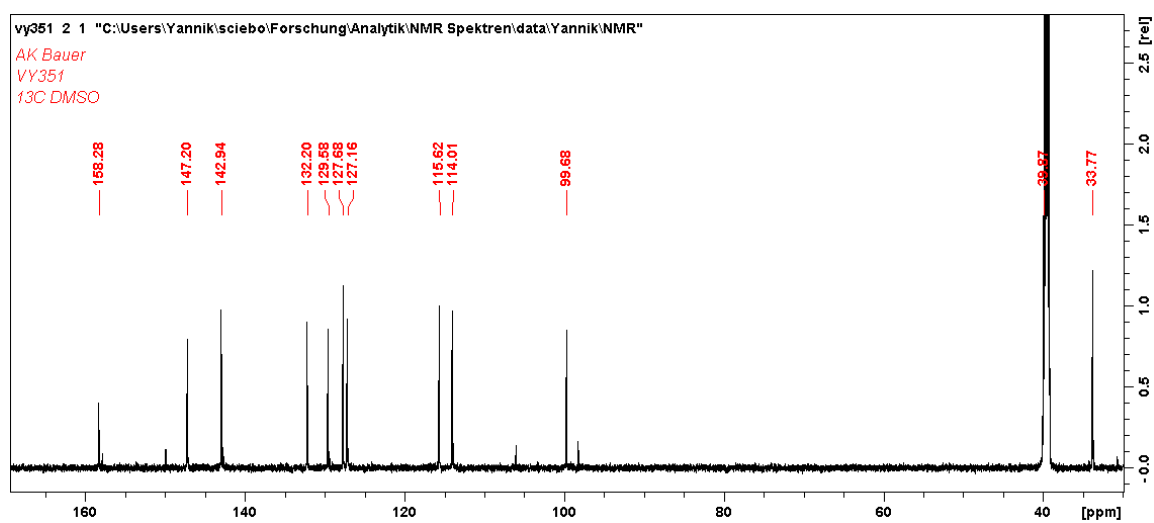
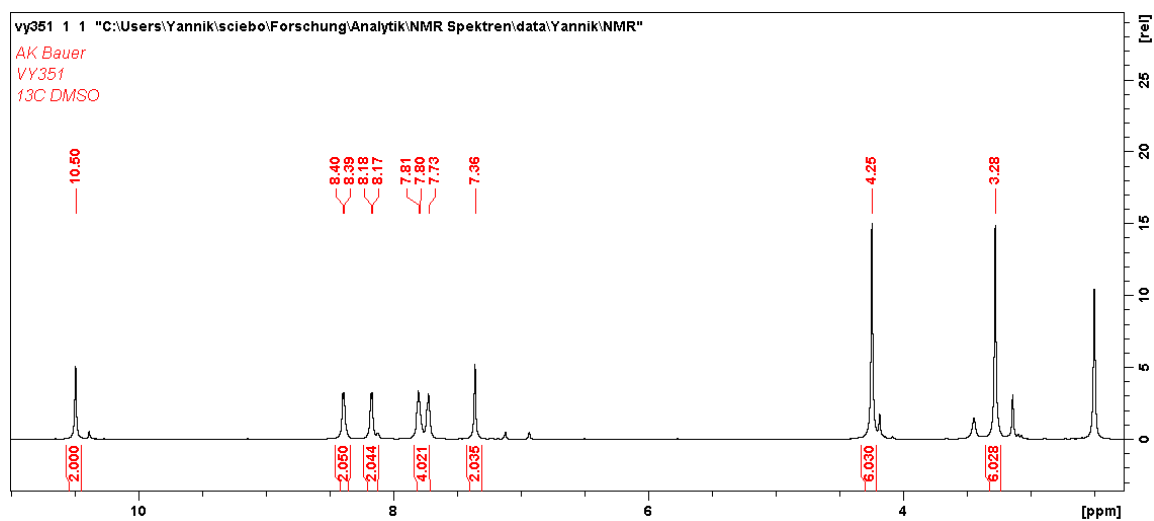
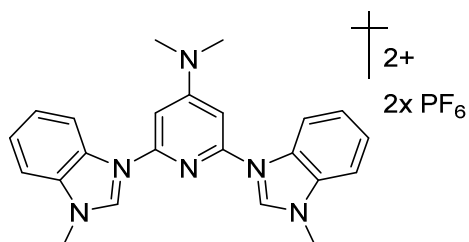


Figure A--0-4: <sup>1</sup>H- (top) and <sup>13</sup>C-NMR spectra (bottom) of BBP<sup>NMe2</sup> (L4) in DMSO at 303 K.

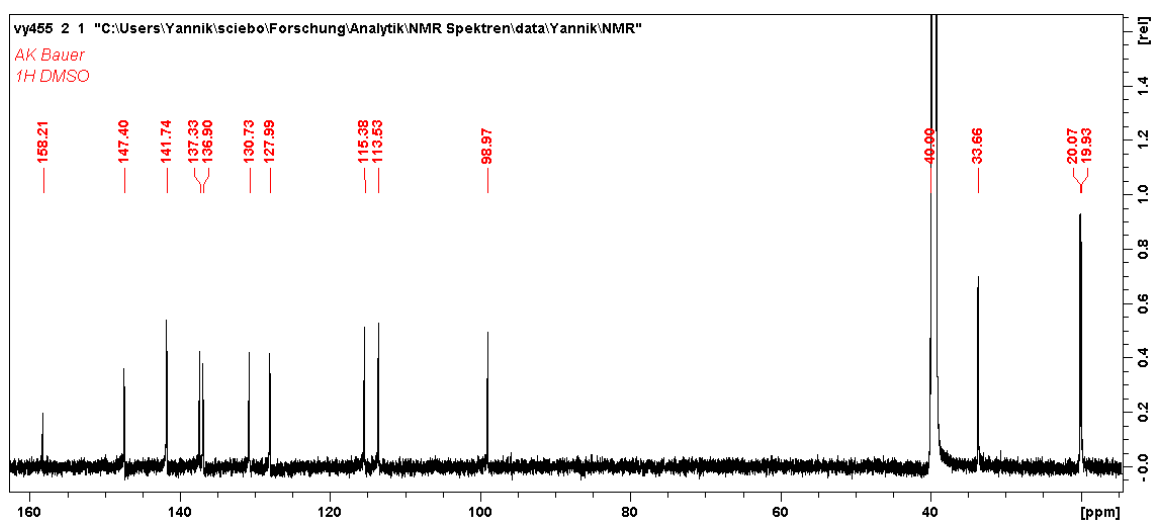
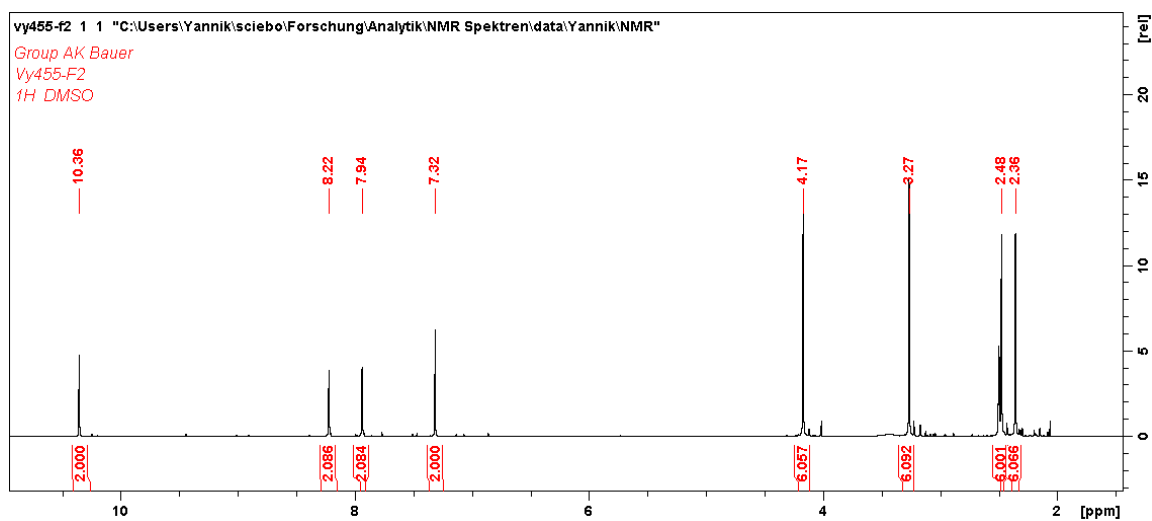
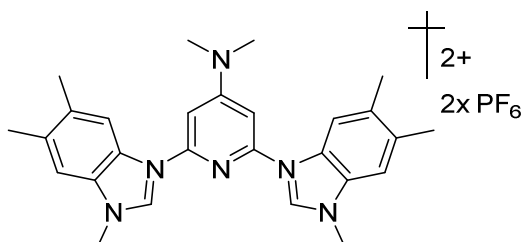


Figure A-0-5: <sup>1</sup>H- (top) and <sup>13</sup>C-NMR spectra (bottom) of **BmbP<sup>NMe2</sup> (L5)** in DMSO at 303 K.

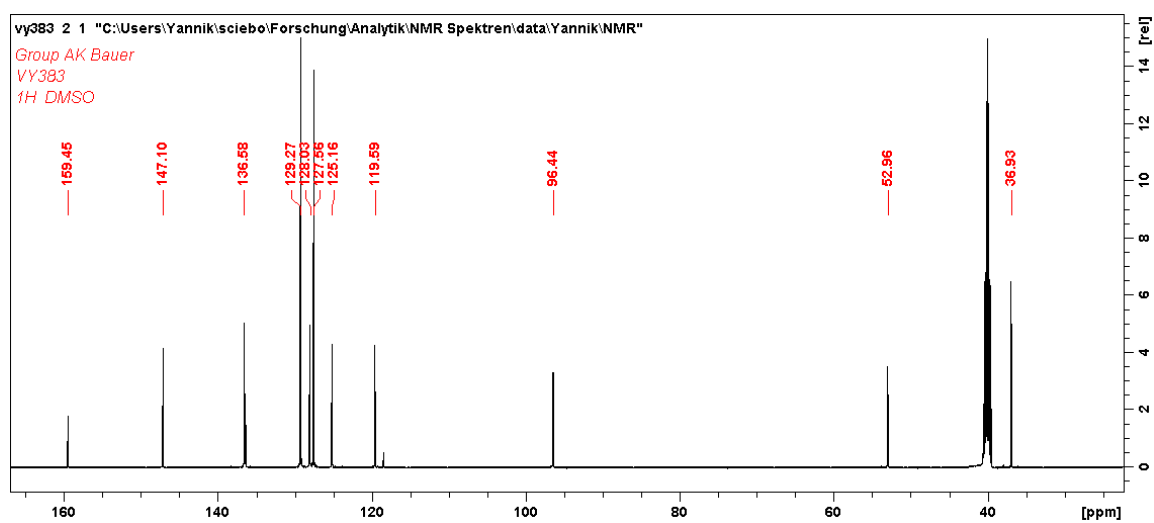
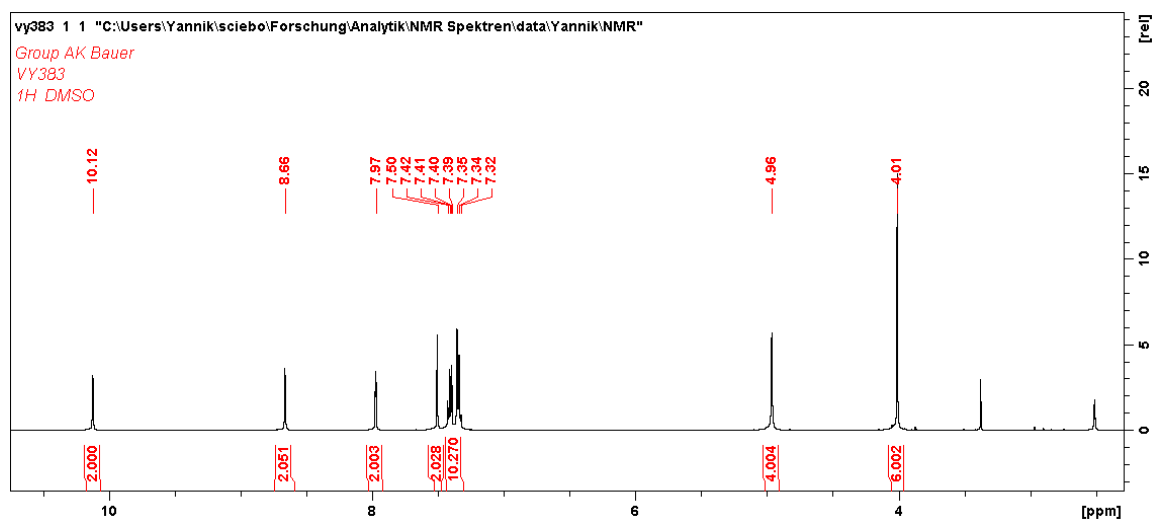
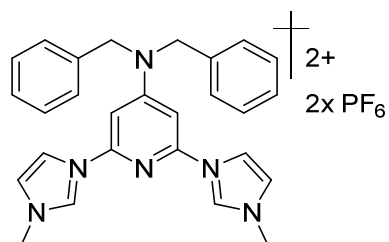


Figure A-0-6:  $^1H$ - (top) and  $^{13}C$ -NMR spectra (bottom) of  $BIP^{NBn2}$  ( $L6$ ) in DMSO at 303 K.

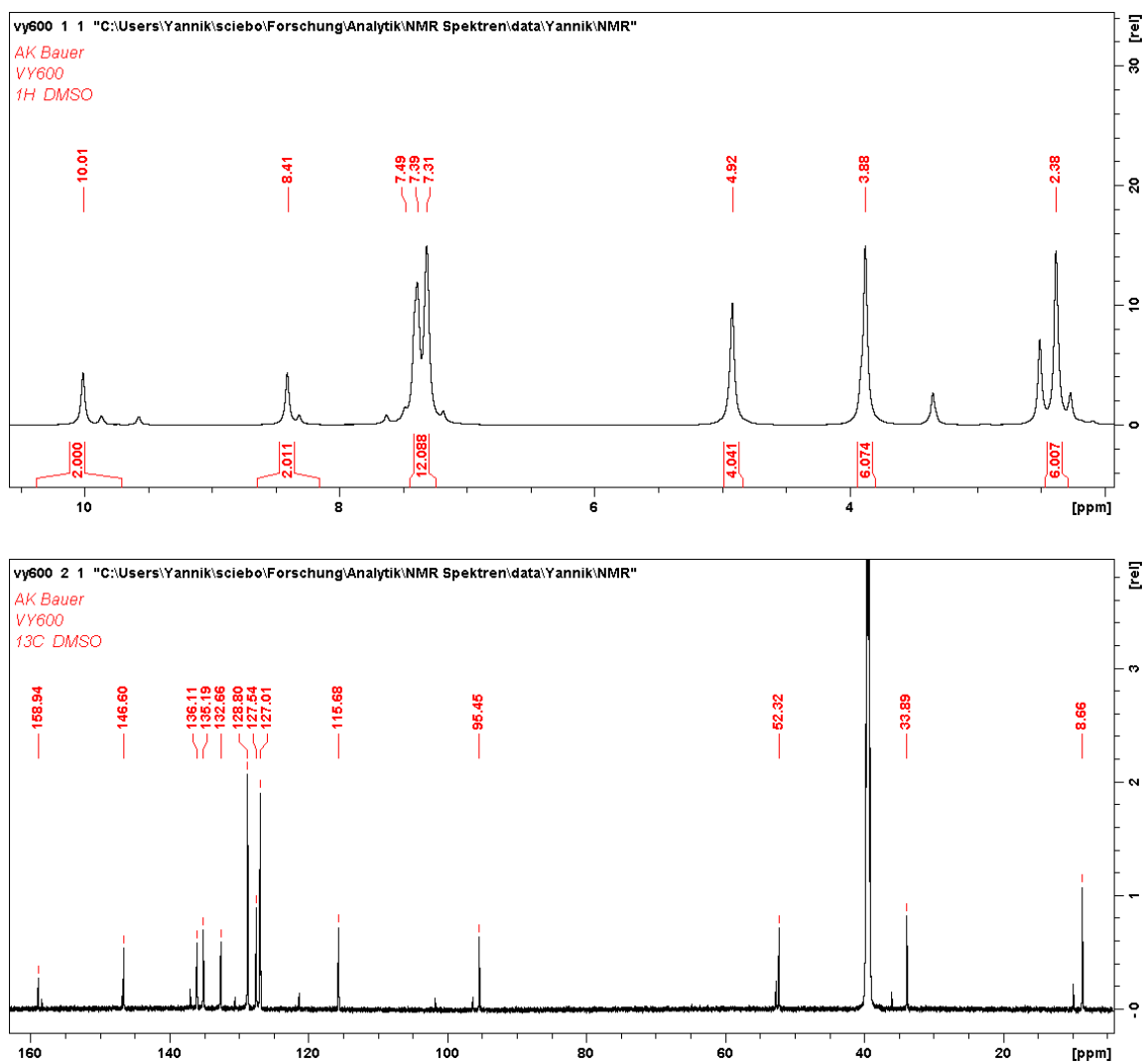
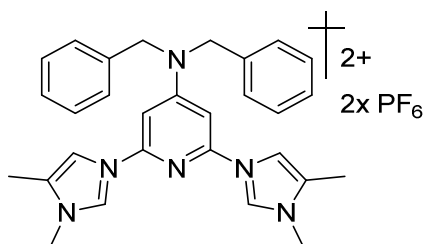


Figure A-0-7:  $^1H$ - (top) and  $^{13}C$ -NMR spectra (bottom) of  $BmiP^{NBn2}$  (L7) in DMSO at 303 K.

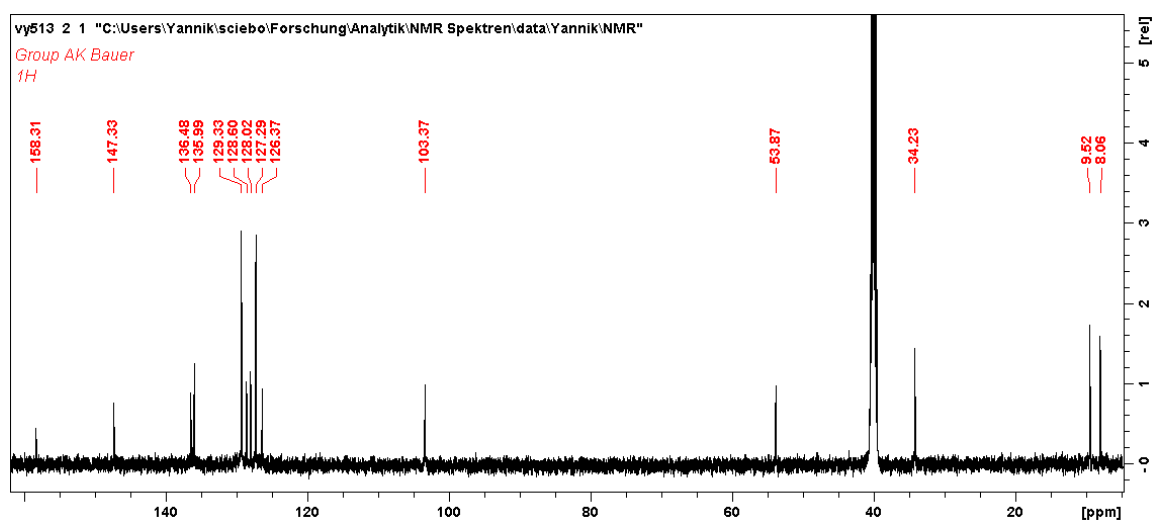
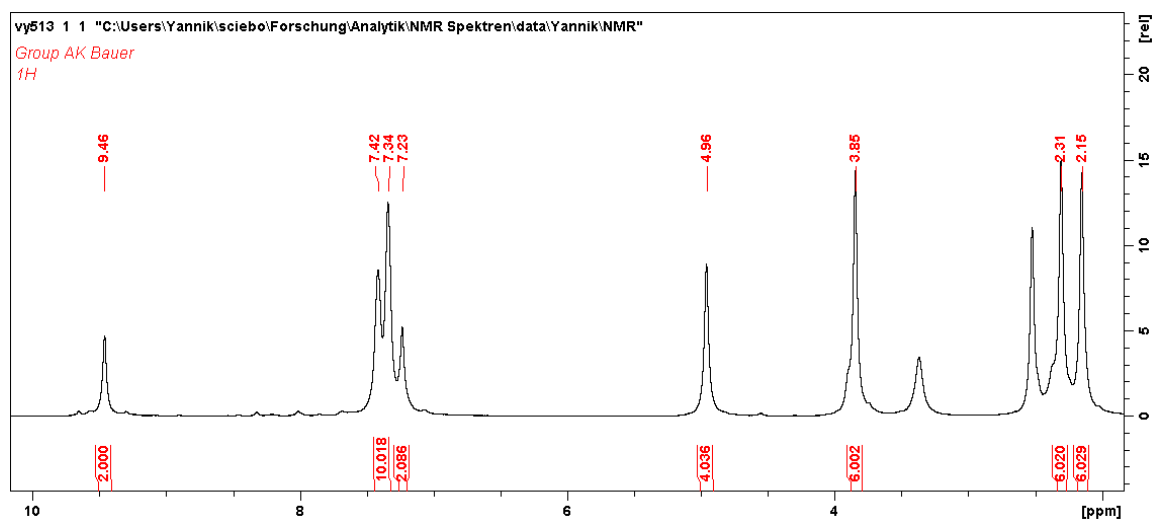
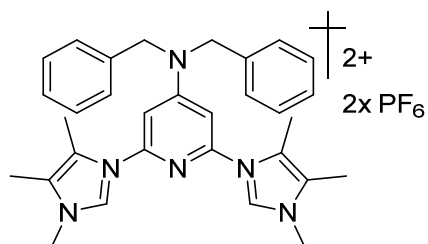


Figure A-0-8:  $^1H$ - (top) and  $^{13}C$ -NMR spectra (bottom) of  $BdmIP^{NBn2}$  (L8) in DMSO at 303 K.

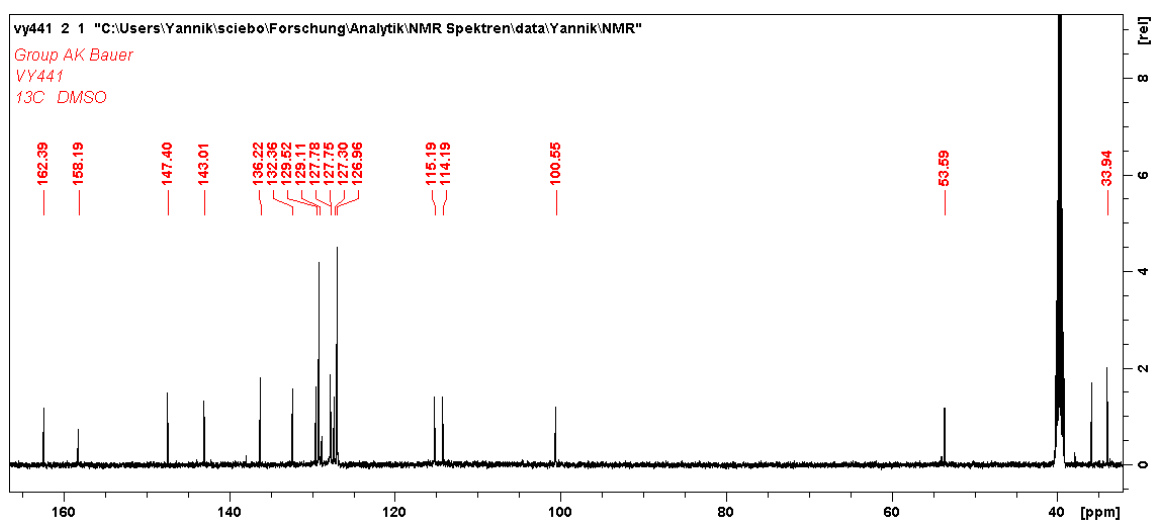
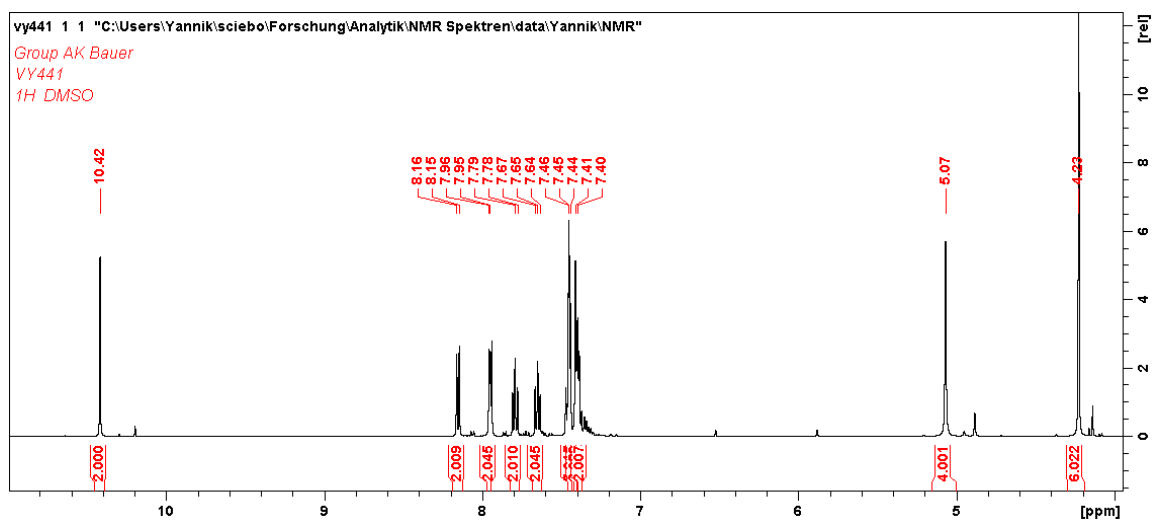
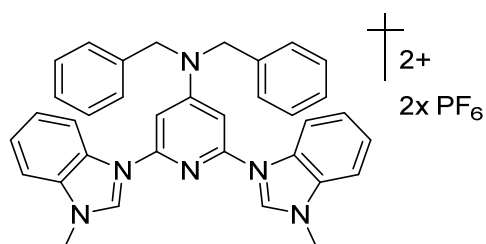


Figure A-0-9:  $^1\text{H}$ - (top) and  $^{13}\text{C}$ -NMR spectra (bottom) of  $\text{BBP}^{\text{NBn}_2}$  (L9) in DMSO at 303 K.

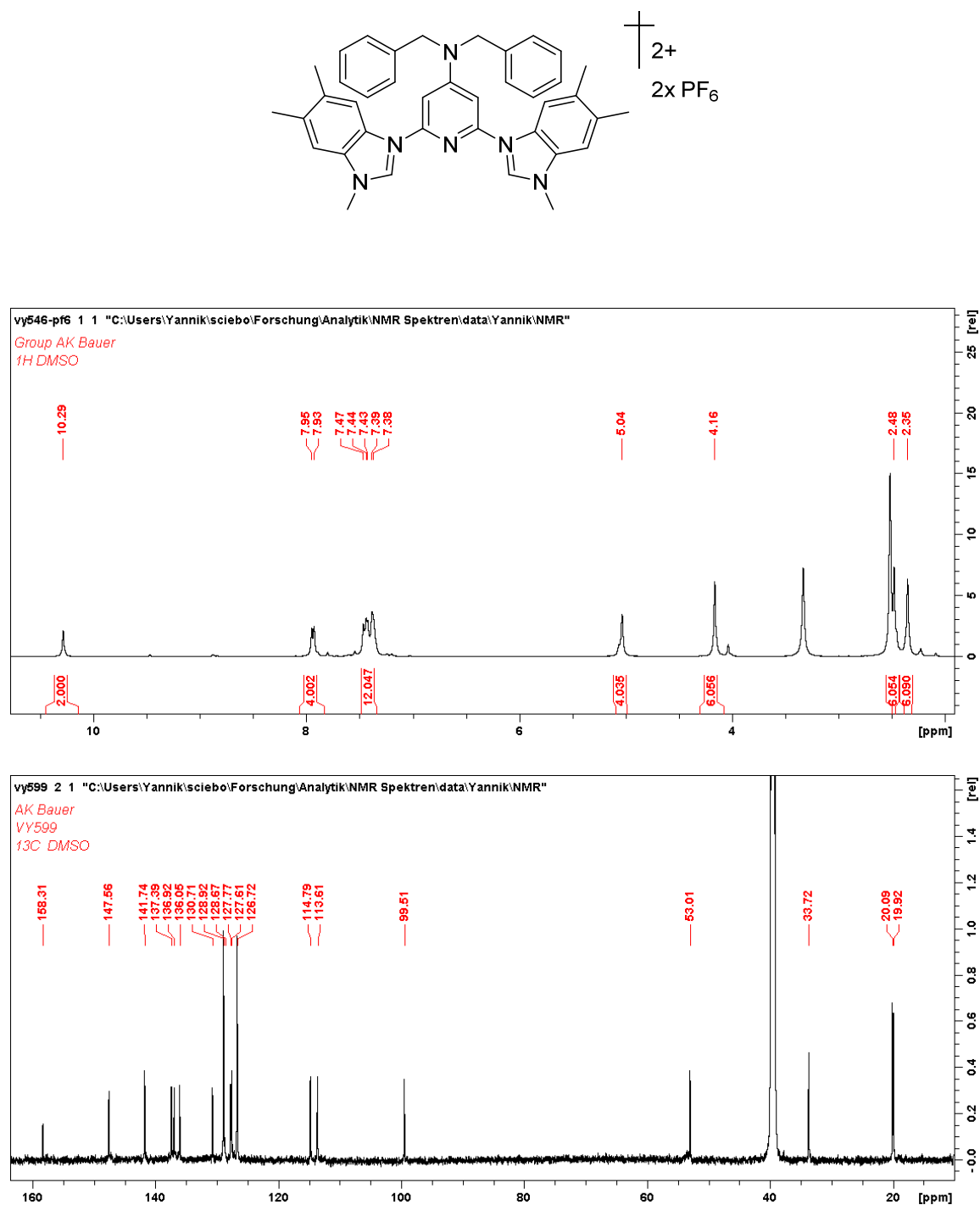


Figure A-0-10: <sup>1</sup>H- (top) and <sup>13</sup>C-NMR spectra (bottom) of **BmbP<sup>NBn2</sup> (L10)** in DMSO at 303 K.

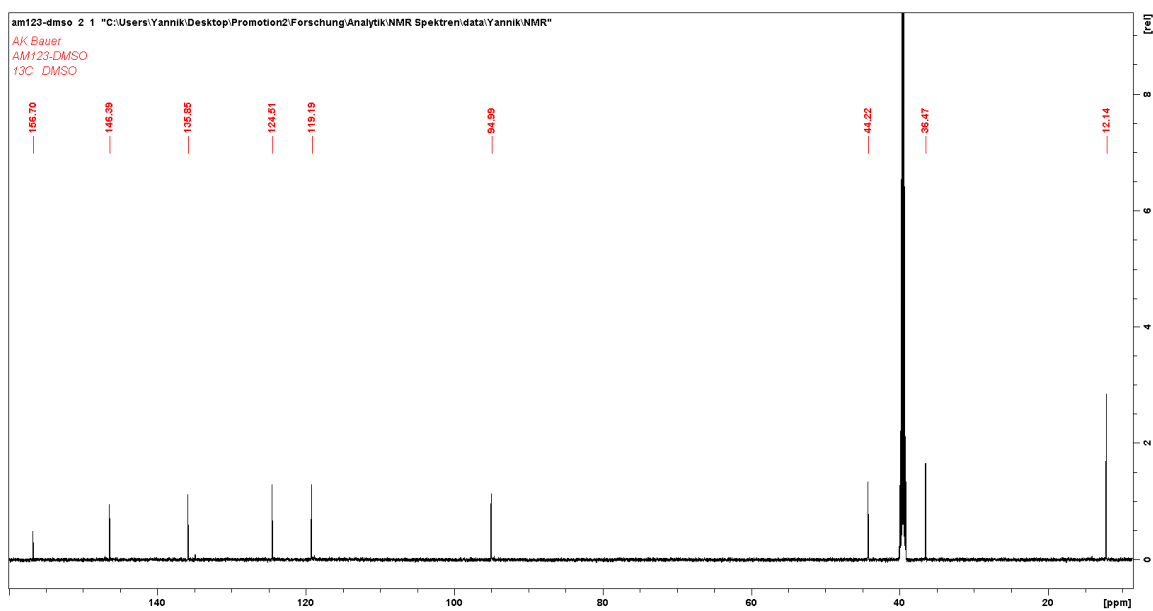
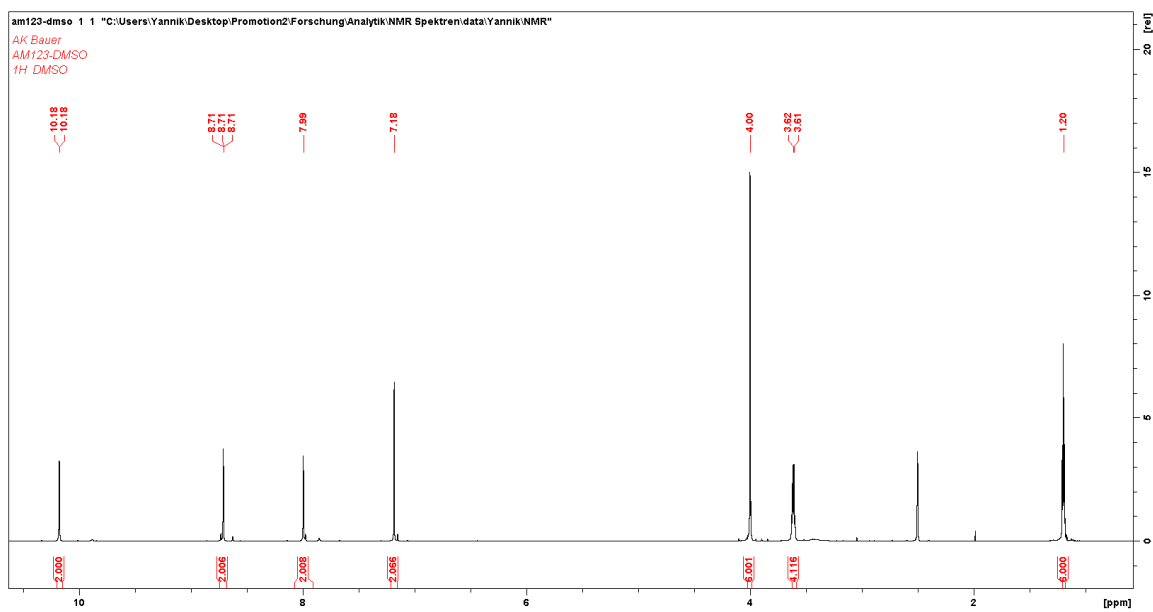
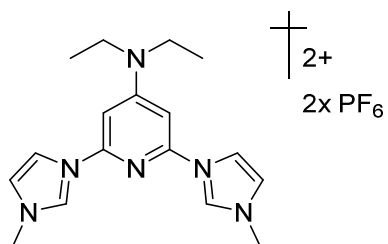


Figure A-0-11:  $^1H$ - (top) and  $^{13}C$ -NMR spectra (bottom) of  $BIP^{NE12}$  (L11) in DMSO at 303 K.

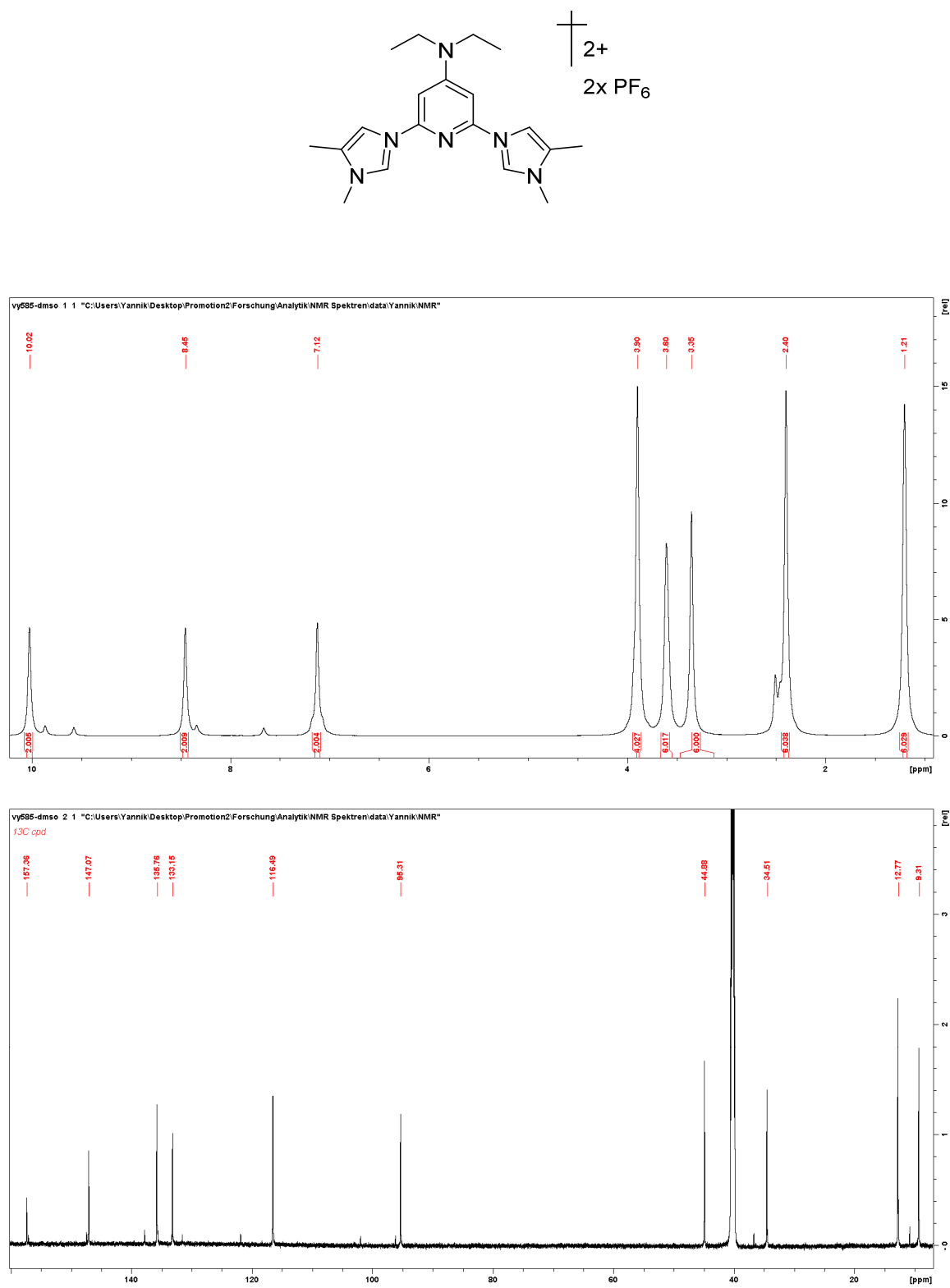


Figure A-0-12:  $^1H$ - (top) and  $^{13}C$ -NMR spectra (bottom) of **BmiP<sup>NEt</sup><sub>2</sub>** (L12) in DMSO at 303 K.

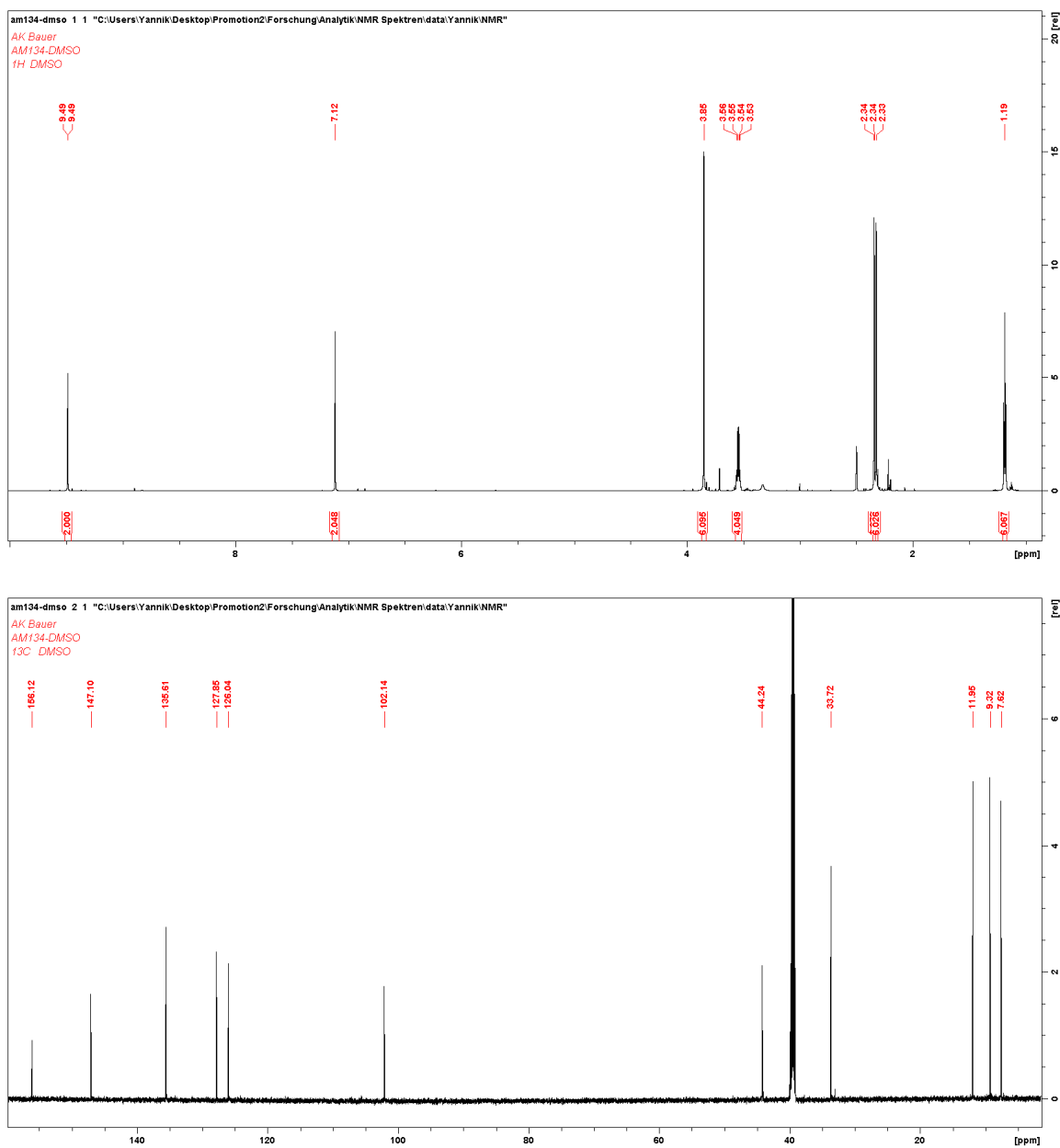
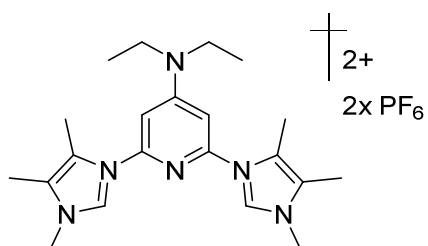


Figure A-0-13: <sup>1</sup>H- (top) and <sup>13</sup>C-NMR spectra (bottom) of BdmIPNE<sub>12</sub> (L13) in DMSO at 303 K.

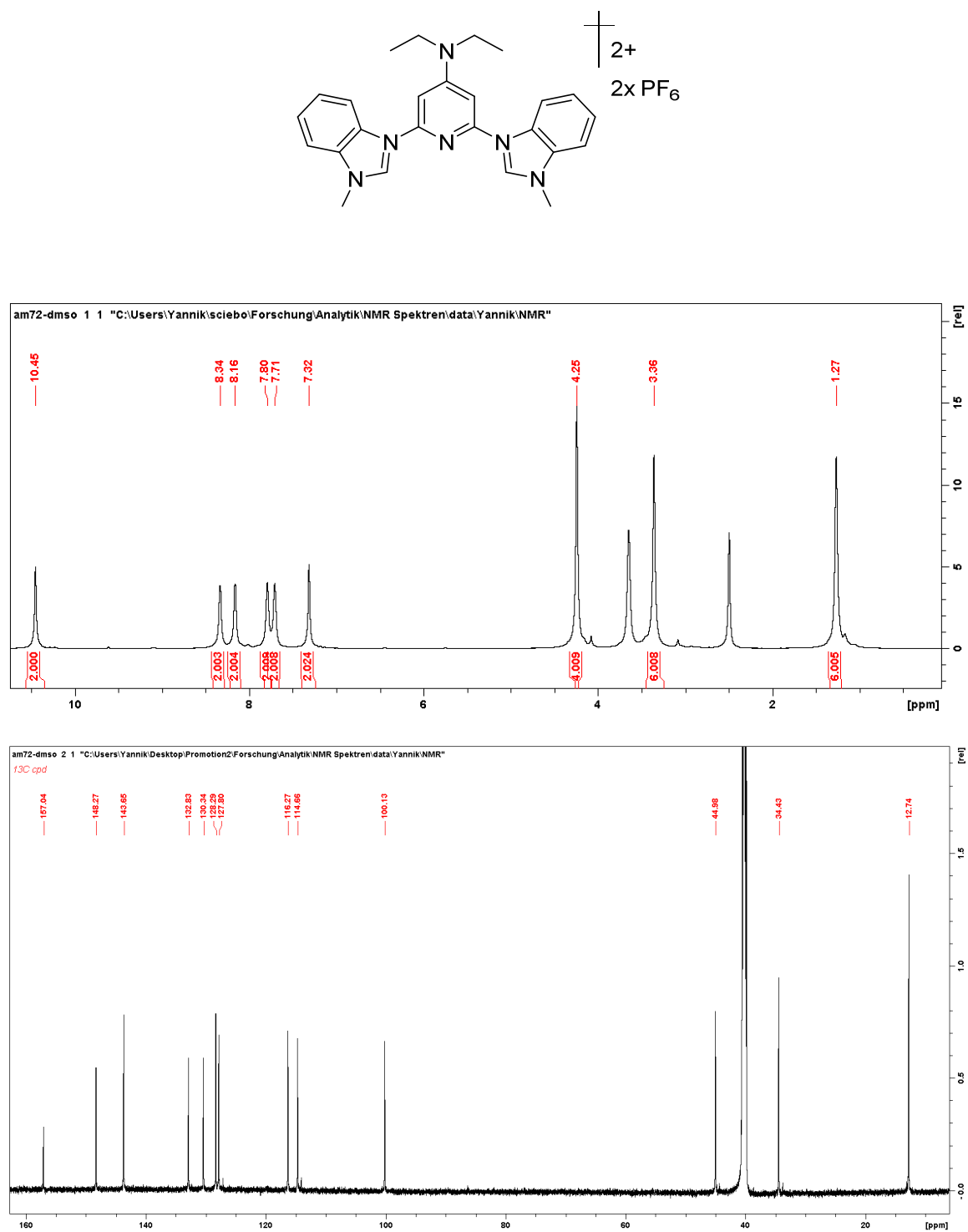


Figure A-0-14:  $^1H$ - (top) and  $^{13}C$ -NMR spectra (bottom) of **BbP<sup>NE12</sup> (L14)** in DMSO at 303 K.

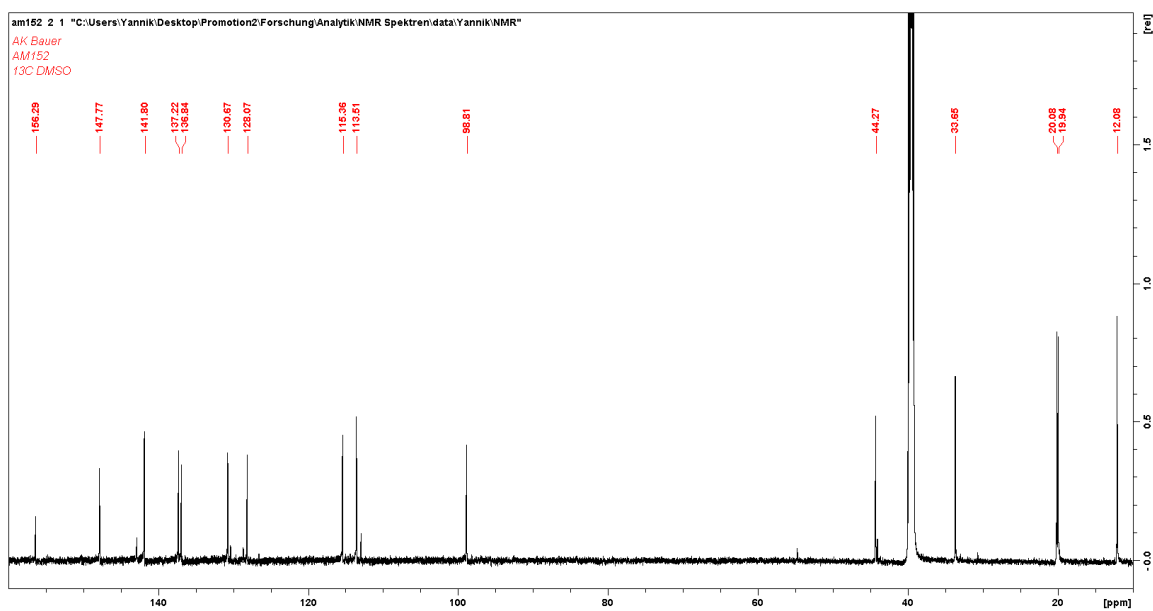
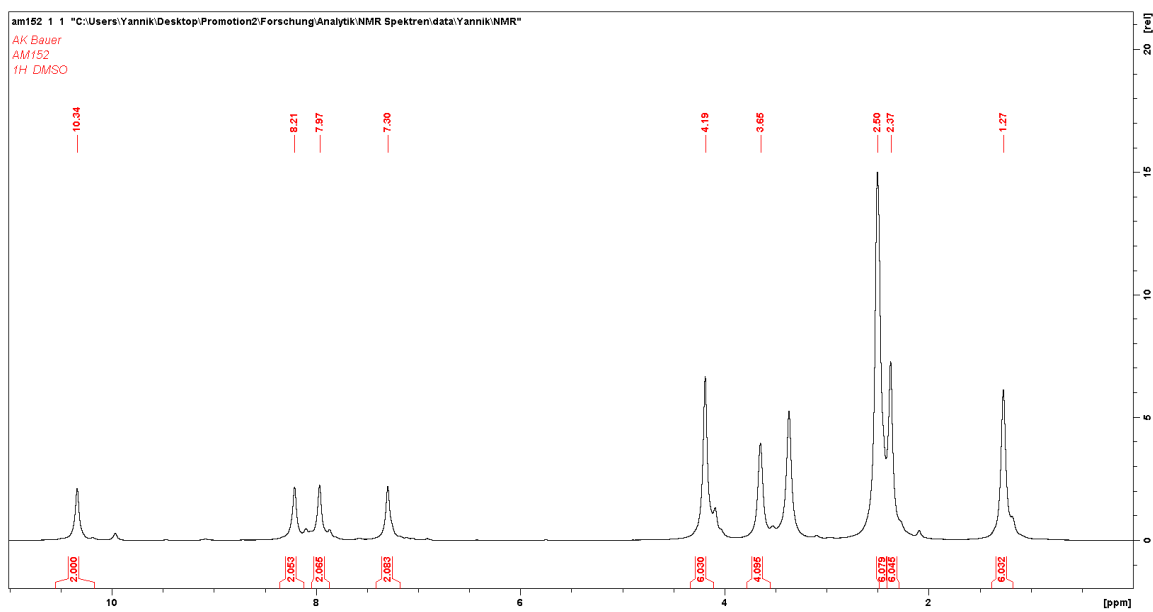
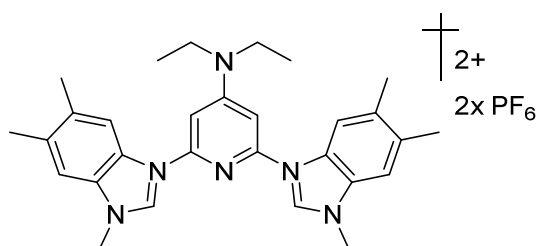


Figure A-0-15: <sup>1</sup>H- (top) and <sup>13</sup>C-NMR spectra (bottom) of **BmbP<sup>NEt</sup><sub>2</sub>** (**L15**) in DMSO at 303 K.

## Crystal data for the iron complex series

**Table A 2:** Crystal data and refinement method of **C1** and **C2**

	<b>C1</b>	<b>C2</b>
Identification code	yv_0075m	Lf_0138a_0138m_a_sq
Empirical formula	C <sub>36</sub> H <sub>45</sub> F <sub>12</sub> FeN <sub>12</sub> P <sub>2</sub>	C <sub>34</sub> H <sub>44</sub> F <sub>12</sub> FeN <sub>12</sub> P <sub>2</sub>
Formula weight [g mol <sup>-1</sup> ]	1033.66	966.60
Temperature [K]	130(2)	130(2)
Wavelength [Å]	0.71073	0.71073
Crystal system	Monoclinic	Monoclinic
Space group	C2/c	C2/c
Unit cell dimensions [Å]; [°]	a = 29.091(3), $\alpha$ = 90	a = 12.463(5), $\alpha$ = 90
	b = 11.4129(14), $\beta$ = 108.154(2)	b = 24.451(9), $\beta$ = 102.222(5)
	c = 27.650(3), $\gamma$ = 90	c = 14.890(6), $\gamma$ = 90
Volume [Å <sup>3</sup> ]	8723.1(18)	4435(3)
Z	8	4
Density (calculated) [Mg m <sup>-3</sup> ]	1.574	1.448
Absorption coefficient [mm <sup>-1</sup> ]	0.519	0.503
F(000)	4240	1984
Crystal size [mm <sup>3</sup> ]	0.5 x 0.28 x 0.24	0.500 x 0.200 x 0.020
$\theta$ range [°]	1.473 to 28.310	1.666 to 25.377
Index ranges	-34 ≤ h ≤ 38, -15 ≤ k ≤ 15, -36 ≤ l ≤ 35	-14 ≤ h ≤ 14, -29 ≤ k ≤ 21, -17 ≤ l ≤ 17
Reflections collected	43658	13127
Independent reflections	10825 [R(int) = 0.0429]	4047 [R(int) = 0.0887]
Completeness to $\theta$ [%]	100.0	100
Refinement method	Full-matrix least-squares on F <sup>2</sup>	Full-matrix least-squares on F <sup>2</sup>
Data / restraints/ parameters	10825 / 210 / 708	4047 / 0 / 277
Goodness of fit on F <sup>2</sup>	1.030	1.041
Final R indices	R1 = 0.0473, wR2 = 0.1115	R1 = 0.0709, wR2 = 0.1817
R indices (all data)	R1 = 0.0684, wR2 = 0.1218	R1 = 0.1180, wR2 = 0.2081
Extinction coefficient	n/a	n/a
Largest diff. peak and hole [e Å <sup>-3</sup> ]	0.528 and -0.432	1.131 and -1.167

**Table A 3: Crystal data and refinement method of C3 and C4**

	<b>C3</b>	<b>C4</b>
Identification code	yv_0080n_0m_a_sq	Yv_0002m
Empirical formula	C <sub>40</sub> H <sub>55</sub> F <sub>12</sub> FeN <sub>13</sub> P <sub>2</sub>	C <sub>60</sub> H <sub>48</sub> F <sub>12</sub> FeN <sub>12</sub> P <sub>2</sub>
Formula weight [g mol <sup>-1</sup> ]	1063.76	1280.57
Temperature [K]	120(2)	130(2)
Wavelength [Å]	0.71073	0.71073
Crystal system	Triclinic	Triclinic
Space group	P-1	P -1
Unit cell dimensions [Å]; [°]	a = 13.3157(7), $\alpha$ = 85.340(2)	a = 12.935(4), $\alpha$ = 74.490(10)
	b = 14.0815(8), $\beta$ = 67.487(2)	b = 13.593(5), $\beta$ = 85.207(8)
	c = 15.5312(9), $\gamma$ = 71.434(2)	c = 16.633(5), $\gamma$ = 72.386(8)
Volume [Å <sup>3</sup> ]	2547.5(3)	2685.9(15)
Z	2	2
Density (calculated) [Mg m <sup>-3</sup> ]	1.387	1.583
Absorption coefficient [mm <sup>-1</sup> ]	0.446	0.630
F(000)	1100	1304
Crystal size [mm <sup>3</sup> ]	0.28 x 0.22 x 0.18	x x
$\theta$ range [°]	2.014 to 29.670	1.270 to 28.431
Index ranges	-18 ≤ h ≤ 18, -19 ≤ k ≤ 19, -21 ≤ l ≤ 21	-17 ≤ h ≤ 17, -18 ≤ k ≤ 18, -22 ≤ l ≤ 22
Reflections collected	282791	27535
Independent reflections	14373 [R(int) = 0.0434]	13294 [R(int) = 0.1796]
Completeness to $\theta$ [%]	99.7	99.9
Refinement method	Full-matrix least-squares on F <sup>2</sup>	Full-matrix least-squares on F <sup>2</sup>
Data / restraints/ parameters	14373 / 0 / 630	13294 / 0 / 720
Goodness of fit on F <sup>2</sup>	1.078	0.932
Final R indices	R1 = 0.0476, wR2 = 0.1266	R1 = 0.1021, wR2 = 0.1837
R indices (all data)	R1 = 0.0624, wR2 = 0.1442	R1 = 0.3204, wR2 = 0.2638
Extinction coefficient	n/a	n/a
Largest diff. peak and hole [e Å <sup>-3</sup> ]	0.812 and -0.543	0.659 and -0.574

**Table A 4:** Crystal data and refinement method of **C6** and **C7**

	<b>C6</b>	<b>C7</b>
Identification code	yv_0004m	Yv_0087m_a
Empirical formula	C <sub>54</sub> H <sub>52</sub> F <sub>12</sub> FeN <sub>12</sub> P <sub>2</sub>	C <sub>58</sub> H <sub>60</sub> F <sub>12</sub> FeN <sub>12</sub> P <sub>2</sub>
Formula weight [g mol <sup>-1</sup> ]	1214.86	1270.97
Temperature [K]	130(2)	130(2)
Wavelength [Å]	0.71073	0.71073
Crystal system	Tetragonal	Triclinic
Space group	I-4 c2	P -1
Unit cell dimensions [Å]; [°]	a = 17.086(3), α = 90	a = 14.0446(15), α = 116.862(2)
	b = 17.086(3), β = 90	b = 15.3561(17), β = 103.285(3)
	c = 18.366(3), γ = 90	c = 15.8979(17), γ = 93.317(2)
Volume [Å <sup>3</sup> ]	5362(2)	2924.8(6)
Z	4	2
Density (calculated) [Mg m <sup>-3</sup> ]	1.505	1.443
Absorption coefficient [mm <sup>-1</sup> ]	0.434	0.401
F(000)	2496	1312
Crystal size [mm <sup>3</sup> ]	0.2 x 0.3 x 0.42	0.460 x 0.420 x 0.240
θ range [°]	1.686 to 27.877	1.499 to 28.305
Index ranges	-22 ≤ h ≤ 22, -22 ≤ k ≤ 22, -24 ≤ l ≤ 23	-18 ≤ h ≤ 18, -20 ≤ k ≤ 20, -21 ≤ l ≤ 21
Reflections collected	25054	30358
Independent reflections	3197 [R(int) = 0.1045]	14417 [R(int) = 0.0406]
Completeness to θ [%]	100	99.9
Refinement method	Full-matrix least-squares on F <sup>2</sup>	Full-matrix least-squares on F <sup>2</sup>
Data / restraints/ parameters	3197 / 0 / 187	1417 / 0 / 796
Goodness of fit on F <sup>2</sup>	1.020	1.028
Final R indices	R1 = 0.0730, wR2 = 0.1761	R1 = 0.0650, wR2 = 0.1539
R indices (all data)	R1 = 0.1363, wR2 = 0.2137	R1 = 0.1131, wR2 = 0.1773
Extinction coefficient	n/a	n/a
Largest diff. peak and hole [e Å <sup>-3</sup> ]	0.613 and -0.272	0.865 and -0.325

**Table A 5: Crystal data and refinement method of C9 and C12**

	<b>C9</b>	<b>C12</b>
Identification code	yv_0150_0150m_a_sq	Am_0141_0141ma_a_pl_sq
Empirical formula	C <sub>73.94</sub> H <sub>68.93</sub> F <sub>12</sub> FeN <sub>12.46</sub> P <sub>2</sub> O <sub>0.75</sub>	C <sub>38</sub> H <sub>52</sub> F <sub>12</sub> FeN <sub>12</sub> P <sub>2</sub>
Formula weight [g mol <sup>-1</sup> ]	1489.96	1022.7
Temperature [K]	130(2)	130(2)
Wavelength [Å]	0.71073	0.71073
Crystal system	Triclinic	Hexagonal
Space group	P-1	P6 <sub>2</sub> 22
Unit cell dimensions [Å]; [°]	a = 14.5433(14), α = 87.047(2) b = 23.060(2), β = 89.532(2) c = 24.632(2), γ = 72.739(2)	a = 12.8103(10), α = 90 b = 12.8103(10), β = 90 c = 28.373(3), γ = 120
Volume [Å <sup>3</sup> ]	7878.2(13)	4032.3(8)
Z	4	3
Density (calculated) [Mg m <sup>-3</sup> ]	1.256	1.263
Absorption coefficient [mm <sup>-1</sup> ]	0.309	0.419
F(000)	3079	1584
Crystal size [mm <sup>3</sup> ]	0.42 x 0.38 x 0.36	0.500 x 0.320 x 0.280
θ range [°]	0.828 to 24.517	1.836 to 25.408
Index ranges	-16 ≤ h ≤ 16, -26 ≤ k ≤ 26, -26 ≤ l ≤ 28	-15 ≤ h ≤ 15, -15 ≤ k ≤ 15, -33 ≤ l ≤ 34
Reflections collected	61572	32938
Independent reflections	26073 [R(int) = 0.0544]	2501 [R(int) = 0.0558]
Completeness to θ [%]	99.3	100
Refinement method	Full-matrix least-squares on F <sup>2</sup>	Full-matrix least-squares on F <sup>2</sup>
Data / restraints/ parameters	26073 / 14 / 1867	2501 / 10 / 157
Goodness of fit on F <sup>2</sup>	1.015	1.085
Final R indices	R1 = 0.0952, wR2 = 0.2641	R1 = 0.0565, wR2 = 0.1615
R indices (all data)	R1 = 0.1428, wR2 = 0.3006	R1 = 0.0683, wR2 = 0.1696
Extinction coefficient	n/a	n/a
Largest diff. peak and hole [e Å <sup>-3</sup> ]	1.812 and -1.188	0.513 and -0.203

**Table A 6:** Crystal data and refinement method of **C13** and **C14**

	<b>C13</b>	<b>C14</b>
Identification code	YV_0038n_0m	Yv_0045n_0m_a_sq
Empirical formula	C <sub>42</sub> H <sub>60</sub> F <sub>12</sub> FeN <sub>12</sub> P <sub>2</sub>	C <sub>50</sub> H <sub>52</sub> F <sub>12</sub> FeN <sub>12</sub> P <sub>2</sub>
Formula weight [g mol <sup>-1</sup> ]	1078.81	1166.82
Temperature [K]	120(2)	120(2)
Wavelength [Å]	0.71073	0.71073
Crystal system	Triclinic	Monoclinic
Space group	P-1	P2 <sub>1/n</sub>
Unit cell dimensions [Å]; [°]	a = 9.7880(12), α = 89.721(4) b = 12.2362(15), β = 77.022(4) c = 20.778(3), γ = 79.294(4)	a = 13.2591(8), α = 90 b = 27.2362(17), β = 107.05(2) c = 16.5914(10), γ = 90
Volume [Å <sup>3</sup> ]	2381.0(5)	5728.3(6)
Z	2	4
Density (calculated) [Mg m <sup>-3</sup> ]	1.505	1.353
Absorption coefficient [mm <sup>-1</sup> ]	0.477	0.403
F(000)	1120	2400
Crystal size [mm <sup>3</sup> ]	0.24 x 0.12 x 0.1	0.300 x 0.280 x 0.080
θ range [°]	1.938 to 26.491	1.971 to 26.415
Index ranges	-12 ≤ h ≤ 12, -15 ≤ k ≤ 15, -25 ≤ l ≤ 25	-15 ≤ h ≤ 16, -34 ≤ k ≤ 34, -20 ≤ l ≤ 20
Reflections collected	147560	170316
Independent reflections	9798 [R(int) = 0.0417]	11697 [R(int) = 0.0787]
Completeness to θ [%]	99.9	99.8
Refinement method	Full-matrix least-squares on F <sup>2</sup>	Full-matrix least-squares on F <sup>2</sup>
Data / restraints/ parameters	9798 / 0 / 641	11697 / 18 / 709
Goodness of fit on F <sup>2</sup>	1.103	1.011
Final R indices	R1 = 0.0323, wR2 = 0.0881	R1 = 0.0754, wR2 = 0.1957
R indices (all data)	R1 = 0.0411, wR2 = 0.0971	R1 = 0.0917, wR2 = 0.2111
Extinction coefficient	n/a	n/a
Largest diff. peak and hole [e Å <sup>-3</sup> ]	0.40 and -0.429	1.434 and -0.855

**Table A 7:** Crystal data and refinement method of **C15**

<b>C15</b>	
Identification code	YV_0042n_0m_a
Empirical formula	C <sub>62</sub> H <sub>74</sub> F <sub>12</sub> FeN <sub>14</sub> P <sub>2</sub>
Formula weight [g mol <sup>-1</sup> ]	1361.14
Temperature [K]	120(2)
Wavelength [Å]	0.71073
Crystal system	Monoclinic
Space group	Cc
	a = 16.2106(5), α = 90
Unit cell dimensions [Å]; [°]	b = 16.2067(5), β = 99.7710(10)
	c = 24.6854(8), γ = 90
Volume [Å <sup>3</sup> ]	6391.3(3)
Z	4
Density (calculated) [Mg m <sup>-3</sup> ]	1.415
Absorption coefficient [mm <sup>-1</sup> ]	0.373
F(000)	2832
Crystal size [mm <sup>3</sup> ]	0.18 x 0.16 x 0.1
θ range [°]	2.299 to 25.040
Index ranges	-19 ≤ h ≤ 19, -19 ≤ k ≤ 19, -29 ≤ l ≤ 29
Reflections collected	88366
Independent reflections	11271 [R(int) = 0.0399]
Completeness to θ [%]	99.6
Refinement method	Full-matrix least-squares on F <sup>2</sup>
Data / restraints/ parameters	11271 / 2 / 824
Goodness of fit on F <sup>2</sup>	1.038
Final R indices	R1 = 0.0459, wR2 = 0.1209
R indices (all data)	R1 = 0.0469, wR2 = 0.1217
Extinction coefficient	n/a
Largest diff. peak and hole [e Å <sup>-3</sup> ]	0.704 and -0.464

# $^1\text{H}$ - and $^{13}\text{C}$ -NMR-Spectra for the iron complex series

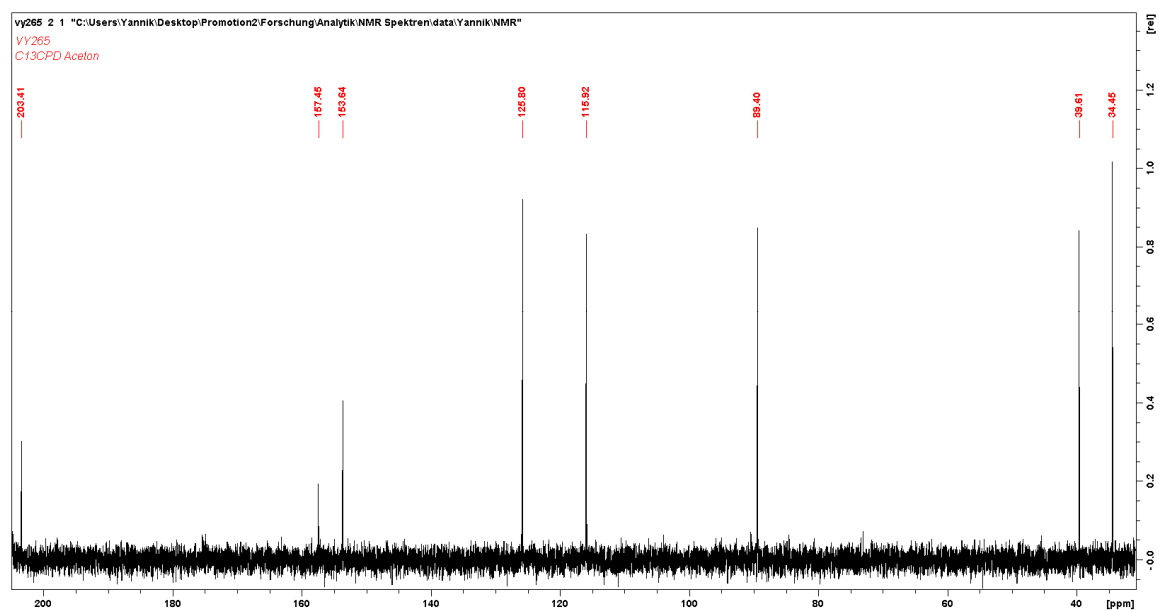
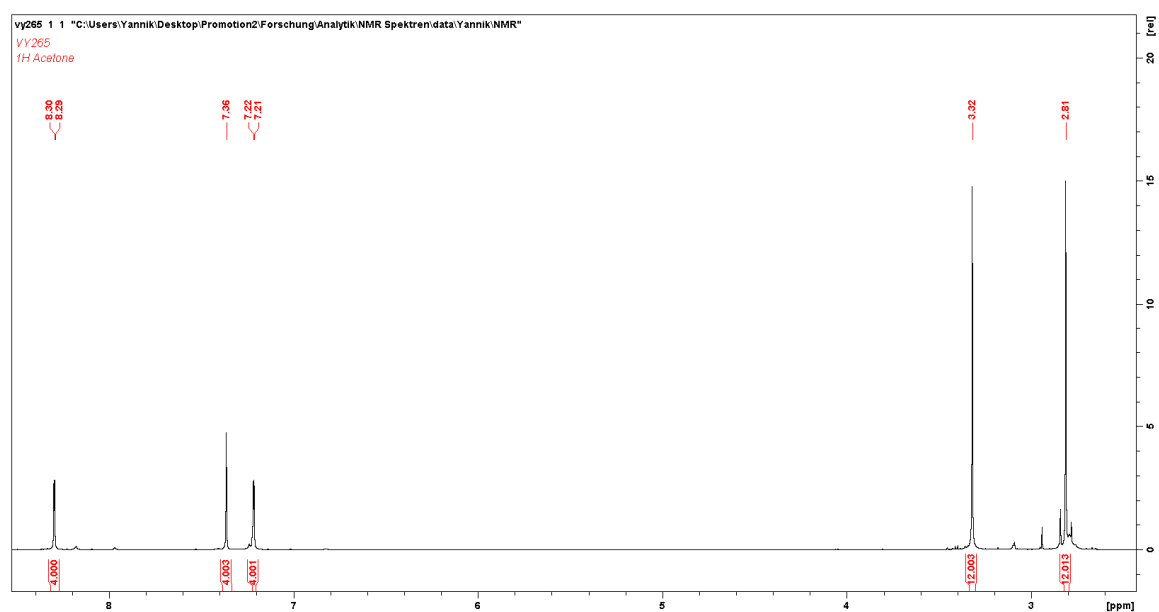
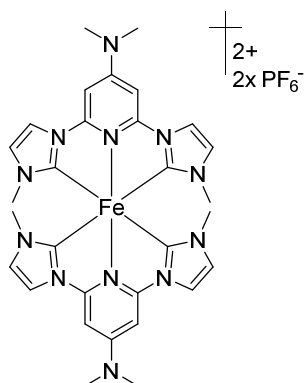


Figure A-0-16:  $^1\text{H}$ - (top) and  $^{13}\text{C}$ -NMR spectra (bottom) of  $[\text{Fe}(\text{BiP}^{\text{NMe}_2})_2][\text{PF}_6]_2$  (C1) in  $(\text{CD}_3)_2\text{CO}$  at 303 K.

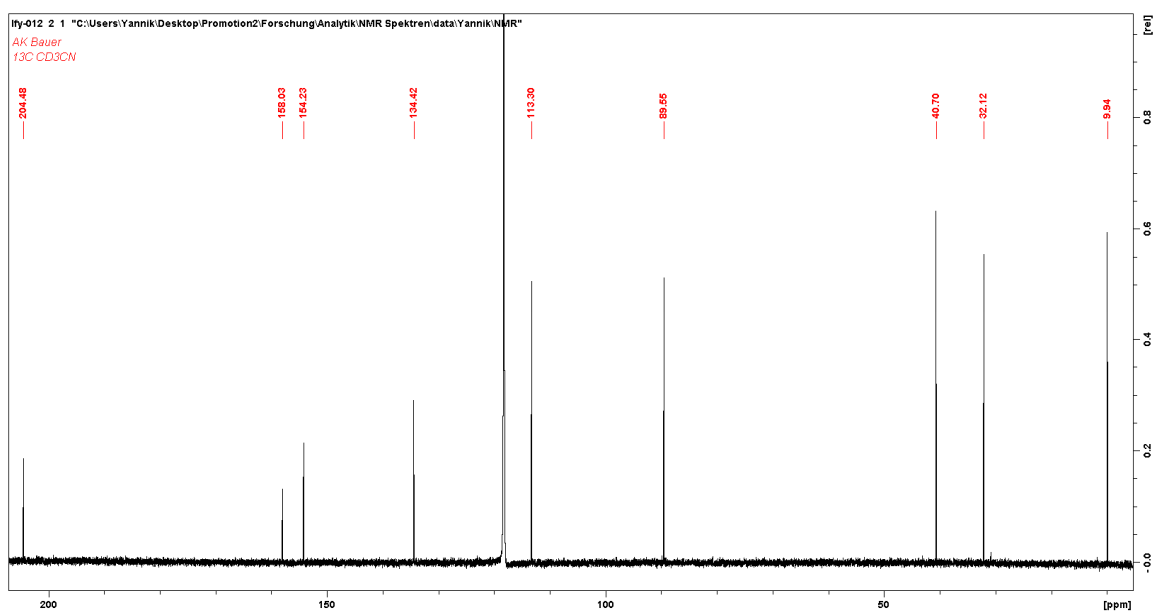
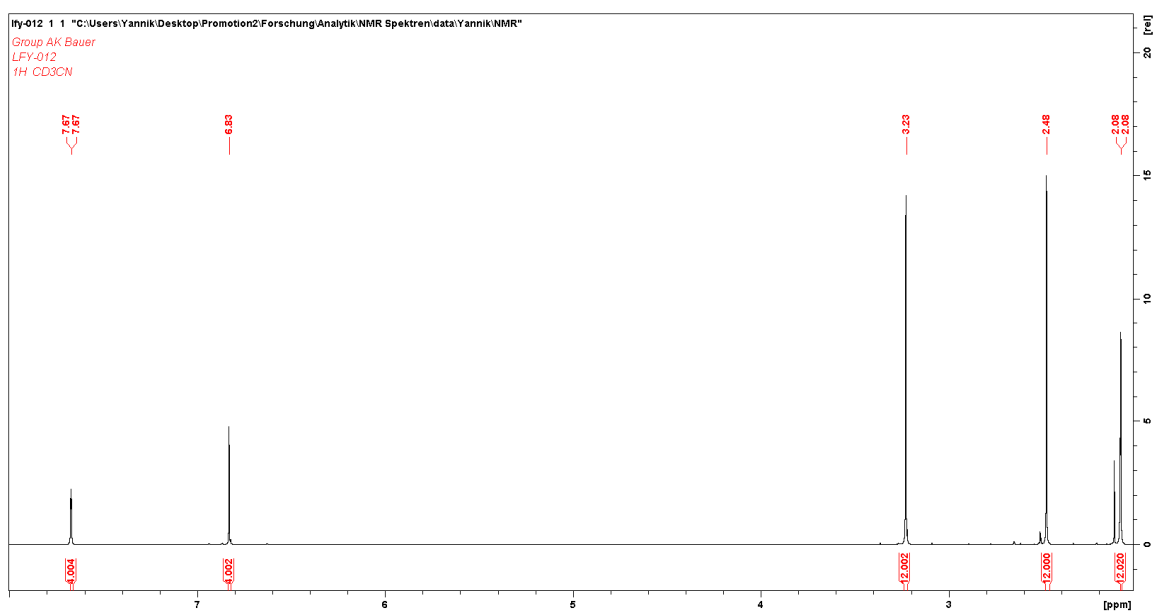
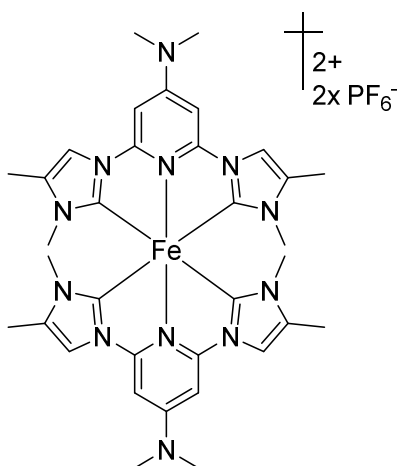


Figure A-0-17:  $^1H$ - (top) and  $^{13}C$ -NMR spectra (bottom) of  $[Fe(BmiP^{NMe_2})_2][PF_6]_2$  (C2) in MeCN at 303 K.

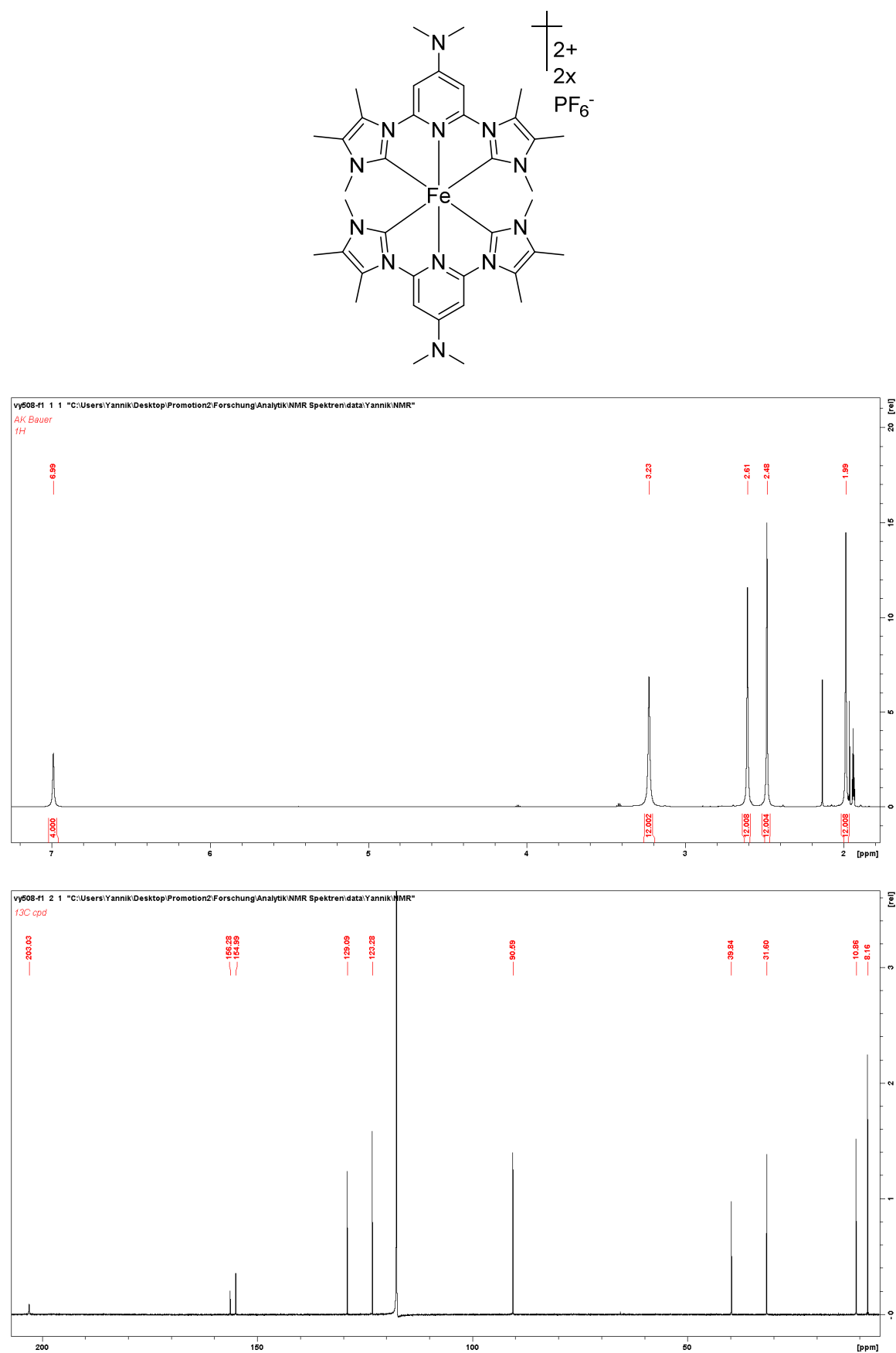


Figure A-0-18: <sup>1</sup>H- (top) and <sup>13</sup>C-NMR spectra (bottom) of [Fe(BdmiP<sup>NMe2</sup>)<sub>2</sub>][PF<sub>6</sub>]<sub>2</sub> (C3) in MeCN at 303 K.

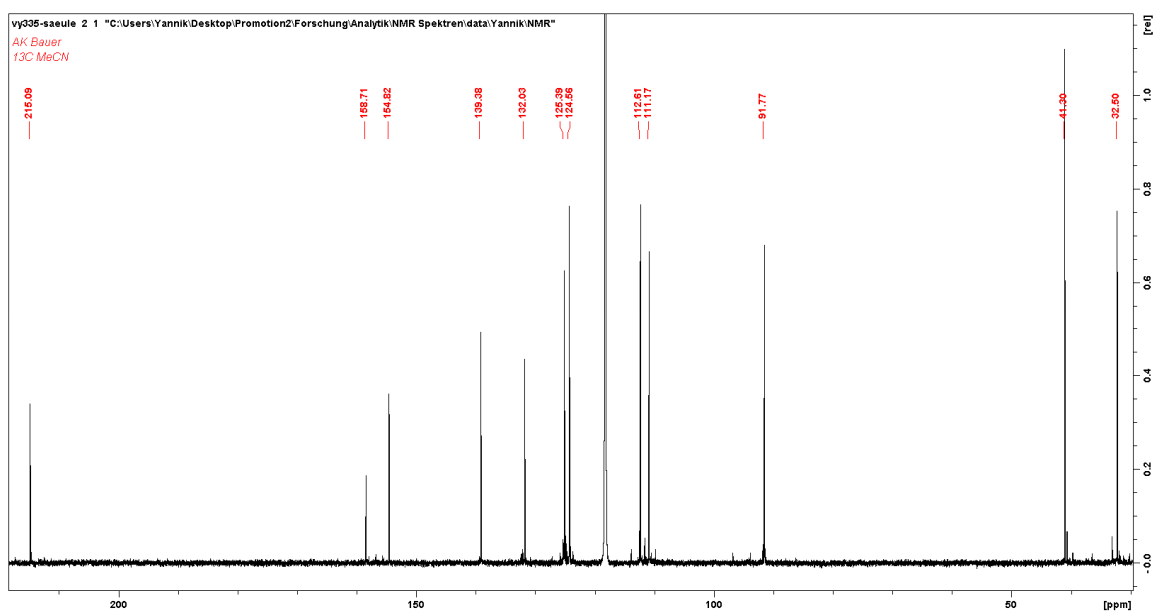
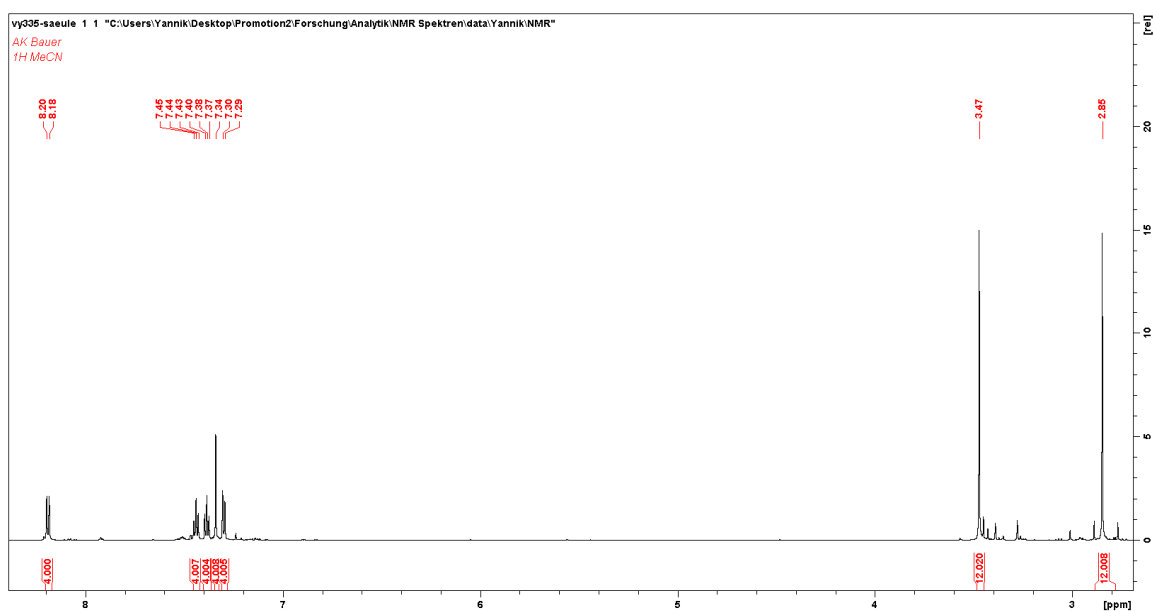
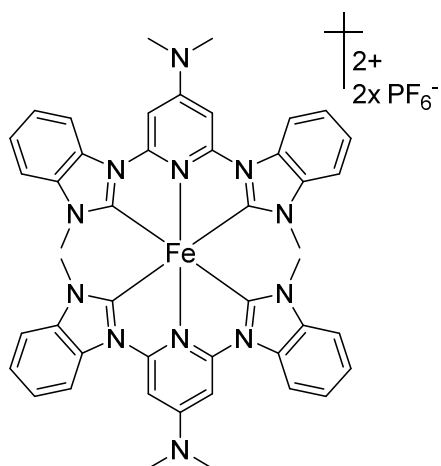


Figure A-0-19:  $^1H$ - (top) and  $^{13}C$ -NMR spectra (bottom) of  $[Fe(BbP^{NMe_2})_2][PF_6]_2$  (C4) in MeCN at 303 K.

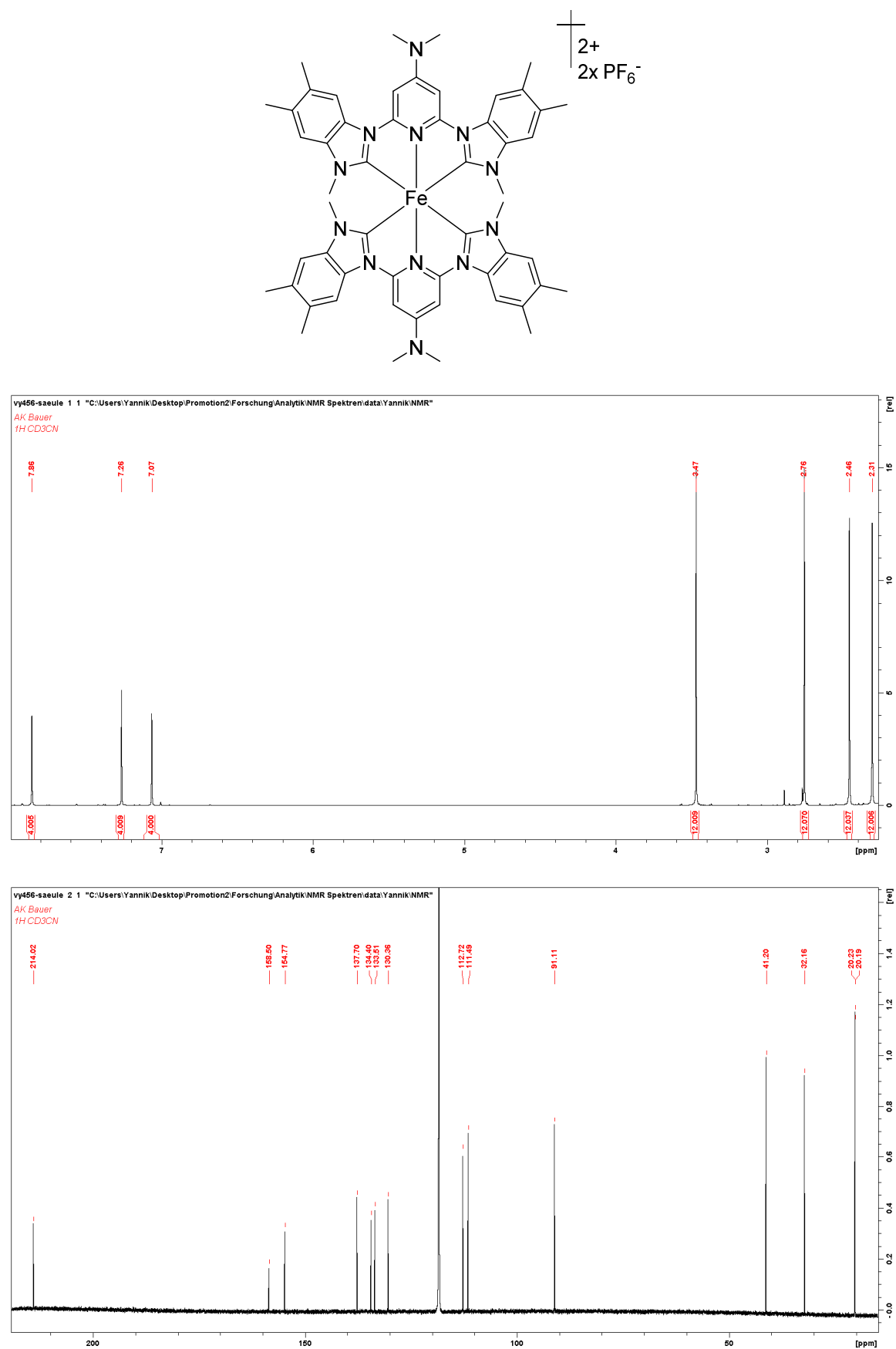


Figure A-0-20:  $^1H$ - (top) and  $^{13}C$ -NMR spectra (bottom) of  $[Fe(BmbP^{NMe_2})_2][PF_6]_2$  (C5) in MeCN at 303 K.

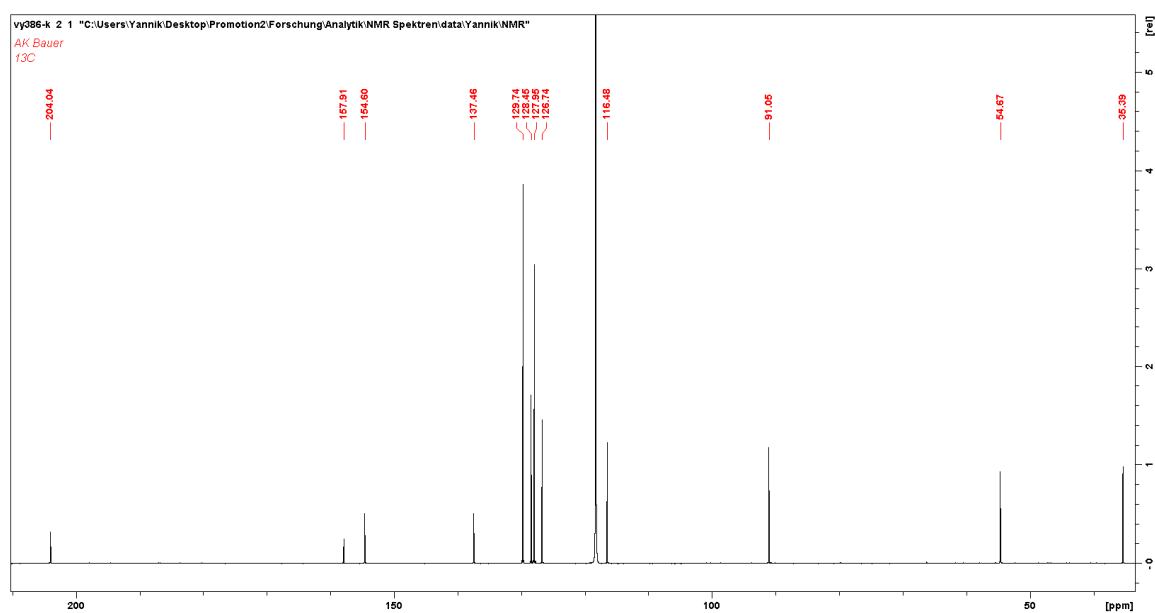
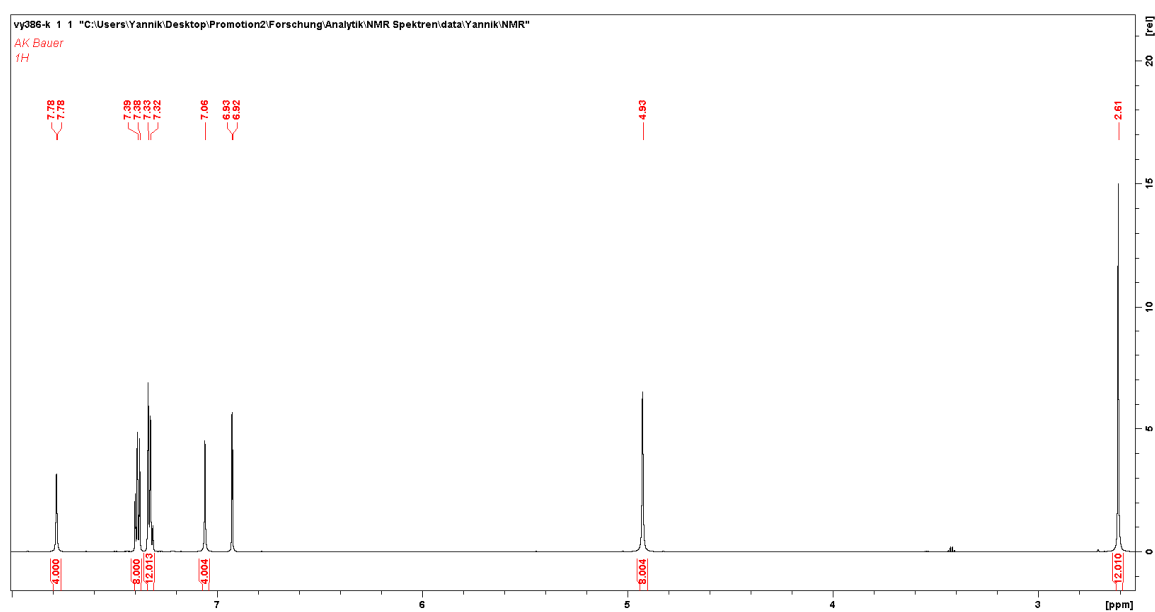
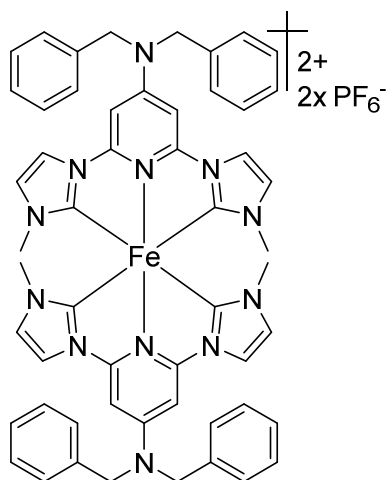


Figure A-0-21:  $^1H$ - (top) and  $^{13}C$ -NMR spectra (bottom) of  $[Fe(BIP^{NBn2})_2][PF_6]_2$  (C6) in MeCN at 303 K.

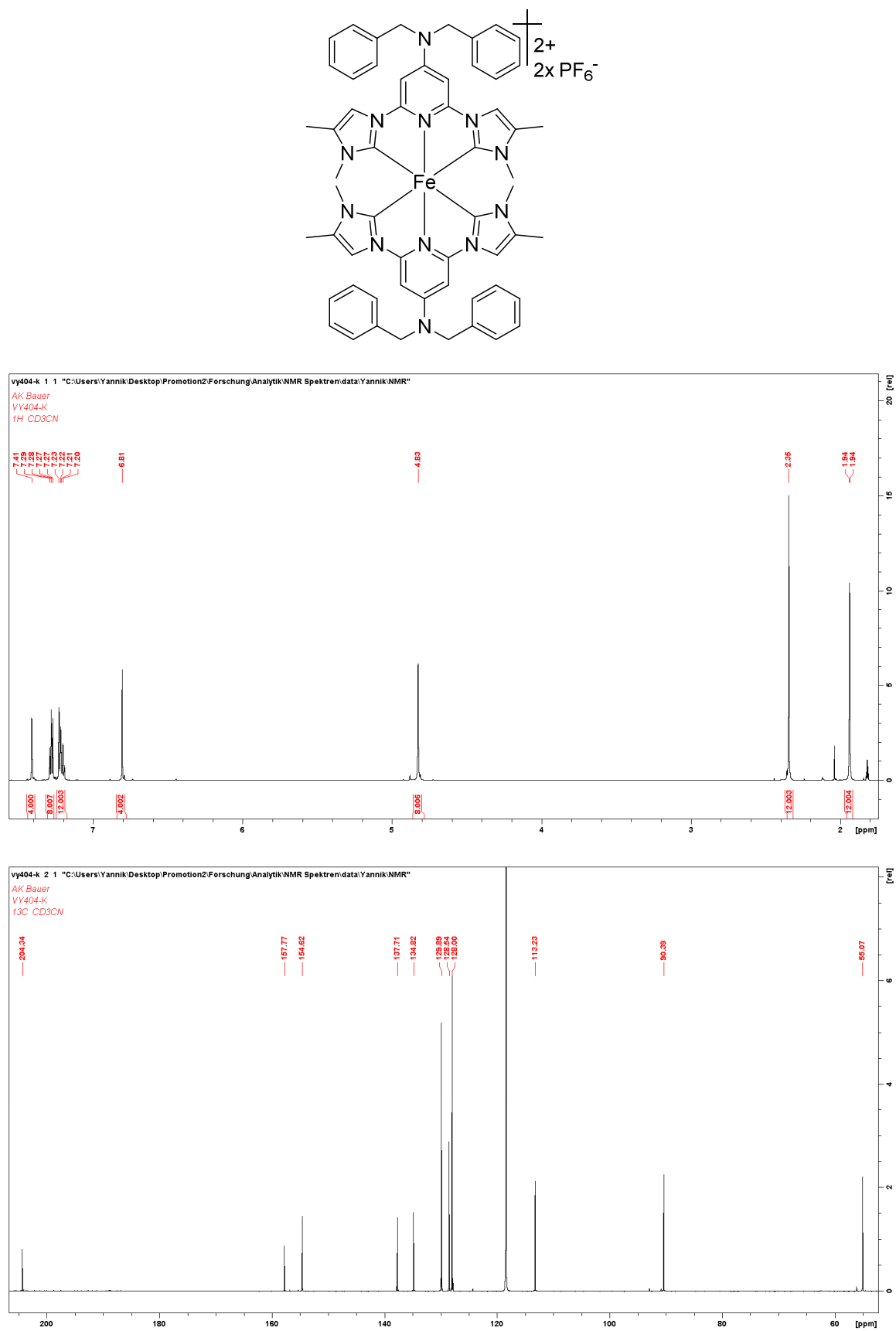


Figure A-0-22:  $^1\text{H}$ - (top) and  $^{13}\text{C}$ -NMR spectra (bottom) of  $[\text{Fe}(\text{BmiP}^{\text{NBn2}})_2][\text{PF}_6]_2$  (C7) in MeCN at 303 K.

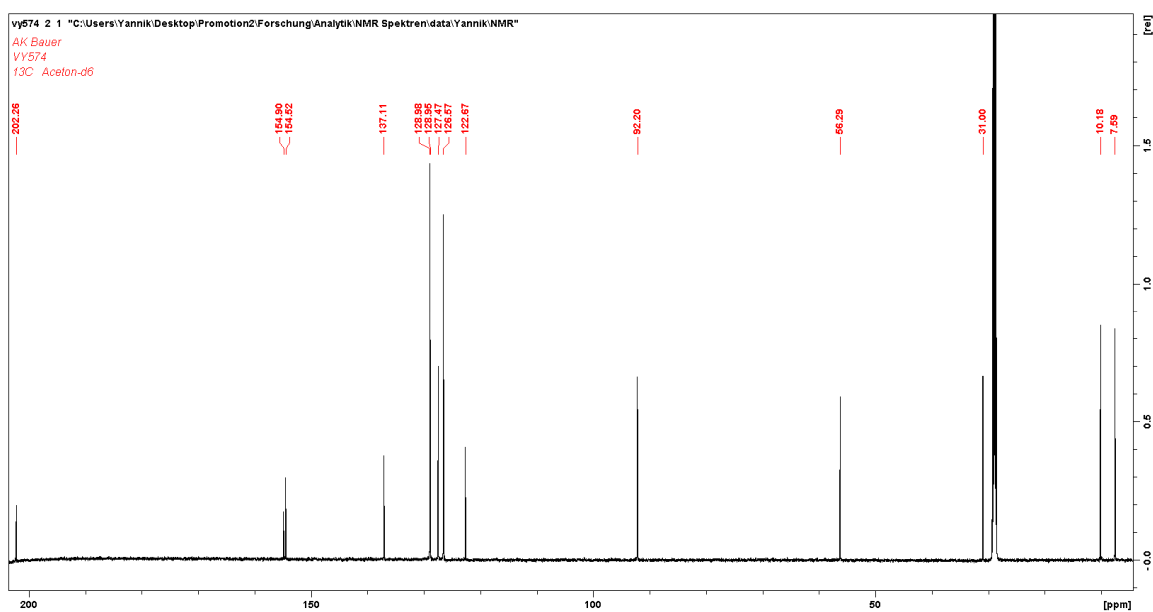
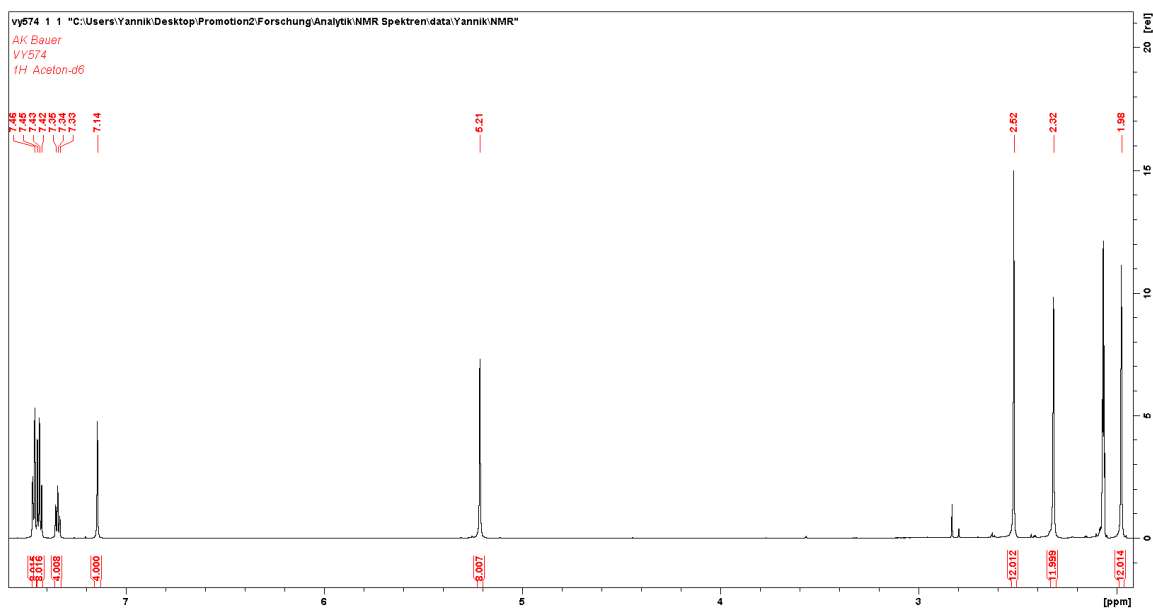
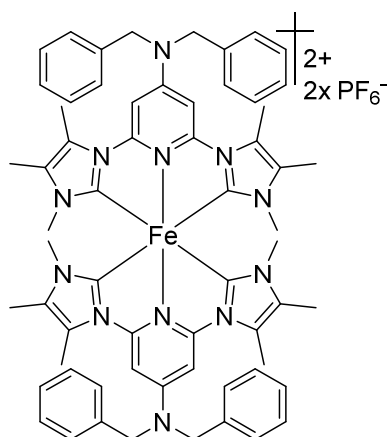


Figure A-0-23: <sup>1</sup>H- (top) and <sup>13</sup>C-NMR spectra (bottom) of  $[\text{Fe}(\text{BdmiP}^{\text{NBn}2})_2][\text{PF}_6]_2$  (C8) in MeCN at 303 K.

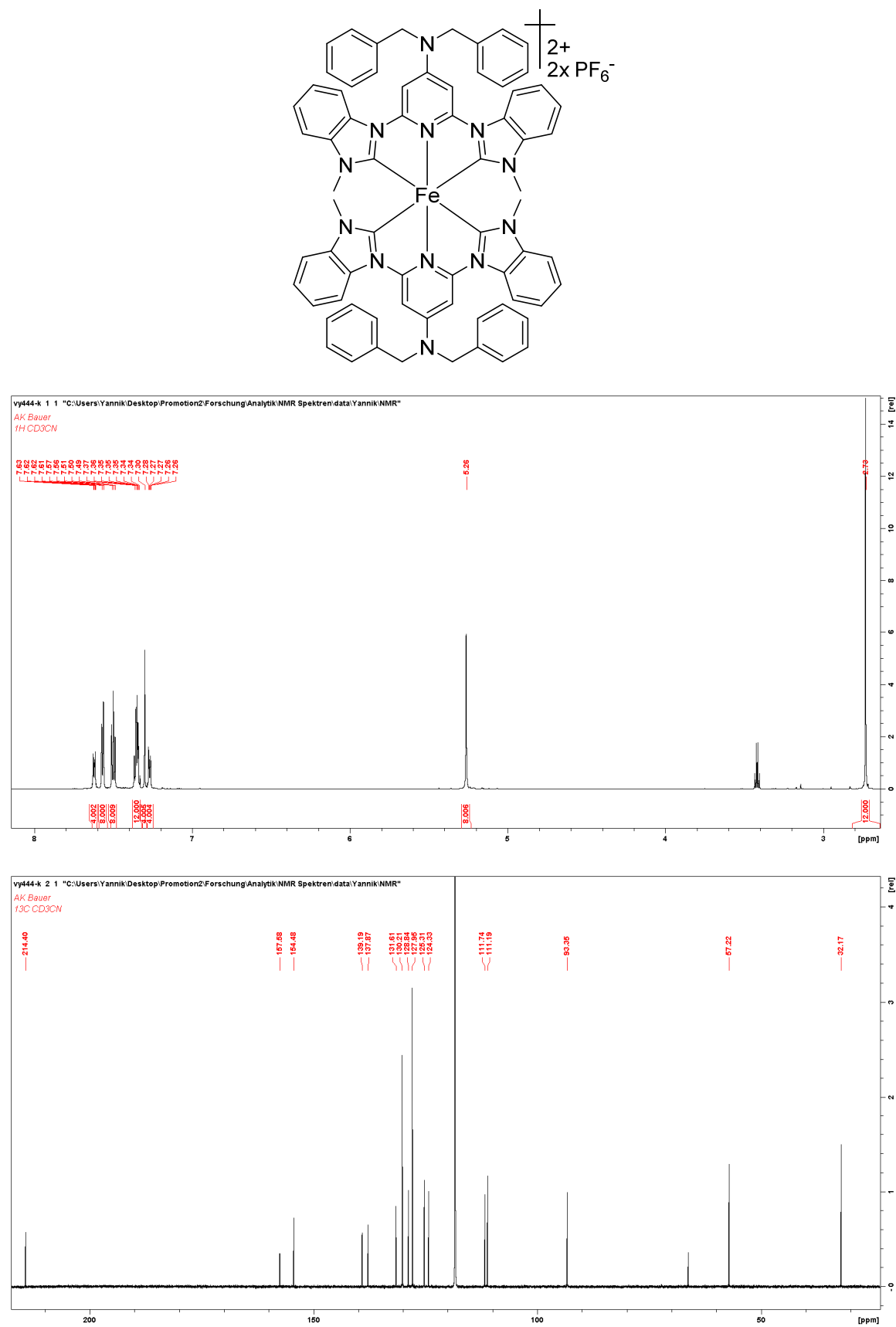


Figure A-0-24: <sup>1</sup>H- (top) and <sup>13</sup>C-NMR spectra (bottom) of [Fe(BbP<sup>NBn2</sup>)<sub>2</sub>][PF<sub>6</sub>]<sub>2</sub> (C9) in MeCN at 303 K.

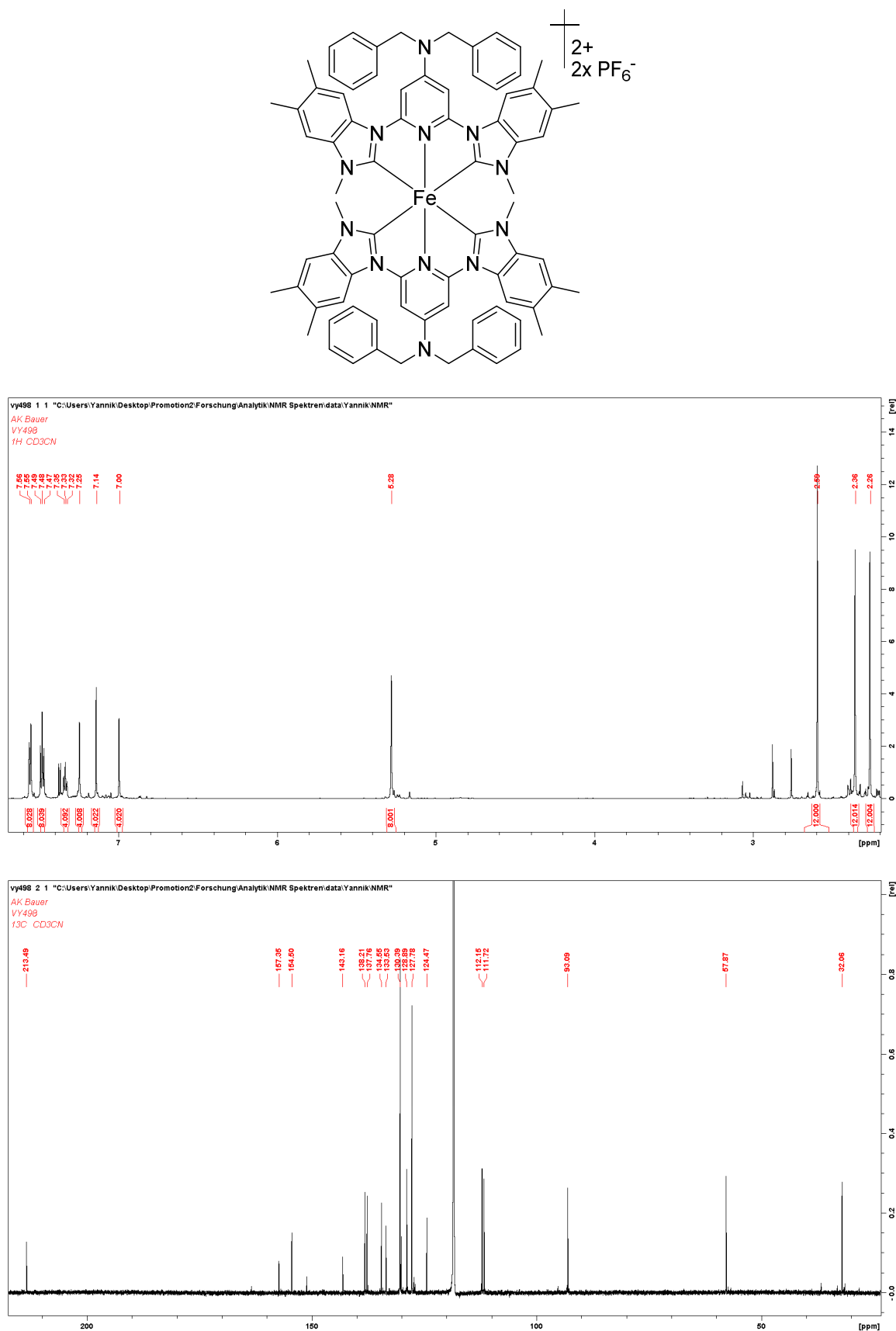


Figure A-0-25:  $^1\text{H}$ - (top) and  $^{13}\text{C}$ -NMR spectra (bottom) of  $[\text{Fe}(\text{BmbP}^{\text{NBn}2})_2][\text{PF}_6]_2$  (C10) in  $\text{MeCN}$  at 303 K.

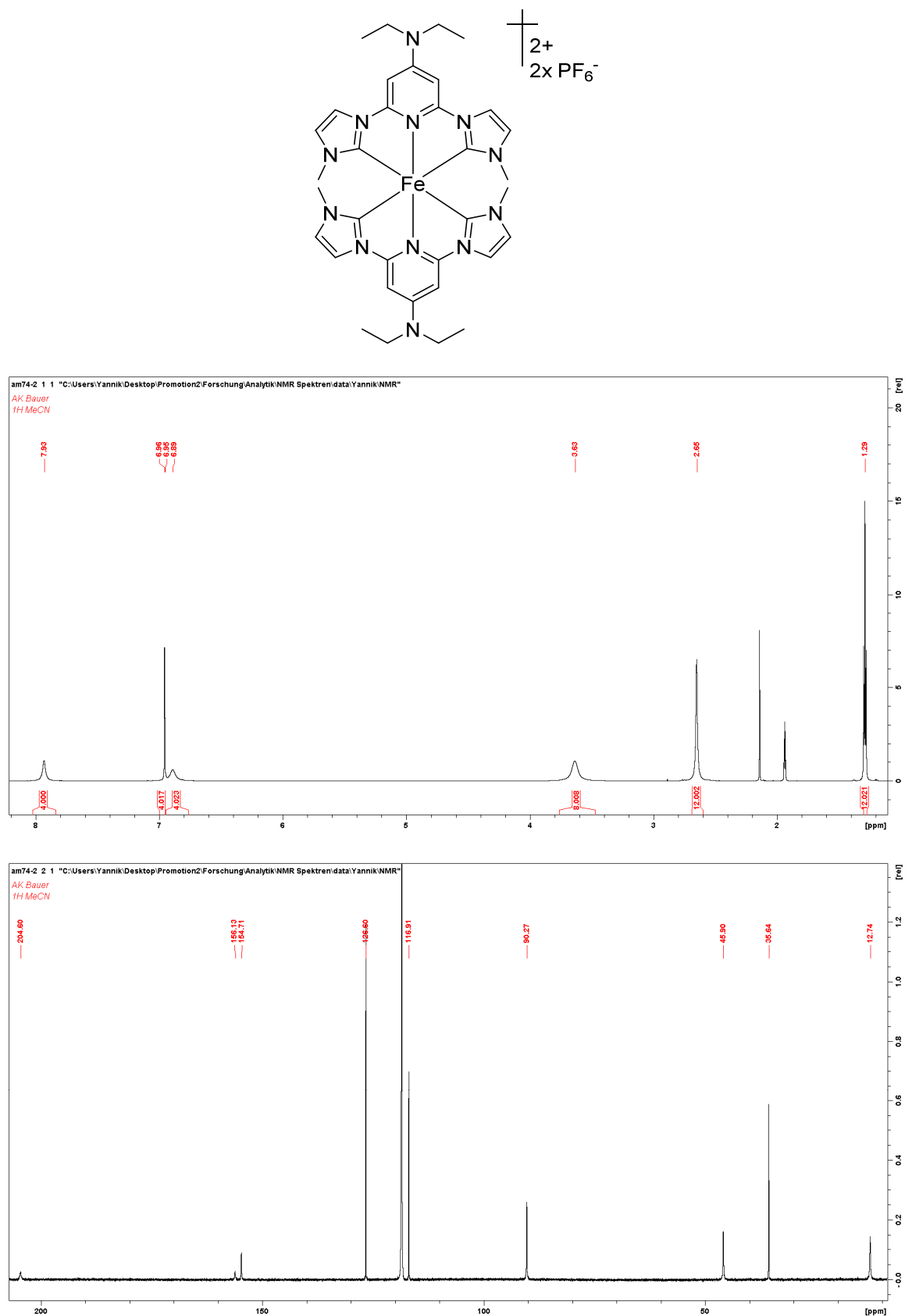


Figure A-0-26: <sup>1</sup>H- (top) and <sup>13</sup>C-NMR spectra (bottom) of  $[Fe(BIP^{NEt_2})_2][PF_6]_2$  (C11) in MeCN at 303 K.

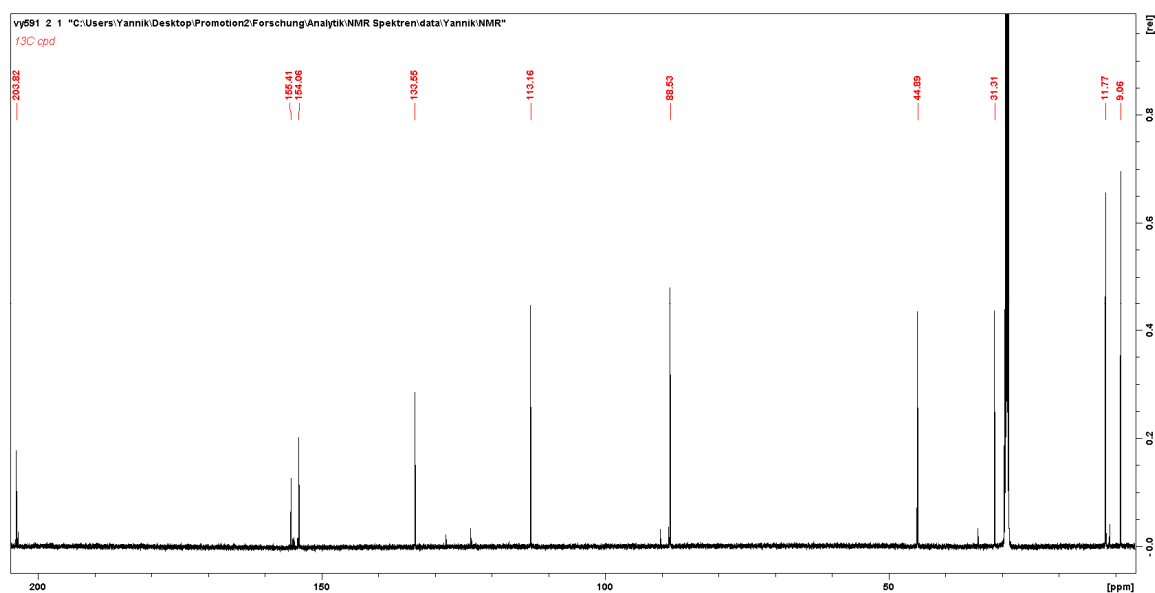
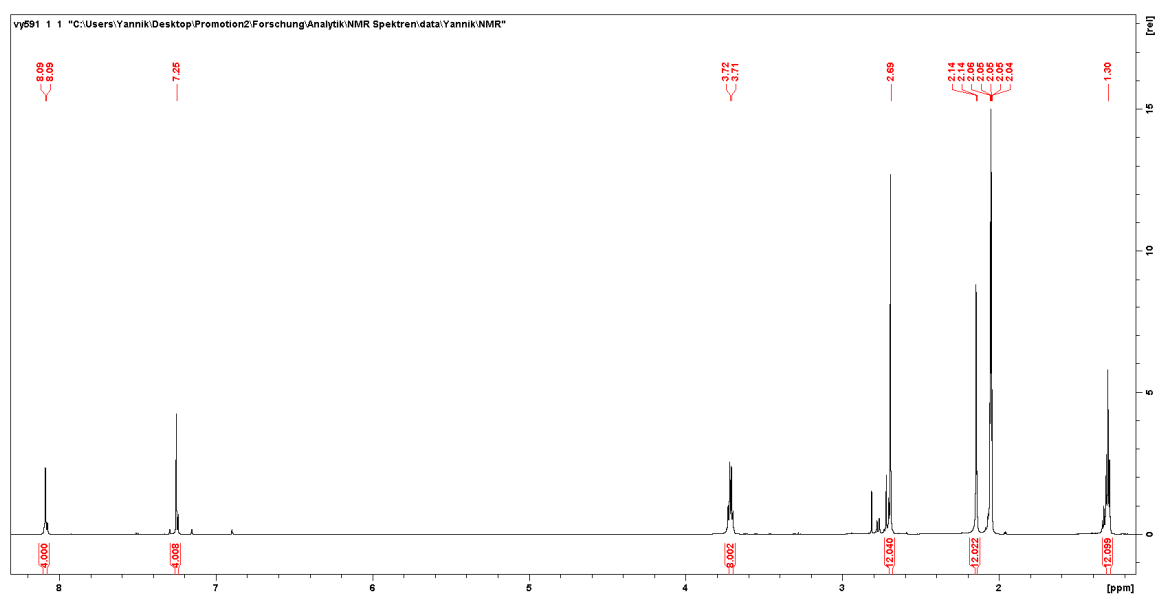
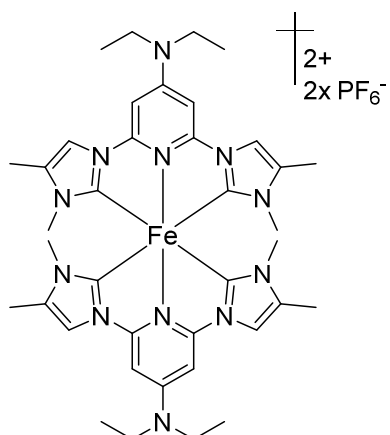


Figure A-0-27: <sup>1</sup>H- (top) and <sup>13</sup>C-NMR spectra (bottom) of [Fe(BmiP<sup>NEt2</sup>)<sub>2</sub>][PF<sub>6</sub>]<sub>2</sub> (C12) in MeCN at 303 K.

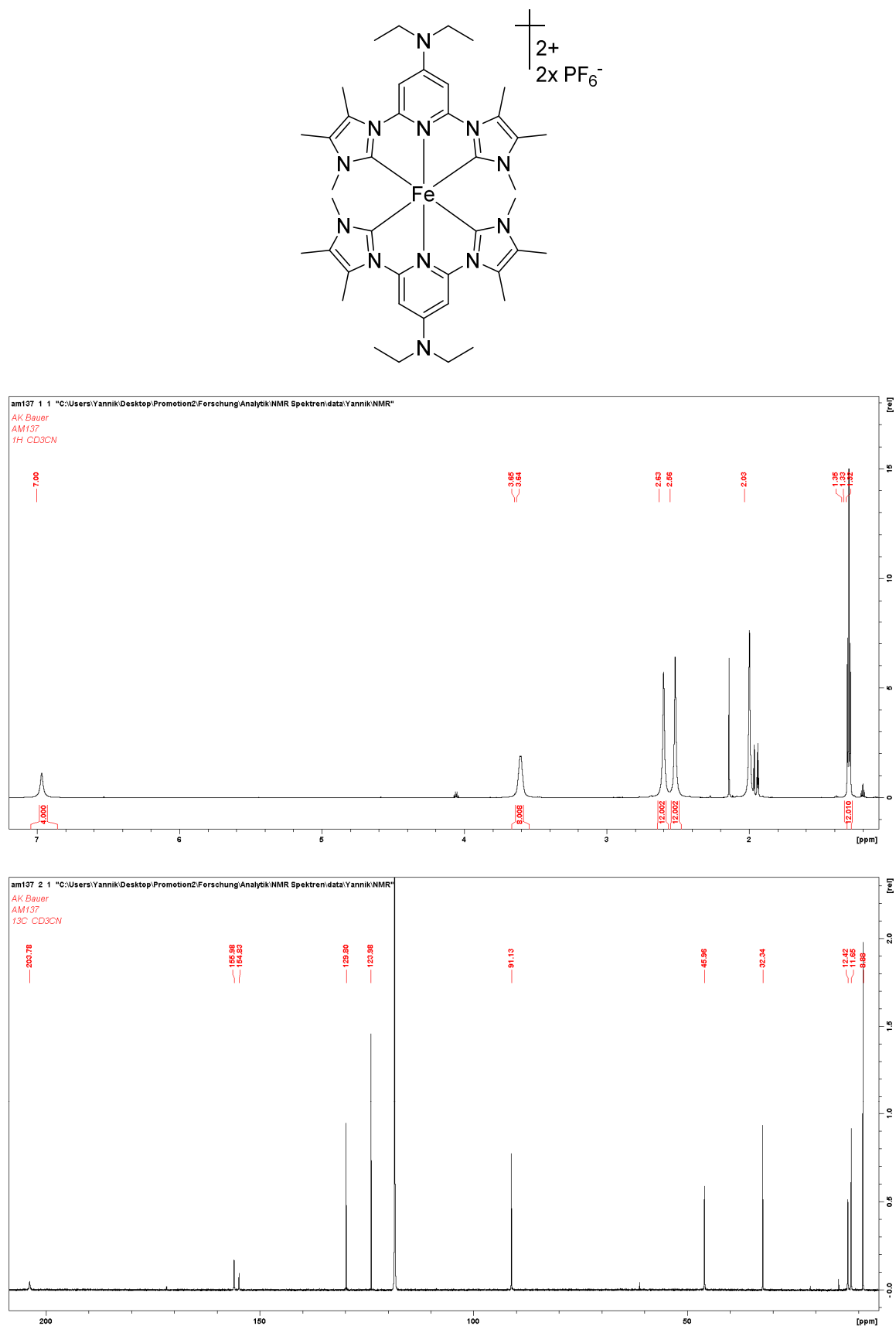


Figure A-0-28:  $^1\text{H}$ - (top) and  $^{13}\text{C}$ -NMR spectra (bottom) of  $[\text{Fe}(\text{BdmiP}^{\text{NEt}_2})_2][\text{PF}_6]_2$  (C13) in MeCN at 303 K.

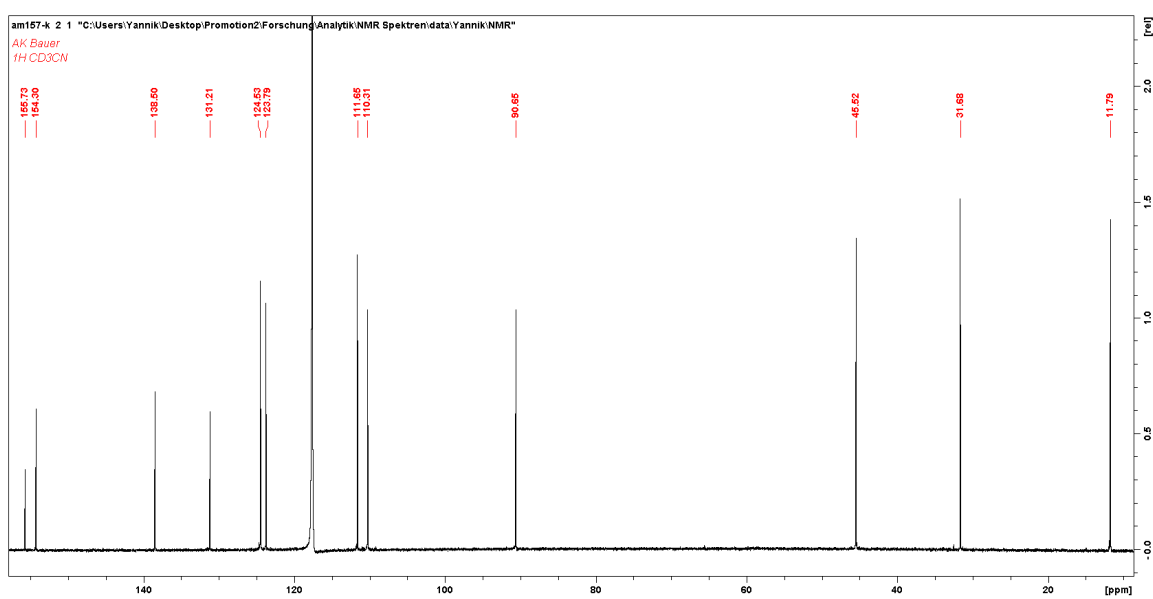
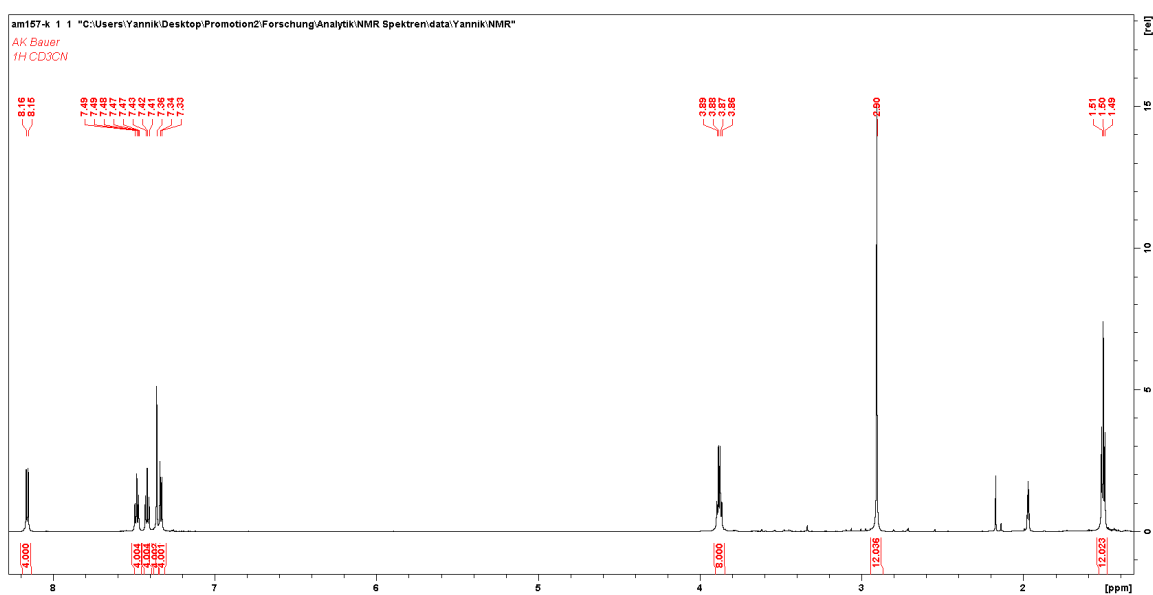
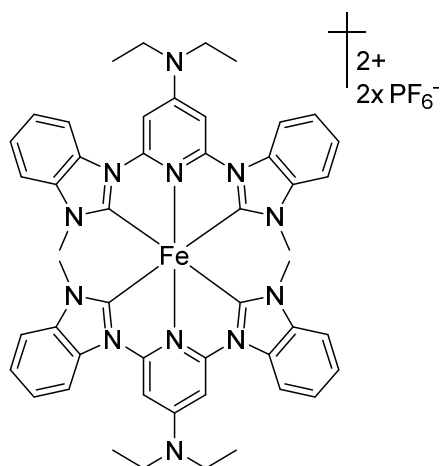


Figure A-0-29: <sup>1</sup>H- (top) and <sup>13</sup>C-NMR spectra (bottom) of [Fe(BbP<sup>NEt2</sup>)<sub>2</sub>][PF<sub>6</sub>]<sub>2</sub> (C14) in MeCN at 303 K.

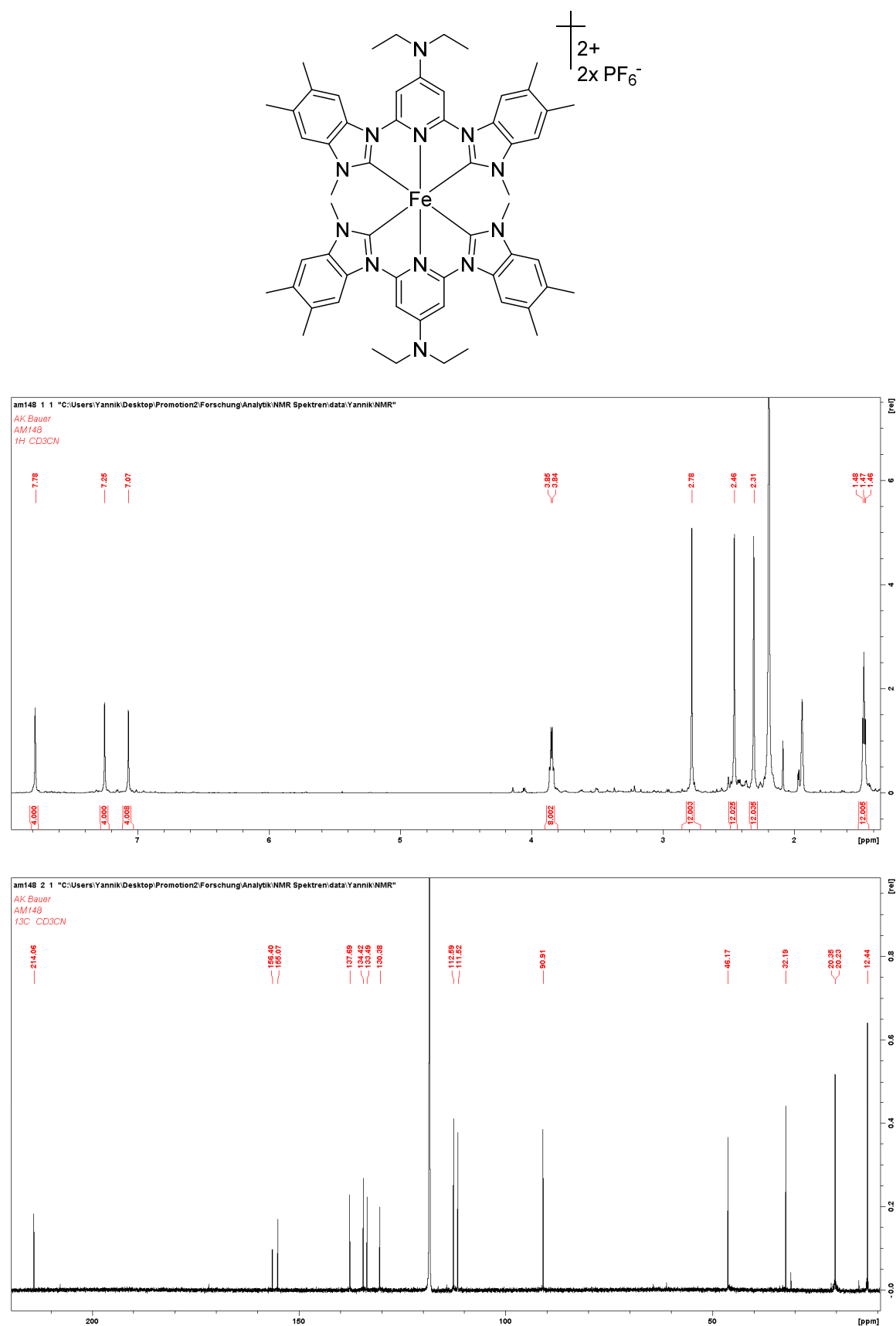


Figure A-0-30:  $^1H$ - (top) and  $^{13}C$ -NMR spectra (bottom) of  $[Fe(BmbP^{NEt_2})_2][PF_6]_2$  (C15) in MeCN at 303 K.

## Electrochemical data for the iron complex series

**Table A 8:** Electrochemical data for the reversible oxidation at  $E^0_{1/2} = -0.023$  V vs Fc/Fc<sup>+</sup> for complex **C1**

V [mV·s <sup>-1</sup> ]	50	100	200	400	800
<b>E<sub>pa</sub> [V]</b>	0.01	0.01	0.012	0.012	0.015
<b>E<sub>pc</sub> [V]</b>	-0.056	-0.059	-0.056	-0.061	-0.061
<b>E<sub>1/2</sub> [V]</b>	-0.023	-0.0245	-0.022	-0.0245	-0.023
<b>ΔE [mV]</b>	66	69	68	73	76
<b>I<sub>pa</sub> [10<sup>-6</sup> A]</b>	1.45	2.19	3.33	4.6	6.53
<b>I<sub>pa</sub>/I<sub>pc</sub></b>	0.94	0.99	0.97	0.98	1
<b>I<sub>pa</sub>/v<sup>0.5</sup></b>	0.205	0.219	0.235	0.23	0.230

**Table A 9:** Electrochemical data for the reversible oxidation at  $E^0_{1/2} = -0.06$  V vs Fc/Fc<sup>+</sup> for complex **C2**

V [mV·s <sup>-1</sup> ]	50	100	200	400	800
<b>E<sub>pa</sub> [V]</b>	-0.026	-0.026	-0.024	-0.026	-0.024
<b>E<sub>pc</sub> [V]</b>	-0.094	-0.094	-0.094	-0.094	-0.096
<b>E<sub>1/2</sub> [V]</b>	-0.06	-0.06	-0.059	-0.06	-0.06
<b>ΔE [mV]</b>	68	68	70	68	72
<b>I<sub>pa</sub> [10<sup>-6</sup> A]</b>	1.09	1.59	2.27	3.18	4.47
<b>I<sub>pa</sub>/I<sub>pc</sub></b>	1.03	1.01	1.01	0.99	0.99
<b>I<sub>pa</sub>/v<sup>0.5</sup></b>	0.154	0.159	0.160	0.159	0.158

**Table A 10:** Electrochemical data for the reversible oxidation at  $E^0_{1/2} = -0.12$  V vs Fc/Fc<sup>+</sup> for complex **C3**

V [mV·s <sup>-1</sup> ]	50	100	200	400	800
<b>E<sub>pa</sub> [V]</b>	-0.092	-0.095	-0.09	-0.09	-0.087
<b>E<sub>pc</sub> [V]</b>	-0.161	-0.163	-0.163	-0.163	-0.166
<b>E<sub>1/2</sub> [V]</b>	-0.1265	-0.129	-0.1265	-0.1265	-0.1265
<b>ΔE [mV]</b>	69	68	73	73	79
<b>I<sub>pa</sub> [10<sup>-6</sup> A]</b>	1.42	1.99	2.78	3.83	5.32
<b>I<sub>pa</sub>/I<sub>pc</sub></b>	1.08	1.08	1.09	1.08	1.09
<b>I<sub>pa</sub>/v<sup>0.5</sup></b>	0.200	0.199	0.196	0.191	0.188

**Table A 11:** Electrochemical data for the reversible oxidation at  $E^{0}_{1/2} = 0.18$  V vs Fc/Fc<sup>+</sup> for complex **C4**

V [mV·s <sup>-1</sup> ]	50	100	200	400	800
E <sub>pa</sub> [V]	0.215	0.217	0.215	0.217	0.219
E <sub>pc</sub> [V]	0.146	0.147	0.146	0.147	0.142
E <sub>1/2</sub> [V]	0.1805	0.182	0.1805	0.182	0.1805
ΔE [mV]	69	70	69	70	77
I <sub>pa</sub> [10 <sup>-6</sup> A]	1.19	1.72	2.47	3.45	4.8
I <sub>pa</sub> /I <sub>pc</sub>	1.14	1	1.01	0.99	0.98
I <sub>pa</sub> /v <sup>0.5</sup>	0.168	0.172	0.174	0.172	0.169

**Table A 12:** Electrochemical data for the reversible oxidation at  $E^{0}_{1/2} = 0.12$  V vs Fc/Fc<sup>+</sup> for complex **C5**

V [mV·s <sup>-1</sup> ]	50	100	200	400	800
E <sub>pa</sub> [V]	0.155	0.157	0.157	0.164	0.172
E <sub>pc</sub> [V]	0.084	0.084	0.076	0.059	0.042
E <sub>1/2</sub> [V]	0.119	0.120	0.117	0.112	0.107
ΔE [mV]	70.8	73.24	80.57	104.99	129.4
I <sub>pa</sub> [10 <sup>-6</sup> A]	0.765	1.11	1.53	2.21	2.969
I <sub>pa</sub> /I <sub>pc</sub>	1.06	1.14	1.06	1.15	1.24
I <sub>pa</sub> /v <sup>0.5</sup>	0.108	0.111	0.108	0.110	0.104

**Table A 13:** Electrochemical data for the reversible oxidation at  $E^{0}_{1/2} = 0.027$  V vs Fc/Fc<sup>+</sup> for complex **C6**

V [mV·s <sup>-1</sup> ]	50	100	200	400	800
E <sub>pa</sub> [V]	0.065	0.062	0.062	0.062	0.06
E <sub>pc</sub> [V]	-0.006	-0.006	-0.008	-0.011	-0.013
E <sub>1/2</sub> [V]	0.029	0.028	0.027	0.025	0.023
ΔE [mV]	71	68	70	73	73
I <sub>pa</sub> [10 <sup>-6</sup> A]	1.02	1.32	1.95	2.82	4.07
I <sub>pa</sub> /I <sub>pc</sub>	0.97	0.99	0.96	0.97	0.97
I <sub>pa</sub> /v <sup>0.5</sup>	0.144	0.132	0.137	0.141	0.143

**Table A 14:** Electrochemical data for the reversible oxidation at  $E^{0}_{1/2} = -0.029$  V vs Fc/Fc<sup>+</sup> for complex **C7**

V [mV·s <sup>-1</sup> ]	50	100	200	400	800
E <sub>pa</sub> [V]	0.006	0.006	0.006	0.006	0.006
E <sub>pc</sub> [V]	-0.062	-0.062	-0.065	-0.065	-0.067
E <sub>1/2</sub> [V]	-0.028	-0.028	-0.029	-0.029	-0.030
ΔE [mV]	68	68	71	71	73
I <sub>pa</sub> [10 <sup>-6</sup> A]	1.36	1.93	2.65	3.74	5.32
I <sub>pa</sub> /I <sub>pc</sub>	1.04	1.02	0.96	0.96	0.97
I <sub>pa</sub> /v <sup>0.5</sup>	0.192	0.193	0.187	0.187	0.188

**Table A 15:** Electrochemical data for the reversible oxidation at  $E^{0}_{1/2} = -0.078$  V vs Fc/Fc<sup>+</sup> for complex **C8**

V [mV·s <sup>-1</sup> ]	50	100	200	400	800
E <sub>pa</sub> [V]	-0.045	-0.042	-0.037	-0.037	-0.028
E <sub>pc</sub> [V]	-0.111	-0.113	-0.118	-0.125	-0.135
E <sub>1/2</sub> [V]	-0.078	-0.077	-0.077	-0.078	-0.081
ΔE [mV]	66	71	81.4	87.9	107.4
I <sub>pa</sub> [10 <sup>-6</sup> A]	0.75	1.048	1.477	2.024	2.58
I <sub>pa</sub> /I <sub>pc</sub>	1.031	1.07	1.1	1.1	1.09
I <sub>pa</sub> /v <sup>0.5</sup>	0.106	0.104	0.104	0.101	0.091

**Table A 16:** Electrochemical data for the reversible oxidation at  $E^{0}_{1/2} = 0.266$  V vs Fc/Fc<sup>+</sup> for complex **C9**

V [mV·s <sup>-1</sup> ]	50	100	200	400	800
E <sub>pa</sub> [V]	0.236	0.233	0.233	0.230	0.230
E <sub>pc</sub> [V]	0.302	0.299	0.302	0.300	0.303
E <sub>1/2</sub> [V]	0.269	0.266	0.267	0.265	0.267
ΔE [mV]	65.91	65.92	68.36	69.49	73.24
I <sub>pa</sub> [10 <sup>-6</sup> A]	0.947	1.375	1.978	2.786	4.13
I <sub>pa</sub> /I <sub>pc</sub>	1.03	1.059	1.06	1.06	1.08
I <sub>pa</sub> /v <sup>0.5</sup>	0.133	0.137	0.139	0.139	0.146

**Table A 17:** Electrochemical data for the reversible oxidation at  $E^{0}_{1/2} = 0.220$  V vs Fc/Fc<sup>+</sup> for complex **C10**

V [mV·s <sup>-1</sup> ]	50	100	200	400	800
E <sub>pa</sub> [V]	0.185	0.180	0.180	0.178	0.166
E <sub>pc</sub> [V]	0.253	0.258	0.263	0.266	0.273
E <sub>1/2</sub> [V]	0.219	0.219	0.221	0.222	0.219
ΔE [mV]	68.4	77.4	82.4	88	107
I <sub>pa</sub> [10 <sup>-6</sup> A]	0.57	0.75	0.99	1.36	1.78
I <sub>pa</sub> /I <sub>pc</sub>	0.8	0.75	0.75	0.74	0.77
I <sub>pa</sub> /v <sup>0.5</sup>	0.08	0.075	0.07	0.07	0.06

**Table A 18:** Electrochemical data for the reversible oxidation at  $E^{0}_{1/2} = -0.038$  V vs Fc/Fc<sup>+</sup> for complex **C11**

V [mV·s <sup>-1</sup> ]	50	100	200	400	800
E <sub>pa</sub> [V]	-0.073	-0.073	-0.080	-0.085	-0.09
E <sub>pc</sub> [V]	0.004	0.002	0.002	0.002	0.004
E <sub>1/2</sub> [V]	-0.034	-0.035	-0.039	-0.041	-0.042
ΔE [mV]	77.8	75.44	82.94	87.44	94.88
I <sub>pa</sub> [10 <sup>-6</sup> A]	1.158	1.58	2.17	2.93	3.93
I <sub>pa</sub> /I <sub>pc</sub>	1.09	0.89	0.87	0.86	0.84
I <sub>pa</sub> /v <sup>0.5</sup>	0.16	0.158	0.2	0.146	0.138

**Table A 19:** Electrochemical data for the reversible oxidation at  $E^{0}_{1/2} = -0.092$  V vs Fc/Fc<sup>+</sup> for complex **C12**

V [mV·s <sup>-1</sup> ]	50	100	200	400	800
E <sub>pa</sub> [V]	-0.124	-0.124	-0.131	-0.139	-0.153
E <sub>pc</sub> [V]	-0.053	-0.053	-0.053	-0.048	-0.039
E <sub>1/2</sub> [V]	-0.089	-0.089	-0.092	-0.093	-0.096
ΔE [mV]	70.8	70.8	78.1	90.3	114.746
I <sub>pa</sub> [10 <sup>-6</sup> A]	1.24	1.68	2.26	2.96	3.7
I <sub>pa</sub> /I <sub>pc</sub>	0.96	0.9	0.88	0.86	0.83
I <sub>pa</sub> /v <sup>0.5</sup>	0.175	0.168	0.159	0.148	0.13

**Table A 20:** Electrochemical data for the reversible oxidation at  $E^{0}_{1/2} = -0.132$  V vs Fc/Fc<sup>+</sup> for complex **C13**

V [mV·s <sup>-1</sup> ]	50	100	200	400	800
<b>E<sub>pa</sub> [V]</b>	-0.168	-0.17	-0.168	-0.173	-0.170
<b>E<sub>pc</sub> [V]</b>	-0.095	-0.097	-0.095	-0.095	-0.090
<b>E<sub>1/2</sub> [V]</b>	-0.131	-0.133	-0.131	-0.134	-0.130
<b>ΔE [mV]</b>	73	73	72.8	77.8	80
<b>I<sub>pa</sub> [10<sup>-6</sup> A]</b>	1.19	1.6	2.19	3.01	4.08
<b>I<sub>pa</sub>/I<sub>pc</sub></b>	0.92	0.89	0.89	0.89	0.88
<b>I<sub>pa</sub>/V<sup>0.5</sup></b>	0.16	0.16	0.154	0.15	0.144

**Table A 21:** Electrochemical data for the reversible oxidation at  $E^{0}_{1/2} = 0.17$  V vs Fc/Fc<sup>+</sup> for complex **C14**

V [mV·s <sup>-1</sup> ]	50	100	200	400	800
<b>E<sub>pa</sub> [V]</b>	0.135	0.13	0.118	0.098	0.079
<b>E<sub>pc</sub> [V]</b>	0.208	0.216	0.2185	0.225	0.238
<b>E<sub>1/2</sub> [V]</b>	0.172	0.173	0.168	0.162	0.158
<b>ΔE [mV]</b>	73.245	86.06	100.1	126.925	158.66
<b>I<sub>pa</sub> [10<sup>-6</sup> A]</b>	0.651	0.87	1.22	1.54	1.9
<b>I<sub>pa</sub>/I<sub>pc</sub></b>	1.21	0.96	0.92	0.89	0.87
<b>I<sub>pa</sub>/V<sup>0.5</sup></b>	0.092	0.087	0.086	0.077	0.067

**Table A 22:** Electrochemical data for the reversible oxidation at  $E^{0}_{1/2} = 0.11$  V vs Fc/Fc<sup>+</sup> for complex **C14**

V [mV·s <sup>-1</sup> ]	50	100	200	400	800
<b>E<sub>pa</sub> [V]</b>	0.074	0.072	0.072	0.067	0.059
<b>E<sub>pc</sub> [V]</b>	0.147	0.150	0.150	0.152	0.154
<b>E<sub>1/2</sub> [V]</b>	0.111	0.111	0.111	0.109	0.107
<b>ΔE [mV]</b>	73.23	78.14	78.1	85.48	95.19
<b>I<sub>pa</sub> [10<sup>-6</sup> A]</b>	0.805	1.13	1.61	2.2	3.03
<b>I<sub>pa</sub>/I<sub>pc</sub></b>	1.07	1.01	1.05	1.04	1.1
<b>I<sub>pa</sub>/V<sup>0.5</sup></b>	0.113	0.113	0.113	0.11	0.107

## Crystal data for the ruthenium complex series

Table A 23: Crystal data and refinement method of C16 and C18

	C16	C18
Identification code	YV_0240_0240m_a	YV_0199_0m
Empirical formula	C <sub>36</sub> H <sub>45</sub> F <sub>12</sub> RuN <sub>15</sub> P <sub>2</sub>	C <sub>40</sub> H <sub>55</sub> F <sub>12</sub> RuN <sub>13</sub> P <sub>2</sub>
Formula weight [g mol <sup>-1</sup> ]	1078.88	1108.98
Temperature [K]	130(2)	130(2)
Wavelength [Å]	0.71073	0.71073
Crystal system	Monoclinic	Triclinic
Space group	C 2/c	P-1
Unit cell dimensions [Å]; [°]	a = 28.6848(15), $\alpha$ = 90 b = 11.6015(6), $\beta$ = 108.0270(10) c = 27.7843(14), $\gamma$ = 90	a = 9.8309(5), $\alpha$ = 73.0170(10) b = 14.1968(8), $\beta$ = 84.8800(10) c = 17.9474(10), $\gamma$ = 85.125(10)
Volume [Å <sup>3</sup> ]	8792.4(8)	2381.5(2)
Z	8	2
Density (calculated) [Mg m <sup>-3</sup> ]	1.630	1.546
Absorption coefficient [mm <sup>-1</sup> ]	0.529	0.489
F(000)	4384	1136
Crystal size [mm <sup>3</sup> ]	0.48 x 0.40 x 0.30	0.440 x 0.260 x 0.220
$\theta$ range [°]	1.493 to 31.173	1.503 to 31.083
Index ranges	-40 ≤ h ≤ 39, -16 ≤ k ≤ 16, -39 ≤ l ≤ 37	-14 ≤ h ≤ 13, -20 ≤ k ≤ 20, -26 ≤ l ≤ 25
Reflections collected	51128	28348
Independent reflections	13349 [R(int) = 0.0353]	13959 [R(int) = 0.0294]
Completeness to $\theta$ [%]	99.9	100.0
Refinement method	Full-matrix least-squares on F <sup>2</sup>	Full-matrix least-squares on F <sup>2</sup>
Data / restraints/ parameters	13349 / 30 / 603	13959 / 0 / 630
Goodness of fit on F <sup>2</sup>	1.032	1.041
Final R indices	R1 = 0.0641, wR2 = 0.1738	R1 = 0.0391, wR2 = 0.0871
R indices (all data)	R1 = 0.0798, wR2 = 0.1896	R1 = 0.0503, wR2 = 0.0947
Extinction coefficient	n/a	n/a
Largest diff. peak and hole [e Å <sup>-3</sup> ]	3.126 and -1.664	0.721 and -0.508

**Table A 24:** Crystal data and refinement method of **C19** and **C20**

	<b>C19</b>	<b>C20</b>
Identification code	YV_0098n_0m_a_sq	YV_0190_0190m_a
Empirical formula	C <sub>50</sub> H <sub>50</sub> F <sub>12</sub> RuN <sub>14</sub> P <sub>2</sub>	C <sub>31.99</sub> H <sub>39.08</sub> F <sub>6</sub> Ru <sub>0.5</sub> N <sub>7.70</sub> PO <sub>0.40</sub>
Formula weight [g mol <sup>-1</sup> ]	1238.05	733.30
Temperature [K]	120(2)	130(2)
Wavelength [Å]	0.71073	0.71073
Crystal system	Triclinic	Triclinic
Space group	P-1	P-1
Unit cell dimensions [Å]; [°]	a = 12.963(7), α = 80.219(18) b = 14.714(8), β = 68.341(17) c = 16.481(9), γ = 71.591(18)	a = 11.4987(6), α = 102.2450(10) b = 11.7511(6), β = 95.1540(10) c = 25.5106(13), γ = 92.859(10)
Volume [Å <sup>3</sup> ]	2767(3)	3346.6(3)
Z	2	4
Density (calculated) [Mg m <sup>-3</sup> ]	1.486	1.455
Absorption coefficient [mm <sup>-1</sup> ]	0.431	0.370
F(000)	1260	1516
Crystal size [mm <sup>3</sup> ]	0.280 x 0.240 x 0.080	0.440 x 0.380 x 0.100
θ range [°]	2.540 to 31.971	0.821 to 31.197
Index ranges	-19 ≤ h ≤ 19, -21 ≤ k ≤ 21, -24 ≤ l ≤ 24	-16 ≤ h ≤ 16, -16 ≤ k ≤ 16, -37 ≤ l ≤ 36
Reflections collected	303983	39944
Independent reflections	19002 [R(int) = 0.0809]	19613 [R(int) = 0.0283]
Completeness to θ [%]	99.9	100.0
Refinement method	Full-matrix least-squares on F <sup>2</sup>	Full-matrix least-squares on F <sup>2</sup>
Data / restraints/ parameters	19002 / 0 / 759	19613 / 2 / 944
Goodness of fit on F <sup>2</sup>	1.089	1.030
Final R indices	R1 = 0.0489, wR2 = 0.1163	R1 = 0.0397, wR2 = 0.0944
R indices (all data)	R1 = 0.0743, wR2 = 0.1374	R1 = 0.0513, wR2 = 0.1005
Extinction coefficient	n/a	n/a
Largest diff. peak and hole [e Å <sup>-3</sup> ]	1.376 and -1.361	0.577 and -0.488

**Table A 25: Crystal data and refinement method of C22 and C24**

	<b>C22</b>	<b>C24</b>
Identification code	YV_0078n_0ma_b	YV_0100n_0m_a_sq
Empirical formula	C <sub>58</sub> H <sub>60</sub> F <sub>12</sub> RuN <sub>12</sub> P <sub>2</sub>	C <sub>78</sub> H <sub>76</sub> F <sub>12</sub> RuN <sub>12</sub> P <sub>2</sub>
Formula weight [g mol <sup>-1</sup> ]	1316.19	1572.51
Temperature [K]	120(2)	120(2)
Wavelength [Å]	0.71073	0.71073
Crystal system	Tetragonal	Triclinic
Space group	I-4c2	P-1
Unit cell dimensions [Å]; [°]	a = 18.2479(8), α = 90 b = 18.2479(8), β = 90 c = 17.4212(7), γ = 90	a = 11.5471(15), α = 81.991(4) b = 11.5619(15), β = 84.110(4) c = 33.918(5), γ = 89.483(4)
Volume [Å <sup>3</sup> ]	5801.0(6)	4460.3(10)
Z	4	2
Density (calculated) [Mg m <sup>-3</sup> ]	1.507	1.171
Absorption coefficient [mm <sup>-1</sup> ]	0.415	0.281
F(000)	2696	1620
Crystal size [mm <sup>3</sup> ]	0.260 x 0.180 x 0.120	0.240 x 0.200 x 0.080
θ range [°]	2.756 to 29.711	1.933 to 28.383
Index ranges	-25 ≤ h ≤ 25, -25 ≤ k ≤ 25, -24 ≤ l ≤ 24	-15 ≤ h ≤ 15, -15 ≤ k ≤ 15, -45 ≤ l ≤ 45
Reflections collected	170757	350590
Independent reflections	4091 [R(int) = 0.0807]	22280 [R(int) = 0.0860]
Completeness to θ [%]	99.0	99.9
Refinement method	Full-matrix least-squares on F <sup>2</sup>	Full-matrix least-squares on F <sup>2</sup>
Data / restraints/ parameters	4091 / 0 / 198	22280 / 9 / 919
Goodness of fit on F <sup>2</sup>	1.074	1.149
Final R indices	R1 = 0.0341, wR2 = 0.0797	R1 = 0.0803, wR2 = 0.1977
R indices (all data)	R1 = 0.0354, wR2 = 0.0809	R1 = 0.0905, wR2 = 0.2035
Extinction coefficient	n/a	n/a
Largest diff. peak and hole [e Å <sup>-3</sup> ]	0.557 and -0.279	1.258 and -1.142

**Table A 26: Crystal data and refinement method of C26 and C28**

	<b>C26</b>	<b>C28</b>
Identification code	shelx	YV_0115n_0ma_a
Empirical formula	C <sub>34</sub> H <sub>44</sub> F <sub>12</sub> RuN <sub>12</sub> P <sub>2</sub>	C <sub>43</sub> H <sub>61.50</sub> F <sub>12</sub> RuN <sub>12.50</sub> P <sub>2</sub>
Formula weight [g mol <sup>-1</sup> ]	1011.82	1144.55
Temperature [K]	130(2)	120(2)
Wavelength [Å]	0.71073	0.71073
Crystal system	Monoclinic	Monoclinic
Space group	C2/m	C2/c
	a = 16.042(3), $\alpha$ = 90	a = 38.570(4), $\alpha$ = 90
Unit cell dimensions [Å]; [°]	b = 39.198(8), $\beta$ = 125.416(3)	b = 14.7013(12), $\beta$ = 91.478(5)
	c = 10.834(2), $\gamma$ = 90	c = 18.0275(15), $\gamma$ = 90
Volume [Å <sup>3</sup> ]	5552(2)	10218.8(15)
Z	4	8
Density (calculated) [Mg m <sup>-3</sup> ]	1.210	1.488
Absorption coefficient [mm <sup>-1</sup> ]	0.413	0.458
F(000)	2056	4712
Crystal size [mm <sup>3</sup> ]	0.35 x 0.28 x 0.24	0.30 x 0.18 x 0.14
$\theta$ range [°]	1.039 to 25.456	1.856 to 28.282
Index ranges	-19 ≤ h ≤ 19, -47 ≤ k ≤ 47, -13 ≤ l ≤ 13	-51 ≤ h ≤ 51, -19 ≤ k ≤ 19, -24 ≤ l ≤ 24
Reflections collected	29465	538558
Independent reflections	5202 [R(int) = 0.0625]	12655 [R(int) = 0.1183]
Completeness to $\theta$ [%]	100.0	100.0
Refinement method	Full-matrix least-squares on F <sup>2</sup>	Full-matrix least-squares on F <sup>2</sup>
Data / restraints/ parameters	5202 / 8 / 337	12655 / 4 / 646
Goodness of fit on F <sup>2</sup>	1.051	1.089
Final R indices	R1 = 0.0562, wR2 = 0.1280	R1 = 0.0675, wR2 = 0.1613
R indices (all data)	R1 = 0.0781, wR2 = 0.1404	R1 = 0.0991, wR2 = 0.1980
Extinction coefficient	n/a	n/a
Largest diff. peak and hole [e Å <sup>-3</sup> ]	0.942 and -0.822	2.944 and -1.954

**Table A 27: Crystal data and refinement method of C29 and C30**

	<b>C29</b>	<b>C30</b>
Identification code	YV_0108n_0m_a_sq	YV_0119n_0m_b
Empirical formula	C <sub>50</sub> H <sub>52</sub> F <sub>12</sub> RuN <sub>12</sub> P <sub>2</sub>	C <sub>62</sub> H <sub>74</sub> F <sub>12</sub> RuN <sub>14</sub> P <sub>2</sub>
Formula weight [g mol <sup>-1</sup> ]	1212.04	1406.36
Temperature [K]	127(2)	120(2)
Wavelength [Å]	0.71073	0.71073
Crystal system	Monoclinic	Monoclinic
Space group	P2 <sub>1</sub> /n	Cc
Unit cell dimensions [Å]; [°]	a = 13.2075(7), α = 90 b = 27.4110(15), β = 107.986(2) c = 16.6750(9), γ = 90	a = 16.2450(19), α = 90 b = 16.2842(19), β = 99.426(4) c = 24.811(3), γ = 90
Volume [Å <sup>3</sup> ]	5741.9(5)	6474.7(13)
Z	4	4
Density (calculated) [Mg m <sup>-3</sup> ]	1.402	1.443
Absorption coefficient [mm <sup>-1</sup> ]	0.412	0.378
F(000)	2472	2904
Crystal size [mm <sup>3</sup> ]	0.300 x 0.240 x 0.020	0.200 x 0.180 x 0.140
θ range [°]	1.964 to 33.231	2.293 to 33.137
Index ranges	-20 ≤ h ≤ 20, -42 ≤ k ≤ 42, -25 ≤ l ≤ 25	-24 ≤ h ≤ 24, -25 ≤ k ≤ 25, -38 ≤ l ≤ 38
Reflections collected	446322	248225
Independent reflections	21993 [R(int) = 0.0735]	24633 [R(int) = 0.0792]
Completeness to θ [%]	99.9	99.9
Refinement method	Full-matrix least-squares on F <sup>2</sup>	Full-matrix least-squares on F <sup>2</sup>
Data / restraints/ parameters	21993 / 11 / 634	24633 / 9 / 848
Goodness of fit on F <sup>2</sup>	1.038	1.080
Final R indices	R1 = 0.0872, wR2 = 0.2485	R1 = 0.0477, wR2 = 0.1130
R indices (all data)	R1 = 0.1020, wR2 = 0.2650	R1 = 0.0635, wR2 = 0.1257
Extinction coefficient	n/a	n/a
Largest diff. peak and hole [e Å <sup>-3</sup> ]	3.345 and -1.859	1.266 and -0.967

# $^1\text{H}$ - and $^{13}\text{C}$ -NMR-Spectra for the ruthenium complex series

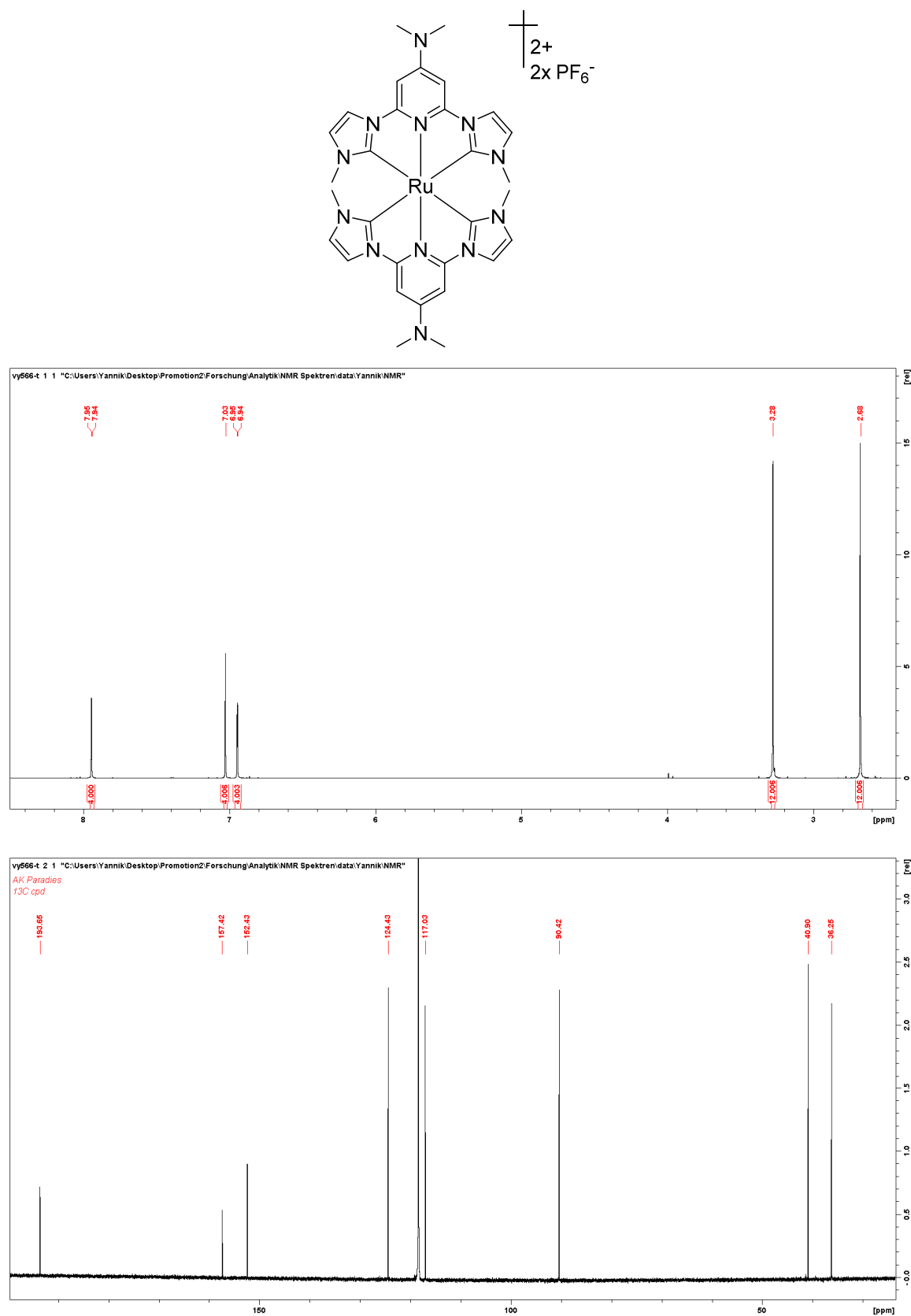


Figure A-0-31:  $^1\text{H}$ - (top) and  $^{13}\text{C}$ -NMR spectra (bottom) of  $[\text{Ru}(\text{BiP}^{\text{NMe}_2})_2][\text{PF}_6]_2$  (C16) in MeCN at 303 K.

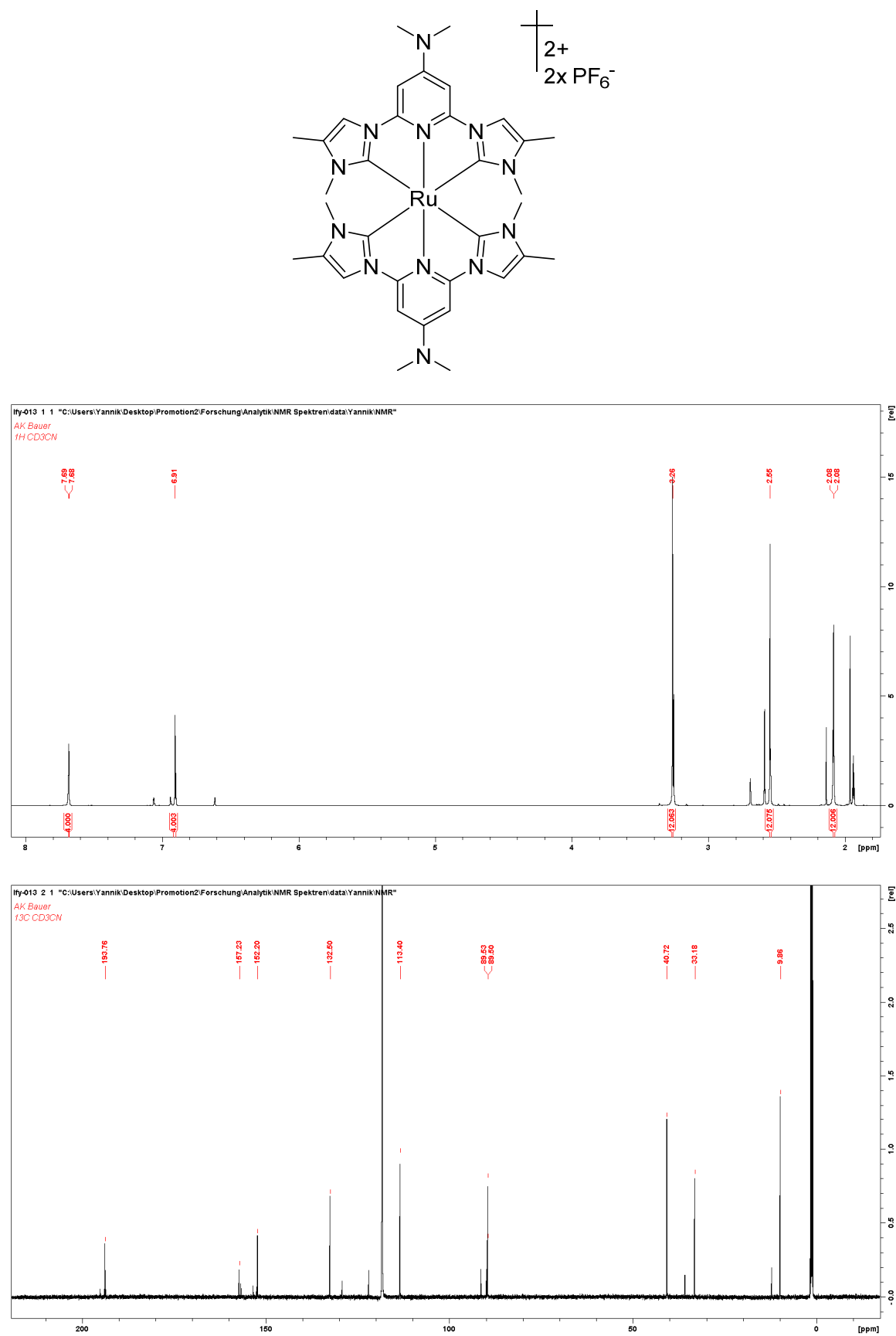


Figure A-0-32:  $^1H$ - (top) and  $^{13}C$ -NMR spectra (bottom) of  $[Ru(BmiP^{NMe_2})_2][PF_6]_2$  (C17) in MeCN at 303 K.

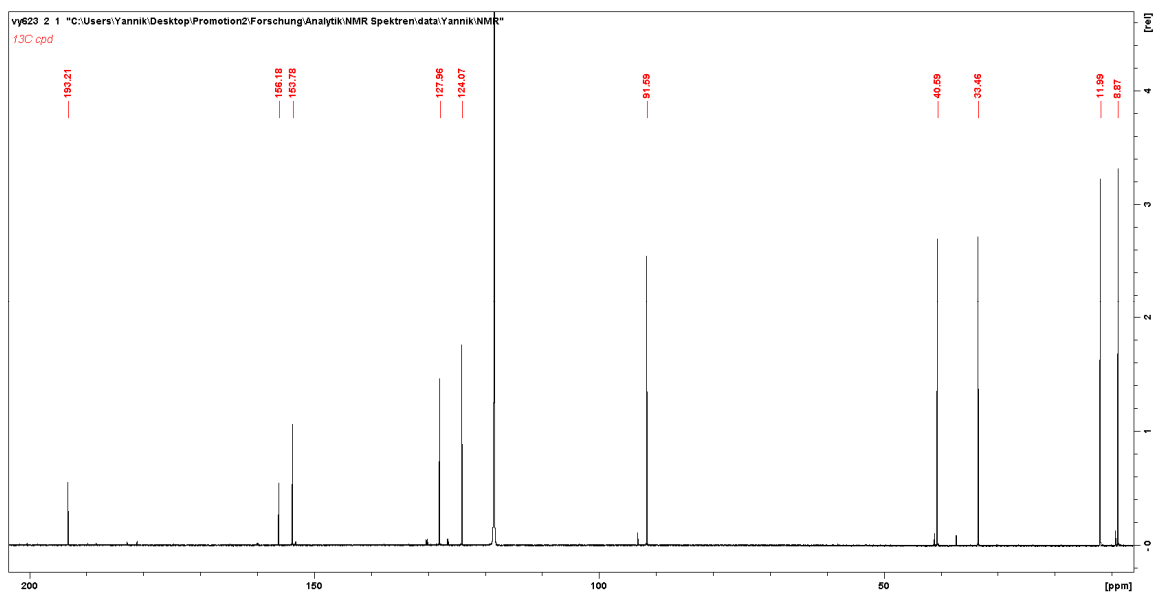
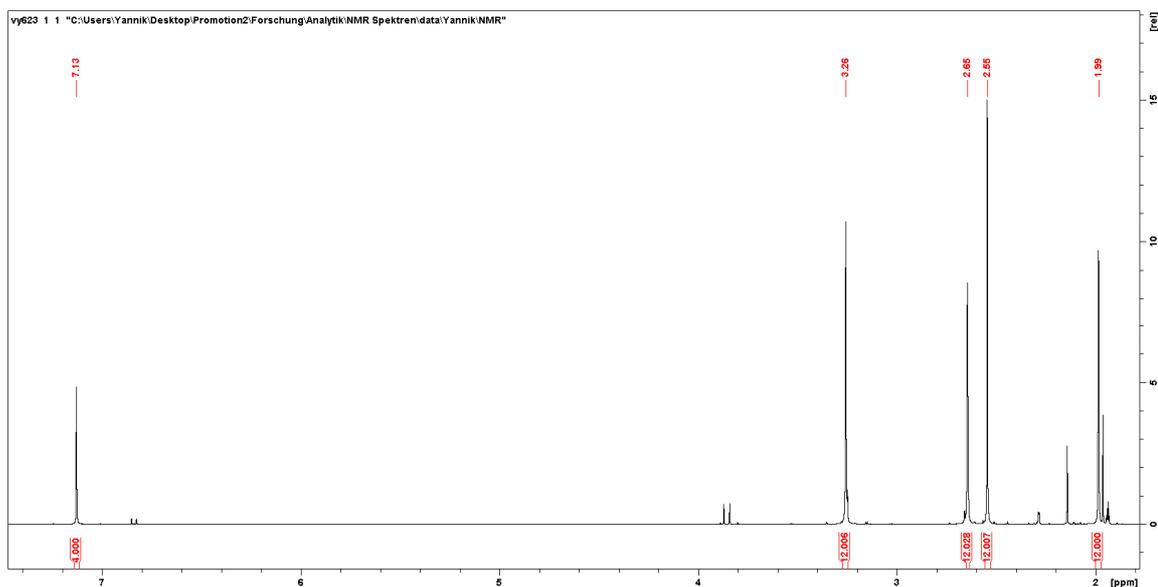
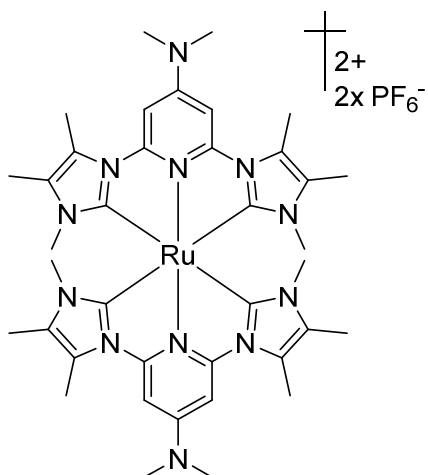


Figure A- 0-33: <sup>1</sup>H- (top) and <sup>13</sup>C-NMR spectra (bottom) of [Ru(BdmiP<sup>NMe2</sup>)<sub>2</sub>][PF<sub>6</sub>]<sub>2</sub> (C18) in MeCN at 303 K.

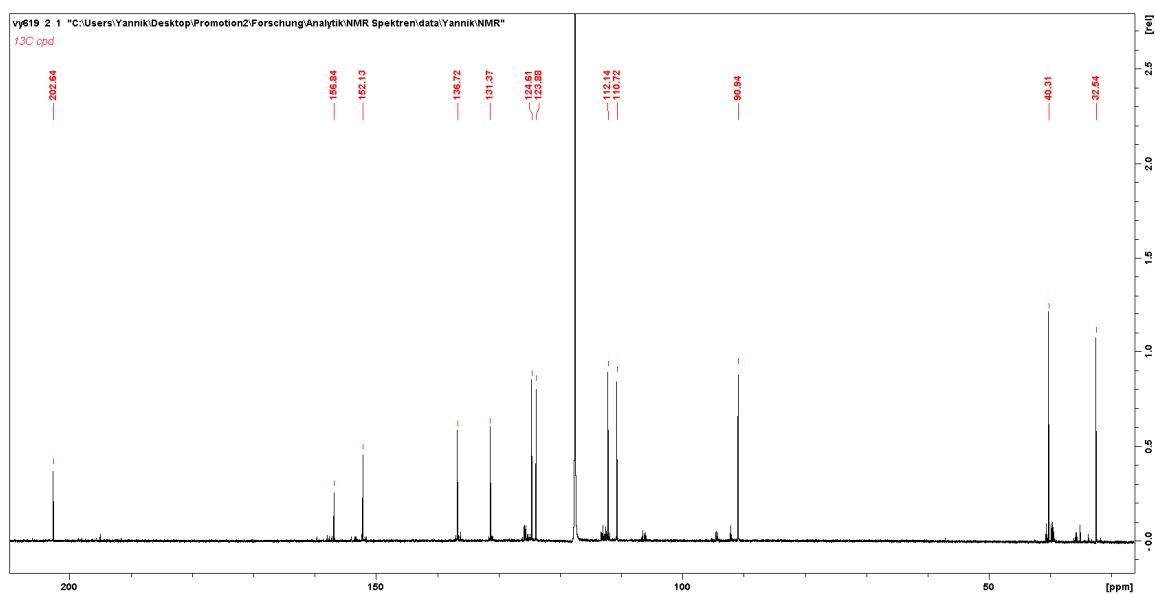
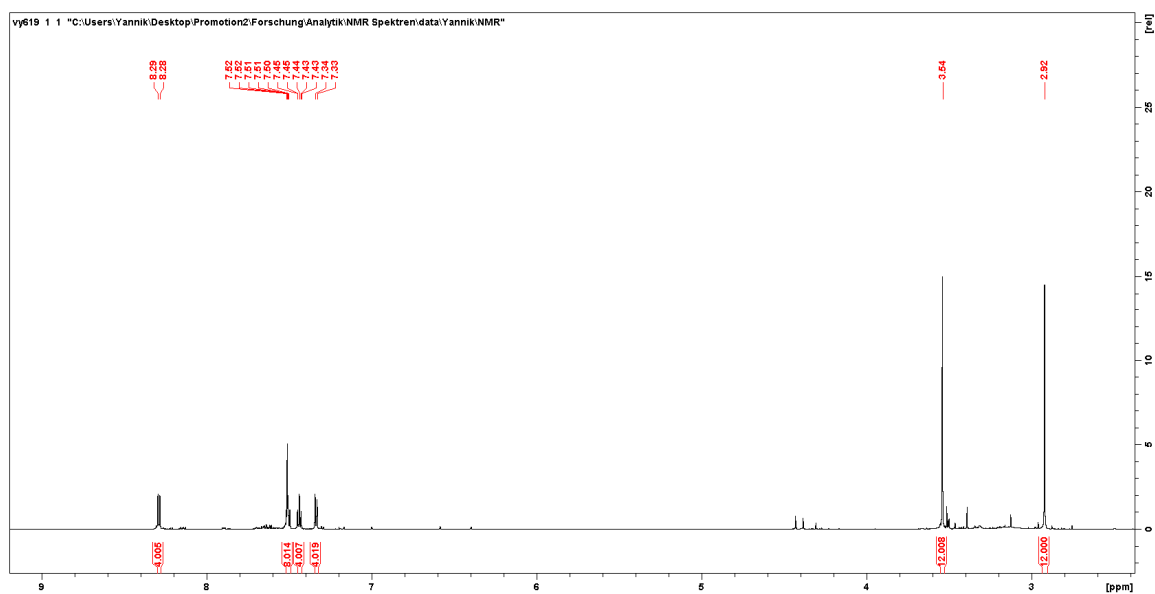
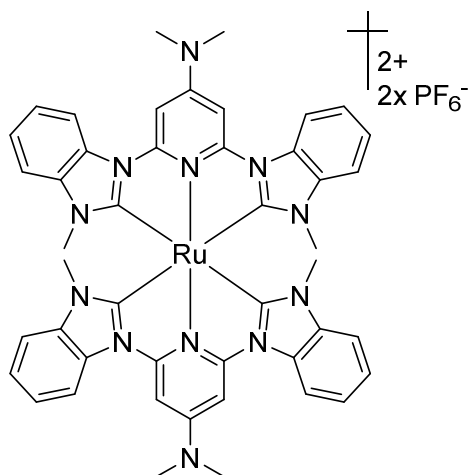


Figure A-0-34:  $^1H$ - (top) and  $^{13}C$ -NMR spectra (bottom) of  $[Ru(BbP^{NMe_2})_2][PF_6]_2$  (C19) in MeCN at 303 K.

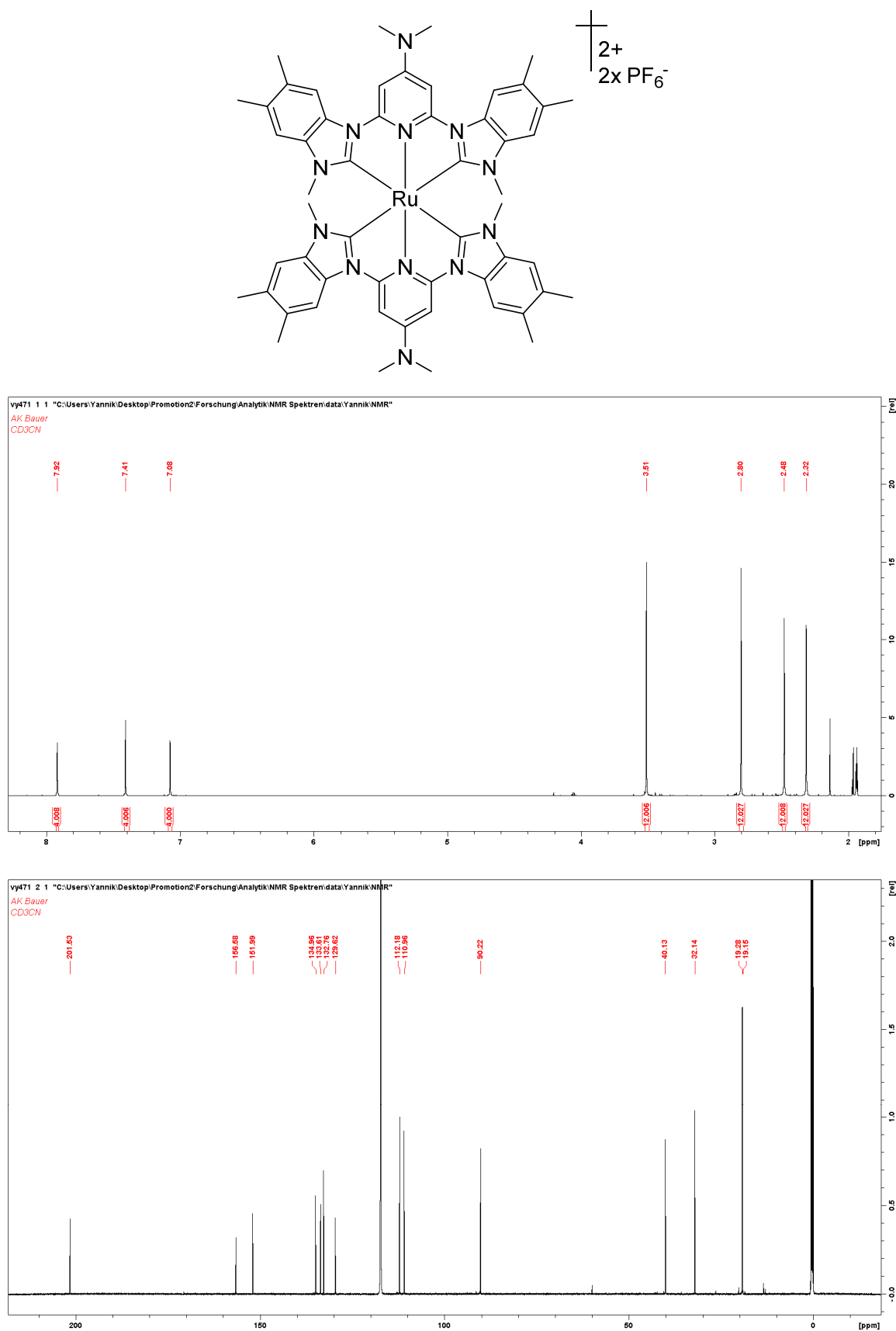


Figure A-0-35: <sup>1</sup>H- (top) and <sup>13</sup>C-NMR spectra (bottom) of [Ru(BmbP<sup>NMe2</sup>)<sub>2</sub>][PF<sub>6</sub>]<sub>2</sub> (C20) in MeCN at 303 K.

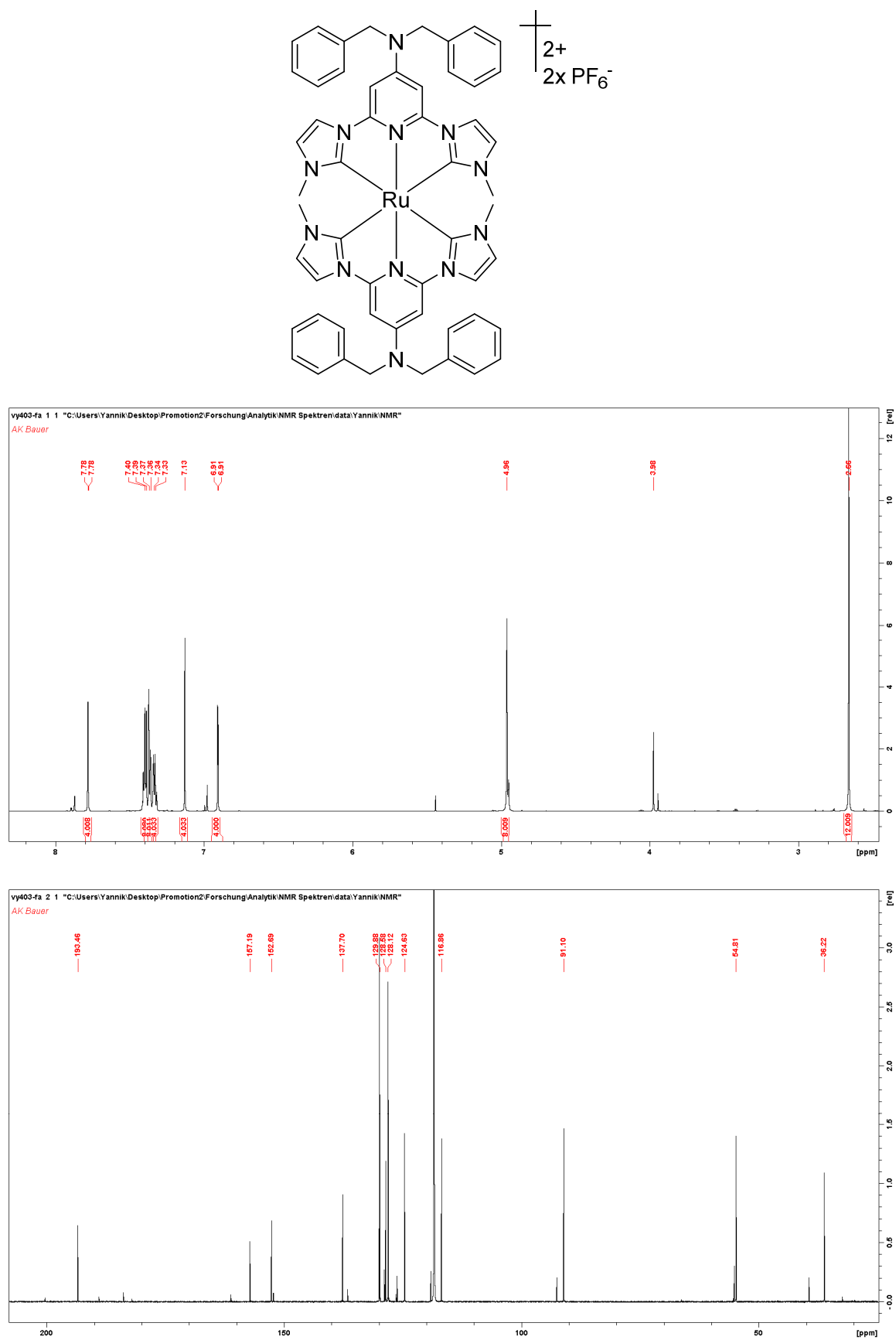


Figure A-0-36:  $^1H$ - (top) and  $^{13}C$ -NMR spectra (bottom) of  $[Ru(BIP^{NBn2})_2][PF_6]_2$  (C21) in MeCN at 303 K.

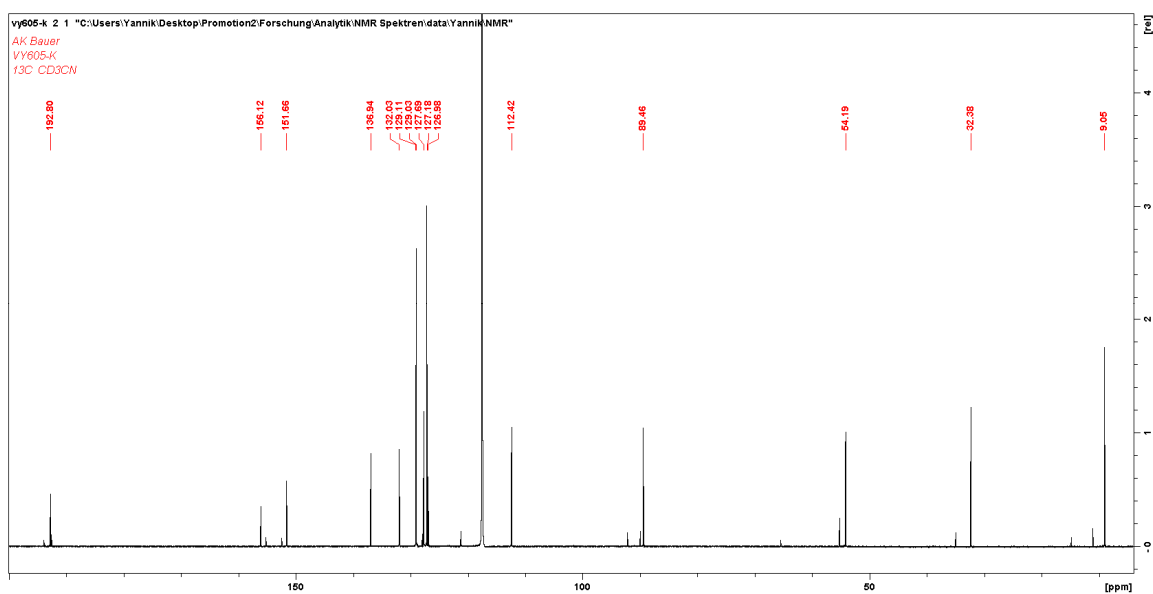
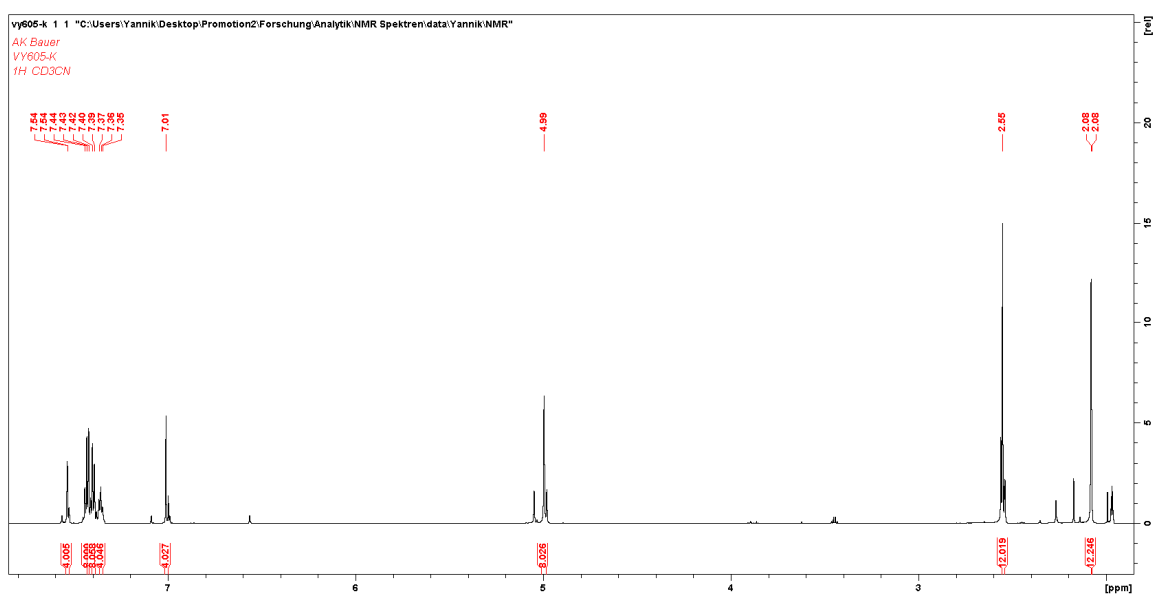
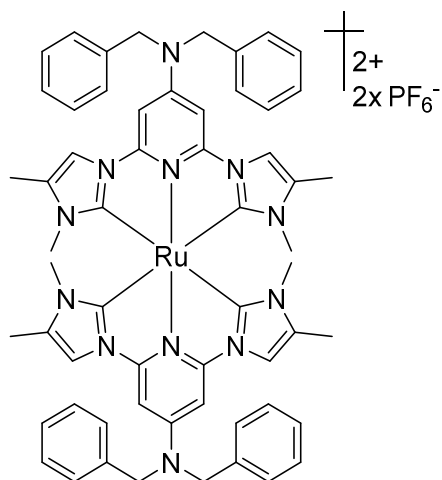


Figure A-0-37:  $^1H$ - (top) and  $^{13}C$ -NMR spectra (bottom) of  $[Ru(BmiP^{NBn2})_2][PF_6]_2$  (C22) in MeCN at 303 K.

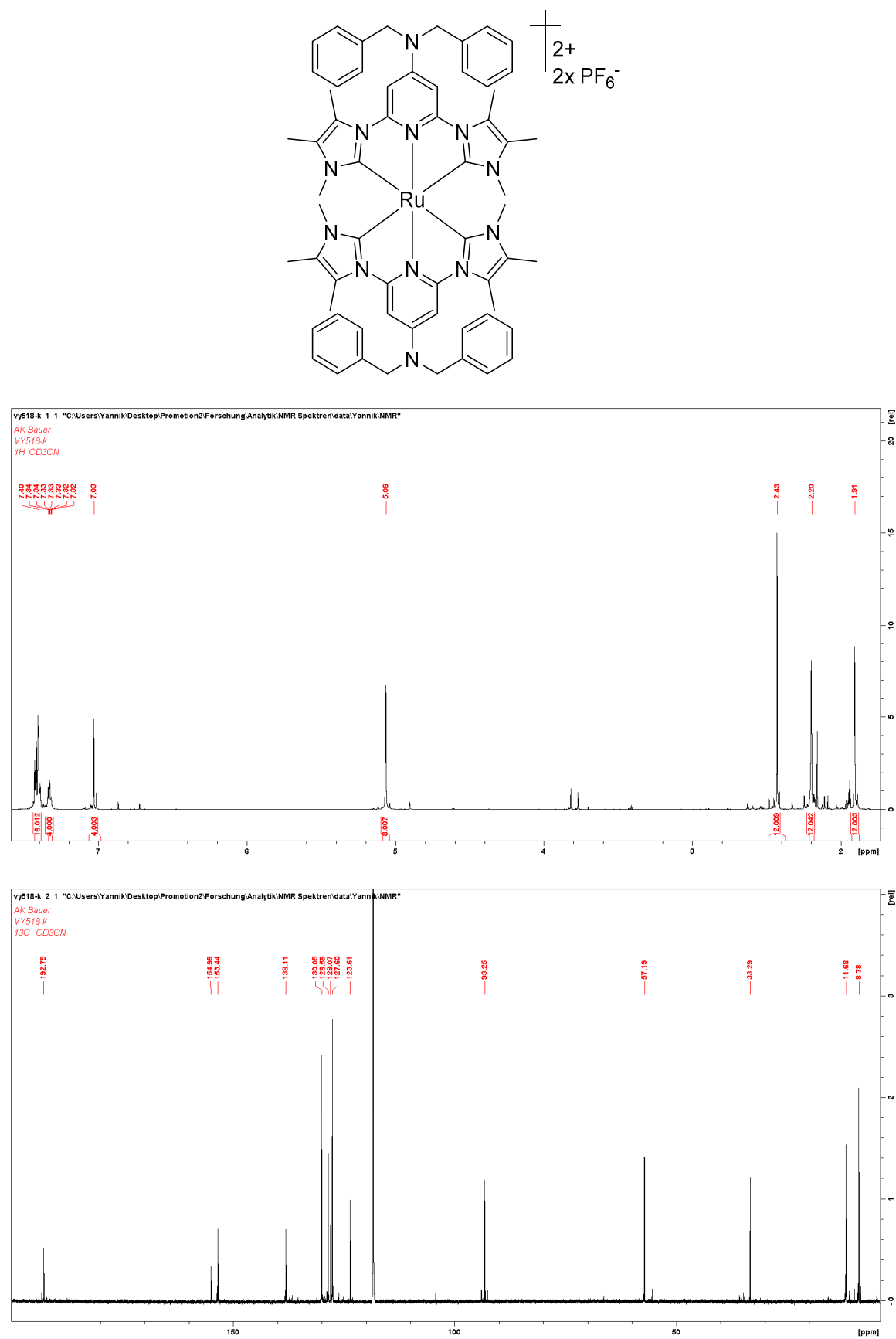


Figure A-0-38:  $^1\text{H}$ - (top) and  $^{13}\text{C}$ -NMR spectra (bottom) of  $[\text{Ru}(\text{BdmiP}^{\text{NBn}2})_2][\text{PF}_6]_2$  (C23) in MeCN at 303 K.

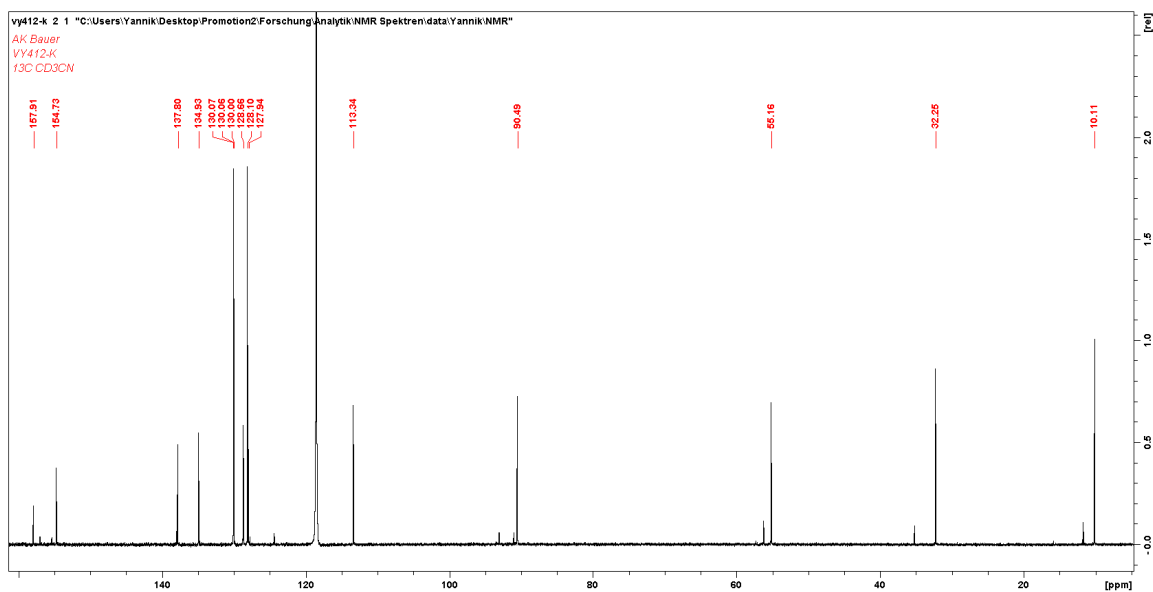
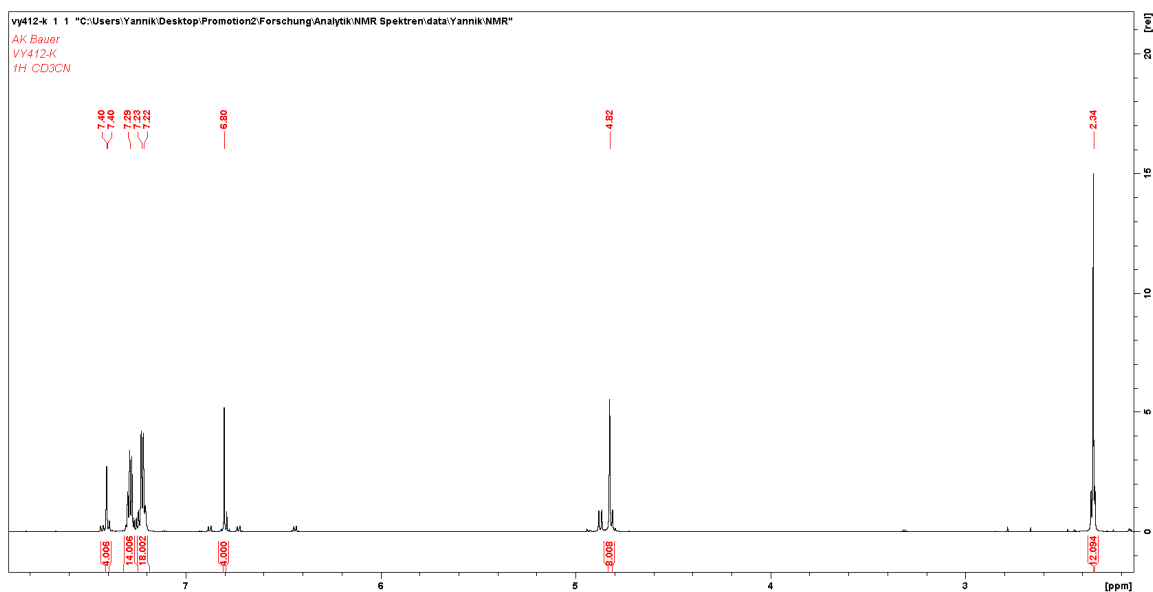
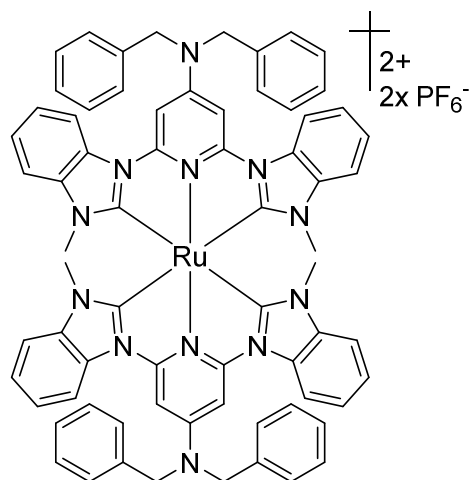


Figure A-0-39:  $^1H$ - (top) and  $^{13}C$ -NMR spectra (bottom) of  $[Ru(BbP^{NBn2})_2][PF_6]_2$  (C24) in MeCN at 303 K.

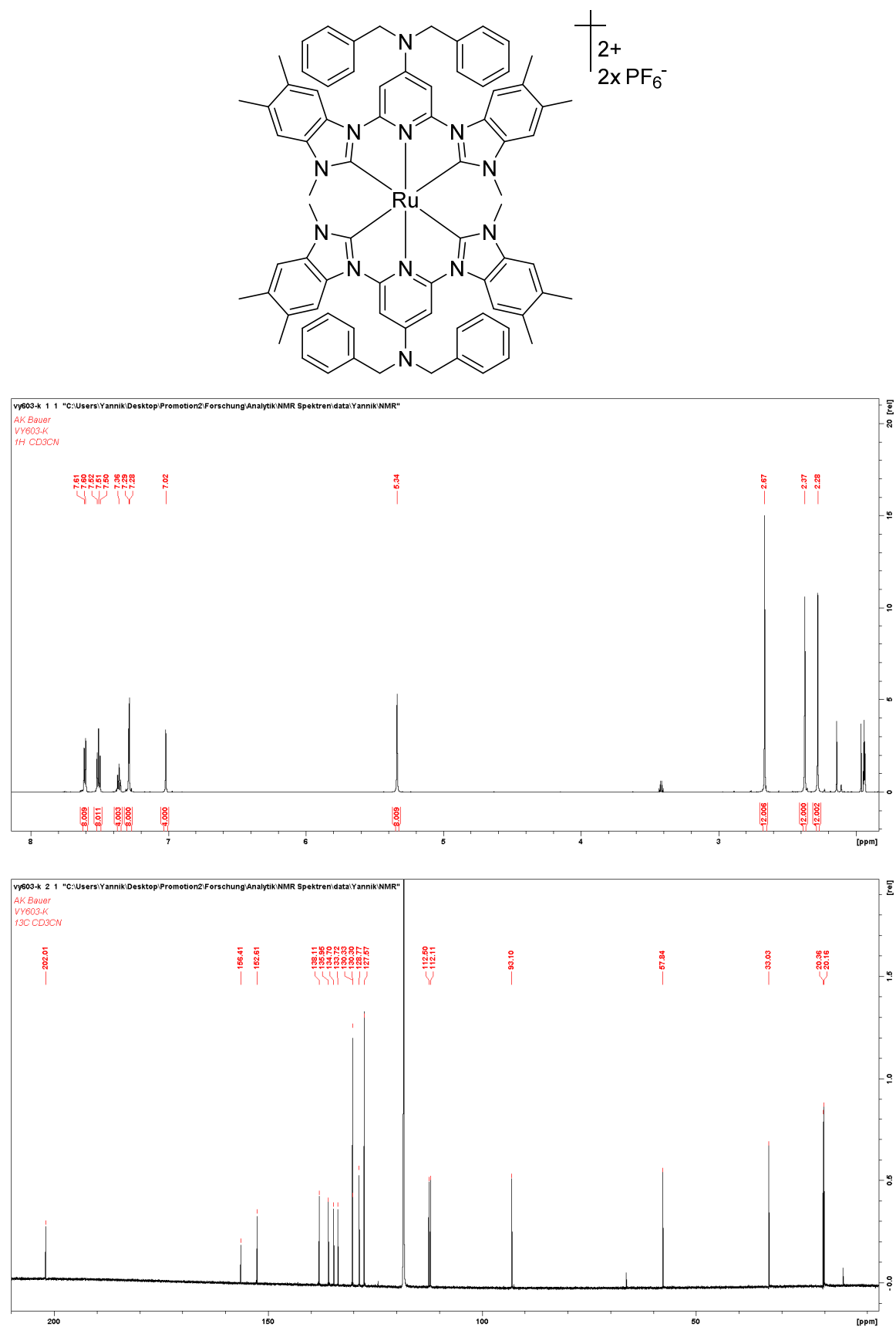


Figure A-0-40: <sup>1</sup>H- (top) and <sup>13</sup>C-NMR spectra (bottom) of  $[Ru(BmbP^{NBn2})_2][PF_6]_2$  (C25) in MeCN at 303 K.

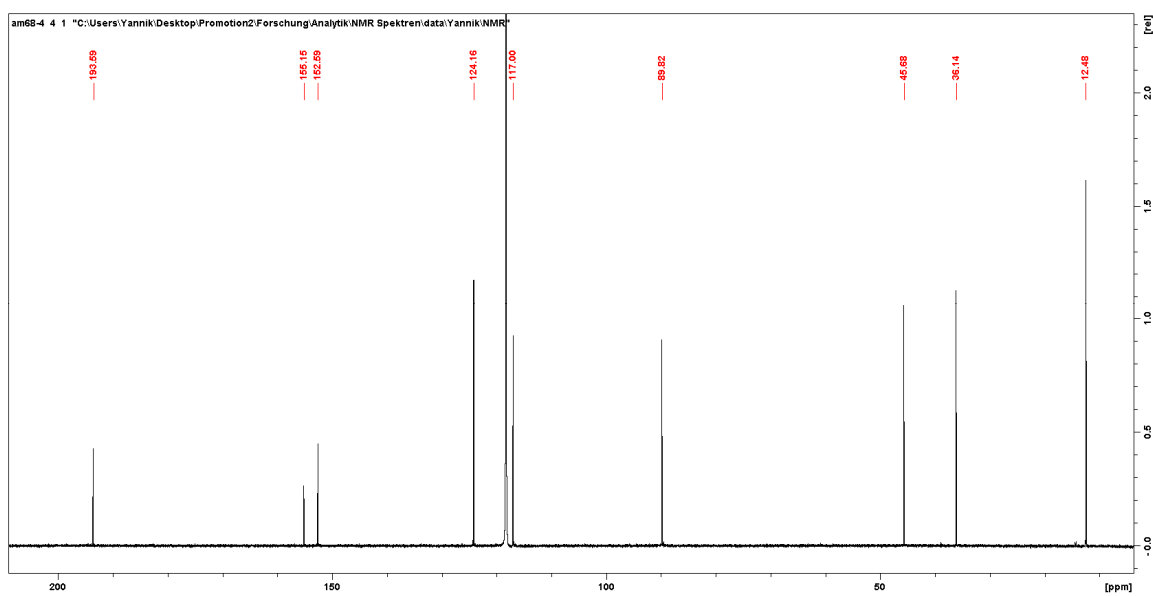
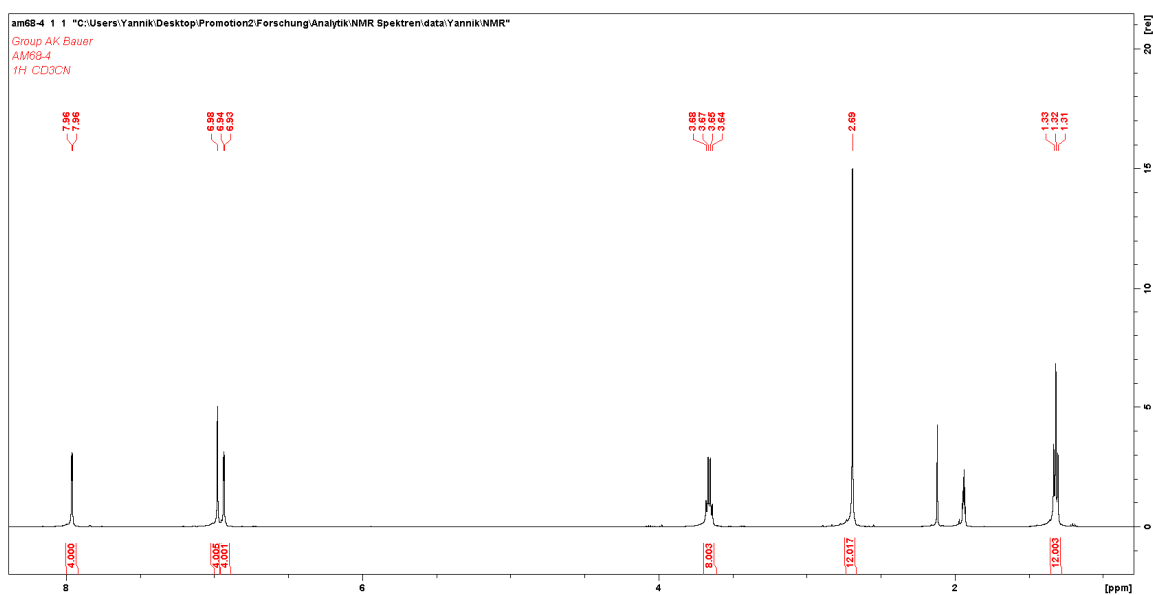
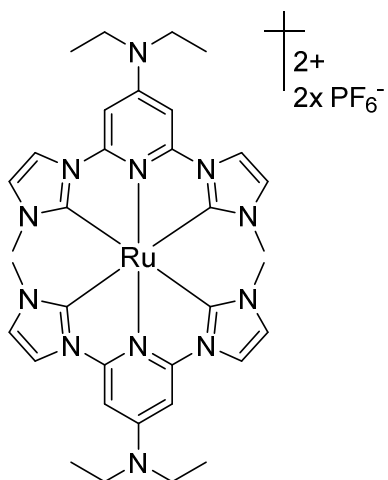


Figure A-0-41:  $^1H$ - (top) and  $^{13}C$ -NMR spectra (bottom) of  $[Ru(BIP^{NEt_2})_2][PF_6]_2$  (C26) in MeCN at 303 K.

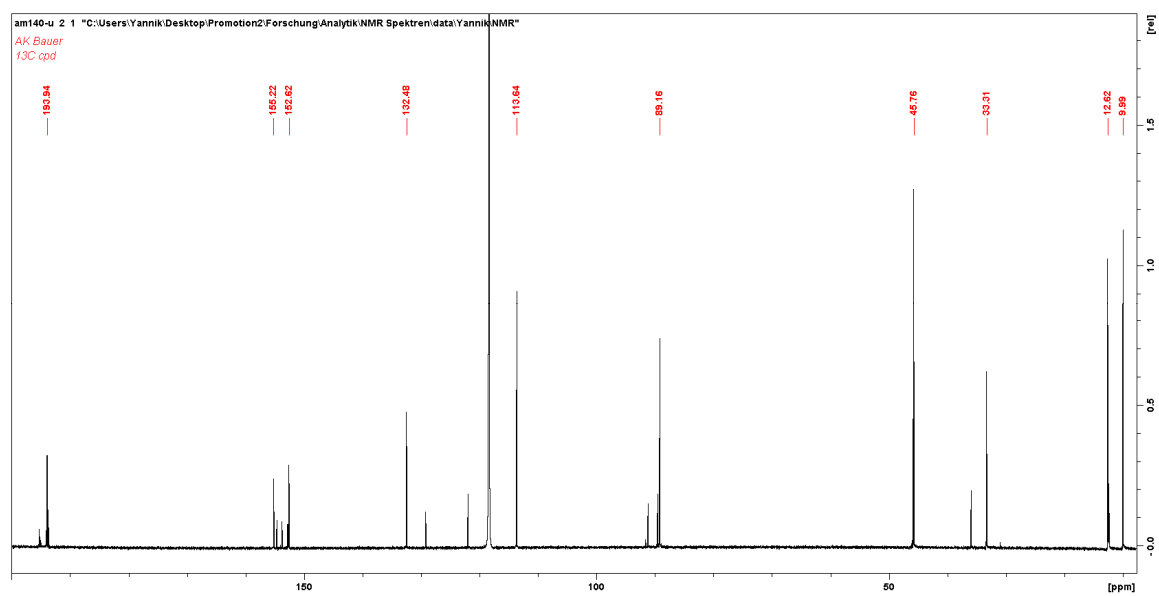
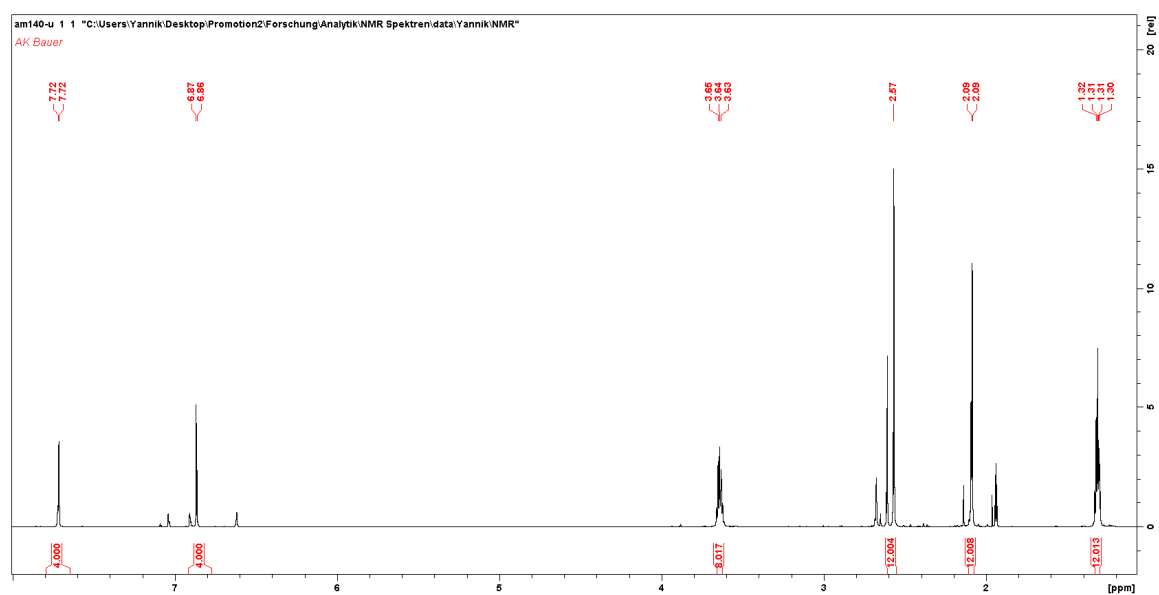
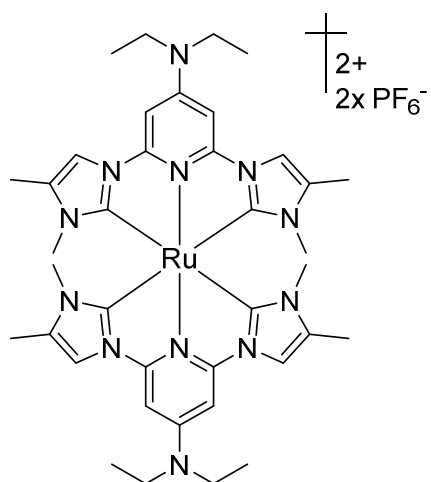


Figure A-0-42:  $^1H$ - (top) and  $^{13}C$ -NMR spectra (bottom) of  $[Ru(BmiPNEt_2)_2][PF_6]_2$  (C27) in MeCN at 303 K.

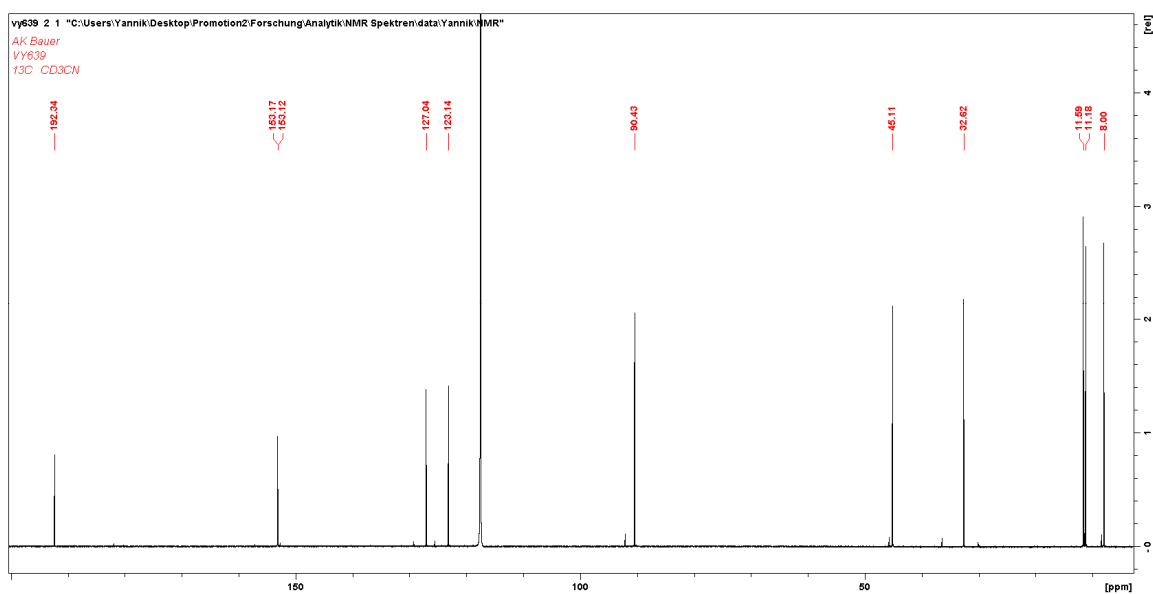
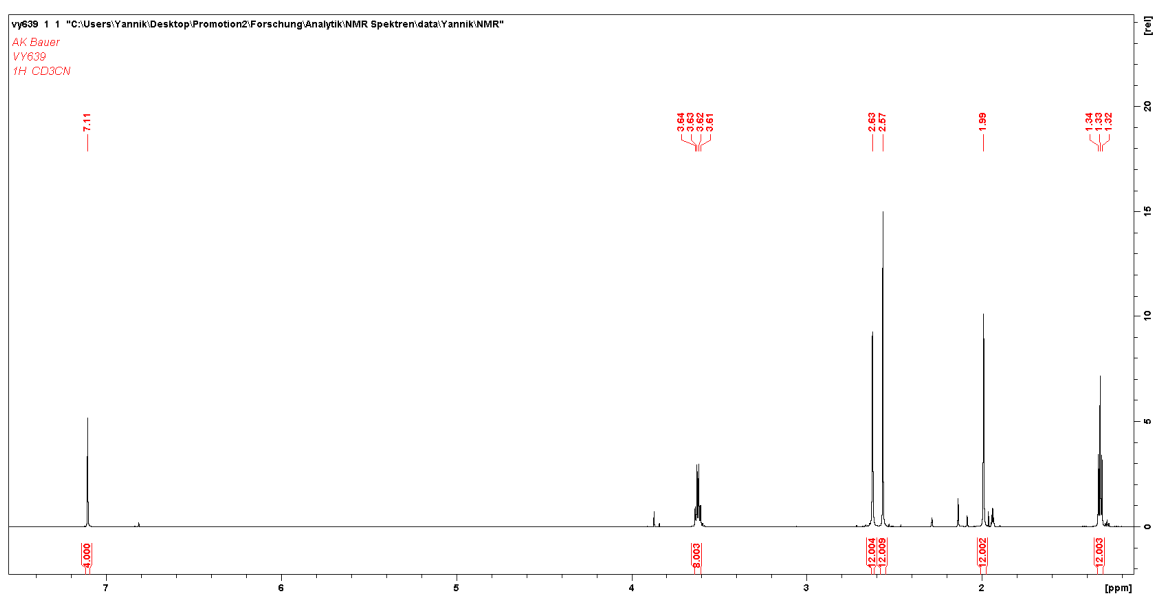
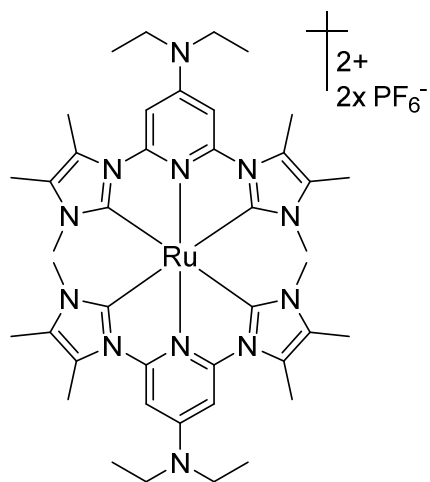


Figure A-0-43: <sup>1</sup>H- (top) and <sup>13</sup>C-NMR spectra (bottom) of [Ru(BdmiP<sup>NEt2</sup>)<sub>2</sub>][PF<sub>6</sub>]<sub>2</sub> (C28) in MeCN at 303 K.

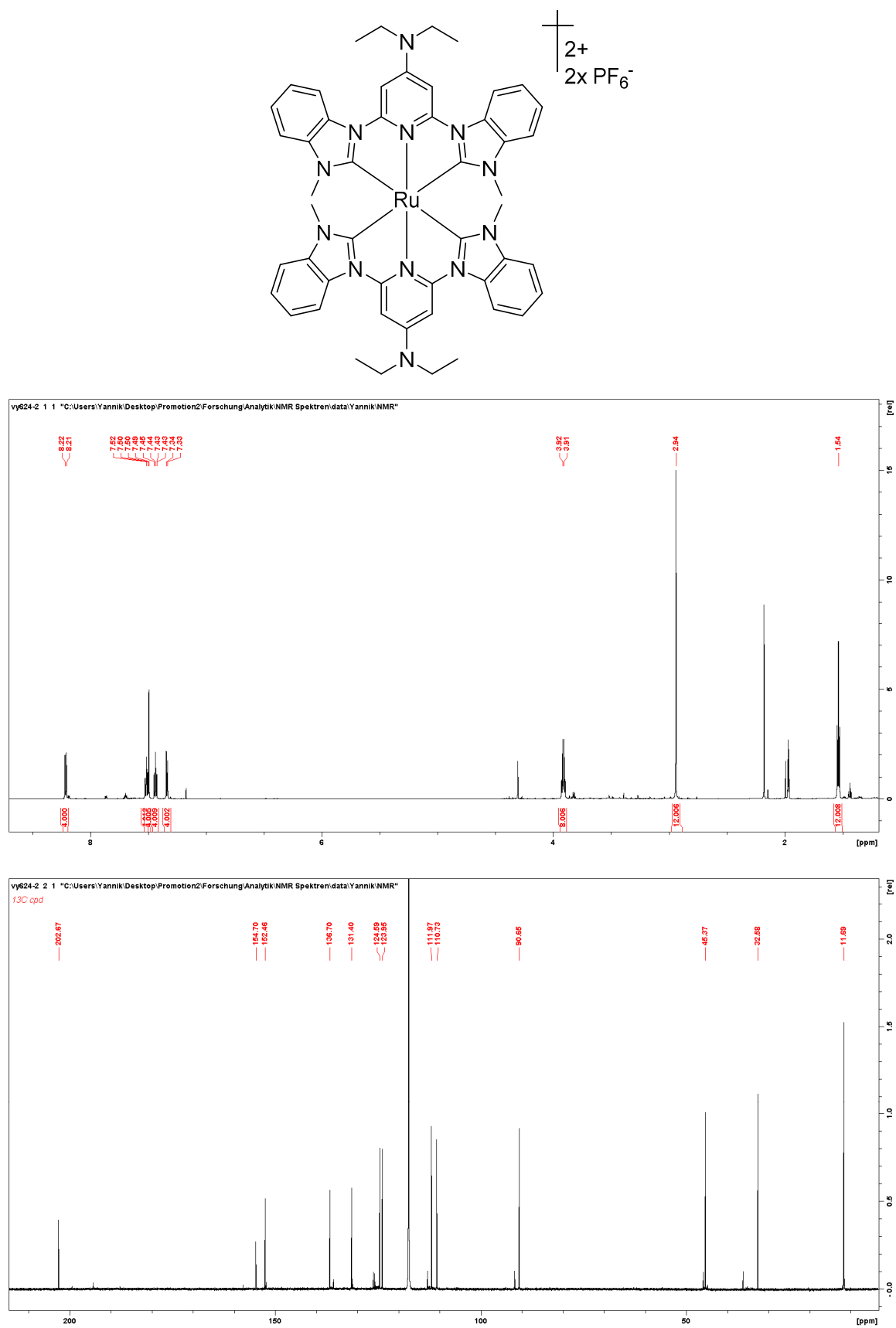
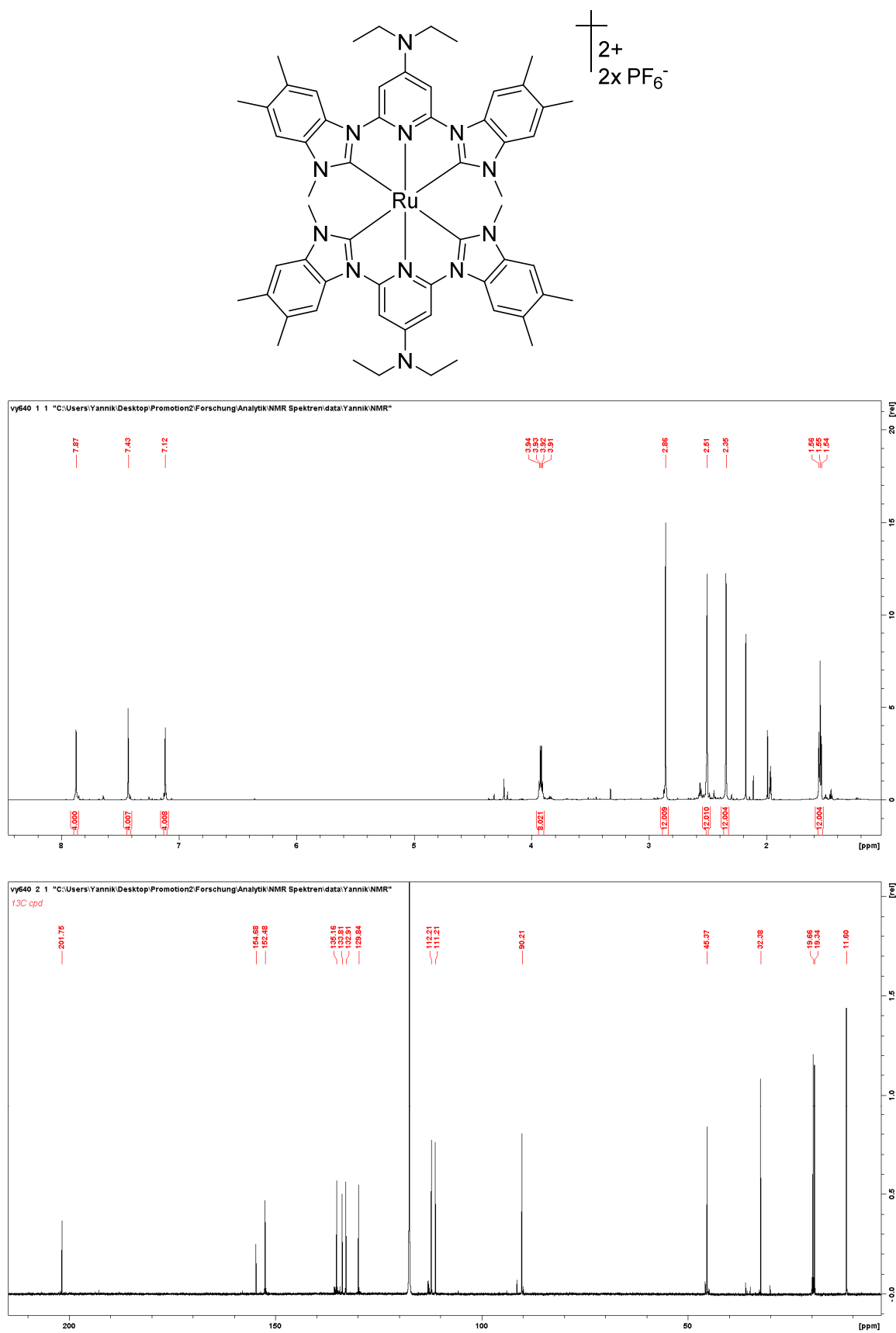


Figure A-0-44: <sup>1</sup>H- (top) and <sup>13</sup>C-NMR spectra (bottom) of  $[Ru(BbP^{NEt_2})_2][PF_6]_2$  (C29) in MeCN at 303 K.



## Electrochemical data for the ruthenium complex series

**Table A 28:** Electrochemical data for the reversible oxidation at  $E_{1/2}^0 = 0.22$  V vs Fc/Fc<sup>+</sup> for complex **C16**

V [mV·s <sup>-1</sup> ]	50	100	200	400	800
$E_{pa}$ [V]	0.192	0.195	0.192	0.195	0.195
$E_{pc}$ [V]	0.263	0.263	0.261	0.263	0.263
$E_{1/2}$ [V]	0.228	0.229	0.227	0.229	0.229
$\Delta E$ [mV]	70.87	68.37	68.4	68	67.7
$I_{pa}$ [10 <sup>-6</sup> A]	1.043	1.46	2.055	2.88	4.05
$I_{pa}/I_{pc}$	1.07	1.05	1.06	1.05	1.06
$I_{pa}/v^{0.5}$	0.147	0.146	0.145	0.144	0.143

**Table A 29:** Electrochemical data for the reversible oxidation at  $E_{1/2}^0 = 0.17$  V vs Fc/Fc<sup>+</sup> for complex **C17**

V [mV·s <sup>-1</sup> ]	50	100	200	400	800
$E_{pa}$ [V]	0.146	0.140	0.141	0.144	0.141
$E_{pc}$ [V]	0.212	0.206	0.209	0.212	0.214
$E_{1/2}$ [V]	0.179	0.173	0.175	0.178	0.178
$\Delta E$ [mV]	65.91	65.92	68.36	68.36	73.23
$I_{pa}$ [10 <sup>-6</sup> A]	1.093	1.558	2.16	3.043	4.27
$I_{pa}/I_{pc}$	1.08	1.08	1.07	1.07	1.08
$I_{pa}/v^{0.5}$	0.154	0.155	0.152	0.152	0.150

**Table A 30:** Electrochemical data for the reversible oxidation at  $E_{1/2}^0 = 0.11$  V vs Fc/Fc<sup>+</sup> for complex **C18**

V [mV·s <sup>-1</sup> ]	50	100	200	400	800
$E_{pa}$ [V]	0.080	0.080	0.078	0.080	0.075
$E_{pc}$ [V]	0.146	0.141	0.144	0.148	0.148
$E_{1/2}$ [V]	0.113	0.111	0.111	0.114	0.112
$\Delta E$ [mV]	65.92	61.03	65.92	68.35	73.25
$I_{pa}$ [10 <sup>-6</sup> A]	0.98	1.53	2.206	3.1991	4.453
$I_{pa}/I_{pc}$	1.16	1.15	1.13	1.159	1.159
$I_{pa}/v^{0.5}$	0.138	0.153	0.156	0.159	0.157

**Table A 31:** Electrochemical data for the reversible oxidation at  $E^{0}_{1/2} = 0.41$  V vs Fc/Fc<sup>+</sup> for complex **C19**

V [mV·s <sup>-1</sup> ]	50	100	200	400	800
E <sub>pa</sub> [V]	0.382	0.377	0.379	0.379	0.377
E <sub>pc</sub> [V]	0.450	0.445	0.450	0.450	0.450
E <sub>1/2</sub> [V]	0.416	0.411	0.415	0.415	0.413
ΔE [mV]	67.451	68.36	70.80	70.81	73.19
I <sub>pa</sub> [10 <sup>-6</sup> A]	1.11	1.51	2.13	3	4.2
I <sub>pa</sub> /I <sub>pc</sub>	1.16	1.13	1.13	1.14	1.13
I <sub>pa</sub> /v <sup>0.5</sup>	0.156	0.151	0.150	0.15	0.148

**Table A 32:** Electrochemical data for the reversible oxidation at  $E^{0}_{1/2} = 0.35$  V vs Fc/Fc<sup>+</sup> for complex **C20**

V [mV·s <sup>-1</sup> ]	50	100	200	400	800
E <sub>pa</sub> [V]	0.316	0.323	0.311	0.306	0.299
E <sub>pc</sub> [V]	0.384	0.384	0.384	0.386	0.389
E <sub>1/2</sub> [V]	0.350	0.354	0.347	0.346	0.344
ΔE [mV]	68.34	60.8	73.22	80.5	90.31
I <sub>pa</sub> [10 <sup>-6</sup> A]	1.03	1.32	1.65	2.31	3.11
I <sub>pa</sub> /I <sub>pc</sub>	1	0.91	0.83	0.87	0.86
I <sub>pa</sub> /v <sup>0.5</sup>	0.146	0.132	0.116	0.115	0.109

**Table A 33:** Electrochemical data for the reversible oxidation at  $E^{0}_{1/2} = 0.29$  V vs Fc/Fc<sup>+</sup> for complex **C21**

V [mV·s <sup>-1</sup> ]	50	100	200	400	800
E <sub>pa</sub> [V]	0.260	0.260	0.260	0.260	0.260
E <sub>pc</sub> [V]	0.328	0.328	0.330	0.330	0.328
E <sub>1/2</sub> [V]	0.294	0.294	0.295	0.295	0.294
ΔE [mV]	68.4	68.4	70.8	70.8	68.4
I <sub>pa</sub> [10 <sup>-6</sup> A]	1.13	1.6	2.2	3.092	4.36
I <sub>pa</sub> /I <sub>pc</sub>	1.1	1.12	1.1	1.09	1.09
I <sub>pa</sub> /v <sup>0.5</sup>	0.159	0.16	0.155	0.154	0.154

**Table A 34:** Electrochemical data for the reversible oxidation at  $E^{0}_{1/2} = 0.29$  V vs Fc/Fc<sup>+</sup> for complex **C22**

V [mV·s <sup>-1</sup> ]	50	100	200	400	800
E <sub>pa</sub> [V]	0.198	0.206	0.203	0.201	0.201
E <sub>pc</sub> [V]	0.272	0.269	0.272	0.269	0.277
E <sub>1/2</sub> [V]	0.235	0.237	0.237	0.235	0.239
ΔE [mV]	74	63	69	68	76
I <sub>pa</sub> [10 <sup>-6</sup> A]	0.3	0.987	1.79	2.92	4.06
I <sub>pa</sub> /I <sub>pc</sub>	1.23	1.06	1.31	1.52	1.56
I <sub>pa</sub> /v <sup>0.5</sup>	0.042	0.098	0.126	0.146	0.143

**Table A 35:** Electrochemical data for the reversible oxidation at  $E^{0}_{1/2} = 0.17$  V vs Fc/Fc<sup>+</sup> for complex **C23**

V [mV·s <sup>-1</sup> ]	50	100	200	400	800
E <sub>pa</sub> [V]	0.133	0.133	0.135	0.125	0.125
E <sub>pc</sub> [V]	0.201	0.206	0.206	0.208	0.211
E <sub>1/2</sub> [V]	0.167	0.169	0.170	0.167	0.168
ΔE [mV]	68	73	70.5	83.04	85.37
I <sub>pa</sub> [10 <sup>-6</sup> A]	0.6	1.09	1.59	2.52	3.39
I <sub>pa</sub> /I <sub>pc</sub>	0.98	1.32	1.24	1.44	1.46
I <sub>pa</sub> /v <sup>0.5</sup>	0.084	0.109	0.112	0.126	0.119

**Table A 36:** Electrochemical data for the reversible oxidation at  $E^{0}_{1/2} = 0.49$  V vs Fc/Fc<sup>+</sup> for complex **C24**

V [mV·s <sup>-1</sup> ]	50	100	200	400	800
E <sub>pa</sub> [V]	0.451	0.452	0.451	0.451	0.448
E <sub>pc</sub> [V]	0.522	0.534	0.534	0.541	0.545
E <sub>1/2</sub> [V]	0.486	0.493	0.492	0.496	0.496
ΔE [mV]	71	82	82.6	89.8	97
I <sub>pa</sub> [10 <sup>-6</sup> A]	0.87	1.29	1.66	2.37	3.04
I <sub>pa</sub> /I <sub>pc</sub>	1.24	1.24	1.05	1.14	1.19
I <sub>pa</sub> /v <sup>0.5</sup>	0.123	0.129	0.117	0.118	0.107

**Table A 37:** Electrochemical data for the reversible oxidation at  $E^{0}_{1/2} = 0.44$  V vs Fc/Fc<sup>+</sup> for complex **C25**

V [mV·s <sup>-1</sup> ]	50	100	200	400	800
<b>E<sub>pa</sub> [V]</b>	0.404	0.399	0.394	0.382	0.374
<b>E<sub>pc</sub> [V]</b>	0.477	0.482	0.487	0.496	0.509
<b>E<sub>1/2</sub> [V]</b>	0.440	0.440	0.440	0.439	0.44185
<b>ΔE [mV]</b>	73.11	82.928	92.41	114.8	134.3
<b>I<sub>pa</sub> [10<sup>-6</sup> A]</b>	0.575	0.866	1.19	1.58	2.19
<b>I<sub>pa</sub>/I<sub>pc</sub></b>	1.14	1.1	1.13	1.16	1.27
<b>I<sub>pa</sub>/v<sup>0.5</sup></b>	0.081	0.086	0.084	0.079	0.077

**Table A 38:** Electrochemical data for the reversible oxidation at  $E^{0}_{1/2} = 0.20$  V vs Fc/Fc<sup>+</sup> for complex **C26**

V [mV·s <sup>-1</sup> ]	50	100	200	400	800
<b>E<sub>pa</sub> [V]</b>	0.170	0.170	0.166	0.161	0.166
<b>E<sub>pc</sub> [V]</b>	0.234	0.236	0.244	0.246	0.246
<b>E<sub>1/2</sub> [V]</b>	0.202	0.203	0.205	0.203	0.206
<b>ΔE [mV]</b>	63.1	65.9	78.1	85.45	80.45
<b>I<sub>pa</sub> [10<sup>-6</sup> A]</b>	1.512	2.21	3.07	4.27	5.93
<b>I<sub>pa</sub>/I<sub>pc</sub></b>	1.07	1.05	1.03	1.04	1.03
<b>I<sub>pa</sub>/v<sup>0.5</sup></b>	0.21	0.22	0.21	0.21	0.20

**Table A 39:** Electrochemical data for the reversible oxidation at  $E^{0}_{1/2} = 0.18$  V vs Fc/Fc<sup>+</sup> for complex **C27**

V [mV·s <sup>-1</sup> ]	50	100	200	400	800
<b>E<sub>pa</sub> [V]</b>	0.144	0.146	0.144	0.146	0.141
<b>E<sub>pc</sub> [V]</b>	0.212	0.214	0.214	0.212	0.214
<b>E<sub>1/2</sub> [V]</b>	0.178	0.18	0.179	0.179	0.177
<b>ΔE [mV]</b>	68	68	70	66	73.8
<b>I<sub>pa</sub> [10<sup>-6</sup> A]</b>	0.59	0.67	0.76	0.8	0.8
<b>I<sub>pa</sub>/I<sub>pc</sub></b>	0.74	0.69	0.65	0.61	0.55
<b>I<sub>pa</sub>/v<sup>0.5</sup></b>	0.08	0.06	0.05	0.04	0.02

**Table A 40:** Electrochemical data for the reversible oxidation at  $E^{0}_{1/2} = 0.09$  V vs Fc/Fc<sup>+</sup> for complex **C28**

V [mV·s <sup>-1</sup> ]	50	100	200	400	800
E <sub>pa</sub> [V]	0.063	0.063	0.061	0.063	0.058
E <sub>pc</sub> [V]	0.131	0.126	0.126	0.134	0.134
E <sub>1/2</sub> [V]	0.097	0.095	0.093	0.098	0.096
ΔE [mV]	68.36	63.48	65.92	70.79	75.68
I <sub>pa</sub> [10 <sup>-6</sup> A]	0.987	1.44	2.158	3.092	4.22
I <sub>pa</sub> /I <sub>pc</sub>	1.09	1.09	1.16	1.17	1.17
I <sub>pa</sub> /v <sup>0.5</sup>	0.13	0.14	0.15	0.15	0.14

**Table A 41:** Electrochemical data for the reversible oxidation at  $E^{0}_{1/2} = 0.39$  V vs Fc/Fc<sup>+</sup> for complex **C29**

V [mV·s <sup>-1</sup> ]	50	100	200	400	800
E <sub>pa</sub> [V]	0.358	0.358	0.356	0.354	0.354
E <sub>pc</sub> [V]	0.424	0.427	0.429	0.429	0.434
E <sub>1/2</sub> [V]	0.391	0.392	0.392	0.391	0.394
ΔE [mV]	66.8	69.2	73.69	75.6	80.57
I <sub>pa</sub> [10 <sup>-6</sup> A]	0.99	1.49	2.19	2.95	4.08
I <sub>pa</sub> /I <sub>pc</sub>	1.15	1.24	1.3	1.29	1.33
I <sub>pa</sub> /v <sup>0.5</sup>	0.14	0.14	0.15	0.14	0.14

**Table A 42:** Electrochemical data for the reversible oxidation at  $E^{0}_{1/2} = 0.33$  V vs Fc/Fc<sup>+</sup> for complex **C30**

V [mV·s <sup>-1</sup> ]	50	100	200	400	800
E <sub>pa</sub> [V]	0.301	0.301	0.301	0.299	0.294
E <sub>pc</sub> [V]	0.364	0.372	0.367	0.369	0.372
E <sub>1/2</sub> [V]	0.333	0.336	0.334	0.334	0.333
ΔE [mV]	63.4	70.7	65.9	70.7	78.1
I <sub>pa</sub> [10 <sup>-6</sup> A]	0.7	1.121	1.634	2.351	3.353
I <sub>pa</sub> /I <sub>pc</sub>	1.022	1.106	1.1367	1.18	1.22
I <sub>pa</sub> /v <sup>0.5</sup>	0.09	0.11	0.11	0.11	0.11